frontiers | Research Topics

Advances in novel pharmacotherapeutics and drug discovery: Computational, experimental, translational, and clinical models

Edited by
Jorge G. Farias, Vanessa Souza-Mello and Francisco Torrens

Coordinated by
Cristian Sandoval

Published in
Frontiers in Pharmacology

ISSN 1664-8714
ISBN 978-2-8325-5344-2
DOI 10.3389/978-2-8325-5344-2

About Frontiers

Frontiers is more than just an open access publisher of scholarly articles: it is a pioneering approach to the world of academia, radically improving the way scholarly research is managed. The grand vision of Frontiers is a world where all people have an equal opportunity to seek, share and generate knowledge. Frontiers provides immediate and permanent online open access to all its publications, but this alone is not enough to realize our grand goals.

Frontiers journal series

The Frontiers journal series is a multi-tier and interdisciplinary set of open-access, online journals, promising a paradigm shift from the current review, selection and dissemination processes in academic publishing. All Frontiers journals are driven by researchers for researchers; therefore, they constitute a service to the scholarly community. At the same time, the *Frontiers journal series* operates on a revolutionary invention, the tiered publishing system, initially addressing specific communities of scholars, and gradually climbing up to broader public understanding, thus serving the interests of the lay society, too.

Dedication to quality

Each Frontiers article is a landmark of the highest quality, thanks to genuinely collaborative interactions between authors and review editors, who include some of the world's best academicians. Research must be certified by peers before entering a stream of knowledge that may eventually reach the public - and shape society; therefore, Frontiers only applies the most rigorous and unbiased reviews. Frontiers revolutionizes research publishing by freely delivering the most outstanding research, evaluated with no bias from both the academic and social point of view. By applying the most advanced information technologies, Frontiers is catapulting scholarly publishing into a new generation.

What are Frontiers Research Topics?

Frontiers Research Topics are very popular trademarks of the *Frontiers journals series*: they are collections of at least ten articles, all centered on a particular subject. With their unique mix of varied contributions from Original Research to Review Articles, Frontiers Research Topics unify the most influential researchers, the latest key findings and historical advances in a hot research area.

Find out more on how to host your own Frontiers Research Topic or contribute to one as an author by contacting the Frontiers editorial office: frontiersin.org/about/contact

Advances in novel pharmacotherapeutics and drug discovery: Computational, experimental, translational, and clinical models

Topic editors
Jorge G. Farias — Universidad de La Frontera, Chile
Vanessa Souza-Mello — Rio de Janeiro State University, Brazil
Francisco Torrens — University of Valencia, Spain

Topic coordinator
Cristian Sandoval — Santo Tomás University, Chile

Citation
Farias, J. G., Souza-Mello, V., Torrens, F., Sandoval, C., eds. (2024). *Advances in novel pharmacotherapeutics and drug discovery: Computational, experimental, translational, and clinical models*. Lausanne: Frontiers Media SA.
doi: 10.3389/978-2-8325-5344-2

Table of contents

frontiers | Frontiers in Pharmacology

TYPE Editorial
PUBLISHED 09 August 2024
DOI 10.3389/fphar.2024.1465835

OPEN ACCESS

EDITED AND REVIEWED BY
Filippo Drago,
University of Catania, Italy

*CORRESPONDENCE
Cristian Sandoval,
cristian.sandoval@ufrontera.cl
Jorge Farías,
jorge.farias@ufrontera.cl

RECEIVED 16 July 2024
ACCEPTED 29 July 2024
PUBLISHED 09 August 2024

CITATION
Sandoval C, Torrens F, Souza-Mello V and Farías J (2024) Editorial: Advances in novel pharmacotherapeutics and drug discovery: computational, experimental, translational, and clinical models.
Front. Pharmacol. 15:1465835.
doi: 10.3389/fphar.2024.1465835

Editorial: Advances in novel pharmacotherapeutics and drug discovery: computational, experimental, translational, and clinical models

Cristian Sandoval[1,2,3]*, Francisco Torrens[4], Vanessa Souza-Mello[5] and Jorge Farías[3]*

[1]Escuela de Tecnología Médica, Facultad de Salud, Universidad Santo Tomás, Osorno, Chile, [2]Departamento de Medicina Interna, Facultad de Medicina, Universidad de La Frontera, Temuco, Chile, [3]Department of Chemical Engineering, Faculty of Engineering and Science, Universidad de La Frontera, Temuco, Chile, [4]Institut Universitari de Ciència Molecular, Universitat de València, València, Spain, [5]Laboratorio de Morfometría, Metabolismo y Enfermedades Cardiovasculares, Centro Biomédico, Instituto de Biología, Universidade do Estado do Rio de Janeiro, Rio de Janeiro, Brazil

KEYWORDS

drug delivery & targeting, public health, cancer, QSAR & docking, multidisciplinary approach

Editorial on the Research Topic
Advances in novel pharmacotherapeutics and drug discovery: computational, experimental, translational, and clinical models

This Research Topic includes contributions to pharmacotherapeutics, as well as the development of new drug discovery and delivery systems. The aim is to enhance the efficiency of screening, identification, development, and advancements in these areas using *in silico*, *in vitro*, and *in vivo* models. This Research Topic consists of a total of 11 papers. Among them, there are 7 original research pieces, 2 literature reviews, and 1 systematic review.

The first article on this Research Topic (Baek et al.) examines the impact of oxidative stress-induced mitochondrial damage on hair cells. It also explores the potential for developing medications that specifically target components of the mitochondrial redox network to address hearing loss pathology. They suggest mitochondria as a key target to protect auditory cells and maintain hearing function, where antioxidants can provide protection against drug-induced ototoxicity. However, because antioxidants are not selective for specific target molecules and can affect multiple signaling pathways simultaneously with low specificity, it is difficult to determine drug efficacy and safety at low concentrations.

As we continue to discuss pharmacological strategies and their potential against various disorders, a number of therapeutic tools and approaches have been tested in clinical trials, in example for the disorder known as Fragile X Syndrome (Milla et al.), which is brought on by the hypermethylation of a CGG repeat expansion in the 5′-untranslated region of the Fragile X Messenger Ribonucleoprotein 1 (FMR1) gene, leading to transcriptional silencing of the gene, which is the most common cause of hereditary intellectual impairments, such as autism spectrum disease. While there is not a cure, treatment and medication can help

control symptoms. So far, pharmacological methods have mostly been used to design drugs that change intracellular pathways, change GABA levels, or block mGluR interactions.

Within this Research Topic, we also located original articles evaluating medications for immunoglobulin A nephropathy (Xu et al.), with tetrandrine showing the strongest inhibitory effect against mesangial cell proliferation induced by deglycosylated human IgA1, particularly when contrasted with non-stimulation of deS/deGal IgA. Similar to this, there is a chance of severe kidney damage when using colistin, an antibacterial medication used as a last option. Consequently, it has been discovered that colistin-encapsulated liposomes lessen nephrotoxicity (Mektrirat et al.). In fact, it has been discovered that the application of liposomes shields human embryonic kidney cells from cytotoxicity that is dependent on both time and concentration. It is also important to note that colistin liposomal formulations reduce clinical and pathological nephrotoxicity in rat models, which shows that they could make things safer.

Lung cancer exhibits the highest morbidity rate when compared to other types of cancer and is the primary cause of mortality from malignant neoplasms worldwide. Non-small-cell lung cancer accounts for around 85%–90% of all cases (Reck and Rabe 2017). Cisplatin or other platinum-based combinations have been the most effective systemic chemotherapy for non-small-cell lung cancer for more than 20 years. However, the introduction of targeted therapy and immunotherapy has resulted in changes to the treatment strategies (Saar et al., 2023). Immunotherapies are sophisticated medications that utilize the body's natural defenses to fight against malignant growths by stimulating or inhibiting various pathways of the immune system. Typical techniques involve the use of PD-1 pathway blocking pharmaceuticals, drugs that hinder the CTLA-4 pathway, and calix pyrroles (Sève and Dumontet, 2005). According to Geretto et al. (2018), Fraisinib has unquestionably demonstrated its efficacy against a variety of tumor cell types, with a focus on its noteworthy performance against non-small-cell lung cancer. Without a doubt, Fraisinib exhibits exceptional anti-tumoral properties with low toxicity in mice (Toumia et al.). Additionally, scientists have discovered and confirmed glycyl-tRNA synthetase as the specific protein that this chemical targets. By blocking the enzyme GARS1, Fraisinib changes a number of important biological processes that are linked to tumor growth, aggressiveness, and invasion.

This idea should also be applied to traditional Chinese medicine. In this field, it is common to use a certain mix of six herbs (pinellia ternata, bran fried Fructus aurantii, ginger, raw bamboo, fried licorice, and raw orange peel) to help people with hyperlipidemia feel better. Oxidative stress indeed has a substantial impact on the progression of hyperlipidemia. A pharmacokinetic and pharmacodynamic model was used in an *in vivo* investigation to investigate the antioxidant activity of Wendan Decoction. The study observed a reduction in plasma triglyceride, total cholesterol, and low-density lipoprotein cholesterol levels, while high-density lipoprotein cholesterol levels varied depending on the dosage (Xu et al.).

We hope that the reader will find this Research Topic a useful reference for the state of the art in the emerging field of pharmacotherapeutics and drug discovery through computational, experimental, translational, and clinical models.

Author contributions

CS: Conceptualization, Writing–original draft, Writing–review and editing. FT: Writing–original draft, Writing–review and editing. VS-M: Writing–original draft, Writing–review and editing. JF: Writing–original draft, Writing–review and editing.

Funding

The author(s) declare that no financial support was received for the research, authorship, and/or publication of this article.

Conflict of interest

The authors declare that the research was conducted in the absence of any commercial or financial relationships that could be construed as a potential conflict of interest.

Publisher's note

References

Geretto, M., Ponassi, M., Casale, M., Pulliero, A., Cafeo, G., Malagreca, F., et al. (2018). A novel calix[4]pyrrole derivative as a potential anti-cancer agent that forms genotoxic adducts with DNA. *Sci. Rep.* 8, 11075. doi:10.1038/s41598-018-29314-9

Reck, M., and Rabe, K. F. (2017). Precision diagnosis and treatment for advanced non-small-cell lung cancer. *N. Engl. J. Med.* 377, 849–861. doi:10.1056/NEJMra1703413

Saar, M., Lavogina, D., Lust, H., Tamm, H., and Jaal, J. (2023). Immune checkpoint inhibitors modulate the cytotoxic effect of chemotherapy in lung adenocarcinoma cells. *Oncol. Lett.* 25 (4), 152. doi:10.3892/ol.2023.13738

Sève, P., and Dumontet, C. (2005). Chemoresistance in non-small cell lung cancer. *Curr. Med. Chem. Anticancer Agents* 5 (1), 73–88. doi:10.2174/1568011053352604

frontiers | Frontiers in Pharmacology

TYPE Mini Review
PUBLISHED 31 March 2023
DOI 10.3389/fphar.2023.1176881

OPEN ACCESS

EDITED BY
Francisco Torrens,
University of Valencia, Spain

REVIEWED BY
Amit P. Bhavsar,
University of Alberta, Canada

*CORRESPONDENCE
Un-Kyung Kim,
kimuk@knu.ac.kr

†These authors have contributed equally to this work and share first authorship

SPECIALTY SECTION
This article was submitted to Experimental Pharmacology and Drug Discovery, a section of the journal Frontiers in Pharmacology

RECEIVED 01 March 2023
ACCEPTED 22 March 2023
PUBLISHED 31 March 2023

CITATION
Baek J-I, Kim Y-R, Lee K-Y and Kim U-K (2023), Mitochondrial redox system: A key target of antioxidant therapy to prevent acquired sensorineural hearing loss.
Front. Pharmacol. 14:1176881.
doi: 10.3389/fphar.2023.1176881

Mitochondrial redox system: A key target of antioxidant therapy to prevent acquired sensorineural hearing loss

Jeong-In Baek[1†], Ye-Ri Kim[2,3†], Kyu-Yup Lee[4] and Un-Kyung Kim[2,5*]

[1]Department of Companion Animal Health, College of Rehabilitation and Health, Daegu Haany University, Gyeongsan, Republic of Korea, [2]Department of Biology, College of Natural Sciences, Kyungpook National University, Daegu, Republic of Korea, [3]Advanced Bio-Resource Research Center, Kyungpook National University, Daegu, Republic of Korea, [4]Department of Otorhinolaryngology-Head and Neck Surgery, School of Medicine, Kyungpook National University, Daegu, Republic of Korea, [5]School of Life Sciences, KNU Creative BioResearch Group (BK21 Plus Project), Kyungpook National University, Daegu, Republic of Korea

Noise (noise-induced hearing loss), and ototoxic drugs (drug-induced ototoxicity), and aging (age-related hearing loss) are the major environmental factors that lead to acquired sensorineural hearing loss. So far, there have been numerous efforts to develop protective or therapeutic agents for acquired hearing loss by investigating the pathological mechanisms of each types of hearing loss, especially in cochlear hair cells and auditory nerves. Although there is still a lack of information on the underlying mechanisms of redox homeostasis and molecular redox networks in hair cells, an imbalance in mitochondrial reactive oxygen species (ROS) levels that enhance oxidative stress has been suggested as a key pathological factor eventually causing acquired sensorineural hearing loss. Thus, various types of antioxidants have been investigated for their abilities to support auditory cells in maintenance of the hearing function against ototoxic stimuli. In this review, we will discuss the scientific possibility of developing drugs that target particular key elements of the mitochondrial redox network in prevention or treatment of noise- and ototoxic drug-induced hearing loss.

KEYWORDS

acquired hearing loss, noise, ototoxic drugs, ROS, mitochondria, drug development

1 Introduction

Sensorineural hearing loss (SNHL), the most common type of permanent hearing impairment, is caused by physical and/or functional damage of cochlear hair cells in inner ear or auditory nerves including spiral ganglion neurons. Acquired SNHL, resulting from continuous accumulation of cellular damage due to various environmental stimuli, increases in prevalence with aging: Being identified in approximately 5–8 of 1,000 children, 33% of adults 65–74 years of age, and over 80% of adults 85 years of age (Walling et al., 2012; Baumgartner et al., 2021). This prevalence of acquired SNHL is much higher than congenital SNHL that occurs in two to four of 1,000 newborns. The major environmental factors that lead to acquired SNHL are aging (age-related hearing loss), noise (noise-induced hearing loss), and ototoxic drugs (drug-induced ototoxicity). Over the past few decades, there have been numerous efforts to develop therapeutic agents for each type of acquired hearing loss by

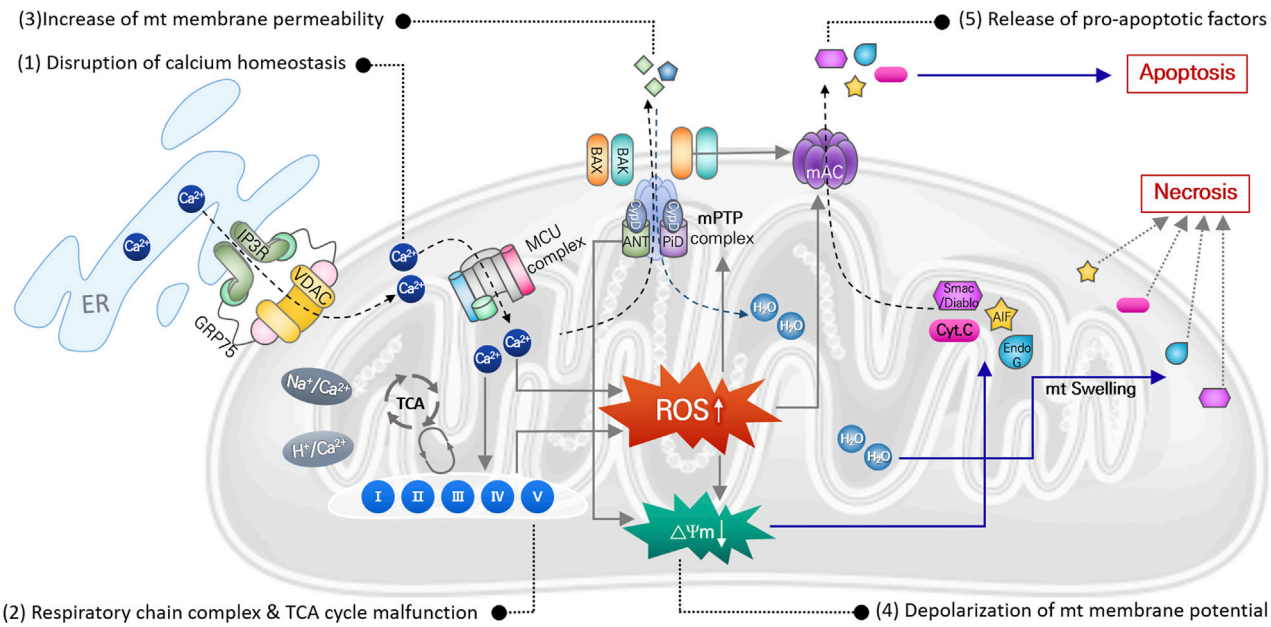

FIGURE 1
Noise, aging and ototoxic drug-induced intracellular signaling pathways leading to hair cell death. It indicates that organelle stress (ER and mitochondria), inflammation, MAPK signaling pathways induced by three environmental stimuli are all mutually interact each other, which finally leads to apoptosis or necroptosis of hair cells. Importantly, increase in mitochondrial ROS is at the center of all the pathways.

investigating the pathological mechanisms of hearing loss at the molecular level. An imbalance in mitochondrial reactive oxygen species (ROS) levels that enhance oxidative stress has been suggested as a key pathological factor that eventually causes hair cell death in all three types of acquired SNHL (Bottger and Schacht, 2013; Fujimoto and Yamasoba, 2014; Kamogashira et al., 2015; Wong and Ryan, 2015). Attempts to decrease ROS levels in order to prevent or slow acquired SNHL led researchers to test the protective or alleviative effects of various antioxidants, such as vitamins, lipoic acids, polyphenols, and other small molecules (Hildebrand et al., 2008; Tavanai and Mohammadkhani, 2017; Ibrahim et al., 2018; Fetoni et al., 2019; Pak et al., 2020). Most of these investigations have been conducted in animal models with only a few studies in humans, and there is still a lack of information on the underlying mechanisms of redox homeostasis and molecular redox networks in hair cells. Due to these limitations, there is currently only one medicine at a clinically applicable level. In 2022, the Food and Drug Administration (FDA) of United States approved the use of sodium thiosulfate, an antioxidant, as a therapeutic agent of cisplatin-induced hearing loss, based on the results of clinical trials (Freyer et al., 2017; Brock et al., 2018a; Brock et al., 2018b). In the clinical test, sodium thiosulfate successfully reduced the incidence of cisplatin-induced ototoxicity by nearly 50% in the hepatoblastoma patients. However, verification of the therapeutic effect was limited to patients under the age of 18 with non-metastic solid cancer, and the effect has also been shown to vary depending on the time intervals between administration of cisplatin and sodium thiosulfate (Hazlitt et al., 2018). It means, the development of otoprotectants that are effective for a wide range of acquired hearing loss is still needed. In this review, we will discuss previous efforts to develop protective or therapeutic agents focusing on oxidative stress-induced mitochondrial damage in hair cells. We will also propose the possibility of developing drugs that target particular elements of the mitochondrial redox network in hearing loss pathology.

2 Oxidative stress in acquired sensorineural hearing loss

The main pathological factors of acquired SNHL, aging, noise exposure, and ototoxic drugs, induce multiple, simultaneous responses in cochlear hair cells, that directly damage macromolecules (nucleic acids, proteins, and lipids), change ion homeostasis, and activate/inhibit intrinsic and extrinsic signaling pathways (Wong and Ryan, 2015; Wu et al., 2020). These responses ultimately produce irreversible hair cell damage when the mechanical or biochemical stimuli overwhelm cellular homeostatic capacity. Disruption of cellular redox homeostasis by either or both increased ROS generation and inhibition of antioxidant defense systems, is known to be mutually influenced by other cellular responses induced by noise, drugs, and aging (Wu et al., 2020) (Figure 1).

2.1 Noise-induced oxidative stress and alleviative effects of antioxidants

Intense noise can directly cause mechanical disruption of the hair cell stereocilia, resulting in their dysfunction in the auditory pathway (Slepecky, 1986; Patuzzi et al., 1989). However, most noise-induced hearing loss is caused by an accumulation of biochemical

damage due to prolonged exposure to sound stimuli below the threshold of mechanical damage. Stimulation of the mitochondrial respiratory system by ischemia/reperfusion (Henderson et al., 2006) and release of free Ca^{2+} from Ca^{2+} stores, such as endoplasmic reticulum (ER) to cytosol and into mitochondria (Gorlach et al., 2015; Wong and Ryan, 2015), are the major noise-induced intracellular responses that cause biochemical hair cell damage. Importantly, these processes are commonly linked to overgeneration of ROS (Yamashita et al., 2004a). Noise exposure also induces insufficiency of the antioxidant system. Consequently, increased ROS randomly reacts with lipids, nucleic acids, and proteins, resulting in dysfunction of these macromolecules, and subsequently inducing release of pro-apoptotic factors. Cytochrome C promotes caspase 3-mediated apoptosis, and translocation of Endonuclease G (EndoG) and apoptosis-inducing factor (AIF) from mitochondria into the nucleus, triggering apoptotic hair cell death with condensed nuclei (Yamashita et al., 2004b; Wong and Ryan, 2015; Sha and Schacht, 2017). Increased ROS has also been shown to activate the c-Jun N-terminal kinase (JNK) signaling pathway, leading to apoptosis in an animal model (Wang et al., 2007; Wu et al., 2020).

Because oxidative stress has been strongly implicated as a cause of noise-induced hearing loss, various types of antioxidant molecules have been used to protect or recover hair cells. Glutathione, D-methionine, resveratrol, salicylate, ebselen, and coenzymeQ_{10} administered in animal studies had significant protective effects on noise-induced hair cell damage (Sha and Schacht, 2017; Pak et al., 2020). Specifically, N-acetyl cysteine (NAC), α-lipoic acid, and ebselen have advanced to clinical trials and shown a substantial otoprotective effect. In two randomized clinical studies, a group of textile workers who received NAC had a reduced temporary threshold shift after noise exposure (Fetoni et al., 2009), as well as army members who received NAC for 14 days who had a reduced temporary threshold shift (Lorito et al., 2008; Kopke et al., 2015). Alpha-lipoic acid also had a protective effect on noise-induced hearing threshold shift. When a group of healthy subjects received oral α-lipoic acid 1 h before noise exposure, their temporary threshold shift at 6 kHz was reduced after noise exposure (Campbell et al., 2007). These results suggest a strong possibility that reducing ROS accumulation may effectively prevent noise-induced hearing loss.

2.2 ROS accumulation in drug-induced ototoxicity and therapeutic effects of antioxidants

Aminoglycoside, broad-spectrum antibiotics, and platinum-based anticancer agents such as cisplatin are the most well-known ototoxic drugs that can cause irreversible, bilateral, and high frequency hearing loss (Musial-Bright et al., 2011). Following entry into the hair cells, both aminoglycosides and cisplatin directly bind to hundreds of intracellular proteins such as kinases, transcription factors, and ion channels that potentially cause dell death (Karasawa et al., 2010; Karasawa et al., 2011; Karasawa et al., 2013; Karasawa and Steyger, 2015).

Although they affect multiple cellular signaling pathways by directly interacting with various proteins, the central affected pathological pathway is the accumulation of oxidative stress caused by accelerated ROS generation and inhibition of antioxidant enzyme activities, eventually leading to apoptosis or necrosis of hair cells (Steyger, 2021). Aminoglycosides are known to accelerate both enzymatic and non-enzymatic ROS formation (Priuska and Schacht, 1995), thereby activating the JNK signaling pathway followed by apoptotic hair cell death (Mielke and Herdegen, 2000). In enzymatic ROS formation, nicotinamide adenine dinucleotide phosphate (NADPH) oxidases are considered a primary source of ROS generation. NADPH oxidase is a protein complex composed of several subunits including a catalytic subunit, NOX (Altenhofer et al., 2015; Steyger, 2021). In previous studies, NOX2 expression was abundantly increased in outer hair cells after neomycin administration in rat cochlea, and inhibition of NOX2 significantly reduced neomycin-induced hair cell damage (Qi et al., 2018). Cisplatin also upregulates NOX3 expression and activates the NOX3 signaling pathway, increasing superoxide production in cultured cells and rat cochlea (Banfi et al., 2004; Mukherjea et al., 2008; Mukherjea et al., 2011).

Disruption of the intracellular antioxidant system also contributes to aminoglycoside- or cisplatin-induced oxidative stress. For example, cisplatin can bind directly to sulfhydryl groups within antioxidant enzymes causing enzyme dysfunction, and can also deplete glutathione (GSH) and NADPH that are essential factors for antioxidant enzyme function (Rybak et al., 2007). Cisplatin and kanamycin are known to decrease expression and activity of the primary antioxidant enzymes: Superoxide dismutase (SOD), glutathione peroxidase (GPx), glutathione reductase (GR), and catalase (CAT) (Rybak et al., 2000; Rybak et al., 2007). Although there are various molecular factors directly affected by drugs, ultimately they cause an excessive accumulation of ROS, and numerous studies have shown that the subsequent cell death signaling pathways shared with noise-induced hearing loss.

Various types of antioxidants were also tested in drug-induced ototoxicity to examine their ability to prevent hearing loss. The widely-used antioxidants, NAC, sodium thiosulfate, and D-methionine, effectively protected or rescued cisplatin-induced ototoxicity, due to their high affinity for platinum molecules, as well as their antioxidative activity (Wu et al., 2020). In our previous studies, we identified several antioxidants that had protective effects against drug-induced ototoxicity. In mouse cochlear explants treated with amikacin, kanamycin, or cisplatin, pre-treatment with galangin (flavonoid antioxidant), fursultiamine (thiamine disulfide derivative), or berberine chloride (alkaline isoquinoline) reduced intracellular ROS levels in hair cells. These treatments prevented ROS-mediated caspase-3 activation, DNA fragmentation, and apoptosis of hair cells, indicating that an antioxidant can be used to prevent both noise- and drug-induced hearing loss. Sodium thiosulfate (STS) is currently the only clinically approved treatment for cisplatin-induced ototoxicity. As an antioxidant, it is known to plays a role in directly removing ROS and promote antioxidative and anti-apoptotic enzymes by activating Nuclear factor erythroid-related factor 2 (Nrf2) (Zhang et al., 2021). Moreover, it directly binds to cisplatin, inhibiting and deactivating the metabolism of cisplatin by formation of platinum (Pt)-STS complex. Cisplatin is metabolized and

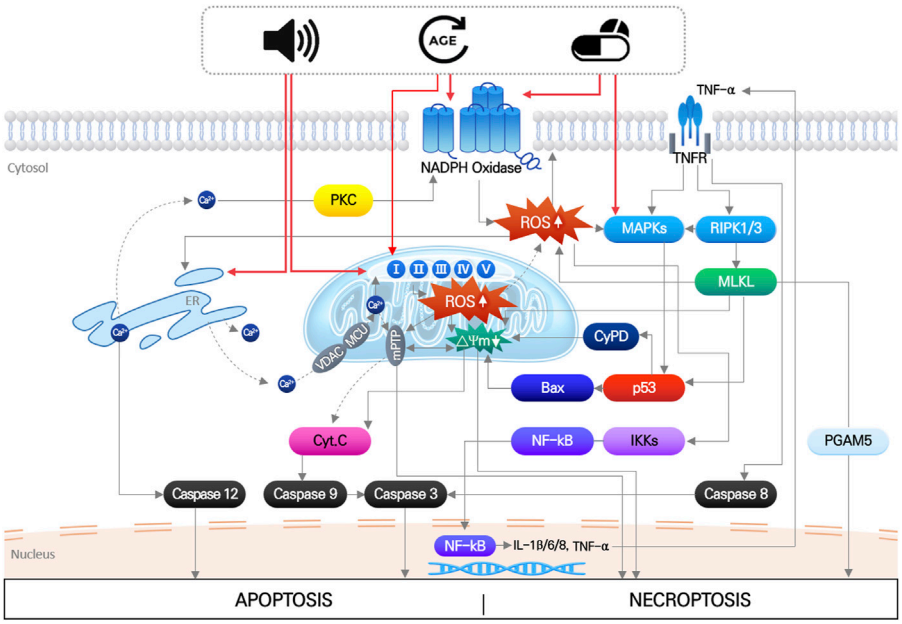

FIGURE 2
Mitochondrial ROS-induced damages causing mitochondrial dysfunction. Direct damages of mitochondrial DNA and antioxidant enzyme, or disruption of ion homeostasis 1), or malfunction of the mitochondrial respiration system 2), can cause increase in mitochondrial ROS. It subsequently leads to increase in mitochondrial membrane potential 3) with depolarization of membrane potential 4), causing osmotic swelling of mitochondria and release of pro-apoptotic factors 5). Finally, cell death signaling pathways are activated by these apoptotic factors.

activated in the body through the process of hydrolysis. In this process, each of activated cisplatin metabolites has different tumor selectivity, finally causing normal cell damages. Since reducing the level of activated form of cisplatin inhibit cytotoxicity of normal cells, it is suggested that the amelioration of cisplatin-induced cytotoxicity by STS could be explained in terms of the rapid formation of inactive Pt-STS complex (Sooriyaarachchi et al., 2012). Therefore, it is thought that STS can play a role as a direct inhibitor of cisplatin, selectively reducing toxicity to normal cells, rather than as an antioxidant.

3 Mitochondrial dysfunction caused by ROS in acquired hearing loss

3.1 Oxidative stress-induced mitochondrial damage triggers hair cell death signals

Mitochondria, referred to as the center of cellular energy metabolism, are organelles that synthesize ATP through the TCA cycle and oxidative phosphorylation processes. Because this aerobic respiration unavoidably produces ROS, mitochondria are the primary cellular source of ROS (Wei et al., 2001; Islam, 2017). Mitochondria also play critical roles in maintaining cellular homeostasis and contribute to homeostatic regulation of calcium and iron concentrations (Contreras et al., 2010), autophagy (Scherz-Shouval and Elazar, 2007), and cell death (Borutaite, 2010). Thus, mitochondrial damage or dysfunction can directly activate cell death signaling pathways. Noise- or cytotoxic drug-induced intracellular responses, including ischemia/reperfusion, DNA damage, ER stress, etc., increase ROS levels and DNA damage in mitochondria within auditory cells. Even though mitochondrial ROS can be easily scavenged by mitochondrial antioxidant systems under normal physiological conditions, excessive ROS generation or failure to remove mitochondrial ROS can cause oxidative stress leading to mitochondrial dysfunction in multiple ways (Figure 2).

In mitochondria, free Ca^{2+} ions are the most likely to trigger ROS elevation. Particularly after intense noise stimulation, Ca^{2+} is released from the ER and translocated into mitochondria through an ion transporter such as VDAC or MCU. Abnormal Ca^{2+} influx can dysregulate Ca^{2+}-regulated enzymes that are involved in ROS metabolism, leading to increased mitochondrial ROS levels, free-radical damage, and ultimately to mitochondrial dysfunction (Tretter and Adam-Vizi, 2004; Bottger and Schacht, 2013). Accumulated mitochondrial ROS can directly damage mitochondrial DNA (mtDNA), causing mtDNA mutations. Accumulation of mtDNA is responsible for dysfunction of various mitochondrial proteins, which disrupts metabolic homeostasis and induces mitochondrial dysfunction (Baker and Staecker, 2012). Finally, mitochondrial damage caused by increased mitochondrial ROS can depolarize mitochondrial membrane potential, which increases mitochondrial membrane permeability and initiates apoptosis or necrosis signaling pathways. Increased ROS activates p53 in the cytosol, leading to translocation of Bcl-2 associated X (BAX) from the cytosol to the mitochondrial outer membrane. Mitochondrial ROS-induced activation of the BAX pore and other mitochondrial pore complexes, e.g., the mitochondrial permeability transition pore (mPTP) and mitochondrial apoptosis-induced channel (mAC), contributes to the release of pro-apoptotic factors (cytochrome C,

EndoG, and AIF) from the mitochondrial matrix to the cytosol to activate the apoptotic signaling pathway (Dejean et al., 2005; Briston et al., 2017). By contrast, loss of mitochondrial membrane potential activates the mPTP pore complex, allowing H_2O and other small molecules to enter the mitochondrial matrix, which induces mitochondrial osmotic swelling and initiates the necrosis signaling pathway (Briston et al., 2017).

Aminoglycosides tend to accumulate in the hair cell mitochondria, and oxidative stress-induced mitochondrial damage and subsequent cell death by antibiotics are also observed consistently in cochlear hair cells (Hobbie et al., 2008). Gentamicin directly inhibits mitochondrial protein synthesis, which triggers opening of the mPTP pore complex that can then release pro-apoptotic factors (Dehne et al., 2002). Cisplatin administration increases mitochondrial ROS, leading to loss of mitochondrial membrane potential and BAX expression, which causes increased cleaved caspase-3 expression and hair cell apoptosis in mouse cochlear explants (Kim et al., 2018).

3.2 Prevention of hair cell death through intensive targeting of mitochondrial ROS

Because mitochondria act as a pathological link between intracellular oxidative stress and apoptotic cell death, inhibiting mitochondrial oxidative stress or decreasing mitochondrial membrane permeability using mitochondria-targeted molecules, could be an effective approach to alleviating noise- and drug-induced hearing loss. Thus, mitochondria-specific targeting of potent compounds has been considered important to maximize effectiveness of the compounds. Especially Lipophilic cation-based modification of compounds is one of the most successful mitochondria-targeting techniques, due to improved ability to cross polarized mitochondrial membrane. Triphenylphosphonium (TPP), a kind of lipophilic cation, has been conjugated to various potent antioxidants (Wang et al., 2020), and numerous TPP-tagged mitochondria-targeted antioxidants including MitoQ, SkQ1, SkQR1, MitoVitE, and MitoPeroxidase, have been tested to prevent or alleviate acquired hearing loss (Zielonka et al., 2017; Fujimoto and Yamasoba, 2019).

We previously used a mitochondria-targeted antioxidant, MitoQ, to evaluate the therapeutic potential of mitochondria-specific antioxidants in oxidative stress-induced hair cell damage. In mouse cochlear explants, H_2O_2 treatment increased mitochondrial ROS leading to loss of mitochondrial membrane potential, which was attributed to decreased expression of the mitochondrial respiratory chain complex I, III, and V. When MitoQ was administered 1 h prior to H_2O_2 treatment, the mitochondrial oxidative stress responses were almost completely neutralized, thus protecting hair cells from apoptotic cell death (Kim et al., 2019). Other studies on drug-induced ototoxicity also suggested that both MitoQ and SkQR1 significantly reduce aminoglycoside- and cisplatin-induced hearing loss in cultured cells and animal models (Jankauskas et al., 2012; Ojano-Dirain and Antonelli, 2012; Ojano-Dirain et al., 2014; Tate et al., 2017; Dirain et al., 2018).

4 Conclusion

Extensive scientific evidence strongly suggests mitochondria as a key target to protect auditory cells and maintain hearing function. Although a number of previous studies have shown that general antioxidants can provide protection against drug-induced ototoxicity, there are two significant limitations. First, since the general antioxidants are not highly selective for specific target molecules and can affect multiple signaling pathways simultaneously with low specificity, it is difficult to determine drug efficacy and safety at low concentrations. Second, general antioxidants have the potential to cause unintended side effects when co-administered with other medicines. For instance, antioxidants such as α-lipoic acid can inhibit the death of cancer cells as well as normal cells, thereby inhibiting the anticancer effect. Thus, α-lipoic acid cannot be administered in combination with the anticancer drugs such as cisplatin.

To overcome these limitations, it will be important to discover and develop novel therapeutic agents that interact with specific mitochondrial factors that contribute to mitochondrial redox homeostasis, such as antioxidant enzymes or mitochondrial pore proteins. This will be essential information for developing common drugs that are widely effective in different types of acquired hearing loss.

Author contributions

J-IB and U-KK contributed to conception and design of the study. J-IB and Y-RK wrote the first draft of the manuscript and created the images. K-YL reviewed and edited the manuscript. U-KK organized the whole process and offered constructive criticism. All authors contributed to manuscript revision, read, and approved the submitted version.

Funding

This research was supported by the National Research Foundation of Korea (NRF) Grant funded by the Korea government (Ministry of Science and ICT): RS-2023-00212674 (to J-IB), NRF-2020R1A2C2003529 (to K-YL), and NRF-2021R1C1C2006677 (to Y-RK). It was also supported by the Bio & Medical Technology Development Program of the National Research Foundation (NRF) funded by the Korean government (MSIT), No. 2022M3E5F2017487 (to U-KK).

Conflict of interest

The authors declare that the research was conducted in the absence of any commercial or financial relationships that could be construed as a potential conflict of interest.

Publisher's note

References

Altenhofer, S., Radermacher, K. A., Kleikers, P. W., Wingler, K., and Schmidt, H. H. (2015). Evolution of NADPH oxidase inhibitors: Selectivity and mechanisms for target engagement. *Antioxid. Redox Signal* 23, 406–427. doi:10.1089/ars.2013.5814

Baker, K., and Staecker, H. (2012). Low dose oxidative stress induces mitochondrial damage in hair cells. *Anat. Rec. Hob.* 295, 1868–1876. doi:10.1002/ar.22594

Banfi, B., Malgrange, B., Knisz, J., Steger, K., Dubois-Dauphin, M., and Krause, K. H. (2004). NOX3, a superoxide-generating NADPH oxidase of the inner ear. *J. Biol. Chem.* 279, 46065–46072. doi:10.1074/jbc.M403046200

Baumgartner, J. E., Baumgartner, L. S., Baumgartner, M. E., Moore, E. J., Messina, S. A., Seidman, M. D., et al. (2021). Progenitor cell therapy for acquired pediatric nervous system injury: Traumatic brain injury and acquired sensorineural hearing loss. *Stem Cells Transl. Med.* 10, 164–180. doi:10.1002/sctm.20-0026

Borutaite, V. (2010). Mitochondria as decision-makers in cell death. *Environ. Mol. Mutagen* 51, 406–416. doi:10.1002/em.20564

Bottger, E. C., and Schacht, J. (2013). The mitochondrion: A perpetrator of acquired hearing loss. *Hear Res.* 303, 12–19. doi:10.1016/j.heares.2013.01.006

Briston, T., Roberts, M., Lewis, S., Powney, B., Szabadkai, G., and Duchen, M. R. (2017). Mitochondrial permeability transition pore: Sensitivity to opening and mechanistic dependence on substrate availability. *Sci. Rep.* 7, 10492. doi:10.1038/s41598-017-10673-8

Brock, P. R., Maibach, R., Childs, M., Rajput, K., Roebuck, D., Sullivan, M. J., et al. (2018a). Sodium thiosulfate for protection from cisplatin-induced hearing loss. *N. Engl. J. Med.* 378, 2376–2385. doi:10.1056/NEJMoa1801109

Brock, P. R., Maibach, R., and Neuwelt, E. A. (2018b). Sodium thiosulfate and cisplatin-induced hearing loss. *N. Engl. J. Med.* 379, 1180–1181. doi:10.1056/NEJMc1809501

Campbell, K. C., Meech, R. P., Klemens, J. J., Gerberi, M. T., Dyrstad, S. S., Larsen, D. L., et al. (2007). Prevention of noise- and drug-induced hearing loss with D-methionine. *Hear Res.* 226, 92–103. doi:10.1016/j.heares.2006.11.012

Contreras, L., Drago, I., Zampese, E., and Pozzan, T. (2010). Mitochondria: The calcium connection. *Biochim. Biophys. Acta* 1797, 607–618. doi:10.1016/j.bbabio.2010.05.005

Dehne, N., Rauen, U., de Groot, H., and Lautermann, J. (2002). Involvement of the mitochondrial permeability transition in gentamicin ototoxicity. *Hear Res.* 169, 47–55. doi:10.1016/s0378-5955(02)00338-6

Dejean, L. M., Martinez-Caballero, S., Guo, L., Hughes, C., Teijido, O., Ducret, T., et al. (2005). Oligomeric Bax is a component of the putative cytochrome c release channel MAC, mitochondrial apoptosis-induced channel. *Mol. Biol. Cell* 16, 2424–2432. doi:10.1091/mbc.e04-12-1111

Dirain, C. O., Ng, M., Milne-Davies, B., Joseph, J. K., and Antonelli, P. J. (2018). Evaluation of mitoquinone for protecting against amikacin-induced ototoxicity in Guinea pigs. *Otol. Neurotol.* 39, 111–118. doi:10.1097/MAO.0000000000001638

Fetoni, A. R., Paciello, F., Rolesi, R., Paludetti, G., and Troiani, D. (2019). Targeting dysregulation of redox homeostasis in noise-induced hearing loss: Oxidative stress and ROS signaling. *Free Radic. Biol. Med.* 135, 46–59. doi:10.1016/j.freeradbiomed.2019.02.022

Fetoni, A. R., Ralli, M., Sergi, B., Parrilla, C., Troiani, D., and Paludetti, G. (2009). Protective effects of N-acetylcysteine on noise-induced hearing loss in Guinea pigs. *Acta Otorhinolaryngol. Ital.* 29, 70–75.

Freyer, D. R., Chen, L., Krailo, M. D., Knight, K., Villaluna, D., Bliss, B., et al. (2017). Effects of sodium thiosulfate versus observation on development of cisplatin-induced hearing loss in children with cancer (ACCL0431): A multicentre, randomised, controlled, open-label, phase 3 trial. *Lancet Oncol.* 18, 63–74. doi:10.1016/S1470-2045(16)30625-8

Fujimoto, C., and Yamasoba, T. (2019). Mitochondria-targeted antioxidants for treatment of hearing loss: A systematic review. *Antioxidants (Basel)* 8, 109. doi:10.3390/antiox8040109

Fujimoto, C., and Yamasoba, T. (2014). Oxidative stresses and mitochondrial dysfunction in age-related hearing loss. *Oxid. Med. Cell Longev.* 2014, 582849. doi:10.1155/2014/582849

Gorlach, A., Bertram, K., Hudecova, S., and Krizanova, O. (2015). Calcium and ROS: A mutual interplay. *Redox Biol.* 6, 260–271. doi:10.1016/j.redox.2015.08.010

Hazlitt, R. A., Min, J., and Zuo, J. (2018). Progress in the development of preventative drugs for cisplatin-induced hearing loss. *J. Med. Chem.* 61, 5512–5524. doi:10.1021/acs.jmedchem.7b01653

Henderson, D., Bielefeld, E. C., Harris, K. C., and Hu, B. H. (2006). The role of oxidative stress in noise-induced hearing loss. *Ear Hear* 27, 1–19. doi:10.1097/01.aud.0000191942.36672.f3

Hildebrand, M. S., Newton, S. S., Gubbels, S. P., Sheffield, A. M., Kochhar, A., de Silva, M. G., et al. (2008). Advances in molecular and cellular therapies for hearing loss. *Mol. Ther.* 16, 224–236. doi:10.1038/sj.mt.6300351

Hobbie, S. N., Akshay, S., Kalapala, S. K., Bruell, C. M., Shcherbakov, D., and Bottger, E. C. (2008). Genetic analysis of interactions with eukaryotic rRNA identify the mitoribosome as target in aminoglycoside ototoxicity. *Proc. Natl. Acad. Sci. U. S. A.* 105, 20888–20893. doi:10.1073/pnas.0811258106

Ibrahim, I., Zeitouni, A., and da Silva, S. D. (2018). Effect of antioxidant vitamins as adjuvant therapy for sudden sensorineural hearing loss: Systematic review study. *Audiol. Neurootol* 23, 1–7. doi:10.1159/000486274

Islam, M. T. (2017). Oxidative stress and mitochondrial dysfunction-linked neurodegenerative disorders. *Neurol. Res.* 39, 73–82. doi:10.1080/01616412.2016.1251711

Jankauskas, S. S., Plotnikov, E. Y., Morosanova, M. A., Pevzner, I. B., Zorova, L. D., Skulachev, V. P., et al. (2012). Mitochondria-targeted antioxidant SkQR1 ameliorates gentamycin-induced renal failure and hearing loss. *Biochem. (Mosc)* 77, 666–670. doi:10.1134/S0006297912060144

Kamogashira, T., Fujimoto, C., and Yamasoba, T. (2015). Reactive oxygen species, apoptosis, and mitochondrial dysfunction in hearing loss. *Biomed. Res. Int.* 2015, 617207. doi:10.1155/2015/617207

Karasawa, T., Sibrian-Vazquez, M., Strongin, R. M., and Steyger, P. S. (2013). Identification of cisplatin-binding proteins using agarose conjugates of platinum compounds. *PLoS One* 8, e66220. doi:10.1371/journal.pone.0066220

Karasawa, T., and Steyger, P. S. (2015). An integrated view of cisplatin-induced nephrotoxicity and ototoxicity. *Toxicol. Lett.* 237, 219–227. doi:10.1016/j.toxlet.2015.06.012

Karasawa, T., Wang, Q., David, L. L., and Steyger, P. S. (2011). Calreticulin binds to gentamicin and reduces drug-induced ototoxicity. *Toxicol. Sci.* 124, 378–387. doi:10.1093/toxsci/kfr196

Karasawa, T., Wang, Q., David, L. L., and Steyger, P. S. (2010). CLIMP-63 is a gentamicin-binding protein that is involved in drug-induced cytotoxicity. *Cell Death Dis.* 1, e102. doi:10.1038/cddis.2010.80

Kim, K. H., Lee, B., Kim, Y. R., Kim, M. A., Ryu, N., Jung, D. J., et al. (2018). Evaluating protective and therapeutic effects of alpha-lipoic acid on cisplatin-induced ototoxicity. *Cell Death Dis.* 9, 827. doi:10.1038/s41419-018-0888-z

Kim, Y. R., Baek, J. I., Kim, S. H., Kim, M. A., Lee, B., Ryu, N., et al. (2019). Therapeutic potential of the mitochondria-targeted antioxidant MitoQ in mitochondrial-ROS induced sensorineural hearing loss caused by Idh2 deficiency. *Redox Biol.* 20, 544–555. doi:10.1016/j.redox.2018.11.013

Kopke, R., Slade, M. D., Jackson, R., Hammill, T., Fausti, S., Lonsbury-Martin, B., et al. (2015). Efficacy and safety of N-acetylcysteine in prevention of noise induced hearing loss: A randomized clinical trial. *Hear Res.* 323, 40–50. doi:10.1016/j.heares.2015.01.002

Lorito, G., Giordano, P., Petruccelli, J., Martini, A., and Hatzopoulos, S. (2008). Different strategies in treating noiseinduced hearing loss with N-acetylcysteine. *Med. Sci. Monit.* 14, BR159–164.

Mielke, K., and Herdegen, T. (2000). JNK and p38 stresskinases--degenerative effectors of signal-transduction-cascades in the nervous system. *Prog. Neurobiol.* 61, 45–60. doi:10.1016/s0301-0082(99)00042-8

Mukherjea, D., Jajoo, S., Sheehan, K., Kaur, T., Sheth, S., Bunch, J., et al. (2011). NOX3 NADPH oxidase couples transient receptor potential vanilloid 1 to signal transducer and activator of transcription 1-mediated inflammation and hearing loss. *Antioxid. Redox Signal* 14, 999–1010. doi:10.1089/ars.2010.3497

Mukherjea, D., Jajoo, S., Whitworth, C., Bunch, J. R., Turner, J. G., Rybak, L. P., et al. (2008). Short interfering RNA against transient receptor potential vanilloid 1 attenuates cisplatin-induced hearing loss in the rat. *J. Neurosci.* 28, 13056–13065. doi:10.1523/JNEUROSCI.1307-08.2008

Musial-Bright, L., Fengler, R., Henze, G., and Hernaiz Driever, P. (2011). Carboplatin and ototoxicity: Hearing loss rates among survivors of childhood medulloblastoma. *Childs Nerv. Syst.* 27, 407–413. doi:10.1007/s00381-010-1300-1

Ojano-Dirain, C. P., Antonelli, P. J., and Le Prell, C. G. (2014). Mitochondria-targeted antioxidant MitoQ reduces gentamicin-induced ototoxicity. *Otol. Neurotol.* 35, 533–539. doi:10.1097/MAO.0000000000000192

Ojano-Dirain, C. P., and Antonelli, P. J. (2012). Prevention of gentamicin-induced apoptosis with the mitochondria-targeted antioxidant mitoquinone. *Laryngoscope* 122, 2543–2548. doi:10.1002/lary.23593

Pak, J. H., Kim, Y., Yi, J., and Chung, J. W. (2020). Antioxidant therapy against oxidative damage of the inner ear: Protection and preconditioning. *Antioxidants (Basel)* 9, 1076. doi:10.3390/antiox9111076

Patuzzi, R. B., Yates, G. K., and Johnstone, B. M. (1989). Outer hair cell receptor current and sensorineural hearing loss. *Hear Res.* 42, 47–72. doi:10.1016/0378-5955(89)90117-2

Priuska, E. M., and Schacht, J. (1995). Formation of free radicals by gentamicin and iron and evidence for an iron/gentamicin complex. *Biochem. Pharmacol.* 50, 1749–1752. doi:10.1016/0006-2952(95)02160-4

Qi, M., Qiu, Y., Zhou, X., Tian, K., Zhou, K., Sun, F., et al. (2018). Regional up-regulation of NOX2 contributes to the differential vulnerability of outer hair cells to neomycin. *Biochem. Biophys. Res. Commun.* 500, 110–116. doi:10.1016/j.bbrc.2018.03.141

Rybak, L. P., Husain, K., Morris, C., Whitworth, C., and Somani, S. (2000). Effect of protective agents against cisplatin ototoxicity. *Am. J. Otol.* 21, 513–520.

Rybak, L. P., Whitworth, C. A., Mukherjea, D., and Ramkumar, V. (2007). Mechanisms of cisplatin-induced ototoxicity and prevention. *Hear Res.* 226, 157–167. doi:10.1016/j.heares.2006.09.015

Scherz-Shouval, R., and Elazar, Z. (2007). ROS, mitochondria and the regulation of autophagy. *Trends Cell Biol.* 17, 422–427. doi:10.1016/j.tcb.2007.07.009

Sha, S. H., and Schacht, J. (2017). Emerging therapeutic interventions against noise-induced hearing loss. *Expert Opin. Investig. Drugs* 26, 85–96. doi:10.1080/13543784.2017.1269171

Slepecky, N. (1986). Overview of mechanical damage to the inner ear: Noise as a tool to probe cochlear function. *Hear Res.* 22, 307–321. doi:10.1016/0378-5955(86)90107-3

Sooriyaarachchi, M., Narendran, A., and Gailer, J. (2012). The effect of sodium thiosulfate on the metabolism of cis-platin in human plasma *in vitro*. *Metallomics* 4, 960–967. doi:10.1039/c2mt20076g

Steyger, P. S. (2021). Mechanisms of aminoglycoside- and cisplatin-induced ototoxicity. *Am. J. Audiol.* 30, 887–900. doi:10.1044/2021_AJA-21-00006

Tate, A. D., Antonelli, P. J., Hannabass, K. R., and Dirain, C. O. (2017). Mitochondria-targeted antioxidant mitoquinone reduces cisplatin-induced ototoxicity in Guinea pigs. *Otolaryngol. Head. Neck Surg.* 156, 543–548. doi:10.1177/0194599816678381

Tavanai, E., and Mohammadkhani, G. (2017). Role of antioxidants in prevention of age-related hearing loss: A review of literature. *Eur. Arch. Otorhinolaryngol.* 274, 1821–1834. doi:10.1007/s00405-016-4378-6

Tretter, L., and Adam-Vizi, V. (2004). Generation of reactive oxygen species in the reaction catalyzed by alpha-ketoglutarate dehydrogenase. *J. Neurosci.* 24, 7771–7778. doi:10.1523/JNEUROSCI.1842-04.2004

Walling, A. D., and Dickson, G. M. (2012). Hearing loss in older adults. *Am. Fam. Physician* 85, 1150–1156.

Wang, J., Ruel, J., Ladrech, S., Bonny, C., van de Water, T. R., and Puel, J. L. (2007). Inhibition of the c-Jun N-terminal kinase-mediated mitochondrial cell death pathway restores auditory function in sound-exposed animals. *Mol. Pharmacol.* 71, 654–666. doi:10.1124/mol.106.028936

Wang, J. Y., Li, J. Q., Xiao, Y. M., Fu, B., and Qin, Z. H. (2020). Triphenylphosphonium (TPP)-Based antioxidants: A new perspective on antioxidant design. *ChemMedChem* 15, 404–410. doi:10.1002/cmdc.201900695

Wei, Y. H., Lu, C. Y., Wei, C. Y., Ma, Y. S., and Lee, H. C. (2001). Oxidative stress in human aging and mitochondrial disease-consequences of defective mitochondrial respiration and impaired antioxidant enzyme system. *Chin. J. Physiol.* 44, 1–11.

Wong, A. C., and Ryan, A. F. (2015). Mechanisms of sensorineural cell damage, death and survival in the cochlea. *Front. Aging Neurosci.* 7, 58. doi:10.3389/fnagi.2015.00058

Wu, J., Ye, J., Kong, W., Zhang, S., and Zheng, Y. (2020). Programmed cell death pathways in hearing loss: A review of apoptosis, autophagy and programmed necrosis. *Cell Prolif.* 53, e12915. doi:10.1111/cpr.12915

Yamashita, D., Jiang, H. Y., Schacht, J., and Miller, J. M. (2004a). Delayed production of free radicals following noise exposure. *Brain Res.* 1019, 201–209. doi:10.1016/j.brainres.2004.05.104

Yamashita, D., Miller, J. M., Jiang, H. Y., Minami, S. B., and Schacht, J. (2004b). AIF and EndoG in noise-induced hearing loss. *Neuroreport* 15, 6452–2722.

Zhang, M. Y., Dugbartey, G. J., Juriasingani, S., and Sener, A. (2021). Hydrogen sulfide metabolite, sodium thiosulfate: Clinical applications and underlying molecular mechanisms. *Int. J. Mol. Sci.* 22, 6452. doi:10.3390/ijms22126452

Zielonka, J., Joseph, J., Sikora, A., Hardy, M., Ouari, O., Vasquez-Vivar, J., et al. (2017). Mitochondria-targeted triphenylphosphonium-based compounds: Syntheses, mechanisms of action, and therapeutic and diagnostic applications. *Chem. Rev.* 117, 10043–10120. doi:10.1021/acs.chemrev.7b00042

frontiers | Frontiers in Pharmacology

TYPE Original Research
PUBLISHED 15 June 2023
DOI 10.3389/fphar.2023.1150829

OPEN ACCESS

EDITED BY
Jorge G. Farias,
University of La Frontera, Chile

REVIEWED BY
Huaxun Wu,
Anhui Medical University, China
Laureline Berthelot,
Institut National de la Santé et de la Recherche Médicale (INSERM), France

*CORRESPONDENCE
Wencheng Xu,
cpuwcxu@hotmail.com,
Xiaoqin Wang,
wangxiao773@hotmail.com,
Pengtao You,
tptyou@hbtcm.edu.cn

†These authors have contributed equally to this work and share first authorship

RECEIVED 27 February 2023
ACCEPTED 07 June 2023
PUBLISHED 15 June 2023

CITATION
Xu W, Song W, Chen S, Jin S, Xue X, Min J, Wang X and You P (2023), Tetrandrine inhibits the proliferation of mesangial cells induced by enzymatically deglycosylated human IgA1 via IgA receptor/MAPK/NF-κB signaling pathway.
Front. Pharmacol. 14:1150829.
doi: 10.3389/fphar.2023.1150829

Tetrandrine inhibits the proliferation of mesangial cells induced by enzymatically deglycosylated human IgA1 via IgA receptor/MAPK/NF-κB signaling pathway

Wencheng Xu[1,2,3*†], Wanci Song[4†], Shuhe Chen[1,2,3], Shanshan Jin[2,3,5], Xue Xue[2,3,5], Jinwen Min[6], Xiaoqin Wang[2,3,5*] and Pengtao You[4*]

[1]Department of Pharmacy, Hubei Provincial Hospital of Traditional Chinese Medicine, Wuhan, China, [2]Hubei Key Laboratory of Theory and Application Research of Liver and Kidney in Traditional Chinese Medicine, Affiliated Hospital of Hubei University of Chinese Medicine, Wuhan, China, [3]Hubei Province Academy of Traditional Chinese Medicine, Wuhan, China, [4]Hubei Key Laboratory of Resources and Chemistry of Chinese Medicine, Hubei University of Chinese Medicine, Wuhan, China, [5]Department of Nephrology, Hubei Provincial Hospital of Traditional Chinese Medicine, Wuhan, China, [6]The First Clinical Medical College, Jinzhou Medical University, Jinzhou, China

Objective: Despite the use of renin-angiotensin system blockade and immunosuppressive drugs, including corticosteroids, the current treatment regimens for Immunoglobulins A nephropathy (IgAN) are severely limited. The proliferation of mesangial cell and deposition of deglycosylated human IgA1 immune complex are the most common pathologic features of IgAN. We examined the tetrandrine potential of suppressing the proliferation of mesangial cells and explored its underlying mechanisms with a focus on IgA receptor/MAPK/NF-κB signaling pathway.

Methods: Standard human IgA (native IgA) were enzymatically desialylated (deS IgA) or further degalactosylated (deS/deGal IgA) using neuraminidase and β-galactosidase. Rat glomerular mesangial cells (HBZY-1) and human renal mesangial cells (HRMC) stimulated by IgA were used to observe the suppressive effect of tetrandrine. The MTT assay was used to detect the cell viability. The protein expression of IgA receptor/MAPK/NF-κB signaling pathway was examined by Western blot. Cell cycle analysis was measured by flow cytometer.

Results: Native IgA and deS IgA showed limited stimulation effect on both HBZY-1 cells and HRMCs, whereas deS/deGal IgA significantly stimulated the proliferation of both HBZY-1 cells and HRMCs ($p < 0.05$). Compared with non-stimulation of deS/deGal IgA, 1–3 μM of tetrandrine had stronger inhibitory effect on the proliferation of HBZY-1 cells and HRMCs with the stimulation of deS/deGal IgA ($p < 0.05$), suggesting that tetrandrine possibly inhibited the proliferation of mesangial cells induced by deglycosylated human IgA1 specifically. Molecular mechanism study revealed that tetrandrine decreased the expression of IgA1 receptor, CD71 and β4GALT1, and inhibited the activation of MAPK/NF-κB significantly ($p < 0.05$). Moreover, these inhibitory effect of tetrandrine caused cell

cycle arrest and stopped the cell growth in the S phase companied with the upregulating of cyclin A2 and downregulating of cyclin D1.

Conclusion: Taken together, tetrandrine inhibited the proliferation of mesangial cells induced by enzymatically deglycosylated human IgA1 via IgA receptor/MAPK/NF-κB signaling pathway. Based on these potential molecular mechanisms, tetrandrine would be an appealing therapeutic option for IgAN.

KEYWORDS

tetrandrine, mesangial cells, IgA nephropathy, IgA receptor, proliferation

1 Introduction

Immunoglobulins A nephropathy (IgAN) is recognized as the most common primary glomerular glomerulonephritis throughout the world. The common clinical manifestation of IgAN patients is asymptomatic hematuria and proteinuria (Zhang et al., 2016; Pattrapornpisut et al., 2021). After a slow progression in 20 years, approximately 30%–40% of IgAN patients were reported to develop end-stage renal failure which had to receive dialysis or kidney transplantation (Zhang et al., 2016).

The histological feature of IgAN is mesangial deposition of the IgA1-containing immune complexes and cell proliferation (Lai et al., 2016). Usually, the structure of human IgA1 has O-glycosylation on the serine and threonine residues in the hinge region of heavy chain. The disaccharide of O-glycan side chains is formed by a primary N-acetylgalactosamine and a secondary β1,3-linked galactose, both of which could be sialylated. However, the hinge region of heavy chain in IgA1 isolated from the serum and the mesangial areas of IgAN patients' renal biopsy were certified to be aberrantly glycosylated or galactose-deficient (Wang et al., 2016). Moreover, the glomerular injury of IgAN is recognized as predominantly mediated by the activation of mesangial cells which are stimulated by the deposited IgA1 in mesangial areas since IgAN is not associated with a significant glomerular cell infiltrate in most cases (Molyneux et al., 2017). Cross-linking of IgA receptors, such as the transferrin receptor (CD71) and β1,4-galactosyltransferase 1 (β4GALT1), elicits proliferation and a proinflammatory in mesangial cells (Tamouza et al., 2012; Molyneux et al., 2017). The mitogen-activated protein kinase (MAPK) and nuclear transcription factor-κB (NF-κB) signal transduction pathways contribute to the activation and proliferation of mesangial cells induced by galactose-deficient IgA1 (Leung et al., 2008; Tamouza et al., 2012).

Tetrandrine, one of the main active components in Fang Ji (*Stephania tetrandrae Root*), has been approved for the treatment of silicosis and rheumatic arthritis in China (Xu et al., 2017). Recent evidence suggests that tetrandrine could suppress the proliferation of T cells stimulated by concanavalin A through multiple cellular signaling, such as NF-κB, MAPK, and PI3K/Akt/mTOR (Xu et al., 2019b; Xu et al., 2021). Moreover, tetrandrine was confirmed to inhibit the activation and proliferation of mesangial cells induced by aberrantly glycosylated human IgA1 or IL-1β (Wu et al., 2011; Xia et al., 2022). In the present study, we evaluated the tetrandrine potential of suppressing the proliferation of mesangial cells induced by enzymatically deglycosylated human IgA1 molecules and explored its underlying mechanisms with a focus on IgA receptor/MAPK/NF-κB signaling pathway.

2 Materials and methods

2.1 Reagents and antibodies

Dulbecco's modified Eagle's medium (DMEM) and fetal bovine serum (FBS) were obtained from Gibco BRL (Grand Island, NY, United States). Tetrandrine (purity: more than 98%) was provided by Chengdu Must Bio-Technology Co., Ltd. EMEM medium was purchased from BeNa Culture Collection (Xinyang, China). National standard human IgA was provided by National Institutes for Food and Drug Control. Neuraminidase and β-galactosidase were all purchased from Shanghai Yuanye Biotechnology Co., Ltd. Primary antibodies against ERK1/2 (dilution 1:1000, #4695), p-ERK1/2 (dilution 1:1000, #4370), JNK (dilution 1:1000, #9258), p-JNK (dilution 1:1000, #4668), p38 (dilution 1:1000, #8690), p-p38 (dilution 1:1000, #4511), NF-κB (dilution 1:1000, #8242), Cyclin D1 (dilution 1:1000, #55506), Cyclin B1 (dilution 1:1000, #12231), Cyclin A2 (dilution 1:1000, #4656) and CD71 (dilution 1:1000, #13113) antibodies were provided by Cell Signaling Technology. Anti β4GALT1 (dilution 1:500, #abs148346) antibody was purchased from Absin. β-actin (dilution 1:5000, #66009-1-Ig) antibody was provided by Proteintech Group. All other reagents are the highest quality reagents provided by commercial suppliers.

2.2 Cell cultures

Rat glomerular mesangial cells (HBZY-1, #4201RAT-CCTCC00124) were obtained from China Center for Type Culture Collection (Wuhan, China). HBZY-1 cells were routinely grown in DMEM medium supplemented with 10% FBS and 1% penicillin/streptomycin and cultured at 37°C in a humidified atmosphere of 5% CO_2 as described before (Li et al., 2022). Human renal mesangial cells (HRMC, #BNCC341276) were provided by BeNa Culture Collection (Xinyang, China). HRMC culture followed with the instructions of manufacturer. Cells between passages three and seven were employed in the present study.

2.3 Deglycosylation of human IgA1

Standard human IgA was enzymatically digested with neuraminidase and β-galactosidase according to the following procedure. Standard human IgA was divided into three groups of 15 mg each. The first group was dissolved in 15 mL of 10 mM/L sodium acetate buffer (SAB, pH 5.0) without any enzymatic process, named as native IgA. The second group was dissolved in SAB, and 7.5 mL of neuraminidase (20 mU/mL) was added to remove

N-acetylneuraminic acid from the IgA protein, named as deS IgA. The third group was dissolved in SAB, and 7.5 mL of neuraminidase (20 mU/mL) and 7.5 mL of β-galactosidase (20 mU/mL) were added to remove N-acetylneuraminic acid and galactose together, nameds as deS/deGal IgA. All samples were incubated overnight at 37°C as described before (Tomana et al., 1999; Sano et al., 2002).

2.4 MTT assay

The 3-(4,5-dimethylthiazol-2-yl)-2,5-diphenyl tetrazolium bromide (MTT, Sigma, MO, United States) assay was used to detect the cell viability. After cell treatment, 10 μL of 5 mg/mL MTT was added to each well with a 4 h-incubation at 37°C. Then, the plates were centrifuged at 375 × g for 5 min followed by discarding the supernatant. Next, precipitated formazan crystals produced by growing cells was dissolved in 150 μL of dimethyl sulfoxide in each well followed by shaking 10 min. Finally, the absorbance was measured at 450 nm by Spark 10 M microplate reader (Tecan, Männedorf, Switzerland). The IC_{50} values of tetrandrine were calculated from dose-response curves as we described before (Xu et al., 2019a).

2.5 Cell cycle analysis

HBZY-1 cells were seeded in 6-well plates and incubated with DMEM medium and stimulated by 1 mg/mL of deS/deGal IgA. Then, the cells were treated by blank solvent, 1, 2.5 and 3 μM of tetrandrine respectively. After 48 h, the cells were harvested and fixed by the treatment with 70% ethanol at 4°C for 1 h. Propidium iodide (100 μg/mL,#P4170, Sigma Chemical Co.) and RNaseA (1 mg/mL,#R5500, Sigma Chemical Co.) were added to stain cellular DNA at 37°C and in dark for 30 min. Finally, the content of cellular DNA was examined by flow cytometry (FACSCalibur, BD Bioscience, CA, US). MODFIT LT™ (V3.1, Verity Software House, Topsham, ME, United States) was used to analyze the data as we described before (Xu et al., 2019b).

2.6 Western blot

After harvest, cells were treated by RIPA lysis kit combined with the protease inhibitor (Beyotime). Protein concentration of cell lysate was examined by BCA protein assay kit (Takara, Kyoto, Japan). The cell extracts were subsequently separated by SDS-polyacrylamide gel electrophoresis and then transferred to nitrocellulose membranes (Millipore, MA, United States). After blocking in 5% nonfat milk at room temperature for 2 h, membranes were incubated with primary antibodies overnight at 4°C, following with the treatment by horseradish peroxidase (HRP) coupled secondary antibody (#7076, Cell Signaling Technology) for 1 h at room temperature. Finally, membranes were treated by ECL reagent (Bio-Rad, CA, United States), signals were detected by FluorChem FC3 system (ProteinSimple, CA, United States) and then quantitatively analyzed by ImageJ software as we described before (Xu et al., 2019b).

2.7 Statistical analysis

Differences in the percentages of viable cells, percentage of cells in cell-cycle phases and the expressions of proteins were examined by Bonferroni Multiple Comparison Tests. These above analyses were performed by using GraphPad PRISM 9.5 (GraphPad Software Inc., San Diego, CA). In each case, two-sided p values < 0.05 were considered to be significant.

3 Results

3.1 Effects of tetrandrine on the proliferation of HBZY-1 cells

We first examined the stimulation effects of deS/deGal IgA on cell proliferation of HBZY-1 cells. Cells were co-cultured with blank solvent, native IgA, deS IgA and deS/deGal IgA for 48, 72, and 96 h respectively. As shown in Figure 1A, only deS/deGal IgA significantly stimulated the proliferation of HBZY-1 cells (p < 0.01). Next, we observed the suppressive effects of tetrandrine on the proliferation of HBZY-1 cells induced by deS/deGal IgA. As shown in Figure 1B, tetrandrine inhibited the proliferation of HBZY-1 cells stimulated by deS/deGal IgA in a dose- and time-dependent manner. Specifically, 1 μM of tetrandrine significantly inhibited the proliferation of HBZY-1 cells stimulated by deS/deGal IgA with little cytotoxic effect on HBZY-1 cells alone (p < 0.001, Figure 1C). Compared with non-stimulation of deS/deGal IgA, 2.5 and 3 μM of tetrandrine showed stronger inhibitory effect on the proliferation of HBZY-1 cells with the stimulation of deS/deGal IgA (p < 0.001, Figure 1C).

3.2 Effects of tetrandrine on the expression of IgA receptor in HBZY-1 cells

To investigate the possible molecular mechanism for the inhibitory effect of tetrandrine against the stimulation of deS/deGal IgA, effects of tetrandrine on the expression of IgA receptor in HBZY-1 cells were examined. Treatment of deS/deGal IgA significantly stimulated the expression of CD71 and β4GALT1 (p < 0.01, Figure 2). 1–3 μM of tetrandrine inhibited the expression of both CD71 and β4GALT1 significantly and dose-dependently (p < 0.01, Figure 2).

3.3 Effects of tetrandrine on MAPK/NF-κB signaling pathway in HBZY-1 cells

MAPK/NF-κB signaling pathway maintains cell proliferation. To investigate the possible mechanism of tetrandrine's inhibitory effect, we examined the effects of tetrandrine on MAPK/NF-κB activation in HBZY-1 cells. As shown in Figure 3, treatment of deS/deGal IgA significantly stimulated the phosphorylation of p38, JNK, ERK and NF-κB (p < 0.01). 1–3 μM of tetrandrine decreased the expression of p-p38, p-JNK, p-ERK and p-NF-κB in a dose-dependent manner with little effect on the expression of p38, JNK, ERK and NF-κB (p < 0.05, Figure 3).

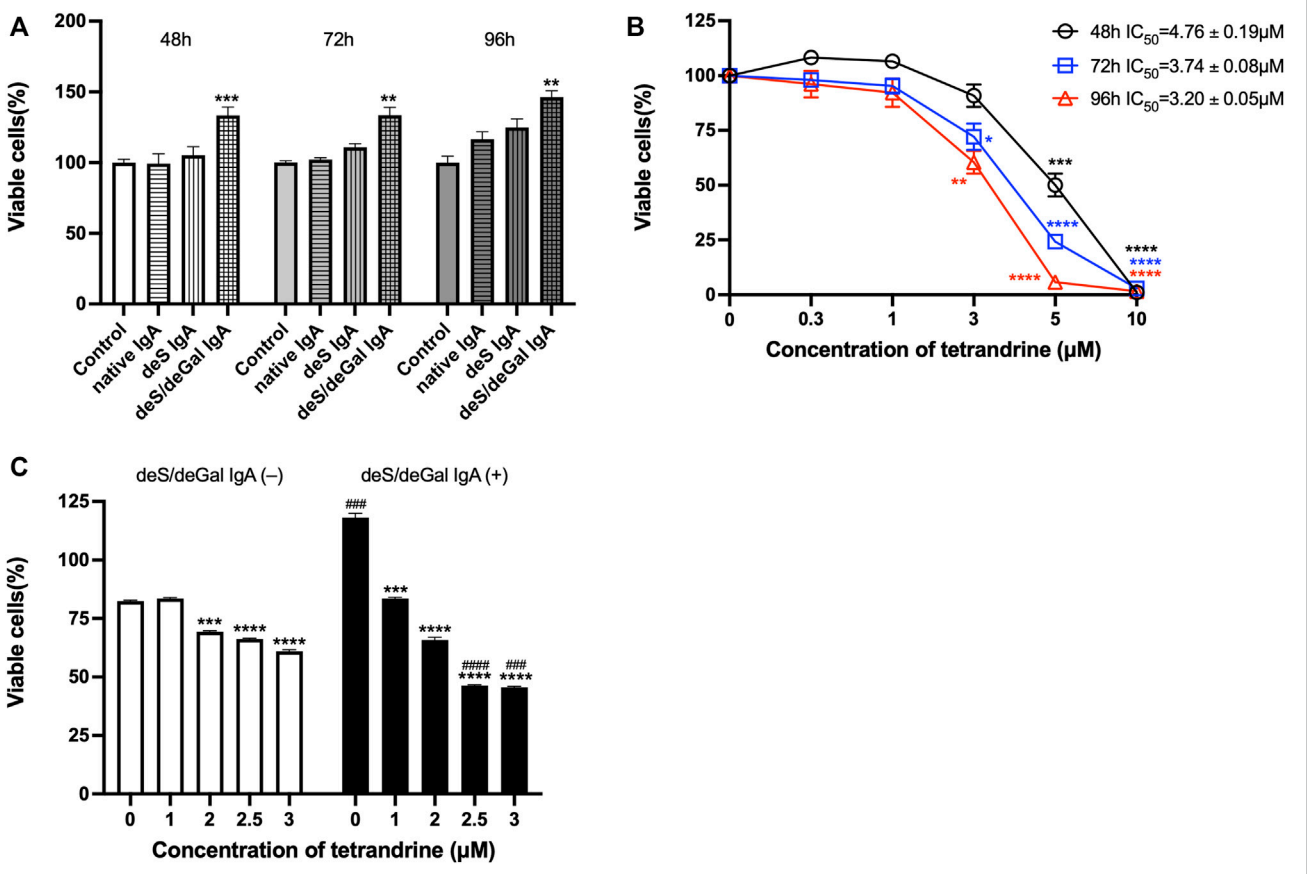

FIGURE 1
Effects of tetrandrine on the proliferation of HBZY-1 cells. **(A)** The stimulation effects of enzymatically deglycosylated human IgA1 on cell proliferation of HBZY-1 cells were examined. Cells were co-cultured with blank solvent, native IgA, deS IgA and deS/deGal IgA for 48, 72, and 96 h respectively. **(B)** HBZY-1 cells were stimulated by deS/deGal IgA and treated with different concentrations of tetrandrine (0, 0.3, 1, 3, 5 and 10 μM) for 48, 72, and 96 h respectively. IC_{50} values of tetrandrine were calculated by GraphPad PRISM 9.5. **(C)** HBZY-1 cells were treated with different concentrations of tetrandrine (0, 1, 2, 2.5 and 3 μM) in the presence or absence of deS/deGal IgA for 48 h. Cell proliferation was determined by MTT assay. The data were expressed as means ± S.E.M. Statistical analyses were performed using Bonferroni's multiple comparison tests, $^{*}p < 0.05$, $^{**}p < 0.01$, $^{***}p < 0.001$ and $^{****}p < 0.0001$, as compared to the group treated by blank solvent, $^{\#\#\#}p < 0.001$ and $^{\#\#\#\#}p < 0.0001$, as compared to the group in the absence of deS/deGal IgA, respectively. (n = 6).

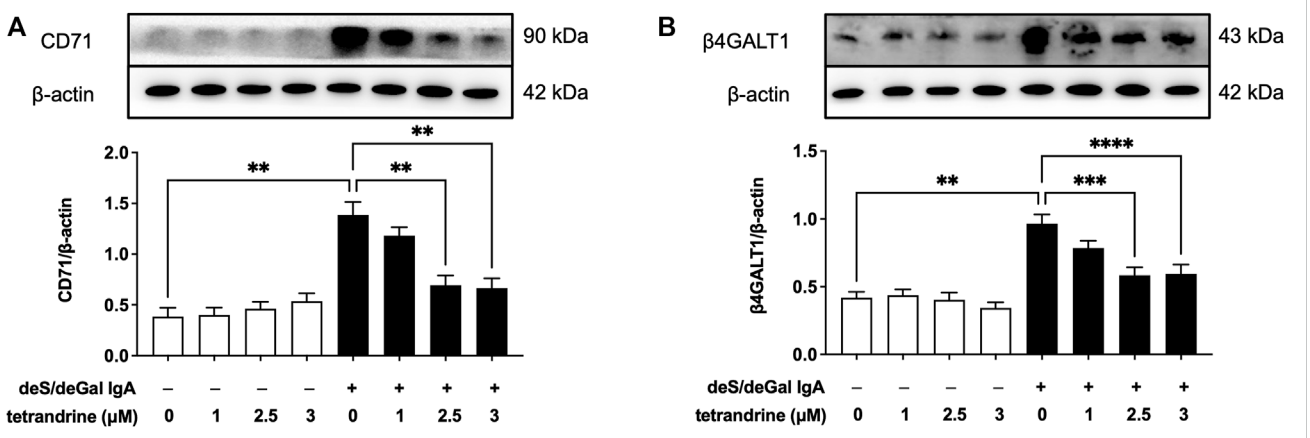

FIGURE 2
Effects of tetrandrine on the expression levels of IgA receptor protein in HBZY-1 cells. Cells were treated with different concentrations of TET (0, 1, 2.5 and 3 μM) in the presence or absence of deS/deGal IgA for 48 h. The cell lysates were examined by Western blot. More than three independent experiments were carried out and representative results were shown in the figures. β-actin was used as internal control. Statistical analyses were performed using Bonferroni's multiple comparison tests, $^{**}p < 0.01$, $^{***}p < 0.001$ and $^{****}p < 0.0001$ respectively. (n = 6).

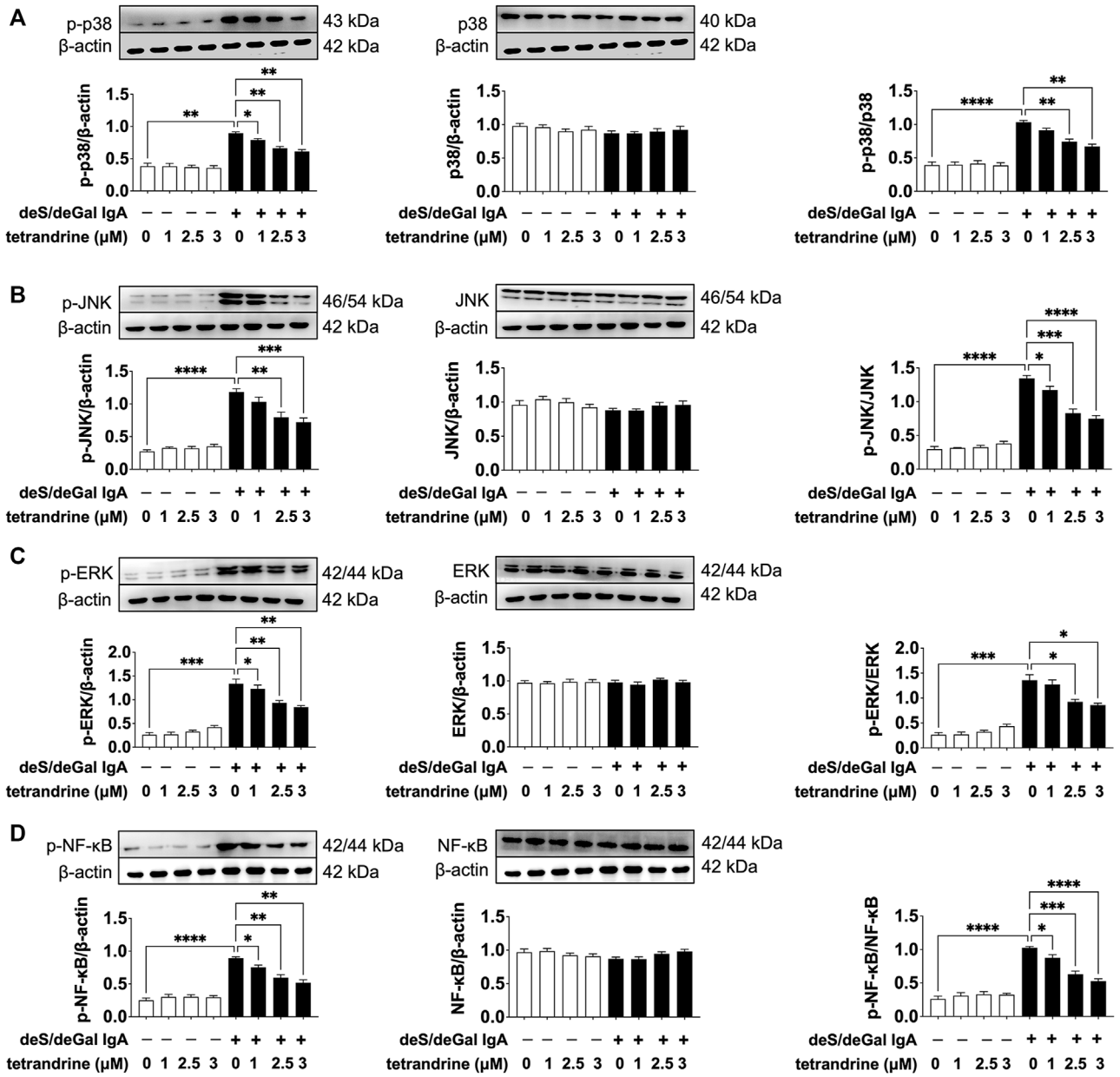

FIGURE 3
Effects of tetrandrine on the expression levels of MAPK/NF-κB in HBZY-1 cells. Cells were treated with different concentrations of TET (0, 1, 2.5 and 3 μM) in the presence or absence of deS/deGal IgA for 48 h. The cell lysates were examined by Western blot. More than three independent experiments were carried out and representative results were shown in the figures. β-actin was used as internal control and re-used to compare the expression levels of MAPK/NF-κB and their phosphorylation protein conveniently. Statistical analyses were performed using Bonferroni's multiple comparison tests, *$p < 0.05$, **$p < 0.01$, ***$p < 0.001$ and ****$p < 0.0001$ respectively. ($n = 6$).

3.4 Effects of tetrandrine on cell cycle arrest in HBZY-1 cells

To examine the effects of tetrandrine on cell cycle arrest in HBZY-1 cells, HBZY-1 cells were stimulated by deS/deGal IgA and treated with 0, 1, 2.5 and 3 μM of tetrandrine respectively. As shown in Figures 4A, B, tetrandrine significantly caused cell cycle arrest and stopped the cell growth in the S phase in a dose-dependent manner ($p < 0.05$). The treatment of tetrandrine also decreased the percentage of cells at G0/G1 phase dose-dependently and significantly ($p < 0.05$). 1–3 μM of tetrandrine showed limited influence on the population of cells at G2/M phase. Accordingly, 1–3 μM of tetrandrine inhibited the expression of cyclin D1 but enhanced the expression of cyclin A2 significantly and dose-dependently ($p < 0.05$, Figure 4C).

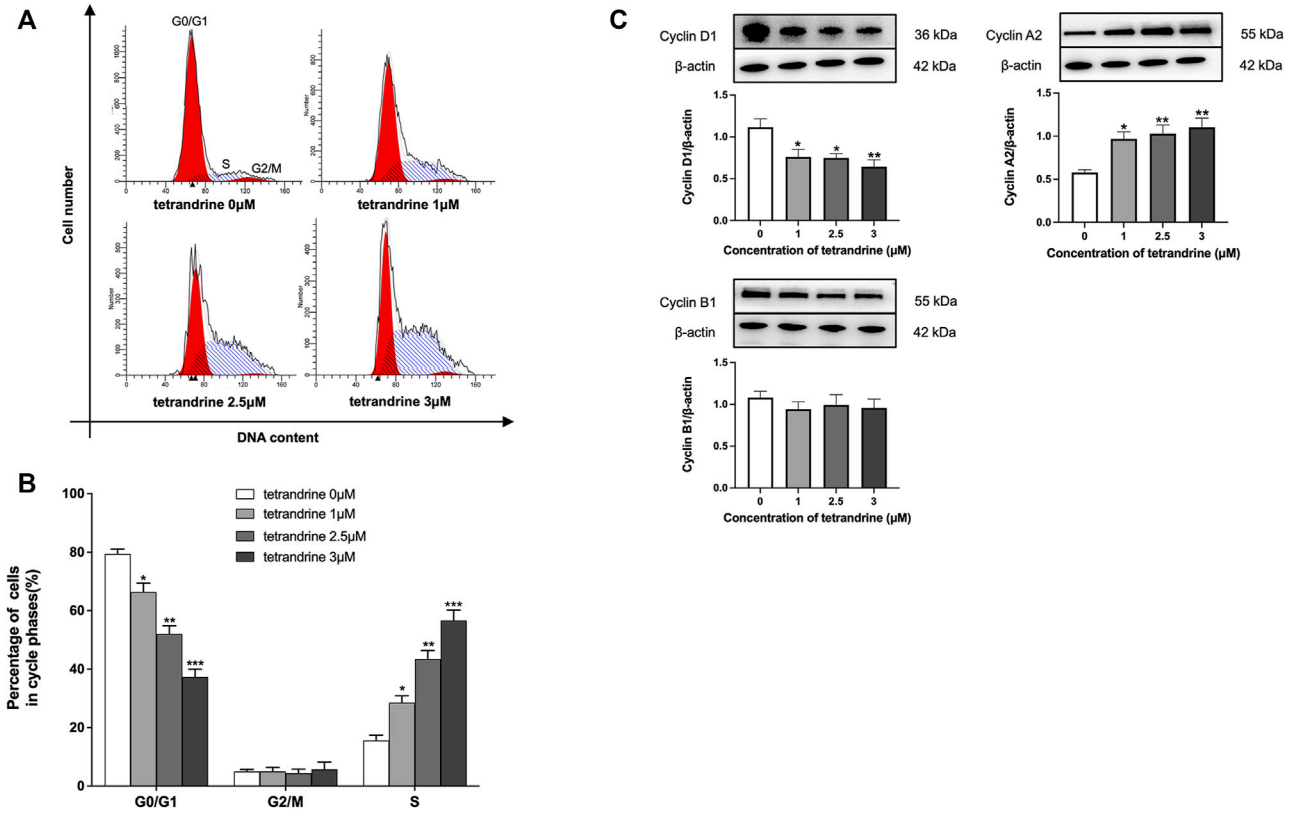

FIGURE 4
Tetrandrine triggers cell cycle in HBZY-1 cells. Cells stimulated by deS/deGal IgA were treated with different concentrations of tetrandrine (0, 1, 2.5 and 3 μM) for 48 h. **(A)** Cell cycle was analyzed by flow cytometer. The peaks marked in the figure represent G0/G1, S and G2/M phases in the cell cycle, respectively. **(B)** Percentages of cell numbers in the cell cycle after 48 h of the agent treatment were. **(C)** The cell lysates were examined by Western blot. *β*-actin was used as internal control. More than three independent experiments were carried out and representative results were shown in the figures. Statistical analyses were performed using Bonferroni's multiple comparison tests, *$p < 0.05$, **$p < 0.01$, and ***$p < 0.001$ as compared to the group treated by blank solvent respectively. ($n = 6$).

3.5 Effects of tetrandrine on the proliferation of HRMCs

To confirm the effects of tetrandrine, we also examined the effects of tetrandrine on the proliferation of HRMCs. deS/deGal IgA significantly stimulated the proliferation of HRMCs ($p < 0.05$, Figure 5A). Tetrandrine inhibited the proliferation of HRMCs stimulated by deS/deGal IgA dose-dependently and time-dependently with IC_{50} value of 3.16 ± 0.10 μM (48 h), 2.42 ± 0.09 μM (72 h) and 2.13 ± 0.24 μM (96 h) (Figure 5B). 1–3 μM of tetrandrine decreased the percentage of viable cells dose-dependently and significantly on HRMCs with non-stimulation of deS/deGal IgA ($p < 0.001$, Figure 5C). Compared with non-stimulation of deS/deGal IgA, 1–3 μM of tetrandrine showed stronger inhibitory effect on the proliferation of HRMCs with the stimulation of deS/deGal IgA ($p < 0.05$, Figure 5C).

3.6 Effects of tetrandrine on the expression of IgA receptor in HRMCs

IgA receptor CD71 and β4GALT1 were largely upregulated significantly with the stimulation of deS/deGal IgA ($p < 0.001$, Figure 6). 2 μM of tetrandrine significantly decreased the expression of CD71 and β4GALT1 obviously and significantly ($p < 0.01$, Figure 6).

3.7 Effects of tetrandrine on MAPK/NF-κB signaling pathway in HRMCs

As shown in Figure 7, treatment of deS/deGal IgA significantly stimulated the phosphorylation of p38, JNK, ERK and NF-κB ($p < 0.001$). 2 μM of tetrandrine decreased the expression of p-p38, p-JNK, p-ERK and p-NF-κB significantly with little effect on the expression of p38, JNK, ERK and NF-κB ($p < 0.001$, Figure 7).

4 Discussion

Renin-angiotensin system blockade and immunosuppressive drugs, including corticosteroids have been list in the guideline for the therapy of IgAN (Rasche et al., 2016). Although the use of these drugs was confirmed to reduce the risk of kidney failure and

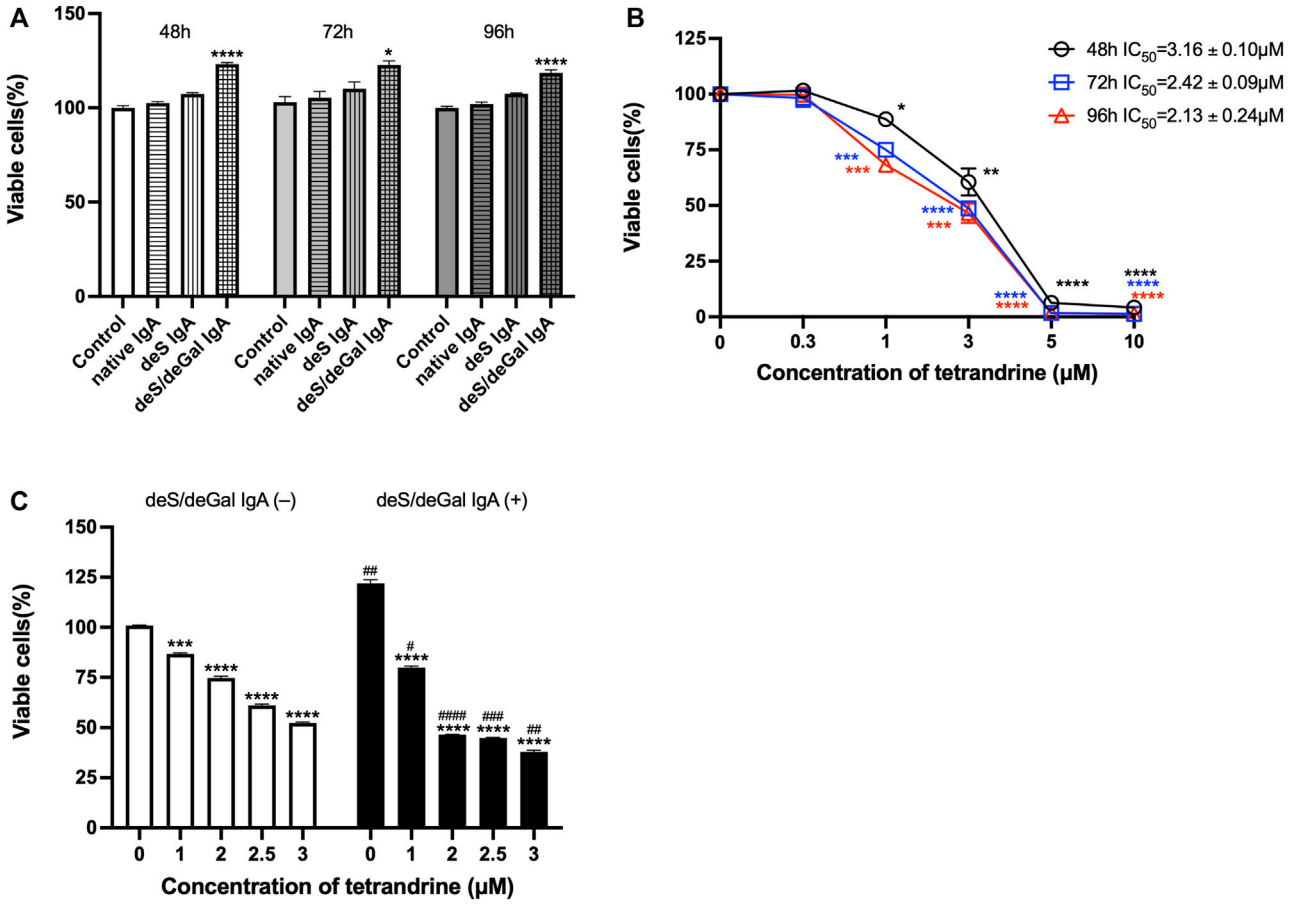

FIGURE 5
Effects of tetrandrine on the proliferation of HRMCs. **(A)** The stimulation effects of enzymatically deglycosylated human IgA1 on cell proliferation of HRMCs were examined. Cells were co-cultured with blank solvent, native IgA, deS IgA and deS/deGal IgA for 48, 72, and 96 h respectively. **(B)** HRMCs were stimulated by deS/deGal IgA and treated with different concentrations of tetrandrine (0, 0.3, 1, 3, 5 and 10 μM) for 48, 72, and 96 h respectively. IC_{50} values of tetrandrine were calculated by GraphPad PRISM 9.5. **(C)** HRMCs were treated with different concentrations of tetrandrine (0, 1, 2, 2.5 and 3 μM) in the presence or absence of deS/deGal IgA for 48 h. Cell proliferation was determined by MTT assay. The data were expressed as means ± S.E.M. Statistical analyses were performed using Bonferroni's multiple comparison tests, $^{*}p < 0.05$, $^{**}p < 0.01$, $^{***}p < 0.001$ and $^{****}p < 0.0001$, as compared to the group treated by blank solvent, $^{\#}p < 0.05$, $^{\#\#}p < 0.01$, $^{\#\#\#}p < 0.001$ and $^{\#\#\#\#}p < 0.0001$, as compared to the group in the absence of deS/deGal IgA, respectively. ($n = 6$).

slow down the progression of renal function in patients with high-risk IgAN, a large proportion of patient was still observed to develop end-stage kidney disease (Lv et al., 2017; O'Shaughnessy and Lafayette, 2017). An "multi-hit" hypothesis of genetic and molecular mechanisms underlying IgAN is undisputed. Firstly, the production of a typical galactose-deficient mucosal-type IgA1 antibodies increased in peripheral blood circulatory system. Secondly, anti-IgA1 autoantibodies formed in immunological system. Thirdly, IgA1-containing immune complexes deposited in the glomerular mesangium, which incited nephritogenic inflammatory response (O'Shaughnessy and Lafayette, 2017). The immune deposition leads to mesangial cell proliferate and over-produce components of extracellular matrix, cytokines and chemokines, causing downstream podocyte injury and induce proteinuria (Lai et al., 2016). Several studies revealed that tetrandrine had therapeutic potential in reducing proteinuria, improving renal function, and alleviating renal pathological damage via attenuating podocyte injury (Yu et al., 2020; Ding et al., 2021; Mao et al., 2022). To the best of our knowledge, the current research firstly suggested that tetrandrine inhibited the proliferation of mesangial cells induced by enzymatically deglycosylated human IgA1 via IgA receptor/MAPK/NF-κB signaling pathway.

Mesangial deposition of aberrantly glycosylated IgA1 is considered as the key pathogenic process of IgA nephropathy (Wang et al., 2016). The IgA1 hinge region has up to six clustered O-glycans which consist of serine and threonine-linked N-acetylgalactosamine usually with β1,3-linked galactose and variable sialylation (Ohyama et al., 2021).

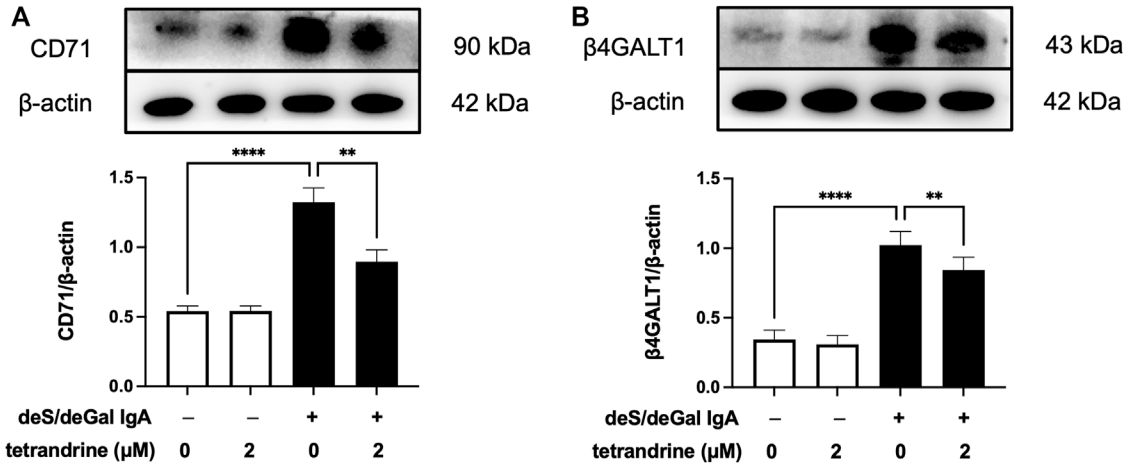

FIGURE 6
Effects of tetrandrine on the expression levels of IgA receptor protein in HRMCs. Cells were treated with 2 μM of tetrandrine in the presence or absence of deS/deGal IgA for 48 h. The cell lysates were examined by Western blot. More than three independent experiments were carried out and representative results were shown in the figures. β-actin was used as internal control. Statistical analyses were performed using Bonferroni's multiple comparison tests, $^{**}p < 0.01$ and $^{****}p < 0.0001$ respectively. ($n = 6$).

When human IgA1 were enzymatically desialylated or further degalactosylated using neuraminidase and β-galactosidase, deglycosylated human IgA1 accumulated in rat glomeruli after injecting into the left renal artery (Sano et al., 2002). In the present study, deS/deGal IgA significantly stimulated the proliferation of both HBZY-1 cells and HRMCs, whereas native IgA and deS IgA showed limited stimulation effects (Figures 1A, 5A). This observation suggested that galactose-deficiency in IgA1 was essential for stimulation function of the deposited IgA1 within the mesangial areas. The stimulation function of galactose-deficiency IgA1 resulted in mesangial cell proliferation, which could be inhibited by the treatment of tetrandrine dose-dependently and time-dependently (Figures 1B, 5B). Compared with non-stimulation of deS/deGal IgA, 1–3 μM of tetrandrine showed stronger inhibitory effect on the proliferation of HRMCs with the stimulation of deS/deGal IgA ($p < 0.05$, Figures 1C, 5C), which suggested that tetrandrine might specifically inhibit the stimulation of deS/deGal IgA.

Pathogenetic IgA only deposit in the mesangial areas of the glomerulus, whereas deposits are rare to find in podocytes or renal tubular epithelial cells, which suggests that IgA receptors are responsible for mesangial cell proliferation induced by galactose-deficiency IgA1 (Lai et al., 2016). CD71 has been identified as a candidate IgA1 receptor expressed on HRMCs. CD71 binds IgA1 and co-localizes with mesangial IgA1 deposits, and is overexpressed in patients with IgAN (Moura et al., 2004). CD71-specific antibodies and transferrin were observed to inhibit the binding of IgA to HRMC partially, suggesting that HRMC expresses at least more than two kinds of IgA receptor. Recently, β4GALT1 was confirmed as an important IgA receptor in HRMC since it played a significant role in the clearance of mesangial IgA and the initial response to IgA deposition (Molyneux et al., 2017). As shown in Figures 2, 6, deS/deGal IgA significantly stimulated the expression of both CD71 and β4GALT1 ($p < 0.01$) in both rat mesangial cell HBZY-1 and human mesangial cell HRMC. 1–3 μM of tetrandrine were observed to downregulate the expression of both CD71 and β4GALT1 obviously, which might contribute to the specific inhibitory effect of tetrandrine against the proliferation of mesangial cell induced by deS/deGal IgA as mentioned in Figures 1C, 5C.

MAPK regulates a variety of cellular processes by transmitting extracellular signals to intracellular reactions and plays an important role in cell proliferation, differentiation, motility, and survival (Cargnello and Roux, 2011). As the common downstream targets, NF-κB family transcription factors are inducible by many different cell-surface receptors, which also regulate cell proliferation, differentiation and death (Xu et al., 2021). Leung et al. reported that polymeric anionic IgA isolated from IgAN patients' venous blood stimulated the activation of MAPK/NF-κB (Leung et al., 2008). Our study also confirmed that enzymatically deglycosylated human IgA1 induced the phosphorylation of p38, JNK, ERK and NF-κB ($p < 0.01$, Figures 3, 7), which might result in the mesangial cell proliferation as shown in Figures 1A, 5A. In the present study, tetrandrine was observed to inhibit the activation of MAPK/NF-κB (Figures 3, 7), thus, inhibit the proliferation of both HBZY-1 cells and HRMC stimulated by deS/deGal IgA (Figures 1, 5). Additionally, these inhibitory effect of tetrandrine caused cell cycle arrest and stopped the cell growth in the S phase companied with the upregulating of cyclin A2 and downregulating of cyclin D1 in HBZY-1 cells (Figure 4).

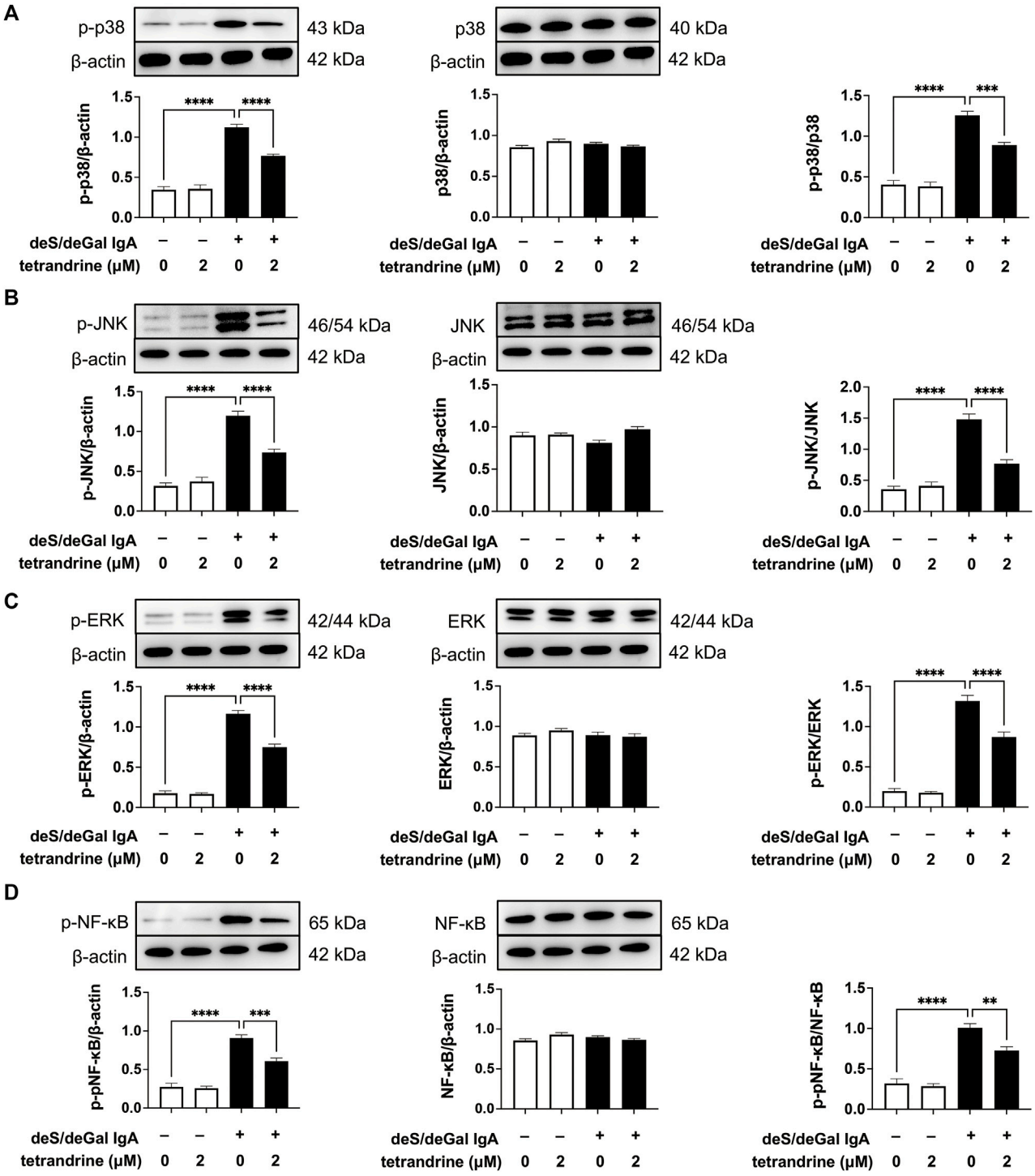

FIGURE 7
Effects of tetrandrine on the expression levels of MAPK/NF-κB in HRMCs. Cells were treated with 2 μM of tetrandrine in the presence or absence of deS/deGal IgA for 48 h. The cell lysates were examined by Western blot. More than three independent experiments were carried out and representative results were shown in the figures. β-actin was used as internal control and re-used to compare the expression levels of MAPK/NF-κB and their phosphorylation protein conveniently. Statistical analyses were performed using Bonferroni's multiple comparison tests, $^{**}p < 0.01$, $^{***}p < 0.001$ and $^{****}p < 0.0001$ respectively. ($n = 6$).

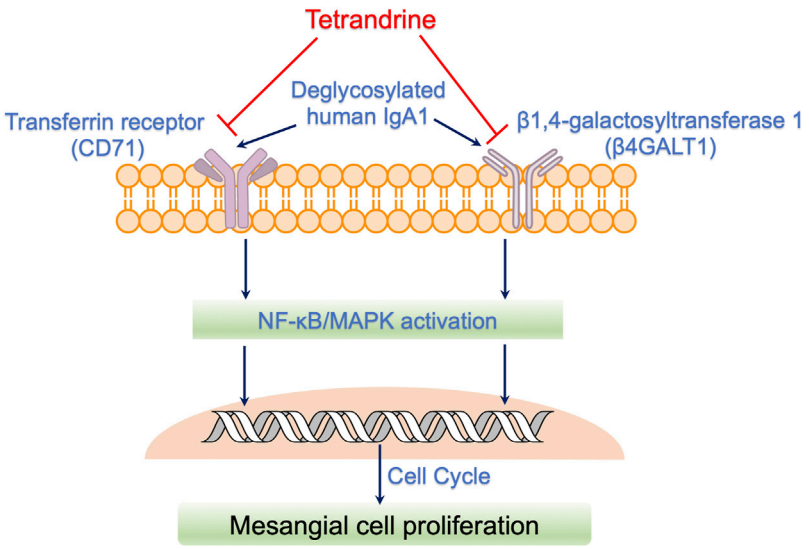

FIGURE 8
Possible action mechanisms of tetrandrine to inhibit the proliferation of mesangial cells induced by deglycosylated human IgA1. Deglycosylated human IgA1 molecule stimulated the expression of IgA1 receptor, CD71 and β4GALT1. Consequently, MAPK/NF-κB signaling pathway was activated, resulting in triggering cell cycle to regulate mesangial cell proliferation. Tetrandrine decreased the expression of IgA1 receptor, CD71 and β4GALT1, and thus, inhibited the activation of MAPK/NF-κB, resulting in triggering cell cycle arrest to stop at S phase companied with the upregulating of cyclin A2 and downregulating of cyclin D. Taken together, tetrandrine possibly inhibited the proliferation of mesangial cells induced by enzymatically deglycosylated human IgA1 via IgA receptor/MAPK/NF-κB signaling pathway.

5 Conclusion

In conclusion, enzymatically deglycosylated human IgA1 molecule stimulated the proliferation of both rat mesangial cell HBZY-1 and human mesangial cell HRMC. Compared with non-stimulation of deS/deGal IgA, 1–3 μM of tetrandrine showed stronger inhibitory effect on the proliferation of HBZY-1 cells and HRMCs with the stimulation of deS/deGal IgA ($p < 0.05$), suggesting that tetrandrine possibly inhibited the proliferation of mesangial cells induced by deglycosylated human IgA1 specifically. Molecular mechanism study revealed that tetrandrine decreased the expression of IgA1 receptor, CD71 and β4GALT1, and inhibited the activation of MAPK/NF-κB, resulting in triggering cell cycle arrest to stop at S phase companied with the upregulating of cyclin A2 and downregulating of cyclin D1. Taken together, tetrandrine inhibited the proliferation of mesangial cells induced by enzymatically deglycosylated human IgA1 via IgA receptor/MAPK/NF-κB signaling pathway (Figure 8). Based on these potential molecular mechanisms, tetrandrine would be an appealing therapeutic option for IgAN.

Data availability statement

The original contributions presented in the study are included in the article/supplementary material, further inquiries can be directed to the corresponding authors.

Author contributions

WX and WS performed the experiments and wrote the manuscript. WX, XW, and PY designed the study and revised the manuscript. SJ, XX, and SC analyzed the data. WX, WS, and JM prepared the figures. All authors contributed to the article and approved the submitted version.

Funding

The 2023~2024 Annual Scientific Research Project of Traditional Chinese Medicine from Hubei Provincial Administration of Traditional Chinese Medicine (Grant Number: ZY2023Z002), the National Natural Science Foundation of China (Grant Number: 82074395), the Natural Science Foundation of Hubei Province (Grant Number: 2021CFB244) and the Dawn Program of Wuhan Knowledge Innovation Project (Grant Number: 2022020801020509).

Conflict of interest

The authors declare that the research was conducted in the absence of any commercial or financial relationships that could be construed as a potential conflict of interest.

Publisher's note

References

Cargnello, M., and Roux, P. P. (2011). Activation and function of the MAPKs and their substrates, the MAPK-activated protein kinases. *Microbiol. Mol. Biol. Rev.* 75 (1), 50–83. doi:10.1128/mmbr.00031-10

Ding, Y., Tang, X., Wang, Y., Yu, D., Zhu, C., and Yu, J. (2021). Tetrandrine alleviates podocyte injury via calcium-dependent calpain-1 signaling blockade. *BMC Complement. Med. Ther.* 21 (1), 296. doi:10.1186/s12906-021-03469-x

Lai, K. N., Tang, S. C. W., Schena, F. P., Novak, J., Tomino, Y., Fogo, A. B., et al. (2016). IgA nephropathy. *Nat. Rev. Dis. Prim.* 2, 16001. doi:10.1038/nrdp.2016.1

Leung, J. C., Tang, S. C., Chan, L. Y., Chan, W. L., and Lai, K. N. (2008). Synthesis of TNF-alpha by mesangial cells cultured with polymeric anionic IgA--role of MAPK and NF-kappaB. *Nephrol. Dial. Transpl.* 23 (1), 72–81. doi:10.1093/ndt/gfm581

Li, H., Zhao, X., Zheng, L., Wang, X., Lin, S., Shen, J., et al. (2022). Bruceine A protects against diabetic kidney disease via inhibiting galectin-1. *Kidney Int.* 102 (3), 521–535. doi:10.1016/j.kint.2022.04.020

Lv, J., Zhang, H., Wong, M., Jardine, M. J., Hladunewich, M., Jha, V., et al. (2017). Effect of oral methylprednisolone on clinical outcomes in patients with iga nephropathy: The testing randomized clinical trial. *JAMA* 318 (5), 432–442. doi:10.1001/jama.2017.9362

Mao, L., Ding, Y., Yu, D., Yin, J., and Yu, J. (2022). Tetrandrine attenuates podocyte injury by inhibiting TRPC6-mediated RhoA/ROCK1 pathway. *Anal. Cell Pathol. (Amst)* 2022, 7534181. doi:10.1155/2022/7534181

Molyneux, K., Wimbury, D., Pawluczyk, I., Muto, M., Bhachu, J., Mertens, P. R., et al. (2017). β1,4-galactosyltransferase 1 is a novel receptor for IgA in human mesangial cells. *Kidney Int.* 92 (6), 1458–1468. doi:10.1016/j.kint.2017.05.002

Moura, I. C., Arcos-Fajardo, M., Sadaka, C., Leroy, V., Benhamou, M., Novak, J., et al. (2004). Glycosylation and size of IgA1 are essential for interaction with mesangial transferrin receptor in IgA nephropathy. *J. Am. Soc. Nephrol.* 15 (3), 622–634. doi:10.1097/01.asn.0000115401.07980.0c

Ohyama, Y., Renfrow, M. B., Novak, J., and Takahashi, K. (2021). Aberrantly glycosylated IgA1 in IgA Nephropathy: What we know and what we don't know. *J. Clin. Med.* 10 (16), 3467. doi:10.3390/jcm10163467

O'Shaughnessy, M. M., and Lafayette, R. A. (2017). Corticosteroids for IgA nephropathy: Testing for benefit, discovering harm. *JAMA* 318 (5), 429–431. doi:10.1001/jama.2017.9359

Pattrapornpisut, P., Avila-Casado, C., and Reich, H. N. (2021). IgA nephropathy: Core curriculum 2021. *Am. J. Kidney Dis.* 78 (3), 429–441. doi:10.1053/j.ajkd.2021.01.024

Rasche, F. M., Keller, F., Rasche, W. G., Schiekofer, S., Boldt, A., Sack, U., et al. (2016). Why, when and how should immunosuppressive therapy considered in patients with immunoglobulin A nephropathy? *Clin. Exp. Immunol.* 186 (2), 115–133. doi:10.1111/cei.12823

Sano, T., Hiki, Y., Kokubo, T., Iwase, H., Shigematsu, H., and Kobayashi, Y. (2002). Enzymatically deglycosylated human IgA1 molecules accumulate and induce inflammatory cell reaction in rat glomeruli. *Nephrol. Dial. Transpl.* 17 (1), 50–56. doi:10.1093/ndt/17.1.50

Tamouza, H., Chemouny, J. M., Kafkova, L. R., Berthelot, L., Flamant, M., Demion, M., et al. (2012). The IgA1 immune complex-mediated activation of the MAPK/ERK kinase pathway in mesangial cells is associated with glomerular damage in IgA nephropathy. *Kidney Int.* 82 (12), 1284–1296. doi:10.1038/ki.2012.192

Tomana, M., Novak, J., Julian, B. A., Matousovic, K., Konecny, K., and Mestecky, J. (1999). Circulating immune complexes in IgA nephropathy consist of IgA1 with galactose-deficient hinge region and antiglycan antibodies. *J. Clin. Invest.* 104 (1), 73–81. doi:10.1172/jci5535

Wang, L., Li, X., Shen, H., Mao, N., Wang, H., Cui, L., et al. (2016). Bacterial IgA protease-mediated degradation of agIgA1 and agIgA1 immune complexes as a potential therapy for IgA Nephropathy. *Sci. Rep.* 6, 30964. doi:10.1038/srep30964

Wu, C. J., Wang, Y. H., Lin, C. J., Chen, H. H., and Chen, Y. J. (2011). Tetrandrine down-regulates ERK/NF-κB signaling and inhibits activation of mesangial cells. *Toxicol Vitro* 25 (8), 1834–1840. doi:10.1016/j.tiv.2011.09.024

Xia, M., Liu, D., Liu, H., Peng, L., Yang, D., Tang, C., et al. (2022). Identification of hub genes and therapeutic agents for IgA nephropathy through bioinformatics analysis and experimental validation. *Front. Med. (Lausanne)* 9, 881322. doi:10.3389/fmed.2022.881322

Xu, W., Chen, S., Wang, X., Tanaka, S., Onda, K., Sugiyama, K., et al. (2021). Molecular mechanisms and therapeutic implications of tetrandrine and cepharanthine in T cell acute lymphoblastic leukemia and autoimmune diseases. *Pharmacol. Ther.* 217, 107659. doi:10.1016/j.pharmthera.2020.107659

Xu, W., Meng, K., Tu, Y., Tanaka, S., Onda, K., Sugiyama, K., et al. (2017). Tetrandrine potentiates the glucocorticoid pharmacodynamics via inhibiting P-glycoprotein and mitogen-activated protein kinase in mitogen-activated human peripheral blood mononuclear cells. *Eur. J. Pharmacol.* 807, 102–108. doi:10.1016/j.ejphar.2017.04.007

Xu, W., Meng, K., Wu, H., Miura, T., Suzuki, S., Chiyotanda, M., et al. (2019a). Vitamin K2 immunosuppressive effect on pediatric patients with atopic dermatitis. *Pediatr. Int.* 61 (12), 1188–1195. doi:10.1111/ped.14014

Xu, W., Wang, X., Tu, Y., Masaki, H., Tanaka, S., Onda, K., et al. (2019b). Tetrandrine and cepharanthine induce apoptosis through caspase cascade regulation, cell cycle arrest, MAPK activation and PI3K/Akt/mTOR signal modification in glucocorticoid resistant human leukemia Jurkat T cells. *Chem. Biol. Interact.* 310, 108726. doi:10.1016/j.cbi.2019.108726

Yu, J., Zhu, C., Yin, J., Yu, D., Wan, F., Tang, X., et al. (2020). Tetrandrine suppresses transient receptor potential cation channel protein 6 overexpression-induced podocyte damage via blockage of RhoA/ROCK1 Signaling. *Drug Des. Devel Ther.* 14, 361–370. doi:10.2147/dddt.S234262

Zhang, R., Zhong, L., Zhou, J., and Peng, Y. (2016). Complement-C1q TNF-related protein 3 alleviates mesangial cell activation and inflammatory response stimulated by secretory IgA. *Am. J. Nephrol.* 43 (6), 460–468. doi:10.1159/000446353

frontiers | Frontiers in Pharmacology

TYPE Review
PUBLISHED 22 June 2023
DOI 10.3389/fphar.2023.1208277

OPEN ACCESS

EDITED BY
Maria Serena Fabbrini,
Universities and Research, Italy

REVIEWED BY
Matteo Ardini,
University of L'Aquila, Italy
Ali Razaghi,
Karolinska Institutet (KI), Sweden

*CORRESPONDENCE
Mauricio Zamorano,
mauriciozamorano@gmail.com

RECEIVED 18 April 2023
ACCEPTED 12 June 2023
PUBLISHED 22 June 2023

CITATION
Lefin N, Miranda J, Beltrán JF, Belén LH, Effer B, Pessoa A Jr, Farias JG and Zamorano M (2023), Current state of molecular and metabolic strategies for the improvement of L-asparaginase expression in heterologous systems. *Front. Pharmacol.* 14:1208277. doi: 10.3389/fphar.2023.1208277

Current state of molecular and metabolic strategies for the improvement of L-asparaginase expression in heterologous systems

Nicolás Lefin[1], Javiera Miranda[1], Jorge F. Beltrán[1], Lisandra Herrera Belén[2], Brian Effer[3], Adalberto Pessoa Jr[4], Jorge G. Farias[1] and Mauricio Zamorano[1]*

[1]Department of Chemical Engineering, Science and Engineering Faculty, Universidad de La Frontera, Temuco, Chile, [2]Departamento de Ciencias Básicas, Facultad de Ciencias, Universidad Santo Tomas, Santiago, Chile, [3]Center of Excellence in Translational Medicine and Scientific and Technological Bioresource Nucleus, Universidad de La Frontera, Temuco, Chile, [4]Department of Biochemical and Pharmaceutical Technology, School of Pharmaceutical Sciences, University of São Paulo, São Paulo, Brazil

Heterologous expression of L-asparaginase (L-ASNase) has become an important area of research due to its clinical and food industry applications. This review provides a comprehensive overview of the molecular and metabolic strategies that can be used to optimize the expression of L-ASNase in heterologous systems. This article describes various approaches that have been employed to increase enzyme production, including the use of molecular tools, strain engineering, and *in silico* optimization. The review article highlights the critical role that rational design plays in achieving successful heterologous expression and underscores the challenges of large-scale production of L-ASNase, such as inadequate protein folding and the metabolic burden on host cells. Improved gene expression is shown to be achievable through the optimization of codon usage, synthetic promoters, transcription and translation regulation, and host strain improvement, among others. Additionally, this review provides a deep understanding of the enzymatic properties of L-ASNase and how this knowledge has been employed to enhance its properties and production. Finally, future trends in L-ASNase production, including the integration of CRISPR and machine learning tools are discussed. This work serves as a valuable resource for researchers looking to design effective heterologous expression systems for L-ASNase production as well as for enzymes production in general.

KEYWORDS

L-asparaginase, molecular strategies, rational design, heterologous expression system, industrial bioprocessing

1 Introduction

L-asparaginase amidohydrolase (L-ASNase), also known as aminohydrolase pertains to the amidase group of enzymes (EC3.5.1.1), is widely recognized as one of the main anticancer drugs and a promising acrylamide mitigator in the food industry. This is due to its role in the hydrolysis of L-asparagine by a two-step mechanism where first the nucleophilic residue (Nuc) attacks the amide carbon atom of L-asparagine, releasing ammonia, thus generating a

beta-acyl-enzyme intermediate. Subsequently, it acts on the ester carbon mediated by a water molecule, forming the L-aspartate molecule as shown in Figure 1 (Shakambari et al., 2019; Chand et al., 2020).

The foundation of ASNase-based treatments is the starvation of amino acids principle (Batool et al., 2016). Due to a mutation in the gene encoding L-asparagine synthetase, many leukemia or lymphoma cells cannot synthesize L-asparaginase and rely on its supply from plasma (Broome, 1968). As a result, leukemia cells undergo starvation and subsequent apoptosis due to altered signaling pathways caused by decreased plasma L-asparagine levels, which are hydrolyzed by L-ASNase (Ueno et al., 1997). This makes L-ASNase a key chemotherapeutic agent for the treatment of acute lymphoblastic leukemia (ALL), and lymphosarcoma. Additionally, its use has been reported in the treatment of acute myelomonocytic leukemia, critical lymphoblastic leukemia, melogenic leukemia, Hodgkin's lymphoma, chronic lymphocytic leukemia, and more (Vimal et al., 2018). Moreover, L-ASNase has several non-medical applications, particularly as a mitigation agent for acrylamide, which is a known carcinogen (level 2 A) and an important neurotoxin (Wang et al., 2021). Acrylamide forms between reducing sugars, and amino acids (such as L-asparagine) when starchy foods are cooked at temperatures over 120°C, and under low humidity. This non-enzymatic mechanism is known as the Maillard reaction. The process involves the formation of a Schiff base and its subsequent decarboxylation. When this progression occurs under heat, either an ammonia or an imine molecule is eliminated, and subsequently replaced to form acrylamide (Jia et al., 2021). Consequently, when L-ASNase is administered, it hydrolyses the present L-asparagine and forms aspartic acid. As a result, the Maillard reaction cannot progress, and the formation of acrylamide is inhibited (Kornbrust et al., 2009). In 2016, the European Food and Drink Federation published a strategy called *"Toolbox Acrylamide"*, driven by industrial enzymes, which promotes the reduction of residual acrylamide in foods to protect public health.

L-ASNase is one of the therapeutic enzymes with the highest global production. It contributes 40% of the total global demand for enzymes with general use. In addition, it represents approximately one-third of the world's requirement for antileukemic and antilymphoma agents. Thus it is one of the enzymatic products with major industrial potential (Vimal and Kumar, 2017). In 2017, its global demand was approximately USD 380 m, and it is estimated to reach USD 420 m by 2025 (Alam et al., 2019). Currently, there are various formulations of L-asparaginase available in the market for clinical use, including those of bacterial origin such as native, PEGylated, and recombinant L-asparaginases from *Escherichia coli* (*E. coli*), as well as native L-asparaginases from *Erwinia chrysanthemi* (*E. chrysanthemi*). Additionally, fungal-derived asparaginases approved for food use, such as those from *Aspergillus oryzae* and *Aspergillus niger*, are also available (Battistel et al., 2021; Jia et al., 2021). All these formulations have been tested to improve their safety profiles (Burke, 2014; Effer et al., 2020; de Almeida Parizotto et al., 2021). However, Due to standard l-asparaginase preparations carries low thermostability, occurrence of side effects and restricted substrate specificity, these applications have been hampered by the diverse conditions frequently seen in the food and healthcare sectors (Zhang et al., 2021). Hence, it is of paramount importance to search for products that allow for the improvement of their properties, such as increased l-ASNase activity, reduced glutaminase activity, and stability for human physiological conditions in the therapeutic case, and improved L-ASNase activity and thermal stability for the food industry, while carefully considering the composition employed in their production, such as the immunological effects triggered by the bacterial-derived L-ASNase itself (Kishore et al., 2015; Wang et al., 2021).

Currently, several reviews have been attempted compiling L-Asparaginases from various sources that are able to improve both pharmacokinetics, reduce side effects and stability (Batool et al., 2016; Wang et al., 2021; Patel et al., 2022). Additionally, thanks to the principles of Quality by Design (QbD), several techniques have been proposed to overcome the disadvantages of

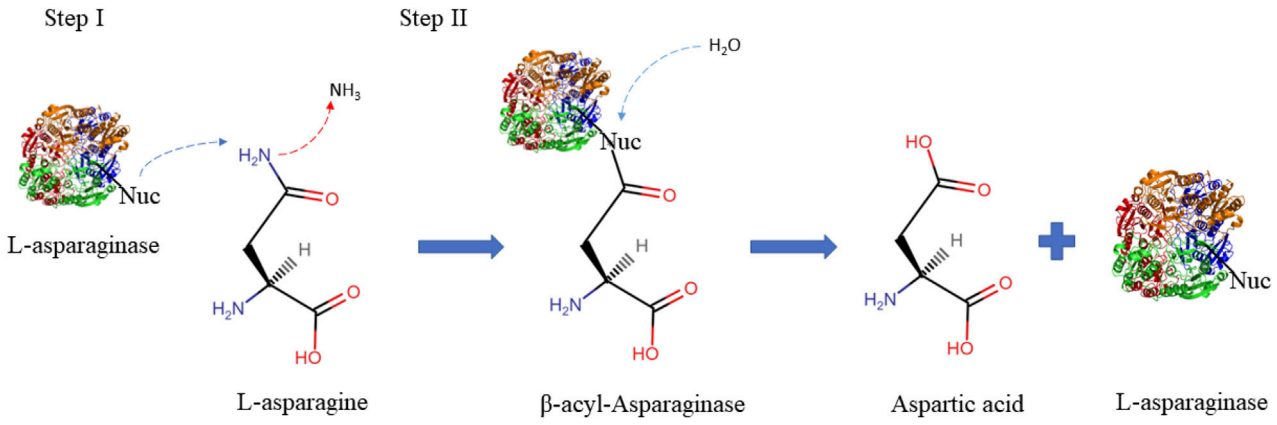

FIGURE 1
Schematic illustration describing the two steps L-asparaginase reaction mechanisms. The first step consists of activating the enzyme's nucleophilic residue with the strong base NH2, which then attacks the l-asparagine amide carbon atom to produce the beta-acyl-enzyme intermediate. The second step involves activating the nucleophile with a water molecule, which attacks the ester carbon repeatedly to produce l-aspartic acid and release ammonia (Nunes et al., 2020). Nuc: nucleophilic residues.

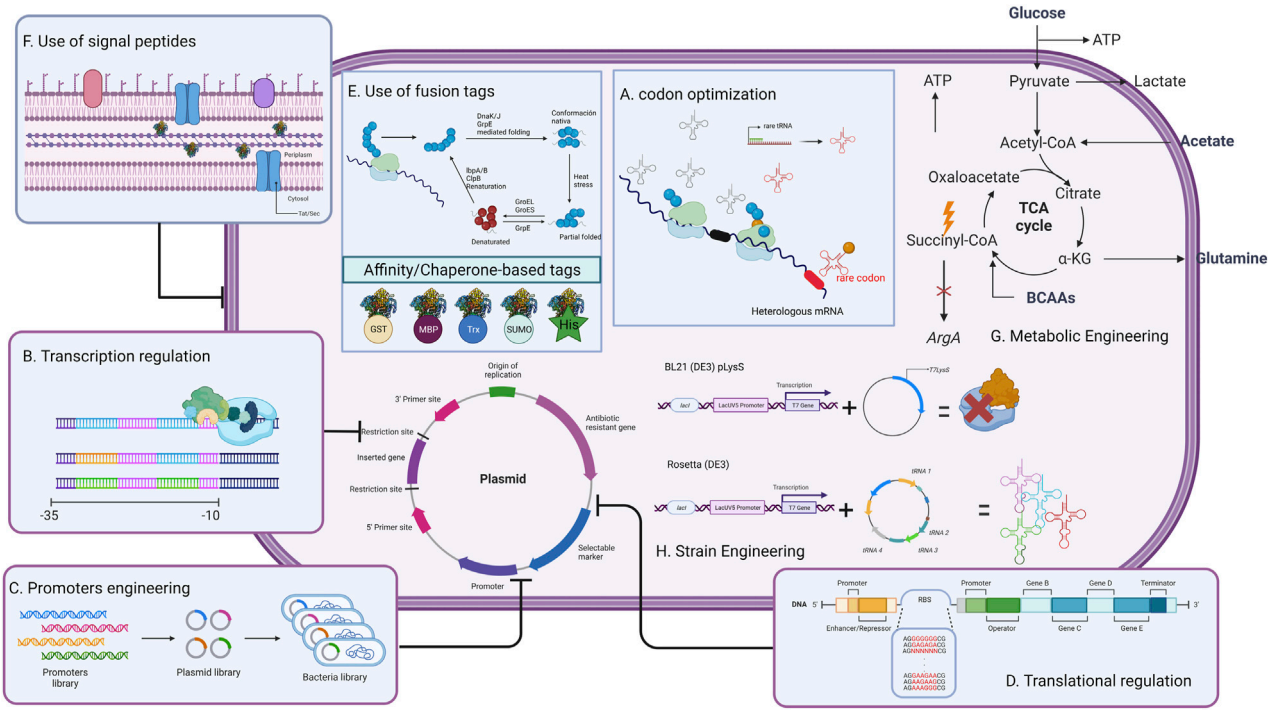

FIGURE 2
General strategies to improve L-ASNase production in heterologous host systems. This strategy can be modified depending on the difficulties that may arise during expression.

the treatment, allowing the development of L-ASNases "bio-betters" (Brumano et al., 2019; Nunes et al., 2020). Each of these attempts aims to express these L-ASNases in heterologous hosts that allow them to be produced efficiently, economically, and easily. However, expressing a different or modified host protein from a different organism presents several challenges.

In this review, the main genetic modifications and current strategies developed to improve L-ASNase expression in microbial heterologous systems, including codon optimization, transcriptional regulation, promoter engineering, translation regulation, optimization of factors affecting expression, and host strains genetic and metabolic engineering (Figure 2), will be discussed. Special attention will be paid to *E. coli*, *Bacillus subtilis* and *P. pastoris*, which are the preferred hosts for L-ASNase expression. Finally, future challenges for the rational design of heterologous systems for L-ASNase expression are discussed.

2 Type and characteristics of L-ASNase in organisms

L-ASNase is widespread, and can be found in animals, plants, and microorganisms such as bacteria, fungi, and yeasts, and even in various thermophilic organisms. Any of these organisms can be a potential source for L-ASNase production. However, not all sources are equivalent (Castro et al., 2021). L-ASNase has been conventionally classified according to amino acid sequence, the organism expressing it, inducibility, cellular localization, substrate affinity, and quaternary structure into three families: 1) bacterial, 2) plant, and 3) rhizobial (Michalska and Jaskolski, 2006; Loch and Jaskolski, 2021). However, this classification has been disputed due to the absence of the thermophilic group. According to Dumina et al. (Dumina et al., 2021), thermophilic L-ASNases differ from mesophiles both in their structural properties (they can be found in a hexameric form (Pritsa and Kyriakidis, 2001)), topological properties, deviation in the canonical arrangement of their active site, etc. For this reason, a new classification for thermophilic L-ASNases (class IV) proposed by the authors would be included in this review (Figure 3). Bacterial class L-ASNases can be subdivided into two different isozymes: Type I and II L-ASNases. Type I L-ASNases (EcA I) is a homodimeric constitutive enzyme located in the cytoplasm, with low affinity for L-asparagine and high affinity for L-glutamine (Pokrovskaya et al., 2022). Among the Type I enzymes, L-ASNases produced by *B. subtilis* (Jia et al., 2013; Feng et al., 2017; Jia et al., 2021; Niu et al., 2021), *Thermococcus kodakarensis* (Chohan and Rashid, 2013; Hong et al., 2014), and *Acinetobacter soli* (Jiao et al., 2020) are the most studied examples. Type II bacterial L-ASNases (EcAII), normally a homotetrameric form and located in periplasmic space with expression induced during anaerobiosis and are secreted only when bacteria are exposed to low nitrogen concentrations (Verma et al., 2007). Their properties have been discussed in *E. coli, Erwinia carotova, Erwinia chrysantemi, Saccharomyces cerevisiae,* etc (Yano et al., 2008). Although both isozymes exhibit enzymatic activity for l-asparagine and l-glutamine, their affinity for L-asparagine is what distinguishes them from one another. Since EcAII has a higher specific affinity for l-asparagine, which results in high antitumor activity and is therefore the one used in medicinal

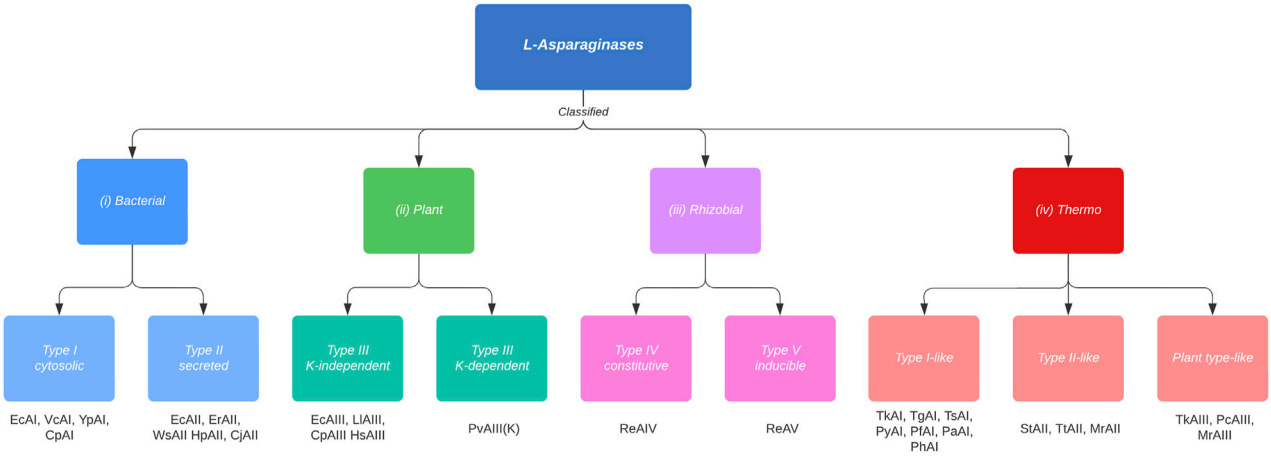

FIGURE 3
Classification and types of L-asparaginases based on the new criteria proposed by Loch and Jaskolski (Loch and Jaskolski, 2021), adding the thermophiles classification (Class IV) proposed by Dumina and Zhgun (Dumina and Zhgun, 2023). Cytosolic Class I, type I enzymes are constitutively expressed, whereas the expression of type II enzymes, which are secreted into the periplasm, is induced under anaerobic conditions. Class II enzymes have dimeric structure, which are subdivided into potassium-dependent and potassium-independent type III enzymes. This dependence arises due to a K^+ coordination to the side chain of Arginine 104, which allows anchoring of the substrate to the active site. In Rizhobial Class III, constitutive type IV enzymes are thermostable, whereas type V enzymes are considered thermolabile and their expression is induced by the presence of l-Asn. Class IV (thermophiles) enzymes are subclassified into type I-like, type II-like and type plant-like. Type I-like enzymes differ from mesophiles in their structure (thermophiles are homodimers) and in their amino acid identity (<37% identity). Type II-like enzymes reveal a rather reduced identity compared to mesophylls and they form structures different from mesophylls (homodimeric and hexameric structures). Finally, the plant-like types present dimeric structures, like mesophylls, however, they can withstand high temperatures due to their amino acid divergence (<50% identity). Examples of enzymes are listed below the boxes. The organism name abbreviations are as follows: Ec, Esherichia coli; Pf, Pyrococcus furiosus; Ph, Pyrococcus horikoshii; Py, Pyrococcus yayanossi; Pa, Pyrococcus abyssi; Pc, Pyrobaculum calidifontis; St, *Streptomyces* thermoletus; Tt, Thermus thermophilus; Tk, Thermococcus kodakarensis; Tz, Thermococcus zilligii; Tg, Thermococcus gammatolerans; Ts, Thermococcus sibiricus; Mr, Melioribacter roseus; Vc, *Vibrio cholerae*; Yp, *Yersinia pestis*; Cp, *Cavia porcellus*; Er, *Erwinia* chrysanthemi; Ew, *Erwinia* carotovora; Cj, *Campylobacter* jejuni; Hp, *Helicobacter pylori*; Ws, Wolinella succinogenes; Ll, Lupinus luteus; Pv, Phaseolus vulgaris; Hs, *Homo sapiens*; Re, Rhizobium etli.

applications (Sharafi et al., 2017). To get an idea, the EcAII K_M (Michaelis-Menten constant) = 10–15 μM *versus* EcAI K_M = 3.5 mM. This means that enzymes EcAII display much higher (2+ orders of magnitude) affinity for L-asparaginase than EcAI (Nunes et al., 2020). Microbial enzymes, like EcAII, are more suitable than their animal and plant counterparts as they provide a consistent profile, stability, relative ease of production and purification, High yields and consistency; simplifying the modification and optimization of the manufacturing process (Lopes et al., 2017; Vachher et al., 2021).

Commercially, there are two products currently available for acrylamide mitigation in the food industry. These are PreventASe TM from DSM (Heerlen, Netherlands) and Acrylaway® from Novozymes A/S (Bagsvaerd, Denmark). PreventASe TM was the first, launched in 2007. It was obtained after analyzing the gene sequence of *Aspergillus niger*. It has an acidic profile (optimum pH 4-5, temperature 50°C). Acrylaway®, on the other hand, is obtained from *Aspergillus oryzae* and has a near-neutral profile (pH optimum 7, temperature 37°C) (Xu et al., 2016). As for its safety, it has been observed over the years that there are no hazards in its use and these are recognized as safe by the U.S. government and are currently used in several countries, including the U.S., Australia, China, Russia, Mexico, etc. (Xu et al., 2016). Additionally, several products are currently available for anti-leukemia treatment. Elspar®, Oncaspar® (Pegaspargase), Crisantaspase®, Kidrolase®, and Erwinase® or Erwinaze® are some of the commercially available brands of ASNase. Elspar® contains L-asparaginase derived from *E. coli*. Oncaspar® is a modified version of Elspar® obtained by covalent conjugation of *E. coli* asparaginase with monomethoxypolyethyleneglycol (PEG), to increase the plasma half-life and decrease the immunogenicity and antigenicity of L-asparaginase. However, a higher prevalence of side effects has been observed (Galindo-Rodríguez et al., 2017). Crisantaspase® and Erwinase® are obtained from *Erwinia chrysanthemi*. The former is often used in combination with other anticancer drugs, while the latter is used in conjunction with chemotherapy or radiotherapy as part of treatment protocols. *Escherichia coli* Kidrolase® is used in the treatment of ALL, leukemic meningitis, and non-Hodgkin's lymphoma (Izadpanah Qeshmi et al., 2018). All these formulations have been tested to improve their safety (Burke, 2014; Effer et al., 2020; de Almeida Parizotto et al., 2021; Munhoz Costa et al., 2022).

Nevertheless, microbial L-ASNase II presents several problems when administered as an antileukemic drug, including severe allergic reactions, nausea, diabetes, pancreatitis, and venous thromboembolism (Goyal and Bhatt, 2015; Schmiegelow et al., 2016).

3 The search for the production of an improved heterologous L-ASNase with commercial value

In recent years, several biological sources of L-ASNase able to tackle some of the mentioned issues through engineering have been

explored. These endeavors have yielded L-ASNases with. 1) reduced immunogenic activity or allergic reactions, 2) high catalytic activity, and 3) low-cost up and downstream processing (Patel et al., 2022). It has been observed that L-ASNases in eukaryotes, such as fungi and yeasts, can result in enzymes with fewer adverse effects and advantageous characteristics (Cachumba et al., 2016). For example, L-ASNase I from the yeast *Saccharomyces cerevisiae* (ScASNaseI) and expressed in *E. coli* BL21 (DE3) has been studied (Munhoz Costa et al., 2016). This is because it was predicted to be a bacterial type II isoform, being a possible candidate as an antileukemic agent. The specific activity of L-asparagine in ScASNaseI was 196.2 U/mg, a value similar to the commercial ASNase activity of *E. coli* (223 U/mg). This enzyme maintains allosteric behavior and localization in the cytosol of the enzyme, as in the case of type I enzymes, but with a k_M of 75 μM as in type II enzymes. In addition, they performed specific activity tests for L-glutamine, presenting 0.38% of L-asparaginase activity, and cytotoxicity tests on MOLT-4 leukemia cells, killing 85% of the cells under physiological conditions (pH 7.4 at 37°C), with optimal activity at pH 8.6 and at 40°C. This enzyme is compatible with the treatment of leukemia. However, alternative sources to bacteria and fungi are currently being explored (Patel et al., 2022). For example, marine microorganisms would produce L-ASNases capable of withstanding pH, salinity, and pressure conditions similar to those of blood plasma. (Qeshmi et al., 2018). A study focused on the cloning, expression, and characterization of L-asparaginase from marine *Pseudomonas aeruginosa* HR03 isolated from fish intestines in *E. coli* BL21 (D3) as a host. The recombinant L-asparaginase (HR03Asnase) was purified and its enzymatic properties were determined. The maximum activity of the enzyme was observed at 40°C and pH 8. The study suggests that HR03Asnase has potential for commercial applications in the food and health industries (Izadpanah Qeshmi et al., 2022). Additionally, thermophilic microorganisms would have been studied which can produce L-ASNases that remain stable at high temperatures, which are potentially suitable for the food industry (Dumina and Zhgun, 2023). A study, identifies a new thermostable L-asparaginase from *Pyrococcus yayanosii* CH1 expressed in *B. subtilis* 168. This L-ASNase was characterized by obtaining a maximum volumetric yield of 1483.81 U/mg, a maximum activity at 95°C and pH 8, making it suitable for industrial food application (Li et al., 2018).

In addition to this, several techniques have been proposed to overcome the disadvantages of native ASNases, improving it obtaining novel bio-betters ASNases. The term bio-better, refers to creating novel drugs by enhancing the features of current peptide- or protein-based biopharmaceuticals, such as affinity, selectivity, immunogenicity, and stability against degradation of proteases (Beck, 2011; Lagassé et al., 2017). These proteins are manufactured from molecular and/or chemical modifications of an original product to improve drug characteristics (Courtois et al., 2015). Molecular strategies like protein engineering by bioinformatics analysis, docking, molecular dynamics and site-directed mutagenesis have been mentioned among the most sophisticated techniques (Nguyen et al., 2016a; Ardalan et al., 2018; Mundaganur et al., 2014; Munhoz Costa et al., 2022). An investigation, by means of directed evolution methodology, succeeded in obtaining a double mutant ASNase from *E. chrysanthemi* expressed in *E. coli* BL21 (DE3). This mutant L-ASNase, besides having a specific activity 46% higher than the wild type L-ASNase, also presents a reduction of the glutaminase activity by 40% and a decrease of the immunogenic effect of 62.5%, being this a promising enzyme in the pharmaceutical industry (Munhoz Costa et al., 2022). Chemical modifications such as scFv-fusion, TRAIL domain-fusion, albumin binding-fusion, PEGylation, PASylation and bioconjugations have been employed (Guo et al., 2000; Abribat, 2023; Trieu, 2010; Lavie and Nguyen 2017; Brumano et al., 2019). A chemical modification of a commercial biosimilar *E. coli* L-ASNase (Leunase® (Kyowa Hakko Kirin, Japan)) was studied by direct conjugation of carboxyl groups to primary amines by 1-ethyl-3-(3-dimethylaminopropyl) carbodiimide (EDC) (Chahardahcherik et al., 2020). In this case, a polymer called carboxymethyl dextran (CMD) was used, which is biologically compatible. The results showed a substantial increase in the specific activity of the modified L-ASNase compared to the commercial one (1609.62 vs 629.8 U/mg). Additionally, an increase in half-life stability in rat serum of 192 h with the modified L-ASNase *versus* 96 h with the native one, and an improvement in temperature and pH stability were observed. In recent years, bio-better proteins have gained considerable industrial attention, as they are patentable and have higher prices in the market due to their clinical advantages (Brumano et al., 2019).

For large-scale processes, biopharmaceutical production from wild strains host is generally avoided. This is mainly due to low yield and high production costs. To overcome the problems faced by conventional L-ASNase production, one approach would be to use recombinant DNA technology, to transfer genes that encode the enzyme, from one microorganism to another. This is called heterologous expression (Li et al., 2019). Heterologous expression allows the relatively stable, safer expression of enzymes, with higher yields (Patel et al., 2022). There are several expression systems available for biopharmaceutical purposes, including bacteria, yeast, filamentous fungi, mammalian cells, plants, insects, transgenic animals, and even microalgae (dos Santos et al., 2018). Each system has its particular features in terms of production capacity, costs, safety, complexity, and specific processing (Schmidt, 2004). The use of complex and costly expression systems, such as mammalian cells (CHO, insects, etc.), are generally used for proteins that require complex post-translational modifications, which in the case of L-ASNase are not necessary. Concerning the use of plant-based expression systems, these display several disadvantages due to the large numbers of proteases present in their cells, making extraction and purification challenging for large-scale enzyme production (Patel et al., 2022). The high secretors and the host strains of bacteria (e.g., *E. coli, Bacillus* and lactic acid bacteria), filamentous fungi (e.g., *Aspergillus*) and yeasts (e.g., *Pichia pastoris*) are most commonly used for the homologous and heterologous expression of recombinant enzymes without complex post-translational modifications (Goswami et al., 2015). Among these, *E. coli*, *B. subtilis* and *P. pastoris* are used for the production of L-ASNase, since these can quickly and easily overexpress (Wang et al., 2021; Patel et al., 2022). However, the yields of L-ASNase production depend not only on host selection. But also of the fermentation process, and the efficiency of the

expression systems (Li et al., 2019). The requirements for a successful high-throughput process for protein production as: 1) high transcription, and translation of genes of specific protein, 2) correct folding, and induction that does not cause stress to the host, 3) desired post-translational modifications, 4) efficient secretion, and limited or no degradation of the product in the culture medium (Kaur et al., 2018).

4 Improvement in systems for L-ASNase heterologous expression

As previously mentioned, the design of an efficient bioprocess strategy is essential for a profitable industry of clinically relevant recombinant proteins. Heterologous protein expression using genetically modified prokaryotic hosts has made it possible to provide a wide range of recombinant proteins. This production, would not be feasible without this technology, as the wild-type cells are not prepared to provide it, in a scalable and rentable manner (Kim et al., 2020). Yet, there are challenges and limitations in the use of these systems. Generally, heterologous expression of proteins has various problems, such as: inadequate folding, heavy molecular weight, or the presence of multiple membrane domains in the protein; cellular metabolic burden, codon usage differences, and sequence repetitiveness that affect translation. For example, one study reported that the heterologous expression of l-asparaginase from *Rhizomucor miehei* in *Pichia pastoris* resulted in low protein expression levels and low enzyme activity due to suboptimal transcriptional and translational regulation (Zhang et al., 2021). Effer et al. (Effer et al., 2019) discusses the evaluation of extracellular expression into *P. pastoris* Glycoswitch VR using two different plasmid constructions containing the *asnB* gene (encoding for L-ASNase of *Erwinia chrysanthemi*), with and without His-tag, to find the best system for producing the extracellular and biologically active protein. The study found that the His-tag could negatively affect the tetrameric conformation of L-asparaginase and possibly affect proper protein folding. This could lead to most of the proteins being accumulated for degradation through ER-associated degradation (ERAD), resulting in low extracellular L-asparaginase production. Another study discusses the effect of hydrophobic region on the signal peptide on L-asparaginase secretion and inclusion bodies (IB's) formation in *E. coli* (Naderi et al., 2022).

Results showed that increasing hydrophobicity of the signal peptides did not necessarily improve secretion efficiency, and in some cases, increased IB's formation. IB's are insoluble protein aggregates generated by the metabolic burden that cells undergo upon induction (Vallejo and Rinas, 2004). The problem of IB's formation or misfolding is further aggravated in the case of L-ASNase. This is mainly because L-ASNase II is fully active in its tetrameric form. This is because the active-site pocket consists mainly of one protomer and is complemented by several residues from the second protomer within a compact dimer (Lubkowski and Wlodawer, 2021) (Figure 4). Therefore, when IB or misfolding occurs, it is required to refold into its native form to maintain its bioactive properties (Mihooliya et al., 2022). Considerable effort has gone into downstream processing involving isolation, solubilization, renaturation (refolding), and purification to obtain the soluble, bioactive protein (Kante et al., 2018). Researchers have achieved up to 50% recovery of functional L-ASNase using various strategies such as the use of strong chaotropic agents (Kante et al., 2018), pulse dilution method (Upadhyay et al., 2014), Freeze-Thaw method (Singhvi et al., 2021), refolding in periodic counter-current chromatography (PCC) (Rajendran et al., 2022), among others. However, these steps are time consuming; require major equipment such as new generation chromatographs, ultrafiltration and diafiltration systems, hydraulic intensifier systems, etc; a large number of reagents such as chaotropic agents, micelles, liposomes, detergents, etc; and use large volumes (generally 1–10 L for mg quantities of protein) (Clark, 2001; Singh et al., 2015; Yuan et al., 2015). Additionally, these strategies are tedious and require large amounts of steps, even more in the case of multimeric proteins, because it requires first a correct renaturation and solubilization of the inactive monomers, for their subsequent refolding of their tetrameric structure under various physiological conditions (Upadhyay et al., 2014; Mihooliya et al., 2022).

Hence, the rational design of vector systems that include the optimization of codons, transcription regulation, optimization of promoters, translation regulation, the optimization of factors that affect expression in the soluble fraction, co-expression of molecular chaperones and secretion strategies, would bolster the production of the proteins of interest (Juturu and Wu, 2018; Kim et al., 2020; Kant Bhatia et al., 2021) (Figure 5). Table 1 presents the production of heterologous L-ASNase from several sources, together with its expression systems, reviewed in this article.

4.1 Codon optimization to improve L-ASNase expression

Messenger RNA (mRNA) of a heterologous gene that contains rare codons can cause significant translation issues, such as stagnation of translation, mRNA and plasmid instability, incorrect amino acid incorporation, displacement of the translation frame, and premature translation completion. In due process, these issues lead to a reduction in the quality and quantity of the synthesized protein (Singha et al., 2017). Codon Optimization can be achieved by replacing rare codons with the original ones, thus adjusting codon bias (Juturu and Wu, 2018).

Codon optimization studies have been performed for the expression of L-ASNase from *Erwinia chrysanthemi* NCPPB1125 in *E. coli* BL21. In this study, codons were optimized and inserted in a pET-21a(+) vector. After adjusting induction and purification conditions, the specific activity reached 312.8 U/mg, which increased 1.5-fold control activity (Nguyen et al., 2016b). Furthermore, the activity of three new uncharacterized extremophilic L-ASNases produced by psychrophilic fungus *Sclerotinia borealis*, thermoacidophilic crenarchaeon *Acidilobus saccharovorans* and thermophilic bacterium *Melioribacter roseu.* The L-ASNase were expressed in *E. coli*, and their codon composition was optimized using the "Twist Codon Optimization" (Twist Bioscience, USA) tool (TwistBioscience, 2022). This strategy allowed to obtain activities of 0.6 U/mL at 24°C and pH 9.6 for *S. borealis*; 2.6 U/mL at 94°C and pH 5.2 for *A. saccharovorans*; and 9.6 U/mL at 37°C and pH 9.6 for *M. roseu* (Dumina et al., 2021).

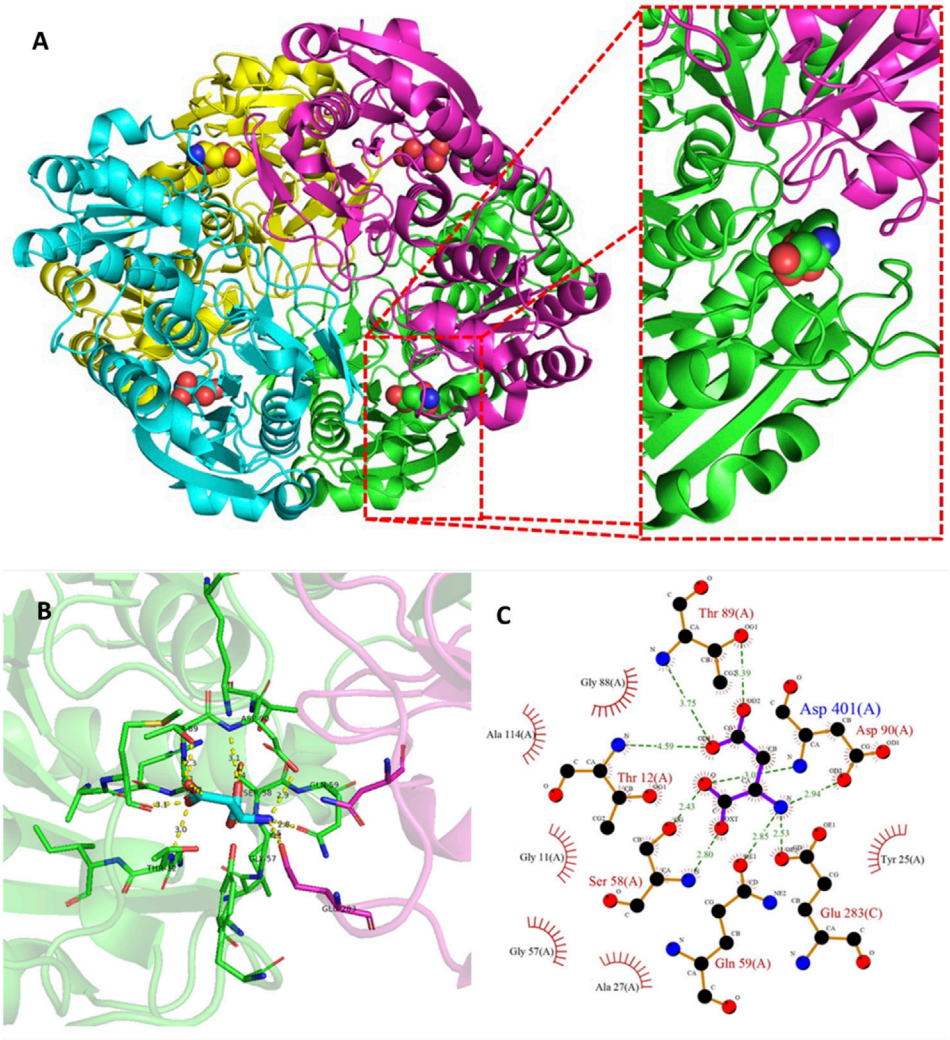

FIGURE 4
Tetramer structure of L-ASNase and the active site of the enzyme. **(A)** A cartoon representation of the *E. coli* type II L-ASNase homotetramer (PBD 3ECA). **(B)** The active-site pocket which is representative for type I and II L-ASNases. The green monomer represents a major part of the active site, contributing five amino acid side chains directly involved in L-ASNase catalysis. On the other hand, a flexible active site loop is found in the purple monomer, which contains two residues, including the primary nucleophile Thr12. These figures were prepared with PyMOL (Schrödinger). **(C)** Ligand-protein interaction diagram of the l-asparagine binding site generated by LigPlot+ (Laskowski and Swindells, 2011). The interaction of l-asparagine with the 2D residues can be seen. Hydrogen bonds are shown as green dotted lines, while radial arcs represent residues that make non-bonded contacts with the ligand.

The L-ASNase of *Z. mobilis* was expressed intracellularly, using pET-28a as vector and extracellularly, using pET-26b, in *E. coli* BL21 (DE3). The yield obtained was 0.13 and 3.6 U/mL, respectively. Results were obtained after codon optimization to better match the host. Therefore, only the extracellularly expressed protein represented an improvement in expression, as native culture in cultures of *Zymomonas mobilis* yield 0.25 U/mL (Einsfeldt et al., 2016)- Recently, a study was conducted *in silico* on the L-ASNase gene of a halophilic bacterium using bioinformatics tools. This study spotted 5 residues associated with rare codons located distant from the active site. These residues can play a role in determining the final structure of the enzyme's binding site and its substrate (Mortazavi et al., 2020).

4.2 Transcription regulation to improve L-ASNase expression

The fine interaction between activator, inducer and repressor molecules, is responsible for the regulation of the biosynthetic pathways at a transcription level. Transcription factors are necessary for the expression and production of enzymes (Kant Bhatia et al., 2021). According to Zhou et al. (Zhou et al., 2019), the transcription strength of a promoter is directly related to its core region (−35 and −10 boxes) for *B. subtilis* hosts, and the optimization of these conserved regions was considered one of the important strategies to increase the yield of recombinant proteins.

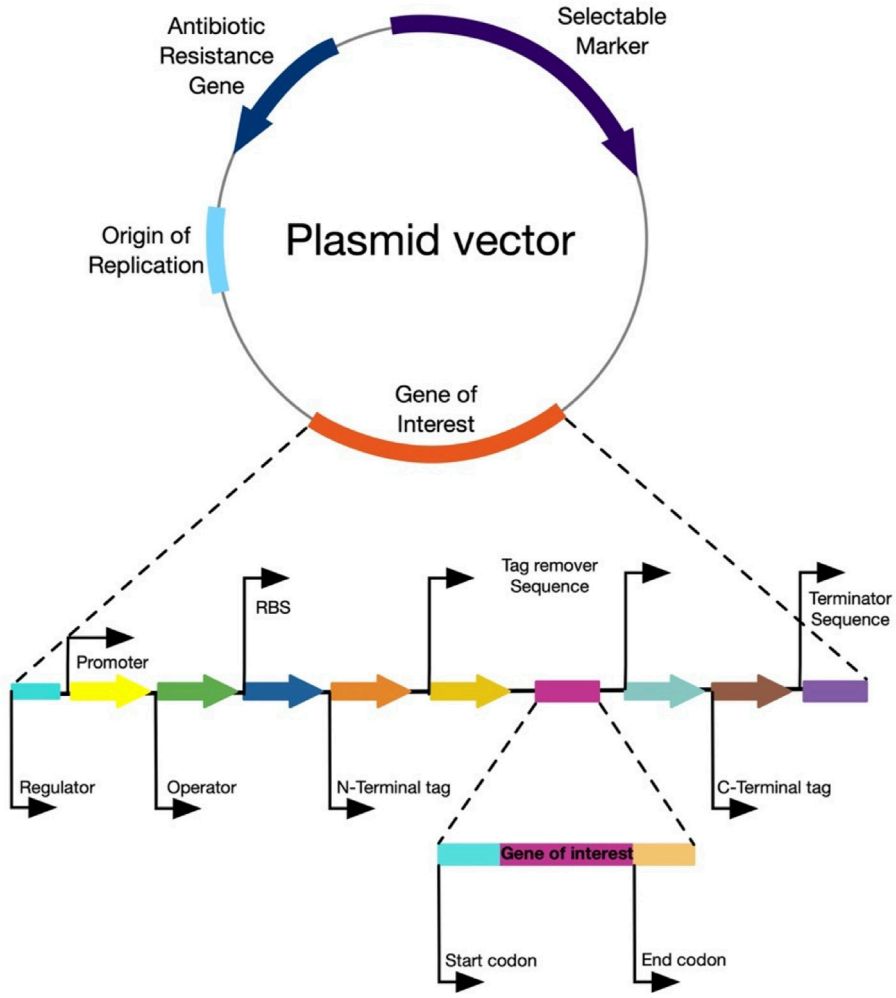

FIGURE 5
General structure of an expression vector. The figure represents the main components of an ideal expression vector for any host microorganism.

A study on L-ASNase production using a dual promoter system, by modifying the −35 and −10 sequences of these promoters, resulted in three mutations. The mutations achieved 6.6%, 7.3%, and 13.3% improvements in expression levels and 4.37-, 4.15-, and 4.86-fold higher transcript intensity compared to the P43 promoter. After 36 h of culture, the expression level in a 10 L fermenter reached 2163.09 U/mL, which was 6.2-fold higher than that of the wild-type strain (based on the P43 promoter) (Niu et al., 2022).

4.3 Engineering of promoters to improve transcription of L-ASNase expression systems

The promoter plays a key role in an expression system as its controls the initiation of transcription of the associated genes. An ideal promoter should possess two desirable features: 1) sufficient strength to allow the accumulation of the product up to 50% of total cellular proteins, and 2) strict regulation to prevent product toxicity (Kaur et al., 2018). The choice of promoter depends on the host being used.

In the case of *E. coli*, the main promoters, when expressing a recombinant protein, are derived from bacteria (lac, tac, trp, araBAD) and bacteriophages (T7, T5, SP6) (Kaur et al., 2018). The T7 promoter, derived from bacteriophage T7, is one of the most used promoters due to its extensive use in the pET expression system. Many studies on L-ASNase production are based on the use of pET systems (Khushoo et al., 2005; Kotzia and Labrou, 2007; Cappelletti et al., 2008; Aghaeepoor et al., 2011; Vidya and Pandey, 2012; Chohan and Rashid, 2013; Roth et al., 2013; Hong et al., 2014; Huang et al., 2014; Upadhyay et al., 2014; Zuo et al., 2014; Ghoshoon et al., 2015; Costa et al., 2016; Sannikova et al., 2016; Radha et al., 2018; Saeed et al., 2018; Shakambari et al., 2018; Goswami et al., 2019; Jiao et al., 2020; Maqsood et al., 2020). This is primarily because of the promoter's efficiency in significantly increasing transcription levels. Several studies have assessed the use of these promoters, and the highest reported L-ASNase reached 978.7 U/mg. This particular L-ASNase is from *T. kodakarensis* KOD1 and was expressed in *E. coli* BLR(DE3) (Hong et al., 2014).

TABLE 1 Production of recombinant L-ASNase and its heterologous expression systems.

Microorganism	Vector	Host cells	Promoter	Secretion signal	Localization		Fermentation type	Enzyme activity	Reference
Anoxybacillus flavithermus	pET-22b (+)	*E. coli* BL21-Codon Plus (DE3)-RIL	T7- IPTG inducible	Without signal peptide	Intracellular	NR	SmF	2.5 U/mL	Maqsood et al. (2020)
Aspergillus terreus	pET-28a (+)	*E. coli* BL21(DE3)	T7- IPTG inducible	Without signal peptide	Extracellular/periplasmic	Shake-flask	SmF	4.81 U/mg	Saeed et al. (2018)
Acinetobacter soli Y-3	pET-30a	*E. coli* BL21(DE3)	T7- IPTG inducible	Without signal peptide	Intracellular	NR	NR	42 U/mg	Jiao et al. (2020)
Bacillus subtilis B11-06	pMA5	*B. subtilis* 168	HpaII-constitutive	Without signal peptide	Extracellular/periplasmic	Shake-flask	SmF	9.98 U/mL	Jia et al. (2013)
Bacillus subtilis 168	pP43NMK	*B. subtilis* WB600	P43- constitutive	WapA signal peptide	Extracellular	Fed-batch (3L)	SmF	407.6 U/mL	Feng et al. (2017)
Bacillus licheniformis Z-1	pP43NMK	*B. subtilis* RIK 1285	P43-constitutive	Native signal peptide	Extracellular/periplasmic	Shake-flask	SmF	426 U/mL	Niu et al. (2021)
Bacillus licheniformis Z-1	pP43NMK-BlA-His	*B. subtilis* RIK 1285	PaprE-PyvyD (dual)-constitutivo	Native signal peptide	Extracellular/periplasmic	Batch (4L)	SmF	2163.09 U/mL	Niu et al. (2022)
Bacillus tequilensis PV9W	pET-28a (+)	*E. coli* BL21(DE3)	T7- IPTG inducible	Without signal peptide	Intracellular	NR	NR	24.55 U/mL	Shakambari et al. (2018)
Cobetia amphilecti AMI6	pQE-80L	*E. coli* BL21(DE3)	T5- IPTG inducible	Without signal peptide	Intracellular	Shake-flask	SmF	778 U/mg	Farahat et al. (2020)
Erwinia carotovora	pET30a	*E. coli* C43 (DE3)	T7- IPTG inducible	Without signal peptide	Cytoplasmic	Fed-batch	SmF	0.9 g/L	Roth et al. (2013)
Erwinia carotovora	pET-22b	*E. coli* BL21(DE3)	T7- IPTG inducible	PelB	Intracellular	Shake-flask	SmF	16.05 U/mL	Goswami et al. (2019)
Erwinia chrysanthemi 3937	Pcrt7/CT-TOPO	*E. coli* BL21 (DE3) pLysS	T7- IPTG inducible	Without signal peptide	Intracellular	NR	NR	25.5 U/mL	Kotzia and Labrou (2007)
Erwinia chrysanthemi	pJAG-s1	*Glycoswitch* SuperMan5 (his-)	AOX1-MeOH inducible	αMF	Extracellular	Shake-flask	SmF	0.456 U/mL	Effer et al. (2019)
Erwinia chrysanthemi	pJAG_s1	*Glycoswitch* SuperMan5 (his+)	AOX1-MeOH inducible	αMF	Extracellular/periplasmic	Fed-batch (2L)	SmF	10.7 U/mL	de Almeida Parizotto et al. (2021)
Erwinia Chrysanthemi NCPPB1125	pPICZαA	*P. pastoris* X33 and *P. pastoris* SMD1168	AOX1-MeOH inducible	αMF	Extracellular	Shake-flask	SmF	1.88 and 3.3 U/mL	Tien Cuong Nguyen (2014)
Escherichia coli (AnsB)	pJAG-s1	*Glycoswitch* SuperMan5 (his-)	AOX1-MeOH inducible	αMF	Extracellular/periplasmic	Shake-flask	SmF	2.98 U/mg	Lima et al. (2020)

(Continued on following page)

10.3389/fphar.2023.1208277

TABLE 1 (*Continued*) Production of recombinant L-ASNase and its heterologous expression systems.

Microorganism	Vector	Host cells	Promoter	Secretion signal	Localization		Fermentation type	Enzyme activity	Reference
Escherichia coli (AnsB)	pET3a	*E. coli* BL21(DE3)	T7- IPTG inducible	PelB	Periplasmic	Fed-batch	SmF	130 U/mL	Aghaeepoor et al. (2011)
Escherichia coli (AnsB)	pET14b	*E. coli* BLR(DE3)	T7- IPTG inducible	PelB	Extracellular	Fed-batch	SmF	870 U/mL	Khushoo et al. (2005)
Escherichia coli K12 (*AnsB*)	pET-26b(+)	*E. coli* BL21 star (DE3)	T7- IPTG inducible	PelB+5 aspartate	Extracellular/periplasmic	Shake-flask	SmF	40.8 U/mL	Kim et al. (2015)
Mutant *Escherichia coli*	pET-SUMO	*E. coli* Rosetta	T7- IPTG inducible	Without signal peptide	Intracellular	Fed-batch	SmF	183.5 U/mg	Caetano (2020)
Escherichia coli MTCC 739	pPink α-HC	*Pichiapink*™	AOX1-MeOH inducible	αMF	Extracellular	NR	SmF	2.18 U/mL	Sajitha et al. (2015)
Escherichia sp. NII	pET-20b	*E. coli* BL21(DE3)	T7- IPTG inducible	PelB	Periplasmic	NR	NR	140 U/mL	Vidya and Pandey (2012)
Escherichia coli AS1. 357	pBV220	*E. coli*	P_RPL-heay inducible	Native signal peptide	Intracellular	NR	NR	228 U/mL	Wang et al. (2001)
Escherichia sp	COLADuet-P21285-asn	*E. coli* BL21(DE3)	P21285-IPTG inducible	Without signal peptide	Intracellular	Shake-flask	SmF	3.68 U/mL	Wang et al. (2019)
Escherichia coli K-12 (JM109)	pET14b	*E. coli* BL21(DE3)	T7- IPTG inducible	Without signal peptide	Cytoplasmic	Shake-flask	SmF	118 g/L	Upadhyay et al. (2014)
Escherichia coli YG 002	pET-15b	*E. coli* BL21(DE3)	T7- IPTG inducible	Native signal peptide	Extracellular	Shake-flask	SmF	17.4 U/mL	Ghoshoon et al. (2015)
Helicobacter pylori CCUG 17874	pET-101	*E. coli* BL21(DE3)	T7- IPTG inducible	Without signal peptide	Intracellular	NR	NR	31.2 U/mg	Cappelletti et al. (2008)
Norcadopsis alba NIOT-VKMA08	pQE-30	*E. coli* M15	T5- IPTG inducible	NR	Extracellular/intracellular	Shake-flask	SmF	158 U/mL	Meena et al. (2016)
Pseudomonas fluorescens MTCC 8127	pET-32a	*E. coli* BL21(DE3)	T7- IPTG inducible	Without signal peptide	Intracellular	NR	SmF	6.4 U/mg	Sindhu and Manonmani (2018)
Penicillium sizovae	pPICZαA	*P. pastoris* X33	AOX1-MeOH inducible	αMF	Extracellular/intracellular	Shake-flask	SmF	3 U/mL	Freitas et al. (2022)
Pectobacterium carotovorum MTCC 1428	pHT43	*B. subtilis* WB800N	grac-IPTG inducible	amyQ	Extracellular	Shake-flask	SmF	105 U/mL	Chityala et al. (2015)
Pectobacterium carotovorum MTCC 1428	pHT43	*B. subtilis* WB800N	grac-IPTG inducible	amyQ	Intracellular	Batch (1L)	SmF	525.98 U/mL	Sushma et al. (2017)
Pyrococcus yayanosii CH1	pMA5	*B. subtilis* 168	P43-constitutive	Without signal peptide	Extracellular/intracellular	Fed-batch (2L)	SmF	5278 U/mL	Li et al. (2019)

(Continued on following page)

10.3389/fphar.2023.1208277

TABLE 1 (*Continued*) Production of recombinant L-ASNase and its heterologous expression systems.

Microorganism	Vector	Host cells	Promoter	Secretion signal	Localization		Fermentation type	Enzyme activity	Reference
Thermococcus kodakarensis KOD1	pET-21a	*E. coli* BLR (DE3)	T7- IPTG inducible	Without signal peptide	Intracellular	Shake-flask	SmF	978.7 U/mg (Purified)	Hong et al. (2014)
Saccharomycescerevisiae (ASP3)	pPIC9	*P. pastoris* GS115	AOX1-MeOH inducible	α-factor signal peptide	Extracellular/periplasmic	Fed-batch (2L)	SmF	85.6 U/mL y 204.4 U/mg (Purified)	[(Ferrara et al., 2006), (Facchinetti de Castro Girão et al., 2016)]
Saccharomycescerevisiae (ASP3)	pPIC9K	*P. pastoris* KM71	AOX1-MeOH inducible	α-factor signal peptide	Periplasmic	Fed-batch (2L)	SmF	3.3 U/mL	Rodrigues et al. (2019)
Saccharomycescerevisiae (ASP3)	pPIC9K	*P. pastoris* KM71	AOX1-MeOH inducible	α-factor signal peptide	Periplasmic	Batch (2L)	SmF	0.71 U/mL	Pillaca-Pullo et al. (2021)
Saccharomycescerevisiae BY4741 (ASP1)	pET-15b	*E. coli* BL21(DE3)	T7- IPTG inducible	NR	Extracellular/periplasmic	Shake-flask	SmF	196.2 U/mg (Purified)	Costa et al. (2016)
Yersinia pseudotuberculosis Q66CJ2	pBAD-24	*E. coli* BL21(DE3)	AraC- arabinose inducible	Without signal peptide	Intracellular	NR	NR	365 U/mL	Pokrovskaya et al. (2012)
Thermococcus kodakaraensis KOD1	pET-21b	*E. coli* BL21-CodonPlus(DE3)-RIL	T7- IPTG inducible	Without signal peptide	Intracellular	NR	NR	2350 U/mL (purified)	Chohan and Rashid (2013)
Rhizomucor miehei CAU432	pET-28a	*E. coli* BL21(DE3)	T7- IPTG inducible	Without signal peptide	Intracellular	Shake-flask	SmF	1985 U/mg (purified)	Huang et al. (2014)
Rhizomucor miehei	pMA5	*B. subtilis* 168	HpaII-constitutive	Without signal peptide	Extracellular	Batch (2L)	SmF	521.9 U/mL	Zhang et al. (2021)
Thermococcus gammatolerans EJ3	pET-22b	*E. coli* BL21(DE3)	T7- IPTG inducible	NR	Intracellular	Shake-flask	SmF	7622 U/mg	Zuo et al. (2014)
Vibrio cholerae	pMCSG7	*E. coli* BL21(DE3)	T7- IPTG inducible	Without signal peptide	Extracellular/periplasmic	Shake-flask	SmF	821 U/mL	Radha et al. (2018)
Wolinella succinogenes	pET28b(+)	*E. coli* BL21(DE3)	T7-IPTG inducible	HB signal peptide	Extracellular/periplasmic	Shake-flask	SmF	238 U/mg	Sannikova et al. (2016)
Zymomonas mobilis	pET26B and pET28a	*E. coli* BL21(DE3)	T7-inducible	pelB signal peptide (pET26b)	Extracellular (pET26b) and intracellular (pET28a)	Shake-flask	SmF	0.13 and 3.6 U/mL	Einsfeldt et al. (2016)

SmF: submerged fermentation; NR: not reported.

10.3389/fphar.2023.1208277

Several studies have been published using promoters other than T7. For example, the production of L-ASNase from *E. coli* AS1.357 in different *E. coli* host strains (JM1105, JM109, TG1, DH5α, and AS1.357) using the pBV220 vector. This vector contains the bacteriophage λ P_RP_L promoter, which is heat-induced. The experiments displayed L-ASNase expression in all the strains examined. However, AS1.357 stood out with the highest expression, achieving an activity of 228 U/mL (Wang et al., 2001). L-ASNase derived from *Cobetia amphilecti* AMI6 was also expressed in *E. coli* BL21 (DE3) using the pQE-80L-kan vector, which features a T5 promoter. They were able to achieve a specific activity of 778 U/mg (Farahat et al., 2020). In another study, using a vector like the previous one (pQE30), L-ASNase from *Nocardiopsis alba* NIOT-VKMA08 was expressed using *E. coli* M15 as the host. In this work, they achieved a high activity of 158.1 U/mL. Nevertheless, developing strategies to synthesize promoters allows for significant upregulation of transcription factors (Meena et al., 2016). A study that following this approach, produced a set of promoters to address the endogenous regulation of different *E. coli* transcription factors (σ^{70}, σ^{38}, σ^{32}, and σ^{24}). Among the designed promoters, P_{21285} was selected as its performance was superior to that achieved with the T7 promoter (Wang et al., 2019).

For the case of *P. pastoris,* promoters for protein expression are limited mainly to the (inducible) AOX1 and (constitutive) GAP promoter. Therefore, for producing L-ASNase using *P. pastoris* as host, only pAOX1 is used. The alcohol oxidase I (AOX1) promoter regulates methanol metabolism and initiates the assimilation of methanol, converting it into formaldehyde. Due to its strict regulation and strong inducibility, when methanol is the sole carbon source, it is widely employed to drive heterologous expression (Yang and Zhang, 2018). Numerous studies have been conducted on L-ASNase production using *P. pastoris* as the host system (Ferrara et al., 2006; Tien Cuong Nguyen, 2014; Sajitha et al., 2015; Effer et al., 2019; Rodrigues et al., 2019; Lima et al., 2020; de Almeida Parizotto et al., 2021; Pillaca-Pullo et al., 2021). Among them, a strategy based on methanol-oxygen control in the bioreactor was devised. This strategy produced a 2-fold increase in maximum volumetric activity compared to the pulse strategy (de Almeida Parizotto et al., 2021).

Recently, strategies for L-ASNase production have been developed using *B. subtilis* as host, since this microorganism, unlike *E. coli*, is GRAS (generally regarded as safe) due to its non-pathogenic and non-toxic properties. Additionally, being Gram-positive, it allows for the secretion of proteins into the extracellular media (Niu et al., 2021; Souza et al., 2021). Numerous efforts have been made to identify strong promoters for transcriptional control. One of the most extensively studied promoters of *B. subtilis* at an industrial scale for producing L-ASNase is P43, a constitutive promoter considered strong (Feng et al., 2017; Li et al., 2019; Niu et al., 2021). By replacing the HpaII promoter with P43 in *B. subtilis*, improved L-ASNase expression was achieved, resulting in a 38.1% increase in activity. Furthermore, the promoter underwent two rounds of error-prone PCR reactions, leading to random mutagenesis. These variants provided an additional 13% increment in activity compared to P_{43}-*B. subtilis* (Feng et al., 2017).

According to Yang et al. (Yang et al., 2021), promoter engineering can modulate the transcriptional capacity of promoters, improving, mutating or changing the DNA sequence of promoters. Using this technique, temperature- and pH-inducible phase-dependent promoters of 114 endogenous promoters were identified and characterized. These were evaluated for the expression of secreted enzymes. This result represents a great potential application for enzyme production, metabolic engineering and synthetic biology (Yang et al., 2017). Using promoter engineering, eight different types of promoters (P_{43}, P_{yxiE}, P_{groEs}, P_{sigX}, P_{trnQ}, P_{131}, P_{242}, $P_{shutttle09}$) were evaluated to enhance L-ASNase expression from *P. yayanosii* CH1. A 2.09-fold improvement in transcript levels over the original strain was achieved using the P_{43} promoter and an optimized ribosomal binding site (RBS) (Li et al., 2019). Niu et al. (Niu et al., 2022) developed an approach similar to the one used by Li et al. (Li et al., 2019), but with the difference that they established a dual-promoter system and optimized the core regions (−35 and −10 boxes). The dual-promoter systems performed ideally when nine of the sixteen dual-promoter systems were used (P_{aprE}-P_{43}, P_{yvyD}-P_{43}, P_{spoVG}-P_{43}, P_{aprE}-P_{aprE}, P_{yvyD}-P_{aprE}, P_{yvyD}-P_{yvyD}, P_{43}-P_{yvyD}, P_{aprE}-P_{yvyD}, and P_{spoVG}-P_{yvyD}). This strategy provided greater yields than the original P_{43} promoter. Among these nine systems, the P_{aprE}-P_{yvyD} promoter achieved the greatest L-ASNase activity of 502.11 U/mL, which was 1.44 times greater than the activity mediated by the original P_{43} promoter.

4.4 Increase in L-ASNase expression by translation regulation

Translation processes are not only responsible for protein synthesis from the mRNA. Also affect folding, structure, and secretion of proteins. To gain greater enzyme production, all mRNA must be translated into proteins and these proteins must be folded into correct structures (Kant Bhatia et al., 2021). To improve the mRNA translation rate and thus increase L-ASNase production, an online RBS calculator is available (DeNovoDNA, 2022), which allows for the design of RBS sequences for *B. subtilis* 168/pMA5-P43-pyasnaseMut. They designed 300 sequences, and theoretically assessed them considering higher yield. Among this sequence, the mutant RBS that achieved the greatest yield was chosen, resulting in a total activity of 5278 U/mL (2-fold higher than the control) (Li et al., 2019). Another free online RBS Calculator, such as "RBS calculator v2.0" (SalisLab, 2022), was used to select a sequence capable of improving expression by 1.39-fold among 22 RBS-assessed sequences (Niu et al., 2022).

Another strategy that improved the production of L-ASNase from *Rhizomucor miehei* was rational design through modification of the 5' untranslated region (UTR). This region consists of the open reading frame (ORF) and facilitates the accessibility of Shine-Dalgarno sequences and start codons, thus enhancing translation initiation efficiency. By modifying the 5' UTR, was possible to express a site-directed mutant L-ASNase from *Rhizomucor miehei*, using *B. subtilis* 168 as the host microorganism, resulting in a 6.33-fold increase in L-ASNase activity. The enzyme was produced in high-density batch culture and reached an activity of 521.9 U/mL (Zhang et al., 2021).

5 Optimization of factors that affect expression in the soluble fraction of L-ASNase

One of the many approaches to improve the solubility of recombinant proteins, is to slow down the protein synthesis process, thereby allowing sufficient time for the protein to reach its native structure. Some of the strategies for this purpose include using weak promoters, low concentration of inducer and low cell culture temperature (Kant Bhatia et al., 2021). However, all these strategies have the problem of low yield of proteins. Other approaches include the use of genetic engineering to optimize factors such as the co-expression of chaperones and the formation of disulfide bonds, the use of fusion tags, and the translocation of proteins to the extracellular medium (Singha et al., 2017).

5.1 Co-expression of chaperones and formation of disulfide bonds in L-ASNase

Co-expression with several types of chaperones involved in protein folding *in vivo* is one of the approaches used to improve the solubility of recombinant proteins (Grigoroudis et al., 2015; Peng et al., 2016; Paraskevopoulou and Falcone, 2018; Wang et al., 2018). Nevertheless, to date only one study has been conducted where they co-expressed chaperones together with L-ASNase (Biglari Goliloo et al., 2021). Biglari Goliloo et al. (Biglari Goliloo et al., 2021) assessed the yield of the co-expression of the GroELS/TF system and L-ASNase (Q59LAsp). Their results showcase that the presence of GroELS and TF chaperones expressed from PG-Tf2 plasmid increased the amount of soluble recombinant Q59LAsp protein in both SHuffle T7 and in *E. coli* BL21 (DE3). In addition, the amount of soluble Q59LAsp protein produced in the SHuffle T7 strain was significantly higher in the presence of chaperones than in *E. coli* BL21 (DE3). This is due to the commercially available SHuffle T7 strain making a chromosome copy of the isomerase with disulfide bond, DsbC along with the *trxB*$^{-y}$ *gor* genotype, which are the genes responsible for providing an oxidative environment, allowing less degradation of L-ASNase (Singha et al., 2017).

5.2 Use of fusion tags

In homologous and heterologous expression reactions, it is possible that the final product does not take place in a single step due to the complex coupled reactions; showcasing several limitations in terms of stability, productivity, functional expression and tolerance to intermediaries (Kant Bhatia et al., 2021). Currently, several fusion partner affinity tags are used, which facilitate purification, increase solubility and reduce proteolysis of the recombinant protein (Singha et al., 2017).

Various fusion tags have been reported in the expression of L-ASNase. The maltose binding protein (MBP) of *E. coli*, has been used widely as a fusion partner to increase solubility of recombinant proteins (Dieterich et al., 2003; Kaur et al., 2018). Additionally, the small ubiquitin-like modifier (SUMO) proteins have been used to alter protein properties such as stability and solubility. Caetano (Caetano, 2020), using a pET-SUMO expression system in combination with a mutated L-ASNase sequence from *E. coli,* expressed it achieving an activity of 183.5 U/mg. In 2016, a study was conducted to improve the activity of human L-ASNase hASNase-3, creating a library of mutants using *E. coli* C41 (DE3) as the heterologous expression host (Karamitros and Konrad, 2016a). The expression system used was pET14b-SUMO, improving catalytic efficiency up to 6 times more than the wild enzyme (Karamitros and Konrad, 2014; Karamitros and Konrad, 2016b). Other N-Terminal fusion proteins that have been employed, such as GST (glutathione S-transferase); and affinity tags to facilitate purification (such as Poly-His, which are often used in the L-ASNase expression hosts) (Feng et al., 2017; Effer et al., 2019; de Almeida Parizotto et al., 2021; Niu et al., 2022). Table 2 Summarizes tags commonly used to modify L-ASNase expression systems.

In one study, the N-terminal heparin-binding peptide (KRKKKKKGKGLGKKKKR) was used to produce a wild-type L-ASNase derived from Wolinella succinogenes expressed in *E. coli* BL21(DE3). This peptide allows the protein to bind heparin and the cancer cell line K562. The enzyme had two different amino acid substitutions (V23Q and K24) that provide resistance to trypsin lysis. The use of the heparin peptide resulted in an improvement in enzyme activity compared to L-ASNase without the peptide (Sannikova et al., 2016).

5.3 Translocation of proteins to the extracellular medium

The efficiency of enzyme production can be limited by their accumulation in inadequate compartments or by inadequate translocation (Kant Bhatia et al., 2021). This limitation can be overcome by slowing down the protein synthesis process, which can also be modified by signal peptides. Secretion facilitates further processing; therefore, in most recombinant production, a secretory signal is cloned along with the gene. This signal can be a native signal or any other efficient signal sequence compatible with the L-ASNase gene frame. In Gram-positive strains like *B. subtilis*, protein secretion is highly efficient and does not require a signal peptide. L-ASNase has been successfully expressed extracellularly in *B. subtilis* through a novel secretion pathway, resulting in a final activity of 426 U/mL. Classical secretion pathways include the Sec-dependent, Tat-translation, and signal recognition particle (SRP) pathways. However, native signal peptides can be replaced with more efficient and validated signal peptides (Niu et al., 2021).

Feng et al. (Feng et al., 2017) succeeded in improving the activity of L-ASNase using *B. subtilis* as the host through combined approaches using combinations of different signal sequences and promoters and using random mutagenesis. In this work, they used eight signal peptides (ywbN, yvgO, amyE, oppA, vpr, lipA and wapA) to assess the amount of protein secretion to the extracellular medium using the HpaII promoter. It was demonstrated that, among the 8 signals, wapA achieved the highest expression, reaching an activity of 407.6 U/mL.

For Gram-negative strains such as *E. coli*, secretion poses a complex challenge. The common scenario is that proteins accumulate in the cytoplasm, which is undesirable for recombinant protein production due to its reducing environment and high concentration of proteases.

TABLE 2 Fusion tag used to improve the solubility of L-ASNase.

Fusion tag	Common expression vector	Description	References
Maltose binding protein (MBP)	pMAL series and pIVEX series	Improves the solubility of the protein	Dieterich et al. (2003)
		Eliminated from the recombinant protein	
		Also aids in purification	
Small ubiquitin-like modifier (SUMO)	pET-SUMO	Promotes folding and structural stability	Caetano (2020)
		SUMO protease enables the elimination of the tag	
Histidine tail (His-tag)	pET pPICZαA pP43NMK pHT43 series	Aids in purification in native or denaturing conditions	[(Niu et al., 2022), (Freitas et al., 2022), (Chityala et al., 2015)]
Glutathione S-transferase (GST)	pGEX series	Protects against intracellular proteolysis	Darwesh et al. (2022)
		Stabilizes the protein in soluble fraction	
		Also aids in purification	
Thioredoxin (Trx)	pET-32a	Aids in the refolding of proteins that require reducing environment	Sindhu and Manonmani (2018)

Moreover, during the extraction process, cell lysis is required, leading to the release of endotoxins and other compounds that complicate purification (Overton, 2014). To enable *E. coli* to express proteins extracellularly, two conditions must be met: 1) maintaining their soluble and active conformation, and 2) providing mechanisms for their delivery into the extracellular space (Kim et al., 2015). Various signal peptides have been employed to facilitate protein translocation to the periplasmic medium, offering a more stable environment. Among these, the signal peptide commonly used in *E. coli* is pelB. For a comprehensive list of articles discussing pelB-based strategies and others, see Table 1. However, new strategies have emerged that further enhance secretion. It has been demonstrated that fusing the pelB sequence with 5 aspartates resulted in nearly double the secretion efficiency of L-ASNase compared to previous approaches (Kim et al., 2015).

Additionally, the secretion of L-ASNase from *E. chrysanthemi* using two signal peptides, OmpA and DsbA, has been investigated (Yari et al., 2020). Signal peptides were selected through an *in silico* approach, taking into account the protein nature, the host organism, and the experimental conditions. Ultimately, it was concluded that DsbA exhibited more efficient targeting of L-ASNase than OmpA (Yari et al., 2020).

The secretory expression of recombinant proteins in yeast necessitates the presence of a signal sequence that facilitates the entry of the recombinant protein into the endoplasmic reticulum (ER), making the initial step for its secretory expression (Yang and Zhang, 2018). The signal sequence of the α-factor of *S. cerevisiae,* along with its truncated versions, has been effectively employed to achieve satisfactory secretion of L-ASNase (see Table 1). In a study, an L-ASNase from *Penicillium sizovae* was expressed using *P. pastoris* as the host organism. The researchers utilized a secretion signal derived from the native α-factor of *S. cerevisiae* to enable efficient secretion of most *P. pastoris* proteins, employing pPICZα as the vector (Freitas et al., 2022).

6 Improvement of the host strains to increase the expression of L-ASNase

The choice of host strain can also play a crucial role in the successful protein production process. The selection of strain should primarily consider the requirements of the plasmid expression system, including: 1) the type of polymerases necessary for protein expression, 2) compatibility between available tRNA anticodons and codons of the heterologous gene, 3) stability of the plasmid or protein within the strain, 4) proper protein capability folding within the strain, 5) requirements for posttranslational modifications, and 6) potential toxicity of the protein to the strain itself (Makino et al., 2011). Nowadays, advancements in genetic and metabolic engineering have enabled the modification of organisms to improve their recombinant protein expression levels. The subsequent secretions will discuss the strategies employed in host strain engineering and metabolic engineering that have been utilized to improve the heterologous expression of L-ASNase.

6.1 Genetic engineering of host strains to improve the expression of L-ASNase

Targeted strain engineering involves modifying a specific DNA sequence in the host that is known to impact the synthesis, degradation, secretion, or folding of proteins. Several commercial strains of *E. coli, P. pastoris,* and *B. subtilis* have been genetically modified with features designed to improve protein expression. The characteristics and advantages of strains used for L-ASNase production are summarized in Table 3. In the context of L-ASNase expression, 11 *E. coli* expression strains were evaluated. Among them, *E. coli* BL21 ArcticExpress (DE3) demonstrated the best results, producing an enzyme comparable to commercially

TABLE 3 Host expression strains used for the production of L-ASNase.

Host strain	Characteristics	Advantages	Source	References
Host strains of *Escherichia coli*				
E. coli BL21(DE3)	Constitutive expression of RNA polymerase T7	Profitable for expression of non-toxic genes	Novagen	Table 1
	Deficient in the Lon and *ompT* genes (proteases)	Stabilizes plasmids		
E. coli BL21-CodonPlus (DE3)-RIL	Expresses rare tRNAs; Useful for genes rich in AT content	Allows codon optimization; therefore, expression of the protein	Agilent	[(Chohan and Rashid, 2013), (Maqsood et al., 2020)]
	Deficient in the Lon and *ompT* genes (proteases)	Profitable for expression of non-toxic genes		
	Constitutive expression of T7 RNA polymerase			
E. coli BLR (DE3)	Derived *recA* from BL21 Constitutive expression of RNA polymerase T7	Stabilizes plasmids that contain repetitive sequences	Novagen	[(Hong et al., 2014), (Khushoo et al., 2005)]
E. coli M15	Constitutively expresses the repressive protein lac	Cannot be infected by lambda phages	Qiagen	Meena et al. (2016)
E. coli C41 (DE3)	Mutation in the lacUV5 promoter	Prevents the death associated with toxic proteins	Lucigen	[(Roth et al., 2013), (Karamitros and Konrad, 2016b), (Karamitros and Konrad, 2014)]
E. coli C43(DE3)				
E. coli Rosetta	Expression of tRNA for rare codons in *E. coli*	Allows codon optimization; therefore, the expression of the protein	Novagen	Caetano (2020)
E. coli BL21 star (DE3)	Mutation in the *rne*131 gene	Improves the stability of mRNA	Invitrogen	Kim et al. (2015)
E. coli ArticExpress (DE3)	Expression of genes *cpn*10 and *cpn*60	Improves folding in the cytosol	Agilent	de Moura et al. (2020)
E. coli Shuffle T7	Expresses *DsbC* and carries mutations in *trxB* and gor	Promotes correct folding	NEB	Biglari Goliloo et al. (2021)
		Resistant to phage T1		
E. coli BL21 (DE3) pLysS	Constitutive expression of T7 lysozymes	Prevents leakage expressions	Novagen	Kotzia and Labrou (2007)
		Improves the expression of genes with toxic inducers		
Bacillus subtilis host strains				
B. subtilis 168	Wild type	Wild type	ATCC® 23857™	[(Effer et al., 2020), (Jia et al., 2013), (Li et al., 2019)]
B. subtilis WB600	Deficient in Δ*nprE*, Δ*aprA*, Δ*epr*, Δ*bpr*, Δ*mpr*, Δ*nprB* (extracellular proteases)	Avoids protein degradation	Wang et al. (2014)	Feng et al. (2017)
B. subtilis RIK 1285	Express *trpC2, ys1, aprEdelta3*	Allows high secretion of proteins	Takara	[(Niu et al., 2021), (Niu et al., 2022)]
	Deficient in *nprR2, nprE18*			
B. subtilis WB800N	Deficient in Δ*nprE*, Δ*aprA*, Δ*epr*, Δ *bpr*, Δ*mpr*, Δ*nprB*, Δ*vpr*, Δ*wprA* (extracellular proteases)	Avoids protein degradation	Murashima et al. (2002)	[(Chityala et al., 2015), (Sushma et al., 2017)]
Pichia pastoris host strains				
P. pastoris KM71 (MUT^S)	Slow growth in methanol	Allows better secretion of complex proteins	Novagen	[(Pillaca-Pullo et al., 2021), (Rodrigues et al., 2019)]
	Contains a deletion in the histidine gene (arg*4, his4, AOX1::ARG4*)			
P. pastoris GS115	Contains a deletion in the histidine gene (*his4*)	Allows better secretion	Invitrogen	[(Ferrara et al., 2006), (Facchinetti de Castro Girão et al., 2016)]
P. pastoris X-33	wild type	Wild type	Invitrogen	[(Tien Cuong Nguyen, 2014), (Freitas et al., 2022)]

(Continued on following page)

TABLE 3 (*Continued*) Host expression strains used for the production of L-ASNase.

Host strain	Characteristics	Advantages	Source	References
P. pastoris Pichiapink™	Contains a deletion in the gene that expresses adenine (*Ade2*)	Allows better secretion	ThermoFisher	Sajitha et al. (2015)
P. pastoris Glycoswitch	Contains a deletion in the histidine gene	Allows better secretion	Pichia	[(Effer et al., 2019), (Lima et al., 2020)]
SuperMan5 (his-)	Interrupts the N-glycosylation pathway of *P. pastoris*, and produces human glycosidic structures. (*his4, och1:: pGAPTrα1,2-mannosidase*)	Possible to "humanize" proteins		
P. pastoris Glycoswitch SuperMan5 (his+)	Interrupts the N-glycosylation pathway of *P. pastoris*, and produces human glycosidic structures. (*och1:: pGAPTrα1,2-mannosidase*)	Possible to "humanize" proteins	Pichia	de Almeida Parizotto et al. (2021)
P. pastoris SMD1168	Contains a deletion in the histidine gene	Enables the stabilization of proteins	Invitrogen	Tien Cuong Nguyen (2014)
	Does not contain protease A (*his4, pep4*) activity	Allows better secretion		

available ones. This strain presented low protein aggregates, proper folding, and a higher specific activity (156 U/mg) (de Moura et al., 2020). Similar studies have been conducted for the expression of *E. chrysanthemi* in *E. coli*, comparing seven different strains: XL1-Blue, TOP10, UT5600, BL21(DE3), BL21(DE3) Star, Rosetta (DE3), and BL21(DE3) pLysS. Among these strains, *E. coli* Rosetta (DE3) yielded the highest enzyme activity, with 17.8 U/mL in the extracellular medium and 4.2 U/mL in the intracellular medium (Karamitros and Labrou, 2014).

6.2 Metabolic engineering in hosts to improve the heterologous expression of L-ASNase

The overexpression of recombinant proteins triggers a cellular stress response (CSR). This response is primarily caused by the diversion of energy and metabolites, including amino acids, ribosomes, and other precursors, towards protein synthesis (Munhoz Costa et al., 2022). Therefore, gaining a better understanding of CSR and developing strategies to control it are crucial for successful recombinant protein production.

Global regulators within the CSR transcriptional regulatory network were discovered by L-ASNase expression in *E. coli*. Specifically, the group of regulators having the greatest impact on gene expression in the regulatory network was identified and their influence on synthesis was assessed. By biological and bioinformatic analyses, it was determined that genes suppressed by *fis*, such as *carB*, *fadB, nrfA, narH* and *queA,* are also activated during the stationary phase. Consequently, this might be considered a possible target for modulating metabolic activity and capacity for protein expression. When *fis* was co-expressed together with L-ASNase at 6 h of induction, the volumetric efficiency of L-ASNase increased 3-fold, compared to the native form of the host (Mahalik et al., 2017). The role of the *lrp* gene was also evaluated, concluding that its co-expression is a suitable target to enhance expression. Achieving a maximum volumetric efficiency of 458.43 mg/L, this result in a 1.5-fold improvement compared to the native expression level (Mahalik et al., 2022). In another study conducted by Sharma et al. (Sharma et al., 2020), studied post-induction upregulated genes as potential candidates for the generation of Cellular Stress Response (CSR) using *E. coli* as strain model. To do this, they evaluated four main double knockouts (ΔelaA + ΔcysW, ΔelaA + ΔcueR, ΔcysW + ΔpurL and ΔyabI + ΔcysW) and six main single knockouts (control strain, ΔpurL, ΔelaA, ΔcysW, ΔcueR, ΔcysJ and ΔyfbN), where they transformed pMAL-p2X plasmid with the L-ASNase gene (*ansB*) cloned under the tac promoter. Double mutants yielded better results, the best of which ΔelaA + ΔcysW improved the activity 2.32-fold over the control strain. Thus, the knock-out strategy would allow the creation of more efficient hosts for L-ASNase production.

7 Future challenges for the rational design of heterologous systems for L-ASNase expression

To achieve successful L-ASNase production, it is crucial to employ a rational approach in designing expression systems, selecting appropriate strains, and making genetic or metabolic modifications. While various strategies have been explored, such as strain engineering, metabolic engineering, and bioinformatics tools, there is still room for improvement in L-ASNase production. Cutting-edge computational, such as In Silico Optimization (ISO) tools, are being adopted to enhance the process. These tools utilize computational methods like simple algorithms, dynamic programming, statistical techniques, and machine learning algorithms (such as artificial neural networks, support vector machines, and deep learning) to generate comprehensive models, reducing the need for time-consuming *in vitro* experimentation (Packiam et al., 2020), *In Silico* Optimization (ISO) tools use appropriate computational methods to generate models based on these approaches, which allow tackling the optimization with a broader and integrative view. Thus, avoiding *in vitro* experimentation and in the process, speeding up the workflow. Examples of computational methods include: 1) simple algorithms,

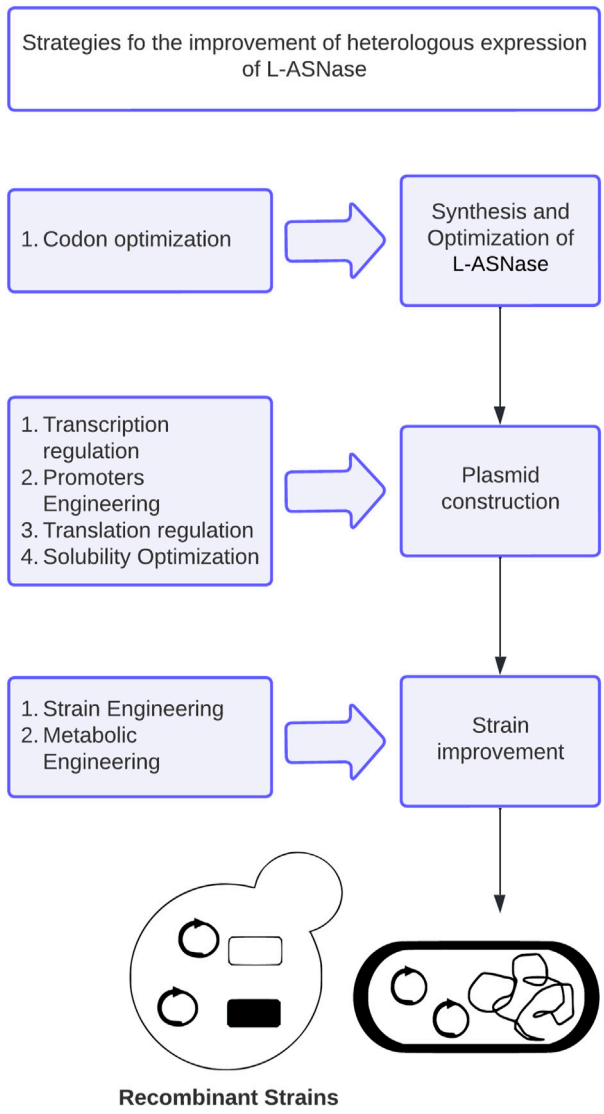

FIGURE 6
Proposed workflow to improve heterologous expression of L-asparaginase.

2) dynamic programming, 3) statistical methods, and iv) ISO tools offer several benefits for optimizing gene expression, allowing modifications based on the host. They evaluate and adjust gene properties like codon usage, GC composition, mRNA stability, cryptic splice sites, and premature polyadenylation signals (Watts et al., 2021; Vasina et al., 2022). Notable tools in this area include "SignalP" and "Phobius," which predict the most efficient signal peptide for a given amino acid sequence, thereby saving time and resources by eliminating the need for constructing multiple vectors (Zhou et al., 2018). Another approach involves using the "nondominated sorting differential search algorithm and flux balance analysis (ndsDSAFBA)", a multi-object optimization model that leverages *in silico* metabolic pathway models to enhance metabolite production. This approach offers a less labor-intensive and cost-effective methodology (Daud et al., 2019) Additionally, deep neural networks have been applied, such as the "mutation predictor for enhanced protein expression (MPEPE)", which can suggest amino acid sequence mutations to improve protein expression (Ding et al., 2022). Moreover, machine learning (ML) is being employed as a rational design strategy, exemplified by the development of MALLPHAS, a strain engineering tool that optimizes protein secretion (Markova et al., 2022).

Another recent strategy involves the use of CRISPR-Cas-based gene editing tools to enhance recombinant protein expression (Gu et al., 2018; Baghban et al., 2019; Fontana et al., 2020). CRISPR has been employed as a synthetic promoter activator for optimizing protein expression. Additionally, small molecule-sensitive gRNAs have been utilized to regulate gene expression in *E. coli* and precisely control multigene pathways (Fontana et al., 2020). The application of CRISPR-Cas9 for genomic engineering in yeast, including *P. pastoris*, has been reported, enabling rapid and marker-free modifications for strain and metabolic engineering purposes (Weninger et al., 2016). *B. subtilis* is another microorganism benefiting from CRISPR technology, with the development of a CRISPR-Cas9 toolkit for comprehensive engineering. This toolkit addresses challenges like low editing efficiency, complex cloning processes, and limited multiplexing capacity, thereby advancing the engineering capabilities of this strain (Gu et al., 2018). The combination of CRISPR and machine learning (ML) facilitates the maturation of metabolic engineering. CRISPR technology enables modifications at numerous genomic sites, simplifying gene editing and metabolic perturbations. ML, on the other hand, aids in the rational selection of optimal genes for desired products or applications through predictions and recommendations (Lawson et al., 2021).

The future challenges in optimizing heterologous protein expression involve integrating the aforementioned bioinformatics tools and designing tools capable of optimizing expression systems comprehensively, from transcriptional regulators to transcription termination. Furthermore, emerging technologies like CRISPR and ML hold promise in facilitating optimization and enhancing the reliability of predictions. In the coming years, the synergy between new algorithms and biotechnological tools should enable the development of advanced software and methodologies that can significantly reduce the time and costs associated with pharmaceutical products like L-ASNASA.

8 Conclusion

Overall, this review provides an overview of molecular and metabolic strategies that can be used to optimize heterologous expression of L-ASNase. This article describes several approaches that have been employed for this means, including the use of molecular tools, strain, and metabolic engineering, and *in silico* optimization. Through a clear and insightful analysis, it highlights the need for a rational design approach to achieve successful expression. In addition, it acknowledges the challenges to large-scale production of bio-betters L-ASNases.

In summary, the use of genetic engineering, rational design of heterologous expression systems, metabolic strategies, would allow motivating and facilitating the pharmaceutical industry to continuously innovate product manufacturing processes, and develop new treatments effectively and using Good Manufacturing Practices (GMP). In this sense Brumano et al.

(Brumano et al., 2019), mentions that the development of bio-betters L-ASNases begins with the development of the process. Therefore, the search for hosts and expression systems that facilitate upstream and downstream processes such as 1) expression systems and the use of bioinformatics tools that allow codon optimization such as "Twist codon optimization" and RBS such as "RBS calculator v2. 0"; 2) hosts capable of producing l-ASNases from new microbiological or molecularly and/or chemically modified sources; 3) enzyme secreting microorganisms such as *B. subtilis* or *P. pastoris* strains; 4) expression systems capable of stabilizing structure conformation and solubility such as the use of pET-SUMO systems or co-expression of chaperones; and 5) that manage to improve L-ASNase production yields such as promoter optimization have been reviewed in this work. These strategies would guarantee the efficacy and safety of the final product that L-ASNase producing industries seek for a continuous improvement of both the process and the product. For this reason, it is of utmost importance to develop a strategy to address all the points mentioned in this review. In Figure 6 it proposes a workflow that would allow an effective rational design of the host and expression system to produce biologically improved L-ASNase.

Author contributions

Drafting: NL Conception and design: NL, JM, MZ Edition: MZ. All authors contributed to the article and approved the submitted version.

Funding

This study was supported by FAPESP-UFRO project No 2020/06982-3, and Fondecyt Postdoctoral project No 3210142.

Acknowledgments

Thanks to ANID (Agencia Nacional de Investigación y Desarrollo) Master Scholarship, grant number 22220584.

Conflict of interest

The authors declare that the research was conducted in the absence of any commercial or financial relationships that could be construed as a potential conflict of interest.

Publisher's note

References

Abribat, T. (2023). *Pegylated l-asparaginase*. United States: Carpmaels and Ransford LLP. Patent No. EP10730170.7. https://www.patentguru.com/EP2451486B2.

Aghaeepoor, M., et al. (2011). High level of extracellular fermentation and alternative purification of *Escherichia coli* asparaginase II. *Biharean Biol.* 5 (2), 96–101. https://www.semanticscholar.org/paper/High-level-of-extracellular-fermentation-and-of-II-Aghaeepoor-Mozafari/19cc63893855a5f184cdf3cdd8b1ac233e21346e.

Alam, S., et al. (2019). "Recent development in the uses of asparaginase as food enzyme," in *Green bio-processes* (Germany: Springer), 55–81.

Ardalan, N., Mirzaie, S., Sepahi, A. A., and Khavari-Nejad, R. A. (2018). Novel mutant of *Escherichia coli* asparaginase II to reduction of the glutaminase activity in treatment of acute lymphocytic leukemia by molecular dynamics simulations and QM-MM studies. *Med. hypotheses* 112, 7–17. doi:10.1016/j.mehy.2018.01.004

Baghban, R., Farajnia, S., Rajabibazl, M., Ghasemi, Y., Mafi, A., Hoseinpoor, R., et al. (2019). Yeast expression systems: Overview and recent advances. *Mol. Biotechnol.* 61 (5), 365–384. doi:10.1007/s12033-019-00164-8

Batool, T., Makky, E. A., Jalal, M., and Yusoff, M. M. (2016). A comprehensive review on l-asparaginase and its applications. *Appl. Biochem. Biotechnol.* 178 (5), 900–923. doi:10.1007/s12010-015-1917-3

Battistel, A. P., Rocha, B. S. d., Santos, M. T. D., Daudt, L. E., and Michalowski, M. B. (2021). Allergic reactions to asparaginase: Retrospective cohort study in pediatric patients with acute lymphoid leukemia. *Hematol. Transfus. Cell Ther.* 43 (1), 9–14. doi:10.1016/j.htct.2019.10.007

Beck, A. (2011). Biosimilar, biobetter and next generation therapeutic antibodies. *mAbs* 3 (2), 107–110. doi:10.4161/mabs.3.2.14785

Biglari Goliloo, E., Tollabi, A., and Zarei Jaliani, H. (2021). Soluble expression and purification of Q59L mutant L-asparaginase in the presence of chaperones in SHuffle™ T7 strain. *ssu-ijml* 8 (2), 138–146. doi:10.18502/ijml.v8i2.6278

Broome, J. D. (1968). Studies on the mechanism of tumor inhibition by L-asparaginase. Effects of the enzyme on asparagine levels in the blood, normal tissues, and 6C3HED lymphomas of mice: Differences in asparagine formation and utilization in asparaginase-sensitive and -resistant lymphoma cells. *J. Exp. Med.* 127 (6), 1055–1072. doi:10.1084/jem.127.6.1055

Brumano, L. P., da Silva, F. V. S., Costa-Silva, T. A., Apolinário, A. C., Santos, J. H. P. M., Kleingesinds, E. K., et al. (2019). Development of L-asparaginase biobetters: Current research status and review of the desirable quality profiles. *Front. Bioeng. Biotechnol.* 6, 212. doi:10.3389/fbioe.2018.00212

Burke, M. J. (2014). How to manage asparaginase hypersensitivity in acute lymphoblastic leukemia. *Future Oncol.* 10 (16), 2615–2627. doi:10.2217/fon.14.138

Cachumba, J. J. M., Antunes, F. A. F., Peres, G. F. D., Brumano, L. P., Santos, J. C. D., and Da Silva, S. S. (2016). Current applications and different approaches for microbial l-asparaginase production. *Braz. J. Microbiol.* 47, 77–85. doi:10.1016/j.bjm.2016.10.004

Caetano, L., Production and characterization of mutants of lower immunogenic potential of L-asparaginase II from *Escherichia coli*: Combination of *in silico* and *in vitro* studies, in postgraduate program in harmacology. 2020, Universidade Federal Do Ceará: Availableat: https://repositorio.ufc.br/handle/riufc/55993.

Cappelletti, D., Chiarelli, L. R., Pasquetto, M. V., Stivala, S., Valentini, G., and Scotti, C. (2008). Helicobacter pyloril-asparaginase: A promising chemotherapeutic agent. *Biochem. Biophysical Res. Commun.* 377 (4), 1222–1226. doi:10.1016/j.bbrc.2008.10.118

Castro, D., Marques, A. S. C., Almeida, M. R., de Paiva, G. B., Bento, H. B. S., Pedrolli, D. B., et al. (2021). L-Asparaginase production review: Bioprocess design and biochemical characteristics. *Appl. Microbiol. Biotechnol.* 105 (11), 4515–4534. doi:10.1007/s00253-021-11359-y

Chahardahcherik, M., Ashrafi, M., Ghasemi, Y., and Aminlari, M. (2020). Effect of chemical modification with carboxymethyl dextran on kinetic and structural properties of L-asparaginase. *Anal. Biochem.* 591, 113537. doi:10.1016/j.ab.2019.113537

Chand, S., Mahajan, R. V., Prasad, J. P., Sahoo, D. K., Mihooliya, K. N., Dhar, M. S., et al. (2020). A comprehensive review on microbial l-asparaginase: Bioprocessing, characterization, and industrial applications. *Biotechnol. Appl. Biochem.* 67 (4), 619–647. doi:10.1002/bab.1888

Chityala, S., Venkata Dasu, V., Ahmad, J., and Prakasham, R. S. (2015). High yield expression of novel glutaminase free l-asparaginase II of Pectobacterium carotovorum MTCC 1428 in Bacillus subtilis WB800N. *Bioprocess Biosyst. Eng.* 38 (11), 2271–2284. doi:10.1007/s00449-015-1464-x

Chohan, S. M., and Rashid, N. (2013). TK1656, a thermostable l-asparaginase from Thermococcus kodakaraensis, exhibiting highest ever reported enzyme activity. *J. Biosci. Bioeng.* 116 (4), 438–443. doi:10.1016/j.jbiosc.2013.04.005

Clark, E. D. B. (2001). Protein refolding for industrial processes. *Curr. Opin. Biotechnol.* 12 (2), 202–207. doi:10.1016/s0958-1669(00)00200-7

Costa, I. M., Schultz, L., de Araujo Bianchi Pedra, B., Leite, M. S. M., Farsky, S. H. P., de Oliveira, M. A., et al. (2016). Recombinant L-asparaginase 1 from *Saccharomyces*

cerevisiae: An allosteric enzyme with antineoplastic activity. *Sci. Rep.* 6 (1), 36239. doi:10.1038/srep36239

Courtois, F., Schneider, C. P., Agrawal, N. J., and Trout, B. L. (2015). Rational design of biobetters with enhanced stability. *J. Pharm. Sci.* 104 (8), 2433–2440. doi:10.1002/jps.24520

Darwesh, D. B., Al-Awthan, Y. S., Elfaki, I., Habib, S. A., Alnour, T. M., Darwish, A. B., et al. (2022). Anticancer activity of extremely effective recombinant L-asparaginase from *Burkholderia pseudomallei*. *J. Microbiol. Biotechnol.* 32 (5), 551–563. doi:10.4014/jmb.2112.12050

Daud, K. M., Mohamad, M. S., Zakaria, Z., Hassan, R., Shah, Z. A., Deris, S., et al. (2019). A non-dominated sorting Differential Search Algorithm Flux Balance Analysis (ndsDSAFBA) for *in silico* multiobjective optimization in identifying reactions knockout. *Comput. Biol. Med.* 113, 103390. doi:10.1016/j.compbiomed.2019.103390

de Almeida Parizotto, L., Krebs Kleingesinds, E., Manfrinato Pedrotti da Rosa, L., Effer, B., Meira Lima, G., Herkenhoff, M. E., et al. (2021). Increased glycosylated l-asparaginase production through selection of Pichia pastoris platform and oxygen-methanol control in fed-batches. *Biochem. Eng. J.* 173, 108083. doi:10.1016/j.bej.2021.108083

de Moura, W. A. F., Schultz, L., Breyer, C. A., de Oliveira, A. L. P., Tairum, C. A., Fernandes, G. C., et al. (2020). Functional and structural evaluation of the antileukaemic enzyme l-asparaginase II expressed at low temperature by different *Escherichia coli* strains. *Biotechnol. Lett.* 42 (11), 2333–2344. doi:10.1007/s10529-020-02955-5

DeNovoDNA (2022). Available at: https://www.denovodna.com/software/).

Dieterich, D. C., Landwehr, M., Reissner, C., Smalla, K. H., Richter, K., Wolf, G., et al. (2003). Gliap – a novel untypical l-asparaginase localized to rat brain astrocytes. *J. Neurochem.* 85 (5), 1117–1125. doi:10.1046/j.1471-4159.2003.01766.x

Ding, Z., Guan, F., Xu, G., Wang, Y., Yan, Y., Zhang, W., et al. (2022). MPEPE, a predictive approach to improve protein expression in *E. coli* based on deep learning. *Comput. Struct. Biotechnol. J.* 20, 1142–1153. doi:10.1016/j.csbj.2022.02.030

dos Santos, N. V., de Carvalho Santos-Ebinuma, V., Pessoa Junior, A., and Pereira, J. F. B. (2018). Liquid–liquid extraction of biopharmaceuticals from fermented broth: Trends and future prospects. *J. Chem. Technol. Biotechnol.* 93 (7), 1845–1863. doi:10.1002/jctb.5476

Dumina, M. V., Zhgun, A. A., Pokrovskay, M. V., Aleksandrova, S. S., Zhdanov, D. D., Sokolov, N. N., et al. (2021). Comparison of enzymatic activity of novel recombinant L-asparaginases of extremophiles. *Appl. Biochem. Microbiol.* 57 (5), 594–602. doi:10.1134/s0003683821050057

Dumina, M., and Zhgun, A. (2023). Thermo-L-Asparaginases: From the role in the viability of thermophiles and hyperthermophiles at high temperatures to a molecular understanding of their thermoactivity and thermostability. *Int. J. Mol. Sci.* 24 (3), 2674. doi:10.3390/ijms24032674

Effer, B., Kleingesinds, E. K., Lima, G. M., Costa, I. M., Sánchez-Moguel, I., Pessoa, A., et al. (2020). Glycosylation of Erwinase results in active protein less recognized by antibodies. *Biochem. Eng. J.* 163, 107750. doi:10.1016/j.bej.2020.107750

Effer, B., Lima, G. M., Cabarca, S., Pessoa, A., Farías, J. G., and Monteiro, G. (2019). L-asparaginase from E. Chrysanthemi expressed in glycoswitch®: Effect of his-tag fusion on the extracellular expression. *Prep. Biochem. Biotechnol.* 49 (7), 679–685. doi:10.1080/10826068.2019.1599396

Einsfeldt, K., Baptista, I. C., Pereira, J. C. C. V., Costa-Amaral, I. C., Costa, E. S. d., Ribeiro, M. C. M., et al. (2016). Recombinant L-asparaginase from Zymomonas mobilis: A potential new antileukemic agent produced in *Escherichia coli*. *PLOS ONE* 11 (6), e0156692. doi:10.1371/journal.pone.0156692

Facchinetti de Castro Girão, L., Gonçalves da Rocha, S. L., Sobral, R. S., Dinis Ano Bom, A. P., Franco Sampaio, A. L., Godinho da Silva, J., et al. (2016). *Saccharomyces cerevisiae* asparaginase II, a potential antileukemic drug: Purification and characterization of the enzyme expressed in Pichia pastoris. *Protein Expr. Purif.* 120, 118–125. doi:10.1016/j.pep.2015.12.012

Farahat, M. G., Amr, D., and Galal, A. (2020). Molecular cloning, structural modeling and characterization of a novel glutaminase-free L-asparaginase from Cobetia amphilecti AMI6. *Int. J. Biol. Macromol.* 143, 685–695. doi:10.1016/j.ijbiomac.2019.10.258

Feng, Y., Liu, S., Jiao, Y., Gao, H., Wang, M., Du, G., et al. (2017). Enhanced extracellular production of L-asparaginase from Bacillus subtilis 168 by B. subtilis WB600 through a combined strategy. *Appl. Microbiol. Biotechnol.* 101 (4), 1509–1520. doi:10.1007/s00253-016-7816-x

Ferrara, M. A., Severino, N. M., Mansure, J. J., Martins, A. S., Oliveira, E. M., Siani, A. C., et al. (2006). Asparaginase production by a recombinant Pichia pastoris strain harbouring *Saccharomyces cerevisiae* ASP3 gene. *Enzyme Microb. Technol.* 39 (7), 1457–1463. doi:10.1016/j.enzmictec.2006.03.036

Fontana, J., Sparkman-Yager, D., Zalatan, J. G., and Carothers, J. M. (2020). Challenges and opportunities with CRISPR activation in bacteria for data-driven metabolic engineering. *Curr. Opin. Biotechnol.* 64, 190–198. doi:10.1016/j.copbio.2020.04.005

Freitas, M., Souza, P., Homem-de-Mello, M., Fonseca-Bazzo, Y. M., Silveira, D., Ferreira Filho, E. X., et al. (2022). L-asparaginase from Penicillium sizovae produced by a recombinant komagataella phaffii strain. *Pharmaceuticals* 15 (6), 746. doi:10.3390/ph15060746

Galindo-Rodríguez, G., Jaime-Pérez, J. C., Salinas-Carmona, M. C., González-Díaz, S. N., Castro-Corona, Á., Cavazos-González, R., et al. (2017). Do immunoglobulin G and immunoglobulin E anti-l-asparaginase antibodies have distinct implications in children with acute lymphoblastic leukemia? A cross-sectional study. *Rev. Bras. Hematol. Hemoter.* 39 (3), 202–209. doi:10.1016/j.bjhh.2016.11.006

Ghoshoon, M. B., Berenjian, A., Hemmati, S., Dabbagh, F., Karimi, Z., Negahdaripour, M., et al. (2015). Extracellular production of recombinant l-asparaginase II in *Escherichia coli*: Medium optimization using response surface methodology. *Int. J. Peptide Res. Ther.* 21 (4), 487–495. doi:10.1007/s10989-015-9476-6

Goswami, R., Hegde, K., and Veeranki, V. D. (2015). Production and characterization of novel glutaminase free recombinant L-asparaginase II of Erwinia carotovora subsp. atroseptica SCRI 1043 in *E. coli* BL21 (DE3). *Br. Microbiol. Res. J.* 6 (2), 95–112. doi:10.9734/bmrj/2015/13867

Goswami, R., Veeranki, V. D., and Mishra, V. K. (2019). Optimization of process conditions and evaluation of pH and thermal stability of recombinant l-Asparaginase II of Erwinia carotovora subsp. atroseptica SCRI 1043 in *E. coli*. *Biocatal. Agric. Biotechnol.* 22, 101377. doi:10.1016/j.bcab.2019.101377

Goyal, G., and Bhatt, V. R. (2015). L-asparaginase and venous thromboembolism in acute lymphocytic leukemia. *Future Oncol.* 11 (17), 2459–2470. doi:10.2217/fon.15.114

Grigoroudis, A. I., McInnes, C., Premnath, P. N., and Kontopidis, G. (2015). Efficient soluble expression of active recombinant human cyclin A2 mediated by *E. coli* molecular chaperones. *Protein Expr. Purif.* 113, 8–16. doi:10.1016/j.pep.2015.01.013

Gu, Y., Xu, X., Wu, Y., Niu, T., Liu, Y., Li, J., et al. (2018). Advances and prospects of Bacillus subtilis cellular factories: From rational design to industrial applications. *Metab. Eng.* 50, 109–121. doi:10.1016/j.ymben.2018.05.006

Guo, L., Wang, J., Yan, X., Chen, R., Qian, S., and Meng, G. (2000). Characterization of l-asparaginase fused with a protective ScFv and the protection mechanism. *Biochem. Biophysical Res. Commun.* 276 (1), 197–203. doi:10.1006/bbrc.2000.3434

Hong, S.-J., Lee, Y. H., Khan, A. R., Ullah, I., Lee, C., Park, C. K., et al. (2014). Cloning, expression, and characterization of thermophilic L-asparaginase from Thermococcus kodakarensis KOD1. *J. Basic Microbiol.* 54 (6), 500–508. doi:10.1002/jobm.201300741

Huang, L., Liu, Y., Sun, Y., Yan, Q., and Jiang, Z. (2014). Biochemical characterization of a novel L-Asparaginase with low glutaminase activity from Rhizomucor miehei and its application in food safety and leukemia treatment. *Appl. Environ. Microbiol.* 80 (5), 1561–1569. doi:10.1128/AEM.03523-13

Izadpanah Qeshmi, F., Homaei, A., Fernandes, P., and Javadpour, S. (2018). Marine microbial L-asparaginase: Biochemistry, molecular approaches and applications in tumor therapy and in food industry. *Microbiol. Res.* 208, 99–112. doi:10.1016/j.micres.2018.01.011

Izadpanah Qeshmi, F., Homaei, A., Khajeh, K., Kamrani, E., and Fernandes, P. (2022). Production of a novel marine Pseudomonas Aeruginosa recombinant L-asparaginase: Insight on the structure and biochemical characterization. *Mar. Biotechnol.* 24 (3), 599–613. doi:10.1007/s10126-022-10129-9

Jia, M., Xu, M., He, B., and Rao, Z. (2013). Cloning, expression, and characterization of l-asparaginase from a newly isolated Bacillus subtilis B11–06. *J. Agric. Food Chem.* 61 (39), 9428–9434. doi:10.1021/jf402636w

Jia, R., Wan, X., Geng, X., Xue, D., Xie, Z., and Chen, C. (2021). Microbial L-asparaginase for application in acrylamide mitigation from food: Current research status and future perspectives. *Microorganisms* 9 (8), 1659. doi:10.3390/microorganisms9081659

Jiao, L., Chi, H., Lu, Z., Zhang, C., Chia, S. R., Show, P. L., et al. (2020). Characterization of a novel type I l-asparaginase from Acinetobacter soli and its ability to inhibit acrylamide formation in potato chips. *J. Biosci. Bioeng.* 129 (6), 672–678. doi:10.1016/j.jbiosc.2020.01.007

Juturu, V., and Wu, J. C. (2018). Heterologous protein expression in Pichia pastoris: Latest research progress and applications. *ChemBioChem* 19 (1), 7–21. doi:10.1002/cbic.201700460

Kant Bhatia, S., Vivek, N., Kumar, V., Chandel, N., Thakur, M., Kumar, D., et al. (2021). Molecular biology interventions for activity improvement and production of industrial enzymes. *Bioresour. Technol.* 324, 124596. doi:10.1016/j.biortech.2020.124596

Kante, R. K., Vemula, S., Somavarapu, S., Mallu, M. R., Boje Gowd, B. H., and Ronda, S. R. (2018). Optimized upstream and downstream process conditions for the improved production of recombinant human asparaginase (rhASP) from *Escherichia coli* and its characterization. *Biologicals* 56, 45–53. doi:10.1016/j.biologicals.2018.10.002

Karamitros, C. S., and Konrad, M. (2014). Bacterial co-expression of the α and β protomers of human l-asparaginase-3: Achieving essential N-terminal exposure of a catalytically critical threonine located in the β-subunit. *Protein Expr. Purif.* 93, 1–10. doi:10.1016/j.pep.2013.10.007

Karamitros, C. S., and Konrad, M. (2016b). Fluorescence-activated cell sorting of human l -asparaginase mutant libraries for detecting enzyme variants with enhanced activity. *ACS Chem. Biol.* 11 (9), 2596–2607. doi:10.1021/acschembio.6b00283

Karamitros, C. S., and Konrad, M. (2016a). Fluorescence-activated cell sorting of human L-asparaginase mutant libraries for detecting enzyme variants with enhanced activity. *Acs Chem. Biol.* 11 (9), 2596–2607. doi:10.1021/acschembio.6b00283

Karamitros, C. S., and Labrou, N. E. (2014). Extracellular expression and affinity purification of L-asparaginase from E. chrysanthemi in *E. coli*. *Sustain. Chem. Process.* 2 (1), 16. doi:10.1186/s40508-014-0016-z

Kaur, J., Kumar, A., and Kaur, J. (2018). Strategies for optimization of heterologous protein expression in *E. coli*: Roadblocks and reinforcements. *Int. J. Biol. Macromol.* 106, 803–822. doi:10.1016/j.ijbiomac.2017.08.080

Khushoo, A., Pal, Y., and Mukherjee, K. (2005). Optimization of extracellular production of recombinant asparaginase in *Escherichia coli* in shake-flask and bioreactor. *Appl. Microbiol. Biotechnol.* 68 (2), 189–197. doi:10.1007/s00253-004-1867-0

Kim, K., Choe, D., Lee, D. H., and Cho, B. K. (2020). Engineering biology to construct microbial chassis for the production of difficult-to-express proteins. *Int. J. Mol. Sci.* 21 (3), 990. doi:10.3390/ijms21030990

Kim, S.-K., Min, W. K., Park, Y. C., and Seo, J. H. (2015). Application of repeated aspartate tags to improving extracellular production of *Escherichia coli* l-asparaginase isozyme II. *Enzyme Microb. Technol.* 79, 49–54. doi:10.1016/j.enzmictec.2015.06.017

Kishore, V., Nishita, K. P., and Manonmani, H. K. (2015). Cloning, expression and characterization of l-asparaginase from Pseudomonas fluorescens for large scale production in *E. coli* BL21. *3 Biotech.* 5 (6), 975–981. doi:10.1007/s13205-015-0300-y

Kornbrust, B. A., et al. (2009). "Asparaginase—An enzyme for acrylamide reduction in food products," in *Enzym. food Technol.* Editor R. J. Whitehurst and M. van Oort (2nd edition). New York: John Wiley and Sons, 59–87. doi:10.1002/9781444309935.ch4

Kotzia, G. A., and Labrou, N. E. (2007). l-Asparaginase from Erwinia Chrysanthemi 3937: Cloning, expression and characterization. *J. Biotechnol.* 127 (4), 657–669. doi:10.1016/j.jbiotec.2006.07.037

Lagassé, H. D., Alexaki, A., Simhadri, V. L., Katagiri, N. H., Jankowski, W., Sauna, Z. E., et al. (2017). Recent advances in (therapeutic protein) drug development. *F1000Research* 6, 113. doi:10.12688/f1000research.9970.1

Laskowski, R. A., and Swindells, M. B. (2011). LigPlot+: Multiple ligand–protein interaction diagrams for drug Discovery. *J. Chem. Inf. Model.* 51 (10), 2778–2786. doi:10.1021/ci200227u

Lavie, A., and Nguyen, H. (2017). *L-ASPARAGINASE variants and FUSION proteins with reduced l-glutaminase activity and enhanced stability*. WO. Patent No. US2017/020090. https://patentscope.wipo.int/search/en/detail.jsf?docId=WO2017151707.

Lawson, C. E., Martí, J. M., Radivojevic, T., Jonnalagadda, S. V. R., Gentz, R., Hillson, N. J., et al. (2021). Machine learning for metabolic engineering: A review. *Metab. Eng.* 63, 34–60. doi:10.1016/j.ymben.2020.10.005

Li, X., Xu, S., Zhang, X., Xu, M., Yang, T., Wang, L., et al. (2019). Design of a high-efficiency synthetic system for l-asparaginase production in Bacillus subtilis. *Eng. Life Sci.* 19 (3), 229–239. doi:10.1002/elsc.201800166

Li, X., Zhang, X., Xu, S., Zhang, H., Xu, M., Yang, T., et al. (2018). Simultaneous cell disruption and semi-quantitative activity assays for high-throughput screening of thermostable L-asparaginases. *Sci. Rep.* 8 (1), 7915. doi:10.1038/s41598-018-26241-7

Lima, G. M., Effer, B., Biasoto, H. P., Feijoli, V., Pessoa, A., Palmisano, G., et al. (2020). Glycosylation of L-asparaginase from *E. coli* through yeast expression and site-directed mutagenesis. *Biochem. Eng. J.* 156, 107516. doi:10.1016/j.bej.2020.107516

Loch, J. I., and Jaskolski, M. (2021). Structural and biophysical aspects of l-asparaginases: A growing family with amazing diversity. *IUCrJ* 8 (4), 514–531. doi:10.1107/S2052252521006011

Lopes, A. M., Oliveira-Nascimento, L. d., Ribeiro, A., Tairum, C. A., Breyer, C. A., Oliveira, M. A. d., et al. (2017). Therapeutic l-asparaginase: Upstream, downstream and beyond. *Crit. Rev. Biotechnol.* 37 (1), 82–99. doi:10.3109/07388551.2015.1120705

Lubkowski, J., and Wlodawer, A. (2021). Structural and biochemical properties of L-asparaginase. *FEBS J.* 288 (14), 4183–4209. doi:10.1111/febs.16042

Mahalik, S., Sharma, A., Das, D. R., Mittra, D., and Mukherjee, K. J. (2022). Co-expressing Leucine Responsive Regulatory protein (Lrp) enhances recombinant L-Asparaginase-II production in *Escherichia coli*. *J. Biotechnol.* 351, 99–108. doi:10.1016/j.jbiotec.2022.04.012

Mahalik, S., Sharma, A. K., Jain, P., and Mukherjee, K. J. (2017). *Identifying genomic targets for protein over-expression by "omics" analysis of Quiescent Escherichia coli cultures*. *Microb. Cell Factories* 16 (1), 133. doi:10.1186/s12934-017-0744-3

Makino, T., Skretas, G., and Georgiou, G. (2011). Strain engineering for improved expression of recombinant proteins in bacteria. *Microb. Cell Factories* 10 (1), 32. doi:10.1186/1475-2859-10-32

Maqsood, B., Basit, A., Khurshid, M., and Bashir, Q. (2020). Characterization of a thermostable, allosteric L-asparaginase from Anoxybacillus flavithermus. *Int. J. Biol. Macromol.* 152, 584–592. doi:10.1016/j.ijbiomac.2020.02.246

Markova, E. A., Shaw, R. E., and Reynolds, C. R. (2022). Prediction of strain engineerings that amplify recombinant protein secretion through the machine learning approach MaLPHAS. *Eng. Biol.* 6, 82–90. doi:10.1049/enb2.12025

Meena, B., Anburajan, L., Vinithkumar, N. V., Shridhar, D., Raghavan, R. V., Dharani, G., et al. (2016). Molecular expression of l-asparaginase gene from Nocardiopsis alba NIOT-VKMA08 in *Escherichia coli*: A prospective recombinant enzyme for leukaemia chemotherapy. *Gene* 590 (2), 220–226. doi:10.1016/j.gene.2016.05.003

Michalska, K., and Jaskolski, M. (2006). Structural aspects of L-asparaginases, their friends and relations. *Acta Biochim. Pol.* 53 (4), 627–640. doi:10.18388/abp.2006_3291

Mihooliya, K. N., Nitika, N., Bhambure, R., and Rathore, A. S. (2022). Post-refolding stability considerations for optimization of *in-vitro* refolding: L-asparaginase as a case study. *Biotechnol. J.* 18, 2200505. doi:10.1002/biot.202200505

Mortazavi, M., Torkzadeh-Mahani, M., Kargar, F., Nezafat, N., and Ghasemi, Y. (2020). *In silico* analysis of codon usage and rare codon clusters in the halophilic bacteria L-asparaginase. *Biologia* 75 (1), 151–160. doi:10.2478/s11756-019-00324-w

Mundaganur, Y. D., Mundaganur, D. S., and Kannarath, A. (2014). *In silico* drug search for better treatment for cancer: L-asparaginase. *Int. J. Res. Stud. Biosci. (IJRSB)* 2, 725.

Munhoz Costa, I., Custódio Moura, D., Meira Lima, G., Pessoa, A., Oresco dos Santos, C., Oliveira, M. A., et al. (2022). Engineered asparaginase from *Erwinia chrysanthemi* enhances asparagine hydrolase activity and diminishes enzyme immunoreactivity- a new promise to treat acute lymphoblastic leukemia. *J. Chem. Technol. Biotechnol.* 97 (1), 228–239. doi:10.1002/jctb.6933

Munhoz Costa, I., Schultz, L., de Araujo Bianchi Pedra, B., Leite, M. S. M., Farsky, S. H. P., de Oliveira, M. A., et al. (2016). Recombinant L-asparaginase 1 from *Saccharomyces cerevisiae*: An allosteric enzyme with antineoplastic activity. *Sci. Rep.* 6 (1), 36239. doi:10.1038/srep36239

Murashima, K., Chen, C. L., Kosugi, A., Tamaru, Y., Doi, R. H., and Wong, S. L. (2002). Heterologous production of Clostridium cellulovorans engB, using protease-deficient Bacillus subtilis, and preparation of active recombinant cellulosomes. *J. Bacteriol.* 184 (1), 76–81. doi:10.1128/jb.184.1.76-81.2002

Naderi, M., Ghaderi, R., Khezri, J., Karkhane, A., and Bambai, B. (2022). Crucial role of non-hydrophobic residues in H-region signal peptide on secretory production of l-asparaginase II in *Escherichia coli*. *Biochem. Biophysical Res. Commun.* 636, 105–111. doi:10.1016/j.bbrc.2022.10.029

Nguyen, H. A., Su, Y., and Lavie, A. (2016a). Design and characterization of Erwinia chrysanthemi l-asparaginase variants with diminished l-glutaminase activity*. *J. Biol. Chem.* 291 (34), 17664–17676. doi:10.1074/jbc.M116.728485

Nguyen, T. T. H., Cuong, T. N., Thanh, S. L. N., and Tuyen, T. D. (2016b). Optimization, purification and characterization of recombinant L-asparaginase II in *Escherichia coli*. *Afr. J. Biotechnol.* 15 (31), 1681–1691. doi:10.5897/ajb2016.15425

Niu, J., Meng, F., Zhou, Y., Zhang, C., Lu, Z., Lu, F., et al. (2021). Non-classical secretion of a type I L-asparaginase in Bacillus subtilis. *Int. J. Biol. Macromol.* 180, 677–683. doi:10.1016/j.ijbiomac.2021.03.104

Niu, J., Yan, R., Shen, J., Zhu, X., Meng, F., Lu, Z., et al. (2022). Cis-element engineering promotes the expression of Bacillus subtilis type I L-asparaginase and its application in food. *Int. J. Mol. Sci.* 23 (12), 6588. doi:10.3390/ijms23126588

Nunes, J. C. F., Cristóvão, R. O., Freire, M. G., Santos-Ebinuma, V. C., Faria, J. L., Silva, C. G., et al. (2020). Recent strategies and applications for l-asparaginase confinement. *Molecules* 25 (24), 5827. doi:10.3390/molecules25245827

Overton, T. W. (2014). Recombinant protein production in bacterial hosts. *Drug Discov. Today* 19 (5), 590–601. doi:10.1016/j.drudis.2013.11.008

Packiam, K. A. R., Ramanan, R. N., Ooi, C. W., Krishnaswamy, L., and Tey, B. T. (2020). Stepwise optimization of recombinant protein production in *Escherichia coli* utilizing computational and experimental approaches. *Appl. Microbiol. Biotechnol.* 104 (8), 3253–3266. doi:10.1007/s00253-020-10454-w

Paraskevopoulou, V., and Falcone, F. H. (2018). Polyionic tags as enhancers of protein solubility in recombinant protein expression. *Microorganisms* 6 (2), 47. doi:10.3390/microorganisms6020047

Patel, P. G., Panseriya, H. Z., Vala, A. K., Dave, B. P., and Gosai, H. B. (2022). Exploring current scenario and developments in the field of microbial L-asparaginase production and applications: A review. *Process Biochem.* 121, 529–541. doi:10.1016/j.procbio.2022.07.029

Peng, S., Chu, Z., Lu, J., Li, D., Wang, Y., Yang, S., et al. (2016). Co-expression of chaperones from P. furiosus enhanced the soluble expression of the recombinant hyperthermophilic α-amylase in *E. coli*. *Cell Stress Chaperones* 21 (3), 477–484. doi:10.1007/s12192-016-0675-7

Pillaca-Pullo, O., Rodrigues, D., Sánchez-Moguel, I., Lopes, A., Pimenta, M., Basi, T., et al. (2021). Recombinantl-asparaginase production using*Pichia pastoris*(*MUT*ˢstrain): Establishment of conditions for growth and induction phases. *J. Chem. Technol. Biotechnol.* 96 (1), 283–292. doi:10.1002/jctb.6540

Pokrovskaya, M. V., Aleksandrova, S. S., Pokrovsky, V. S., Omeljanjuk, N. M., Borisova, A. A., Anisimova, N. Y., et al. (2012). Cloning, expression and characterization of the recombinant Yersinia pseudotuberculosis l-asparaginase. *Protein Expr. Purif.* 82 (1), 150–154. doi:10.1016/j.pep.2011.12.005

Pokrovskaya, M. V., Pokrovsky, V. S., Aleksandrova, S. S., Sokolov, N. N., and Zhdanov, D. D. (2022). Molecular analysis of L-asparaginases for clarification of the mechanism of action and optimization of pharmacological functions. *Pharmaceutics* 14 (3), 599. doi:10.3390/pharmaceutics14030599

Pritsa, A. A., and Kyriakidis, D. A. (2001). L-asparaginase of Thermus thermophilus: Purification, properties and identification of essential amino acids for its catalytic activity. *Mol. Cell. Biochem.* 216 (1), 93–101. doi:10.1023/a:1011066129771

Qeshmi, F. I., Homaei, A., Fernandes, P., and Javadpour, S. (2018). Marine microbial L-asparaginase: Biochemistry, molecular approaches and applications in tumor therapy and in food industry. *Microbiol. Res.* 208, 99–112. doi:10.1016/j.micres.2018.01.011

Radha, R., Arumugam, N., and Gummadi, S. N. (2018). Glutaminase free l-asparaginase from *Vibrio cholerae*: Heterologous expression, purification and biochemical characterization. *Int. J. Biol. Macromol.* 111, 129–138. doi:10.1016/j.ijbiomac.2017.12.165

Rajendran, V., Pushpavanam, S., and Jayaraman, G. (2022). Continuous refolding of L-asparaginase inclusion bodies using periodic counter-current chromatography. *J. Chromatogr. A* 1662, 462746. doi:10.1016/j.chroma.2021.462746

Rodrigues, D., Pillaca-Pullo, O., Torres-Obreque, K., Flores-Santos, J., Sánchez-Moguel, I., Pimenta, M. V., et al. (2019). Fed-batch production of *Saccharomyces cerevisiae* L-asparaginase II by recombinant Pichia pastoris MUTs strain. *Front. Bioeng. Biotechnol.* 7, 16. doi:10.3389/fbioe.2019.00016

Roth, G., Nunes, J. E. S., Rosado, L. A., Bizarro, C. V., Volpato, G., Nunes, C. P., et al. (2013). Recombinant Erwinia carotovora l-asparaginase II production in *Escherichia coli* fed-batch cultures. *Braz. J. Chem. Eng.* 30, 245–256. doi:10.1590/s0104-66322013000200003

Saeed, H., Ali, H., Soudan, H., Embaby, A., El-Sharkawy, A., Farag, A., et al. (2018). Molecular cloning, structural modeling and production of recombinant Aspergillus terreus l. asparaginase in *Escherichia coli*. *Int. J. Biol. Macromol.* 106, 1041–1051. doi:10.1016/j.ijbiomac.2017.08.110

Sajitha, S., Vidya, J., Varsha, k., Binod, P., and Pandey, A. (2015). Cloning and expression of l-asparaginase from *E. coli* in eukaryotic expression system. *Biochem. Eng. J.* 102, 14–17. doi:10.1016/j.bej.2015.02.027

SalisLab (2022). Available at: https://salislab.net/software/.

Sannikova, E. P., Bulushova, N. V., Cheperegin, S. E., Gubaydullin, I. I., Chestukhina, G. G., Ryabichenko, V. V., et al. (2016). The modified heparin-binding l-asparaginase of Wolinella succinogenes. *Mol. Biotechnol.* 58 (8), 528–539. doi:10.1007/s12033-016-9950-1

Schmidt, F. (2004). Recombinant expression systems in the pharmaceutical industry. *Appl. Microbiol. Biotechnol.* 65 (4), 363–372. doi:10.1007/s00253-004-1656-9

Schmiegelow, K., Attarbaschi, A., Barzilai, S., Escherich, G., Frandsen, T. L., Halsey, C., et al. (2016). Consensus definitions of 14 severe acute toxic effects for childhood lymphoblastic leukaemia treatment: A delphi consensus. *Lancet Oncol.* 17 (6), e231–e239. doi:10.1016/S1470-2045(16)30035-3

Shakambari, G., Ashokkumar, B., and Varalakshmi, P. (2019). L-asparaginase – a promising biocatalyst for industrial and clinical applications. *Biocatal. Agric. Biotechnol.* 17, 213–224. doi:10.1016/j.bcab.2018.11.018

Shakambari, G., Sameer Kumar, R., Ashokkumar, B., Ganesh, V., Vasantha, V. S., and Varalakshmi, P. (2018). Cloning and expression of L-asparaginase from Bacillus tequilensis PV9W and therapeutic efficacy of Solid Lipid Particle formulations against cancer. *Sci. Rep.* 8 (1), 18013. doi:10.1038/s41598-018-36161-1

Sharafi, Z., Barati, M., Khoshayand, M. R., and Adrangi, S. (2017). Screening for type II L-asparaginases: Lessons from the genus halomonas. *Iran. J. Pharm. Res. IJPR* 16 (4), 1565–1573. https://www.ncbi.nlm.nih.gov/pmc/articles/PMC5843318/.

Sharma, A. K., Shukla, E., Janoti, D. S., Mukherjee, K. J., and Shiloach, J. (2020). A novel knock out strategy to enhance recombinant protein expression in *Escherichia coli*. *Microb. Cell Factories* 19 (1), 148. doi:10.1186/s12934-020-01407-z

Sindhu, R., and Manonmani, H. K. (2018). Expression and characterization of recombinant l-asparaginase from Pseudomonas fluorescens. *Protein Expr. Purif.* 143, 83–91. doi:10.1016/j.pep.2017.09.009

Singh, A., Upadhyay, V., Upadhyay, A. K., Singh, S. M., and Panda, A. K. (2015). Protein recovery from inclusion bodies of *Escherichia coli* using mild solubilization process. *Microb. Cell Factories* 14 (1), 41. doi:10.1186/s12934-015-0222-8

Singha, T. K., Gulati, P., Mohanty, A., Khasa, Y. P., Kapoor, R. K., and Kumar, S. (2017). Efficient genetic approaches for improvement of plasmid based expression of recombinant protein in *Escherichia coli*: A review. *Process Biochem.* 55, 17–31. doi:10.1016/j.procbio.2017.01.026

Singhvi, P., Verma, J., Panwar, N., Wani, T. Q., Singh, A., Qudratullah, M., et al. (2021). Molecular attributes associated with refolding of inclusion body proteins using the freeze–thaw method. *Front. Microbiol.* 12, 618559. doi:10.3389/fmicb.2021.618559

Souza, C. C. d., Guimarães, J. M., Pereira, S. D. S., and Mariúba, L. A. M. (2021). The multifunctionality of expression systems in Bacillus subtilis: Emerging devices for the production of recombinant proteins. *Exp. Biol. Med.* 246 (23), 2443–2453. doi:10.1177/15353702211030189

Sushma, C., Anand, A. P., and Veeranki, V. D. (2017). Enhanced production of glutaminase free L-asparaginase II by Bacillus subtilis WB800N through media optimization. *Korean J. Chem. Eng.* 34 (11), 2901–2915. doi:10.1007/s11814-017-0211-1

Tien Cuong Nguyen (2014). Expression, purification and evaluation of recombinant L-asparaginase in menthylotrophic Pichia pastoris. *J. vietnamiese enviorment* 6, 228–292. doi:10.13141/jve.vol6.no3.pp288-292

Trieu, V. (2010). *Albumin binding peptide-mediated disease targeting*. CA: Ridout and Maybee LLP. Patent No. 2867252. https://www.ic.gc.ca/opic-cipo/cpd/eng/patent/2867252/summary.html?type=number_searchandtabs1Index=tabs1_1.

TwistBioscience (2022). TwistBioscience. Available at: https://www.twistbioscience.com/.

Ueno, T., Ohtawa, K., Mitsui, K., Kodera, Y., Hiroto, M., Matsushima, A., et al. (1997). Cell cycle arrest and apoptosis of leukemia cells induced by L-asparaginase. *Leukemia* 11 (11), 1858–1861. doi:10.1038/sj.leu.2400834

Upadhyay, A. K., Singh, A., Mukherjee, K. J., and Panda, A. K. (2014). Refolding and purification of recombinant L-asparaginase from inclusion bodies of *E. coli* into active tetrameric protein. *Front. Microbiol.* 5, 486. doi:10.3389/fmicb.2014.00486

Vachher, M., Sen, A., Kapila, R., and Nigam, A. (2021). Microbial therapeutic enzymes: A promising area of biopharmaceuticals. *Curr. Res. Biotechnol.* 3, 195–208. doi:10.1016/j.crbiot.2021.05.006

Vallejo, L. F., and Rinas, U. (2004). Strategies for the recovery of active proteins through refolding of bacterial inclusion body proteins. *Microb. Cell factories* 3, 11–12. doi:10.1186/1475-2859-3-11

Vasina, M., Velecký, J., Planas-Iglesias, J., Marques, S. M., Skarupova, J., Damborsky, J., et al. (2022). Tools for computational design and high-throughput screening of therapeutic enzymes. *Adv. Drug Deliv. Rev.* 183, 114143. doi:10.1016/j.addr.2022.114143

Verma, N., Kumar, K., Kaur, G., and Anand, S. (2007). L-Asparaginase: A promising chemotherapeutic agent. *JC Rev. Biotechnol.* 27 (1), 45–62. doi:10.1080/07388550601173926

Vidya, J., and Pandey, A. (2012). Recombinant expression and characterization of l-asparaginase II from a moderately thermotolerant bacterial isolate. *Appl. Biochem. Biotechnol.* 167 (5), 973–980. doi:10.1007/s12010-012-9617-8

Vimal, A., and Kumar, A. (2017). Biotechnological production and practical application of L-asparaginase enzyme. *Biotechnol. Genet. Eng. Rev.* 33 (1), 40–61. doi:10.1080/02648725.2017.1357294

Vimal, A., Kumar, A., and l-Asparaginase, P. (2018). l-Asparaginase: a feasible therapeutic molecule for multiple diseases. *3 Biotech.* 8 (6), 278. doi:10.1007/s13205-018-1282-3

Wang, Y., Liu, Q., Weng, H., Shi, Y., Chen, J., Du, G., et al. (2019). Construction of synthetic promoters by assembling the sigma factor binding −35 and −10 boxes. *Biotechnol. J.* 14 (1), 1800298. doi:10.1002/biot.201800298

Wang, Y., Liu, Y., and Wang, Z. (2014). Influence of promoter and signal peptide on the expression of pullulanase in Bacillus subtilis. *Biotechnol. Lett.* 36 (9), 1783–1789. doi:10.1007/s10529-014-1538-x

Wang, Y., Qian, S., Meng, G., and Zhang, S. (2001). Cloning and expression of L-asparaginase gene in *Escherichia coli*. *Appl. Biochem. Biotechnol.* 95 (2), 93–101. doi:10.1385/abab:95:2:093

Wang, Y., Xu, W., Wu, H., Zhang, W., Guang, C., and Mu, W. (2021). Microbial production, molecular modification, and practical application of l-asparaginase: A review. *Int. J. Biol. Macromol.* 186, 975–983. doi:10.1016/j.ijbiomac.2021.07.107

Wang, Z., Zhang, M., Lv, X., Fan, J., Zhang, J., Sun, J., et al. (2018). GroEL/ES mediated the *in vivo* recovery of TRAIL inclusion bodies in *Escherichia coli*. *Sci. Rep.* 8 (1), 15766. doi:10.1038/s41598-018-34090-7

Watts, A., Sankaranarayanan, S., and Raipuria, R. K. (2021). Optimizing protein expression in heterologous system: Strategies and tools. *Meta Gene* 29, 100899. doi:10.1016/j.mgene.2021.100899

Weninger, A., Hatzl, A. M., Schmid, C., Vogl, T., and Glieder, A. (2016). Combinatorial optimization of CRISPR/Cas9 expression enables precision genome engineering in the methylotrophic yeast Pichia pastoris. *J. Biotechnol.* 235, 139–149. doi:10.1016/j.jbiotec.2016.03.027

Xu, F., Oruna-Concha, M.-J., and Elmore, J. S. (2016). The use of asparaginase to reduce acrylamide levels in cooked food. *Food Chem.* 210, 163–171. doi:10.1016/j.foodchem.2016.04.105

Yang, H., Qu, J., Zou, W., Shen, W., and Chen, X. (2021). An overview and future prospects of recombinant protein production in Bacillus subtilis. *Appl. Microbiol. Biotechnol.* 105 (18), 6607–6626. doi:10.1007/s00253-021-11533-2

Yang, S., Du, G., Chen, J., and Kang, Z. (2017). Characterization and application of endogenous phase-dependent promoters in Bacillus subtilis. *Appl. Microbiol. Biotechnol.* 101 (10), 4151–4161. doi:10.1007/s00253-017-8142-7

Yang, Z., and Zhang, Z. (2018). Engineering strategies for enhanced production of protein and bio-products in Pichia pastoris: A review. *Biotechnol. Adv.* 36 (1), 182–195. doi:10.1016/j.biotechadv.2017.11.002

Yano, S., Minato, R., Thongsanit, J., Tachiki, T., and Wakayama, M. (2008). Overexpression of type I L-asparaginase of Bacillus subtilis in *Escherichia coli*, rapid purification and characterisation of recombinant type I L-asparaginase. *Ann. Microbiol.* 58, 711–716. doi:10.1007/bf03175579

Yari, M., Ghoshoon, M. B., Nezafat, N., and Ghasemi, Y. (2020). Experimental evaluation of in silico selected signal peptides for secretory expression of Erwinia asparaginase in *Escherichia coli*. *Int. J. Peptide Res. Ther.* 26 (3), 1583–1591. doi:10.1007/s10989-019-09961-w

Yuan, T. Z., Ormonde, C. F. G., Kudlacek, S. T., Kunche, S., Smith, J. N., Brown, W. A., et al. (2015). Shear-stress-mediated refolding of proteins from aggregates and inclusion bodies. *ChemBioChem* 16 (3), 393–396. doi:10.1002/cbic.201402427

Zhang, X., Wang, Z., Wang, Y., Li, X., Zhu, M., Zhang, H., et al. (2021). Heterologous expression and rational design of l-asparaginase from rhizomucor miehei to improve thermostability. *Biology* 10 (12), 1346. doi:10.3390/biology10121346

Zhou, C., Ye, B., Cheng, S., Zhao, L., Liu, Y., Jiang, J., et al. (2019). Promoter engineering enables overproduction of foreign proteins from a single copy expression cassette in Bacillus subtilis. *Microb. Cell Factories* 18 (1), 111. doi:10.1186/s12934-019-1159-0

Zhou, Y., Lu, Z., Wang, X., Selvaraj, J. N., and Zhang, G. (2018). Genetic engineering modification and fermentation optimization for extracellular production of recombinant proteins using *Escherichia coli*. *Appl. Microbiol. Biotechnol.* 102 (4), 1545–1556. doi:10.1007/s00253-017-8700-z

Zuo, S., Xue, D., Zhang, T., Jiang, B., and Mu, W. (2014). Biochemical characterization of an extremely thermostable l-asparaginase from Thermococcus gammatolerans EJ3. *J. Mol. Catal. B Enzym.* 109, 122–129. doi:10.1016/j.molcatb.2014.08.021

frontiers | Frontiers in Neuroscience

TYPE Mini Review
PUBLISHED 02 August 2023
DOI 10.3389/fnins.2023.1213410

OPEN ACCESS

EDITED BY
Kimberly M. Huber,
University of Texas Southwestern Medical Center, United States

REVIEWED BY
Christina Gross,
Cincinnati Children's Hospital Medical Center, United States
Cara Jean Westmark,
University of Wisconsin-Madison, United States

*CORRESPONDENCE
Christian A. Cea-Del Rio
✉ christian.cea@usach.cl

RECEIVED 28 April 2023
ACCEPTED 17 July 2023
PUBLISHED 02 August 2023

CITATION
Milla LA, Corral L, Rivera J, Zuñiga N, Pino G, Nunez-Parra A and Cea-Del Rio CA (2023) Neurodevelopment and early pharmacological interventions in Fragile X Syndrome. *Front. Neurosci.* 17:1213410. doi: 10.3389/fnins.2023.1213410

Neurodevelopment and early pharmacological interventions in Fragile X Syndrome

Luis A. Milla[1], Lucia Corral[2], Jhanpool Rivera[2], Nolberto Zuñiga[2], Gabriela Pino[2], Alexia Nunez-Parra[3,4] and Christian A. Cea-Del Rio[2]*

[1]Centro de Investigacion Biomedica y Aplicada (CIBAP), Escuela de Medicina, Facultad de Ciencias Medicas, Universidad de Santiago de Chile, Santiago, Chile, [2]Laboratorio de Neurofisiopatologia, Centro de Investigacion Biomedica y Aplicada (CIBAP), Escuela de Medicina, Facultad de Ciencias Medicas, Universidad de Santiago de Chile, Santiago, Chile, [3]Physiology Laboratory, Department of Biology, Faculty of Science, Universidad de Chile, Santiago, Chile, [4]Cell Physiology Center, Universidad de Chile, Santiago, Chile

Fragile X Syndrome (FXS) is a neurodevelopmental disorder and the leading monogenic cause of autism and intellectual disability. For years, several efforts have been made to develop an effective therapeutic approach to phenotypically rescue patients from the disorder, with some even advancing to late phases of clinical trials. Unfortunately, none of these attempts have completely succeeded, bringing urgency to further expand and refocus research on FXS therapeutics. FXS arises at early stages of postnatal development due to the mutation and transcriptional silencing of the Fragile X Messenger Ribonucleoprotein 1 gene (*FMR1*) and consequent loss of the Fragile X Messenger Ribonucleoprotein (FMRP) expression. Importantly, FMRP expression is critical for the normal adult nervous system function, particularly during specific windows of embryogenic and early postnatal development. Cellular proliferation, migration, morphology, axonal guidance, synapse formation, and in general, neuronal network establishment and maturation are abnormally regulated in FXS, underlying the cognitive and behavioral phenotypes of the disorder. In this review, we highlight the relevance of therapeutically intervening during critical time points of development, such as early postnatal periods in infants and young children and discuss past and current clinical trials in FXS and their potential to specifically target those periods. We also discuss potential benefits, limitations, and disadvantages of these pharmacological tools based on preclinical and clinical research.

KEYWORDS

neurodevelopment, Fragile X syndrome, clinical trials, pharmacological interventions, GABA, mGluR, PI3K

Introduction

Brain development occurs in a highly coordinated fashion, with a wide range of molecular and environmental factors contributing to neuronal network morphology, connectivity, and functional maturation. Fragile X Syndrome (FXS) is the leading genetic cause of intellectual disability and autism and is classified as a neurodevelopmental disorder due to the appearance of behavioral and cognitive phenotypes during early postnatal development. The syndrome exhibits a range of behavioral and cognitive alterations, including abnormalities in social behaviors, increased anxiety, cognitive deficits, hyperexcitability, and sensory

hyper-responsiveness (Miller et al., 1999; Kau et al., 2004; Kaufmann et al., 2004; Hagerman and Stafstrom, 2009).

FXS is caused by the transcriptional silencing of the Fragile X Messenger Ribonucleoprotein 1 (*FMR1*) gene due to the hypermethylation of a CGG repeat expansion in its 5'-untranslated region (5'UTR; (Oberlé et al., 1991; Verkerk et al., 1991; Vincent et al., 1991; Yu et al., 1991). This epigenetic control mechanism is developmentally regulated (Mor-Shaked and Eiges, 2018) and occurs during early stages of gestation in different cells and to varying degrees (Schultz et al., 2015), even within the same tissue (Chen et al., 2011). The silencing of *FMR1* results in the loss of expression of the Fragile X Messenger Ribonucleoprotein (FMRP), an RNA-binding protein that primarily regulates both mRNA mobilization and local translation (Feng et al., 1997; Brown et al., 2001; Stefani et al., 2004), but it has been also involve in mRNA stability (De Rubeis and Bagni, 2010; Shu et al., 2020), DNA damage response (Alpatov et al., 2014), and direct ion channel regulation (Kalmbach and Brager, 2020; Kshatri et al., 2020). FMRP mRNA targets are involved in processes that occur during critical periods of postnatal neurodevelopment such as axonal guidance, synaptic connectivity, and neuronal network plasticity (Till, 2010) strongly suggesting that therapeutic intervention during these time windows could be relevant for completely or partially reversing the molecular and cellular alterations underlying the physiological symptoms observed in individuals with FXS.

In this review, we briefly discuss the role of FMRP during postnatal neurodevelopment, and then, based on age-group recruitment requirements, summarize the results of current and past pharmacological clinical trials in FXS. Finally, we discuss the potential benefits, limitations, and disadvantages of early postnatal pharmacological interventions.

Role of FMRP in neurodevelopment

Since FMRP is a RNA-binding protein that regulates protein translation by association with mRNAs, its absence impacts different neurodevelopmental processes along this time frame (Russo and DiAntonio, 2019; Sears et al., 2019; Doll et al., 2020, 2021; Prashad and Gopal, 2021). In FXS, FMRP is progressively developmentally regulated with epigenetic silencing of the *FMR1* gene that begins around 10 to 13 weeks of gestation (Willemsen et al., 2002; Li et al., 2020), and cognitive and behavioral FXS characteristics emerging during early childhood (2- to 3-year-old).

To study the role of FMRP during brain development, researchers have widely used rodents as an experimental model where the *Fmr1* gene is knocked-out from zygote stages in the FXS mice model (The Dutch-Belgian Fragile X Consorthium et al., 1994). Evidence from rodents developmental brain suggest that the first postnatal week is roughly equivalent to the third semester human infant (Clancy et al., 2007; Semple et al., 2013), including processes such as oligodendrocyte maturation (postnatal day (pnd) 1-3) and increased axonal and dendritic density (pnd 7-10) (Semple et al., 2013). However, there are still some processes that occur postnatally in both humans and rodents such as peaks in synaptogenesis, peak in myelination rate, neurotransmitter receptor changes (humans: 2-3 year old; rodents: pnd 20-21), and plateau for synaptic pruning (humans: 12–18 year old; rodents: pnd 35-49) (Semple et al., 2013; Silbereis et al., 2016). In the mouse model, FMRP brain expression peaks seem to coincide with critical periods of synaptogenesis (Zito and Svoboda, 2002), which occurs at the end of the first postnatal week (Bonaccorso et al., 2015), and gradually declines thereafter (Nimchinsky et al., 2001; Gholizadeh et al., 2015). Recent studies have shown that re-expression of FMRP in cortical excitatory cells during early postnatal development ameliorates structural, functional, and behavioral abnormalities seen in the FXS mouse model (Rais et al., 2022).

FMRP expression also seems to peak perinatally in healthy human subjects, as suggested by the relative expression levels of the gene (Figure 1A) obtained from the publicly available Brainspan – Allen Brain Atlas website (Miller et al., 2014). This correlates with neurodevelopmental milestones such as synaptogenesis, synaptic pruning, myelination and apoptosis (Silbereis et al., 2016). Furthermore, this role of FMRP during neurodevelopment is highlighted by one of the most characteristic neuronal phenotypes found in FXS: an abundance of hyper elongated and immature dendritic spines observed in both animal models (Zito and Svoboda, 2002; Kang et al., 2021) and human cortical brain regions (Irwin et al., 2000, 2001). Additionally, studies from forebrain organoids from patient-derived induced pluripotent stem cells (iPSC) reveal that loss of FMRP leads to dysregulated neurogenesis, abnormal neuronal differentiation, increased neuronal excitability and pervasive gene expression alterations in a cell-specific manner (Sunamura et al., 2018; Kang et al., 2021). More specifically, iPSC from FXS patients showed a delayed GABA polarization switch, decrease number of GABAergic inhibitory interneuron populations and hyperexcitable membrane properties in differentiated neurons (Zhang et al., 2022). These findings correlate with diminished GABA, GABA receptors, and glutamate decarboxylase (GAD) expression levels, the delayed GABA polarization switch, and the overall neuronal hyperactivity reported in animal models (Cea-Del Rio et al., 2014; Contractor et al., 2015; Di et al., 2020).

Altogether, evidence suggests that FMRP plays an important function during neurodevelopment, particularly at the synaptogenesis peri- and postnatal critical periods, which may underlie the clinical symptomatology observed in the mature FXS nervous system, providing an attractive window for therapeutic intervention.

Current and potential use of small molecules during neurodevelopment for FXS

Since 2002, several therapeutic tools and approaches have been tested in clinical trials for FXS (Supplementary Table S1; The data included in this table was obtained on August 2022 from www.ClinicalTrials.gov; search terms *"Fragile X Syndrome," "FXS."* The table is available in the following repository https://doi.org/10.6084/m9.figshare.23643210.v1). Although the results have mostly been unfavorable because reason such as outcome measures chosen, enrollment criteria fidelity, enhanced placebo response rates and what age range is most appropriate to treatment success, they have helped to redefine or concentrate efforts on newer and multidisciplinary approaches (Reviewed in Erickson et al., 2017). Thus, clinical trials have begun to focus on addressing early postnatal temporal windows that may coincide with critical periods of neurodevelopment (Figures 2B,C). To this day, only 5 and 16% of the FXS clinical trials have focused on populations younger than 3 years old or between 3 to

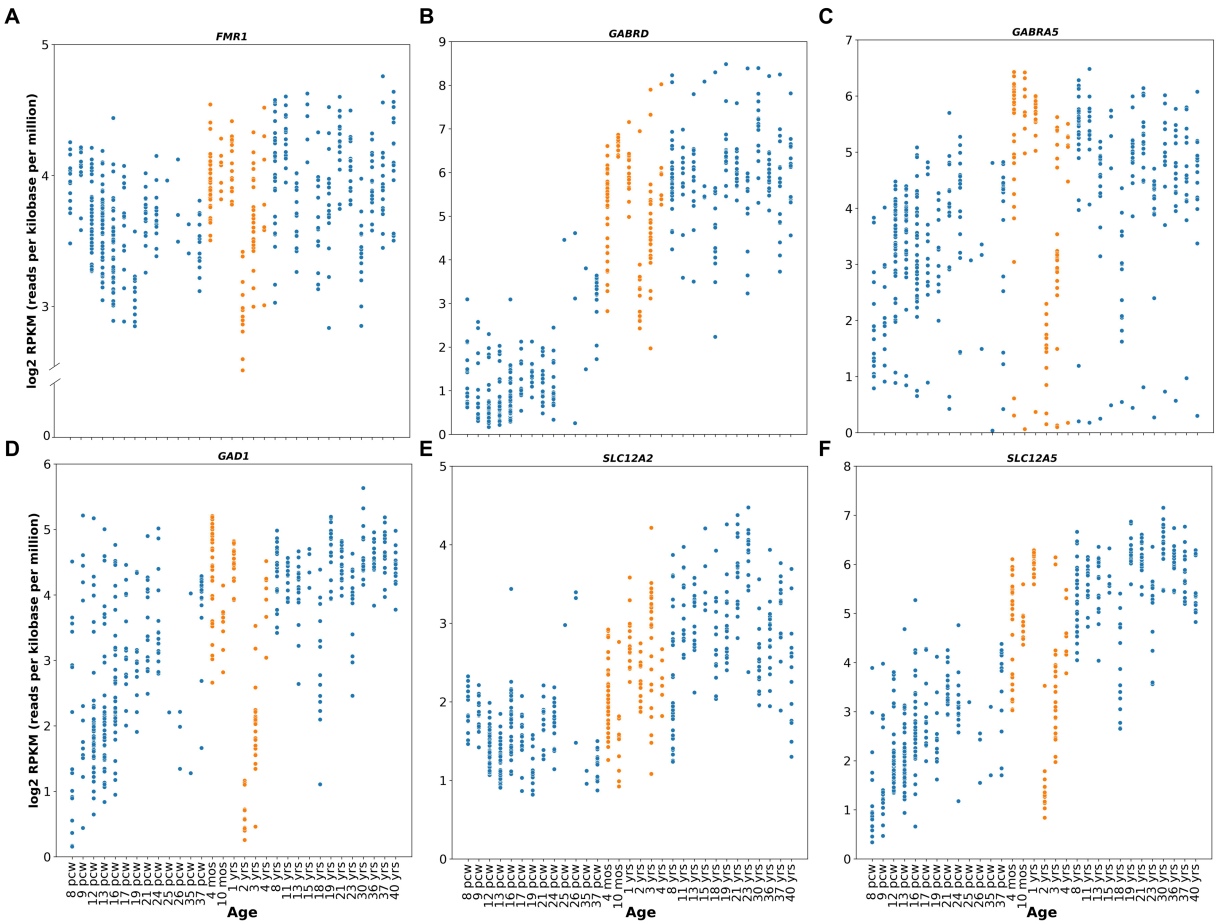

FIGURE 1
Human relative gene expression throughout development. FMR1, GABRD, GABRA5, GAD1, SLC12A2 and SLC12A5 genes from embryonic stages (post conceptional weeks, pcw) to adulthood of healthy human subjects. RNA-seq data were obtained from Brainspan Developmental Transcriptome, containing log2 RPKM (reads per kilobase per million) values. Orange dots shows expression from 4 months to 4 years. Genes analyzed were: **(A)** FMR1 (ENSG00000102081), **(B)** GABRD (ENSG00000187730), **(C)** GABRA5 (ENSG00000186297), **(D)** GAD1 (ENSG00000128683), **(E)** SLC12A2 (ENSG00000064651), **(F)** SLC12A5 (ENSG00000124140). RNA-seq data were obtained from Brainspan Developmental Transcriptome, publicly available at https://human.brain-map.org/.

6 years old children, respectively (Figure 2B), although numbers have started to trend upward in recent years (Figure 2C).

Pharmacological approaches have concentrated on drug design, addressing mGluR antagonism, GABA modulation, and intracellular pathway modulation (Berry-Kravis et al., 2017; Ligsay et al., 2017; Hagerman et al., 2018; Youssef et al., 2018). The details of the pharmacological agents tested and results from preclinical studies and clinical trials have been widely and recently reviewed (Erickson et al., 2017; Munshi et al., 2017; Berry-Kravis et al., 2018; Protic et al., 2022), so we will focus on discussing literature that highlights the potential pharmacological use during critical time windows of neurodevelopment and the possible outcomes.

Metabotropic glutamate receptor neurotransmission and signaling

Synaptic activation regulates FMRP expression via mGluRs (Weiler et al., 1997) that rely on intracellular pathways associated with mTOR and ERK1/2 signaling (Nosyreva and Huber, 2006; Sharma et al., 2010), a pathway that is particularly relevant during neurodevelopmental periods of synaptogenesis. These findings form the basis of the most prominent theory explaining FXS, the "mGluR theory," which involves the upregulation of mGluR-dependent mechanisms and increased protein synthesis (Bear et al., 2004). This theory has been validated in preclinical studies in mice and *Drosophila melanogaster* models where several FXS cellular and behavioral phenotypes were corrected when mGluR neurotransmission was either antagonized or knocked out (Chuang, 2005; McBride et al., 2005; Dölen et al., 2007).

Over the years, different clinical trials have targeted the metabotropic glutamatergic hypothesis, including the testing of Mavoglurant, a selective antagonist of the mGlu5 receptor (ClinicalTrials.gov Identifiers: NCT01253629, NCT01433354), and Basimglurant (ClinicalTrials.gov Identifier: NCT01517698, NCT01015430, NCT01750957) and Fenobam (Berry-Kravis et al., 2009), both negative allosteric modulators of the same receptor. Fenobam was discontinued after a pilot study that did not report results due to financial problems with the manufacturer company, and Basimglurant's trial status has not been updated since 2016.

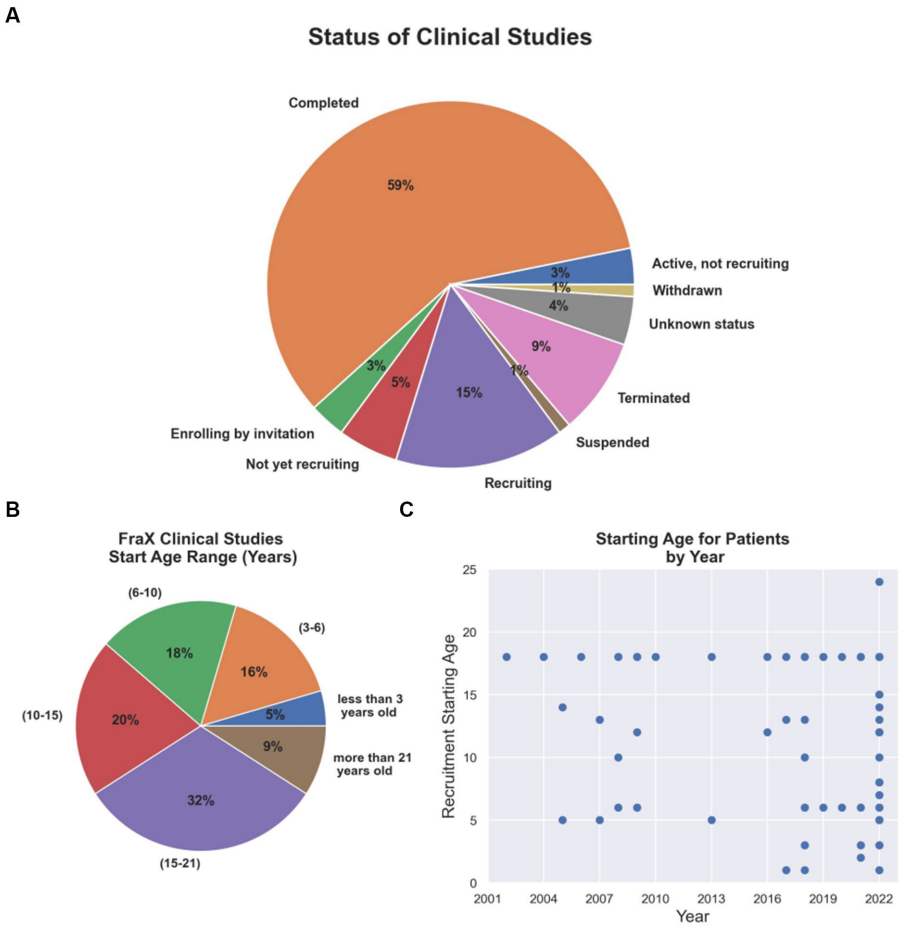

FIGURE 2
Current FXS clinical trial status and age group addressed. **(A)** Completion and recruiting status for FXS clinical trials. **(B)** Percentage of FXS clinical trials per age group. **(C)** Starting age required for patients recruited in clinical trials by year from 2002 to 2022.

Mavoglurant has reported a lack of efficacy for behavioral phenotypes in several clinical trial studies, regardless of FMRP methylation status when evaluated in adolescent/adult groups (Berry-Kravis et al., 2016).

Interestingly, despite being a neurodevelopmental disorder, clinical trials have only recently begun to focus on exploring pharmacological interventions during early developmental periods (Figure 2B). Indeed, a double-blind, placebo-controlled research design for Mavoglurant paired with an intensive language intervention is currently ongoing in children between 32 months and 6 years old (ClinicalTrials.gov Identifier: NCT02920892) assessing early postnatal windows of neurodevelopment that may overlap with periods of synaptogenesis and synaptic plasticity. The expected outcomes of this trial are to determine whether the drug improves language learning and communication that involve the child's use of gestures, eye contact, vocalizations, and/or words and word combinations to communicate a message to a listener (ClinicalTrials.gov Identifier: NCT02920892).

This pursuit of an early postnatal intervention is supported by evidence showing that group 1 mGluRs (mGluR1 and mGluR5) have an important role in synaptogenesis, synaptic pruning, and plasticity (Riedel and Reymann, 1996; Bortolotto et al., 1999, 2005; Cea-Del Rio et al., 2020), which occur during perinatal and early postnatal development. Indeed, mGluR5 protein expression levels are high during the first 2 weeks of postnatal life (Lu et al., 1997; Friedman et al., 2016; Lum et al., 2016) and studies in mGluR5 KO mice have shown impaired learning behavior and defects in the formation of the somatosensory cortical barrels, underscoring its importance for cortical development (Catania et al., 1994; Romano et al., 2002). Moreover, downregulation of mGluR expression (Dölen et al., 2007) or administration of mGluR antagonists to neonate *Fmr1* KO mice (Su et al., 2011) had a greater effect on reducing the average neuronal spine length and density of the FXS phenotype when compared to adults. On the contrary, mGluR antagonism during early stages of wild type mice development, although at higher concentrations to those reported in *Fmr1* KO, have also shown diminished proliferation and differentiation of progenitor neuronal cells (PNCs) (Di Giorgi-Gerevini et al., 2005; Friedman et al., 2016), similar to those exhibited by mice lacking mGluR5 (Di Giorgi-Gerevini et al., 2005). Furthermore, a study in FXS forebrain organoids from human showed that MPEP treatment failed to rescue the synaptic, excitability, and neuronal developmental phenotypes seen in these organoids (Kang et al., 2021), altogether, suggesting none or potential negative effect of mGluR antagonist drugs used during these windows of development.

In addition, considerations need to be made in light of recent human studies using positron emission tomography (PET) after administration of a novel specific mGluR5 PET ligand, 3-[^{18}F]

fluoro-5-(2-pyridinylethynyl) benzonitrile ([^{18}F]FPEB), which showed reduced mGluR5 availability and distribution in humans with FXS (Brašić et al., 2021, 2022; Mody et al., 2021) either reflecting mGluR5 high occupancy, as a result of a hyperexcited network, or mGluR decreased protein expression. Interestingly, this last scenario would not be consistent with the proposed mGluR theory and the preclinical studies that gave rise to the clinical trials on mGluR antagonists (Huber et al., 2002; Bear et al., 2004; Osterweil et al., 2010). It is worth notice, that these PET studies were performed in FXS adult patients between 18 and 60 years old, which may explain the unsuccessful results in mGluR5 antagonist clinical trials that have addressed a similar age range (Bailey et al., 2015; Berry-Kravis et al., 2016; Youssef et al., 2018). Although this does not necessarily mean that pharmacological interventions during early development (children and infants) would be unsuccessful, a complex scenario for trials in younger patients could be expected. Beyond these considerations, further evaluation of mGluR5 expression in younger FXS patients is required to better understand the implications of the use of mGluR antagonists at these developmental stages.

Excitatory-inhibitory balance and GABAergic neurotransmission

Excitatory-inhibitory (E-I) balance establishment depends on genetic and homeostatic mechanisms while experiences shape it throughout synaptogenesis and plasticity development (Sohal and Rubenstein, 2019). Indeed, E-I balance is crucial for maintaining stable levels of activity and as a signal-to-noise detector mechanism in the neuronal network (Sohal and Rubenstein, 2019). FXS is characterized by a hyperexcitable neuronal phenotype that primarily reflects disturbances on the E-I balance and its molecular components (Contractor et al., 2015; Antoine et al., 2019). Data form FXS animal models indicate that FMRP interacts with and regulates several of these components including NMDA, AMPA, $GABA_A$ receptor subunits ($GABA_AR$; The Dutch-Belgian Fragile X Consorthium et al., 1994; Gross et al., 2011; Deng and Klyachko, 2016; Zhu et al., 2018) and ion channel expression (Bureau et al., 2008; Harlow et al., 2010; Deng et al., 2013; Bausch et al., 2015). For instance, FMRP interacts with potassium channel subunits (Deng et al., 2013), and large-conductance BK calcium-activated channels (Bureau et al., 2008; Harlow et al., 2010) which regulate cell excitability. During neurodevelopment these alterations in the E-I balance have been shown to translate into delayed cortical functional maturation and disrupted synaptic plasticity in FXS (Olmos-Serrano et al., 2010; Cellot and Cherubini, 2013). Clinically, this hyperexcitable phenotype is proposed as a neurobiological substrate for behavioral traits such as anxiety, irritability, hyperactivity, and hypersensitivity, which explains why it has been considered a primary target in several clinical trials attempting to modulate either or both excitatory and inhibitory neurotransmission (ClinicalTrials.gov Identifiers: NCT00054730, NCT00895752, NCT00584948, NCT01911455, NCT03697161, NCT01725152, NCT01282268, NCT01325220, NCT03697161, and NCT01911455).

In particular, $GABA_AR$ was first postulated as a therapeutic target for the treatment of FXS in 2007 (D'Hulst and Kooy, 2007). These attempts were supported for several studies showing that *Fmr1*KO mice exhibit diminished levels of the GAD enzyme expression (Semple et al., 2013), and concomitant alterations in intracellular GABA availability and a reduction in synaptically released GABA (Olmos-Serrano et al., 2010). Also, FMRP interacts with $GABA_AR$ subunits (D'Hulst et al., 2006; Gantois et al., 2006; Curia et al., 2009; Olmos-Serrano et al., 2010; Kratovac and Corbin, 2013) that are typically associated with providing non-synaptic tonic forms of inhibition (Gantois et al., 2006; Curia et al., 2009; Martin et al., 2014; Zhang et al., 2017), a mechanism that delivers a persistent inhibitory background conductance that directly regulates the E-I balance (Mitchell and Silver, 2003; Semyanov et al., 2004; Bonin et al., 2007). These preclinical findings have been validated in humans, which show reduced $GABA_AR$ binding, as evaluated using PET scan (D'Hulst et al., 2015) and transcranial magnetic stimulation (TMS), revealing abnormal functional inhibition in adults with FXS (Morin-Parent et al., 2019). Subsequent preclinical studies with the GABA-mimetic Gaboxadol, a $GABA_AR$ agonist with higher affinity for delta(δ)-containing $GABA_AR$ (Stórustovu and Ebert, 2006), Ganaxolone, an allosteric $GABA_AR$ superagonist, and Arbaclofen, a $GABA_BR$ agonist, demonstrated correction of the locomotor hyperactivity, irritability, anxiety-like behaviors (Olmos-Serrano and Corbin, 2011; Cogram et al., 2019), audiogenic seizures (Heulens et al., 2012), repetitive/preservative behavior (Braat et al., 2015), and excessive basal protein synthesis and abnormal spine density (Pacey et al., 2009; Henderson et al., 2012; Qin et al., 2015) phenotypes.

In humans, clinical studies of Arbaclofen and Ganaxolone were undertaken in 2013 and 2016, respectively (ClinicalTrials.gov, NCT01725152, NCT01282268 and NCT01325220), with results reported in 2017 (Berry-Kravis et al., 2017; Ligsay et al., 2017). Unfortunately, neither of these drugs have resulted in significant improvements in the overall population, although promising results were observed when children population subgroups were separately analyzed (ages 6-9 years for Ganaxolone, and ages 5-11 years for arbaclofen) (Berry-Kravis et al., 2017; Ligsay et al., 2017). Specifically, Ganaxolone produced an improvement in stereotypic behaviors such as anxiety and cognitive abilities, and Arbaclofen showed specificity for irritability behaviors, which are relevant to social avoidance in human FXS. Berry-Kravis and collaborators argue that this effect could be explained because of the higher doses given to these groups compared to the adult group, or because these patients had higher levels of baseline irritability, which makes it easier to observe a positive response to the drug (Berry-Kravis et al., 2017). However, these results might also be explained by the age at which they received treatment. This last argument is especially relevant considering that the role of GABA in early development includes migration stimulation and guidance and the sculpting of the glutamatergic synaptic network (Owens and Kriegstein, 2002; Cellot and Cherubini, 2013), potentially correcting alterations in neurodevelopment. In this scenario, other potential GABA agents that could be tested in preclinical studies include modulators of tonic inhibition, such as selective agonists for alpha5 and delta subunits, which have relative gene expression peak levels (GABRD and GABRA5) at early postnatal stages in healthy human subjects (Figures 1B,C; https://human.brain-map.org/; Miller et al., 2014), but appear to be downregulated during neurodevelopment in FXS patients (Bonin et al., 2007; Martin et al., 2014). A new double-blind, placebo-controlled phase 2 clinical trials for Gaboxadol, which targets tonic inhibition specifically, is currently ongoing (ClinicalTrials.

gov Identifier: NCT03697161). However, this study only includes adolescent and adult subjects (ages 13 to 22 years), limiting the possibility of assessing the potential for early postnatal therapeutic interventions in the GABAergic system.

Moreover, studies addressing early developmental stages using GABA-mimetic drugs should consider that proper maturation of the GABAergic system is critical to the E-I balance. Interventions during these periods could either promote or hinder these processes. For instance, in the immature mouse brain (P0 - P5) GABA acts to depolarize most neurons, due to the chloride (Cl^-) electrochemical driving force which promotes an inward Cl^- conductance on activation of GABA receptors. This phenomenon is dominated by the developmental expression of 2 Cl^- co-transporter proteins, NKCC1 (SLC12A1) and KCC2 (SLC12A5). The differential developmental projection of their relative expression results in a switch of the Cl^- electrochemical gradient during the first postnatal week in mice (He et al., 2014) determining whether activation of the $GABA_AR$ is depolarizing or hyperpolarizing (Rivera et al., 1999). In the FXS mouse model, the normal progression of the $GABA_AR$-mediated polarity switch is delayed, occurring during the second postnatal week instead (He et al., 2014), a delay also seen in differentiated iPSC from FXS patients (Zhang et al., 2022). In this context, preclinical studies addressed this alteration using Bumetanide and Furosemide to inhibit the chloride co-transporter NKCC1 during early postnatal development. Thus, both compounds were able to rectify the disrupted driving force through $GABA_ARs$ in cortical neurons, restoring their synaptic development and cortical circuit function in FXS mice (He et al., 2019). Considering that these drugs are already FDA-approved to treat other disorders, and that the establishment of new indications for existing drugs has been proposed as an efficient alternative over the *de novo* drug development (a concept known as drug repurposing), these are not only new pharmacological treatment options but also support the hypothesis of early developmental interventions.

Studies also show that GABA itself can regulate the GABA polarity switch by modulating the expression of the KCC2 transporter (Ganguly et al., 2001; Heubl et al., 2017; Wright et al., 2017). This suggests that the decrease in GABA neurotransmission observed in *Fmr1* KO may explain the observation of delayed dynamics and temporal polarity switch of the $GABA_AR$-mediated inhibitory responses in these animals. This will then impact the E-I balance of the network generating neuronal hyperexcitability as is seen in FXS. From here, although it may seem paradoxical to suggest the use of GABA mimetic drugs at early developmental stages since they may cause further excitability on the already hyperexcitable network in FXS, it can be speculated that administration of GABA-mimetic drugs early in postnatal development may have a beneficial effect by upregulating the KCC2 co-transporter. Upregulating KCC2 would promote the reversal of the Cl-electrochemical gradient and the mature hyperpolarizing GABA response. Such a manipulation may act to re-establish the temporality of the GABA switch and in turn rescue or restore the E/I balance and ameliorate the hyperexcitable phenotype. Despite the above, currently it is not known when this developmental switch occurs in humans. However, some evidence indicates that the expression of these transporters is developmentally regulated (Figures 1E,F; https://human.brain-map.org/; Miller et al., 2014). High NKCC1 and negligible levels of KCC2 protein are seen during perinatal stages, and gradual downregulation of NKCC1 and upregulation of KCC2 take place after the early postnatal period (Dzhala et al., 2005; Jansen et al., 2010; Sedmak et al., 2016), further suggesting a potential temporal window for postnatal pharmacological GABA-mimetic intervention.

Intracellular pathways

The FXS cellular phenotype also relies in faulty functioning of intracellular pathways including hyperactivation of mitogen-activated protein kinase (MAPK) and extracellular signal-regulated kinases (ERK) (Soong et al., 2008; Weng et al., 2008; Wang et al., 2012), as well as low levels of cAMP (Berry-Kravis et al., 1995; Wang et al., 2012; Gurney et al., 2017). These pathways are essential in several neurodevelopmental processes, including the transition from pluripotent stem cells to neuronal progenitors and synaptic plasticity, greatly impacting the cortical cytoarchitecture, organization and function (Iroegbu et al., 2021).

Clinical trials have tested different drugs targeting the restoration or correction of these pathways including: BPN14770, a Phosphodiesterase 4D (PDE4D) allosteric inhibitor (Clinical Trial Identifier: NCT03569631); Lovastatin, a FDA-approved specific inhibitor of the rate-limiting enzyme in cholesterol biosynthesis, 3-hydroxy-3-methylglutaryl coenzymeA [3HMG-CoA] reductase (Clinical Trial Identifier: NCT02680379 and NCT02642653); and Metformin, an insulin-normalizing drug that downregulates the insulin/IGF-I signaling pathway (Clinical Trial Identifier: NCT03862950 and NCT03479476). BPN14770 has only been tested in adult subjects (18-to 41-year-old) meeting the primary outcome measure for tolerability and the secondary outcome for cognitive performance and language in phase 2 clinical trials (Berry-Kravis et al., 2021). Importantly, PDE4D has been implicated in cognitive ability with the observations that (i) missense mutations of PDE4D cause rare neurodevelopmental disorder with intellectual disabilities (Acrodysostosis type 2) and (ii) PDE4D plays a role in regulating levels of cAMP which is an important neurobiological substrate of learning and memory early in development. Thus, future studies looking at the effects of BPN14770 at earlier ages are warranted to further explore potential benefits of an early pharmacological intervention.

On the other hand, both Metformin and Lovastatin clinical trials have addressed early time periods of development including younger children of 6, 8 and 10-year-old (Clinical Trial Identifier: NCT02680379, NCT02642653, NCT03862950 and NCT03479476). These studies showed a decrease in the aberrant behavior checklist total score (ABC) in the case of Metformin (Proteau-Lemieux et al., 2021), and significant improvements in ABC-community global score (ABC-C) when Lovastatin is combined with Minocycline, an antibiotic that inhibit matrix metallopeptidase 9 (MMP-9) showing potency in correct dendritic spine abnormalities in the *Fmr1* KO mouse (Champigny et al., 2022). Moreover, when Lovastatin was combined with parent-implemented language intervention (PILI), language and communication skills were improved (Thurman et al., 2020) supporting the benefits of interventions in early development. These treatments downregulate the phosphatidylinositol-3 kinase (PI3K) serine–threonine-specific protein kinase (AKT1) pathway,

which is hyperactivated in animal models of FXS (Pellerin et al., 2016; Gantois et al., 2019; Altable and de la Serna, 2021). Furthermore, preclinical studies showed that inhibition of PI3K signaling normalizes the abnormal protein synthesis and altered neurogenic cell fate during development in FXS organoids (Kang et al., 2021; Raj et al., 2021). These results highlight again the therapeutic potential for intervention in early stages of development in humans, although in this case addressing embryonic periods would add complexity to pharmacologically intervene. Finally, a recently published controlled trial with Metformin showed improvements in memory, social novelty deficits, and neuroanatomical abnormalities in nine young children with FXS (2- to 7-year-old) (Biag et al., 2019). This has led to a new clinical trial for Metformin in children from 2 to 16-year-old with FXS to assess treatment of behavior, cognitive and language phenotypes (ClinicalTrial Identifier: NCT05120505).

Finally, it is worth to mention that some newer pharmacological intervention attempts, discussed in detail in other recent review articles (McBride et al., 2016; Berry-Kravis et al., 2018; Tartaglia et al., 2019; Protic et al., 2022), have tested compounds acting upon monoaminergic, oxytocinergic and endocannabinoid neurotransmission systems, including sertraline, oxyctocin, a cannabidiol transdermal gel (ZYN002), sulindac and methylphenidate, among others (ClinicalTrial Identifiers: NCT01474746, NCT01254045, NCT04823052, NCT03614663, NCT04977986 and NCT05301361). Most of these newer alternatives have made further efforts in addressing earlier time points in development, recruiting toddlers and preschoolers from as early as 3 or 6-year-old (Figure 2). Only two clinical trials have reported results in this population: sertraline which showed no benefit to the outcomes proposed (Potter et al., 2019), and oxytocin which reported some promising effects on social anxiety (Hall et al., 2012).

Conclusion

More efforts need to be done to address the weaknesses and pitfalls of translating preclinical results from animal models studies to clinical research in order to properly identify and confirm the potential benefits of pharmacological treatments during critical periods of neurodevelopment. The *Fmr1* KO mice and *fmr1 Drosophila* models have allowed important progress in the FXS field but it is unclear how their molecular, cellular, and physiological features, as well as timeline or trajectories of development, translate to humans. For instance, in the FXS mice the *Fmr1* gene is knocked out resulting in the loss of FMRP expression since the zygote stage as opposed to the gradual decline in gene expression observed in humans. This limits the translation of developmental studies in FXS mice to humans. *Drosophila melanogaster* has been extensively used to study genetic and molecular aspects of human disease by implementing state-of-the-art technologies. Still, limitations arise since the results necessarily need to be further tested in mammalian-derived neurons, to better translate this information to physiological analyzes in complete tissues and finally to escalate to complex behavior studies. Currently, utilization of FXS iPSC-derived neurons and human brain organoid models are particularly informative since they both retain the epigenetic memory and exhibit a methylated FMR1 gene. Moreover, iPSCs can potentially differentiate into all cell types in large numbers providing a powerful platform for drug screening. This is particularly relevant for FXS research, where human neurons are inaccessible for studies other than from aborted fetuses or postmortem brain samples. There are, however, limitations with these experimental models in regard that they usually represent early fetal brain development stages, but it is unclear how they may shed light on optimal postnatal neurodevelopmental time windows for human pharmacological interventions in FXS. Fortunately, a recent study has shown that cortical organoids from neurotypical humans could mature to parallel *in vivo* postnatal development and maintain developmental milestones for 250 to 300 days postnatal (Gordon et al., 2021), further validating its value for late-onset associated critical neurodevelopmental periods and drug screening.

Finally, there are several barriers in performing clinical trials in a younger population, including physiological heterogeneity within the pediatric population (which can be divided at least in four different categories), scarce knowledge on pharmacokinetics and pharmacodynamics, the need for higher safety standards, the potential short and long-term negative side effects on the developing brain, and regarding legal consent for participation and balancing risk and benefits for this pediatric population. However, considering that FXS is a neurodevelopmental disorder, a new venue for interventions targeting relevant neurodevelopment time windows associated with the FXS phenotypes need to be more deeply considered. Although this strategy is already utilized in several clinical trials that have included 2-and 3-year-old children, further preclinical investigation is required to better understand at what age time point and how long therapeutic intervention should be given, in addition to knowing the potential positive and negative outcomes of such a treatment. Information from these studies could provide better strategies on how to avoid unwanted side effects, improve FXS phenotypes, and overall, how to improve the lifestyle of patients.

Author contributions

CC-D developed the idea and topic of the manuscript. CC-D, LM, and AN-P contributed to the ideas expressed in the manuscript. LM design and create figures. LC, JR, NZ, and GP contributed to collecting, analyzing, and selecting the literature included in this manuscript. LC and JR write an original draft. CC-D, LM, and AN-P write, review, and edit the final version of the manuscript. All authors contributed to the article and approved the submitted version.

Funding

This work is supported by Universidad de Santiago de Chile, Vicerrectoría de Investigación, Desarrollo e Innovación, DICYT 022001CDR to CC-D and DICYT 021801MB to LM.

Acknowledgments

We thank the critical reading of the manuscript and feedback of Miguel Reyes-Parada and Maneesh Kumar.

Conflict of interest

The authors declare that the research was conducted in the absence of any commercial or financial relationships that could be construed as a potential conflict of interest.

Publisher's note

All claims expressed in this article are solely those of the authors and do not necessarily represent those of their affiliated organizations, or those of the publisher, the editors and the reviewers. Any product that may be evaluated in this article, or claim that may be made by its manufacturer, is not guaranteed or endorsed by the publisher.

Supplementary material

The Supplementary material for this article can be found online at: https://www.frontiersin.org/articles/10.3389/fnins.2023.1213410/full#supplementary-material

SUPPLEMENTARY TABLE S1
Pharmacological interventions in Clinical FXS trials since 2002. Dta included in this table was obtained on August 2022 from www.ClinicalTrials.gov; search terms "Fragile X Syndrome," "FXS."

References

Alpatov, R., Lesch, B. J., Nakamoto-Kinoshita, M., Blanco, A., Chen, S., Stützer, A., et al. (2014). A chromatin-dependent role of the Fragile X mental retardation protein FMRP in the DNA damage response. *Cells* 157, 869–881. doi: 10.1016/j.cell.2014.03.040

Altable, M., and de la Serna, J. M. (2021). Neuroinflammation links COVID-19 and fragile X syndrome: role of MMP-9, IGF-1, IL-10, metformin, statins and curcumin. *Qeios*. doi: 10.32388/KO4C77.2

Antoine, M. W., Langberg, T., Schnepel, P., and Feldman, D. E. (2019). Increased excitation-inhibition ratio stabilizes synapse and circuit excitability in four autism mouse models. *Neuron* 101, 648–661.e4. doi: 10.1016/j.neuron.2018.12.026

Bailey, D. B., Berry-Kravis, E., Wheeler, A., Raspa, M., Merrien, F., Ricart, J., et al. (2015). Mavoglurant in adolescents with fragile X syndrome: analysis of clinical global impression-improvement source data from a double-blind therapeutic study followed by an open-label, long-term extension study. *J. Neurodev. Disord.* 8, 1–10. doi: 10.1186/s11689-015-9134-5

Bausch, A. E., Dieter, R., Nann, Y., Hausmann, M., Meyerdierks, N., Kaczmarek, L. K., et al. (2015). The sodium-activated potassium channel slack is required for optimal cognitive flexibility in mice. *Learn. Mem.* 22, 323–335. doi: 10.1101/lm.037820.114

Bear, M. F., Huber, K. M., and Warren, S. T. (2004). The mGluR theory of fragile X mental retardation. *Trends Neurosci.* 27, 370–377. doi: 10.1016/j.tins.2004.04.009

Berry-Kravis, E., Hagerman, R., Visootsak, J., Budimirovic, D., Kaufmann, W. E., Cherubini, M., et al. (2017). Arbaclofen in fragile X syndrome: results of phase 3 trials. *J. Neurodev. Disord.* 9:3. doi: 10.1186/s11689-016-9181-6

Berry-Kravis, E., Des Portes, V., Hagerman, R., Jacquemont, S., Charles, P., Visootsak, J., et al. (2016). Mavoglurant in fragile X syndrome: results of two randomized, double-blind, placebo-controlled trials. *Sci. Transl. Med.* 8:321ra5. doi: 10.1126/scitranslmed.aab4109

Berry-Kravis, E. M., Harnett, M. D., Reines, S. A., Reese, M. A., Ethridge, L. E., Outterson, A. H., et al. (2021). Inhibition of phosphodiesterase-4D in adults with fragile X syndrome: a randomized, placebo-controlled, phase 2 clinical trial. *Nat. Med.* 27, 862–870. doi: 10.1038/s41591-021-01321-w

Berry-Kravis, E., Hessl, D., Coffey, S., Hervey, C., Schneider, A., Yuhas, J., et al. (2009). A pilot open label, single dose trial of fenobam in adults with fragile X syndrome. *J. Med. Genet.* 46, 266–271. doi: 10.1136/jmg.2008.063701

Berry-Kravis, E., Hicar, M., and Ciurlionis, R. (1995). Reduced cyclic AMP production in fragile X syndrome: cytogenetic and molecular correlations. *Pediatr. Res.* 38, 638–643. doi: 10.1203/00006450-199511000-00002

Berry-Kravis, E. M., Lindemann, L., Jønch, A. E., Apostol, G., Bear, M. F., Carpenter, R. L., et al. (2018). Drug development for neurodevelopmental disorders: Lessons learned from fragile X syndrome. *Nat. Rev. Drug Discov.* 17, 280–298. doi: 10.1038/nrd.2017.221

Biag, H. M. B., Potter, L. A., Wilkins, V., Afzal, S., Rosvall, A., Salcedo-Arellano, M. J., et al. (2019). Metformin treatment in young children with fragile X syndrome. *Mol. Genet. Genomic. Med.* 7, 1–13. doi: 10.1002/mgg3.956

Bonaccorso, C. M., Spatuzza, M., Di Marco, B., Gloria, A., Barrancotto, G., Cupo, A., et al. (2015). Fragile X mental retardation protein (FMRP) interacting proteins exhibit different expression patterns during development. *Int. J. Dev. Neurosci.* 42, 15–23. doi: 10.1016/j.ijdevneu.2015.02.004

Bonin, R. P., Martin, L. J., MacDonald, J. F., and Orser, B. A. (2007). α5GABAA receptors regulate the intrinsic excitability of mouse hippocampal pyramidal neurons. *J. Neurophysiol.* 98, 2244–2254. doi: 10.1152/jn.00482.2007

Bortolotto, Z. A., Collett, V. J., Conquet, F., Jia, Z., Van Der Putten, H., and Collingridge, G. L. (2005). The regulation of hippocampal LTP by the molecular switch, a form of metaplasticity, requires mGlu5 receptors. *Neuropharmacology* 49, 13–25. doi: 10.1016/j.neuropharm.2005.05.020

Bortolotto, Z. A., Fitzjohn, S. M., and Collingridge, G. L. (1999). Roles of metabotropic glutamate receptors in LTP and LTD in the hippocampus. *Curr. Opin. Neurobiol.* 9, 299–304. doi: 10.1016/S0959-4388(99)80044-0

Braat, S., D'Hulst, C., Heulens, I., de Rubeis, S., Mientjes, E., Nelson, D. L., et al. (2015). The GABAA receptor is an FMRP target with therapeutic potential in fragile X syndrome. *Cell Cycle* 14, 2985–2995. doi: 10.4161/15384101.2014.989114

Bražić, J. R., Goodman, J. A., Nandi, A., Russell, D. S., Jennings, D., Barret, O., et al. (2022). Fragile X mental retardation protein and cerebral expression of metabotropic glutamate receptor subtype 5 in men with Fragile X syndrome: a pilot study. *Brain Sci.* 12:314. doi: 10.3390/brainsci12030314

Bražić, J. R., Nandi, A., Russell, D. S., Jennings, D., Barret, O., Martin, S. D., et al. (2021). Cerebral expression of metabotropic glutamate receptor subtype 5 in idiopathic autism spectrum disorder and fragile x syndrome: a pilot study. *Int. J. Mol. Sci.* 22, 1–16. doi: 10.3390/ijms22062863

Brown, V., Jin, P., Ceman, S., Darnell, J. C., O'donnell, W. T., Tenenbaum, S. A., et al. (2001). Microarray identification of FMRP-associated brain mRNAs and altered mRNA translational profiles in Fragile X syndrome Howard Hughes Medical Institute Department of human genetics FMRP is largely cytoplasmic, incorporated into large messenger-ribonucleopr. *Cells* 107:27710. Available at: http://www.cell.com/cgi/content/full/107/4/

Bureau, I., Shepherd, G. M. G., and Svoboda, K. (2008). Circuit and plasticity defects in the developing somatosensory cortex of Fmr1 knock-out mice. *J. Neurosci.* 28, 5178–5188. doi: 10.1523/JNEUROSCI.1076-08.2008

Catania, M. V., Landwehrmeyer, G. B., Testa, C. M., Standaert, D. G., Penney, J. B., and Young, A. B. (1994). Metabotropic glutamate receptors are differentially regulated during development. *Neuroscience* 61, 481–495. doi: 10.1016/0306-4522(94)90428-6

Cea-Del Rio, C. A., Huntsman, M. M., Rio, C. A. C., and Huntsman, M. M. (2014). The contribution of inhibitory interneurons to circuit dysfunction in Fragile X syndrome. *Front. Cell. Neurosci.* 8, 1–7. doi: 10.3389/fncel.2014.00245

Cea-Del Rio, C. A., Nunez-Parra, A., Freedman, S. M., Kushner, J. K., Alexander, A. L., Restrepo, D., et al. (2020). Disrupted inhibitory plasticity and homeostasis in Fragile X syndrome. *Neurobiol. Dis.* 142:104959. doi: 10.1016/j.nbd.2020.104959

Cellot, G., and Cherubini, E. (2013). Functional role of ambient GABA in refining neuronal circuits early in postnatal development. *Front. Neural. Circuits* 7:136. doi: 10.3389/fncir.2013.00136

Champigny, C., Morin-Parent, F., Bellehumeur-Lefebvre, L., Çaku, A., Lepage, J. F., and Corbin, F. (2022). Combining lovastatin and minocycline for the treatment of Fragile X syndrome: results from the LovaMiX clinical trial. *Front. Psych.* 12, 1–10. doi: 10.3389/fpsyt.2021.762967

Chen, L., Hadd, A. G., Sah, S., Houghton, J. F., Filipovic-Sadic, S., Zhang, W., et al. (2011). High-resolution methylation polymerase chain reaction for fragile X analysis: evidence for novel FMR1 methylation patterns undetected in southern blot analyses. *Genet. Med.* 13, 528–538. doi: 10.1097/GIM.0b013e31820a780f

Chuang, S.-C. (2005). Prolonged epileptiform discharges induced by altered group I metabotropic glutamate receptor-mediated synaptic responses in hippocampal slices of a Fragile X mouse model. *J. Neurosci.* 25, 8048–8055. doi: 10.1523/JNEUROSCI.1777-05.2005

Clancy, B., Finlay, B. L., Darlington, R. B., and Anand, K. J. S. (2007). Extrapolating brain development from experimental species to humans. *Neurotoxicology* 28, 931–937. doi: 10.1016/j.neuro.2007.01.014

Cogram, P., Deacon, R. M. J., Warner-Schmidt, J. L., von Schimmelmann, M. J., Abrahams, B. S., and During, M. J. (2019). Gaboxadol normalizes behavioral abnormalities in a mouse model of fragile x syndrome. *Front. Behav. Neurosci.* 13, 1–9. doi: 10.3389/fnbeh.2019.00141

Contractor, A., Klyachko, V. A., and Portera-Cailliau, C. (2015). Altered neuronal and circuit excitability in Fragile X syndrome. *Neuron* 87, 699–715. doi: 10.1016/j.neuron.2015.06.017

Curia, G., Papouin, T., Séguéla, P., and Avoli, M. (2009). Downregulation of tonic GABAergic inhibition in a mouse model of fragile X syndrome. *Cereb. Cortex* 19, 1515–1520. doi: 10.1093/cercor/bhn159

D'Hulst, C., De Geest, N., Reeve, S. P., Van Dam, D., De Deyn, P. P., Hassan, B. A., et al. (2006). Decreased expression of the GABAA receptor in fragile X syndrome. *Brain Res.* 1121, 238–245. doi: 10.1016/j.brainres.2006.08.115

D'Hulst, C., Heulens, I., Van Der Aa, N., Goffin, K., Koole, M., Porke, K., et al. (2015). Positron emission tomography (PET) quantification of GABAA receptors in the brain of fragile X patients. *PLoS One* 10, 1–12. doi: 10.1371/journal.pone.0131486

D'Hulst, C., and Kooy, R. F. (2007). The GABAA receptor: a novel target for treatment of fragile X? *Trends Neurosci.* 30, 425–431. doi: 10.1016/j.tins.2007.06.003

De Rubeis, S., and Bagni, C. (2010). Fragile X mental retardation protein control of neuronal mRNA metabolism: insights into mRNA stability. *Mol. Cell. Neurosci.* 43, 43–50. doi: 10.1016/j.mcn.2009.09.013

Deng, P. Y., and Klyachko, V. A. (2016). Genetic upregulation of BK channel activity normalizes multiple synaptic and circuit defects in a mouse model of fragile X syndrome. *J. Physiol.* 594, 83–97. doi: 10.1113/JP271031

Deng, P. Y., Rotman, Z., Blundon, J. A., Cho, Y., Cui, J., Cavalli, V., et al. (2013). FMRP regulates neurotransmitter release and synaptic information transmission by modulating action potential duration via BK channels. *Neuron* 77, 696–711. doi: 10.1016/j.neuron.2012.12.018

Di Giorgi-Gerevini, V., Melchiorri, D., Battaglia, G., Ricci-Vitiani, L., Ciceroni, C., Busceti, C. L., et al. (2005). Endogenous activation of metabotropic glutamate receptors supports the proliferation and survival of neural progenitor cells. *Cell Death Differ.* 12, 1124–1133. doi: 10.1038/sj.cdd.4401639

Di, J., Li, J., O'Hara, B., Alberts, I., Xiong, L., Li, J., et al. (2020). The role of GABAergic neural circuits in the pathogenesis of autism spectrum disorder. *Int. J. Dev. Neurosci.* 80, 73–85. doi: 10.1002/jdn.10005

Dölen, G., Osterweil, E., Rao, B. S. S., Smith, G. B., Auerbach, B. D., Chattarji, S., et al. (2007). Correction of Fragile X syndrome in mice. *Neuron* 56, 955–962. doi: 10.1016/j.neuron.2007.12.001

Doll, C. A., Scott, K., and Appel, B. (2021). Fmrp regulates oligodendrocyte lineage cell specification and differentiation. *Glia* 69, 2349–2361. doi: 10.1002/glia.24041

Doll, C. A., Yergert, K. M., and Appel, B. H. (2020). The RNA binding protein fragile X mental retardation protein promotes myelin sheath growth. *Glia* 68, 495–508. doi: 10.1002/glia.23731

Dzhala, V. I., Talos, D. M., Sdrulla, D. A., Brumback, A. C., Mathews, G. C., Benke, T. A., et al. (2005). NKCC1 transporter facilitates seizures in the developing brain. *Nat. Med.* 11, 1205–1213. doi: 10.1038/nm1301

Erickson, C. A., Davenport, M. H., Schaefer, T. L., Wink, L. K., Pedapati, E. V., Sweeney, J. A., et al. (2017). Fragile X targeted pharmacotherapy: lessons learned and future directions. *J. Neurodev. Disord.* 9, 1–14. doi: 10.1186/s11689-017-9186-9

Feng, Y., Gutekunst, C. A., Eberhart, D. E., Yi, H., Warren, S. T., and Hersch, S. M. (1997). Fragile X mental retardation protein: nucleocytoplasmic shuttling and association with somatodendritic ribosomes. *J. Neurosci.* 17, 1539–1547. doi: 10.1523/jneurosci.17-05-01539.1997

Friedman, L. K., Sharma, A., Corcia, M., Webster, T., Qazi, L., Simsovits, D., et al. (2016). Selective inhibition of metabotropic glutamate type 1 alpha receptor (mGluR1α) reduces cell proliferation and migration following status epilepticus in early development. *Int. J. Dev. Neurosci.* 54, 6–21. doi: 10.1016/j.ijdevneu.2016.08.002

Ganguly, K., Schinder, A. F., Wong, S. T., and Poo, M. (2001). GABA itself promotes the developmental switch of neuronal GABAergic responses from excitation to inhibition. *Cells* 105, 521–532. doi: 10.1016/S0092-8674(01)00341-5

Gantois, I., Popic, J., Khoutorsky, A., and Sonenberg, N. (2019). Metformin for treatment of fragile x syndrome and other neurological disorders. *Annu. Rev. Med.* 70, 167–181. doi: 10.1146/annurev-med-081117-041238

Gantois, I., Vandesompele, J., Speleman, F., Reyniers, E., D'Hooge, R., Severijnen, L. A., et al. (2006). Expression profiling suggests underexpression of the GABAA receptor subunit δ in the fragile X knockout mouse model. *Neurobiol. Dis.* 21, 346–357. doi: 10.1016/j.nbd.2005.07.017

Gholizadeh, S., Halder, S. K., and Hampson, D. R. (2015). Expression of fragile X mental retardation protein in neurons and glia of the developing and adult mouse brain. *Brain Res.* 1596, 22–30. doi: 10.1016/j.brainres.2014.11.023

Gordon, A., Yoon, S.-J., Tran, S. S., Makinson, C. D., Park, J. Y., Andersen, J., et al. (2021). Long-term maturation of human cortical organoids matches key early postnatal transitions. *Nat. Neurosci.* 24, 331–342. doi: 10.1038/s41593-021-00802-y

Gross, C., Yao, X., Pong, D. L., Jeromin, A., and Bassell, G. J. (2011). Fragile X mental retardation protein regulates protein expression and mRNA translation of the potassium channel Kv4.2. *J. Neurosci.* 31, 5693–5698. doi: 10.1523/JNEUROSCI.6661-10.2011

Gurney, M. E., Cogram, P., Deacon, R. M., Rex, C., and Tranfaglia, M. (2017). Multiple behavior phenotypes of the Fragile-X syndrome mouse model respond to chronic inhibition of phosphodiesterase-4D (PDE4D). *Sci. Rep.* 7, 1–11. doi: 10.1038/s41598-017-15028-x

Hagerman, R., Jacquemont, S., Berry-Kravis, E., Des Portes, V., Stanfield, A., Koumaras, B., et al. (2018). Mavoglurant in Fragile X syndrome: results of two open-label, extension trials in adults and adolescents. *Sci. Rep.* 8, 1–9. doi: 10.1038/s41598-018-34978-4

Hagerman, P. J., and Stafstrom, C. E. (2009). Origins of epilepsy in Fragile X syndrome. *Epilepsy. Curr.* 9, 108–112. doi: 10.1111/j.1535-7511.2009.01309.x

Hall, S. S., Lightbody, A. A., McCarthy, B. E., Parker, K. J., and Reiss, A. L. (2012). Effects of intranasal oxytocin on social anxiety in males with fragile X syndrome. *Psychoneuroendocrinology* 37, 509–518. doi: 10.1016/j.psyneuen.2011.07.020

Harlow, E. G., Till, S. M., Russell, T. A., Wijetunge, L. S., Kind, P., and Contractor, A. (2010). Critical period plasticity is disrupted in the barrel cortex of Fmr1 knockout mice. *Neuron* 65, 385–398. doi: 10.1016/j.neuron.2010.01.024

He, Q., Arroyo, E. D., Smukowski, S. N., Xu, J., Piochon, C., Savas, J. N., et al. (2019). Critical period inhibition of NKCC1 rectifies synapse plasticity in the somatosensory cortex and restores adult tactile response maps in fragile X mice. *Mol. Psychiatry* 24, 1732–1747. doi: 10.1038/s41380-018-0048-y

He, Q., Nomura, T., Xu, J., and Contractor, A. (2014). The developmental switch in GABA polarity is delayed in fragile X mice. *J. Neurosci.* 34, 446–450. doi: 10.1523/JNEUROSCI.4447-13.2014

Henderson, C., Wijetunge, L., Kinoshita, M. N., Shumway, M., Hammond, R. S., Postma, F. R., et al. (2012). Reversal of disease-related pathologies in the fragile X mouse model by selective activation of GABAB receptors with arbaclofen. *Sci. Transl. Med.* 4:152ra128. doi: 10.1126/scitranslmed.3004218

Heubl, M., Zhang, J., Pressey, J. C., Al Awabdh, S., Renner, M., Gomez-Castro, F., et al. (2017). GABAA receptor dependent synaptic inhibition rapidly tunes KCC2 activity via the cl--sensitive WNK1 kinase. *Nat. Commun.* 8:1776. doi: 10.1038/s41467-017-01749-0

Heulens, I., D'Hulst, C., Van Dam, D., De Deyn, P. P., and Kooy, R. F. (2012). Pharmacological treatment of fragile X syndrome with GABAergic drugs in a knockout mouse model. *Behav. Brain Res.* 229, 244–249. doi: 10.1016/j.bbr.2012.01.031

Huber, K. M., Gallagher, S. M., Warren, S. T., and Bear, M. F. (2002). Altered synaptic plasticity in a mouse model of fragile X mental retardation. *Proc. Natl. Acad. Sci. U. S. A.* 99, 7746–7750. doi: 10.1073/pnas.122205699

Iroegbu, J. D., Ijomone, O. K., Femi-Akinlosotu, O. M., and Ijomone, O. M. (2021). ERK/MAPK signalling in the developing brain: perturbations and consequences. *Neurosci. Biobehav. Rev.* 131, 792–805. doi: 10.1016/j.neubiorev.2021.10.009

Irwin, S. A., Galvez, R., and Greenough, W. T. (2000). Dendritic spine structural anomalies in fragile-X mental retardation syndrome. *Cereb. Cortex* 10, 1038–1044. doi: 10.1093/cercor/10.10.1038

Irwin, S. A., Patel, B., Idupulapati, M., Harris, J. B., Crisostomo, R. A., Larsen, B. P., et al. (2001). Abnormal dendritic spine characteristics in the temporal and visual cortices of patients with fragile-X syndrome: a quantitative examination. *Am. J. Med. Genet.* 98, 161–167. doi: 10.1002/1096-8628(20010115)98:2<161::AID-AJMG1025>3.0.CO;2-B

Jansen, L. A., Peugh, L. D., Roden, W. H., and Ojemann, J. G. (2010). Impaired maturation of cortical GABAA receptor expression in pediatric epilepsy. *Epilepsia* 51, 1456–1467. doi: 10.1111/j.1528-1167.2009.02491.x

Kalmbach, B. E., and Brager, D. H. (2020). Fragile X mental retardation protein modulates somatic D-type K + channels and action potential threshold in the mouse prefrontal cortex. *J. Neurophysiol.* 124, 1766–1773. doi: 10.1152/jn.00494.2020

Kang, Y., Zhou, Y., Li, Y., Han, Y., Xu, J., Niu, W., et al. (2021). A human forebrain organoid model of fragile X syndrome exhibits altered neurogenesis and highlights new treatment strategies. *Nat. Neurosci.* 24, 1377–1391. doi: 10.1038/s41593-021-00913-6

Kau, A. S. M., Tierney, E., Bukelis, I., Stump, M. H., Kates, W. R., Trescher, W. H., et al. (2004). Social behavior profile in Young males with Fragile X syndrome: characteristics and specificity. *Am. J. Med. Genet.* 126 A, 9–17. doi: 10.1002/ajmg.a.20218

Kaufmann, W. E., Cortell, R., Kau, A. S. M., Bukelis, I., Tierney, E., Gray, R. M., et al. (2004). Autism spectrum disorder in fragile X syndrome: communication, social interaction, and specific behaviors. *Am. J. Med. Genet.* 129 A, 225–234. doi: 10.1002/ajmg.a.30229

Kratovac, S., and Corbin, J. G. (2013). Developmental changes in expression of inhibitory neuronal proteins in the Fragile X syndrome mouse basolateral amygdala. *Brain Res.* 1537, 69–78. doi: 10.1016/j.brainres.2013.08.052

Kshatri, A., Cerrada, A., Gimeno, R., Bartolomé-Martín, D., Rojas, P., and Giraldez, T. (2020). Differential regulation of BK channels by fragile X mental retardation protein. *J. Gen. Physiol.* 152:e201912502. doi: 10.1085/jgp.201912502

Li, M., Shin, J., Risgaard, R. D., Parries, M. J., Wang, J., Chasman, D., et al. (2020). Identification of FMR1-regulated molecular networks in human neurodevelopment. *Genome Res.* 30, 361–374. doi: 10.1101/gr.251405.119

Ligsay, A., Van Dijck, A., Nguyen, D. V., Lozano, R., Chen, Y., Bickel, E. S., et al. (2017). A randomized double-blind, placebo-controlled trial of ganaxolone in children and adolescents with fragile X syndrome. *J. Neurodev. Disord.* 9, 1–13. doi: 10.1186/s11689-017-9207-8

Lu, Y. M., Jia, Z., Janus, C., Henderson, J. T., Gerlai, R., Wojtowicz, J. M., et al. (1997). Mice lacking metabotropic glutamate receptor 5 show impaired learning and reduced CA1 long-term potentiation (LTP) but normal CA3 LTP. *J. Neurosci.* 17, 5196–5205. doi: 10.1523/jneurosci.17-13-05196.1997

Lum, J. S., Fernandez, F., Matosin, N., Andrews, J. L., Huang, X. F., Ooi, L., et al. (2016). Neurodevelopmental expression profile of dimeric and monomeric group 1 mGluRs: relevance to schizophrenia pathogenesis and treatment. *Sci. Rep.* 6, 1–10. doi: 10.1038/srep34391

Martin, B. S., Corbin, J. G., and Huntsman, M. M. (2014). Deficient tonic GABAergic conductance and synaptic balance in the fragile X syndrome amygdala. *J. Neurophysiol.* 112, 890–902. doi: 10.1152/jn.00597.2013

McBride, S. M. J., Choi, C. H., Wang, Y., Liebelt, D., Braunstein, E., Ferreiro, D., et al. (2005). Pharmacological rescue of synaptic plasticity, courtship behavior, and mushroom body defects in a Drosophila model of Fragile X syndrome. *Neuron* 45, 753–764. doi: 10.1016/j.neuron.2005.01.038

McBride, S. M. J., Choi, C. H., Wang, Y., Liebelt, D., Braunstein, E., Ferreiro, D., et al. (2016). Developmental studies in fragile X syndrome. *J. Neurosci.* 9, 1–13. doi: 10.1186/s11689-020-09310-9

Miller, J. A., Ding, S.-L., Sunkin, S. M., Smith, K. A., Ng, L., Szafer, A., et al. (2014). Transcriptional landscape of the prenatal human brain. *Nature* 508, 199–206. doi: 10.1038/nature13185

Miller, L. J., McIntosh, D. N., McGrath, J., Shyu, V., Lampe, M., Taylor, A. K., et al. (1999). Electrodermal responses to sensory stimuli in individuals with fragile X syndrome: a preliminary report. *Am. J. Med. Genet.* 83, 268–279. doi: 10.1002/(SICI)1096-8628(19990402)83:4<268::AID-AJMG7>3.0.CO;2-K

Mitchell, S. J., and Silver, R. A. (2003). Shunting inhibition modulates neuronal gain during synaptic excitation. *Neuron* 38, 433–445. doi: 10.1016/S0896-6273(03)00200-9

Mody, M., Petibon, Y., Han, P., Kuruppu, D., Ma, C., Yokell, D., et al. (2021). In vivo imaging of mGlu5 receptor expression in humans with Fragile X syndrome towards development of a potential biomarker. *Sci. Rep.* 11, 1–7. doi: 10.1038/s41598-021-94967-y

Morin-Parent, F., Champigny, C., Lacroix, A., Corbin, F., and Lepage, J. F. (2019). Hyperexcitability and impaired intracortical inhibition in patients with fragile-X syndrome. *Transl. Psychiatry* 9:312. doi: 10.1038/s41398-019-0650-z

Mor-Shaked, H., and Eiges, R. (2018). Reevaluation of FMR1 hypermethylation timing in fragile X syndrome. *Front. Mol. Neurosci.* 11, 1–7. doi: 10.3389/fnmol.2018.00031

Munshi, K., Pawlowski, K., Gonzalez-Heydrich, J., and Picker, J. D. (2017). Review of salient investigational drugs for the treatment of Fragile X syndrome. *J. Child Adolesc. Psychopharmacol.* 27, 850–863. doi: 10.1089/cap.2016.0200

Nimchinsky, E. A., Oberlander, A. M., and Svoboda, K. (2001). Abnormal development of dendritic spines in FMR1 knock-out mice. *J. Neurosci.* 21, 5139–5146. doi: 10.1523/jneurosci.21-14-05139.2001

Nosyreva, E. D., and Huber, K. M. (2006). Metabotropic receptor-dependent long-term depression persists in the absence of protein synthesis in the mouse model of fragile X syndrome. *J. Neurophysiol.* 95, 3291–3295. doi: 10.1152/jn.01316.2005

Oberlé, I., Rousseau, F., Heitz, D., Kretz, C., Devys, D., Hanauer, A., et al. (1991). Instability of a 550-base pair DNA segment and abnormal methylation in fragile X syndrome. *Science* 1979, 1097–1102. doi: 10.1126/science.252.5009.1097

Olmos-Serrano, J. L., and Corbin, J. G. (2011). Amygdala regulation of fear and emotionality in fragile X syndrome. *Dev. Neurosci.* 33, 365–378. doi: 10.1159/000329424

Olmos-Serrano, J. L., Paluszkiewicz, S. M., Martin, B. S., Kaufmann, W. E., Corbin, J. G., and Huntsman, M. M. (2010). Defective GABAergic neurotransmission and pharmacological rescue of neuronal hyperexcitability in the amygdala in a mouse model of fragile X syndrome. *J. Neurosci.* 30, 9929–9938. doi: 10.1523/JNEUROSCI.1714-10.2010

Osterweil, E. K., Krueger, D. D., Reinhold, K., and Bear, M. F. (2010). Hypersensitivity to mGluR5 and ERK1/2 leads to excessive protein synthesis in the hippocampus of a mouse model of fragile X syndrome. *J. Neurosci.* 30, 15616–15627. doi: 10.1523/JNEUROSCI.3888-10.2010

Owens, D. F., and Kriegstein, A. R. (2002). Is there more to gaba than synaptic inhibition? *Nat. Rev. Neurosci.* 3, 715–727. doi: 10.1038/nrn919

Pacey, L. K. K., Heximer, S. P., and Hampson, D. R. (2009). Increased GABAB receptor-mediated signaling reduces the susceptibility of fragile X knockout mice to audiogenic seizures. *Mol. Pharmacol.* 76, 18–24. doi: 10.1124/mol.109.056127

Pellerin, D., Çaku, A., Fradet, M., Bouvier, P., Dubé, J., and Corbin, F. (2016). Lovastatin corrects ERK pathway hyperactivation in fragile X syndrome: potential of platelet's signaling cascades as new outcome measures in clinical trials. *Biomarkers* 21, 497–508. doi: 10.3109/1354750X.2016.1160289

Potter, L. A., Scholze, D. A., Biag, H. M. B., Schneider, A., Chen, Y., Nguyen, D. V., et al. (2019). A randomized controlled trial of sertraline in Young children with autism Spectrum disorder. *Front. Psych.* 10:810. doi: 10.3389/fpsyt.2019.00810

Prashad, S., and Gopal, P. P. (2021). RNA-binding proteins in neurological development and disease. *RNA Biol.* 18, 972–987. doi: 10.1080/15476286.2020.1809186

Proteau-Lemieux, M., Lacroix, A., Galarneau, L., Corbin, F., Lepage, J. F., and Çaku, A. (2021). The safety and efficacy of metformin in fragile X syndrome: an open-label study. *Prog. Neuro-Psychopharmacol. Biol. Psychiatry* 110:110307. doi: 10.1016/j.pnpbp.2021.110307

Protic, D. D., Aishworiya, R., Salcedo-Arellano, M. J., Tang, S. J., Milisavljevic, J., Mitrovic, F., et al. (2022). Fragile X syndrome: from molecular aspect to clinical treatment. *Int. J. Mol. Sci.* 23, 1–20. doi: 10.3390/ijms23041935

Qin, M., Huang, T., Kader, M., Krych, L., Xia, Z., Burlin, T., et al. (2015). R-baclofen reverses a social behavior deficit and elevated protein synthesis in a mouse model of fragile X syndrome. *Int. J. Neuropsychopharmacol.* 18, 1–13. doi: 10.1093/ijnp/pyv034

Rais, M., Lovelace, J. W., Shuai, X. S., Woodard, W., Bishay, S., Estrada, L., et al. (2022). Functional consequences of postnatal interventions in a mouse model of Fragile X syndrome. *Neurobiol. Dis.* 162:105577. doi: 10.1016/j.nbd.2021.105577

Raj, N., McEachin, Z. T., Harousseau, W., Zhou, Y., Zhang, F., Merritt-Garza, M. E., et al. (2021). Cell-type-specific profiling of human cellular models of fragile X syndrome reveal PI3K-dependent defects in translation and neurogenesis. *Cell Rep.* 35:108991. doi: 10.1016/j.celrep.2021.108991

Riedel, G., and Reymann, K. G. (1996). Metabotropic glutamate receptors in hippocampal long-term potentiation and learning and memory. *Acta Physiol. Scand.* 157, 1–19. doi: 10.1046/j.1365-201X.1996.484231000.x

Rivera, C., Voipio, J., Payne, J. A., Ruusuvuori, E., Lahtinen, H., Lamsa, K., et al. (1999). The K+/cl-co-transporter KCC2 renders GABA hyperpolarizing during neuronal maturation. *Nature* 397, 251–255. doi: 10.1038/16697

Romano, C., Smout, S., Miller, J. K., and O'Malley, K. L. (2002). Developmental regulation of metabotropic glutamate receptor 5b protein in rodent brain. *Neuroscience* 111, 693–698. doi: 10.1016/S0306-4522(02)00042-8

Russo, A., and DiAntonio, A. (2019). Wnd/DLK is a critical target of FMRP responsible for neurodevelopmental and behavior defects in the Drosophila model of Fragile X syndrome. *Cell Rep.* 28, 2581–2593.e5. doi: 10.1016/j.celrep.2019.08.001

Schultz, M. D., He, Y., Whitaker, J. W., Hariharan, M., Mukamel, E. A., Leung, D., et al. (2015). Human body epigenome maps reveal noncanonical DNA methylation variation. *Nature* 523, 212–216. doi: 10.1038/nature14465

Sears, J. C., Choi, W. J., and Broadie, K. (2019). Fragile X mental retardation protein positively regulates PKA anchor rugose and PKA activity to control actin assembly in learning/memory circuitry. *Neurobiol. Dis.* 127, 53–64. doi: 10.1016/j.nbd.2019.02.004

Sedmak, G., Jovanov-Milošević, N., Ulamec, M. P. M., Krušlin, B., Kaila, K., and Judaš, M. (2016). Developmental expression patterns of KCC2 and functionally associated molecules in the human brain. *Cereb. Cortex* 26, 4574–4589. doi: 10.1093/cercor/bhv218

Semple, B. D., Blomgren, K., Gimlin, K., Ferriero, D. M., and Noble-Haeusslein, L. J. (2013). Brain development in rodents and humans: identifying benchmarks of maturation and vulnerability to injury across species. *Prog. Neurobiol.* 106–107, 1–16. doi: 10.1016/j.pneurobio.2013.04.001

Semyanov, A., Walker, M. C., Kullmann, D. M., and Silver, R. A. (2004). Tonically active GABAA receptors: modulating gain and maintaining the tone. *Trends Neurosci.* 27, 262–269. doi: 10.1016/j.tins.2004.03.005

Sharma, A., Hoeffer, C. A., Takayasu, Y., Miyawaki, T., McBride, S. M., Klann, E., et al. (2010). Dysregulation of mTOR signaling in fragile X syndrome. *J. Neurosci.* 30, 694–702. doi: 10.1523/JNEUROSCI.3696-09.2010

Shu, H., Donnard, E., Liu, B., Jung, S., Wang, R., and Richter, J. D. (2020). FMRP links optimal codons to mRNA stability in neurons. *Proc. Natl. Acad. Sci.* 117, 30400–30411. doi: 10.1073/pnas.2009161117

Silbereis, J. C., Pochareddy, S., Zhu, Y., Li, M., and Sestan, N. (2016). The cellular and molecular landscapes of the developing human central nervous system. *Neuron* 89, 248–268. doi: 10.1016/j.neuron.2015.12.008

Sohal, V. S., and Rubenstein, J. L. R. (2019). Excitation-inhibition balance as a framework for investigating mechanisms in neuropsychiatric disorders. *Mol. Psychiatry* 24, 1248–1257. doi: 10.1038/s41380-019-0426-0

Soong, H. K., Markham, J. A., Weiler, I. J., and Greenough, W. T. (2008). Aberrant early-phase ERK inactivation impedes neuronal function in fragile X syndrome. *Proc. Natl. Acad. Sci. U. S. A.* 105, 4429–4434. doi: 10.1073/pnas.0800257105

Stefani, G., Fraser, C. E., Darnell, J. C., and Darnell, R. B. (2004). Fragile X mental retardation protein is associated with translating polyribosomes in neuronal cells. *J. Neurosci.* 24, 7272–7276. doi: 10.1523/JNEUROSCI.2306-04.2004

Stórustovu, S. Í., and Ebert, B. (2006). Pharmacological characterization of agonists at δ-containing GABAA receptors: functional selectivity for extrasynaptic receptors is dependent on the absence of γ2. *J. Pharmacol. Exp. Ther.* 316, 1351–1359. doi: 10.1124/jpet.105.092403

Su, T., Fan, H.-X., Jiang, T., Sun, W.-W., Den, W.-Y., Gao, M.-M., et al. (2011). Early continuous inhibition of group 1 mGlu signaling partially rescues dendritic spine abnormalities in the Fmr1 knockout mouse model for fragile X syndrome. *Psychopharmacology* 215, 291–300. doi: 10.1007/s00213-010-2130-2

Sunamura, N., Iwashita, S., Enomoto, K., Kadoshima, T., and Isono, F. (2018). Loss of the fragile X mental retardation protein causes aberrant differentiation in human neural progenitor cells. *Sci. Rep.* 8, 1–13. doi: 10.1038/s41598-018-30025-4

Tartaglia, N., Bonn-Miller, M., and Hagerman, R. (2019). Treatment of Fragile X syndrome with Cannabidiol: a case series study and brief review of the literature. *Cannabis. Cannabinoid. Res.* 4, 3–9. doi: 10.1089/can.2018.0053

The Dutch-Belgian Fragile X ConsorthiumBakker, C. E., Verheij, C., Willemsen, R., van der Helm, R., Oerlemans, F., et al. (1994). Fmr1 knockout mice: a model to study fragile X mental retardation. *Cells* 78, 23–33. doi: 10.1016/0092-8674(94)90569-X

Thurman, A. J., Potter, L. A., Kim, K., Tassone, F., Banasik, A., Potter, S. N., et al. (2020). Controlled trial of lovastatin combined with an open-label treatment of a parent-

implemented language intervention in youth with fragile X syndrome. *J. Neurodev. Disord.* 12, 1–17. doi: 10.1186/s11689-020-09315-4

Till, S. M. (2010). The developmental roles of FMRP. *Biochem. Soc. Trans.* 38, 507–510. doi: 10.1042/BST0380507

Verkerk, A. J. M. H., Pieretti, M., Sutcliffe, J. S., Fu, Y. H., Kuhl, D. P. A., Pizzuti, A., et al. (1991). Identification of a gene (FMR-1) containing a CGG repeat coincident with a breakpoint cluster region exhibiting length variation in fragile X syndrome. *Cells* 65, 905–914. doi: 10.1016/0092-8674(91)90397-H

Vincent, A., Hertz, D., Petit, C., Kretz, C., Oberlé, I., and Mandel, J. L. (1991). Abnormal pattern detected in fragile-X patients by pulsed-field gel electrophoresis. *Nature* 349, 624–626. doi: 10.1038/349624a0

Wang, X., Snape, M., Klann, E., Stone, J. G., Singh, A., Petersen, R. B., et al. (2012). Activation of the extracellular signal-regulated kinase pathway contributes to the behavioral deficit of fragile x-syndrome. *J. Neurochem.* 121, 672–679. doi: 10.1111/j.1471-4159.2012.07722.x

Weiler, I. J., Irwin, S. A., Klintsova, A. Y., Spencer, C. M., Brazelton, A. D., Miyashiro, K., et al. (1997). Fragile X mental retardation protein is translated near synapses in response to neurotransmitter activation. *Proc. Natl. Acad. Sci. U. S. A.* 94, 5395–5400. doi: 10.1073/pnas.94.10.5395

Weng, N., Weiler, I. J., Sumis, A., Berry-Kravis, E., and Greenough, W. T. (2008). Early-phase ERK activation as a biomarker for metabolic status in Fragile X syndrome. *Am. J. Med. Genet. B Neuropsychiatr. Genet.* 147, 1253–1257. doi: 10.1002/ajmg.b.30765

Willemsen, R., Bontekoe, C. J. M., Severijnen, L. A., and Oostra, B. A. (2002). Timing of the absence of FMR1 expression in full mutation chorionic villi. *Hum. Genet.* 110, 601–605. doi: 10.1007/s00439-002-0723-5

Wright, R., Newey, S. E., Ilie, A., Wefelmeyer, W., Raimondo, J. V., Ginham, R., et al. (2017). Neuronal chloride regulation via KCC2 is modulated through a GABAB receptor protein complex. *J. Neurosci.* 37, 5447–5462. doi: 10.1523/JNEUROSCI.2164-16.2017

Youssef, E. A., Berry-Kravis, E., Czech, C., Hagerman, R. J., Hessl, D., Wong, C. Y., et al. (2018). Effect of the mGluR5-NAM basimglurant on behavior in adolescents and adults with Fragile X syndrome in a randomized, double-blind, placebo-controlled trial: FragXis phase 2 results. *Neuropsychopharmacology* 43, 503–512. doi: 10.1038/npp.2017.177

Yu, S., Pritchard, M., Kremer, E., Lynch, M., Nancarrow, J., Baker, E., et al. (1991). Fragile X genotype characterized by an unstable region of DNA. *Science* 1979, 1179–1181. doi: 10.1126/science.252.5009.1179

Zhang, N., Peng, Z., Tong, X., Lindemeyer, A. K., Cetina, Y., Huang, C. S., et al. (2017). Decreased surface expression of the δ subunit of the GABAA receptor contributes to reduced tonic inhibition in dentate granule cells in a mouse model of fragile X syndrome. *Exp. Neurol.* 297, 168–178. doi: 10.1016/j.expneurol.2017.08.008

Zhang, A., Sokolova, I., Domissy, A., Davis, J., Rao, L., Hana Utami, K., et al. (2022). Maturation delay of human GABAergic neurogenesis in Fragile X syndrome pluripotent stem cells. *Stem Cells Transl. Med.* 11, 613–629. doi: 10.1093/stcltm/szac022

Zhu, P., Li, J., Zhang, L., Liang, Z., Tang, B., Liao, W. P., et al. (2018). Development-related aberrations in Kv1.1 α-subunit exert disruptive effects on bioelectrical activities of neurons in a mouse model of fragile X syndrome. *Prog. Neuro-Psychopharmacol. Biol. Psychiatry* 84, 140–151. doi: 10.1016/j.pnpbp.2018.02.011

Zito, K., and Svoboda, K. (2002). Activity-dependent synaptogenesis in the adult mammalian cortex. *Neuron* 35, 1015–1017. doi: 10.1016/S0896-6273(02)00903-0

frontiers | Frontiers in Pharmacology

TYPE Original Research
PUBLISHED 15 August 2023
DOI 10.3389/fphar.2023.1220796

OPEN ACCESS

EDITED BY
Francisco Torrens,
University of Valencia, Spain

REVIEWED BY
Liang Guo,
Bristol Myers Squibb, United States
Clemens Möller,
Hochschule Albstadt-Sigmaringen, Germany
Jean-Pierre Valentin,
UCB Biopharma SPRL, Belgium
Annie Delaunois,
UCB Biopharma SPRL, Belgium
Gary Richard Mirams,
University of Nottingham, United Kingdom
Zhihua Li,
United States Food and Drug Administration, United States

*CORRESPONDENCE
Ki-Suk Kim,
idkks@kitox.re.kr
Seong-Jun Park,
parksj@cnu.ac.kr

RECEIVED 11 May 2023
ACCEPTED 07 August 2023
PUBLISHED 15 August 2023

CITATION
Yoon S-H, Lee H-L, Jeong DU, Lim KM, Park S-J and Kim K-S (2023), Assessment of the proarrhythmic effects of repurposed antimalarials for COVID-19 treatment using a comprehensive *in vitro* proarrhythmia assay (CiPA).
Front. Pharmacol. 14:1220796.
doi: 10.3389/fphar.2023.1220796

Assessment of the proarrhythmic effects of repurposed antimalarials for COVID-19 treatment using a comprehensive *in vitro* proarrhythmia assay (CiPA)

Seung-Hyun Yoon[1,2], Hyun-Lee Lee[1], Da Un Jeong[3], Ki Moo Lim[4], Seong-Jun Park[2]* and Ki-Suk Kim[1]*

[1]R&D Center for Advanced Pharmaceuticals and Evaluation, Korea Institute of Toxicology, Daejeon, Republic of Korea, [2]College of Veterinary Medicine, Research Institute of Veterinary Medicine, Chungnam National University, Daejeon, Republic of Korea, [3]Intelligent Human Twin Research Center, Electronics and Telecommunications Research Institute, Daejeon, Republic of Korea, [4]Department of IT Convergence Engineering, Kumoh National Institute of Technology, Gumi, Republic of Korea

Due to the outbreak of the SARS-CoV-2 virus, drug repurposing and Emergency Use Authorization have been proposed to treat the coronavirus disease 2019 (COVID-19) during the pandemic. While the efficiency of the drugs has been discussed, it was identified that certain compounds, such as chloroquine and hydroxychloroquine, cause QT interval prolongation and potential cardiotoxic effects. Drug-induced cardiotoxicity and QT prolongation may lead to life-threatening arrhythmias such as torsades de pointes (TdP), a potentially fatal arrhythmic symptom. Here, we evaluated the risk of repurposed pyronaridine or artesunate-mediated cardiac arrhythmias alone and in combination for COVID-19 treatment through *in vitro* and *in silico* investigations using the Comprehensive *in vitro* Proarrhythmia Assay (CiPA) initiative. The potential effects of each drug or in combinations on cardiac action potential (AP) and ion channels were explored using human induced pluripotent stem cell-derived cardiomyocytes (hiPSC-CMs) and Chinese hamster ovary (CHO) cells transiently expressing cardiac ion channels (Nav1.5, Cav1.2, and hERG). We also performed *in silico* computer simulation using the optimized O'Hara-Rudy human ventricular myocyte model (ORd model) to classify TdP risk. Artesunate and dihydroartemisinin (DHA), the active metabolite of artesunate, are classified as a low risk of inducing TdP based on the torsade metric score (TMS). Moreover, artesunate does not significantly affect the cardiac APs of hiPSC-CMs even at concentrations up to 100 times the maximum serum concentration (C_{max}). DHA modestly prolonged at APD_{90} (10.16%) at 100 times the C_{max}. When considering C_{max}, pyronaridine, and the combination of both drugs (pyronaridine and artesunate) are classified as having an intermediate risk of inducing TdP. However, when considering the unbound concentration (the free fraction not bound to carrier proteins or other tissues inducing pharmacological activity), both drugs are classified as having a low risk of inducing TdP. In summary, pyronaridine, artesunate, and a combination of both drugs have been confirmed to pose a low proarrhythmogenic risk at therapeutic and supratherapeutic (up to 4 times) free C_{max}. Additionally, the CiPA initiative may be suitable for regulatory use and provide novel insights for evaluating drug-induced cardiotoxicity.

KEYWORDS
CiPA, cardiotoxicity, COVID-19, electrophysiology, antimalarials

1 Introduction

Drug-induced QT/QTc interval prolongation and cardiotoxicity are associated with arrhythmic events, such as torsade de point (TdP), and sudden cardiac death (Yap and Camm, 2003). To evaluate these risk factors, the International Council for Harmonisation of Technical Requirements for Pharmaceuticals for Human Use (ICH) has published S7B and E14 guidelines, which provide a framework for predicting cardiotoxicity assessment for drugs (Cavero and Crumb, 2005). Unfortunately, the low specificity of ICH S7B/E14 leads to the undesirable regulation of drugs that are unlikely to cause cardiac arrhythmias (Jeong et al., 2022). This is typically understood to result from focusing on only one of the many ion channels governing action potential (AP) formation (Colatsky et al., 2016; Jeong et al., 2022). To resolve this issue, the Comprehensive *in vitro* Proarrhythmia Assay (CiPA) project was proposed by the US Food and Drug Administration (FDA) and has grown into an international research project with the participation of the FDA and various researchers led by pharmaceutical companies. The CiPA project comprises four interrelated components, the first of which assesses the effects of drugs through *in vitro* experiments using ion currents participating in human ventricular AP formation (Cavero et al., 2016). The second component predicts drug-induced cardiotoxicity using an *in silico* model, the O'Hara-Rudy human ventricular myocyte model (ORd model), with results obtained from an *in vitro* ion current dataset as input (Cavero et al., 2016; Yoo et al., 2021). The *in silico* model allows the classification of each drug as having no/low, intermediate, or high proarrhythmic risk. The third component investigates the electrophysiological effects of human induced pluripotent stem cells (hiPSC-CMs), which can also be used to confirm unexpected adverse cardiac effects compared with *in vitro* multiple cardiac ion channel screening data and *in silico* prediction models (Strauss et al., 2019). The fourth component confirms *in vivo* human electrophysiological impact of drugs that may result from metabolic characteristics through human surface electrocardiography in phase I clinical trials and compares it to preclinical data (Park et al., 2019; Strauss et al., 2019). The CiPA initiative suggests a novel human-based paradigm for systematically evaluating drugs with the potential proarrhythmic risk rather than focusing on drug-induced hERG block and QT prolongation (Cavero et al., 2016; Fermini et al., 2016; Authier et al., 2017). This new paradigm can overcome the limitations of existing methods used to assess drug-induced cardiotoxicity. Moreover, the newly ICH E14/S7B Q&As incorporate CiPA assays as follow-up studies for risk evaluation best practice considerations for experimental factors (ICH E14/S7B Implementation Working Group, 2022).

Since 2019, the world has been facing a pandemic caused by coronavirus disease 2019 (COVID-19) (Touret et al., 2020; Yanagida

TABLE 1 Test concentrations of drugs used in the electrophysiological recordings (in nM).

Cardiac ion channel recordings						
Drug		C_{max}	Conc.1	Conc.2	Conc.3	Conc.4
Pyronaridine		800	800	1,600	2,400	3,200
Artesunate		780	780	1,560	2,340	3,120
Dihydroartemisinin (DHA)		4,200	4,200	8,400	12,600	16,800
Mixture (3:1)	Pyronaridine	800	800	1,600	2,400	3,200
	Artesunate	780	600	1,200	1,800	2,400
Drug		Unbound concentration	Conc.1	Conc.2	Conc.3	Conc.4
Pyronaridine		13.2	13.2	26.4	39.6	52.8
Mixture (3:1)	Pyronaridine	13.2	13.2	26.4	39.6	52.8
	Artesunate	N/A	10.4	20.8	31.2	41.6
AP recordings						
Drug		C_{max}	Conc.1	Conc.2	Conc.3	Conc.4
Artesunate		780	780	7,800	23,400	78,000
Dihydroartemisinin (DHA)		4,200	4,200	42,000	126,000	420,000
Drug		Unbound concentration	Conc.1	Conc.2	Conc.3	Conc.4
Pyronaridine		13.2	13.2	132	396	1,320
Mixture (3:1)	Pyronaridine	13.2	13.2	132	396	1,320
	Artesunate	N/A	10.4	104	312	1,040

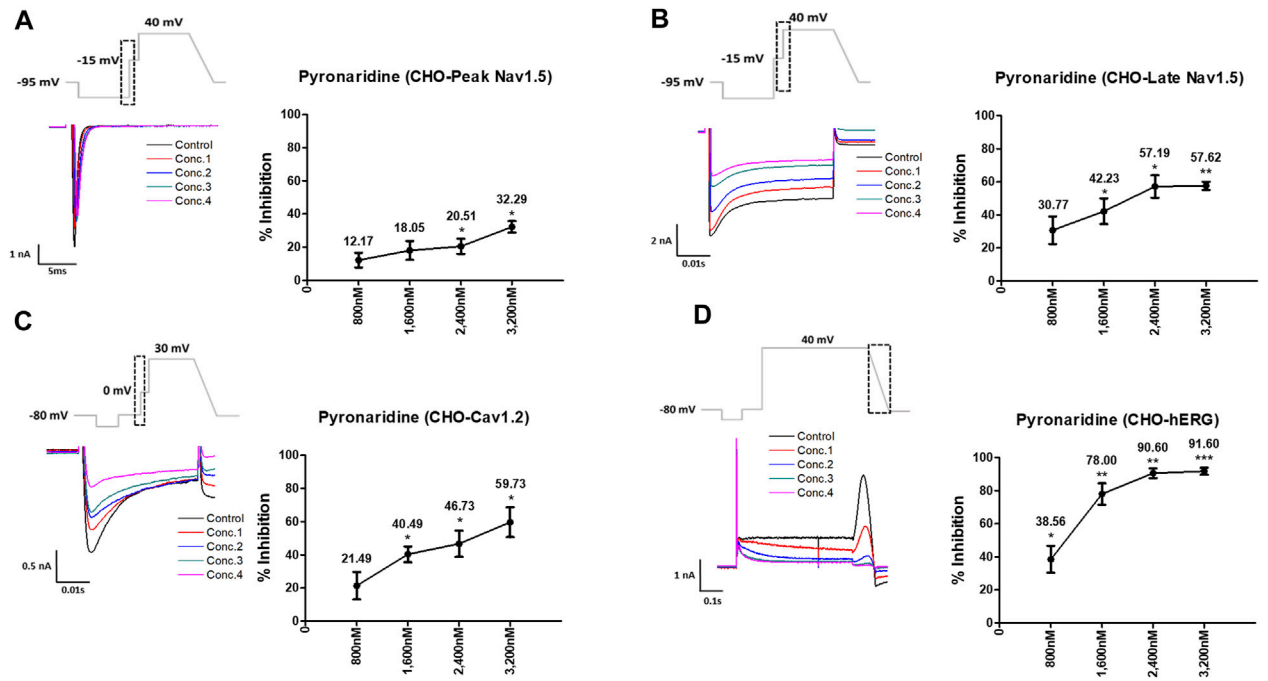

FIGURE 1
Effects of pyronaridine tested considering C_{max} on cardiac ionic currents in CHO cells. **(A–D)** Representative traces demonstrating of ionic currents showing the effect of pyronaridine on Peak Nav1.5 **(A)**, Late Nav1.5 **(B)**, Cav1.2 **(C)**, and hERG **(D)** at concentrations of 800, 1,600, 2,400, and 3,200 nM, respectively (left), and the concentration-response relationship for each ionic current (right). Data are presented as mean ± standard error of the mean (SEM) and analyzed using Student's t-test. *$p < 0.05$, **$p < 0.01$ or ***$p < 0.001$ compared to control ($n = 3$).

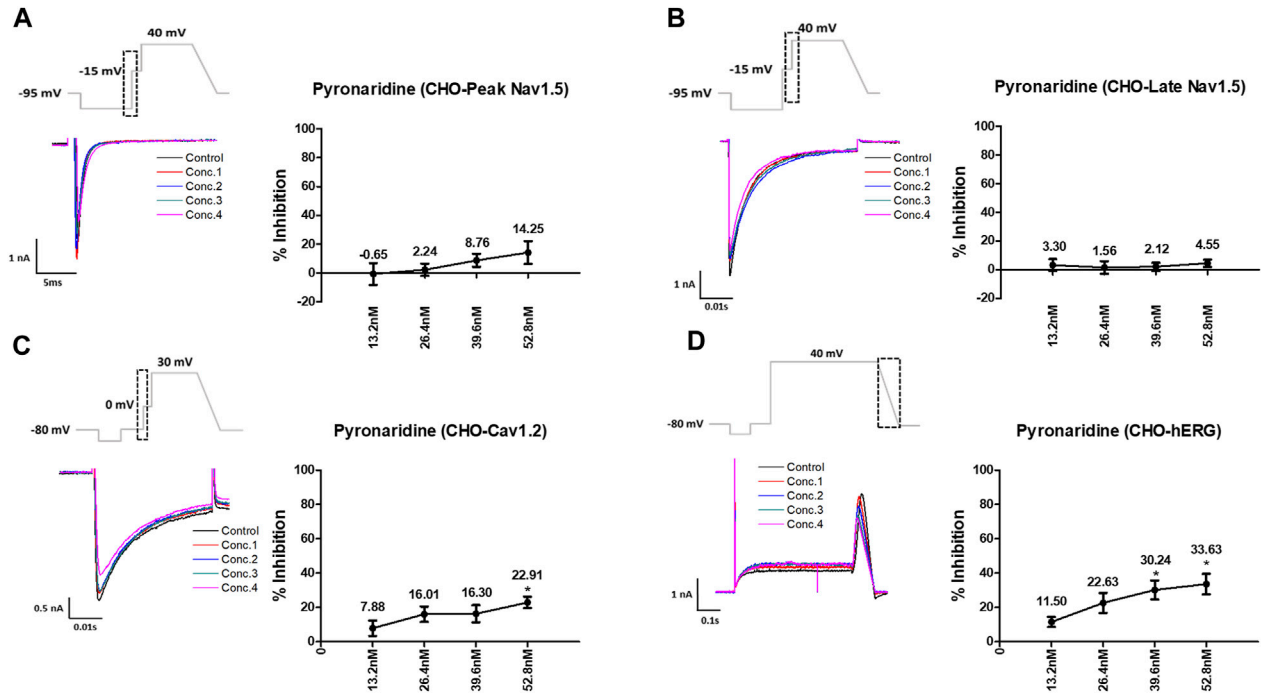

FIGURE 2
Effects of pyronaridine tested considering unbound concentration on cardiac ionic currents in CHO cells. **(A–D)** Representative traces of ionic currents demonstrating the effect of pyronaridine on Peak Nav1.5 **(A)**, Late Nav1.5 **(B)**, Cav1.2 **(C)**, and hERG **(D)** at concentrations of 13.2, 26.4, 39.6, and 52.8 nM, respectively (left), and the concentration-response relationship for each ionic current (right). Data are presented as mean ± standard error of the mean (SEM) and analyzed using Student's t-test. *$p < 0.05$, **$p < 0.01$ or ***$p < 0.001$ compared to control ($n = 3$).

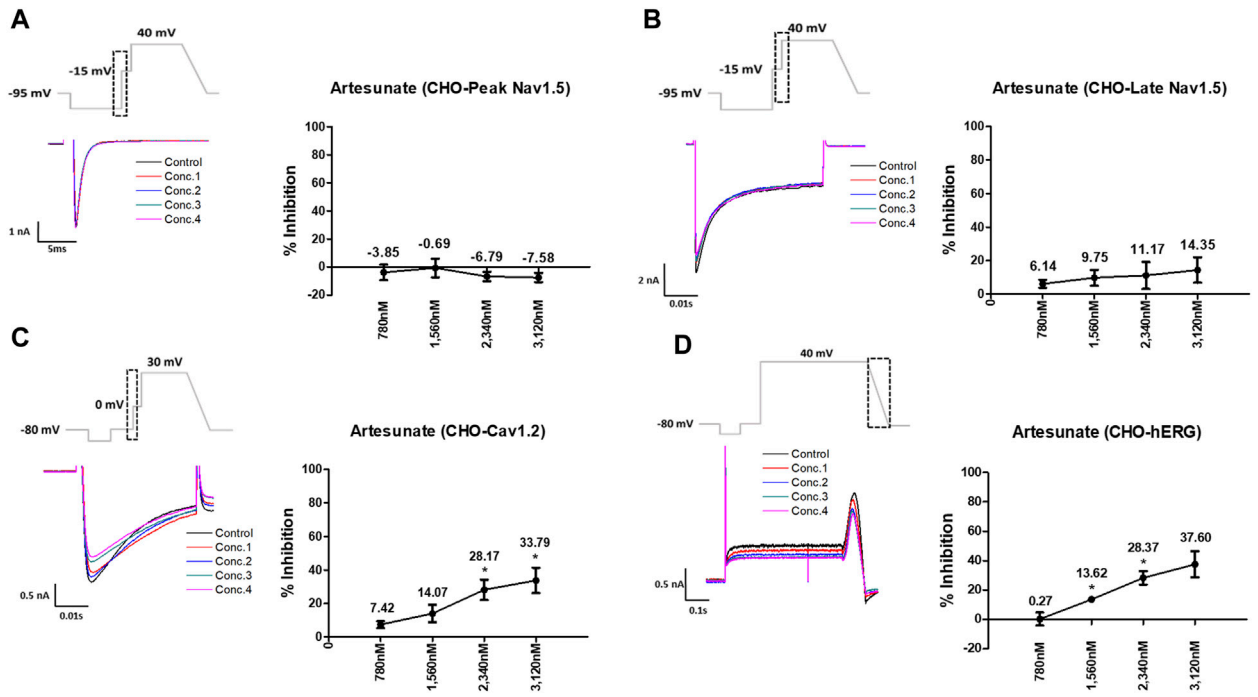

FIGURE 3
Effects of artesunate tested considering C_{max} on cardiac ionic currents in CHO cells. **(A–D)** Representative traces of ionic currents demonstrating the effect of artesunate on Peak Nav1.5 **(A)**, Late Nav1.5 **(B)**, Cav1.2 **(C)**, and hERG **(D)** at concentrations of 780, 1,560, 2,340, and 3,120 nM, respectively (left) and the concentration-response relationship for each ionic current (right). Data are presented as mean ± standard error of the mean (SEM) and analyzed using Student's t-test. *$p < 0.05$, **$p < 0.01$ or ***$p < 0.001$ compared to control ($n = 3$).

et al., 2021); many nonclinical and clinical trials have been conducted to treat COVID-19, including the repurposing of drugs such as chloroquine (CQ), hydroxychloroquine (HCQ), and remdesivir (Yanagida et al., 2021). Drug repurposing is a useful tool for identifying new therapeutic methods (Serafin et al., 2020). Previous studies have reported that the quinoline-related antimalarial drugs CQ and HCQ block ion channels related to cardiac AP formation and can cause fatal arrhythmias associated with QT prolongation (Kinoshita et al., 2010; Borba et al., 2020; Chorin et al., 2020; Mercuro et al., 2020; Wang et al., 2020; Tleyjeh et al., 2021; Sala et al., 2022). Compliant data from the CiPA initiative have shown that using CQ and HCQ at therapeutic concentrations related to malaria or repurposing for COVID-19 is associated with the risk of QT prolongation and TdP (Delaunois et al., 2021). Those drugs inhibited mainly potassium channels, *in silico* prediction model predicted that have the potential to prolong repolarization (Thomet et al., 2021; Varshneya et al., 2021; Whittaker et al., 2021; TeBay et al., 2022). Additionally, CQ, HCQ, or azithromycin (AZM) co-administration can trigger to high arrhythmogenic risk in conditions with impaired repolarization (Sutanto and Heijman, 2020; Montnach et al., 2021). Consequently, on 15 June 2020, the FDA revoked the Emergency Use Authorization (EUA) for HCQ and CQ because they were ineffective in treating COVID-19 and could cause serious adverse cardiac events (The Food and Drug Administration, 2020a). Pyronaridine-artesunate is also an antimalarial drug that has been considered for treating COVID-19, and clinical trials are currently ongoing. Pyronaridine–artesunate is an artemisinin-based combination therapy used to treat malaria (Rueangweerayut et al., 2012). *In vitro* studies comparing the effectiveness of pyronaridine, artesunate, and HCQ against SARS-CoV-2 indicated that pyronaridine and artesunate were more effective in human lung epithelial (Calu-3) cells (Bae et al., 2020; Krishna et al., 2021). However, there is limited information on drug-induced cardiotoxicity and QT prolongation associated with repurposing for COVID-19 treatment. Therefore, it is important to determine the potential cardiotoxicity of this drug to avoid severe adverse events.

Our study aimed to perform *in vitro* and *in silico* investigations of the effects of pyronaridine, artesunate, and a combination of both drugs on cardiac electrophysiological properties and to predict arrhythmic potentials using the principles and methods of the CiPA initiative. Moreover, our study aimed to improve our understanding of cardiotoxicity and QT prolongation mechanisms, providing even greater insight into standardized nonclinical assays based on the CiPA approach.

2 Methods

2.1 Chemicals

Pyronaridine and artesunate were obtained from Sigma-Aldrich (St. Louis, MO, USA). The mixture consists of pyronaridine and artesunate in a ratio of 3:1. Dihydroartemisinin (DHA) was obtained from Selleck Chemicals (Houston, TX, USA). The drugs

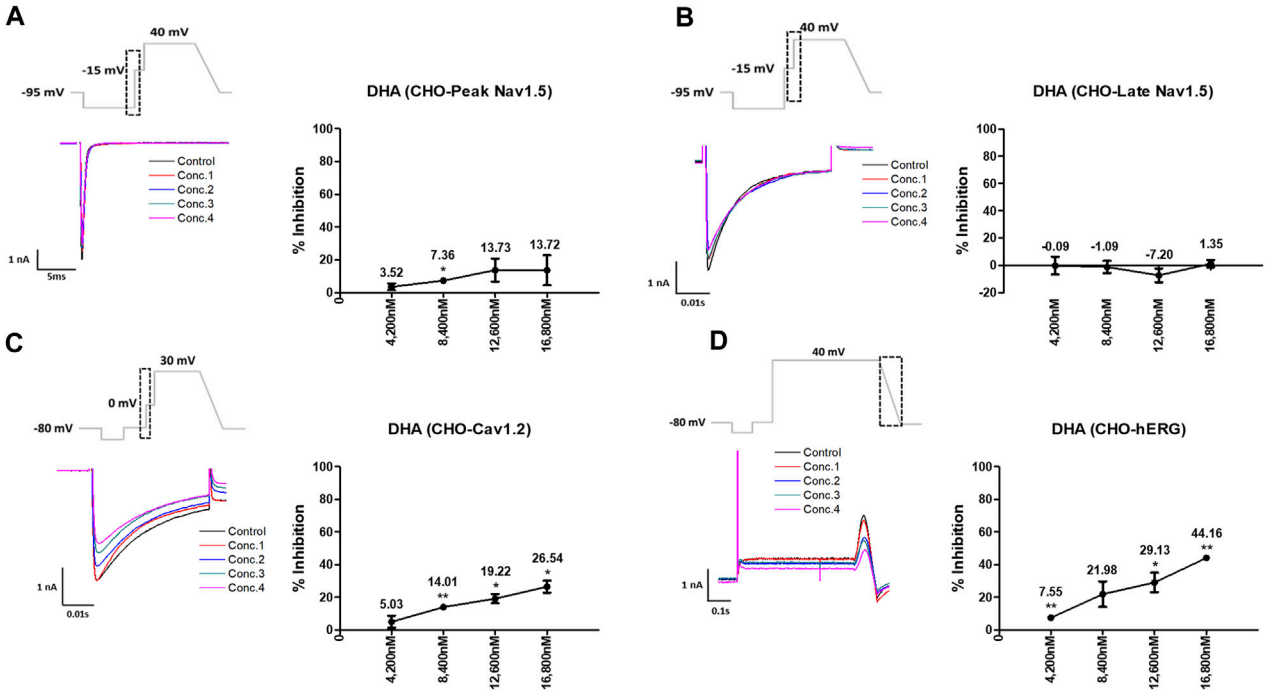

FIGURE 4
Effects of dihydroartemisinin (DHA) tested considering C_{max} on cardiac ionic currents in CHO cells. **(A–D)** Representative traces of ionic currents demonstrating the effect of DHA on Peak Nav1.5 **(A)**, Late Nav1.5 **(B)**, Cav1.2 **(C)**, and hERG **(D)** at concentrations of 780, 1,560, 2,340, and 3,120 nM, respectively (left) and the concentration-response relationship for each ionic current (right). Data are presented as mean ± standard error of the mean (SEM) and analyzed using Student's t-test. *$p < 0.05$, **$p < 0.01$ or ***$p < 0.001$ compared to control ($n = 3$).

were formulated into a stock solution using dimethyl sulfoxide (DMSO) and stored at −20°C. On the day of the experiment, the stock solution was freshly diluted in the external solution containing 0.1% DMSO and the desired drug concentrations. All chemicals required for preparing the external/internal solutions were obtained from Sigma-Aldrich. The drugs were tested at four different concentrations, taking into account the maximum serum concentration after drug administered (C_{max}) and the concentration of the drug that is not bound to plasma or tissue proteins or not uptake by red blood cells (unbound concentration) (Table 1) (The European Medicines Agency, 2012). According to The European Medicines Agency (2012), therapeutic Cmax of pyronaridine in humans is 726 ng/mL (800 nM), and unbound concentration is 12 ng/mL (13.2 nM). Pyronaridine exhibited high plasma protein binding in various organisms, including humans, dogs, rats, and rabbits ranging from 92% to 96%, and it showed preferentially associated with red blood cells. The therapeutic Cmax of artesunate in humans is 0.3 μg/mL (780 nM). The Cmax of DHA, the active metabolite of artesunate, in humans is 1.2 μg/mL (4,200 nM).

2.2 Cell preparation

To investigate the effect of drugs on multiple cardiac ion currents (peak Nav1.5, late Nav1.5, Cav1.2, and hERG), the hERG-CHO cell line was purchased from B'SYS GmbH (Witterswil, Switzerland), while the Nav1.5-CHO and Cav1.2-CHO cell lines were purchased from Charles River Laboratories (Cleveland, OH, USA).

The hERG-CHO cells were maintained in Dulbecco's Modified Eagle's Medium and Nutrient Mixture F-12 (DMEM/F12) (Gibco, Gaithersburg, MD, USA) supplemented with 10% fetal bovine serum (FBS) (Gibco), 1% penicillin/streptomycin (Gibco) and 50 μg/mL hygromycin B (Invitrogen, Carlsbad, CA, USA) in a humidified 5% CO_2 atmosphere at 37°C. The Nav1.5-CHO cells were maintained in Ham's F-12 medium (Gibco) supplemented with 10% FBS, 1% penicillin/streptomycin, and 0.25 mg/mL Geneticin™ Selective antibiotic (Gibco) in a humidified 5% CO_2 atmosphere at 37°C. The Cav1.2-CHO cells were maintained in Ham's F-12 medium supplemented with 10% tetracycline screened FBS (Takara Bio Inc., Otsu, Japan), 1% penicillin/streptomycin, 0.25 mg/mL hygromycin B, 0.25 mg/mL Geneticin™ Selective antibiotic, 0.40 mg/mL Zeocin (Invivogen, San Diego, CA, USA), and 0.01 mg/mL Blasticidin (Thermo Fisher Scientific, Waltham, MA, USA) in a humidified 5% CO_2 atmosphere at 37°C. To induce Cav1.2 expression, 1 μg/mL tetracycline (Sigma-Aldrich) was added to selection antibiotic-free media 24 h prior to testing. Additionally, to prevent Ca^{2+}-induced toxicity, 3 μM verapamil hydrochloride (Sigma-Aldrich) was included.

2.3 Recording of ionic currents

Conventional whole-cell voltage-clamp recordings were performed for four different currents: hERG, peak Nav1.5, late

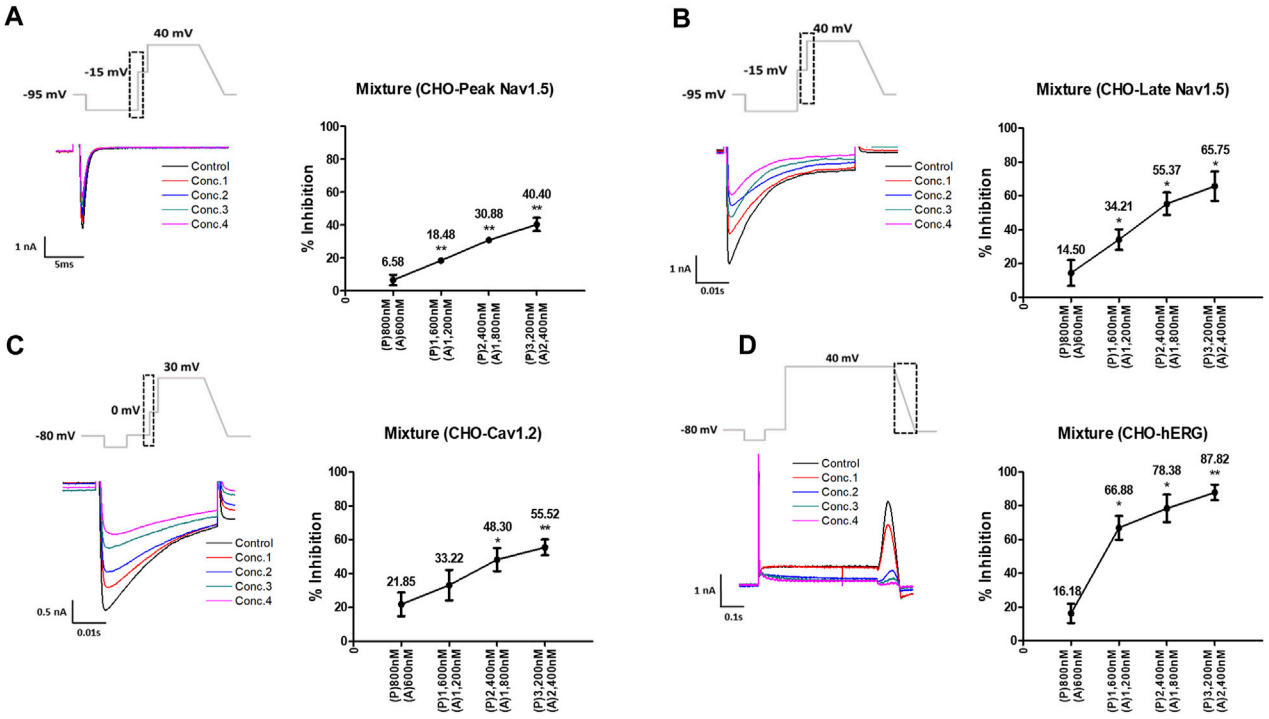

FIGURE 5
Effects of the mixture tested considering C_{max} on cardiac ionic currents in CHO cells. **(A–D)** Representative traces of ionic currents demonstrating the effect of the mixture on Peak Nav1.5 **(A)**, Late Nav1.5 **(B)**, Cav1.2 **(C)**, and hERG **(D)** with pyronaridine concentrations of 800, 1,600, 2,400, and 3,200 nM, and artesunate concentrations of 600, 1,200, 1,800, and 2,400 nM, respectively (left). Concentration-response relationship for each ionic current (right). Data are presented as mean ± standard error of the mean (SEM) and analyzed using Student's t-test. *$p < 0.05$, **$p < 0.01$ or ***$p < 0.001$ compared to control ($n = 3$). P, pyronaridine; A, artesunate.

Nav1.5 and Cav1.2 currents were recorded and analyzed as recommended by the FDA (The Food and Drug Administration, 2020b). The recording pipette with a tip resistance of 3–5 MΩ was filled with internal solutions. The external solution for peak Nav1.5 consisted of the following (in mM): 130 NaCl, 10 HEPES, 4 CsCl, 1 $MgCl_2$*$6H_2O$, 2 $CaCl_2$*H_2O, and 10 dextrose (pH 7.4 with NaOH). The internal solution for peak Nav1.5 contained the following (in mM): 130 CsCl, 7 NaCl, 1 $MgCl_2$*$6H_2O$, 5 HEPES, 5 EGTA, 5 Mg-ATP, and 0.4 Tris-GTP (pH 7.2 with CsOH). The same voltage protocol and solutions were used for recording the late Nav1.5 current as for as the peak Nav1.5. To induce the late Nav1.5 current, 150 nM ATX-II (Alomone labs, Jerusalem, Israel) was added. The external solution for Cav1.2 consisted of the following (in mM): 137 NaCl, 10 HEPES, 4 KCl, 1 $MgCl_2$*$6H_2O$, 1.8 $CaCl_2$*H_2O, and 10 dextrose (pH 7.4 with NaOH). The internal solution for Cav1.2 contained the following (in mM): 120 Aspartic Acid, 120 CsOH, 10 CsCl, 10 HEPES, 10 EGTA, 5 Mg-ATP, and 0.4 Tris-GTP (pH 7.2 with CsOH). The external solution for hERG contained the following (in mM): 130 NaCl, 10 HEPES, 5 KCl, 1 $MgCl_2$*$6H_2O$, 1 $CaCl_2$*H_2O, and 12.5 dextrose (pH 7.4 with NaOH). The internal solution for hERG consisted of the following (in mM): 120 K-gluconate, 20 KCl, 10 HEPES, 5 EGTA, and 1.5 Mg-ATP (pH 7.3 with KOH). All four currents were recorded at physiological temperature (37°C ± 1°C).

2.4 Recording of spontaneous APs in hiPSC-CMs

For single-cell AP recordings, hiPSC-CMs (Cardiosight-S; NEXEL, Co., Ltd., Seoul, Korea) were cultured. The cells were transferred to four-well culture plates with Matrigel (Corning, NY, USA)-coated glass coverslips for AP recording. They were maintained in a culture incubator in a humidified 5% CO_2 atmosphere at 37°C, and utilized within 7 days after thawing. The medium was changed every 2–3 days. The external solution for APs recording contained the following (in mM): 145 NaCl, 5.4 KCl, 10 HEPES, 1 $MgCl_2$*$6H_2O$, 1.8 $CaCl_2$*H_2O, and 5 dextrose (pH 7.4 with NaOH). The internal solution for AP recording consisted of the following (in mM): 20 KCl, 120 K-Aspartic Acid, 5 NaCl, 2 $CaCl_2$*H_2O, 5 EGTA, and 5 Mg-ATP (pH 7.25 with KOH). The maximum rate of depolarization during the upstroke of the AP (Vmax), maximum diastolic potential (MDP), AP amplitude (APA), the AP duration at 50% (APD_{50}), and 90% (APD_{90}) repolarization were measured when they were stable. The spontaneous contractions of hiPSC-CMs were recorded in I = 0 mode, and only cells that exhibited stable beating were used in the analysis. APs were recorded at a physiological temperature (37°C ± 1°C).

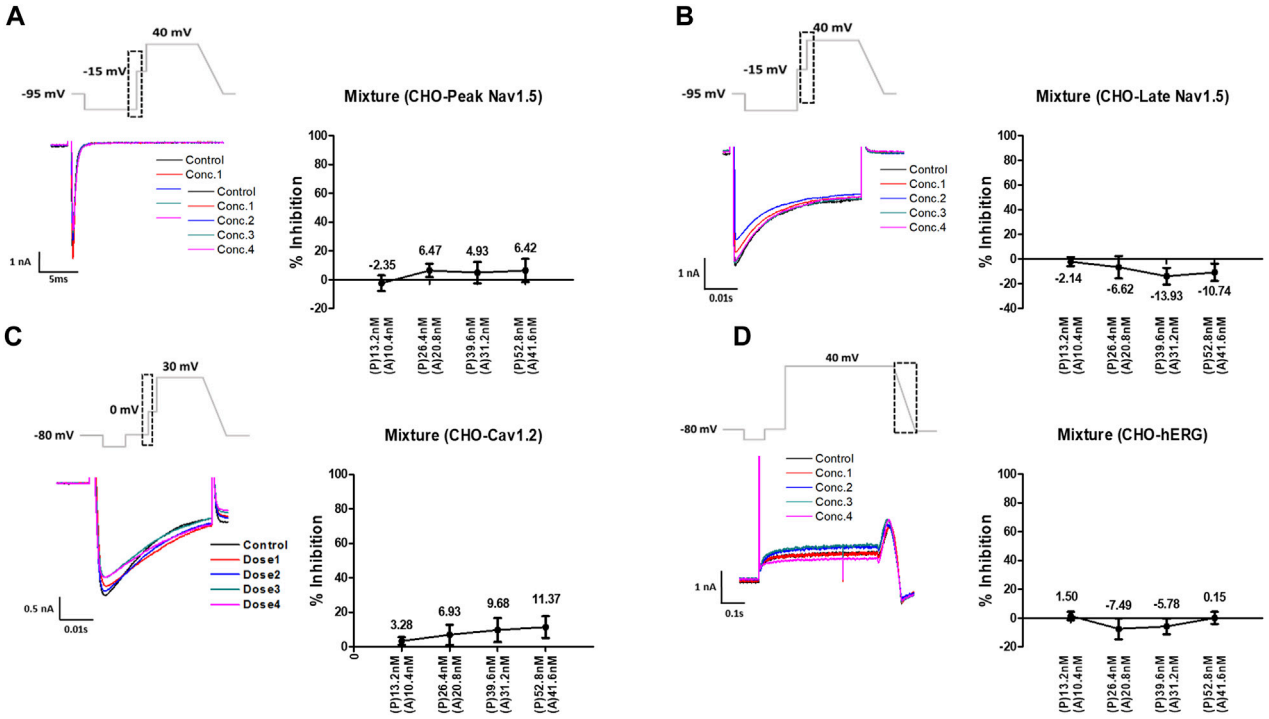

FIGURE 6
Effects of the mixture tested considering unbound concentration on cardiac ionic currents in CHO cells. **(A–D)** Representative traces of ionic currents demonstrating the effect of the mixture on Peak Nav1.5 **(A)**, Late Nav1.5 **(B)**, Cav1.2 **(C)**, and hERG **(D)** with pyronaridine concentrations of 13.2, 26.4, 39.6, and 52.8 nM and artesunate concentrations of 10.4, 20.8, 31.2, and 41.6 nM, respectively (left). Concentration-response relationship for each ionic current (right). Data are presented as mean ± standard error of the mean (SEM) and analyzed using Student's t-test. *$p < 0.05$, **$p < 0.01$ or ***$p < 0.001$ compared to control ($n = 3$). P, pyronaridine; A, artesunate.

2.5 Hill fitting and generating samples

Hill fitting was conducted using the same method as proposed by Chang et al. (2017) with R programming language (https://github.com/FDA/CiPA/tree/Model-Validation-2018/Hill_Fitting). *In vitro* datasets obtained from the whole-cell voltage-clamp experiment were fitted and sampled with the Markov chain Monte Carlo (MCMC) model proposed by Haario et al. (2006); Laine and Tamminen (2008); Soetaert and Petzoldt (2010) to obtain Hill curves for dosage-to-response for each ion channel. The results were 2,000 samples with half-maximal inhibitory concentration (IC50) and Hill coefficients data per drug used as input for *in silico* model.

2.6 *In silico* model

The optimized ORd model for drug effects was used as a cellular electrophysiological *in silico* model for the human ventricular myocytes (Dutta et al., 2017), generating the AP, the sum of the potentials for all ion channels inhibited by the drugs in cardiomyocytes (O'Hara et al., 2011). The inhibited ion channel was expressed by multiplying the inhibition factor in the general ionic current equation; the inhibition factor consists of Hill coefficients ($\boldsymbol{h}$), IC_{50}, and drug concentration ($\boldsymbol{D}$) (equation 1) (Li et al., 2019).

$$\textbf{Inhibition factor} = \left[1 + \left(\frac{\boldsymbol{D}}{\boldsymbol{IC50}}\right)^{\boldsymbol{h}}\right]^{-1}$$

2.7 Torsade metric score (TMS)

The qNet is the total amount of net charges that pass through six ion channels most affected by drugs in the cell membrane (The six ion channels are as follows: I_{NaL}; the inward sodium current, I_{CaL}; the L-type calcium current, I_{Kr}; the rapidly activating delayed rectifier potassium current, I_{Ks}; the slowly activating delayed rectifier potassium current, I_{K1}; the inward rectifier potassium current, I_{to}; the transient outward potassium current) during one cycle length ($\boldsymbol{CL}$), and is computed as equation 2 (Li et al., 2019; Yoo et al., 2021). The mean of qNet values at 1, 2, 3, and 4 multiples of C_{max} or unbound concentration for each drug, the TMS value, showed high accuracy in predicting TdP risks in the prior study of Li et al. (2019). Accordingly, this study calculated the TMS value for CiPA 12 training set drugs and derived logistic regression curves to obtain Threshold 1 and Threshold 2 for classifying TdP risk. Threshold 1 is the TMS value to separate low risk from intermediate/high risk, and Threshold 2 separates high risk from intermediate/low risk. The classifier was based on ordinal logistic regression using the lrm function from version 4.5-0 of the rms package (Chang et al., 2017). To give the logistic

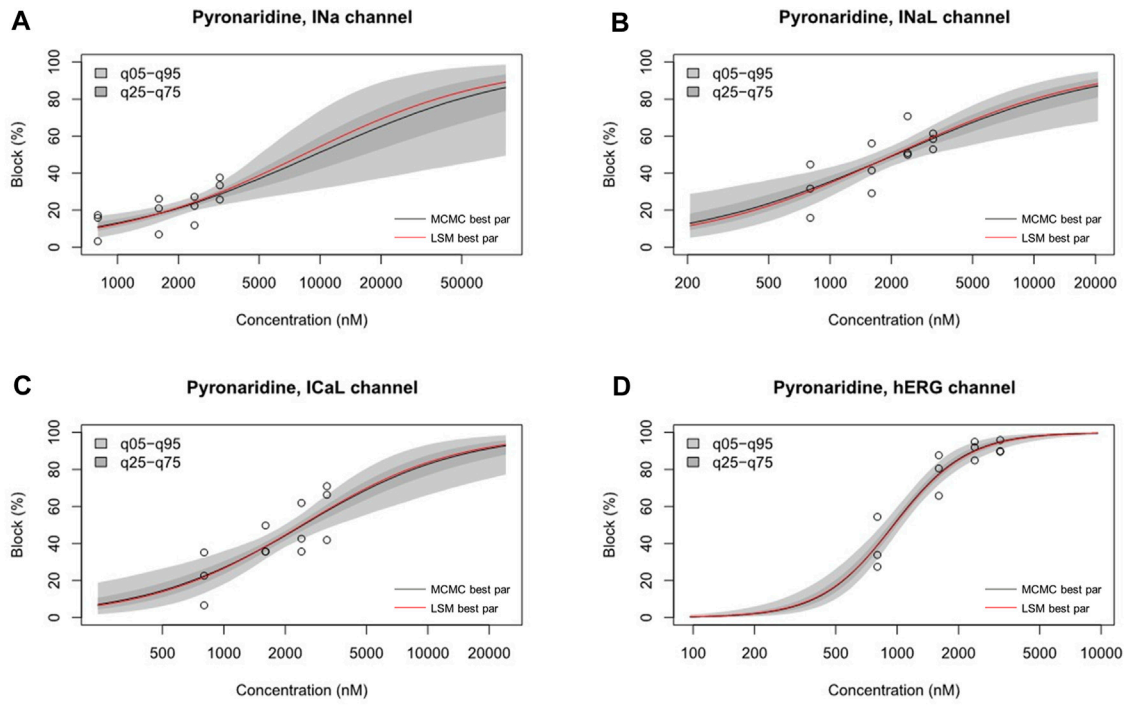

FIGURE 7
Hill curve for dosage-to-response for pyronaridine on I_{Na} **(A)**, pyronaridine on I_{NaL} **(B)**, pyronaridine on I_{CaL} **(C)**, pyronaridine on I_{Kr} **(D)**. Experimental data points for each cell by circles. 95% confidence interval of the fitting on the gray shaded area. Within each panel, the solid red line was fitted using the best parameter of the half-maximal inhibitory concentration (IC_{50}) and Hill coefficient from the nonlinear least square method, whereas the solid black line was the median value from Markov chain Monte Carlo (MCMC) sampling.

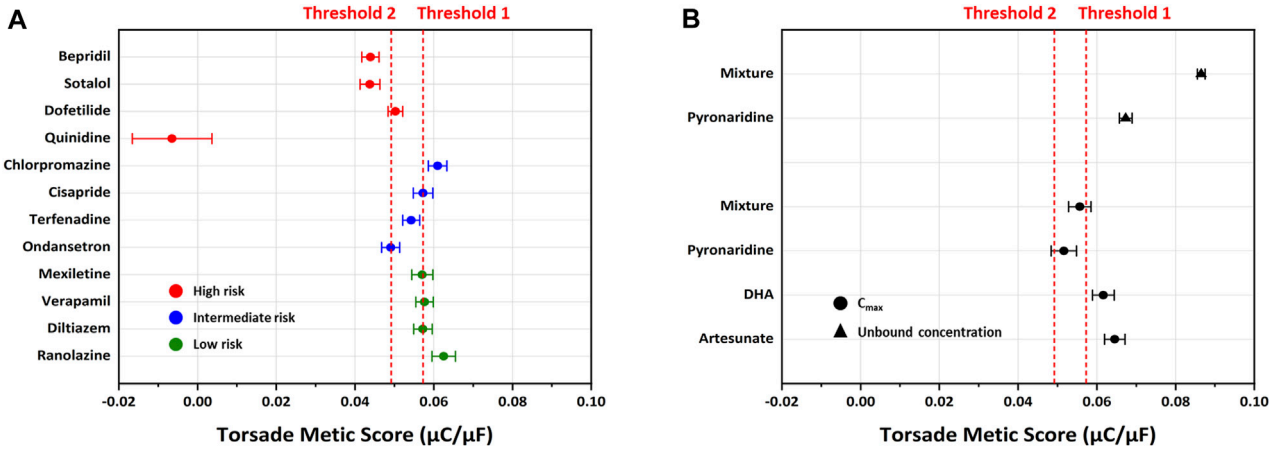

FIGURE 8
Distribution of the torsade metric score (TMS) for drugs using the optimized ORd model. Drugs are sorted based on the mean of TMS in each dataset. **(A)** Threshold 1 and threshold 2 were calculated using logistic regression to classify the TdP risk categories (red for high risk, blue for intermediate risk, green for low risk) using CiPA 12 training set drugs. Threshold 1 (separating low from intermediate/high risk) has a value of 0.0573 μC/μF, and threshold 2 (separating high from intermediate/low risk) has a value of 0.0492 μC/μF. **(B)** The drugs tested considering C_{max} are represented by solid black circle clusters, while drugs tested considering unbound concentration are represented by solid black triangle clusters.

answer for ordinal logistic regression, the high, intermediate, and low-risk levels were categorically encoded to the numerical values of 2, 1, and 0, respectively.

$$qNet = \int_0^{CL} (INaL + ICaL + IKr + IKs + IK1 + Ito)dt$$

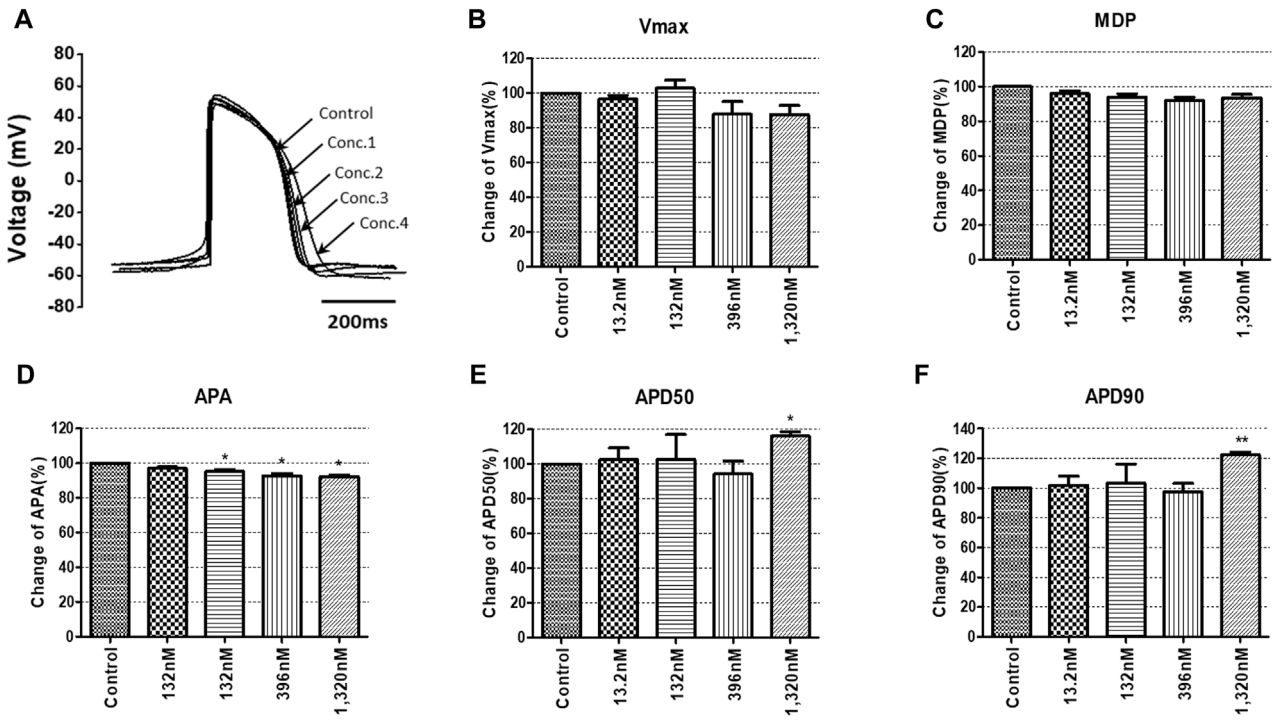

FIGURE 9
Effects of pyronaridine on action potential (AP) parameters of hiPSC-CMs. **(A)** Typical AP traces of hiPSC-CMs in the control and after exposure to 13.2, 132, 396, and 1,320 nM pyronaridine. **(B–F)** Bar graphs illustrating mean normalized values for AP parameters of hiPSC-CMs, including MDP, maximal diastolic potential; APA, AP amplitude; Vmax, maximum rate of depolarization during the upstroke of the AP; APD_{50} and APD_{90}, AP duration at 50% and 90%. Data are presented as mean ± standard error of the mean (SEM) and analyzed using Student's t-test. $^{*}p < 0.05$, $^{**}p < 0.01$ or $^{***}p < 0.001$ compared to control ($n = 3$).

2.8 Statistical analysis

Data analysis was performed using pCLAMP (Axon Instruments, Foster City, CA, USA), Origin 2022 (OriginLab Corp, Northampton, MA, USA), Excel (Microsoft, Redmond, WA, USA) and GraphPad Prism (GraphPad Software, San Diego, CA, USA). Statistical significance was determined using Student's t-test. The values were presented as mean ± standard error of the mean (SEM) and were considered statistically significant when the *p*-value was less than 0.05. Statistically significant differences were assessed using the paired *t*-test at $^{*}p < 0.05$, $^{**}p < 0.01$ or $^{***}p < 0.001$.

3 Results

3.1 Multiple effects of drugs on cardiac ion channels

To investigate the effects of the drugs on ion channels involved in cardiac AP formation a whole-cell voltage-clamp technique was employed. In our previous studies, conducted cardiac ionic currents screening using CiPA 12 training set drugs at various multiple of C_{max} (1, 2, 3, and 4). These datasets were then utilized in the optimized ORd model, to predict drug-induced TdP risks with high accuracy. In order to enhance the accuracy of TdP prediction, it was deemed appropriate to perform cardiac ionic currents screening within the same range (1, 2, 3 and 4 multiples of C_{max} or unbound concentration) as TMS. Therefore, in this study, cardiac ionic currents screening was conducted at these specified multiples of C_{max} or unbound concentration to enable more precise prediction of TdP risks.

Pyronaridine was tested at four different concentrations (C_{max} and 2, 3, and 4 multiples of C_{max}) (Figure 1). Peak Nav1.5 currents were measured as the peak inward current at the −15 mV step, and late Nav1.5 currents were measured as the inward current at the end of the −15 mV step (Figures 1A, B). Pyronaridine decreased the peak Nav1.5 at 800, 1,600, 2,400, and 3,200 nM by 12.17, 18.05, 20.51, and 32.29%, respectively. In addition, pyronaridine concentration-dependently decreased Late Nav1.5. The Cav1.2 currents were recorded as the peak inward current at 0 mV step and significantly decreased at 1,600, 2,400, and 3,200 nM by 40.49, 46.73, and 59.73%, respectively (Figure 1C). The hERG currents were measured as peak outward currents during the ramp-down phase. Pyronaridine decreased the cardiac hERG currents by 38.56, 78.00, 90.60, and 91.60% at 800, 1,600, 2,400, and 3,200 nM, respectively (Figure 1D). Pyronaridine significantly decreased the peak Nav1.5, late Nav1.5, and Cav1.2 currents; however, its sensitivity to three currents was less than that of the hERG currents. In addition, pyronaridine was tested at unbound concentrations and 2, 3, and 4 multiples of unbound concentrations (Figure 2). Pyronaridine did not significantly affect the peak Nav1.5 and late Nav1.5 currents (Figures 2A, B). The Cav1.2 currents

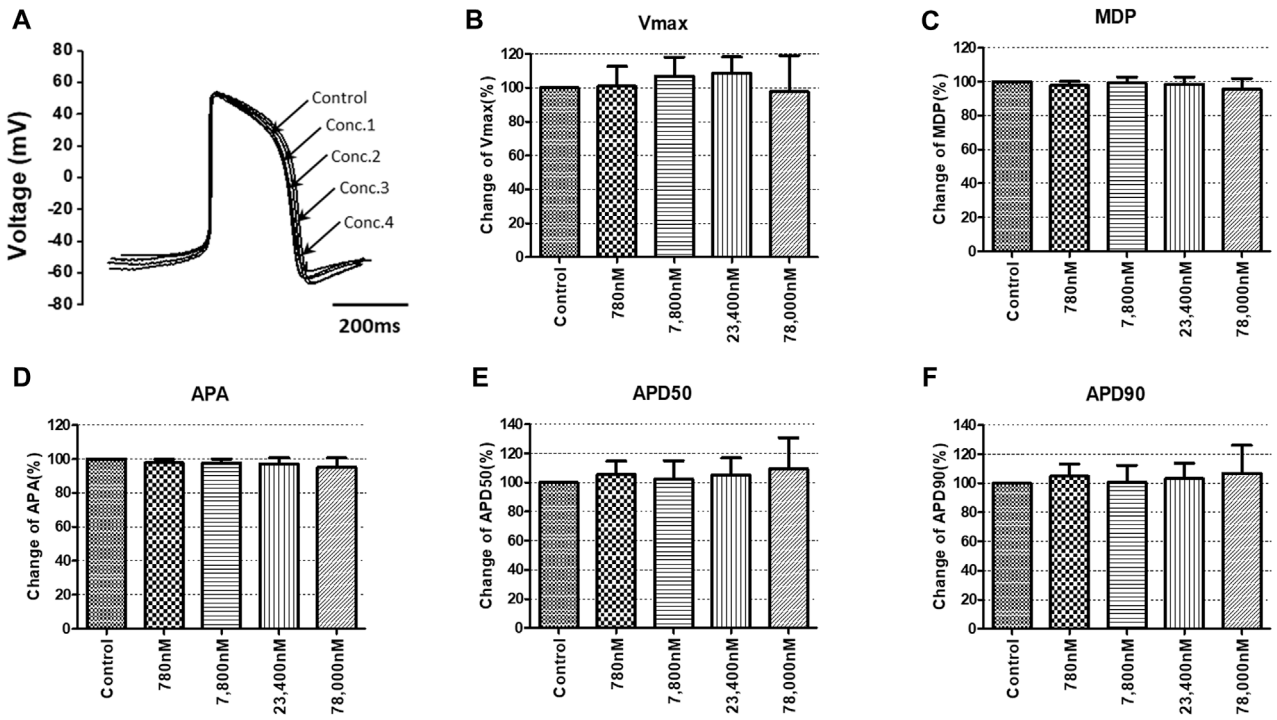

FIGURE 10
Effects of artesunate on action potential (AP) parameters of hiPSC-CMs. **(A)** Typical AP traces of hiPSC-CMs in the control and after exposure to 780, 7,800, 23,400, and 78,000 nM artesunate. **(B–F)** Bar graphs illustrating mean normalized values for AP parameters of hiPSC-CMs, including MDP, maximal diastolic potential; APA, AP amplitude; Vmax, maximum rate of depolarization during the upstroke of the AP; APD_{50} and APD_{90}, AP duration at 50% and 90%. Data are presented as mean ± standard error of the mean (SEM) and analyzed using Student's t-test. *$p < 0.05$, **$p < 0.01$ or ***$p < 0.001$ compared to control ($n = 3$).

decreased at 52.8 nM by 22.91% (Figure 2C), and the hERG currents decreased at 39.6 and 52.8 nM by 30.24% and 33.63%, respectively (Figure 2D).

Artesunate was tested at four different concentrations (C_{max} and 2, 3, and 4 multiples of C_{max}). As shown in Figure 3, artesunate did not significantly affect the peak Nav1.5 and late Nav1.5 currents (Figures 3A, B) but significantly decreased Cav1.2 currents at 2,340 and 3,120 nM by 28.17% and 33.79%, respectively (Figure 3C). Moreover, hERG currents decreased at 1,560 and 2,340 nM by 13.62% and 28.37%, respectively (Figure 3D). DHA was tested at four different concentrations (C_{max} and 2, 3, and 4 multiples of Cmax). DHA significantly decreased the peak Nav1.5 currents at 8,400 nM by 7.36% (Figure 4A). Additionally, Cav1.2 currents decreased at 8,400, 12,600, and 16,800 nM by 14.01, 19.22, and 26.54%, respectively (Figure 4C). The hERG currents significantly inhibited at 4,200, 12,600, and 16,800 nM by 7.55, 29.13, and 44.16%, respectively (Figure 4D). However, DHA did not affect the late Nav1.5 currents (Figure 4B).

Considering the C_{max}, the mixture tested decreased the four cardiac ionic currents in a concentration-dependent manner (Figure 5). Additionally, considering the unbound concentration, the mixture tested did not significantly affect the peak Nav1.5, late Nav1.5, Cav1.2, or hERG currents (Figure 6).

3.2 TdP risk prediction by TMS

The inhibition rates of four ion channel currents were sampled using the uncertainty quantification algorithm based on the MCMC model to generate 2,000 Hill curves. From each Hill curve, we obtained IC_{50} and Hill coefficient (Figure 7). The risk of drug-induced cardiac arrhythmias such as TdP was evaluated using a novel *in silico* biomarker, qNet, and TMS as proposed by CiPA (Dutta et al., 2017; Li et al., 2019) (Figure 8). As shown in Figure 8A, the two thresholds that classify drugs into three TdP risk categories were also calculated based on the CiPA 12 training set drugs: Threshold 1 has a value of 0.0573 μC/μF and Threshold 2 has a value of 0.0492 μC/μF. When tested considering C_{max}, artesunate and DHA was classified as a low risk of inducing TdP (TMS = 0.064523 μC/μF for artesunate 0.061648 μC/μF for DHA) (Figure 8B). However, pyronaridine and the mixture were classified as having an intermediate risk of inducing TdP (TMS was 0.051608 μC/μF for pyronaridine and 0.055643 μC/μF for the mixture) (Figure 8B). In contrast, considering unbound concentration, both pyronaridine and mixture were classified as having a low risk of inducing TdP with 0.067301 μC/μF and 0.086473 μC/μF of TMS, respectively. Despite the utilization of the same drug, it was confirmed that the case tested considering the unbound concentration had a lower risk of inducing TdP than the case tested considering C_{max}.

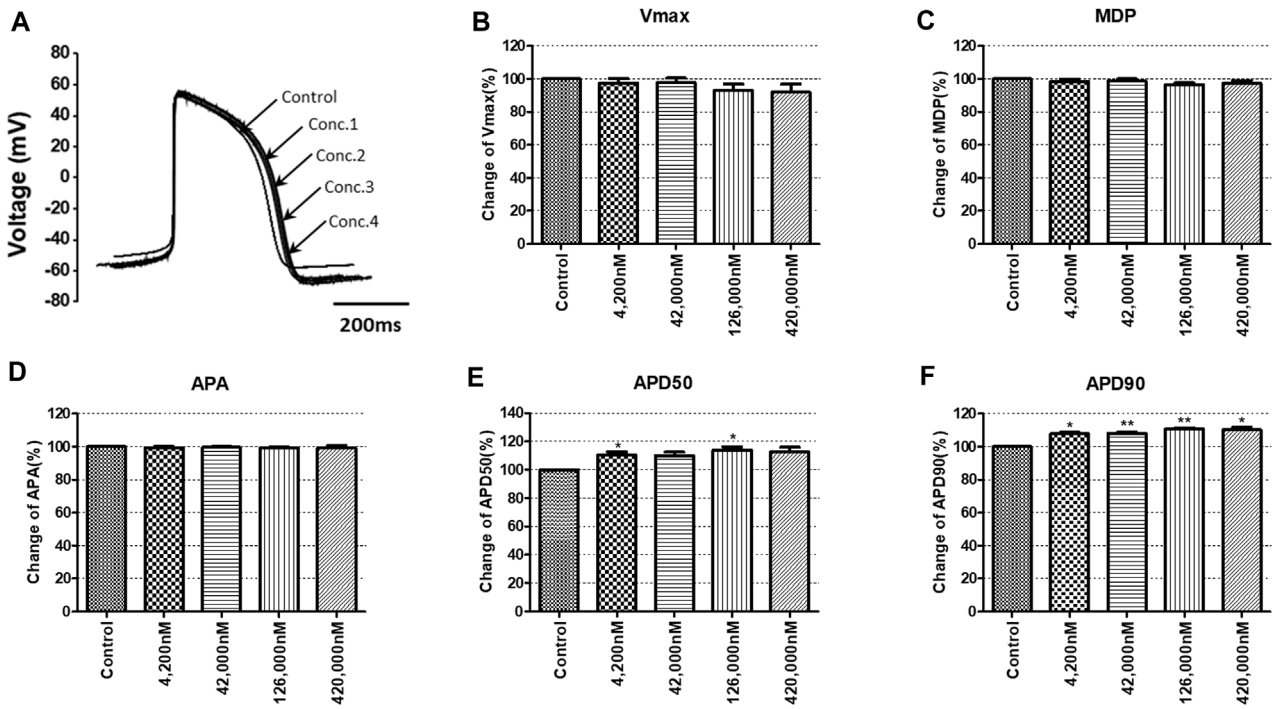

FIGURE 11
Effects of DHA on action potential (AP) parameters of hiPSC-CMs. **(A)** Typical AP traces of hiPSC-CMs in the control and after exposure to 4,200, 42,000, 126,000 and 420,000 nM DHA. **(B–F)** Bar graphs illustrating mean normalized values for AP parameters of hiPSC-CMs, including MDP, maximal diastolic potential; APA, AP amplitude; Vmax, maximum rate of depolarization during the upstroke of the AP; APD_{50} and APD_{90}, AP duration at 50% and 90%. Data are presented as mean ± standard error of the mean (SEM) and analyzed using Student's t-test. *$p < 0.05$, **$p < 0.01$ or ***$p < 0.001$ compared to control ($n = 3$).

3.3 Effects of drugs on cardiac APs in ventricular hiPSC-CMs

To confirm the integrated electrophysiological effects of the drugs, we measured the spontaneous beating of hiPSC-CMs using the whole-cell current-clamp method. Under control conditions, the values of the AP parameters were as follows: −63.1 ± 1.6 mV for MDP, 45.8 ± 4.1 mV/ms for Vmax, 287.0 ± 17.9 ms for APD_{90}, 236.1 ± 12.5 ms for APD_{50}, 1.2 ± 0.03 for APD_{90}/APD_{50} ratio and 113.8 ± 1.1 mV for APA (n = 9, mean ± SEM). Previous studies using hiPSC-CMs have demonstrated that ventricular-type cells exhibit certain characteristics, including a plateau phase, $APD_{90} > 150$ ms, and APD_{90}/APD_{50} ratio of 1.07~1.31 (Peng et al., 2010; Honda et al., 2011). The AP waveforms and parameters in our research were consistent with those reported in previous studies. For the analysis and pharmacological testing, only ventricular-type cells were included. The effects of the drugs on AP parameters were normalized with respect to the control value within each individual cell. These normalized values were then presented as bar graphs, depicting the changes in AP shape induced by the drugs. Pyronaridine was tested at four different concentrations, considering its unbound concentration. Applying 1,320 nM pyronaridine induced significant changes in APs; APD_{50} and APD_{90} increased by 16.07% and 22.34%, respectively, compared to the control (n = 3) (Figure 9). Additionally, pyronaridine significantly decreased the APA of hiPSC-CMs in a concentration-dependent manner. There were no significant changes in the Vmax or MDP with pyronaridine. Artesunate was tested at four different concentrations considering the C_{max}. As shown in Figure 10, artesunate did not significantly alter the cardiac APs of hiPSC-CMs ($n = 3$). DHA was tested at four different concentrations considering the C_{max}. As shown Figure 11, DHA significantly prolonged the APD_{50} of hiPSC-CMs at 4,200 and 126,000 nM by 10.26% and 13.83%, respectively. Additionally, DHA induced significant changes in APD_{90} at 4,200, 42,000, 126,000, and 420,000 nM by 7.88, 8.02, 10.74, and 10.16%, respectively. However, it did not significant changes in the Vmax, MDP, or APA. Additionally, the mixture was tested at four different concentrations considering the unbound concentration. It significantly prolonged the APD_{50} of hiPSC-CMs at Conc.2, 3, and 4 by 2.99, 7.56, and 8.32%, respectively, but did not change any other AP parameters (MDP, Vmax, APA, or APD_{90}) (Figure 12).

4 Discussion

In our study, we utilized the CiPA initiative, a novel approach for assessing the proarrhythmic risk of drugs, to evaluate the cardiotoxicity of pyronaridine and artesunate, which were repurposed for COVID-19 treatment during the pandemic. Antimalarial drugs are frequently combined with other drugs to increase their efficacy, reduce the risk of resistant parasites, and shorten the duration of malaria treatment (Kremsner and Krishna,

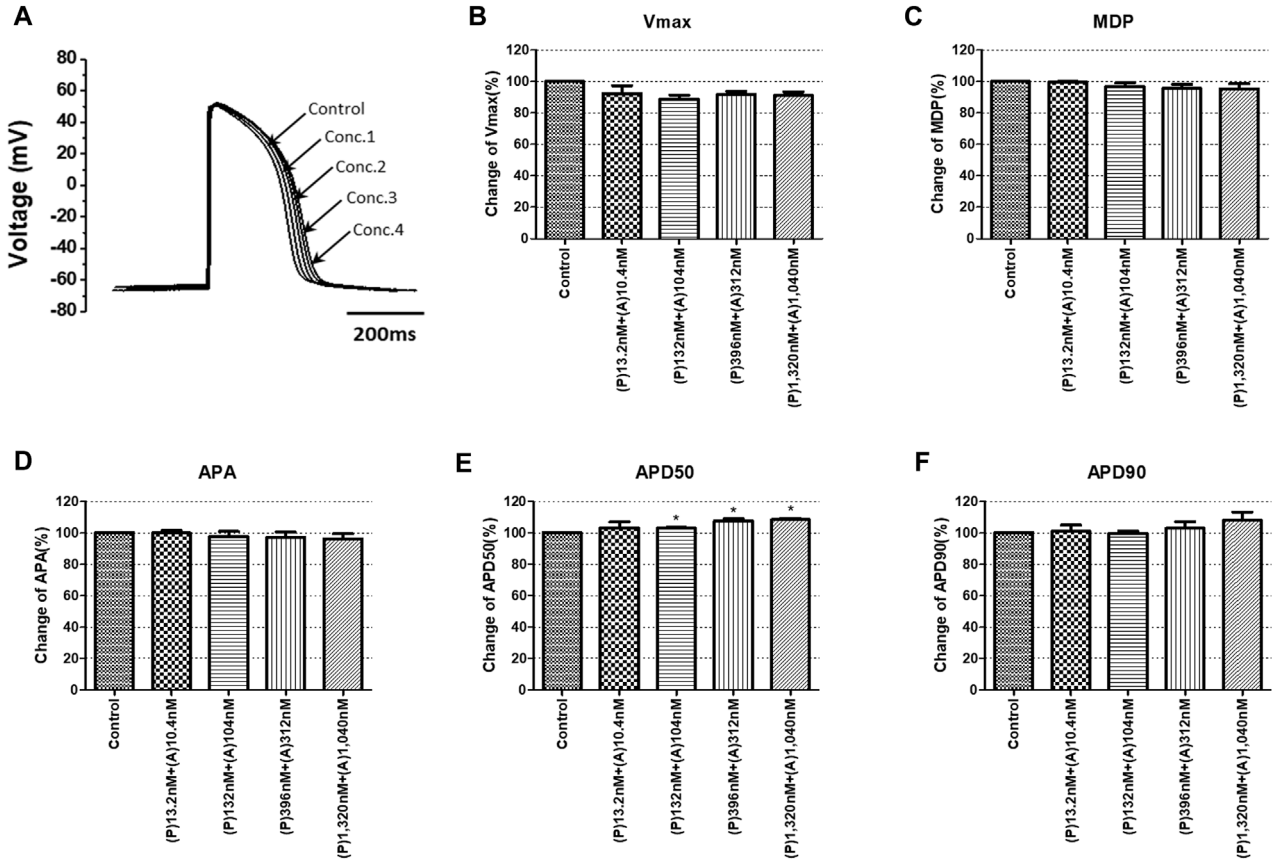

FIGURE 12
Effects of the mixture on action potential (AP) parameters of hiPSC-CMs. **(A)** Typical AP traces of hiPSC-CMs in the control and after exposure to 13.2, 132, 396, and 1,320 nM pyronaridine and 10.4, 104, 312, and 1,040 nM artesunate. **(B–F)** Bar graphs illustrating mean normalized values for AP parameters of hiPSC-CMs, including MDP, maximal diastolic potential; APA, AP amplitude; Vmax, maximum rate of depolarization during the upstroke of the AP; APD_{50} and APD_{90}, AP duration at 50% and 90%. Data are presented as mean ± standard error of the mean (SEM) and analyzed using Student's t-test. $*p < 0.05$, $**p < 0.01$ or $***p < 0.001$ compared to control ($n = 3$). P, pyronaridine; A, artesunate.

2004). Among the various antimalarial drug combination therapies, artemisinin-based combination treatments (ACTs) are generally considered the most effective, offering high therapeutic efficacy and real-life safety against malaria (Dini et al., 2018). ACTs consist of an artemisinin derivative paired with a partner drug, such as pyronaridine-artesunate. It has been reported that the combination of pyronaridine and artesunate exhibits a stronger antiviral effect (Nosten and White, 2007; Kurth et al., 2011; Lane et al., 2019). These drugs have been repurposed for COVID-19 treatment, making it crucial to evaluate their cardiovascular adverse reactions, and drug-induced cardiotoxicity. The CiPA initiative proves to be an ideal method for evaluating cardiac safety during drug screening. In our study, we evaluated the drug-induced effects on cardiac arrhythmia for each drug individually and in combination, employing the CiPA initiative. Artesunate was evaluated at four different concentrations considering the C_{max} and was classified as having a low risk of inducing TdP (Figure 8B). Moreover, it had no significant impact on the cardiac APs of hiPSC-CMs (Figure 10). According to Lakhan et al. (2013), intravenous administration of artesunate did not affect the QTc interval, and no significant cardiovascular effects were observed in patients with *falciparum* malaria. Another study found that intravenous artesunate did not prolong the QT interval, even at high doses (Maude et al., 2009). DHA is the active metabolite of artemisinin compounds (e.g., artemotil, artesunate, artemether) (Woo et al., 1998). DHA was classified as a low TdP risk (Figure 8B). It significantly inhibited cardiac ion channels, but modestly prolonged at APD_{90} (10.16%) at 100 times the C_{max}. According to Borsini et al. (2012), the IC_{50} on hERG current at 0.1 Hz for DHA is 7.7 ± 0.9 μM; however, it did not significantly prolong the APD_{90}. Compared to our research, DHA appears that it significantly interacts with other cardiac ion channels. Furthermore, there have been no adverse cardiovascular effects reported in malaria patients treated with these drugs in clinical trials (White, 2007). Hence, artesunate and DHA have little cardiotoxicity, as indicated in previous reports.

We investigated and compared the effects of pyronaridine and the combination of both drugs on cardiac ion channels and APs at various concentrations based on the C_{max} and unbound concentration. Drugs can bind partially to various plasma or tissue proteins, and typically, it is the unbound (free) fraction of the drug that exerts pharmacological effects (Cervelli and Russ, 2010). Conversely, some drugs tend to accumulate in the myocardium and cells, prolonging their drug action (Tylutki and

Polak, 2015). The heart serves as a central pharmacokinetic compartment that is easily accessible to drugs and can also be a site for their side effects (The European Medicines Agency, 2012). Therefore, it is essential to assess drugs at various concentrations, including the free fractions and higher active concentrations. As shown in Figure 8, pyronaridine and its mixtures evaluated based on C_{max} were classified as having intermediate TdP risk. However, when considering unbound concentrations, were classified as having a low risk of inducing TdP. We assessed pyronaridine and mixture at four different concentrations considering the unbound concentration for AP recordings. These significantly inhibited hERG, Nav1.5, and Cav1.2 currents, but remained relatively modest or non-existent effects on APD_{90} in hiPSC-CM (Figures 9, 12). It is expected that multiple interactions with cardiac ion channels. Similarly, verapamil is well-known hERG blocker but does not prolong the QT interval in clinical settings due to its multi-channel effects (Honda et al., 2011). While the potential extrapolation to human is not elucidated, it has been observed that pyronaridine and its metabolites are distributed in high concentrations in the liver, spleen, adrenal gland, kidney, and thyroid gland of rats (The European Medicines Agency, 2012). However, there have been no reports of high concentrations accumulating in the heart. According to the European Medicines Agency (2012), the active concentration of pyronaridine available in the systemic circulation is only 12 ng/mL, as a result of plasma protein or tissue binding. Therefore, when considering electrophysiological recordings, TdP risk prediction using TMS, and pharmacological contexts, it is expected that pyronaridine and the mixture will pose a low proarrhythmogenic risk at supratherapeutic (up to 4 times) free C_{max}.

This study is the first to report the potential cardiotoxicity in electrophysiological terms of pyronaridine and artesunate, which have been repurposed for COVID-19 treatment under the new CiPA initiative (involving multiple ion channel screening, hiPSC-CMs, and a new *in silico* human-based prediction model that has finished the training phase using CiPA 12 training set drugs).

In summary, this study suggests that pyronaridine, artesunate, and their combination, repurposed for COVID-19 treatment, pose a low risk of adverse cardiac events and cardiotoxicity. Furthermore, the utilization of the CiPA initiative in drug safety assessment platforms can help identify potential cardiotoxicity and serve as an alternative to current *in vitro* and *in vivo* systems.

Data availability statement

The original contributions presented in the study are included in the article/Supplementary Material, further inquiries can be directed to the corresponding authors.

Author contributions

All authors listed have made a substantial, direct, and intellectual contribution to the work and approved it for publication.

Funding

This work was supported by a grant (22213MFDS391) from the Ministry of Food and Drug Safety and the Ministry of Trade, Industry and Energy, Republic of Korea (20009748).

Conflict of interest

The authors declare that the research was conducted in the absence of any commercial or financial relationships that could be construed as a potential conflict of interest.

Publisher's note

All claims expressed in this article are solely those of the authors and do not necessarily represent those of their affiliated organizations, or those of the publisher, the editors and the reviewers. Any product that may be evaluated in this article, or claim that may be made by its manufacturer, is not guaranteed or endorsed by the publisher.

References

Authier, S., Pugsley, M. K., Koerner, J. E., Fermini, B., Redfern, W. S., Valentin, J.-P., et al. (2017). Proarrhythmia liability assessment and the comprehensive *in vitro* proarrhythmia assay (CiPA): an industry survey on current practice. *J. Pharmacol. Toxicol. Methods* 86, 34–43. doi:10.1016/j.vascn.2017.02.021

Bae, J.-Y., Lee, G. E., Park, H., Cho, J., Kim, Y.-E., Lee, J.-Y., et al. (2020). Pyronaridine and artesunate are potential antiviral drugs against COVID-19 and influenza, 2020 2007 2028.225102 bioRxiv. doi:10.1101/2020.07.28.225102

Borba, M. G. S., Val, F. F. A., Sampaio, V. S., Alexandre, M. a. A., Melo, G. C., Brito, M., et al. (2020). Effect of high vs low doses of chloroquine diphosphate as adjunctive therapy for patients hospitalized with severe acute respiratory syndrome coronavirus 2 (SARS-CoV-2) infection: a randomized clinical trial. *JAMA Netw. Open.* 3, e208857. doi:10.1001/jamanetworkopen.2020.8857

Borsini, F., Crumb, W., Pace, S., Ubben, D., Wible, B., Yan, G.-X., et al. (2012). *In vitro* cardiovascular effects of dihydroartemisin-piperaquine combination compared with other antimalarials. *Antimicrob. Agents Chemother.* 56, 3261–3270. doi:10.1128/aac.05688-11

Cavero, I., and Crumb, W. (2005). ICH S7B draft guideline on the non-clinical strategy for testing delayed cardiac repolarisation risk of drugs: a critical analysis. *Expert Opin. Drug Saf.* 4, 509–530. doi:10.1517/14740338.4.3.509

Cavero, I., Guillon, J.-M., Ballet, V., Clements, M., Gerbeau, J.-F., and Holzgrefe, H. (2016). Comprehensive *in vitro* proarrhythmia assay (CiPA): pending issues for successful validation and implementation. *J. Pharmacol. Toxicol. Methods* 81, 21–36. doi:10.1016/j.vascn.2016.05.012

Cervelli, M. J., and Russ, G. R. (2010). *Chapter 73–principles of drug therapy, dosing, and prescribing in chronic kidney disease and renal replacement therapy*. Philadelphia: Elsevier.

Chang, K. C., Dutta, S., Mirams, G. R., Beattie, K. A., Sheng, J., Tran, P. N., et al. (2017). Uncertainty quantification reveals the importance of data variability and experimental design considerations for *in silico* proarrhythmia risk assessment. *Front. Physiol.* 8, 917. doi:10.3389/fphys.2017.00917

Chorin, E., Dai, M., Shulman, E., Wadhwani, L., Bar-Cohen, R., Barbhaiya, C., et al. (2020). The QT interval in patients with COVID-19 treated with hydroxychloroquine and azithromycin. *Nat. Med.* 26, 808–809. doi:10.1038/s41591-020-0888-2

Colatsky, T., Fermini, B., Gintant, G., Pierson, J. B., Sager, P., Sekino, Y., et al. (2016). The comprehensive *in vitro* proarrhythmia assay (CiPA) initiative—Update on progress. *J. Pharmacol. Toxicol. Methods* 81, 15–20. doi:10.1016/j.vascn.2016.06.002

Delaunois, A., Abernathy, M., Anderson, W. D., Beattie, K. A., Chaudhary, K. W., Coulot, J., et al. (2021). Applying the CiPA approach to evaluate cardiac proarrhythmia risk of some antimalarials used off-label in the first wave of COVID-19. *Clin. Transl. Sci.* 14, 1133–1146. doi:10.1111/cts.13011

Dini, S., Zaloumis, S., Cao, P., Price, R. N., Fowkes, F. J., Van Der Pluijm, R. W., et al. (2018). Investigating the efficacy of triple artemisinin-based combination therapies for treating Plasmodium falciparum malaria patients using mathematical modeling. *Antimicrob. Agents Chemother.* 62, e01068-18. doi:10.1128/AAC.01068-18

Dutta, S., Chang, K. C., Beattie, K. A., Sheng, J., Tran, P. N., Wu, W. W., et al. (2017). Optimization of an *in silico* cardiac cell model for proarrhythmia risk assessment. *Front. Physiol.* 8, 616. doi:10.3389/fphys.2017.00616

Fermini, B., Hancox, J. C., Abi-Gerges, N., Bridgland-Taylor, M., Chaudhary, K. W., Colatsky, T., et al. (2016). A new perspective in the field of cardiac safety testing through the comprehensive *in vitro* proarrhythmia assay paradigm. *J. Biomol. Screen.* 21, 1–11. doi:10.1177/1087057115594589

Haario, H., Laine, M., Mira, A., and Saksman, E. (2006). Dram: efficient adaptive MCMC. *Statistics Comput.* 16, 339–354. doi:10.1007/s11222-006-9438-0

Honda, M., Kiyokawa, J., Tabo, M., and Inoue, T. (2011). Electrophysiological characterization of cardiomyocytes derived from human induced pluripotent stem cells. *J. Pharmacol. Sci.* 117, 149–159. doi:10.1254/jphs.11038FP

ICH E14/S7B Implementation Working Group (2022). Questions and answers: clinical and nonclinical evaluation of QT/QTc interval prolongation and proarrhythmic potential. Available at: https://database.ich.org/sites/default/files/E14-S7B_QAs_Step4_2022_0221.pdf (Accessed June 27, 2022).

Jeong, D. U., Yoo, Y., Marcellinus, A., Kim, K. S., and Lim, K. M. (2022). Proarrhythmic risk assessment of drugs by d V m/dt shapes using the convolutional neural network. *CPT Pharmacometrics Syst. Pharmacol.* 11, 653–664. doi:10.1002/psp4.12803

Kinoshita, A., Yamada, H., Kotaki, H., and Kimura, M. (2010). Effects of anti-malarial drugs on the electrocardiographic QT interval modelled in the isolated perfused Guinea pig heart system. *Malar. J.* 9, 318. doi:10.1186/1475-2875-9-318

Kremsner, P. G., and Krishna, S. (2004). Antimalarial combinations. *Lancet* 364, 285–294. doi:10.1016/S0140-6736(04)16680-4

Krishna, S., Augustin, Y., Wang, J., Xu, C., Staines, H. M., Platteeuw, H., et al. (2021). Repurposing antimalarials to tackle the COVID-19 pandemic. *Trends Parasitol.* 37, 8–11. doi:10.1016/j.pt.2020.10.003

Kurth, F., Bélard, S., Basra, A., and Ramharter, M. (2011). Pyronaridine–artesunate combination therapy for the treatment of malaria. *Curr. Opin. Infect. Dis.* 24, 564–569. doi:10.1097/QCO.0b013e32834cabdb

Laine, M., and Tamminen, J. (2008). Aerosol model selection and uncertainty modelling by adaptive MCMC technique. *Atmos. Chem. Phys.* 8, 7697–7707. doi:10.5194/acp-8-7697-2008

Lakhan, S., Lalit, J., Hemlata, S., and Prashant, N. (2013). Effect of artesunate on electrocardiographic QT interval in patients with plasmodium falciparum malaria. *Int. J. Physiol.* 1, 156–160. doi:10.5958/j.2320-608X.1.2.033

Lane, T. R., Massey, C., Comer, J. E., Anantpadma, M., Freundlich, J. S., Davey, R. A., et al. (2019). Repurposing the antimalarial pyronaridine tetraphosphate to protect against Ebola virus infection. *PLoS Negl. Trop. Dis.* 13, e0007890. doi:10.1371/journal.pntd.0007890

Li, Z., Ridder, B. J., Han, X., Wu, W. W., Sheng, J., Tran, P. N., et al. (2019). Assessment of an *in silico* mechanistic model for proarrhythmia risk prediction under the CiPA initiative. *Clin. Pharmacol. Ther.* 105, 466–475. doi:10.1002/cpt.1184

Maude, R. J., Plewes, K., Faiz, M. A., Hanson, J., Charunwatthana, P., Lee, S. J., et al. (2009). Does artesunate prolong the electrocardiograph QT interval in patients with severe malaria? *Am. J. Trop. M. Hyg.* 80, 126–132. doi:10.4269/ajtmh.2009.08-0326

Mercuro, N. J., Yen, C. F., Shim, D. J., Maher, T. R., Mccoy, C. M., Zimetbaum, P. J., et al. (2020). Risk of QT interval prolongation associated with use of hydroxychloroquine with or without concomitant azithromycin among hospitalized patients testing positive for coronavirus disease 2019 (COVID-19). *JAMA Cardiol.* 5, 1036–1041. doi:10.1001/jamacardio.2020.1834

Montnach, J., Baro, I., Charpentier, F., De Waard, M., and Loussouarn, G. (2021). Modelling sudden cardiac death risks factors in patients with coronavirus disease of 2019: the hydroxychloroquine and azithromycin case. *EP Eur.* 23, 1124–1133. doi:10.1093/europace/euab043

Nosten, F., and White, N. J. (2007). Artemisinin-based combination treatment of falciparum malaria. *Am. J. Trop. Med. Hyg.* 77, 181–192. doi:10.4269/ajtmh.2007.77.181

O'hara, T., Virág, L., Varró, A., and Rudy, Y. (2011). Simulation of the undiseased human cardiac ventricular action potential: model formulation and experimental validation. *PLoS Comput. Biol.* 7, e1002061. doi:10.1371/journal.pcbi.1002061

Park, J. S., Jeon, J. Y., Yang, J. H., and Kim, M. G. (2019). Introduction to *in silico* model for proarrhythmic risk assessment under the CiPA initiative. *Transl. Clin. Pharmacol.* 27, 12–18. doi:10.12793/tcp.2019.27.1.12

Peng, S., Lacerda, A. E., Kirsch, G. E., Brown, A. M., and Bruening-Wright, A. (2010). The action potential and comparative pharmacology of stem cell-derived human cardiomyocytes. *J. Pharmacol. Toxicol. Methods* 61, 277–286. doi:10.1016/j.vascn.2010.01.014

Rueangweerayut, R., Phyo, A. P., Uthaisin, C., Poravuth, Y., Binh, T. Q., Tinto, H., et al. (2012). Pyronaridine–artesunate versus mefloquine plus artesunate for malaria. *N. Engl. J. Med.* 366, 1298–1309. doi:10.1056/NEJMoa1007125

Sala, L., Leonov, V., Mura, M., Giannetti, F., Khudiakov, A., Moretti, A., et al. (2022). Use of hiPSC-derived cardiomyocytes to rule out proarrhythmic effects of drugs: the case of hydroxychloroquine in COVID-19. *Front. Physiol.* 12, e730127. doi:10.3389/fphys.2021.730127

Serafin, M. B., Bottega, A., Foletto, V. S., Da Rosa, T. F., Hörner, A., and Hörner, R. (2020). Drug repositioning is an alternative for the treatment of coronavirus COVID-19. *Int. J. Antimicrob. Agents* 55, 105969. doi:10.1016/j.ijantimicag.2020.105969

Soetaert, K., and Petzoldt, T. (2010). Inverse modelling, sensitivity and Monte Carlo analysis in R using package FME. *J. Stat. Softw.* 33, 1–28. doi:10.18637/jss.v033.i03

Strauss, D. G., Gintant, G., Li, Z., Wu, W., Blinova, K., Vicente, J., et al. (2019). Comprehensive *in vitro* proarrhythmia assay (CiPA) update from a cardiac safety research consortium/health and environmental sciences institute/FDA meeting. *Ther. Innov. Regul. Sci.* 53, 519–525. doi:10.1177/2168479018795117

Sutanto, H., and Heijman, J. (2020). Beta-adrenergic receptor stimulation modulates the cellular proarrhythmic effects of chloroquine and azithromycin. *Front. Physiol.* 11, 587709. doi:10.3389/fphys.2020.587709

Tebay, C., Mcarthur, J. R., Mangala, M., Kerr, N., Heitmann, S., Perry, M. D., et al. (2022). Pathophysiological metabolic changes associated with disease modify the proarrhythmic risk profile of drugs with potential to prolong repolarisation. *Br. J. Pharmacol.* 179, 2631–2646. doi:10.1111/bph.15757

The European Medicines Agency (2012). Pyramax. Available at: https://www.ema.europa.eu/en/documents/outside-eu-product-information/pyramax-product-information_en.pdf (Accessed Feburary 16, 2012).

The Food and Drug Administration (2020a). Fact sheet for health care providers emergency use authorization (EUA) of hydroxychloroquine sulfate supplied from the strategic national stockpile for treatment of COVID-19 in certain hospitalised patients. Available at: https://www.fda.gov/media/136537/download (Accessed June 15, 2020).

The Food and Drug Administration (2020b). Recommended voltage protocols to study drug-cardiac ion channel interactions using recombinant cell lines. Available at: https://www.fda.gov/media/131157/download (Accessed July 9, 2020).

Thomet, U., Amuzescu, B., Knott, T., Mann, S. A., Mubagwa, K., and Radu, B. M. (2021). Assessment of proarrhythmogenic risk for chloroquine and hydroxychloroquine using the CiPA concept. *Eur. J. Pharmacol.* 913, 174632. doi:10.1016/j.ejphar.2021.174632

Tleyjeh, I. M., Kashour, Z., Aldosary, O., Riaz, M., Tlayjeh, H., Garbati, M. A., et al. (2021). Cardiac toxicity of chloroquine or hydroxychloroquine in patients with COVID-19: a systematic review and meta-regression analysis. *Mayo Clin. Proc. Innov. Qual. Outcomes.* 5, 137–150. doi:10.1016/j.mayocpiqo.2020.10.005

Touret, F., Gilles, M., Barral, K., Nougairède, A., Van Helden, J., Decroly, E., et al. (2020). *In vitro* screening of a FDA approved chemical library reveals potential inhibitors of SARS-CoV-2 replication. *Sci. Rep.* 10, 13093. doi:10.1038/s41598-020-70143-6

Tylutki, Z., and Polak, S. (2015). Plasma vs heart tissue concentration in humans–literature data analysis of drugs distribution. *Biopharm. Drug Dispos.* 36, 337–351. doi:10.1002/bdd.1944

Varshneya, M., Irurzun-Arana, I., Campana, C., Dariolli, R., Gutierrez, A., Pullinger, T. K., et al. (2021). Investigational treatments for COVID-19 may increase ventricular arrhythmia risk through drug interactions. *CPT Pharmacometrics Syst. Pharmacol.* 10, 100–107. doi:10.1002/psp4.12573

Wang, G., Lu, C.-J., Trafford, A. W., Tian, X., Flores, H. M., Maj, P., et al. (2020). Mechanistic insights into ventricular arrhythmogenesis of hydroxychloroquine and azithromycin for the treatment of COVID-19. Biorxiv. doi:10.1101/2020.05.21.108605

White, N. J. (2007). Cardiotoxicity of antimalarial drugs. *Lancet Infect. Dis.* 7, 549–558. doi:10.1016/S1473-3099(07)70187-1

Whittaker, D. G., Capel, R. A., Hendrix, M., Chan, X. H. S., Herring, N., White, N. J., et al. (2021). Cardiac TdP risk stratification modelling of anti-infective compounds including chloroquine and hydroxychloroquine. *R. Soc. Open Sci.* 8, 210235. doi:10.1098/rsos.210235

Woo, S. H., Parker, M. H., Ploypradith, P., Northrop, J., and Posner, G. H. (1998). Direct conversion of pyranose anomeric OH→ F→ R in the artemisinin family of antimalarial trioxanes. *Tetrahedron Lett.* 39, 1533–1536. doi:10.1016/S0040-4039(98)00132-4

Yanagida, S., Satsuka, A., Hayashi, S., Ono, A., and Kanda, Y. (2021). Comprehensive cardiotoxicity assessment of COVID-19 treatments using human-induced pluripotent stem cell-derived cardiomyocytes. *Toxicol. Sci.* 183, 227–239. doi:10.1093/toxsci/kfab079

Yap, Y. G., and Camm, A. J. (2003). Drug induced QT prolongation and torsades de pointes. *Heart* 89, 1363–1372. doi:10.1136/heart.89.11.1363

Yoo, Y., Marcellinus, A., Jeong, D. U., Kim, K.-S., and Lim, K. M. (2021). Assessment of drug Proarrhythmicity using artificial neural networks with *in silico* deterministic model outputs. *Front. Physiol.* 12, e761691. doi:10.3389/fphys.2021.761691

frontiers | Frontiers in Pharmacology

TYPE Systematic Review
PUBLISHED 25 September 2023
DOI 10.3389/fphar.2023.1225288

OPEN ACCESS

EDITED BY
Jorge G. Farias,
University of La Frontera, Chile

REVIEWED BY
Marc Royo,
Penn State Milton S. Hershey Medical Center, United States
Somchai Amornyotin,
Mahidol University, Thailand
Luis Laranjeira,
Eli Lilly, Portugal

*CORRESPONDENCE
Cheuk-Kwan Sun,
researchgate000@gmail.com

†These authors have contributed equally to this work

RECEIVED 19 May 2023
ACCEPTED 15 September 2023
PUBLISHED 25 September 2023

CITATION
Hung K-C, Chen J-Y, Wu S-C, Huang P-Y, Wu J-Y, Liu T-H, Liu C-C, Chen I-W and Sun C-K (2023), A systematic review and meta-analysis comparing the efficacy and safety of ciprofol (HSK3486) versus propofol for anesthetic induction and non-ICU sedation.
Front. Pharmacol. 14:1225288.
doi: 10.3389/fphar.2023.1225288

A systematic review and meta-analysis comparing the efficacy and safety of ciprofol (HSK3486) versus propofol for anesthetic induction and non-ICU sedation

Kuo-Chuan Hung[1,2], Jen-Yin Chen[1,2], Shao-Chun Wu[3], Po-Yu Huang[4], Jheng-Yan Wu[5], Ting-Hui Liu[6], Chien-Cheng Liu[7], I-Wen Chen[8†] and Cheuk-Kwan Sun[9,10*†]

[1]School of Medicine, College of Medicine, National Sun Yat-sen University, Kaohsiung, Taiwan, [2]Department of Anesthesiology, Chi Mei Medical Center, Tainan, Taiwan, [3]Department of Anesthesiology, Kaohsiung Chang Gung Memorial Hospital, Chang Gung University College of Medicine, Kaohsiung, Taiwan, [4]Department of Internal Medicine, Chi Mei Medical Center, Tainan, Taiwan, [5]Department of Nutrition, Chi Mei Medical Center, Tainan, Taiwan, [6]Department of Psychiatry, Chi Mei Medical Center, Tainan, Taiwan, [7]Department of Anesthesiology, E-Da Hospital, I-Shou University, Kaohsiung, Taiwan, [8]Department of Anesthesiology, Chi Mei Medical Center, Liouying, Tainan City, Taiwan, [9]Department of Emergency Medicine, E-Da Dachang Hospital, I-Shou University, Kaohsiung, Taiwan, [10]School of Medicine for International Students, College of Medicine, I-Shou University, Kaohsiung, Taiwan

Background: Ciprofol (HSK3486) is a novel intravenous anesthetic agent that bears structural similarity to propofol and displays favorable pharmacodynamic characteristics such as rapid onset and offset. The meta-analysis aimed at comparing the efficacy and safety of ciprofol versus propofol in clinical practice.

Methods: Medline, EMBASE, Google Scholar, Cochrane Library were searched from inception to April 2023. The primary outcome was success rate of sedation/anesthetic induction and differences in sedation/induction time. The secondary outcomes included risks of hemodynamic instability, respiratory complications, and pain on injection, as well as recovery profiles, satisfaction score, and top-up dose requirement.

Results: Twelve RCTs (sedation: n = 6, anesthetic induction, n = 6, all conducted in China) involving 1,793 patients (age: 34–58 years) published from 2021 to 2023 were analyzed. Pooled results revealed no differences in success rate [risk ratio (RR) = 1, 95% confidence interval (CI): 0.99 to 1.01, I^2 = 0%, 1,106 patients, p = 1] and time required for successful anesthetic induction/sedation [mean difference (MD) = 7.95 s, 95% CI: −1.09 to 16.99, I^2 = 97%, 1,594 patients, p = 0.08]. The risks of top-up dose requirement (RR = 0.94, p = 0.48), cardiopulmonary complications [i.e., bradycardia (RR = 0.94, p = 0.67), tachycardia (RR = 0.83, p = 0.68), hypertension (RR = 1.28, p = 0.2), hypoxemia/pulmonary depression (RR = 0.78, p = 0.24)], and postoperative nausea/vomiting (RR = 0.85, p = 0.72), as well as discharge time (MD = 1.39 min, p = 0.14) and satisfaction score (standardized MD = 0.23, p = 0.16) did not differ significantly between the two groups. However, the ciprofol group had lower risks of hypotension (RR = 0.85, p = 0.02) and pain on injection (RR = 0.17, p < 0.00001) than the propofol group. The time to full alertness

was statistically shorter in the propofol group (i.e., 0.66 min), but without clinical significance.

Conclusion: Our results demonstrated similar efficacy between ciprofol and propofol for sedation and anesthetic induction, while ciprofol was associated with lower risks of hypotension and pain on injection. Future studies are warranted to evaluate the efficacy and safety of ciprofol in pediatric or the elderly populations.

Systematic Review Registration: (https://www.crd.york.ac.uk/prospero/), identifier (CRD42023421278).

KEYWORDS

ciprofol, meta-analysis, sedation, anesthetic induction, propofol

1 Introduction

Propofol, which is a potent intravenous hypnotic agent, is commonly used for anesthetic induction because of its rapid onset of action, a relatively low incidence of pharyngeal morbidity, as well as the ease of administering and monitoring (Joo and Perks, 2000; Chen et al., 2021). In addition, propofol is often the sedative agent of choice for painful diagnostic procedures (e.g., colonoscopy) where patients need to be cooperative with minimal movement. Propofol is particularly useful in outpatient settings due to its ability to achieve a fast recovery with a low risk of postoperative nausea/vomiting (PONV) (Abad-Santos et al., 2003; Sahinovic et al., 2018; Zhang et al., 2018; Dong et al., 2023). Propofol primarily exerts its pharmacological effects by activating the gamma-aminobutyric acid (GABAA)-receptor subunit β1, which in turn increases inhibitory synaptic transmission through the chloride channels, leading to anesthesia and sedation (Hansen, 2015). Despite the known clinical benefits, the use of propofol may be associated with cardiopulmonary depression in a dose-dependent manner, which can result in adverse events such as hypotension, bradycardia, and apnea (Coté et al., 2010; Sneyd et al., 2022). In the anesthesia setting, a previous study of 42,825 patients who underwent elective non-cardiac surgery found a significant correlation between post-induction hypotension and the risk of acute kidney injury (Maheshwari et al., 2018), highlighting the safety concern about propofol use. Besides, propofol administration is associated with injection pain (Euasobhon et al., 2016). These drawbacks have prompted the search for alternative anesthetic agents that can provide similar efficacy without compromising patient safety and comfort.

Ciprofol (HSK3486) is a novel intravenous anesthetic agent that bears structural similarity to propofol and displays favorable pharmacodynamic characteristics such as rapid onset and offset (Qin et al., 2017; Bian et al., 2021). Clinical studies have compared the efficacy and safety of ciprofol with those of propofol in patients receiving various elective surgery or sedative procedures (e.g., gastrointestinal endoscopy) (Teng et al., 2021; Chen et al., 2022a; Luo et al., 2022; Wu et al., 2022; Liang et al., 2023). Some studies reported no difference in success rate or time required for anesthetic induction/sedation between ciprofol and propofol, while ciprofol seems to have a more stable hemodynamic profile and a lower incidence of adverse events (Chen et al., 2022a; Wu et al., 2022). Despite the promising findings from previous clinical studies, the efficacy and safety of ciprofol in clinical practice have yet to be fully established due to the absence of large-scale randomized controlled trials (RCTs). The current meta-analysis aimed at assessing the efficacy and safety of ciprofol relative to propofol by combining the results of various studies. Moreover, the present investigation attempted to identify the probable origins of heterogeneity and inconsistencies across different studies to provide more accurate evaluations of the treatment outcomes.

2 Methods

The protocol for the present meta-analysis was officially registered on PROSPERO (CRD42023421278). The report of this meta-analysis adhered to the PRISMA (Preferred Reporting Items for Systematic Reviews and Meta-Analyses) criteria.

2.1 Data source and literature searches

Two investigators, working independently, systematically conducted a comprehensive literature search in databases including MEDLINE, EMBASE, Cochrane Library, and the Google Scholar. The search was performed from the inception of these databases up to 26 April 2023 with a specific focus being placed on articles that compared the efficacy and safety of ciprofol with those of propofol in patients receiving sedation or anesthetic induction. The search terms included: ("Sedation" or "Sedative" or "Deep sedation" or "procedural sedation" or "depression of consciousness" or "sedative" or "Conscious sedation" or "Moderate sedation" or "General anesthesia*" or "Anesthesia*" or "tracheal intubation" or "laryngeal mask airway" or "anesthetic induction") and ("HSK3486"or "ciprofol"). To ensure an exhaustive search, a combination of controlled vocabulary and synonyms was employed, with no limitations on language or publication date. The search strategy for one of the databases, MEDLINE, is detailed in Supplemental Table S1. Furthermore, to identify potential additional references meeting the inclusion criteria, the investigators meticulously scrutinized the reference lists of all included studies and those of relevant reviews.

2.2 Eligibility criteria

The inclusion criteria used were as follows: (a) Population: individuals aged 18 years or above receiving surgeries or procedures under general anesthesia or sedation; (b) Intervention: the administration of ciprofol, either as a standalone agent or in combination with opioids, for the purpose of sedation or anesthetic

induction; (c) Comparator: the use of propofol with or without opioid for sedation or anesthetic induction; (d) Outcomes: availability of details on the success rate of sedation/anesthetic induction, risk of hemodynamic instability, recovery profiles, or adverse events; and (e) Type of study: only RCTs were included.

The exclusion criteria were 1) studies that focused on patients in the intensive care unit (ICU) setting; 2) studies that had no control group (i.e., propofol not used); 3) pharmacokinetics studies; 4) number of patients in each group less than 20. The cutoff of <20 patients per group was chosen based on recommendations that RCT arms should have at least 20 subjects to ensure adequate statistical power (Julious, 2005); and 5) articles presented as reviews, case reports, conference abstracts, non-peer-reviewed articles, or letters. In cases where studies reported multiple subgroups with varying sample sizes, we only included arms with >20 patients and did not extract data from arms with <20 patients. Importantly, we did not exclude full studies from eligibility just because they had some smaller arms, as long as they also had arms with sufficient sample sizes that could be analyzed.

2.3 Studies selection and data extraction

The titles and/or abstracts of studies were screened separately by two reviewers to identify studies that potentially meet the predefined inclusion criteria, the full text of which were retrieved and independently assessed for eligibility by the two reviewers. Any disagreement on study eligibility between the two reviewers was settled by a discussion that may involve a third reviewer if necessary.

Relevant information, including the clinical setting (i.e., sedation or anesthetic induction), first author' name, publication year, patient characteristics (e.g., gender), sample size, American Society of Anesthesiologists (ASA) physical status, episodes of hemodynamic instability (e.g., bradycardia), respiratory complications (i.e., hypoxemia and respiratory depression), recovery profiles (e.g., time to full alertness and satisfaction score), pain on injection, top-up dose requirement, type of surgery/procedure, dosage of study drugs, and country of publication, was systematically extracted. In cases of disagreement, a discussion was conducted to reach a consensus.

2.4 Outcomes and definitions

The dual primary outcomes were the success rate of sedation/anesthetic induction as well as the differences in sedation/induction time. Secondary outcomes included the risk of hemodynamic instability (e.g., hypotension), respiratory complications, recovery profiles (e.g., time to full alertness, risk of PONV, discharge time, satisfaction score), pain on injection, and top-up dose requirement. The definition and criteria used for each outcome was based on the definitions provided in the individual studies, rather than imposing a single standardized definition across all studies. For the current study, discharge time referred to the time from the end of procedures or/and the last instance of drug administration up until the fulfilment of discharge criteria according to the definition of individual studies.

2.5 Risk of bias and certainty of evidence

In accordance with the revised Cochrane risk of bias tool for randomized trials (RoB 2.0 tool) (Sterne et al., 2019), two reviewers conducted an independent assessment of the risk of bias for the included studies. Disagreements pertaining to the RoB assessment were resolved by a third reviewer. The quality of the included trials was categorized into three levels: "low risk of bias," "some concerns," and "high risk of bias," based on six domains including the randomization process, deviations from the intended interventions, missing outcome data, measurement of the outcome, selective reporting of results, as well as the overall risk of bias.

The evaluation of the certainty of evidence was performed independently by the same two reviewers based on five criteria, namely, the risk of bias, inconsistency, indirectness, imprecision, and publication bias. In the event of disagreements, a third reviewer intervened to reach a final decision.

2.6 Strategy for data synthesis

The data was analyzed using the random-effects model to determine the pooled risk ratio (RR), mean difference (MD), or standardized mean difference (SMD). Additionally, the 95% confidence interval (CI) was reported for each outcome. To assess heterogeneity for each outcome, I^2 statistics values of 50% or higher were deemed indicative of substantial heterogeneity as previously reported (Hung et al., 2022). Sensitivity analysis was employed to determine the reliability of primary and secondary outcomes through a leave-one-out approach. Potential publication bias was evaluated for outcomes reported in 10 or more studies/dataset using visual analysis of a funnel plot. Subgroup analysis was performed based on the clinical setting (i.e., sedation or anesthetic induction). Statistical analyses were performed using Review Manager (RevMan) or comprehensive Meta-Analysis (CMA) V3 software (Biostat, Englewood, NJ, United States). Statistical significance was set at a probability value (p) of less than 0.05.

3 Results

3.1 Study selection

The literature search and selection process involving multiple databases, including Medline, Embase, Cochrane library, and the Google Scholar, resulted in the identification of a total of 153 records (Figure 1). After removing 39 duplicates, screening of the title and abstract of the remaining 114 records led to further exclusion of 88 articles. The full texts of the remaining 26 articles were assessed for eligibility, of which 14 were excluded due to: lack of a control group (2 studies), patients did not undergo any procedure or surgery (1 study), being pharmacokinetics studies (4 studies), conducted in

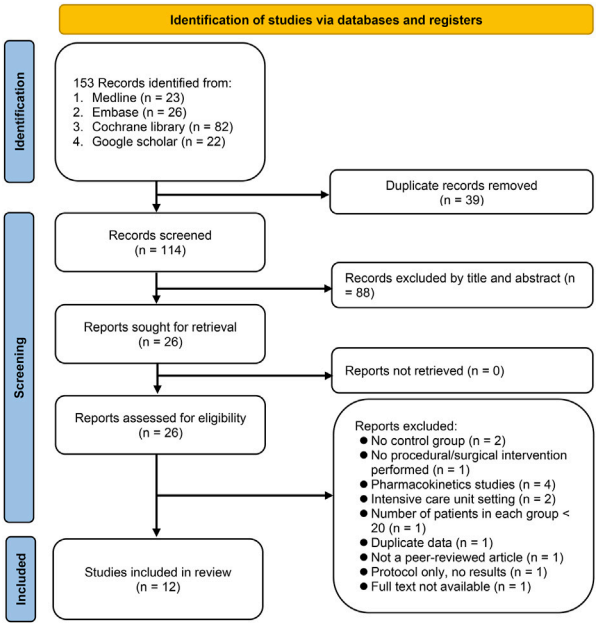

FIGURE 1
From a search across Medline, Embase, Cochrane library, and Google Scholar, 153 records were identified. After deduplication and preliminary screening, 88 of 114 articles were excluded. Of the 26 articles assessed in full, 14 were excluded for reasons including lack of control group, non-surgical patients, being pharmacokinetic studies, intensive care unit (ICU) setting, or having small sample sizes. Four more were excluded for duplicate data, being non-peer-reviewed, being only protocols, or unavailable full texts.

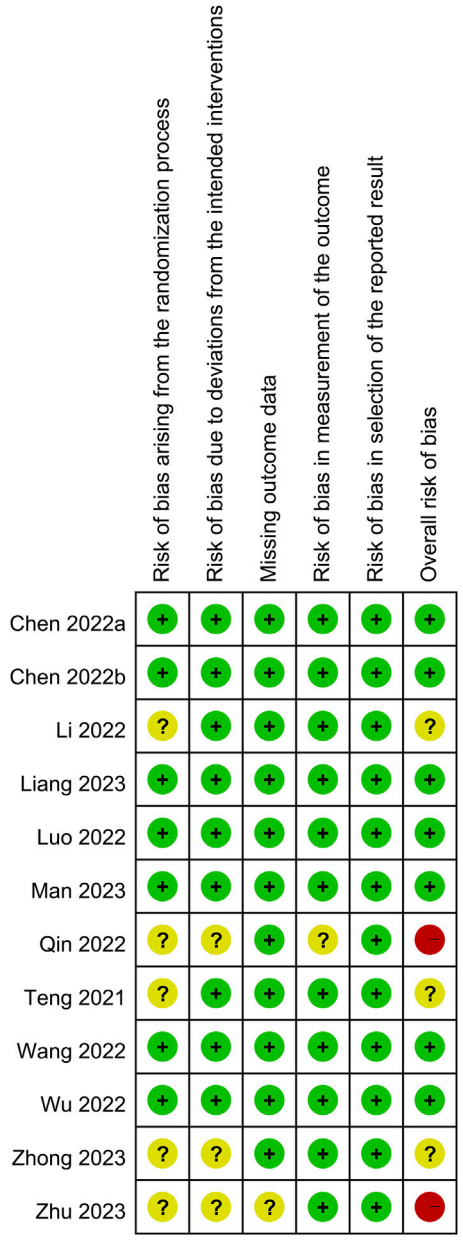

FIGURE 2
Risks of bias of the included randomized controlled trial. Seven randomized controlled trials (RCTs) were regarded as having a low overall risk of bias. In contrast, three RCTs raised concerns in some domains such as the risk of bias arising from the randomization process, which led to some concerns in the overall risk of bias. Notably, two RCTs were deemed to have a high overall risk of bias. Green indicates low risk of bias; yellow indicates some concerns or uncertain risk of bias; red indicates high risk of bias.

an ICU setting (2 studies), and having fewer than 20 patients per group (1 study). An additional 4 studies were excluded for other reasons including duplicate data (1 study), non-peer-reviewed study (1 study), only a protocol (1 study), or full text not available (1 study). Finally, a total of 12 RCTs published between 2021 and 2023 were included in the current meta-analysis (Teng et al., 2021; Chen et al., 2022a; Chen et al., 2022b; Li et al., 2022; Luo et al., 2022; Qin et al., 2022; Wang et al., 2022; Wu et al., 2022; Liang et al., 2023; Man et al., 2023; Zhong et al., 2023; Zhu et al., 2023).

3.2 Characteristics and quality of studies

All twelve studies were conducted in China with the inclusion of a total of 1793 participants. Among the 12 RCTs, six employed ciprofol as a sedative for diverse procedures, including gastrointestinal (GI) endoscopy (n = 3) (Teng et al., 2021; Chen et al., 2022b; Li et al., 2022), fiberoptic bronchoscopy (n = 2) (Luo et al., 2022; Wu et al., 2022), and mixed procedures (GI endoscopy or fiberoptic bronchoscopy) (n = 1) (Zhong et al., 2023). The other six RCTs evaluated the efficacy of ciprofol as an induction agent in gynecological surgery (n = 2) (Chen et al., 2022a; Man et al., 2023), elective surgery (n = 3) (Wang et al., 2022; Liang et al., 2023; Zhu et al., 2023), and kidney transplantation (n = 1) (Qin et al., 2022). Of these six studies, three also use ciprofol as an agent for anesthetic maintenance (Qin et al., 2022; Liang et al., 2023; Man et al., 2023). The mean or median age of the participants ranged from 34 to 58 years. The male percentage varied from 0% to 54.3% with two studies focusing on female patients receiving gynecological surgery (Chen et al., 2022a; Man et al., 2023). The ASA physical status classification varied from I to IV with ASA II being the most common. Nine studies included patients with ASA I-II (Teng et al., 2021; Chen et al., 2022a; Chen et al., 2022b; Li et al., 2022; Wang et al., 2022; Wu et al., 2022; Liang et al., 2023;

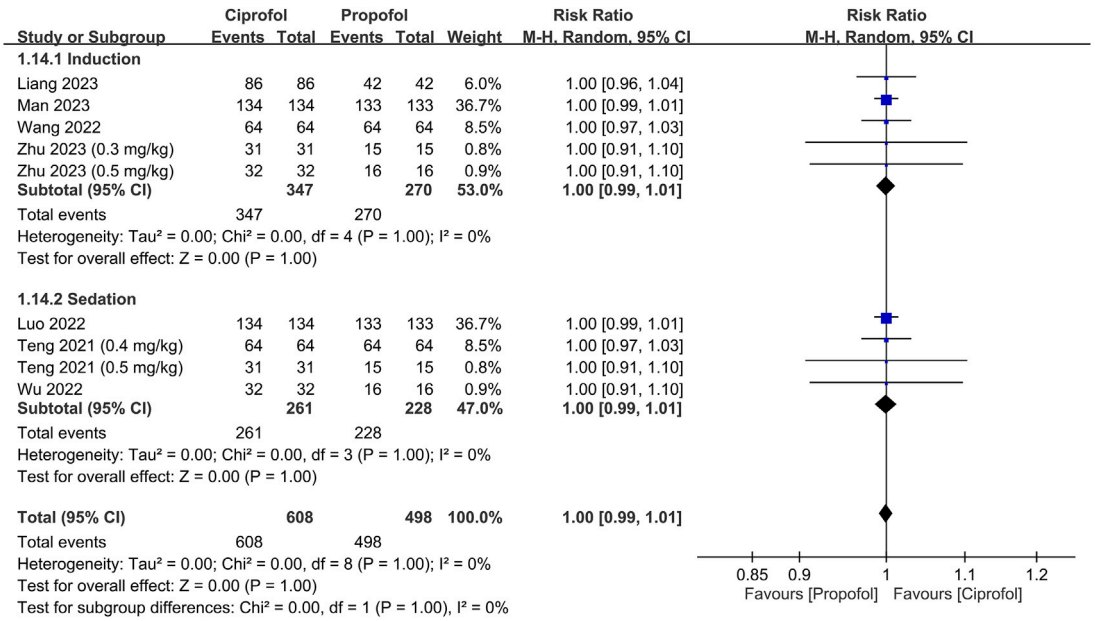

FIGURE 3
Forest plot comparing the success rate between the ciprofol and propofol groups. M-H, Mantel-Haenszel; CI, confidence interval.

Man et al., 2023; Zhu et al., 2023), while two studies recruited patients with ASA I-III (Luo et al., 2022; Zhong et al., 2023). In contrast, one study only enrolled high-risk patients (i.e., ASA III-IV) undergoing kidney transplantation (Qin et al., 2022).

Among the 12 RCTs, three employed a three-arm study design to compare the efficacy of different dosages of ciprofol with propofol (Teng et al., 2021; Zhong et al., 2023; Zhu et al., 2023). The dosage of ciprofol and propofol employed in the studies varied widely. For sedation or anesthetic induction, the dosage of ciprofol ranged from 0.3 to 0.5 mg/kg in 10 studies (Teng et al., 2021; Chen et al., 2022a; Li et al., 2022; Luo et al., 2022; Qin et al., 2022; Wang et al., 2022; Wu et al., 2022; Liang et al., 2023; Man et al., 2023; Zhu et al., 2023), whereas one study implemented dosages of 6 and 8 mg/kg/h for sedation (Zhong et al., 2023). However, one study did not provide relevant information regarding ciprofol dosage (Chen et al., 2022b). On the other hand, the dosage of propofol ranged from 1.2 to 2.0 mg/kg for sedation or anesthetic induction in 11 studies (Teng et al., 2021; Chen et al., 2022a; Chen et al., 2022b; Li et al., 2022; Luo et al., 2022; Qin et al., 2022; Wang et al., 2022; Wu et al., 2022; Liang et al., 2023; Man et al., 2023; Zhu et al., 2023) with one study utilizing a dosage of 40 mg/kg/h for sedation (Zhong et al., 2023).

The results of an overall evaluation of all domains of bias for the 12 RCTs are summarized in Figure 2. Seven RCTs were regarded as having a low overall risk of bias (Chen et al., 2022a; Chen et al., 2022b; Luo et al., 2022; Wang et al., 2022; Wu et al., 2022; Liang et al., 2023; Man et al., 2023), indicating well-conducted studies with reliable results. In contrast, three RCTs (Teng et al., 2021; Li et al., 2022; Zhong et al., 2023) raised concerns in some domains such as the risk of bias arising from the randomization process, which led to some concerns in the overall risk of bias. Notably, two RCTs (Qin et al., 2022; Zhu et al., 2023) were deemed to have a high overall risk of bias, highlighting significant concerns regarding the validity and reliability of the findings.

3.3 Outcomes

3.3.1 Primary outcomes: success rate and time required for successful anesthetic induction/sedation

The success rate and time required for successful anesthetic induction/sedation are shown in Figures 3, 4, respectively. There were no differences in the success rate (RR = 1, 95% CI: 0.99 to 1.01, I^2 = 0%, p = 1.0, 1,106 patients, sensitivity analysis: consistent) (Teng et al., 2021; Luo et al., 2022; Wang et al., 2022; Wu et al., 2022; Liang et al., 2023; Man et al., 2023; Zhu et al., 2023) and time required for successful anesthetic induction/sedation (MD = 7.95 s, 95% CI: −1.09 to 16.99, I^2 = 97%, p = 0.08, 1,594 patients) (Chen et al., 2022a; Chen et al., 2022b; Li et al., 2022; Luo et al., 2022; Wang et al., 2022; Wu et al., 2022; Liang et al., 2023; Man et al., 2023; Zhong et al., 2023; Zhu et al., 2023) between the ciprofol and propofol groups. Sensitivity analysis revealed a shorter time to achieve anesthetic induction/sedation with the use of propofol than that with ciprofol when one study was removed (Luo et al., 2022). Similarly, subgroup analysis based on the clinical setting (i.e., sedation or anesthetic induction) demonstrated no difference in success rate or time for successful anesthetic induction/sedation between the two groups. The levels of certainty on the success rate and time required for successful anesthetic induction/sedation were evaluated as high and moderate, respectively.

3.3.2 Secondary outcomes: top-up doses required, risk of adverse event, and recovery parameters

The risks of top-up dose requirement, cardiopulmonary complications, and pain on injection, as well as recovery parameters between the ciprofol and propofol groups are summarized in Table 2. There were no differences in the risks of top-up dose requirement (RR = 0.94, 95% CI: 0.80 to 1.11, p = 0.48) (Figure 5), bradycardia (RR = 0.94, 95% CI: 0.73 to 1.23, p = 0.67)

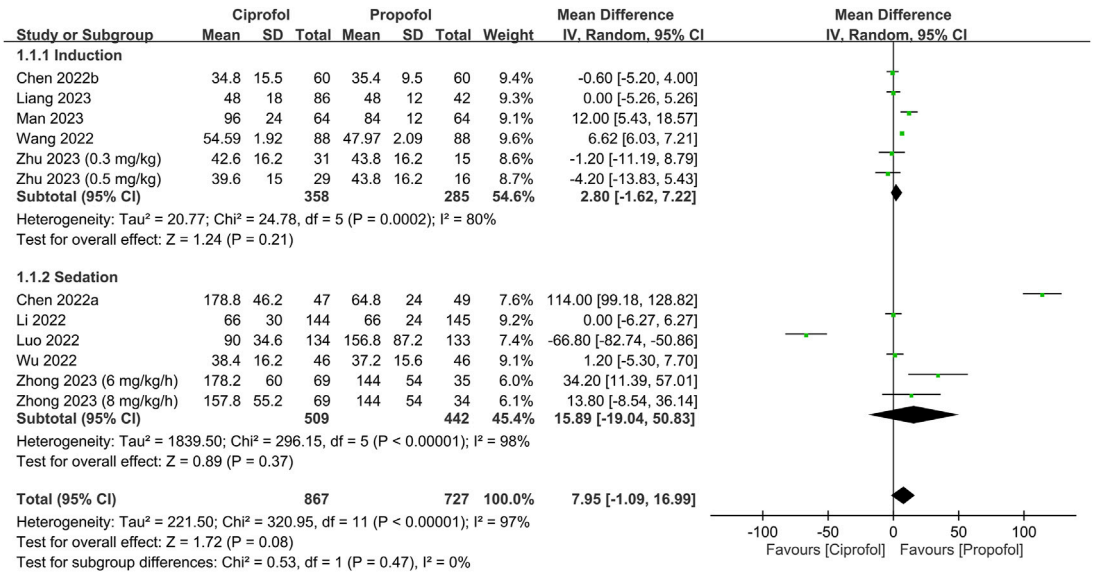

FIGURE 4
Forest plot showing the difference in time required for anesthetic induction/sedation between the ciprofol and propofol groups. IV, inverse variance; CI, confidence interval.

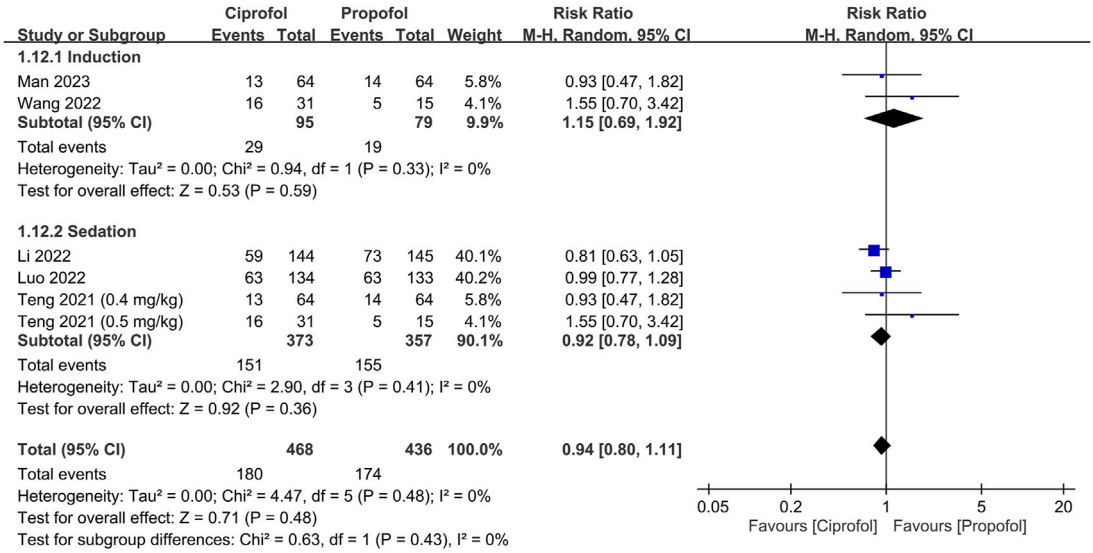

FIGURE 5
Forest plot comparing the risk of top-up dose requirement between the ciprofol and propofol groups. M-H, Mantel-Haenszel; CI, confidence interval.

(Supplementary Figure S1), tachycardia (RR = 0.83, 95% CI: 0.34 to 2.04, $p = 0.68$) (Supplementary Figure S2), hypertension (RR = 1.28, 95% CI: 0.88 to 1.86, $p = 0.2$) (Supplementary Figure S3), pulmonary complications (RR = 0.78, 95% CI: 0.51 to 1.19, $p = 0.24$) (Supplementary Figure S4), and PONV (RR = 0.85, 95% CI: 0.35 to 2.06, $p = 0.72$) (Supplementary Figure S5), as well as discharge time (MD = 1.39 min, 95% CI: −0.45 to 3.22, $p = 0.14$) (Supplementary Figure S6) and satisfaction score (SMD = 0.23, 95% CI:−0.10 to 0.56, $p = 0.16$) (Supplementary Figure S7) between the two groups. In contrast, the risks of hypotension (RR = 0.85, 95% CI: 0.73 to 0.98, $p = 0.02$) (Figure 6) and pain on injection (RR = 0.17, 95% CI: 0.11 to 0.27, $p < 0.00001$) (Figure 7) were lower in the ciprofol group compared to those in the propofol group. The time to full alertness was statistically shorter by a clinically non-significant 0.66 min (95% CI: 0.14 to 1.18, $p = 0.01$) (Supplementary Figure S8) in patients being given propofol than those receiving ciprofol.

The results of sensitivity analysis showed a wide variation with regard to the risk of hypotension, time to full alertness, discharge

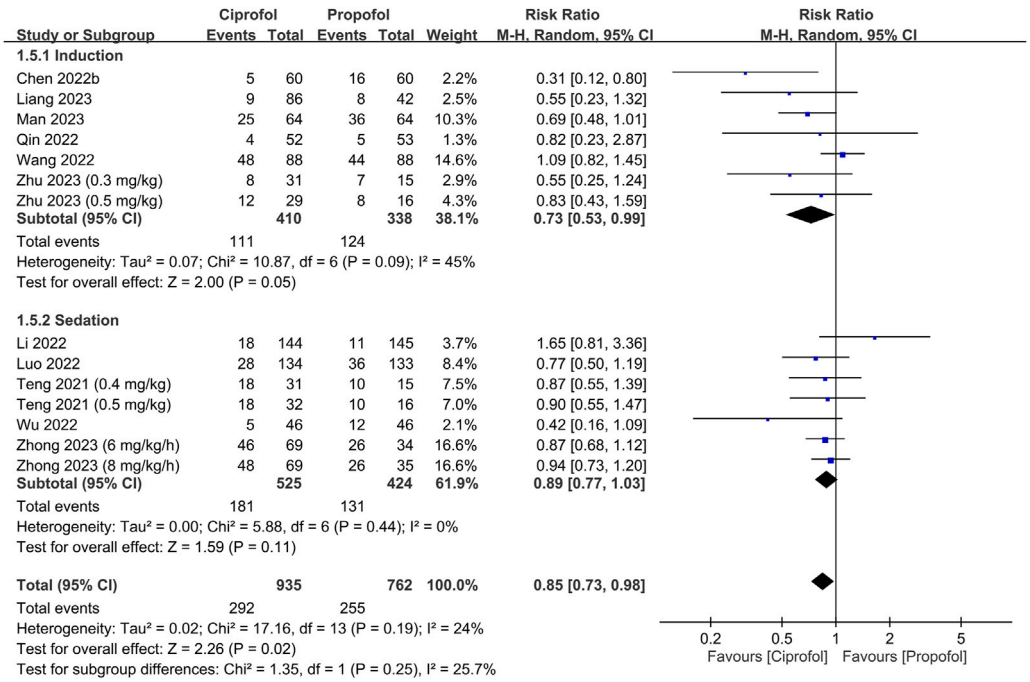

FIGURE 6
Forest plot comparing the risk of hypotension between the ciprofol and propofol groups. M-H, Mantel-Haenszel; CI, confidence interval.

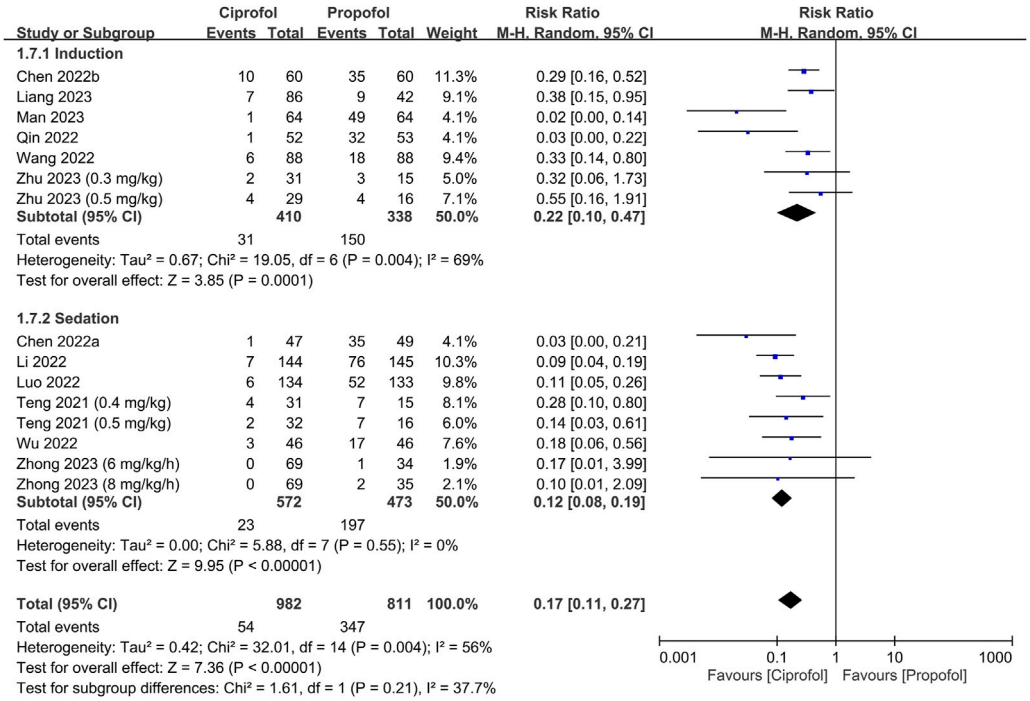

FIGURE 7
Forest plot comparing the risk of pain on injection between the ciprofol and propofol groups. M-H, Mantel-Haenszel; CI, confidence interval.

time, and satisfaction score, suggesting a lack of consistency. Conversely, sensitivity analysis of other outcomes demonstrated consistent findings.

Table 1 presents a summary of the certainty of evidence pertaining to different outcomes of the current study. Notably, a high level of certainty was assigned to the outcomes on the risks of

TABLE 1 Study characteristics.

	Clinical setting	Mean or median age (years)	N	Male (%)	ASA I/II/III/IV	Procedures	Ciprofol (mg/kg)	Propofol (mg/kg)	Country
Chen et al., 2022a	Sedation	41 vs. 43	96	40.6	86/10/0/0	GI scopy	NA	1.5~2	China
Chen et al., 2022b	AI	34 vs. 34	120	0	66/54/0/0	GYN surgery	0.4	2	China
Li et al., 2022	Sedation	44 vs. 44	289	40.8	233/56/0/0	GI scopy	0.4	1.5	China
Liang et al., 2023	AI	39 vs. 41	128	25.8	70/58/0/0	Elective surgery	0.4	2	China
							0.8 mg/kg/h	5 mg/kg/h	
Luo et al., 2022	Sedation	47 vs. 47	267	50.6	113/150/4/0	FB	0.4	2	China
Man et al., 2023	AI	42 vs. 44	128	0	32/96/0/0	GYN surgery	0.5	2	China
Qin et al., 2022	AI	39 vs. 41	105	34.3	0/0/86/19	KT	0.4	2.0	China
Teng et al., 2021	Sedation	46 vs. 48 vs. 48	94	44.7	75/19/0/0	GI scopy	0.4; 0.5	2.0	China
Wang et al., 2022	AI	39 vs. 41	176	35.8	99/77/0/0	Elective surgery	0.4	2.0	China
Wu et al., 2022	Sedation	58 vs. 57	92	54.3	18/74/0/0	FB	0.3	1.2	China
Zhong et al., 2023	Sedation	57 vs. 58 vs. 57	207	53.6	38/150/19/0	GI scopy/FB	6 mg/kg/h; 8 mg/kg/h	40 mg/kg/h	China
Zhu et al., 2023	AI	45 vs. 47 vs. 45	91	50.5	38/53/0/0	Elective surgery	0.3; 0.5	2	China

AI, anesthetic induction; FB, fiberoptic bronchoscopy; KT, kidney transplantation; GYN, surgery, Gynecological surgery; GI, gastrointestinal; ASA, American society of anesthesiologists; NA, not available.

top-up dose requirement, bradycardia, hypertension, and pain on injection. Conversely, the certainty of evidence for outcomes such as tachycardia, hypotension, hypoxemia, time to full alertness, and PONV was considered moderate. In contrast, the certainty of evidence was deemed low for discharge time and satisfaction score.

4 Discussion

This meta-analysis, which included 12 RCTs published from 2021 to 2023, found no significant differences in success rate and time for anesthetic induction/sedation between the ciprofol and propofol groups. Similarly, the risks of top-up dose requirement, cardiopulmonary complications (i.e., bradycardia, tachycardia, hypertension, hypoxemia/pulmonary depression), and PONV, as well as discharge time and satisfaction score did not differ significantly between the two groups. However, the ciprofol group had lower risks of hypotension and pain on injection than the propofol group. Although the time to full alertness was statistically shorter in the propofol group, it was clinically insignificant. This meta-analysis is the first to investigate the efficacy and safety of ciprofol use as an induction/sedative agent in clinical practice.

Sedative medications such as propofol are commonly used in a variety of medical settings, including diagnostic, surgical, and other therapeutic procedures, as well as anesthetic induction and critical care (Ghojazadeh et al., 2019; Freitas et al., 2022; Guo et al., 2023). Despite the ability of sedatives to provide relief from procedure-related anxiety and discomfort through the induction of sedation and anxiolysis, safety concerns remain an important issue as they can cause varying degrees of depression in the respiratory and cardiovascular systems as well as a loss of airway reflexes (Godoroja-Diarto et al., 2022; Sneyd et al., 2022; Hara et al., 2023). The efficacy and safety of sedatives can be evaluated based on their possession of optimal properties for clinical use, including a rapid onset of action, minimal cardiopulmonary depression, rapid and smooth awakening from sedation, minimal cognitive dysfunction, and a low risk of PONV (Khorsand et al., 2022; Thomson et al., 2010; Minami and Takigawa, 2023). In addition to a low risk of adverse events, sedatives should be easy to administer and monitor with predictable effects to minimize possible medication errors and risk of complications, thereby improving patient outcomes (Gan, 2006; Manzi et al., 2021).

Similar to propofol, ciprofol functions as a positive allosteric modulator of GABA-A receptors, binding to them and augmenting the inhibitory effect of the neurotransmitter GABA, thereby inducing sedative, hypnotic, and anesthetic effects (Lu et al., 2023). Ciprofol is estimated to possess approximately 4–5 times greater potency than propofol, although its precise potency ratio is still being fully characterized (Qin et al., 2017). After intravenous

TABLE 2 Effect Estimate, subgroup analysis, sensitivity, risk of publication bias, and certainty of evidence of secondary outcomes.

Overall outcome or subgroup	Studies	Participants	Effect estimate (MD, SMD, RR)	*p*-value	I^{2a}	Sensitivity analysis	PB	Favor[b]	Certainty of evidence
Top-up dose requirement	6	904	RR 0.94 (0.80, 1.11)	0.48	0%	Consistent	-	NS	High
Induction	2	174	RR 1.15 (0.69, 1.92)	0.59	0%	-	-	NS	-
Sedation	4	730	RR 0.92 (0.78, 1.09)	0.36	0%	-	-	NS	-
Risk of cardiopulmonary complications and pain on injection									
Bradycardia	14	1,697	RR 0.94 (0.73, 1.23)	0.67	0%	Consistent	Low	NS	High
Induction	7	748	RR 0.82 (0.58, 1.15)	0.25	0%	-	-	NS	-
Sedation	7	949	RR 1.15 (0.77, 1.72)	0.5	0%	-	-	NS	-
Tachycardia	5	515	RR 0.83 (0.34, 2.04)	0.68	0%	Consistent	-	NS	Moderate
Induction	5	515	RR 0.83 (0.34, 2.04)	0.68	0%	-	-	NS	-
Sedation	0	0	RR Not estimable	-	-	-	-	-	-
Hypertension	8	814	RR 1.28 (0.88, 1.86)	0.2	0%	Consistent	-	NS	High
Induction	5	515	RR 1.30 (0.86, 1.97)	0.22	0%	-	-	NS	-
Sedation	3	299	RR 1.20 (0.52, 2.82)	0.67	0%	-	-	NS	-
Hypotension	14	1,697	RR 0.85 (0.73, 0.98)	0.02	24%	Inconsistent	Low	C	Moderate
Induction	7	748	RR 0.73 (0.53, 0.99)	0.05	45%	-	-	C	-
Sedation	7	949	RR 0.89 (0.77, 1.03)	0.11	0%	-	-	NS	-
Respiratory complications[c]	7	1,330	RR 0.78 (0.51, 1.19)	0.24	0%	Consistent	-	NS	High
Hypoxemia	5	855	RR 0.81 (0.47, 1.40)	0.45	13%	-		NS	Moderate
Pulmonary depression	4	475	RR 0.7 (0.31, 1.59)	0.39	0%	-		NS	
Pain on injection	15	1793	RR 0.17 (0.11, 0.27)	<0.00001	56%	Consistent	low	C	High
Induction	7	748	RR 0.22 (0.10, 0.47)	0.003	69%	-	-	C	-
Sedation	8	1,045	RR 0.12 (0.08, 0.19)	0.0009	0%	-	-	C	-
Characteristics of recovery									
Time to full alertness	11	1,296	MD 0.66 (0.14, 1.18)	0.01	34%	Inconsistent	low	P	Moderate
Induction	4	347	MD 0.67 (−0.04, 1.37)	0.06	0%	-	-	NS	-
Sedation	7	949	MD 0.70 (−0.08, 1.48)	0.08	58%	-	-	NS	-
PONV	5	639	RR 0.85 (0.35, 2.06)	0.72	0%	Consistent	-	NS	Moderate
Induction	4	372	RR 0.92 (0.37, 2.31)	0.86	0%	-	-	NS	-
Sedation	1	267	RR 0.33 (0.01, 8.05)	0.5	-	-	-	-	-
Discharge time	7	792	MD 1.39 (−0.45, 3.22)	0.14	80%	Inconsistent	-	NS	Low
Induction	1	128	MD 0.30 (−1.65, 2.25)	0.76	-	-	-	NS	-
Sedation	6	664	MD 1.57 (−0.48, 3.62)	0.13	81%	-	-	NS	-
Satisfaction scores	7	814	SMD 0.23 (−0.10, 0.56)	0.16	74%	Inconsistent	-	NS	Low
Patients	4	453	SMD 0.49 (0.28, 0.70)	<0.00001	0%	-	-	C	-
Anesthesiologists	3	361	SMD −0.04 (−0.29, 0.20)	0.73	10%	-	-	NS	-

[a]Heterogeneity; PB, publication bias; NS, no significance between both groups; MD, mean difference; SMD, standardized mean difference; RR, risk ratio; PONV, postoperative nausea and vomiting.

[b]Favor Ciprofol (C) or propofol (P).

[c]Data from patients receiving sedation.

administration of ciprofol, its anesthetic effects begin within 30–60 s (Lu et al., 2023). Owing to its high lipophilicity, ciprofol undergoes a rapid distribution phase characterized by extensive tissue distribution, including easy passage across the blood-brain barrier, thereby facilitating its central nervous system effects (Lu et al., 2023). Ciprofol undergoes substantial hepatic metabolism, primarily through glucuronidation, resulting in a terminal half-life of approximately 2 h (Lu et al., 2023).

Several studies examining patients undergoing gastrointestinal endoscopy or fiberoptic bronchoscopy have indicated comparable efficacy as a sedative agent between ciprofol at a dose of 0.4 mg/kg and propofol at 2.0 mg/kg (Teng et al., 2021; Luo et al., 2022). In the present meta-analysis, the regimens of ciprofol at 0.4 mg/kg and propofol at 2.0 mg/kg predominated across the included studies. The pooled results showed no significant differences in success rate between the two groups, suggesting comparable probability of achieving successful anesthetic induction/sedation between the two agents. Furthermore, our subgroup and sensitivity analyses demonstrated consistent findings. Moreover, there were no significant differences in the time required for successful anesthetic induction/sedation and the risk of top-up dose requirement between the two groups, further supporting similar efficacy of both agents for anesthetic induction and sedation. The high degree of heterogeneity (I^2 = 97%) on the time required for successful anesthetic induction/sedation may be partially attributed to the variations in sedative dosage and procedure (e.g., fiberoptic bronchoscopy or gastrointestinal endoscopy) across our included studies.

Minimal cardiopulmonary depression is a prerequisite for drugs utilized in sedation and anesthetic induction. Despite no significant difference in the risks of bradycardia, tachycardia, hypertension, and hypoxemia between the two groups (Table 2), individuals who received ciprofol exhibited a lower risk of hypotension compared to those being given propofol. Prior studies have indicated that hypotension is linked to a heightened risk of myocardial and renal injury (Ahuja et al., 2020), as well as elevated mortality rates (Wesselink et al., 2018). Furthermore, the longer the exposure and the lower the blood pressure, the greater the risk of mortality (Wesselink et al., 2018). Therefore, our finding of a lower risk of hypotension associated with ciprofol may suggest a safety profile superior to that of propofol. It is noteworthy that the enrollment of relatively healthy patients (e.g., ASA I-II) in the majority of studies included in the current meta-analysis may in part explain the subtle disparity between ciprofol and propofol, which may be more conspicuous in the diseased population. Indeed, only one study recruited patients with ASA III to IV; hence, the benefits of ciprofol in the management of patients with severe comorbidities warrant further evaluations.

In addition to the risk of dose-dependent hemodynamic instability, propofol administration is frequently associated with injection pain, which is a commonly reported adverse reaction. Such discomfort, which is likely due to the high concentration of propofol, can result in anxiety and body movements during drug administration (Tan and Onsiong, 1998; Marik, 2004). Compared with propofol, the demonstration of a lower risk of injection pain linked to ciprofol may be another benefit of its clinical use. With regard to recovery characteristics, no significant differences in the risk of PONV, discharge time, and satisfaction score were observed between the two agents. Although the time to full alertness was slightly shorter with propofol than ciprofol (MD: 0.66 min), the difference was not considered clinically relevant. Surprisingly, despite limited data from only four studies, the apparently higher degree of satisfaction associated with ciprofol than propofol may be partially attributed to the lower incidence of injection pain linked to ciprofol use. Focusing on the effects of sedatives on cognitive function, despite the reported impacts of different sedatives on subsequent psychomotor and cognitive function as well as explicit and implicit memory (Sarasin et al., 1996; Wang et al., 2019), the effects of both agents on those recovery characteristics were not evaluated due to a lack of related information in all studies. Therefore, further investigations are needed to address these issues to provide clinical implications for better outpatient care.

Several key factors should be considered when comparing propofol and ciprofol. First, propofol and ciprofol have different potencies, with ciprofol estimated to be 4–5 times more potent than propofol (Qin et al., 2017). This should be considered when calculating doses for comparison. Equating the dosages on a simple mg/kg basis would fail to provide an accurate assessment. Second, while the two drugs have similar pharmacokinetic properties, such as rapid onset and short duration of action, there are some differences in parameters, such as clearance and volume of distribution, that can impact the comparison. Third, patient factors, including age, health status, and type of procedure, can influence drug performance and side-effect profiles, potentially leading to variations in comparisons across different patient populations.

Through a comprehensive synthesis of existing evidence, our meta-analysis established that ciprofol presented comparable efficacy to propofol for sedation and anesthetic induction, supported by equivalent success rates and induction times. Notably, ciprofol offers safety benefits, including reduced hypotension risk and lower injection pain incidence compared to propofol. In addition, the recovery characteristics and overall safety profiles were generally similar. Accordingly, ciprofol can be considered when propofol is contraindicated or not well tolerated. The reduced risk of hypotension suggests that ciprofol may be preferred in patients at high risk of complications from hypotension, such as the elderly or those with cardiovascular disease. For patients experiencing pain upon propofol injection, switching to ciprofol is an option to improve comfort. Dosage adjustments between the two drugs must account for the higher potency of ciprofol than that of propofol. Equivalent doses may lead to over-sedation with ciprofol. Monitoring for respiratory and cardiovascular side effects is still required as with other sedative medications.

The current meta-analysis was associated with several limitations that may impact the extrapolation and reliability of its findings. First, the fact that all of the included studies were conducted in China may limit extrapolation of the results to other populations. Second, the relatively narrow age range of the study participants (i.e., 34–58 years) may restrict the applicability of the findings to other age groups. Third, the wide variation in ciprofol

and propofol dosages across the included studies may introduce heterogeneity that biased our results. Fourth, the diversity in anesthetic techniques for both sedation and anesthetic induction in the included trials may be another source of heterogeneity that could impede comparability of the findings between studies. Fifth, the recruitment of patients with different ASA physical status across the studies may obscure the significance of our findings. For instance, patients belonging to higher ASA classes, who were recruited in one of our included trials, may have more comorbidities that could affect their response to sedation or anesthesia compared to relatively healthy individuals. Finally, the small sample sizes in some studies may limit the power for discerning significant differences or associations between the variables of interest.

In conclusion, this meta-analysis of 12 RCTs including a total of 1,793 participants showed no significant differences in success rate and time for anesthetic induction/sedation between the ciprofol and propofol groups. The risks of various adverse events also did not significantly differ between the two groups, except for lower risks of hypotension and pain on injection in the ciprofol group. Despite the statistically shorter time to full alertness associated with propofol use, it was not of clinical significance. Future studies are warranted to evaluate the efficacy and safety of ciprofol in specific patient populations, such as pediatric or elderly patients.

Data availability statement

The original contributions presented in the study are included in the article/Supplementary Material, further inquiries can be directed to the corresponding author.

Author contributions

Conceptualization and literature search: K-CH and J-YC; methodology: S-CW; Trial selection: P-YH and J-YW; Data analysis: T-HL and C-CL; Data extraction: I-WC and C-KS; Writing—original draft preparation: K-CH and C-KS; Writing—review and editing: I-WC and C-KS. All authors contributed to the article and approved the submitted version.

Conflict of interest

The authors declare that the research was conducted in the absence of any commercial or financial relationships that could be construed as a potential conflict of interest.

Publisher's note

All claims expressed in this article are solely those of the authors and do not necessarily represent those of their affiliated organizations, or those of the publisher, the editors and the reviewers. Any product that may be evaluated in this article, or claim that may be made by its manufacturer, is not guaranteed or endorsed by the publisher.

Supplementary material

The Supplementary Material for this article can be found online at: https://www.frontiersin.org/articles/10.3389/fphar.2023.1225288/full#supplementary-material

References

Abad-Santos, F., Gálvez-Múgica, M. A., Santos, M. A., Novalbos, J., Gallego-Sandín, S., Méndez, P., et al. (2003). Pharmacokinetics and pharmacodynamics of a single bolus of propofol 2% in healthy volunteers. *J. Clin. Pharmacol.* 43, 397–405. doi:10.1177/0091270003251391

Ahuja, S., Mascha, E. J., Yang, D., Maheshwari, K., Cohen, B., Khanna, A. K., et al. (2020). Associations of intraoperative radial arterial systolic, diastolic, mean, and pulse pressures with myocardial and acute kidney injury after noncardiac surgery: A retrospective cohort analysis. *Anesthesiology* 132, 291–306. doi:10.1097/ALN.0000000000003048

Bian, Y., Zhang, H., Ma, S., Jiao, Y., Yan, P., Liu, X., et al. (2021). Mass balance, pharmacokinetics and pharmacodynamics of intravenous HSK3486, a novel anaesthetic, administered to healthy subjects. *Br. J. Clin. Pharmacol.* 87, 93–105. doi:10.1111/bcp.14363

Chen, B-z., Yin, X-y., Jiang, L-h., Liu, J-h., Shi, Y-y., and Yuan, B-y. (2022a). The efficacy and safety of ciprofol use for the induction of general anesthesia in patients undergoing gynecological surgery: A prospective randomized controlled study. *BMC Anesthesiol.* 22, 245–247. doi:10.1186/s12871-022-01782-7

Chen, X., Guo, P., Yang, L., Liu, Z., and Yu, D. (2022b). Comparison and clinical value of ciprofol and propofol in intraoperative adverse reactions, operation, resuscitation, and satisfaction of patients under painless gastroenteroscopy anesthesia. *Contrast Media & Mol. Imaging* 2022, 9541060. doi:10.1155/2022/9541060

Chen, Y-T., Sun, C-K., Wu, K-Y., Chang, Y-J., Chiang, M-H., Chen, I-W., et al. (2021). The use of propofol versus dexmedetomidine for patients receiving drug-induced sleep endoscopy: A meta-analysis of randomized controlled trials. *J. Clin. Med.* 10, 1585. doi:10.3390/jcm10081585

Coté, G. A., Hovis, R. M., Ansstas, M. A., Waldbaum, L., Azar, R. R., Early, D. S., et al. (2010). Incidence of sedation-related complications with propofol use during advanced endoscopic procedures. *Clin. Gastroenterology Hepatology* 8, 137–142. doi:10.1016/j.cgh.2009.07.008

Dong, S. A., Guo, Y., Liu, S. S., Wu, L. L., Wu, L. N., Song, K., et al. (2023). A randomized, controlled clinical trial comparing remimazolam to propofol when combined with alfentanil for sedation during ERCP procedures. *J. Clin. Anesth.* 86, 111077. doi:10.1016/j.jclinane.2023.111077

Euasobhon, P., Dej-Arkom, S., Siriussawakul, A., Muangman, S., Sriraj, W., Pattanittum, P., et al. (2016). Lidocaine for reducing propofol-induced pain on induction of anaesthesia in adults. *Cochrane database Syst. Rev.* 2, Cd007874. doi:10.1002/14651858.CD007874.pub2

Freitas, T. M., David, C., Almeida, A. G., Pinto, F. J., Costa, J., and Caldeira, D. (2022). Cardiovascular and respiratory safety of sedation strategies used in transesophageal echocardiography: A systematic review incorporating network meta-analysis. *J. Cardiothorac. Vasc. Anesth.* 36, 4129–4140. doi:10.1053/j.jvca.2022.07.003

Gan, T. J. (2006). Pharmacokinetic and pharmacodynamic characteristics of medications used for moderate sedation. *Clin. Pharmacokinet.* 45, 855–869. doi:10.2165/00003088-200645090-00001

Ghojazadeh, M., Sanaie, S., Paknezhad, S. P., Faghih, S. S., and Soleimanpour, H. (2019). Using ketamine and propofol for procedural sedation of adults in the emergency department: A systematic review and meta-analysis. *Adv. Pharm. Bull.* 9, 5–11. doi:10.15171/apb.2019.002

Godoroja-Diarto, D., Constantin, A., Moldovan, C., Rusu, E., and Sorbello, M. (2022). Efficacy and safety of deep sedation and anaesthesia for complex endoscopic procedures-A narrative review. *Diagn. (Basel, Switz.* 12, 1523. doi:10.3390/diagnostics12071523

Guo, Q., An, Q., Zhao, L., Wu, M., Wang, Y., and Guo, Z. (2023). Safety and efficacy of dexmedetomidine for bronchoscopy: A systematic review and meta-analysis. *J. Clin. Med.* 12 (4), 1607. doi:10.3390/jcm12041607

Hansen, T. G. (2015). Sedative medications outside the operating room and the pharmacology of sedatives. *Curr. Opin. Anaesthesiol.* 28, 446–452. doi:10.1097/ACO.0000000000000202

Hara, T., Ozawa, A., Shibutani, K., Tsujino, K., Miyauchi, Y., Kawano, T., et al. (2023). Practical guide for safe sedation. *J. Anesth.* 37, 340–356. doi:10.1007/s00540-023-03177-5

Hung, K-C., Wang, L-K., Lin, Y-T., Yu, C-H., Chang, C-Y., Sun, C-K., et al. (2022). Association of preoperative vitamin D deficiency with the risk of postoperative delirium and cognitive dysfunction: A meta-analysis. *J. Clin. Anesth.* 79, 110681. doi:10.1016/j.jclinane.2022.110681

Joo, H. S., and Perks, W. J. (2000). Sevoflurane versus propofol for anesthetic induction: A meta-analysis. *Anesth. Analgesia* 91, 213–219. doi:10.1097/00000539-200007000-00040

Julious, S. A. (2005). Sample size of 12 per group rule of thumb for a pilot study. *Pharm. Statistics J. Appl. Statistics Pharm. Industry* 4, 287–291. doi:10.1002/pst.185

Khorsand, S., Karamchandani, K., and Joshi, G. P. (2022). Sedation-analgesia techniques for nonoperating room anesthesia: An update. *Curr. Opin. Anaesthesiol.* 35, 450–456. doi:10.1097/ACO.0000000000001123

Li, J., Wang, X., Liu, J., Wang, X., Li, X., Wang, Y., et al. (2022). Comparison of ciprofol (HSK3486) versus propofol for the induction of deep sedation during gastroscopy and colonoscopy procedures: A multi-centre, non-inferiority, randomized, controlled phase 3 clinical trial. *Basic & Clin. Pharmacol. Toxicol.* 131, 138–148. doi:10.1111/bcpt.13761

Liang, P., Dai, M., Wang, X., Wang, D., Yang, M., Lin, X., et al. (2023). Efficacy and safety of ciprofol vs. propofol for the induction and maintenance of general anaesthesia: a multicentre, single-blind, randomised, parallel-group, phase 3 clinical trial. *Eur. J. Anaesthesiol.* 40 (6), 399–406. doi:10.1097/EJA.0000000000001799

Lu, M., Liu, J., Wu, X., and Zhang, Z. (2023). Ciprofol: A novel alternative to propofol in clinical intravenous anesthesia? *BioMed Res. Int.* 2023, 7443226. doi:10.1155/2023/7443226

Luo, Z., Tu, H., Zhang, X., Wang, X., Ouyang, W., Wei, X., et al. (2022). Efficacy and safety of HSK3486 for anesthesia/sedation in patients undergoing fiberoptic bronchoscopy: A multicenter, double-blind, propofol-controlled, randomized, phase 3 study. *CNS drugs* 36, 301–313. doi:10.1007/s40263-021-00890-1

Maheshwari, K., Turan, A., Mao, G., Yang, D., Niazi, A. K., Agarwal, D., et al. (2018). The association of hypotension during non-cardiac surgery, before and after skin incision, with postoperative acute kidney injury: A retrospective cohort analysis. *Anaesthesia* 73, 1223–1228. doi:10.1111/anae.14416

Man, Y., Xiao, H., Zhu, T., and Ji, F. (2023). Study on the effectiveness and safety of ciprofol in anesthesia in gynecological day surgery: A randomized double-blind controlled study. *BMC Anesthesiol.* 23, 92. doi:10.1186/s12871-023-02051-x

Manzi, J. E., Jones, M. R., Cornett, E. M., and Kaye, A. D. (2021). Moderate and deep procedural sedation-the role of proper monitoring and safe techniques in clinical practice. *Curr. Opin. Anaesthesiol.* 34, 497–501. doi:10.1097/ACO.0000000000001011

Marik, P. E. (2004). Propofol: Therapeutic indications and side-effects. *Curr. Pharm. Des.* 10, 3639–3649. doi:10.2174/1381612043382846

Minami, D., and Takigawa, N. (2023). Safe sedation during diagnostic and therapeutic flexible bronchoscopy in Japan: A review of the literature. *Respir. Investig.* 61, 52–57. doi:10.1016/j.resinv.2022.09.003

Qin, K., Qin, W., Ming, S., Ma, X., and Du, X. (2022). Effect of ciprofol on induction and maintenance of general anesthesia in patients undergoing kidney transplantation. *Eur. Rev. Med. Pharmacol. Sci.* 26, 5063–5071. doi:10.26355/eurrev_202207_29292

Qin, L., Ren, L., Wan, S., Liu, G., Luo, X., Liu, Z., et al. (2017). Design, synthesis, and evaluation of novel 2,6-disubstituted phenol derivatives as general anesthetics. *J. Med. Chem.* 60, 3606–3617. doi:10.1021/acs.jmedchem.7b00254

Sahinovic, M. M., Struys, M., and Absalom, A. R. (2018). Clinical pharmacokinetics and pharmacodynamics of propofol. *Clin. Pharmacokinet.* 57, 1539–1558. doi:10.1007/s40262-018-0672-3

Sarasin, D. S., Ghoneim, M. M., and Block, R. I. (1996). Effects of sedation with midazolam or propofol on cognition and psychomotor functions. *J. oral Maxillofac. Surg. official J. Am. Assoc. Oral Maxillofac. Surg.* 54, 1187–1193. doi:10.1016/s0278-2391(96)90348-1

Sneyd, J. R., Absalom, A. R., Barends, C. R. M., and Jones, J. B. (2022). Hypotension during propofol sedation for colonoscopy: A retrospective exploratory analysis and meta-analysis. *Br. J. Anaesth.* 128, 610–622. doi:10.1016/j.bja.2021.10.044

Sterne, J. A. C., Savović, J., Page, M. J., Elbers, R. G., Blencowe, N. S., Boutron, I., et al. (2019). RoB 2: A revised tool for assessing risk of bias in randomised trials. *BMJ Clin. Res. ed)* 366, l4898. doi:10.1136/bmj.l4898

Tan, C. H., and Onsiong, M. K. (1998). Pain on injection of propofol. *Anaesthesia* 53, 468–476. doi:10.1046/j.1365-2044.1998.00405.x

Teng, Y., Ou, M., Wang, X., Zhang, W., Liu, X., Liang, Y., et al. (2021). Efficacy and safety of ciprofol for the sedation/anesthesia in patients undergoing colonoscopy: Phase IIa and IIb multi-center clinical trials. *Eur. J. Pharm. Sci.* 164, 105904. doi:10.1016/j.ejps.2021.105904

Thomson, A., Andrew, G., and Jones, D. B. (2010). Optimal sedation for gastrointestinal endoscopy: Review and recommendations. *J. gastroenterology hepatology* 25, 469–478. doi:10.1111/j.1440-1746.2009.06174.x

Wang, W., Liu, Y., Liu, Y., Liu, F., and Ma, Y. (2019). Comparison of cognitive impairments after intensive care unit sedation using dexmedetomidine and propofol among older patients. *J. Clin. Pharmacol.* 59, 821–828. doi:10.1002/jcph.1372

Wang, X., Liu, J., Zuo, Y. X., Zhu, Q. M., Wei, X. C., Zou, X. H., et al. (2022). Effects of ciprofol for the induction of general anesthesia in patients scheduled for elective surgery compared to propofol: A phase 3, multicenter, randomized, double-blind, comparative study. *Eur. Rev. Med. Pharmacol. Sci.* 26 (5), 1607–1617. doi:10.26355/eurrev_202203_28228

Wesselink, E. M., Kappen, T. H., Torn, H. M., Slooter, A. J. C., and van Klei, W. A. (2018). Intraoperative hypotension and the risk of postoperative adverse outcomes: A systematic review. *Br. J. Anaesth.* 121, 706–721. doi:10.1016/j.bja.2018.04.036

Wu, B., Zhu, W., Wang, Q., Ren, C., Wang, L., and Xie, G. (2022). Efficacy and safety of ciprofol-remifentanil versus propofol-remifentanil during fiberoptic bronchoscopy: A prospective, randomized, double-blind, non-inferiority trial. *Front. Pharmacol.* 13, 1091579. doi:10.3389/fphar.2022.1091579

Zhang, W., Zhu, Z., and Zheng, Y. (2018). Effect and safety of propofol for sedation during colonoscopy: A meta-analysis. *J. Clin. Anesth.* 51, 10–18. doi:10.1016/j.jclinane.2018.07.005

Zhong, J., Zhang, J., Fan, Y., Zhu, M., Zhao, X., Zuo, Z., et al. (2023). Efficacy and safety of Ciprofol for procedural sedation and anesthesia in non-operating room settings. *J. Clin. Anesth.* 85, 111047. doi:10.1016/j.jclinane.2022.111047

Zhu, Q., Luo, Z., Wang, D., Li, J., Wei, X., Tang, J., et al. (2023). Efficacy and safety of ciprofol versus propofol for the induction of anesthesia in adult patients: A multicenter phase 2a clinical trial. *Int. J. Clin. Pharm.* 45, 473–482. doi:10.1007/s11096-022-01529-x

frontiers | Frontiers in Pharmacology

TYPE Original Research
PUBLISHED 22 November 2023
DOI 10.3389/fphar.2023.1282464

OPEN ACCESS

EDITED BY
Jorge G. Farias,
University of La Frontera, Chile

REVIEWED BY
Cristian Sandoval,
University of La Frontera, Chile
Christian I. Nkanga,
University of Kinshasa, Democratic Republic of Congo

*CORRESPONDENCE
Wasan Katip,
wasankatip@gmail.com
Raktham Mektrirat,
raktham.m@cmu.ac.th

†These authors share first authorship

RECEIVED 24 August 2023
ACCEPTED 30 October 2023
PUBLISHED 22 November 2023

CITATION
Mektrirat R, Paengjun N, Chongrattanameteekul P, Umsumarng S, Cheunsri S, Photichai K, Lewchalermvong K, Sansamur C, Okonogi S and Katip W (2023), Utilizing liposomal encapsulation approach to address nephrotoxic challenges of colistimethate sodium through a preclinical study.
Front. Pharmacol. 14:1282464.
doi: 10.3389/fphar.2023.1282464

Utilizing liposomal encapsulation approach to address nephrotoxic challenges of colistimethate sodium through a preclinical study

Raktham Mektrirat[1,2,3*†], Noppanut Paengjun[1], Peerawit Chongrattanameteekul[1†], Sonthaya Umsumarng[1,2], Suppara Cheunsri[1], Kornravee Photichai[4], Kittima Lewchalermvong[5†], Chalutwan Sansamur[6,7], Siriporn Okonogi[3,8] and Wasan Katip[3,9*]

[1]Department of Veterinary Bioscience and Public Health, Faculty of Veterinary Medicine, Chiang Mai University, Chiang Mai, Thailand, [2]Research Center for Veterinary Biosciences and Veterinary Public Health, Faculty of Veterinary Medicine, Chiang Mai University, Chiang Mai, Thailand, [3]Center of Excellence in Pharmaceutical Nanotechnology, Faculty of Pharmacy, Chiang Mai University, Chiang Mai, Thailand, [4]Center of Veterinary Diagnosis and Technology Transfer, Faculty of Veterinary Medicine, Chiang Mai University, Chiang Mai, Thailand, [5]School of Agricultural Technology, King Mongkut's Institute of Technology Ladkrabang, Bangkok, Thailand, [6]Akkhraratchakumari Veterinary College, Walailak University, Nakhon Si Thammarat, Thailand, [7]Centre for One Health, Walailak University, Nakhon Si Thammarat, Thailand, [8]Department of Pharmaceutical Sciences, Faculty of Pharmacy, Chiang Mai University, Chiang Mai, Thailand, [9]Department of Pharmaceutical Care, Faculty of Pharmacy, Chiang Mai University, Chiang Mai, Thailand

The use of Colistin, a last-resort antimicrobial drug, carries the risk of acute kidney injury. The objective of the study was to assess the effectiveness of colistin-encapsulated liposomes (CL) in reducing nephrotoxicity. Additionally, a liposomal preparation of colistimethate sodium was formulated using the reverse phase evaporation method with a 3:1 ratio of phospholipids to cholesterol. The liposomal properties were evaluated using scanning electron microscopy, photon correlation spectroscopy, and release kinetic assay. The killing kinetics of the formulations on embryonic kidney cells were assessed using *in vitro* MTT reduction assay. The nephrotoxicity of CL and colistimethate sodium solution (CS) was evaluated *in vivo* by administering a dose of 20 mg/kg to rats every 12 h for 3 days, with a negative control group receiving a 0.9% saline solution (NSS). The study results revealed that monodisperses of CL showed a smooth surface and distinct boundaries, with an average size of 151.50 $\pm$ 0.46 nm and a narrow size distribution of 0.25 $\pm$ 0.01. The liposomal particles showed high entrapment efficiency of 96.45% $\pm$ 0.41%, with a ζ-potential of −60.80 $\pm$ 1.01 mV and a release rate of 50% of colistimethate sodium within the first 480 min. The CL induced nephrocytotoxicity in a concentration- and time-dependent manner. However, CS had notably lower IC_{50} values compared to its liposome preparations at 48 and 72 h ($p < 0.05$). *In vivo* study results show that serum levels of symmetric dimethylarginine (SDMA) and total white blood cell count (WBC) were significantly lower in the CL group (SDMA = 8.33 $\pm$ 1.70 μg/dL; WBC = 7.29 $\pm$ 0.99 $\log_{10}$ cells/mL) compared to the CS group (SDMA = 15.00 $\pm$ 1.63 μg/dL; WBC = 9.73 $\pm$ 0.51 $\log_{10}$ cells/mL). Our study findings enhance the understanding

of the safety profile of CL and its potential to improve patient outcomes through the use of liposomal colistin medication. Additional clinical studies are necessary to establish the optimal safety regiment in humans.

KEYWORDS

acute kidney injury, antimicrobial, cytotoxicity, liposome, rat, symmetric dimethylarginine

Introduction

Following the widespread usage of broad-spectrum antimicrobial drugs, the prevalence of multidrug resistance (MDR) in bacterial infections is currently a leading cause of morbidity and mortality on a global scale. Moreover, the bacterial production of plasmid-mediated ESBLs limits the number of antimicrobials that can be used to treat infections successfully. Whereas the resistance to last-resort antibiotics is particularly concerning because it might soon restrict the use of antimicrobial therapy for bacterial serious diseases (Fair and Tor, 2014). Due to a lack of other choices, colistin (also known as polymyxin E) has resurfaced as a last-line of defense against multidrug-resistant Gram-negative bacteria (Li et al., 2006). Guidelines for the most effective clinical use of colistin treatment are provided by international consensus recommendations (Tsuji et al., 2019). For the treatment of serious multidrug-resistant Enterobacterales, *Pseudomonas aeruginosa*, *Acinetobacter baumannii* infections, intravenous colistin has been performed. However, it is most commonly utilized in serious clinical conditions including sepsis, and also pneumonia related with mechanical ventilation (VAP) in the intensive care unit (ICU).

Unfortunately, clinical use of colistin has been limited due to its potential to cause acute kidney injury (Falagas and Kasiakou, 2006; Hartzell et al., 2009; Arrayasillapatorn et al., 2021; Ustundag et al., 2022). Colistin can induce acute kidney injury via several potential mechanisms, including direct tubular toxicity, oxidative stress, and disruption of cell membrane integrity. Factors such as pre-existing renal disease and the concomitant use of other nephrotoxic medications can further increase the risk of acute kidney injury (AKI) (Jafari and Elyasi, 2021). Recently developed clinical practice guidelines from the kidney disease community have highlighted the importance of monitoring kidney function in patients treated with colistin to prevent and manage its nephrotoxicity (Pogue et al., 2017; Shields et al., 2017; Eljaaly et al., 2021). Laboratory studies using cell-based assay and animal models have extensively reported colistin-induced nephrotoxicity, providing insights into the mechanisms underlying its toxicity (Keirstead et al., 2014; Heybeli et al., 2019). These laboratory findings align with clinical concerns, suggesting a need for greater awareness of the risks associated with colistin treatment and a greater understanding of the mechanisms of AKI to improve patient outcomes. Ultimately, this highlights the importance of a collaborative effort between clinical and laboratory approaches to better understand and manage the risks of colistin-induced nephrotoxicity.

Liposomes are a promising drug delivery system that could mitigate the toxicity associated with colistin use (Ferreira et al., 2021; Zong et al., 2022). Since, the liposomes are small spherical vesicles consisting of a phospholipid bilayer that can encapsulate and deliver drugs to target cells. They have been shown to improve drug efficacy, reduce toxicity, and enhance drug stability (Bozzuto and Molinari, 2015; Faustino and Pinheiro, 2020). Recent developments in liposomal colistin have shown promising results in animal models and clinical trials, animal models have been extensively used to evaluate the efficacy of liposome-based drug delivery systems in enhancing the therapeutic efficacy of antimicrobials while reducing their toxic side effects (Alarfaj et al., 2022; Joshi et al., 2023). Several clinical trials have also been conducted to evaluate the efficacy of liposome-based drug delivery systems in reducing the occurrence of antimicrobial-induced nephrotoxicity (Bulbake et al., 2017; Zong et al., 2022). The aim of this study was to evaluate the renal cytotoxicity of colistimethate sodium, as well as to assess the safety of colistin liposome formulations (CL) in reducing its toxic side effects, particularly in relation to nephrotoxicity in a rat model.

Materials and methods

Cell lines and culture condition

A human embryonic kidney cell line (Name, 2A; Number, CRL-12013) was purchased from American Type Culture Collection (ATCC, Manassas, VA, United States). The culture plates of human embryonic kidney cells were adjusted to 4×10^4 cells/well in RPMI 1640 supplemented with 1% heat inactivated fetal bovine serum (FBS) (Gibco, Waltham, MA, United States) and 1% penicillin/streptomycin (Sigma-Aldrich, St. Louis, MO, United States) with a final concentration of 100 units per ml. The cells were maintained at 37°C and 5% CO_2 in a humidified incubator (Thermo Fischer Scientific, San Jose, CA, United States).

Dose-response nephrocytoxicity test of colistimethate sodium

The culture plates of human embryonic kidney cells were treated with 0–200 μg/mL colistimethate sodium (Able Medical Co.,Ltd., Mahasarakham, Thailand) and incubated in 5% CO_2 incubator under humidified conditions at 37°C. The cell viability was measured by MTT [3-(4,5-dimethylthiazol-2-yl)-2,5-diphenyl tetrazolium bromide] reduction assay at 24 h after exposure of the tested solution. The volume of 10 μL of 5 mg/mL MTT was added into 200 μL of cell suspension and incubated for 4 h The volume of 100 μL 0.1 M HCl in absolute isopropanol was added after incubation. The colorimetric determination of formazan product was spectrophotometrically measured at 570 nm. Cell viability was expressed as a percentage of the control culture with normal saline solution. This experiment was done with four independent replications.

Preparation of colistin-encapsulated liposome

The CL was prepared using the reverse phase evaporation method with modifications as described previously (Shi and Qi, 2018). First, a

mixture of exact phospholipid and cholesterol at various molar ratios in methanol was vortex-mixed for 30 s. The lipid solution was then evaporated under vacuum at 40°C for 20 min using a rotary evaporator. Next, a solution of colistimethate sodium in normal saline was mixed with the exact amount of diethyl ether before being added to the lipid film. The final mixture was then sonicated until a stable emulsion formed. The organic solvent was removed by using a rotary evaporator until a film was formed. The film was sonicated with 10 mL of normal saline at 40°C for 10 min to create the CL suspension. Finally, unentrapped colistimethate sodium was removed using a mini-column centrifugation method employing a Sephadex G-50 column (Sigma-Aldrich, St. Louis, MO, United States). The experiment was conducted thrice, with a fresh syringe packed with gel for each repetition.

Visualization of surface liposomal morphology

The specimen was freeze-dried, sputter-coated with gold particles, and then examined for its cell morphological appearance under a field-emission scanning electron microscope (FE-SEM) (JSM-6335F, JEOL Ltd., Tokyo, Japan).

Physicochemical characterization of the formulation

The present investigation concerns the comprehensive examination of the internal phase droplets diluted in Millipore water at a ratio of 1:100 (v/v), focusing on the measurement of particle size, size distribution, and ζ-potential. Photon correlation spectroscopy (PCS) was employed as the primary technique for this purpose, utilizing a Zetasizer Nano ZS instrument (Malvern Instruments Ltd., Malvern, Worcestershire, United Kingdom) at a temperature of 25°C. To determine the particle size and size distribution of each mixture, the sample was transferred into a cuvette and measured on a fixed angle of 173°. The particle size was expressed as an average diameter in nm, while the particle size distribution was expressed as polydispersity index (PdI). For the determination of ζ-potential, each mixture was transferred into DT51070 folded capillary cells (Malvern, Worcestershire, United Kingdom) prior to being subjected to PCS. The ζ-potential of the samples was automatically calculated based on the Smoluchowski equation (Rizvi and Saleh, 2018) using the Zetasizer software version 7.1 (Malvern, Worcestershire, United Kingdom). All experiments were conducted in triplicate in order to ensure the reliability of the obtained results.

Determination of liposomal entrapment efficiency

The measurement of entrapment efficiency for CL was conducted using the mini-column centrifugation technique, following the procedures outlined in previous reports (Torchilin and Weissig, 2003). Briefly, the mini-columns were created by utilizing 15 mL plastic syringe barrels filled with Sephadex G-50 (Sigma-Aldrich, St. Louis, MO, United States). To remove excess fluid from the Sephadex beads, centrifugation was performed at 3,000 rpm at 25°C for 3 min. Next, 0.4 mL of CL suspension was added to the column beds and centrifuged at 1,500 rpm at 25°C for 3 min. Following this step, the columns were washed twice with 0.2 mL of distilled water. The elutes containing CL were collected and digested, and the resulting clear solution was then analyzed using high-performance liquid chromatography (HPLC).

Colistin-encapsulated liposome release kinetic assay

The mixed solutions of phosphate-buffered saline (PBS, pH 7.4) were used as the *in vitro* release media. An aliquot of 4 mL of liposomal preparation was mixed with 16 mL of PBS and gently stirred (200 rpm) at 37°C. A 1 mL sample was withdrawn to determine the total drug content, while an additional 0.5 mL sample was mixed with Triton X-100 (LOBA Chemie Pvt. Ltd., MB, India) and centrifuged at 12,000 rpm for 10 min. After centrifugation, 0.1 mL of the supernatant was collected and diluted with 0.9 mL. The diluted sample was then transferred to nylon membrane (0.22 μm) ultra-centrifugation filters for the determination of free drug content using HPLC with Prominence-i (LC-2030) (Shimadzu, Kyoto, Japan). Three replicates of each sample were evaluated at each time point for 0, 5, 120, 240, 480, 720, and 1,440 min.

Time-dependent nephrocytoxicity test of the formulation

The killing kinetic of the formulations was performed to determine the time killing rates on human embryonic kidney cells. The cells were inoculated into wells of a 96-well plate at a density of 4×10^4 cells/well. The experiment was performed in four independent replicates in the culture plates administered the formulations of CS and CL. The culture plates were incubated at 37°C in a 5% CO_2 incubator for 48 and 72 h. The cell viability was measured by MTT reduction assay as described above.

Animal preparation and ethical approval

Twelve male Sprague Dawley rats (*Rattus norvegicus*) were procured from Nomura Siam International Co., Ltd., Bangkok, Thailand, and were average aged 8 weeks with an average body weight of 250 g. The animals were housed in a controlled environment, maintained at a temperature of 24°C ± 1°C with 50% ± 10% relative humidity and a 12:12 h light-dark cycle with light intensities ranging between 250 and 350 Lux. The rats were fed with a standard pelleted diet *ad libitum* and provided with access to drinking water. A 1-week acclimation period was provided before the start of any experimental procedure. Animal procedures were approved by the Walailak University Institutional Animal Care and Use Committee, Thailand (Permit No. WU-ACUC-65064).

Induction of acute kidney injury

The experiment was divided into 2 groups. The control group consisted of 6 rats that received a 0.9% saline solution (NSS), while the experimental group consisted of 6 rats that received a 20 mg/kg

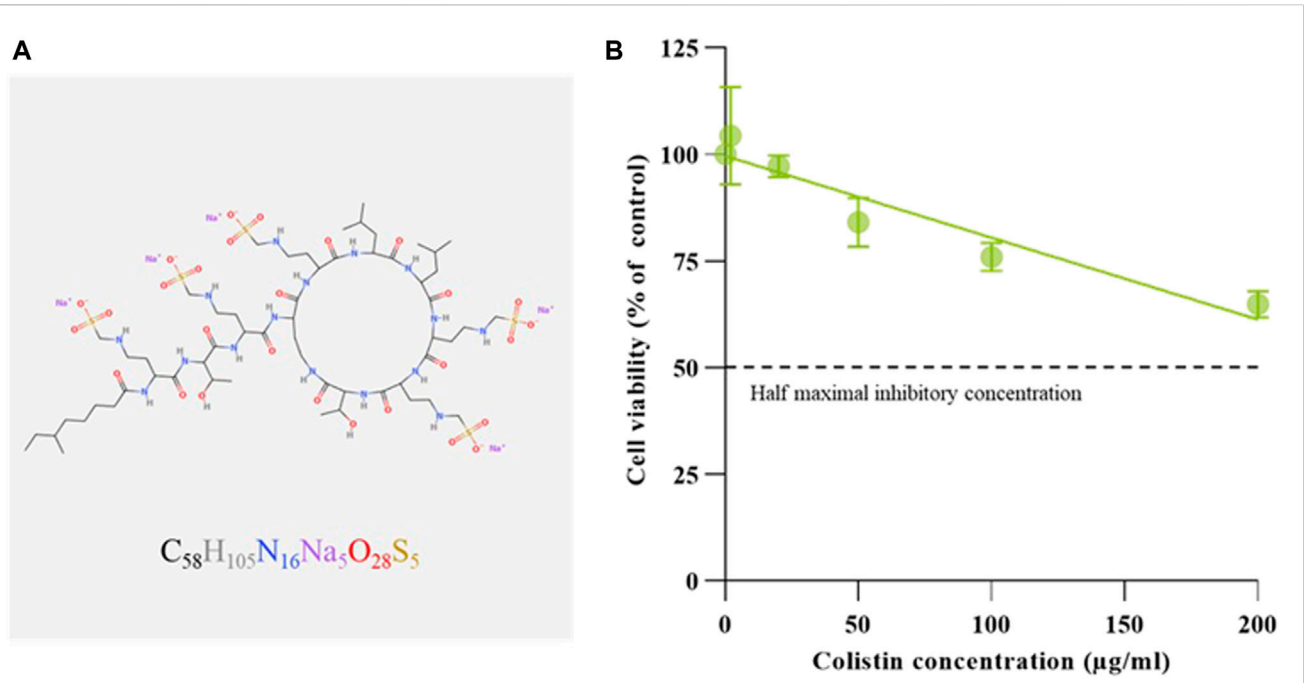

FIGURE 1
Molecular configuration and renal cytotoxicity of Colistimethate sodium. **(A)** Schematic diagram of chemical structure generated by MolView [(www.molview.org) (Smith, 1995)], along with the simplified molecular-input line-entry system strings obtained from the NCBI PubChem database (National Center for Biotechnology Information, 2023). **(B)** Dose-response curve of colistimethate sodium on human embryonic kidney cells. Percentages of cell viability calculated from cells exposed to with normal saline (control), and 2, 20, 50, 100, and 200 μg/mL of colistimethate sodium. Data represents the mean ± SD of four independent experiments. Half maximal inhibitory concentration (IC_{50}) values of CS on human embryonic kidney cells calculated by linear approximation regression of the percentage cell viability versus the drug concentration.

dose of colistimethate sodium. Both groups were given intraperitoneal injections every 12 h continuously for a total of 3 days, with no change in the dosages or frequency of injections being allowed during this period of time.

Clinical and pathological evaluations

The rats were observed for 7 days to check for any toxic effects, changes in behavior, physical appearance, injuries, pain, and signs of illness. Additionally, their daily water and food intake as well as body weight were monitored (Organisation for Economic Co-operation and Development, 2002). Blood samples were collected from the tail vein on days 0 and 7 to analyze symmetric dimethylarginine (SDMA), blood urea nitrogen (BUN), creatinine, aspartate aminotransferase (AST), alanine aminotransferase (ALT), and alkaline phosphatase (ALP) levels. On day 7, the rats were euthanized, and their vital organs (heart, kidneys, liver, lung, and spleen) were removed and fixed in 10% buffered formalin for subsequent histopathological analysis. The relative kidney weight of each rat was calculated by dividing the kidney weight (in grams) by the body weight of the rat (in grams) and then multiplying by 100.

Statistical analysis

Descriptive statistics were used to describe data, including percentage, proportion, ratio, and the half-maximal inhibitory concentration (IC_{50}), while continuous data were expressed as means and standard deviations (SDs). IC_{50} values of colistimethate sodium on human embryonic kidney cells were calculated by linear approximation regression of the percentage cell viability versus the drug concentration. The unpaired *t*-test was utilized to compare the mean ζ-potential between plain liposomes and CL. Additionally, for each time point, unpaired *t*-tests were used to compare cell viability and IC_{50} values between CS and CL. One-way analysis of variance (ANOVA) for independent samples was performed to compare mean clinical parameters according to three different experimental groups. Two-tailed tests were performed, and a *p*-value of <0.05 was considered statistically significant. Statistical analysis was performed with R statistical software (RStudio, Boston, MA, United States). The graph generation was performed using the commercial software GraphPad Prism (San Diego, CA, United States).

Results

Dose-response nephrocytoxicity of colistimethate sodium

To examine the colistimethate sodium induced cytotoxicity, cell viability for human embryonic kidney cells was determined using MTT reduction assay. The cell viability was represented by the detection of enzyme mitochondrial dehydrogenase activity. The cytotoxic effect of the colistimethate sodium on kidney cell line for 24 h was shown in Figure 1. The results show that

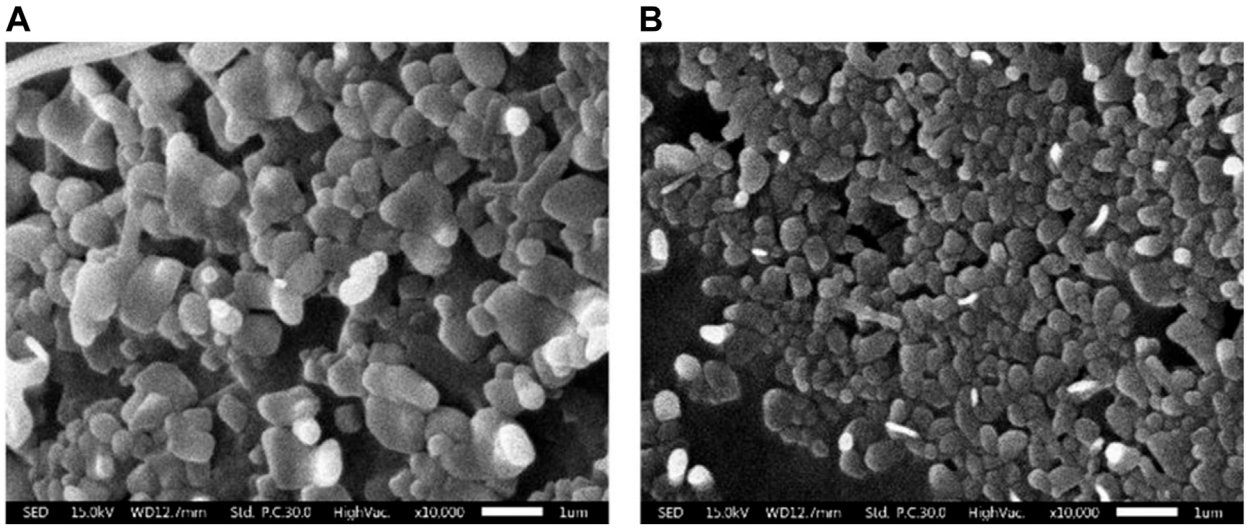

FIGURE 2
Scanning electron micrographs of liposomal morphology. **(A)** Plain liposome and **(B)** colistin-encapsulated liposome prepared through reverse phase evaporation with a 3:1 ratio of phospholipids to cholesterol.

colistimethate sodium induced cytotoxicity in a concentration-dependent manner. The viability rate of the kidney cell line from the control group was 100%, while that of the kidney cell line treated with 2, 20, 50, 100, and 200 μg/mL of the colistimethate sodium was 104.34% ± 11.46%, 97.11% ± 2.58%, 84.10% ± 5.70%, 75.96% ± 3.32%, and 64.81% ± 3.13%, respectively. Since, the viability rates of the cells exposed to 200 μg/mL of colistimethate sodium were more than 50% throughout the trial period. However, the IC_{50} or 50% cytotoxic concentration (CC_{50}) value was able to calculate by estimated linear regression equation [$Y = (-0.1916 \times X) + 99.60$, $R^2 = 0.8307$].

Liposomal morphology

SEM was utilized to investigate the external morphology of liposomal formation. The SEM image revealed liposomes as spherical structures, which appeared as monodisperse particles with smooth surfaces and distinct boundaries. In particular, the study focused on CL, comparing to plain liposomes. Notably, the micelles within the CL were observed to be smaller than those found in the plain liposomes (Figure 2).

Liposomal size and stability

To evaluate the physicochemical properties of the obtained liposomes in terms of size, size distribution and ζ-potential, the dynamic light scattering (DLS) of preparation was also performed using Zetasizer Nano ZS instrument. The result demonstrated that the average size was 151.50 ± 0.46 nm with narrow size distribution of 0.25 ± 0.01 and ζ-potential of −60.80 ± 1.01 mV. Whereas the liposomal preparation without colistimethate sodium had an average size 124.87 ± 2.26 nm with narrow size distribution of 0.44 ± 0.06 and ζ-potential of −71.43 ± 0.64 mV (Figure 3). This finding has important implications for the design and formulation of liposomal drug delivery systems, where balancing the composition of the lipid bilayer is critical for efficient drug delivery.

Controlled release kinetics of colistimethate sodium

Among different molar ratios of a mixture of precise phospholipid and cholesterol, the combination containing 75% phospholipid and 25% cholesterol exhibited the highest drug entrapment efficiency (EE) with an average value of 96.45 ± 0.41. Drug release from liposomes containing colistimethate sodium was measured at 37°C to evaluate the presence of the drug in the PBS release media. It can be seen that the release of colistimethate sodium from the cholesterol-enhanced liposome carrier system occurred in a time-dependent manner. The first 50% release was observed within 480 min, after which it plateaued (Figure 4).

Time-dependent nephrocytoxicity of the formulation

The study of dose-response cytotoxicity of colistimethate sodium suggested that a value corresponding to the maximum safety concentration on human embryonic kidney cells are given at 200 μg/mL of the colistimethate sodium. Therefore, the cytotoxic effect of the liposome formulations containing 200 μg/mL of the colistimethate sodium on kidney cell line for 24, 48, and 72 h was performed. Figure 5A demonstrated time-dependent killing by colistimethate sodium, while at 24 h, the CL formulation (73.77 ± 3.98) exhibited higher cell viability than the CS formulation (64.81 ± 3.13)

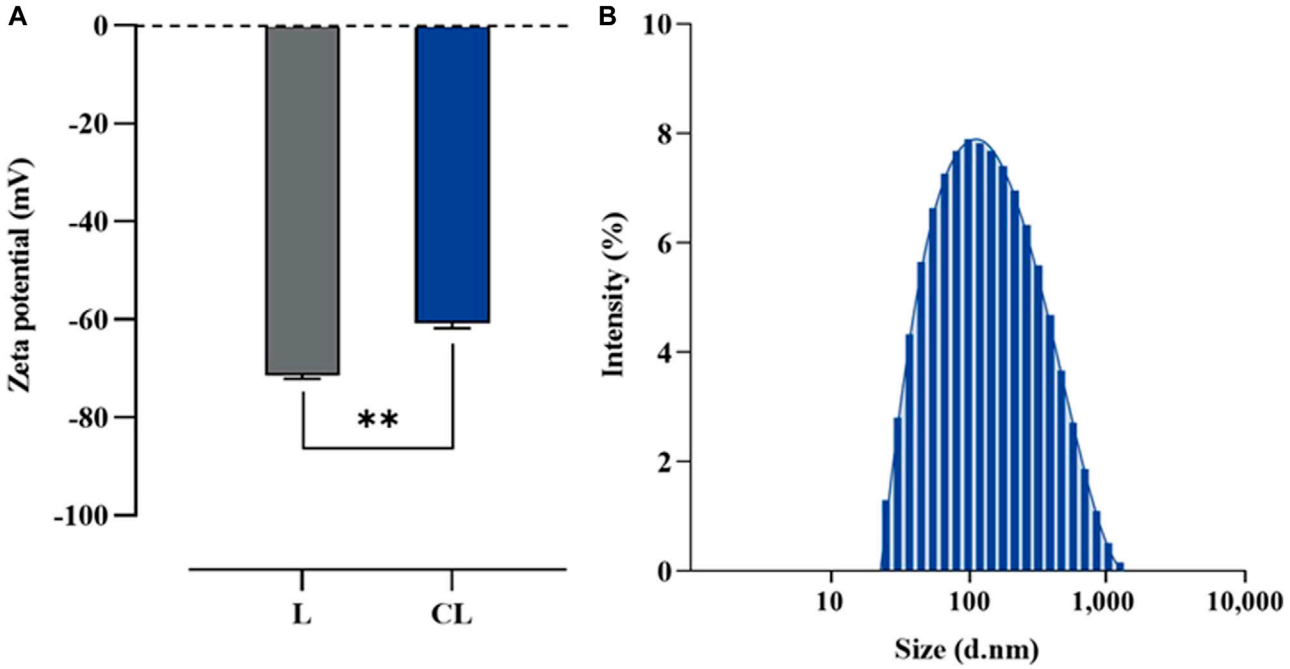

FIGURE 3
Particular characterization of liposome formulated using a reverse phase evaporation method. **(A)** Z-potential of plain liposome (L) and colistin-encapsulated liposome (CL), and **(B)** Size distribution of CL measured using photon correlation spectroscopy. Horizontal lines with asterisk denote (**) illustrate the significant differences ($p < 0.01$) compared between L and CL preparations, determined through unpaired *t*-tests.

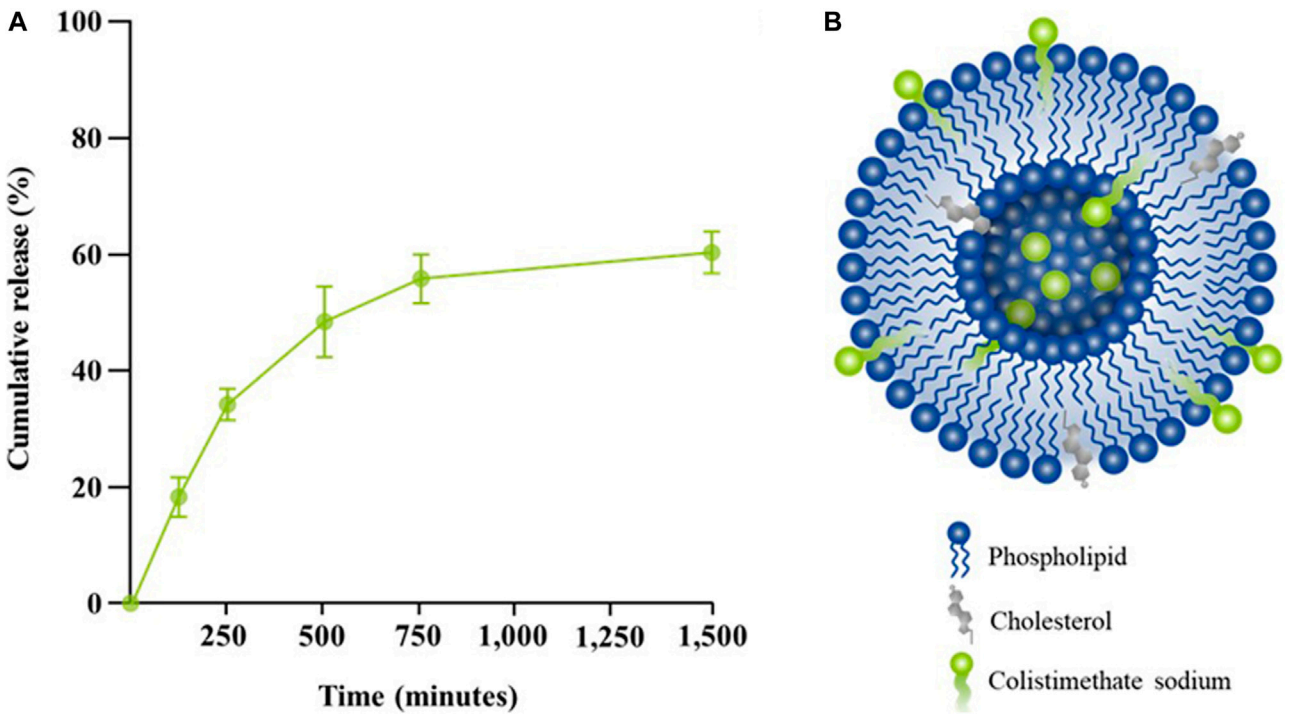

FIGURE 4
Release kinetic profiles of colistin-encapsulated liposome. **(A)** Percentage of cumulative release of colistimethate sodium from the liposomal formulation measured at 0, 5, 120, 240, 480, 720, and 1,440 min. **(B)** A schematic diagram of colistimethate sodium entrapped within the complex micellar structure of a cholesterol-enhanced liposome carrier system.

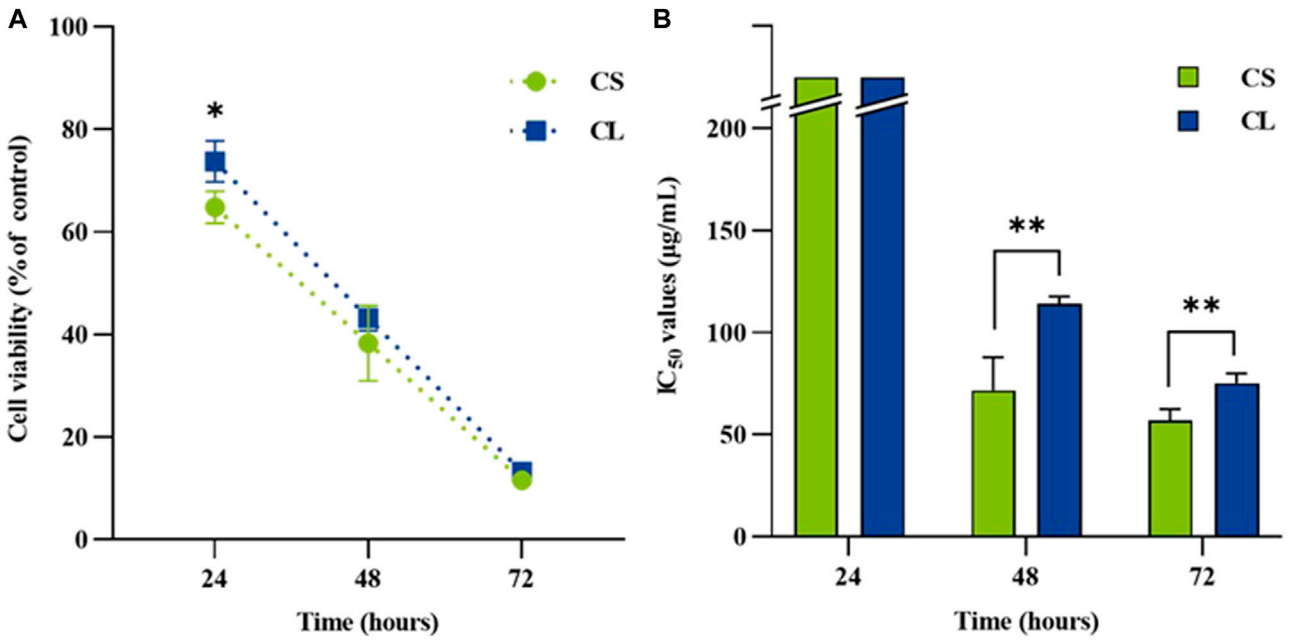

FIGURE 5
The renal cytotoxicity on human embryonic kidney cells exposed to colistimethate sodium solution (CS), colistin-encapsulated liposome (CL) for 24, 48, and 72 h. For each time point, **(A)** the line chart depicting time-kill kinetics of CS and CL at 200 μg/mL and **(B)** the bar chart displaying the half maximal inhibitory concentration (IC50). The data represents the mean ± SD of four independent experiments, and the analyses employed an unpaired *t*-test. The asterisk (*) indicates a statistically significant difference between CS and CL at $p < 0.05$, while (**) represents significance at $p < 0.01$, both determined through unpaired *t*-tests at each time point.

TABLE 1 Incidence density comparison of clinical signs in rats treated with 0.9% saline solution (negative control), 20 mg/kg colistimethate sodium solution, and 20 mg/kg colistin-encapsulated liposome, administered every 12 hours for 3 days.

Clinical signs	Incidence rate (Case number/animal day at risk)			CL baring with NSS			CL baring with CS		
	NSS	CS	CL	δ_{abs}	IRR	*p*-value	δ_{abs}	IRR	*p*-value
Lethargy	0.00 (0/42)	7.89 (3/38)	0.00 (0/42)	0.00	-	1.00	7.89	-	0.10
Disheveled fur	0.00 (0/42)	7.69 (3/39)	5.13 (2/39)	7.69	0.00	0.23	2.56	1.50	1.00
Cyanosis	0.00 (0/42)	5.00 (2/40)	0.00 (0/42)	0.00	-	1.00	5.00	-	0.23
Redness	0.00 (0/42)	5.13 (2/39)	0.00 (0/42)	0.00	-	1.00	5.13	-	0.23
Edema	0.00 (0/42)	7.69 (3/39)	2.50 (1/40)	2.50	0.00	0.49	5.19	3.08	0.36
Fatality	0.00 (0/42)	2.63 (1/38)	0.00 (0/42)	0.00	-	1.00	2.63	-	0.48

CL, colistin-encapsulated liposome; CS, colistimethate sodium solution; NSS, 0.9% saline solution; IRR, incidence rate ratios; δ_{abs}, absolute difference.

($p = 0.0375$). IC50 values for CS and CL at 24 h could not be estimated due to the concentration limit of 200 μg/mL. However, at 48 and 72 h, CS had significantly lower IC_{50} values (71.67 ± 16.07 μg/mL and 53.33 ± 15.28 μg/mL) than its liposome preparations (114.0 ± 3.61 μg/mL at 48 h, $p = 0.0112$; 118.33 ± 2.89 μg/mL at 72 h, $p = 0.0019$), as shown in Figure 5B.

Nephrotoxicity of the formulation in rat model

In order to assess the safety of CL, rats received a 20 mg/kg dose of the CL formulation every 12 h for 3 days. The positive control and negative control groups were given CS at the equivalent dose to CL and NSS, respectively. Rat lethality and clinical signs were closely monitored for a period of 7 days. The findings indicated no fatalities in either the NSS or CL groups. However, the CS group exhibited an incident density of fatality at 2.63. The CS group displayed clinical signs of lethargy, disheveled fur, cyanosis, redness, and edema, while no clinical signs were observed in the NSS groups. Intriguingly, in the CL group compared to the CS group, the reduction rates of disheveled fur and edema incident density were 32.47% ($p = 1.00$) and 66.67% ($p = 0.36$), respectively (Table 1).

Hematological and blood chemistry parameters were compared among the experimental rat groups at day 7 post-administration. Acute kidney injury was successfully induced in the CS group, as evidenced by a significantly elevated serum level of symmetric

TABLE 2 Comparison of rat blood parameters at 7 days post-administration of 0.9% saline solution (negative control), 20 mg/kg colistimethate sodium solution, and 20 mg/kg colistin-encapsulated liposome, administered every 12 h for 3 days.

Blood parameter	Experimental groups			p-value
	NSS	CS	CL	
RBC (log10 cells/mL)	7.21 ± 0.24	7.48 ± 0.32	7.52 ± 0.57	0.62
Hb (g/dL)	14.05 ± 0.50	14.40 ± 0.27	14.68 ± 1.04	0.56
Hct (%)	42.33 ± 1.54	44.00 ± 0.19	45.03 ± 2.48	0.19
WBC (log10 cells/mL)	7.37 ± 0.47[a]	9.73 ± 0.51[b]	7.29 ± 0.99[a]	<0.01
PLT (log10 cells/mL)	805.00 ± 121.15	801.50 ± 68.06	780.00 ± 73.09	0.97
Cr (mg/dL)	<0.10 ± 0.00	<0.10 ± 0.00	<0.10 ± 0.00	N/A
BUN (mg/dL)	27.75 ± 2.28	23.25 ± 3.49	25.00 ± 3.00	0.23
ALT (U/L)	88.00 ± 17.85	97.75 ± 9.78	75.75 ± 30.89	0.48
AST (U/L)	207.00 ± 34.26	218.00 ± 27.90	166.50 ± 57.78	0.33
ALP (U/L)	272.75 ± 20.14	255.25 ± 30.96	231.00 ± 12.69	0.13
GGT (U/L)	4.00 ± 1.22	1.25 ± 1.64	6.50 ± 4.56	0.18
SDMA (μg/dL)	10.67 ± 0.47[a]	15.00 ± 1.63[b]	8.33 ± 1.70[a]	<0.01

[a,b]Distinctive superscript letters shared within the same row are significantly different ($p < 0.05$). ALP, Alkaline phosphatase; ALT, Alanine transaminase; AST, Aspartate transaminase; BUN, Blood urea nitrogen concentration; CL, Colistin-encapsulated liposome; Cr, Creatinine; CS, Colistimethate sodium solution; GGT, Gamma-glutamyl transferase; Hb, Hemoglobin concentration; Hct, Hematocrit; NSS, 0.9% saline solution; PLT, Platelet count; RBC, Red blood Cell Count; SDMA, Symmetric dimethyl arginine; WBC, White blood cell count.

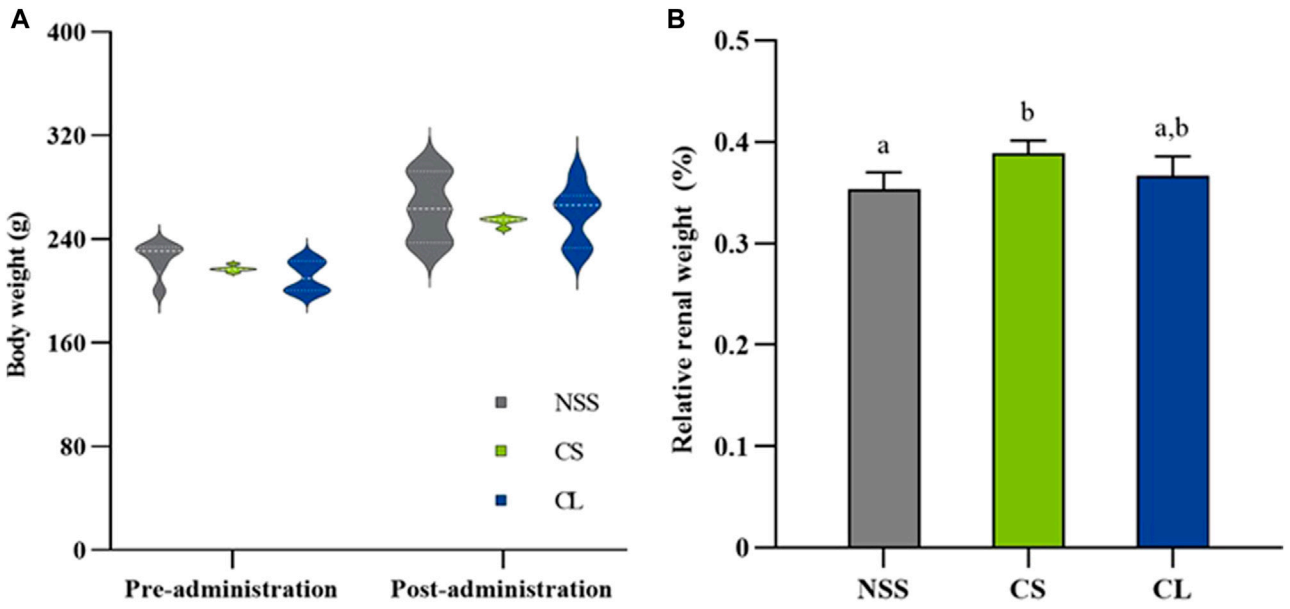

FIGURE 6
Comparison of body and renal weights in rats treated with 0.9% saline solution (NSS), 20 mg/kg colistimethate sodium solution (CS), and 20 mg/kg colistin-encapsulated liposome (CL), administered every 12 h for 3 days. **(A)** Mean body weights at pre-administration (day 0) and post-administration (day 7) and **(B)** relative renal weights post-administration of the three experimental groups. The data underwent analysis through a two-way ANOVA followed by Tukey's multiple comparison test. Bars without a common letter indicated significant differences ($p < 0.05$).

dimethylarginine (SDMA) (15.00 ± 1.63 μg/dL) compared to the NSS group (10.67 ± 0.47 μg/dL) ($p < 0.01$). Conversely, no significant difference in serum SDMA levels was observed between the NSS and CL groups (8.33 ± 1.70 μg/dL). Moreover, the mean value of total white blood cell count (WBC) was also not different in the NSS group (7.37 ± 0.47 $\log_{10}$ cells/mL) and the CL group (7.29 ± 0.99 $\log_{10}$ cells/mL). In the CS group, WBC levels was 9.73 ± 0.51 $\log_{10}$ cells/mL, which were significantly higher than those

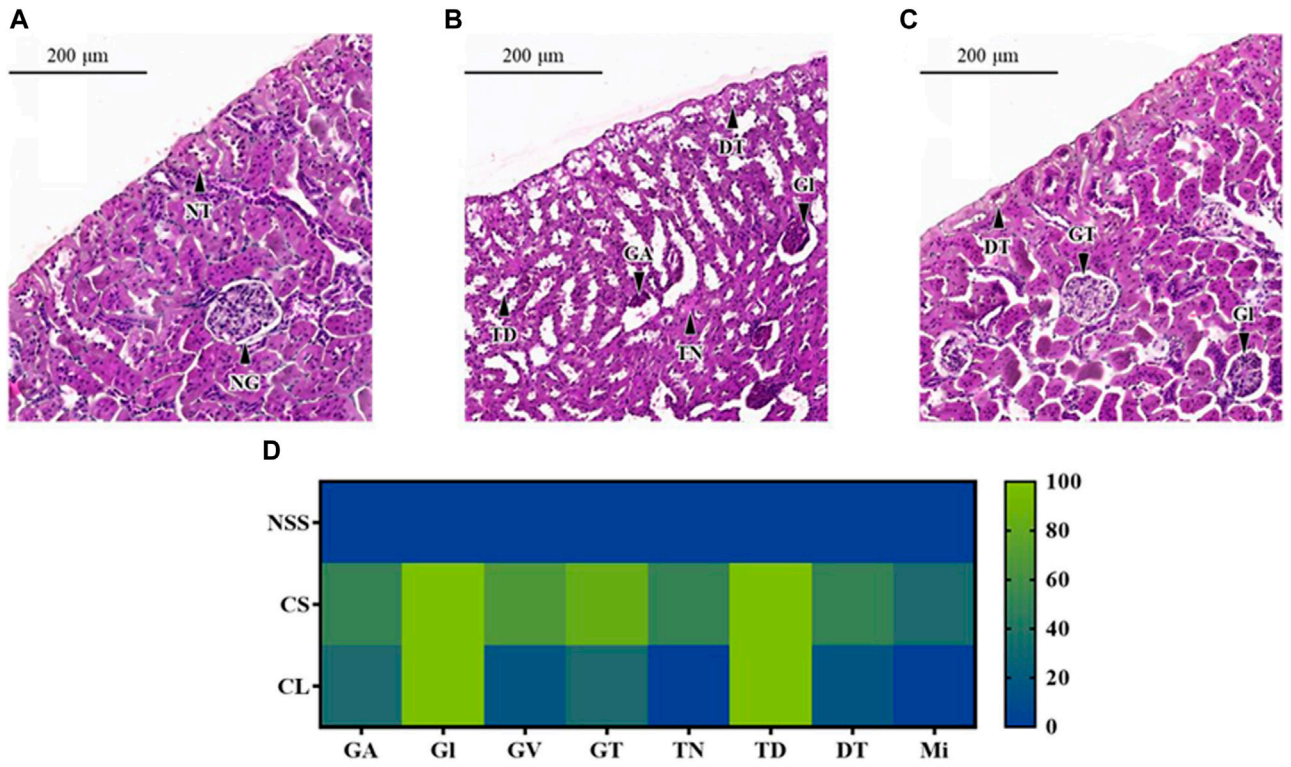

FIGURE 7
Microscopic characterization of rat renal tissues. Photomicrography of representative renal cross section with hematoxylin and eosin staining from rats after administrated with **(A)** 0.9% saline solution (NSS), **(B)** 20 mg/kg colistimethate sodium solution (CS), and **(C)** 20 mg/kg colistin-encapsulated liposome (CL) every 12 h for 3 days. **(D)** The heat map illustrated the occurrence percentage of histopathological renal lesions found in each individual kidney relative to the total number of kidneys. Features noted here include GA, Glomerular atrophy; DT, Degenerative renal tubules; Gl, Glomerulitis; GT, Glomerular basement thickening; GV, Glomerular vacuolation; Mi, Mineralization; NG, Normal glomerulus; NT, Normal renal tubules; TD, Tubular dilatation; TN, Tubular necrosis.

of the NSS and CL groups ($p < 0.01$). However, no significant differences were observed in other blood parameters (Table 2).

During 7 observation days, the mean body weight did not differ significantly among the three experimental groups (Figure 6A). Additionally, the calculation of average daily gain (ADG) for the NSS (7.94 ± 1.47 g), CS (7.53 ± 0.65 g), and CL (7.69 ± 1.20 g) groups showed no significant differences. The results revealed that the CS group (0.39 ± 0.01 g) exhibited a greater relative renal weight after 7 days compared to the NSS group (0.35 ± 0.02 g) ($p < 0.05$). However, CS group relative renal weight was, which were not significantly different from NSS and CL (0.37 ± 0.02 g) groups (Figure 6B).

The microscopic examination of rats in the NSS group reveals normal glomerular and renal tubular structures (Figure 7A). Conversely, histopathological renal lesions are observed in the CS and CL groups, as shown in Figures 7B, C, respectively. In addition, the occurrence percentage of these histopathological renal lesions in each individual kidney, relative to the total number of kidneys, was illustrated in Figure 7D.

In both the CS and CL groups, full occurrence rate of Glomerulitis (Gl) and tubular dilatation (TD) were observed. The percentage of glomerular basement thickening (83.33%), glomerular vacuolation (66.67%), glomerular atrophy (50.00%), and degenerative renal tubules (50.00%) was higher in the CS group compared to the CL group, which had incidence rates of 33.33%, 16.67%, 33.33%, and 16.67%, respectively. The CS group had a half occurrence rate of tubular necrosis (TN) and a one-third occurrence rate of mineralization (Mi), whereas these pathological changes were absent in the CL group.

Discussion

The colistin is composed of both hydrophobic and hydrophilic regions. The fatty acyl chain at the N-terminal end constitutes the hydrophobic region, responsible for interacting with the bacterial membrane. Meanwhile, the cyclic heptapeptide ring constitutes the hydrophilic region, imparting colistin with its antimicrobial activity (Ayoub Moubareck, 2020). In this study, CL were prepared using the reverse phase evaporation method with a 3:1 ratio of phospholipids to cholesterol. Our results also demonstrate that the CL had approximately a size of 150 nm, a ζ-potential of −60 mV, and an EE of 95%. While the size was consistent with the previous experiment, the EE showed improvement compared to the earlier findings (Wallace et al., 2012; Li et al., 2016; Menina et al., 2019). The CL morphology from SEM images is also consistent with previous research conducted on liposomes prepared through the lipid film hydration method (Menina et al., 2019). Our preparation method is

particularly suitable for colistin as it has the advantage of being able to encapsulate both hydrophilic and hydrophobic drugs. This is because liposomes are formed by a water-in-oil emulsion, which allows for the incorporation of both water-soluble and lipid-soluble compounds (Akbarzadeh et al., 2013; Lu and Qu, 2021). This finding aligns with previous research which average size of colistin-loaded liposomes, prepared using dioleoylphosphatidylcholine with or without cholesterol at a molar ratio of 2:1, to be around 180 nm (Wallace et al., 2012). Furthermore, previous research has also suggested that using a 70:30% ratio of lipids to cholesterols is optimal for increasing stability without altering the lipid composition, while ensuring controlled and reproducible drug release (Briuglia et al., 2015). The presence of cholesterol to liposomes can increase in liposome size (Choi et al., 2023) and have significant effects on liposomes stability fluidity, permeability, and stability. This effect is due to ability of cholesterol to increase the packing density of phospholipids in the bilayer and may interact with phospholipids through hydrogen bonding (Pandit et al., 2004), leading to increased membrane rigidity and decreased fluidity that can affect permeability (Lombardo and Kiselev, 2022).

The cell-based toxicity assay on human embryonic kidney cells was performed for prognosticating toxicity of colistin prior to study in the killing kinetic of the formulations. The cytotoxicity result of the CS on human embryonic kidney cells at 24 h after exposure was in dose-dependent manner. The percentage of cytotoxicity at highest concentration of the colistin (200 μg/mL) is lower the half maximal inhibitory concentration this study. These findings are in agreement with previous study on colistin-induced renal proximal tubular cells (RPTEC/TERT1) toxicity, which the IC_{50} value of colistin was at concentrations above 200 μg/mL (Worakajit et al., 2021). The median toxic concentration (TC_{50}) of 70 μM colistin on human proximal tubule kidney cell line (HK-2) upon 24-h treatment was also previously documented (Keirstead et al., 2014). Whereas the previous study demonstrated that cytotoxicity of colistin has weak toxic activity on human erythrocyte (Mohamed et al., 2016). The effects of colistin in combination on Vero cells were also toxic at 1 mg/mL (Naghmouchi et al., 2013). These results suggest that 200 μg/mL colistin has strong safety on the kidney cells exposed directly. The MTT assay is the commonly applied for evaluating of cytotoxicity for screening the drugs (Berridge et al., 2005). In this assay, the reduction of MTT is linked to the metabolic activity of intracellular reductases, including mitochondrial dehydrogenase (Rai et al., 2018). While this method has limitations in elucidating the mechanisms of colistin-induced kidney cell death, previous research suggests that colistin causes mitochondrial and endoplasmic reticulum dysfunction (Gai et al., 2019).

Exposure of human embryonic kidney cells to the colistin formulations reduced cellular metabolic activity concentration and time-dependently. Moreover, the liposome formulation of colistin (IC_{50} > 200 μg/mL) had unacceptable cytotoxicity at 24 h. Interestingly, the viability of human embryonic kidney cells after exposure with colistin solution was higher than that of their liposome preparation. These results indicated that the liposome preparations of colistin had biocompatibility and low toxicity. Overall, our results are in accordance with previously reported cytotoxicity of the liposomal amphotericin B studied (Roberts et al., 2015). It has been hypothesized that the nephrocytotoxicity of colistin in liposomal form is lower than that of unencapsulated colistin. Since, liposomes are tiny vesicles that encapsulate nephrotoxic drugs and are made of phospholipid bilayer. It may have a higher therapeutic index and less toxicity since the reticuloendothelial system and macrophages can absorb it preferentially (Ameen, 2017). In addition, the liposomal drug-delivery systems offer a very interesting opportunity for delivering drugs with reduced nephrotoxicity. However, *in vivo* nephrotoxic effect of the colistin formulations needs to be investigated for the best possible therapeutic approach.

In a nephrotoxicity study, rats were given 20 mg/kg of colistin every 12 h for 3 days and compared to a negative control group. The results showed clinical signs of toxicity, including disheveled fur, lethargy, redness, edema, cyanosis, and fatality. Although the levels of BUN and Cr in the CS group remained unchanged, the study also found significantly elevated levels of WBC, and all histopathology lesions in the central nervous system were associated with acute kidney injury (Heybeli et al., 2019). The results of this study were consistent with previous studies that used 20-mg/kg/8-h, 30-mg/kg/12-h, and 150-mg/kg/12-h colistin methanesulfonate via a jugular vein cannula for 7 days (Wallace et al., 2008), as well as another study that used 12–36 mg/kg/day colistimethate sodium intramuscular injection every 12 h for 7 days (Ghlissi et al., 2013). Since, the development of colistin-induced nephrotoxicity can be attributed to the binding of colistin to the cell membrane of glomerular and proximal tubule cells, which results in an increased membrane permeability and the loss of water and ions from the cells. This process can lead to kidney damage, as evidenced by previous studies (Ordooei Javan et al., 2015; Petejova et al., 2019). The results of this experiment further support the potential risk of acute kidney injury, as shown by the significant increase in SDMA levels. This finding is consistent with previous research that demonstrated the effectiveness of serum SDMA as a biomarker of renal excretory function in a rat model of gentamicin-induced proximal tubular injury, as well as the validation of a high-throughput SDMA immunoassay for rat serum (Hamlin et al., 2022).

Interestingly, the reduction in all clinical signs, WBC count, SDMA levels, and histopathological lesions was observed in the CL group. These results suggest that the liposome formulation can effectively protect against the nephrotoxic effects of colistimethate sodium, which is consistent with previous studies on doxorubicin (Gabizon et al., 2003), cisplatin (Uchino et al., 2005), polymyxin E sulfate (Wang et al., 2009), amphotericin B (Stone et al., 2016), and vancomycin (Joshi et al., 2023). The precise mechanism by which liposomes reduce colistin nephrotoxicity is not yet fully understood, although several possibilities have been proposed. One possibility is that liposomes interact with cells through various mechanisms. When liposomes come into contact with cells, they can merge with the cell membrane and release their contents into the cell. This characteristic can be beneficial for delivering drugs or other therapeutic agents directly to the interior of cells (Pei and Buyanova, 2019). Additionally, liposomal encapsulation enhances the stability and safety of antimicrobials, resulting in more appropriate pharmacokinetic and pharmacodynamic profiles by prolonging the circulation time in the bloodstream (Ferreira et al., 2021). The results suggest that liposomal drug delivery systems can effectively reduce both *in vitro* and *in vivo* nephrotoxicity. In addition, this information can be used to improve patient outcomes through the use of liposomal colistin medication.

Further clinical studies are warranted to determine the best possible safety approach.

Conclusion

This study has highlighted that the preparation of colistin-encapsulated liposomes is successful and plays an important role in ensuring effective pharmaceutical properties. Additionally, the use of liposomes has been found to protect human embryonic kidney cells from concentration- and time-dependent cytotoxicity. Notably, the liposomal formulation of colistin has also been found to particularly decrease clinical and pathological nephrotoxicity in rat models, which underscores their potential in enhancing safety. Overall, these findings provide a comprehensive understanding of the benefits of liposomal systems and emphasize the need for further research into optimizing drug delivery systems for use in human clinical studies.

Data availability statement

The original contributions presented in the study are included in the article/Supplementary material, further inquiries can be directed to the corresponding authors.

Ethics statement

Ethical approval was not required for the studies on humans in accordance with the local legislation and institutional requirements because only commercially available established cell lines were used. The animal study was approved by Walailak University Institutional Animal Care and Use Committee, Thailand. The study was conducted in accordance with the local legislation and institutional requirements.

Author contributions

RM: Conceptualization, Data curation, Formal Analysis, Investigation, Methodology, Project administration, Resources, Software, Validation, Visualization, Writing–original draft, Writing–review and editing. NP: Data curation, Writing–review and editing. PC: Data curation, Formal Analysis, Software, Validation, Visualization, Writing–original draft, Writing–review and editing. SU: Investigation, Methodology, Writing–review and editing. SC: Data curation, Writing–review and editing. KP: Data curation, Writing–review and editing. KL: Investigation, Methodology, Writing–review and editing. CS: Investigation, Methodology, Writing–review and editing. SO: Investigation, Methodology, Resources, Supervision, Writing–review and editing. WK: Conceptualization, Funding acquisition, Methodology, Project administration, Writing–original draft, Writing–review and editing.

Funding

The author(s) declare financial support was received for the research, authorship, and/or publication of this article. This research project is supported by Thailand Science Research and Innovation (TSRI) with grant number 71689.

Acknowledgments

We would like to express our gratitude for the partial support provided by Chiang Mai University for this research. The authors are also thankful for the Center of Excellence in Research Center for Pharmaceutical Nanotechnology, Faculty of Pharmacy, Chiang Mai University for the facility and instrument support.

Conflict of interest

The authors declare that the research was conducted in the absence of any commercial or financial relationships that could be construed as a potential conflict of interest.

Publisher's note

All claims expressed in this article are solely those of the authors and do not necessarily represent those of their affiliated organizations, or those of the publisher, the editors and the reviewers. Any product that may be evaluated in this article, or claim that may be made by its manufacturer, is not guaranteed or endorsed by the publisher.

References

Akbarzadeh, A., Rezaei-Sadabady, R., Davaran, S., Joo, S. W., Zarghami, N., Hanifehpour, Y., et al. (2013). Liposome: classification, preparation, and applications. *Nanoscale Res. Lett.* 8, 102. doi:10.1186/1556-276X-8-102

Alarfaj, R. E., Alkhulaifi, M. M., Al-Fahad, A. J., Aljihani, S., Yassin, A. E. B., Alghoribi, M. F., et al. (2022). Antibacterial efficacy of liposomal formulations containing tobramycin and N-acetylcysteine against tobramycin-resistant *Escherichia coli*, *Klebsiella pneumoniae*, and acinetobacter baumannii. *Pharmaceutics* 14, 130. doi:10.3390/pharmaceutics14010130

Ameen, M. (2017). Liposomal amphotericin B and delayed presentation of renal tubular acidosis: a case report. *MOJ Clin. Med. Case Rep.* 7. doi:10.15406/mojcr.2017.07.00189

Arrayasillapatorn, N., Promsen, P., Kritmetapak, K., Anunnatsiri, S., Chotmongkol, W., and Anutrakulchai, S. (2021). Colistin-induced acute kidney injury and the effect on survival in patients with multidrug-resistant gram-negative infections: significance of drug doses adjusted to ideal body weight. *Int. J. Nephrol.* 2021, 7795096. doi:10.1155/2021/7795096

Ayoub Moubareck, C. (2020). Polymyxins and bacterial membranes: a review of antibacterial activity and mechanisms of resistance. *Membr. (Basel)* 10, 181. doi:10.3390/membranes10080181

Berridge, M. V., Herst, P. M., and Tan, A. S. (2005). Tetrazolium dyes as tools in cell biology: new insights into their cellular reduction. *Biotechnol. Annu. Rev.* 11, 127–152. doi:10.1016/S1387-2656(05)11004-7

Bozzuto, G., and Molinari, A. (2015). Liposomes as nanomedical devices. *Int. J. Nanomedicine* 10, 975–999. doi:10.2147/IJN.S68861

Briuglia, M. L., Rotella, C., Mcfarlane, A., and Lamprou, D. A. (2015). Influence of cholesterol on liposome stability and on *in vitro* drug release. *Drug Deliv. Transl. Res.* 5, 231–242. doi:10.1007/s13346-015-0220-8

Bulbake, U., Doppalapudi, S., Kommineni, N., and Khan, W. (2017). Liposomal formulations in clinical use: an updated review. *Pharmaceutics* 9, 12. doi:10.3390/pharmaceutics9020012

Choi, S., Kang, B., Yang, E., Kim, K., Kwak, M. K., Chang, P. S., et al. (2023). Precise control of liposome size using characteristic time depends on solvent type and membrane properties. *Sci. Rep.* 13, 4728. doi:10.1038/s41598-023-31895-z

Eljaaly, K., Bidell, M. R., Gandhi, R. G., Alshehri, S., Enani, M. A., Al-Jedai, A., et al. (2021). Colistin nephrotoxicity: meta-analysis of randomized controlled trials. *Open Forum Infect. Dis.* 8, ofab026. doi:10.1093/ofid/ofab026

Fair, R. J., and Tor, Y. (2014). Antibiotics and bacterial resistance in the 21st century. *Perspect. Med. Chem.* 6, 25–64. doi:10.4137/PMC.S14459

Falagas, M. E., and Kasiakou, S. K. (2006). Toxicity of polymyxins: a systematic review of the evidence from old and recent studies. *Crit. Care* 10, R27. doi:10.1186/cc3995

Faustino, C., and Pinheiro, L. (2020). Lipid systems for the delivery of amphotericin B in antifungal therapy. *Pharmaceutics* 12, 29. doi:10.3390/pharmaceutics12010029

Ferreira, M., Ogren, M., Dias, J. N. R., Silva, M., Gil, S., Tavares, L., et al. (2021). Liposomes as antibiotic delivery systems: a promising nanotechnological strategy against antimicrobial resistance. *Molecules* 26, 2047. doi:10.3390/molecules26072047

Gabizon, A., Shmeeda, H., and Barenholz, Y. (2003). Pharmacokinetics of pegylated liposomal Doxorubicin: review of animal and human studies. *Clin. Pharmacokinet.* 42, 419–436. doi:10.2165/00003088-200342050-00002

Gai, Z., Samodelov, S. L., Kullak-Ublick, G. A., and Visentin, M. (2019). Molecular mechanisms of colistin-induced nephrotoxicity. *Molecules* 24, 653. doi:10.3390/molecules24030653

Ghlissi, Z., Hakim, A., Mnif, H., Ayadi, F. M., Zeghal, K., Rebai, T., et al. (2013). Evaluation of colistin nephrotoxicity administered at different doses in the rat model. *Ren. Fail* 35, 1130–1135. doi:10.3109/0886022X.2013.815091

Hamlin, D. M., Schultze, A. E., Coyne, M. J., Mccrann, D. J., 3rd, Mack, R., Drake, C., et al. (2022). Evaluation of renal biomarkers, including symmetric dimethylarginine, following gentamicin-induced proximal tubular injury in the rat. *Kidney360* 3, 341–356. doi:10.34067/KID.0006542020

Hartzell, J. D., Neff, R., Ake, J., Howard, R., Olson, S., Paolino, K., et al. (2009). Nephrotoxicity associated with intravenous colistin (colistimethate sodium) treatment at a tertiary care medical center. *Clin. Infect. Dis.* 48, 1724–1728. doi:10.1086/599225

Heybeli, C., Oktan, M. A., and Cavdar, Z. (2019). Rat models of colistin nephrotoxicity: previous experimental researches and future perspectives. *Eur. J. Clin. Microbiol. Infect. Dis.* 38, 1387–1393. doi:10.1007/s10096-019-03546-7

Jafari, F., and Elyasi, S. (2021). Prevention of colistin induced nephrotoxicity: a review of preclinical and clinical data. *Expert Rev. Clin. Pharmacol.* 14, 1113–1131. doi:10.1080/17512433.2021.1933436

Joshi, M. D., Iacoban, P., and Scheetz, M. H. (2023). Pharmacokinetic and biomarker quantification studies on vancomycin-loaded PEGylated liposomes and its potential to reduce vancomycin-induced kidney injury: a rat study. *Pharmaceutics* 15, 1582. doi:10.3390/pharmaceutics15061582

Keirstead, N. D., Wagoner, M. P., Bentley, P., Blais, M., Brown, C., Cheatham, L., et al. (2014). Early prediction of polymyxin-induced nephrotoxicity with next-generation urinary kidney injury biomarkers. *Toxicol. Sci.* 137, 278–291. doi:10.1093/toxsci/kft247

Li, J., Nation, R. L., Turnidge, J. D., Milne, R. W., Coulthard, K., Rayner, C. R., et al. (2006). Colistin: the re-emerging antibiotic for multidrug-resistant Gram-negative bacterial infections. *Lancet Infect. Dis.* 6, 589–601. doi:10.1016/S1473-3099(06)70580-1

Li, Y., Huang, L., Tang, C., Zhang, E., Ding, L., and Yang, L. (2016). Preparation and characterisation of the colistin-entrapped liposome driven by electrostatic interaction for intravenous administration. *J. Microencapsul.* 33, 427–437. doi:10.1080/02652048.2016.1205153

Lombardo, D., and Kiselev, M. A. (2022). Methods of liposomes preparation: formation and control factors of versatile nanocarriers for biomedical and nanomedicine application. *Pharmaceutics* 14, 543. doi:10.3390/pharmaceutics14030543

Lu, W.-L., and Qi, X.-R. (2021). *Liposome-based drug delivery systems*. Berlin, Heidelberg: Springer Berlin Heidelberg : Imprint: Springer.

Menina, S., Eisenbeis, J., Kamal, M. a.M., Koch, M., Bischoff, M., Gordon, S., et al. (2019). Bioinspired liposomes for oral delivery of colistin to combat intracellular infections by *Salmonella enterica*. *Adv. Healthc. Mater* 8, e1900564. doi:10.1002/adhm.201900564

Mohamed, Y. F., Abou-Shleib, H. M., Khalil, A. M., El-Guink, N. M., and El-Nakeeb, M. A. (2016). Membrane permeabilization of colistin toward pan-drug resistant Gram-negative isolates. *Braz J. Microbiol.* 47, 381–388. doi:10.1016/j.bjm.2016.01.007

Naghmouchi, K., Baah, J., Hober, D., Jouy, E., Rubrecht, C., Sane, F., et al. (2013). Synergistic effect between colistin and bacteriocins in controlling Gram-negative pathogens and their potential to reduce antibiotic toxicity in mammalian epithelial cells. *Antimicrob. Agents Chemother.* 57, 2719–2725. doi:10.1128/AAC.02328-12

National Center for Biotechnology Information (2023). *PubChem compound summary for CID 216258, colistimethate*.

Ordooei Javan, A., Shokouhi, S., and Sahraei, Z. (2015). A review on colistin nephrotoxicity. *Eur. J. Clin. Pharmacol.* 71, 801–810. doi:10.1007/s00228-015-1865-4

Organisation for Economic Co-operation and Development (2002). *Test No. 420: acute oral toxicity - fixed dose procedure*. Paris: OECD Publishing.

Pandit, S. A., Bostick, D., and Berkowitz, M. L. (2004). Complexation of phosphatidylcholine lipids with cholesterol. *Biophys. J.* 86, 1345–1356. doi:10.1016/S0006-3495(04)74206-X

Pei, D., and Buyanova, M. (2019). Overcoming endosomal entrapment in drug delivery. *Bioconjug Chem.* 30, 273–283. doi:10.1021/acs.bioconjchem.8b00778

Petejova, N., Martinek, A., Zadrazil, J., and Teplan, V. (2019). Acute toxic kidney injury. *Ren. Fail* 41, 576–594. doi:10.1080/0886022X.2019.1628780

Pogue, J. M., Ortwine, J. K., and Kaye, K. S. (2017). Clinical considerations for optimal use of the polymyxins: a focus on agent selection and dosing. *Clin. Microbiol. Infect.* 23, 229–233. doi:10.1016/j.cmi.2017.02.023

Rai, Y., Pathak, R., Kumari, N., Sah, D. K., Pandey, S., Kalra, N., et al. (2018). Mitochondrial biogenesis and metabolic hyperactivation limits the application of MTT assay in the estimation of radiation induced growth inhibition. *Sci. Rep.* 8, 1531. doi:10.1038/s41598-018-19930-w

Rizvi, S. a.A., and Saleh, A. M. (2018). Applications of nanoparticle systems in drug delivery technology. *Saudi Pharm. J.* 26, 64–70. doi:10.1016/j.jsps.2017.10.012

Roberts, J., Bingham, J., Mclaren, A. C., and Mclemore, R. (2015). Liposomal formulation decreases toxicity of amphotericin B *in vitro* and *in vivo*. *Clin. Orthop. Relat. Res.* 473, 2262–2269. doi:10.1007/s11999-015-4232-y

Shi, N.-Q., and Qi, X.-R. (2018). Preparation of drug liposomes by reverse-phase evaporation. *Liposome-Based Drug Deliv. Syst.*, 1–10. doi:10.1007/978-3-662-49231-4_3-1

Shields, R. K., Anand, R., Clarke, L. G., Paronish, J. A., Weirich, M., Perone, H., et al. (2017). Defining the incidence and risk factors of colistin-induced acute kidney injury by KDIGO criteria. *PLoS One* 12, e0173286. doi:10.1371/journal.pone.0173286

Smith, T. J. (1995). MolView: a program for analyzing and displaying atomic structures on the Macintosh personal computer. *J. Mol. Graph* 13, 122–125. doi:10.1016/0263-7855(94)00019-o

Stone, N. R., Bicanic, T., Salim, R., and Hope, W. (2016). Liposomal amphotericin B (AmBisome(®)): a review of the pharmacokinetics, pharmacodynamics, clinical experience and future directions. *Drugs* 76, 485–500. doi:10.1007/s40265-016-0538-7

Torchilin, V. P., and Weissig, V. (2003). *Liposomes: a practical approach*. Oxford ; New York: Oxford University Press.

Tsuji, B. T., Pogue, J. M., Zavascki, A. P., Paul, M., Daikos, G. L., Forrest, A., et al. (2019). International consensus guidelines for the optimal use of the polymyxins: endorsed by the American college of clinical pharmacy (ACCP), European society of clinical microbiology and infectious diseases (ESCMID), infectious diseases society of America (IDSA), international society for anti-infective Pharmacology (ISAP), society of critical care medicine (SCCM), and society of infectious diseases pharmacists (SIDP). *Pharmacotherapy* 39, 10–39. doi:10.1002/phar.2209

Uchino, H., Matsumura, Y., Negishi, T., Koizumi, F., Hayashi, T., Honda, T., et al. (2005). Cisplatin-incorporating polymeric micelles (NC-6004) can reduce nephrotoxicity and neurotoxicity of cisplatin in rats. *Br. J. Cancer* 93, 678–687. doi:10.1038/sj.bjc.6602772

Ustundag, G., Oncel, E. K., Sahin, A., Keles, Y. E., Aksay, A. K., and Ciftdogan, D. Y. (2022). Colistin treatment for multidrug-resistant gram-negative infections in children: caution required for nephrotoxicity. *Sisli Etfal Hastan. Tip. Bul.* 56, 427–434. doi:10.14744/SEMB.2021.69851

Wallace, S. J., Li, J., Nation, R. L., Prankerd, R. J., and Boyd, B. J. (2012). Interaction of colistin and colistin methanesulfonate with liposomes: colloidal aspects and implications for formulation. *J. Pharm. Sci.* 101, 3347–3359. doi:10.1002/jps.23203

Wallace, S. J., Li, J., Nation, R. L., Rayner, C. R., Taylor, D., Middleton, D., et al. (2008). Subacute toxicity of colistin methanesulfonate in rats: comparison of various intravenous dosage regimens. *Antimicrob. Agents Chemother.* 52, 1159–1161. doi:10.1128/AAC.01101-07

Wang, D., Kong, L., Wang, J., He, X., Li, X., and Xiao, Y. (2009). Polymyxin E sulfate-loaded liposome for intravenous use: preparation, lyophilization, and toxicity assessment *in vivo*. *PDA J. Pharm. Sci. Technol.* 63, 159–167.

Worakajit, N., Chabang, N., Soodvilai, S., Tuchinda, P., and Soodvilai, S. (2021). Pinocembrin attenuates colistin-induced human renal proximal tubular cell apoptosis. *Thai Bull. Pharm. Sci.* 16, 1–9. doi:10.14456/tbps.2021.11

Zong, T. X., Silveira, A. P., Morais, J. a.V., Sampaio, M. C., Muehlmann, L. A., Zhang, J., et al. (2022). Recent advances in antimicrobial nano-drug delivery systems. *Nanomater. (Basel)* 12, 1855. doi:10.3390/nano12111855

frontiers | Frontiers in Pharmacology

TYPE Original Research
PUBLISHED 03 January 2024
DOI 10.3389/fphar.2023.1258108

OPEN ACCESS

EDITED BY
Jorge G. Farias,
University of La Frontera, Chile

REVIEWED BY
Mauricio Zamorano,
University of La Frontera, Chile
Vasudevarao Penugurti,
Duke University, United States

*CORRESPONDENCE
Marco Ponassi,
marco.ponassi@hsanmartino.it

†These authors have contributed equally to this work and share first authorship

RECEIVED 13 July 2023
ACCEPTED 17 November 2023
PUBLISHED 03 January 2024

CITATION
Ben Toumia I, Bachetti T, Chekir-Ghedira L, Profumo A, Ponassi M, Di Domizio A, Izzotti A, Sciacca S, Puglisi C, Forte S, Giuffrida R, Colarossi C, Milardi D, Grasso G, Lanza V, Fiordoro S, Drago G, Tkachenko K, Cardinali B, Romano P, Iervasi E, Vargas GC, Barboro P, Kohnke FH and Rosano C (2024), Fraisinib: a calixpyrrole derivative reducing A549 cell-derived NSCLC tumor *in vivo* acts as a ligand of the glycine-tRNA synthase, a new molecular target in oncology.
Front. Pharmacol. 14:1258108.
doi: 10.3389/fphar.2023.1258108

Fraisinib: a calixpyrrole derivative reducing A549 cell-derived NSCLC tumor *in vivo* acts as a ligand of the glycine-tRNA synthase, a new molecular target in oncology

Iméne Ben Toumia[1†], Tiziana Bachetti[1†], Leila Chekir-Ghedira[2], Aldo Profumo[1], Marco Ponassi[1*], Alessandro Di Domizio[3], Alberto Izzotti[1,4], Salvatore Sciacca[5], Caterina Puglisi[5], Stefano Forte[5], Raffaella Giuffrida[5], Cristina Colarossi[5], Danilo Milardi[6], Giuseppe Grasso[7], Valeria Lanza[6], Stefano Fiordoro[4], Giacomo Drago[4], Kateryna Tkachenko[1], Barbara Cardinali[1], Paolo Romano[1], Erika Iervasi[1], Gabriela Coronel Vargas[1], Paola Barboro[1], Franz Heinrich Kohnke[8] and Camillo Rosano[1]

[1]IRCCS Ospedale Policlinico San Martino, Genova, Italy, [2]Unit of Bioactive Natural Substances and Biotechnology, Faculty of Dental Medicine of Monastir, University of Monastir, Monastir, Tunisia, [3]SPILLOproject, Milano, Italy, [4]Department of Experimental Medicine, University of Genova, Genova, Italy, [5]Istituto Oncologico del Mediterraneo, Viagrande, Italy, [6]Istituto di Cristallografia, Consiglio Nazionale delle Ricerche, Catania, Italy, [7]Department of Chemical Sciences, University of Catania, Catania, Italy, [8]Dipartimento di Scienze Chimiche, Farmaceutiche ed Ambientali (CHIBIOFARAM), University of Messina, Messina, Italy

Background and purpose: Lung cancer is the leading cause of death in both men and women, constituting a major public health problem worldwide. Non-small-cell lung cancer accounts for 85%–90% of all lung cancers. We propose a compound that successfully fights tumor growth *in vivo* by targeting the enzyme GARS1.

Experimental approach: We present an in-depth investigation of the mechanism through which Fraisinib [meso-(p-acetamidophenyl)-calix(4)pyrrole] affects the human lung adenocarcinoma A549 cell line. In a xenografted model of non-small-cell lung cancer, Fraisinib was found to reduce tumor mass volume without affecting the vital parameters or body weight of mice. Through a computational approach, we uncovered that glycyl-tRNA synthetase is its molecular target. Differential proteomics analysis further confirmed that pathways regulated by Fraisinib are consistent with glycyl-tRNA synthetase inhibition.

Key results: Fraisinib displays a strong anti-tumoral potential coupled with limited toxicity in mice. Glycyl-tRNA synthetase has been identified and validated as a protein target of this compound. By inhibiting GARS1, Fraisinib modulates different key biological processes involved in tumoral growth, aggressiveness, and invasiveness.

Conclusion and implications: The overall results indicate that Fraisinib is a powerful inhibitor of non-small-cell lung cancer growth by exerting its action on the enzyme GARS1 while displaying marginal toxicity in animal models. Together with the proven ability of this compound to cross the blood–brain barrier, we can assess that Fraisinib can kill two birds with one stone: targeting the primary tumor and its metastases "in one shot." Taken together, we suggest that inhibiting GARS1 expression and/or GARS1 enzymatic activity may be innovative molecular targets for cancer treatment.

KEYWORDS

non-small-cell lung cancer, calix[4]pyrroles, proteomics, target discovery, drug discovery, cancer

1 Introduction

Lung cancer is the leading fatal tumor and in the top five ranked tumors for incidence in the world (Sung et al., 2021), and it has a 5-year survival rate of less than 15% (Wood et al., 2015); overall, non-small-cell lung cancer (NSCLC) accounts for approximately 85%–90% of all cases (Reck et al., 2014). The most effective systemic chemotherapy for NSCLC has been cisplatin (CDDP) or other platinum-based combinations for more than two decades. However, CDDP resistance is a major obstacle to its clinical effectiveness (Sève and Dumontet, 2005). Other chemotherapies include paclitaxel (Taxol), docetaxel (Taxotere), gemcitabine, vinorelbine, etoposide (VP-16), and pemetrexed (Derks et al., 2017), but all of these cause severe adverse effects (AEs), including nausea, fatigue, ulcers, and hair loss. In recent years, treatment strategies have changed with the introduction of specific targeted therapy and immunotherapy (Saar et al., 2023). Immunotherapies are "state-of-the-art" therapies that use the body's natural defenses to fight the tumor by stimulating/inhibiting different immune system pathways. Some of the most adopted strategies are based on drugs that block the PD-1 pathway and drugs that block the CTLA-4 pathway. In this category of therapies, we can also include therapeutic cancer vaccines and chimeric antigen receptor (CAR) T-cell therapy. Along with chemotherapeutics, immunotherapies can induce side effects that are known as "immune-related adverse effects." In addition, immunotherapies are often combined with classical chemotherapeutics (Saar et al., 2023).

In general, stage I and stage II NSCLC are treated with surgery, while patients with stage IV NSCLC typically do not undergo surgery or radiation therapy but are instead treated with conventional chemotherapeutics, targeted therapies, or immunotherapy. Palliative care is also important to help relieve symptoms and side effects. Patients with stage III NSCLC may undergo surgery or not, depending on their clinical state and on the size and location of the tumor and the lymph nodes that are involved. For those patients whose tumors cannot be removed with surgery, ASCO recommends radiotherapy using a platinum-based chemotherapy combination.

Nowadays, targeted therapy is considered the standard first-line treatment for epidermal growth factor receptor (EGFR)- or anaplastic lymphoma kinase (ALK)-positive patients. However, only 15%–50% of patients with NSCLC exhibit an activating EGFR mutation (Reck and Rabe, 2017), and ALK translocations occur in just 2%–20% of patients (Blackhall et al., 2014; Steuer and Ramalingam, 2014; Wu et al., 2016). Despite this, CDDP remains the standard first-line chemotherapy for advanced NSCLC (Wang et al., 2004).

Calix (Sève and Dumontet, 2005) pyrroles (C4PYs) are members of a very interesting chemical family of macrocycles. They consist of four pyrrole units linked by quaternary carbon atoms at their 2,5 positions, thus forming a ring structure (Figure 1A). These compounds gained considerable interest after the discovery of their ability to bind anions (Gale et al., 1996; Gale et al., 2001), act as ditopic (ion-pair) receptors (Custelcean et al., 2005), and form complexes and "host" neutral molecules containing hydrogen bond acceptor moieties that can interact with NH units of the pyrroles (Allen et al., 1996; Gale, 2011). The ability of C4PYs to bind anionic compounds inspired us to use these macrocycles as "vectors" for the delivery of a trans-Pt moiety to the DNA (Cafeo et al., 2013). Initially, a *meso*-p-nitroaniline-calix (Sève and Dumontet, 2005) pyrrole derivative trans-coordinated to a Pt(II) center was prepared (Figure 1B) that showed its potential as an anticancer drug. This work paved the way for the use of C4PYs in medicinal chemistry. Following this experience, an in-depth investigation into C4PYs was conducted, both as potential vectors for drug delivery (Cafeo et al., 2014; Cafeo et al., 2015) and as innovative drugs (Lappano et al., 2015; Geretto et al., 2018). This led to our discovery that *meso*-(p-acetamidophenyl)-calix (Sève and Dumontet, 2005) pyrrole (Figure 1C), named Fraisinib, is effective against several tumor cell lines (Geretto et al., 2018), particularly on NSCLC. Initially, we were convinced that the main molecular mechanism of cytotoxicity of Fraisinib was due to its capability to form adducts to the DNA, as these were found experimentally. However, the selectivity toward a limited number of tumors, also confirmed by further studies, could not be explained by the generic formation of DNA adducts. The molecular mechanisms underlying Fraisinib's effects were hypothesized to be mediated by its binding to a specific protein, and this prompted us to investigate Fraisinib targets on a proteome-wide scale using SPILLO-PBSS software (Di Domizio et al., 2014) as this approach had already been successfully used in other similar projects (Giatti et al., 2021; Malacrida et al., 2022). In contrast with traditional structure-based approaches (e.g., molecular docking simulations), this software is more likely to identify targets and off-targets of any small molecule due to its ability to recognize protein binding sites even when they are hidden or highly distorted (cryptic binding sites). This analysis led us to the identification of the protein glycyl-tRNA synthetase 1 (GARS1) as the main target of

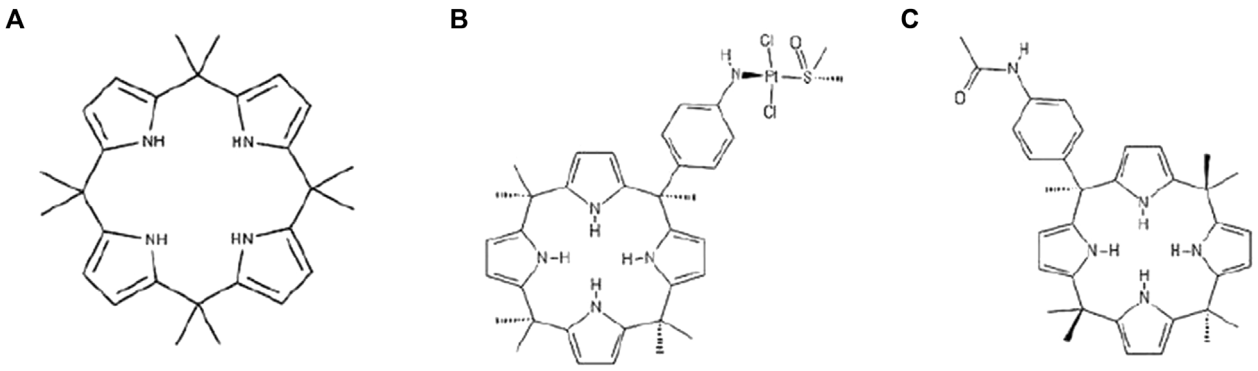

FIGURE 1
Formula of **(A)** calix[4]pyrrole (C4PY), **(B)** a *meso*-p-nitroaniline-calix[4]pyrrole derivative trans-coordinated to a Pt(II) center, and **(C)** *meso*-(p-acetamidophenyl)-calix[4]pyrrole (Fraisinib).

Fraisinib. GARS1 is an enzyme that is essential in protein synthesis by charging tRNA with glycine amino acid. There is considerable experimental evidence correlating its overexpression with poor prognosis in patients with breast, lung, renal, and liver cancer (Sung et al., 2022). The role of GARS1 in cancer progression was recently linked to the additional functionality of this protein in regulating neddylation, a post-translational modification involved in cell cycle regulation and proliferation (Mo et al., 2016). Furthermore, unlike other tRNA synthases, GARS1 uses direct ATP condensation to synthesize the metabolite diadenosine tetraphosphate (Ap4A) by a unique amino acid-independent mechanism. Ap4A is a secondary signaling molecule that is thought to act as an "alarmone," signaling cellular stress to evoke an intracellular response (Götz et al., 2019).

This work demonstrates, through a functional test, that Fraisinib suppresses the synthesis of Ap4A by GARS1 and, consequently, that GARS1 is indeed the protein target for this lead compound, as predicted by SPILLO-PBSS. Data obtained by differential mass spectrometry experiments were further explored using computational system biology and bioinformatics to shed more light on the molecular pathways that are influenced by the action of Fraisinib on the human NSCLC cell line A549.

2 Materials and methods

2.1 Chemistry

Calixpyrrole-derivative Fraisinib and the related molecules shown in Supplementary Figure S1A were prepared as previously reported by Geretto et al. (2018), and their purity was confirmed by both chromatographic and spectroscopic analyses. All compounds used were >95% pure as per HPLC.

2.2 A549 cell culture

The human lung adenocarcinoma A549 cell line was purchased from ATCC and cultured in DMEM (Sigma-Aldrich, Milan, Italy) supplemented with 10% fetal calf serum (Euroclone, Milan, Italy), 2 mM L-glutamine (Euroclone, Milan, Italy), and 1% penicillin–streptomycin (Euroclone, Milan, Italy) at 37°C in a 5% CO_2 incubator. In each experiment, they were used at 70%–80% confluency. A549 cells were chosen because they were well documented to be suitable for studies on lung tumors and drug discovery (Małgorzata Juszczak et al., 2016).

2.3 Fraisinib solution for cell treatment and multicaspase assay

A stock solution of Fraisinib in DMSO 10 mM was diluted 1: 100 with a culture medium. 20 µL of this solution was added to the wells containing the cells in 180 µL of culture medium to obtain a final concentration of 10 µM for Fraisinib and 0.1% DMSO. A mixture of the culture medium containing the same amount of DMSO but without Fraisinib was used for the sham test indicated as "DMSO." Therefore, the concentration of DMSO in the cell wells was identical for Fraisinib-treated and DMSO-treated cells. An additional set of cells were not treated with any solution, and they are referred to in the main text as control (see Figure 2A).

After 48 h treatment, the Muse™ MultiCaspase Assay Kit (Millipore Merck, Vimodrone MI, Italy) was used for the detection of multiple caspase activation (caspase-1, -3, -4, -5, -6, -7, -8, and -9), following the manufacturer's instructions. The percentage of cells with multicaspase activity was then examined using a Muse™ Cell Analyzer (Millipore Merck, Vimodrone MI, Italy) flow cytometer. The signal intensity for each antigen-specific antibody spot is proportional to the relative concentration of the antigen, and thus of the protein, in the sample.

2.4 Cell cycle arrest analysis

Cell cycle analysis was performed using nuclear DNA intercalating stain propidium iodide (PI) provided in the Muse Cell Cycle Kit (Millipore). Fraisinib cell cycle arrest analysis was carried out as previously described by Parodi et al. (2016). Cells were at 80% confluency for 48 h with Fraisinib compared to the controls; after fixation for 3 h in 70% EtOH at −20°C and washing in PBS, cells

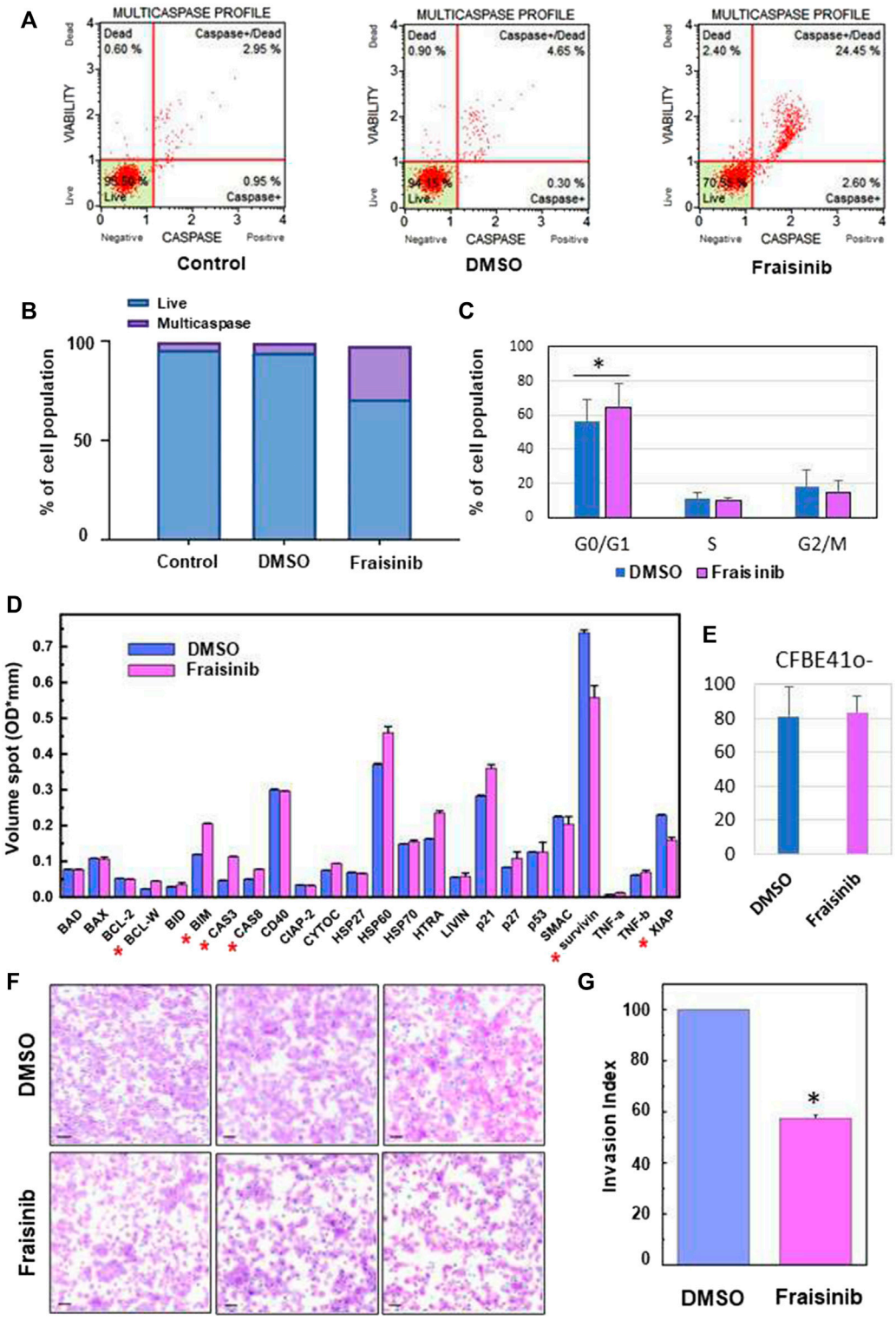

FIGURE 2
Fraisinib treatment induces caspase cascade activation, cell cycle arrests at the G0/G1 phase, and apoptosis activation and invasiveness inhibition in A549 cells. **(A)** FACS-based activation assays of the multicaspase complex in A549 cells. Profiles were determined in untreated cells (control) and after 48 h treatment with DMSO or 10 μM Fraisinib. **(B)** Bar charts depict the percentage of live cells and multicaspase enzyme activation. **(C)** Relative fractions of cells in G0/G1, S, and G2/M stages determined for cells exposed to DMSO or 10 μM Fraisinib. Statistical difference between DMSO- and Fraisinib-treated cells in G0/G1 was calculated by paired Student's t-test (asterisk: p-value = 0.01). **(D)** Comparison of the expression level of apoptotic proteins extracted from DMSO- and Fraisinib-treated A549 cells. Results are the mean ± SD of two independent wells within the array; asterisks indicate the protein level ratio between treated vs. untreated cells higher than 20%. **(E)** Bar diagram showing the percentage of damaged cells revealed by c.Live Tox reagent 250 nM (Cytena) in DMSO- and Fraisinib-treated cells after 48 h treatments. Values are the mean ± SD of three experiments performed in quadruplicate. **(F)** Images representing cell migration in three independent experiments performed to evaluate invasion inhibition in A549 cells with added DMSO (top images) or exposed to Fraisinib (bottom images). The bars correspond to 100 μm. **(G)** Histogram reporting the mean value ± SD of the migration index of the three independent experiments (asterisks: p-value< 0.001).

TABLE 1 Differentially expressed proteins and merged-network characteristics.

Network feature	24 h		48 h		72 h	
	DEP network	Merged network	DEP network	Merged network	DEP network	Merged network
Protein building network (node)	426	526	465	563	396	490
Protein excluded from the network	49	36	57	47	58	49
Number of interactions (edge)*	1,171	2,436	1,252	2,531	962	2,012
Average number of neighbors*	5.6	9.3	5.4	9	4.9	8.3
Clustering coefficient*	0.216	0.244	0.203	0.243	0.192	0.241
PPI enrichment *p*-value**	1.8E-11	<1E-16	4.8E-10	<1E-16	1.7E-7	<1E-16

*Provided by the Cytoscape Analyze-Network tool.
**The PPI enrichment *p*-values represent the statistical significance provided by STRING.

were added with the Muse Cell Cycle reagent and incubated for 30′ at RT. The cell cycle was then measured and determined following the manufacturer's instructions using the Muse Cell Analyzer (Millipore Merck, Vimodrone MI, Italy).

2.5 Human apoptotic protein array

To detect simultaneously the relative levels of expression of many apoptosis-related proteins in a single sample, their quantification was carried out using a Human Apoptosis Antibody Array Kit (RayBiotech, GA, United States of America) following the manufacturer's instructions. A549 cells were seeded (10^5 cells/mL) and treated with Fraisinib 10 μM; cells added with only DMSO were used as the negative control. After 48 h of treatment, cells were harvested, spun down at 1,500 rpm at 4°C for 5 min, and washed twice with ice-cold PBS. Centrifugation was carried out again at 1,500 rpm at 4°C for 5 min, and the supernatant was discarded. Cell proteins were extracted, and approximately 500 μg of proteins from each sample were incubated with the human apoptosis array overnight. Chemiluminescence detections were carried out by scanning the membrane on an Odyssey Fc Imaging System (LI-COR, United States of America). Results are represented as the medium ±SD of results from two independent wells within the membrane.

2.6 Cell invasion assay

Cell invasion assay was carried out in Matrigel chambers (BD Bio Coat), as previously described by Ferrari et al. (2017). A549 cells were seeded (3 × 104 cells/well) in Matrigel chambers in a serum-free medium containing 0.1% DMSO as the control or 2.3 μM of Fraisinib and the same amount of DMSO. Invasion assay was carried out using a medium supplemented with 20% FBS as the chemoattractant for 18 h. The A549 cells that invaded the lower chamber were fixed with 100% methanol and stained with 1% Toluidine blue in 1% borax. The invasion index was calculated as the ratio between the counts of Fraisinib- and DMSO-treated cells invading the Matrigel chamber, and it was expressed as a percentage.

2.7 Fraisinib solution for animal treatment

The injectable solution was prepared by dissolving Fraisinib in DMSO (18.75 mg in 200 μL) and then diluted to 1 mL with olive oil. Thus, 6.66 μL of this solution was required for each gram of mice body weight (BW) to achieve a dosage of 125 mg/kg of mice BW. The solution was used immediately. For the control, a mixture of olive oil and DMSO in the ratio of 9:1 was also prepared.

2.8 Mouse strain and toxicity experiments

After an acclimation period, 12 Balb/c mice were randomly divided into two groups of six mice each. One group received subcutaneous injections with 125 mg/kg BW of Fraisinib (one injection every 2 days for 1 month), and the second group was injected with the same volume of solvent mixture (oil/DMSO, 9:1) at the same time intervals.

2.9 Hematological and biochemical analysis

After sacrificing the mice, blood aliquots were collected in 300 μL tubes (VACUPLAST) containing ethylenediaminetetraacetic acid (EDTA-K2) and carefully mixed by inversion in a homogenizer (Electra—Homolaby 22T) for hematological tests that were performed in an automated hematology analyzer (Sysmex XE-5000 hematology analyzer, Sysmex, Kobe, Japan) to establish the following parameters: RBC, red blood cells; HB, hemoglobin; HCT, hematocrit; MCH, mean corpuscular hemoglobin; MCHC, mean corpuscular hemoglobin concentration; PLT, platelet count; VGM, mean corpuscular volume; WBC, white blood cells; LYM, lymphocytes; NEU, neutrophils; EOS, eosinophils; MON, monocytes; and BASO, basophiles. For biochemical analysis of serum, aliquots of blood were deposited in tubes (10 × 45 mm, maximum volume 500 μL—VACUPLAST) containing coagulation activators and separator gel. The aliquots were then centrifuged at 2,500 rpm for 5 min (Eppendorf® Minispin® model SPIN 1.000, Hamburg, Germany) to separate the serum. These biological samples were then tested by automated analysis using a commercial Cobas Integra kit (Roche, Boulogne-Billancourt, France) to evaluate the following parameters: creatinine, AST: aspartate aminotransferase, ALT: alanine

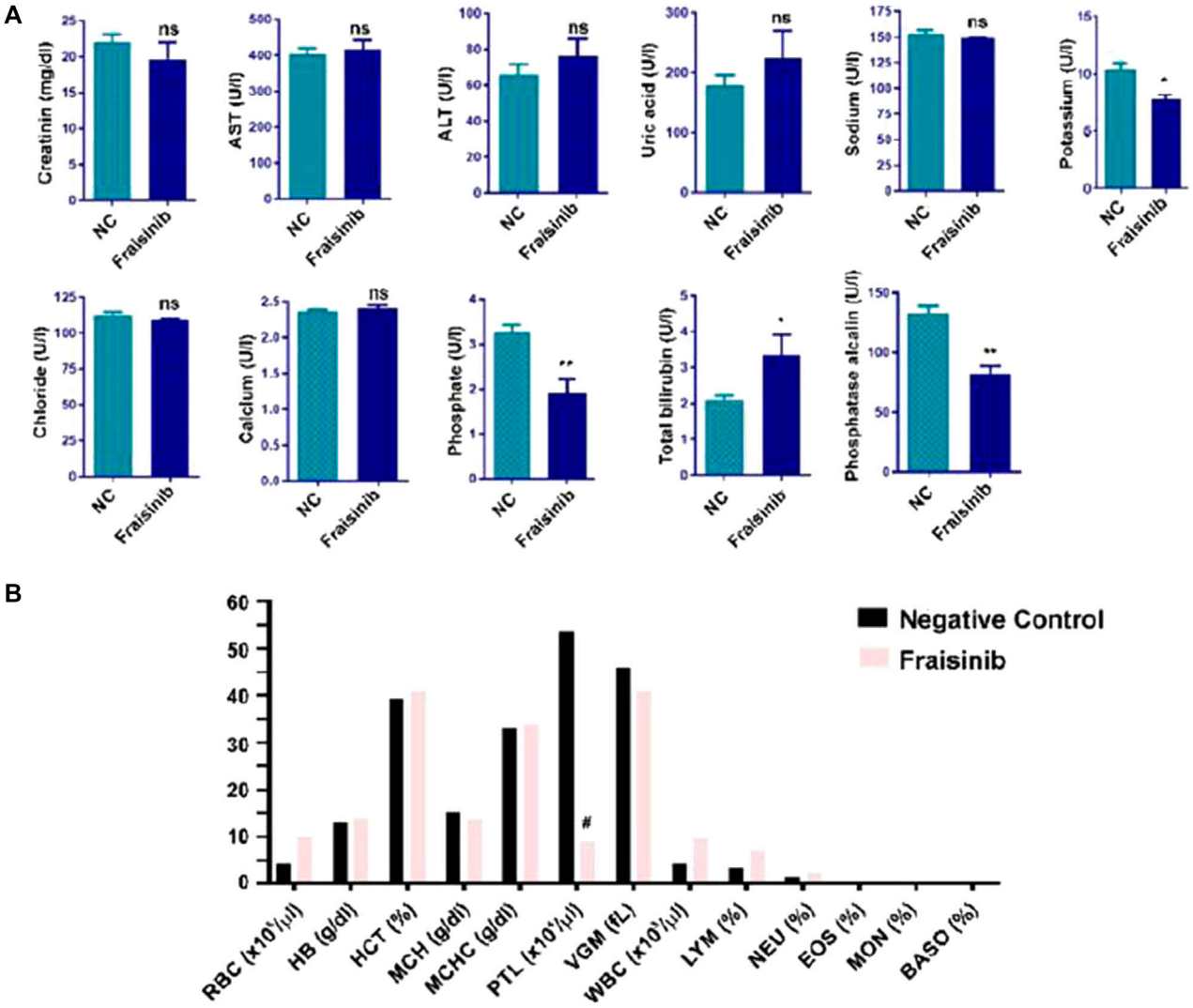

FIGURE 3
Hematological and biochemical analysis of mice blood from two groups of mice (each group n = 6), one treated with 125 mg/kg Fraisinib/BW and the other with vehicle (NC negative control). **(A)** Serum levels of creatinine; AST, aspartate aminotransferase; ALT, alanine aminotransferase; uric acid; sodium; potassium; chloride; calcium; phosphate; total bilirubin; and phosphatase alkaline. **(B)** Blood count results: RBC, red blood cells; HB, hemoglobin; HCT, hematocrit; MCH, mean corpuscular hemoglobin; MCHC, mean corpuscular hemoglobin concentration; PLT, platelet count; VGM, mean corpuscular volume; WBC, white blood cell; LYM, lymphocytes; NEU, neutrophils; EOS, eosinophils; MON, monocytes; and BASO, basophiles. The figures shown are mean ± standard error. #, values that differed significantly from the NC group. Statistical comparisons between groups were analyzed using a one-way analysis of variance (ANOVA). Statistical significance was considered for p-value <0.05. *$p < 0.05$; **$p < 0.01$. ns: not significant compared to the NC group.

aminotransferase, uric acid, sodium potassium, chloride, calcium, phosphate, total bilirubin, and phosphatase alkaline.

2.10 Tumor growth experiments

Immunodeficient (CD-1 nude) female mice, 12 individuals, were randomly divided into two groups of seven and five mice. The larger group was inoculated with 1×10^6 A549 cells. After 1 week, we started treating the seven-mice group with subcutaneous injections (125 mg/kg of Fraisinib/BW) three times per week. The five-mice group was treated with the same volumes of oil/DMSO (9:1) without Fraisinib (positive control group or DMSO group).

The overall duration of the experiment was 1 month. During the 3-week treatment, tumor growth inhibition was monitored by measuring tumor volumes using the formula V (mm3) = d2 × D/2, where d and D are the shortest and the longest diameters, respectively. At the end of the treatment, tumors were also weighed by using a caliber. Mice B.W. were also monitored.

2.11 Protein database preparation

The protein database used for SPILLO-PBSS screening was generated by collecting all protein 3D structures available in the RCSB Protein Data Bank (Berman et al., 2000) (update June 2020)

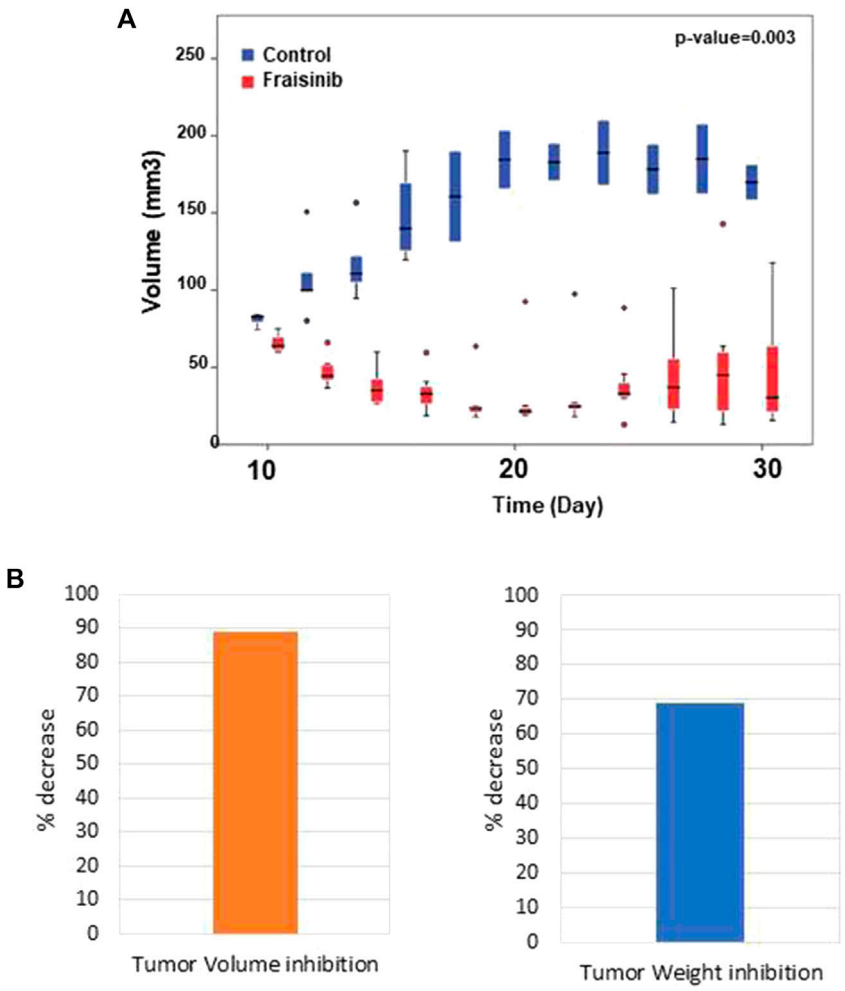

FIGURE 4
Inhibitory effect of Fraisinib treatment on tumor growth. **(A)** Box plot representing the tumor size of treated (red) and untreated (blue) animal groups at each time point. Circles represent the outliers. Unpaired *t*-test on the overall days' comparison between groups *p*-value = 0.003 **(B)** Tumor inhibition observed at the end of treatment compared to the untreated group: 89% and 69% volume and weight, respectively.

for the organisms *Homo sapiens* (45,872 entries), *Mus musculus* (6,474 entries), and *Rattus norvegicus* (2,970 entries) experimentally solved by either X-ray diffraction or solution NMR, including sequence redundancies, for a total of 55,316 holo- and apo-protein 3D structures. Biological assemblies for proteins showing multimeric structures were then generated in accordance with the BIOMT transformation matrices included in the PDB files. For multi-model PDB files from solution NMR experiments, only the first model was included in the database. No further protein structure refinements were carried out to improve the quality of protein 3D structures in the database.

2.12 RBS generation

The reference binding site (RBS) used by SPILLO-PBSS to search the protein database for potential targets of Fraisinib was obtained by molecular modeling techniques and the standard RBS generation protocol described in the SPILLO-PBSS reference paper (Di Domizio et al., 2014). It included 22 amino acid residues directly interacting with Fraisinib without any water-mediated contact.

2.13 *In silico* screening and ranking of the protein database

An unbiased and systematic search for Fraisinib potential binding sites (PBSs) within all protein 3D structures included in the database was carried out using SPILLO-PBSS. Calculations were performed using a rotation step of 30° and a grid spacing of 2.0 Å, with the geometric tolerance set to 4.0 Å. SPILLO-PBSS analyzed all proteins in the database, and a ranking of the PBSs for the molecule was obtained for each protein and stored by the program. The proteins were then ranked according to the highest PBS score, representing the highest similarity to the corresponding RBS, obtained from each analyzed protein 3D structure.

2.14 Target validation

GARS1 aliquots (0.5 μM) were incubated in the reaction buffer (5 mM HEPES, pH 7.5, 2 mM KCl, 0.5 mM $MgCl_2$, and 100 μM DTT) in the presence of 5 mM ATP and different concentrations of

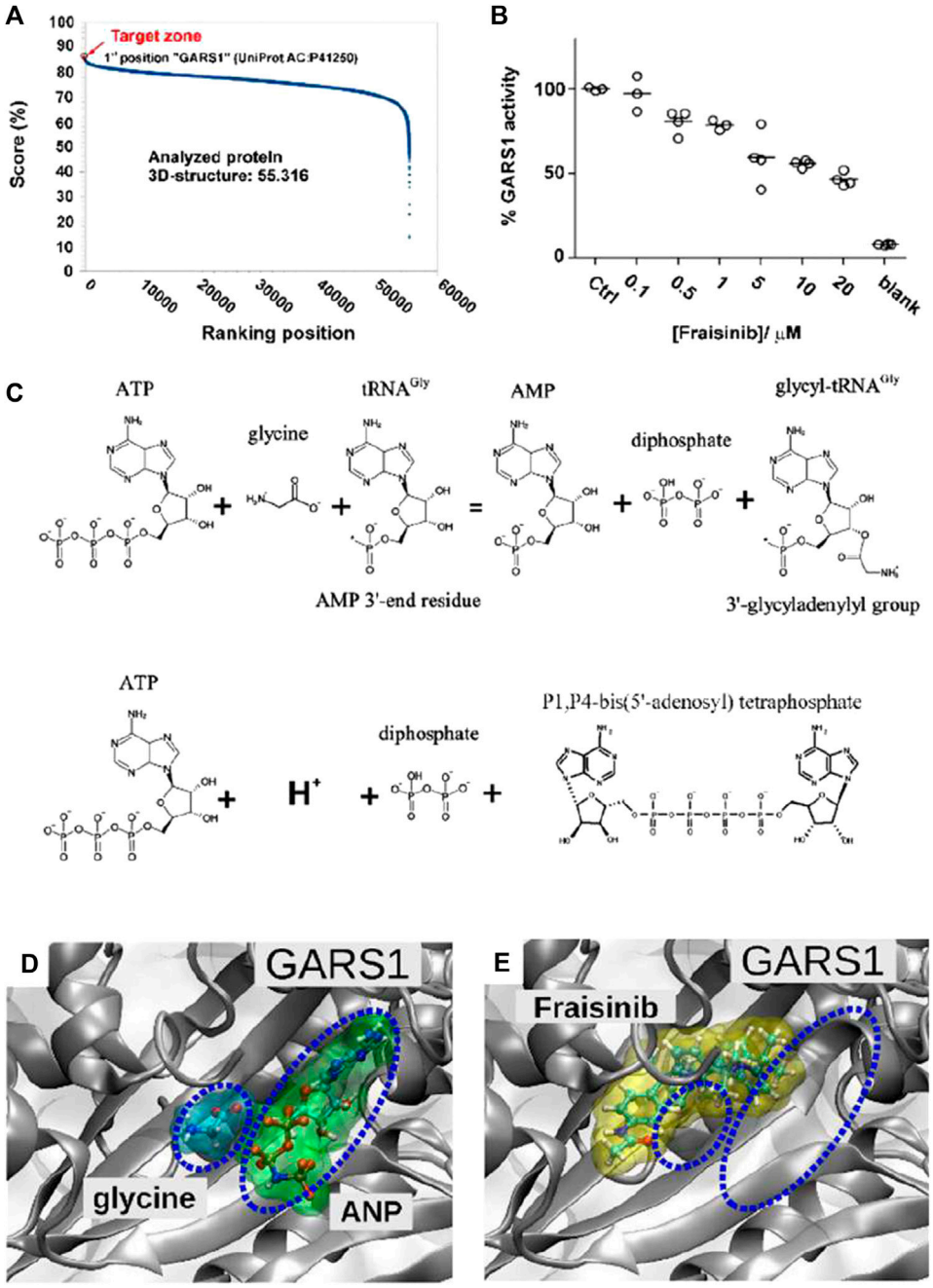

FIGURE 5
Target determination and validation. **(A)** SPILLO-PBSS screening and ranking for Fraisinib. The plot resulted from the *in silico* screening for Fraisinib on the available structural proteomes. Proteins are ranked in descending order of score. Glycyl-tRNA synthetase GARS1 (PDB code: 4KR3 - UniProtKB AC: P41250) was identified as the top-ranked potential target for Fraisinib. **(B)** Enzyme activity obtained by monitoring the amount of pyrophosphate (PPi) released during ATP consumption by GARS1 (circles) in the presence of increasing concentrations of inhibitor Fraisinib (0.1–20 µM). Enzyme activities are reported as average percentages (straight lines) normalized against enzyme activity measured in the absence of an inhibitor. **(C)** Two enzymatic reactions catalyzed by GARS1. **(D)** Positions of glycine and ATP (in this specific structure replaced by the nonhydrolyzable ATP analog 5′-adenylyl-imidodiphosphate (ANP)) and **(E)** Fraisinib within their corresponding binding sites obtained by X-ray diffraction (PDB code: 4KR3) and SPILLO-PBSS calculation, respectively. The partial overlap between the binding sites of glycine/ANP and Fraisinib is shown, which implies a competition between the various molecules for the same binding region, leading to the inhibition of the catalytic activity of the enzyme [drawings were produced using VMD (Götz et al., 2019)].

inhibitor (from 0.1 to 20 µM) at 25°C. Aliquots of the reaction mixtures (4 µL) were quenched after 30 min by adding 4 µL of a 200 mM EDTA solution and analyzed in a 96-well plate by using a Varioskan (Thermo Fisher Scientific). PPi released during the reaction was measured by the molybdate spectrophotometric assay, as previously reported by Guan et al. (2012). Quenched

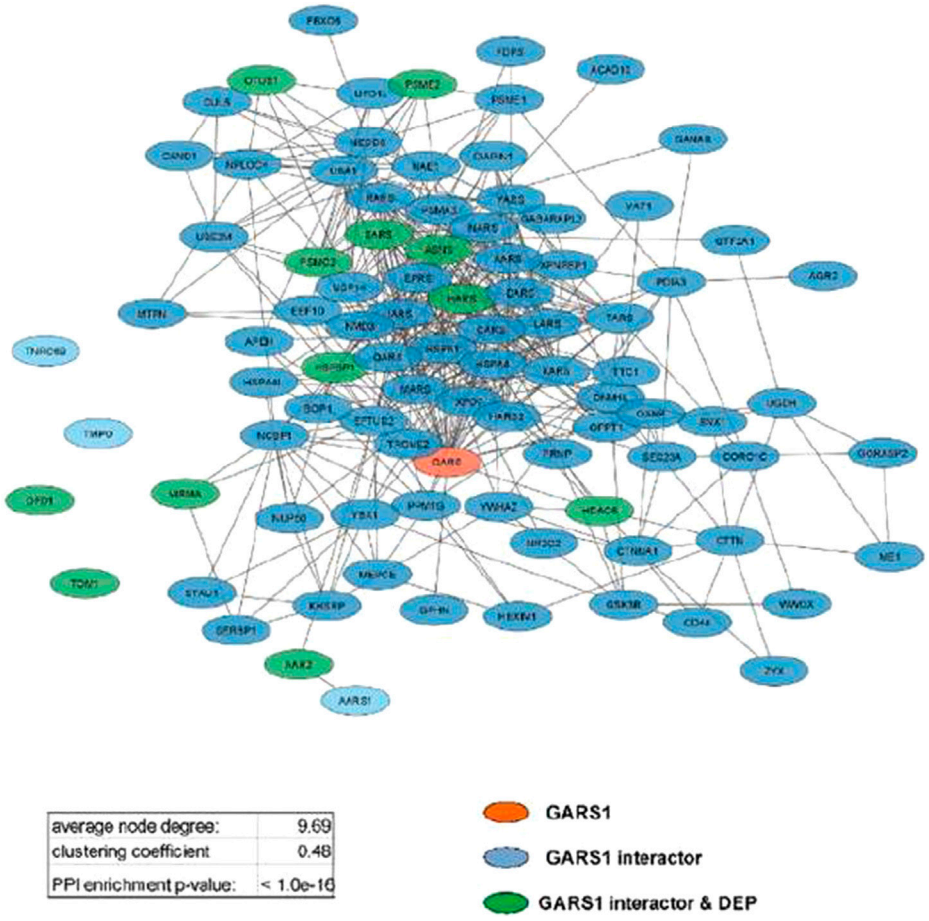

FIGURE 6
GARS1 interactome in the A549 cell line. Network parameters are reported in the inset table.

reaction mixtures were incubated for 10 min with 200 µL of 3 mM ammonium molybdate in 0.6 M HCl (60% CH3CN W/W). The formation of the blue molybdene complex was assayed by measuring the optical absorbance at λ = 790 nm. Calibration curves were obtained using standard PPi solutions (0–50 µM). All molecules tested (Supplementary Figure S1) were prepared in DMSO stock solutions to ensure that the final DMSO concentration did not exceed 1% and that the volumes added in each well were the same.

2.15 A549 cell treatments and protein extraction

For cell treatments, Fraisinib stock solution 10 mM in DMSO was diluted to the final 10 µM concentration in the culture medium. DMSO (0.1%) was added to control samples at each time point at the same concentration of the diluted drug. After 24, 48, and 72 h, cells were harvested with a cell scraper, washed with PBS added with protease (20 µg/mL leupeptin, 25 µg/mL aprotinin, 10 µg/mL pepstatin, 0.5 mM benzamide) and phosphatase inhibitors (1 mM Na_3VO_4), and collected by centrifugation at 4°C at 1,500 rpm for 15 min. The pellet of cells was lysed by RIPA buffer (50 mM Tris-HCl, 150 mM NaCl, 1% Triton X100, 0.1% SDS, and 0.5% sodium deoxycholate, pH 8.0), incubated at 4°C for 60 min, and then, sonicated for 30 s in ice. Following centrifugation at 7,000 rpm for 15 min, the supernatant containing the total proteins was transferred into a new tube; 100 µL DTT 1M:0.9 mL ratio was added to the proteins and then incubated at RT for 30 min. Subsequently, 400 µL 0.5 M iodoacetamide:0.6 mL volume was added followed by incubation at RT for 30 min. Solution C 2X (SDS 20%; DTT 6%) was added at the ratio of 1:1, vortexed, and incubated at 95°C for 5 min to remove lipids and nucleic acids. Proteins were then precipitated with 5 volumes MATF (1 mL methanol:12 mL acetone: 1 mL tributyl phosphate), rotated at 4°C for 60 min, and then, centrifuged at 7,000 rpm for 15 min. Pellets were resuspended in 1 mL MATF, centrifuged at 12,000 rpm at 4°C for 15 min, and dried in a SpeedVac. The obtained proteins were resuspended in ammonium bicarbonate (AMBIC) 50 mM to the final concentration of 2 µg/µL, digested with trypsin at 37°C for 1 h, and blocked with acetic acid 50% in a 1:10 ratio. Following agitation for 10 min, tryptic peptides were dried under a vacuum.

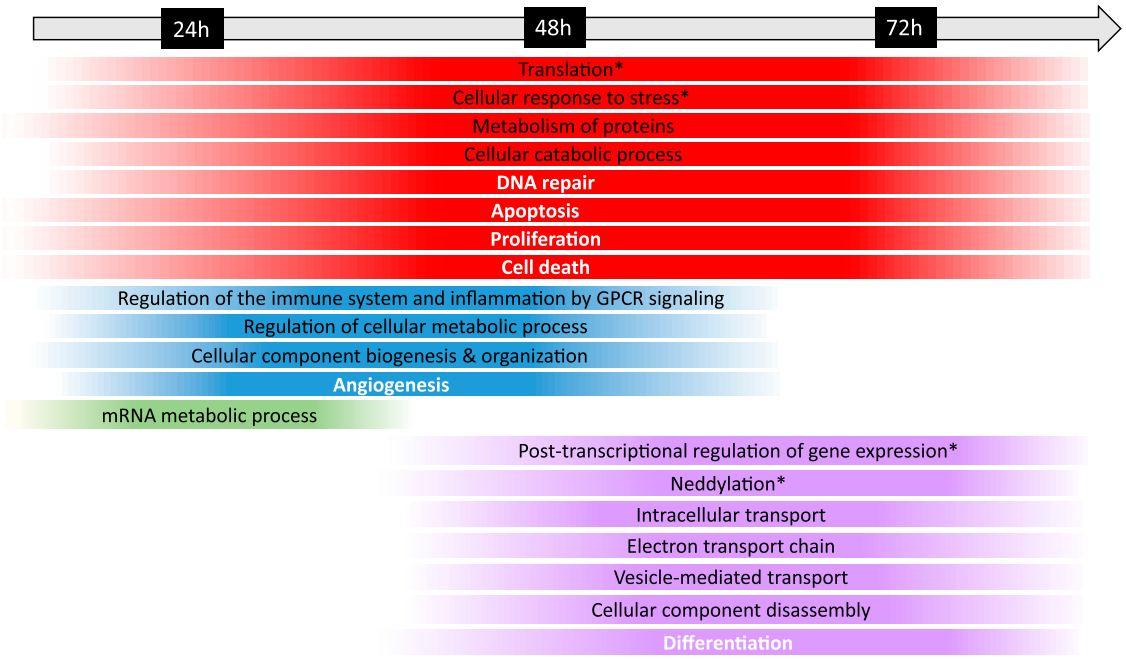

FIGURE 7
Timeline of the biological mechanisms dysregulated in the A549 cells following Fraisinib treatment. The chronological progression of pathway dysregulation, observed by comparing the DMSO control and Fraisinib-treated cells at 24, 48, and 72 h, is shown over time. Under the timeline, each strip spans the first and last treatment time point at which the biological mechanism resulted dysregulated; the strips are color coded as follows: red for biological mechanisms altered at all time points; blue at 24 and 48 h, green only at 24 h, and violet at 48 and 72 h. The colors at the edges of each strip are faded as the data were obtained at definite time points and both the start and the end of each process cannot be exactly defined. General biological mechanisms are written in black, and cancer hallmarks are written in bold white; the biological mechanisms specifically regulated by GARS1 are indicated with an asterisk (retrieved from Cancer Gene Net, https://signor.uniroma2.it/CancerGeneNet/).

2.16 Mass spectrometry analysis

Tandem mass analysis of tryptic digests was performed on an UltiMate 3000 nano chromatography system (Thermo Fisher Scientific) equipped with a PepMap RSL C18 column (75 µm × 150 mm; 2 µm particle size) (Thermo Fisher Scientific) at a flow rate of 250 nL/min and a temperature of 60°C. Mobile phase A was 0.1% v/v formic acid in water, and mobile phase B was 80% ACN, 20% H_2O, and 0.08% v/v formic acid. The following 105 min gradient was selected: 0.0–3.0 min isocratic 2% B; 3.0–7.0 min 7% B; 7.0–65.0 min 30% B; 65.0–78.0 min 45% B; 78.0–83.0 min 80% B; 83.0–85.0 isocratic 80% B; 85.0–85.1 2% B; and finally, 85.1–105.0 isocratic 2% B.

After separation, the flow was sent directly to an EASY-Spray (ESI) source connected to an Exactive Plus Orbitrap Q Mass Spectrometer (both Thermo Fisher Scientific). The software Xcalibur (version 4.1, Thermo Fisher Scientific) was used for operating the UHPLC/HR-MS. MS scans were acquired at a resolution of 70,000 between 200 and 2,000 m/z, with an automatic gain control (AGC) target of 3.0E6 and a maximum injection time (maxIT) of 100 ms. MS/MS spectra were acquired at a resolution of 17,500 and an AGC target of 1.0E5 and a maxIT of 50 ms. A quadrupole isolation window of 2.0 m/z was used, and HCD was performed using 30 normalized collision energy (NCE).

Data from the mass spectrometer in *.raw format was processed with Thermo Fisher Proteome Discoverer® software version 2.4.1.15 using a workflow adapted to LTQ ORBITRAP label-free quantification. The software divides the data analysis into two steps: processing and consensus.

The processing step established the database for PMS identification in MS/MS spectra and concatenated decoy (*Homo sapiens* - sp_canonical v2022-03-02, target FDR strict = 0.01, and target FDR relaxed = 0.05 for proteins, peptides, and PSMs), static modification (Carbamidomethyl/+57.021Da on C), and dynamic modifications (oxidation/+15.995 Da (M); Phospho/+79.966 Da (S, T, Y)), as well as identification engines (MS Amanda 2.0 (Dorfer et al., 2014)) Sequest HT® and tolerances (precursor mass tolerance = 10 ppm and fragment mass tolerance = 0.0 2Da).

In the consensus step, precursor abundance was calculated by intensity, using unique + razor peptides and considering protein for peptide uniqueness. Peptide normalization (based on total peptide amount, scaling on all average), peptide filters (high confidence, minimum length = 6), protein quantification (Unique + Razor, precursor abundance based on intensity), and differential analysis (protein abundance calculation based on summed abundances, pairwise ratio based, and *t*-test background based) were also assessed in this step using PD Precursor Ions Quantifier and IMP-apQuant nodes (https://ms.imp.ac.at/index.php?action=apQuant). The entire workflow is described in Supplementary Table S5. The mass spectrometry proteomics data were deposited in the ProteomeXchange Consortium via the PRIDE (Deutsch et al.,

2020; Perez-Riverol et al., 2022) partner repository with the dataset identifier PXD037653 (see "Data availability").

2.17 Functional network construction and enrichment analysis

As explained earlier, identified proteins were used to perform pairwise ratio-based comparisons between untreated and Fraisinib-treated A549 cells at 24, 48, and 72 h. Among the 4,352 high-FDR master proteins identified from all the spectrum files, the 1,077 (24.7%) significantly dysregulated ones (p-value <0.05) with an expression change of more than two-fold were collected in the following three groups: differentially expressed protein (DEP) 24 h, DEP 48 h, and DEP 72 h (Supplementary Table S1).

The STRING database was queried using the DEP lists to obtain the protein–protein interaction (PPI) data (medium confidence: 0.4) considering text mining, experiments, databases, co-expression, and co-occurrence as setting, while the GARS1 interactome was also constructed using data from the Protein Interaction Network Analysis (PINA) database. The functional networks reported in Figure 5 and Supplementary Figure S5 were built using Cytoscape software (v3.9.9), and the topological features, reported in Table 1, were evaluated by the Analyze-Network tool.

Enrichment analysis and the resulting functional group visualization were performed by Cytoscape ClueGO plugin (v.2.5.7) using the following criteria: p-value adjusted using the Bonferroni step down <0.02, Gene Ontology (GO) Biological Process and Reactome Pathways, Min GO level 3, Max GO level 6, and kappa score threshold 0.55.

2.18 Statistical analysis

To assess the significance of Fraisinib effects on cells, paired Student's t-test and one-way ANOVA were performed on values obtained from experimental replicates by comparing treated and untreated (DMSO added) samples. To evaluate the statistical significance in animal model experiments, treated and untreated (DMSO added) samples at each time point were compared by using unpaired Student's t-test.

3 Results

3.1 Fraisinib induces cell cycle arrest and apoptosis through the caspase cascade activation

To unravel the mechanism underlying the cytotoxicity of Fraisinib, the apoptotic activity was evaluated in A549 cells. The activation of apoptosis initiator and executioner caspases (caspase-1, -3, -4, -5, -6, -7, -8, and -9) was evaluated. As shown in Figures 2A, B, Fraisinib treatment significantly increased the percentage of cells having an activated caspase cascade compared to untreated checks and vehicles.

Due to the very low solubility of Fraisinib in the aqueous medium, it was initially dissolved in a small volume of DMSO and diluted to the required concentration with the culture medium (see Materials and methods). Solutions containing the same amount of DMSO but without Fraisinib were used for the sham tests. In both cases, the final concentration of DMSO in the wells was 0.01%. A second negative control was also used that was not treated with either DMSO or Fraisinib. In Figure 2A, the caspase profiles for these differently treated cells are indicated as Fraisinib, DMSO, and control, respectively.

To further study the mechanisms of action of Fraisinib in A549 cancer cells, a Muse™ MultiCaspase Assay Kit (Millipore Merck, Vimodrone MI, Italy) was used to examine the cell cycle arrest ability of Fraisinib (at 10 μM concentration in normoxic conditions). Fraisinib efficiently and significantly increased a percentage of the cell population in the G0/G1 phase compared to the DMSO-treated cells (Figure 2C). These combined results clearly illustrate the capacity of Fraisinib to control cell cycle progression via caspase cascade (Hashimoto et al., 2011). To evaluate the expression levels of several proteins involved in apoptosis, a semi-quantitative analysis of apoptotic proteins in A549 cells treated with 10 μM Fraisinib for 48 h was carried out using a human apoptotic protein array.

In particular, the difference in signal intensities relative to each protein between Fraisinib- and DMSO-treated cells (Supplementary Figures S1A, 1B) was evaluated to determine the differences in relative protein expression across the full array of human apoptotic proteins (Figure 2D).

After evaluating protein levels in treated vs. DMSO cells, only proteins that showed at least 20% up- or downregulation after Fraisinib treatment were considered possible players in the apoptotic process regulated by Fraisinib. Among these, the upregulated BCL-W, BIM, caspase-3, and Caspase-8 and the downregulated XIAP and survivin suggest that the apoptotic pathway is activated by the drug through both the induction of pro-apoptotic proteins and the reduction of proteins acting as apoptosis inhibitors.

Last but not least, Fraisinib treatment did not show toxic effects on the normal lung cells CFBE41o (Figure 2E).

3.2 Fraisinib inhibits the invasive ability of A549 cells

We evaluated the inhibitory effect of Fraisinib on the invasive ability of A549 cells using a Matrigel invasion assay. In line with previous results (Geretto et al., 2018; Ben Toumia et al., 2022), this test was conducted using the IC80 (2.3 μM). Compared to cells treated with DMSO, Fraisinib displayed a marked inhibitory effect against A549 cell invasiveness, decreasing the invasion rate by 57.4% (Figures 2F, G). This *in vitro* assay suggests that Fraisinib may inhibit the metastatic potential of A549 cells.

3.3 Toxicity evaluation

In a previous study, we demonstrated that Fraisinib showed no cytotoxic effect on lymphocytes (peripheral blood mononuclear cells, PBMCs) in the 0.1–300 μM concentration range. *In vivo* studies in mice showed no alterations in behavior or change in

BW after treatment for 72 h at a dose of 50 mg/kg of BW, and no significant changes were detected in transaminases and creatinine serum levels (Ben Toumia et al., 2022).

In this work, to proceed further with the evaluation of toxicity, a group of six mice was treated for 30 days with a higher dose of 125 mg/kg BW three times a week and compared to a control group of six mice. Compared to the previous study, a wider range of physiological parameters was considered. Creatinine, AST, ALT, uric acid, sodium, potassium, chloride, calcium, and total bilirubin were within the norm, while phosphate and phosphatase alkaline were slightly lower, and total bilirubin was slightly higher than in the control group (Figure 3A). No significant changes in hematological and biochemical parameters were detected, and the blood count of RBC, HB, HCT, MCH, MCHC, VGM, WBC, LYM, NEU, EOS, MON, and BASO were in the norm, with PLT lower than in the control (Figure 3B). Overall, these results confirm that the drug should be well tolerated if used for cancer treatment.

3.4 Anti-tumor potential *in vivo*

The anti-tumor effect of Fraisinib was evaluated *in vivo* in immunodeficient CD-1 nude mice (Crl:CD1-Foxn1nu). The tumor was considered to be developed 7 days after injection with the tumor cells. From that point in time, mice in the treatment group (n = 7) were administered a dose of 125 mg/kg BW of Fraisinib three times a week for 24 days. The control group (n = 5) received an equivalent volume of the vehicle mixture. Fraisinib treatment dramatically reduced the size and the weight of tumors from the first week of treatment compared to the control group (Figures 4A–B). Moreover, the data in Figure 4B showing the variation of tumor size as a percentage with respect to time 0 indicate that 10 days from the beginning of the treatment, the control group had a tumor size that was nearly nine-fold larger than in the treated group. Although the Fraisinib effect was evident, pairwise comparisons between the control and treatment groups at each time point did not reveal statistically significant differences, likely due to the low number of samples. This is due to the death of 3/5 control samples. Nevertheless, the statistical analysis of the tumor size in the overall groups over time showed a p-value of 0.03, thus suggesting that the medium values between the different groups were significantly different.

3.5 Target identification: *in silico* protein database screening and ranking

With the aim of identifying the potential target proteins of Fraisinib that could account for its anti-tumoral effect on the A549 cell line, the SPILLO-PBSS software was used (Di Domizio et al., 2014) to screen and rank a large protein database, including the available structural proteomes (Protein Data Bank 55,316 protein 3D structures, June 2020, see Materials and methods) of three different organisms, namely, *Homo sapiens*, *Mus musculus*, and *Rattus norvegicus*. This analysis generated the plot in Figure 5A, where points correspond to proteins ranked in descending order based on the greatest similarity between the reference binding site (RBS) and the best potential binding site (PBS) identified within each protein 3D structure. Interestingly, the non-linearity of the curve highlights the presence of a minority of proteins with scores higher than all the others, corresponding to the potential targets of Fraisinib.

3.6 GARS1 as a potential target for Fraisinib: competitive inhibition hypothesis

A potential binding site for Fraisinib was identified within the catalytic site of the enzyme, where the glycilation of tRNA in the presence of ATP takes place. Notably, GARS1 was identified by SPILLO-PBSS as a possible target of Fraisinib despite the presence of many steric clashes in the PBS, which would have prevented its detection by traditional structure-based methods. Importantly, the PBS turned out to partially overlap the region occupied by glycine and ATP, which in the reported structure was replaced by the isosteric ANP to improve the quality of diffraction data (Qin et al., 2014). We were, thus, able to hypothesize an inhibition of the catalytic activity of GARS1 by Fraisinib (Figures 5D, E) as the possible cause of the experimentally observed biological effects induced by Fraisinib. It cannot be excluded that the possible binding of Fraisinib may make GARS1 less flexible, interfering with its ability to interact with certain components of the neddylation pathway. Overall, these findings prompted us to conduct experiments to test the SPILLO-PBSS-predicted interaction between GARS1 and Fraisinib.

3.7 Effects of Fraisinib on the enzymatic activity of GARS1

Previous reports (Guo et al., 2009) showed that GARS1 catalyzes direct condensation of two ATP molecules to produce diadenosine tetraphosphate (Ap4a) and inorganic pyrophosphate (PPi) (Figure 5C). This reaction can easily be monitored by measuring PPi production by spectrophotometric assays (Upson et al., 1996; Grasso et al., 2015). The spectrophotometric assay was employed to investigate the inhibitory effect of Fraisinib against GARS1 activity. We observed that Fraisinib in the concentration range (0.1–20 μM) inhibited GARS1 activity dose-dependently (Figure 5B). In contrast, an isomer of Fraisinib (FHK563 in Supplementary Figure S2) and another four molecules mimicking diverse portions of this compound (Supplementary Figure S2A) were shown to be ineffective, further corroborating the hypothesis that Fraisinib is a specific and effective inhibitor of the GARS1 (Supplementary Figure S2B).

3.8 Evaluation of the biological role of GARS1 in the A549 cell line treated with Fraisinib

Adopting a multi-proteomic approach, the possible involvement of GARS1 in the regulation of phenotypic alterations that reduced *in vivo* tumorigenicity of A549 cells exposed to Fraisinib over time was evaluated. For this purpose, a differential proteomic analysis followed by the generation of functional networks and

enrichment analysis was performed. Results obtained after including the known GARS1 interactors identified in the A549 cell line were subsequently compared with the previous one (Supplementary Figure S3). These results allowed for the identification of proteins deregulated by the treatment that are part of the interactome of the GARS1 protein.

In detail, a label-free differential proteomics analysis of the A549 cell line treated with 10 μM Fraisinib for 24, 48, and 72 h, compared to a DMSO control (Supplementary Table S1), was performed by mass spectrometry (MS). Among the 4,352 proteins identified, 1,076 (24.7%) were significantly dysregulated (p-value <0.05), with an expression change of more than two-fold. For each single time point analyzed, ~11% of proteins were found altered; of these, 61.7% were downregulated after 24 h and approximately 50% were downregulated after 48 h and 72 h. Fifty-one proteins were altered at each of the three time points analyzed, while about 250 proteins were found altered at one of the time points (Supplementary Figure S4).

Analyzing protein interaction data obtained by the STRING database, three different functional networks were built using Cytoscape (Supplementary Figures S5A, C, E) to show the DEPs induced by Fraisinib treatment at 24, 48, and 72 h, hereafter defined as DEP24 h, DEP48 h, and DEP72 h. The DEP-network analysis results (see Table 1) revealed that ~90% of DEP participated in network construction (node) with an average of ~5 interactions among themselves (average number of neighbors), displaying a good density degree of connections (clustering coefficient ~0.2) and a very low PPI enrichment p-value, indicating that DEP24 h, DEP48 h, and DEP72 h are indeed functionally and biologically connected groups of proteins. In network-based studies, there is increasing evidence demonstrating that it is critical to evaluate a set of genes/proteins based on their context-specificity expression, and it is also necessary to assess their neighbors even if these are non-significantly differentially expressed (Guan et al., 2012; Sonawane et al., 2017). As GARS1 expression was unchanged throughout Fraisinib treatment, we checked for the presence of its interactors in the DEP lists. For this purpose, from the STRING and PINA (Wu et al., 2009) databases, 140 proteins physically and functionally associated with GARS1 were retrieved, and from these, the 91 proteins (Supplementary Table S2) present in the protein list identified by MS were selected in order to build the GARS1 A549-specific interactome (Figure 6). Of note, 12 out of these 91 GARS1 interactors were also DEPs, suggesting that connections between DEP and GARS1 exist. This hypothesis was confirmed by building three merged networks integrating the three DEP lists and GARS1 interactors (Supplementary Figures S5B, D, F). Exploiting the resulting merged networks, newly participating nodes were found (Table 1) associated with a densely interconnected network where the central nodes were mainly GARS1 interactors and GARS1 itself. On measuring the topological features (Table 1), the thus obtained results, confirmed that the merged-network nodes tend to cluster together more efficiently than in DEP networks, indicating a crosstalk between GARS1 interactors and DEPs at all time points of treatment.

In addition, to further evaluate the biological mechanisms underlying Fraisinib treatment, the enrichment analysis of the 91 GARS1 interactors and the DEP24 h, DEP48 h, and DEP72 h was performed using the Cytoscape ClueGO plugin. The results obtained for GARS1 interactors revealed its involvement in regulating not only tRNA amino-acetylation, as expected, but also other cellular functions related to protein and mRNA metabolism (Supplementary Figure S6). Comparing the ClueGO network results linked to the analysis of the three DEP lists with or without GARS1 interactors (Supplementary Tables S1, S2; Supplementary Figures S11–S13) showed an evident improvement in enriched terms for the latter due to the addition of GARS1 interactors to DEP lists (bubble graphs in Supplementary Figures S7–S9), allowing a better characterization of the cellular and functional mechanisms that were dysregulated during treatment with Fraisinib (Figure 7).

At the time points of 24, 48, and 72 h, the dysregulation of distinct pathways mediated by the interactions of GARS1 (Supplementary Table S3) and its neighborhood (i.e., DEP24 h, DEP48 h, and DEP72 h) was observed, and the results are in line with other studies reporting the dependency of ARS functions on cellular expression patterns (Lee et al., 2006; Kwon et al., 2019; Wang and Yang, 2020; Sung et al., 2022).

In particular, the timeline showed a prompt response of mRNA processing at 24 h, leading to post-transcriptional regulation processes occurring over a longer time span, as expected from the succession of events involved in mRNA maturation and functioning (Alpert et al., 2017).

At 24 and 48 h, molecular profiling of the response to Fraisinib treatment showed dysregulated processes related to cellular metabolism, immune response, inflammation, and angiogenesis. At 48 and 72 h, other biological mechanisms involved in the control of cellular fate, such as differentiation and gene expression, showed dysregulation (Figure 7). Interestingly, at these time points, enrichment analysis highlighted neddylation, an important biological process controlling protein function that is involved in cellular activity (Mo et al., 2016) and lung cancer tumorigenesis (Li et al., 2014).

4 Discussion

The modern drug discovery process is still full of hurdles and is becoming increasingly harder every year. Finding a biological system that has not previously been assessed as a therapeutic target is an extraordinary challenge despite the growing number of scientists involved in the field and the large number of novel discoveries. In this context, our group has pioneered the application in the medicinal chemistry of calix[n]pyrroles. Although this class of molecules has been known for over a century (Baeyer, 1886), it is only recently that we proposed their use as possible drug carriers (Cafeo et al., 2013) and, later, as potential drugs (Lappano et al., 2015). More recently, a macrocyclic compound called Fraisinib [*meso*-(p-acetamidophenyl)-calix (Sève and Dumontet, 2005) pyrrole] that can successfully kill cancer cells while inducing very limited (or no) toxicity (Geretto et al., 2018; Ben Toumia et al., 2022) has been synthesized and tested *in vitro*, *ex vivo*, and *in vivo*. The present study demonstrates how Fraisinib is able to drastically reduce the volume and weight of NSCLC tumors within the first week of treatment without inducing severe toxicity in mice (Figures 4A, B). To provide a possible biomolecular interpretation of the experimentally observed biological effects induced by Fraisinib in

the human lung carcinoma A549 cell line, we performed a 3D *in silico* screening on a proteome-wide scale using SPILLO-PBSS software. As subsequently confirmed experimentally, the software succeeded in identifying an inhibitory interaction between Fraisinib and the catalytic site of the GARS1 enzyme, which was predicted as the top-ranked target of Fraisinib out of more than 55,000 protein structures analyzed (Figure 5A). Fraisinib should, therefore, be considered a "first-in-class" compound that can inhibit GARS1 enzymatic functions and, hence, also regulate Ap4A levels in the cells.

NSCLC treatment options and recommendations depend on several factors, including the type and the stage of cancer, the possible side effects induced by the drug(s), and the patient's overall health. The therapeutic options for this tumor include surgery, radiation therapy, chemotherapy, targeted therapy, and immunotherapy. Additionally, chemo-treatments can be administered before and after surgery to lower the risk of tumor recurrence and to help reduce the extent of surgery.

In particular, chemotherapies are based on the use of cytotoxic compounds, and they are based on a regimen that usually consists of a specific number of cycles given over a set period of time. The most popular drugs available for NSCLC are Carboplatin, Cisplatin, Taxotere, Etoposide, and Taxol (Sève and Dumontet, 2005; Derks et al., 2017). These drugs may also damage healthy cells in the body, thus causing unpalatable side effects.

Targeted therapies are focused on blocking specific proteins that are essential to cancer growth and survival, and often, targeted therapies are administered together with conventional chemotherapeutics such as platinum-based drugs. The novel drug reported here to be effective on cancer cell growth could be inserted in the category of target therapy due to the identification of GARS1 as its specific molecular target and, similar to other treatments, we cannot exclude the possibility that it could be suitable to be used in combination with conventional approaches.

In particular, the identification of the Fraisinib target GARS1 is absolutely in accordance with the role of GARS1 in cancerogenesis. As a consequence of GARS1 inhibition, Fraisinib can modulate different biological and molecular pathways related to GARS1 functions in a unique way. The glycyl-tRNA synthetase GARS1 belongs to the aminoacyl-tRNA synthetases (ARSs) enzyme family that plays essential roles in cells, catalyzing the aminoacylation of tRNA substrates by juxtaposing ATP, amino acids, and tRNAs (Figure 5C), and the produced aminoacylated tRNAs are used in protein synthesis by the ribosomes (Cader et al., 2007). In the absence of its aminoacid cognate, glycine, GARS1 produces the metabolite diadenosine tetraphosphate (Ap4A) by the direct condensation of two ATP moieties, releasing pyrophosphate (Guo et al., 2009). Ap4A is produced in response to various environmental and genotoxic stresses. Although its biological role has still not been fully elucidated, Ap4A is reported to possibly be involved in different signaling pathways (Ferguson et al., 2020).

GARS1 emerges prominently in all analyses as the aminoacyl-tRNA synthetase (aaRS) most strongly associated with cancer. This prominence may be attributed to its dual role in facilitating protein synthesis in both the cytosol and mitochondria. In contrast to other ARSs, GARS1 predominantly exhibits gene amplification in various cancer types, while other proteins tend to feature more deletions and mutations rather than amplifications. Furthermore, higher levels of GARS1 mRNA are associated with significantly poorer survival rates in different cancer types, among which is lung adenocarcinoma, thus confirming the pathogenic role of this protein in cancer development.

Notably, prior research has uncovered multiple seemingly unrelated functions for GARS1 beyond its conventional role in protein synthesis. GARS1 appears to play a critical role in the neddylation pathway (Wang et al., 2011), which facilitates the attachment of the ubiquitin-like protein NEDD8 to specific protein substrates (Mo et al., 2016). NEDD8 is a ubiquitin-like protein that participates in post-translational protein modification, a process referred to as neddylation. Neddylation not only controls ubiquitination modifications but also influences a range of biological processes, thus playing a crucial role in the onset and prognosis of lung cancer. In particular, the inhibition of the neddylation pathway exhibited a potent anti-proliferative effect on platinum drug-resistant A549 and H460 cells, and the clinical investigation of protein neddylation inhibition was proposed as a novel strategy for the treatment of Pt-resistant NSCLC (Jazaeri et al., 2013).

Resistance to platinum drugs leads to cancer recurrence and the failure of the therapeutic plan treatment and, therefore, a poor prognosis. The upregulation of the NEDD8-binding enzyme UBE2F is a significant pathway for lung cancer cells to evade platinum-induced apoptosis. Following platinum-based drug treatment, UBE2F, as a substrate, exhibits reduced binding capacity to CUL3, leading to the accumulation of UBE2F. However, the accumulation of UBE2F, in conjunction with RBX2, promotes the neddylation of CUL5, subsequently facilitating the degradation of the substrate NOXA. This results in reduced cellular oxidative stress resistance and diminished cell survival. These findings also suggest that UBE2F could serve as a promising new therapeutic target. From the proteomics analysis on A549 cells, Fraisinib has been shown to be a potential inhibitor of neddylation; therefore, it could, thereby, indirectly suppress UBE2F activity and allow NOXA to further promote apoptosis.

Studies have suggested that GARS1 modulates the cell cycle through its involvement in neddylation, raising the possibility that targeting GARS1 could inhibit cancer, as exemplified by small molecule neddylation inhibitors. Furthermore, bovine GARS1 has been found to enhance mTOR activation by translocating to the nucleus in response to amino acid signaling (Yu et al., 2019). While this activity has yet to be definitively demonstrated in humans, the conservation of the localization signal in human GARS1 implies that mTOR activation through GARS1 could be an advantageous pathway exploited by cancer cells.

Contrary to these previous findings, secreted GARS1 has also been observed to induce apoptosis in tumor cells by binding to K-cadherin on the cell surface and releasing phosphatase 2A (PP2A), resulting in ERK dephosphorylation and apoptosis (Park et al., 2012).

It is noteworthy that there exists a strong correlation between glycine consumption and the expression of the mitochondrial glycine biosynthesis pathway across various cancer cells, suggesting that GARS1's involvement in cancer may also relate to glycine metabolism. Presently, it remains unclear which of these activities prevails in the context of cancer or whether there is a discernible pattern of tissue specificity among them. Nonetheless,

our analyses indicate that GARS1 represents a promising target for multiple cancer types, possibly owing to one or more of these functional roles.

These findings pointed us toward GARS1 as an important factor in the Fraisinib-induced biological effect observed in A549 cells.

Growing evidence supports the role of ARSs in sustaining cancer phenotype and, consequently, makes them promising targets for cancer therapies (Wang and Yang, 2020; Sangha and Kantidakis, 2022; Sung et al., 2022). Multi-omics analysis, evaluating genetic alteration and prognostic value of transcriptional dysregulation, shows GARS1 to have the highest association with cancer out of all the ARSs (Wang et al., 2020), especially for lung adenocarcinoma (Zhang et al., 2021). GARS1 mRNA overexpression, found at the tissue level, has recently been linked to poor prognosis for hepatocellular carcinoma (Wang et al., 2022) and was selected as a urinary protein marker for the diagnosis of urothelial carcinoma (Chen et al., 2021). Although the enzymatic activity of GARS1 is principally involved in the first essential step of protein synthesis, other functions associated with cancer evolution and cellular homeostasis have been described in the last decade (Sung et al., 2022).

Data from differential proteomics and bioinformatics analyses unraveled that Fraisinib, affecting the catalytic activity of GARS1, can modulate different biological and molecular functions involved in antagonizing the tumoral phenotype of NSCLC A549 cells over time. Evaluating the effects of Fraisinib treatment in A549 cells over time, protein metabolism, the cellular catabolic process, and four pathways involved in sustaining the cancerous phenotype (proliferation, apoptosis, DNA repair, and cell death) were altered throughout the treatment (Figure 7; Supplementary Table S4). The relationship between the alterations of these cellular processes and cancer formation mechanisms described for other ARSs (Lee et al., 2006; Wang and Yang, 2020; Sung et al., 2022) indicates that Fraisinib's anti-tumoral activity could depend on GARS1 targeting. In addition, the timeline representing the effects of the drug is consistent with the progression of biological processes, starting from pathways involved in protein expression immediately modulated by the molecule toward more complex processes involving vesicle-mediated pathways such as intracellular trafficking, which are modulated later.

Of note, 145 and 68 DEPs involved in cell cycle and apoptosis regulation, respectively, were found to be modulated by Fraisinib in agreement with the results obtained in cell-based assays, thus allowing the mode of action of the molecule to be better defined and its biological target to be identified. It was also demonstrated that Fraisinib can inhibit the invasive ability of A549 cells. The pathogenetic role of GARS1 in oncology has recently been confirmed by a publication reporting that the silencing of GARS1 expression is effective in counteracting the progression of prostate cancer (Khosh Kish et al., 2023). These data, together with the proven ability of this compound to cross the blood–brain barrier (BBB) (Geretto et al., 2018), suggest that Fraisinib can kill two birds with one stone: targeting the primary tumor and its metastases "in one shot." Taken together, this work suggests that the inhibition of GARS1 expression and/or GARS1 enzymatic activity may be innovative molecular targets for cancer treatment.

5 Conclusion

In this work, we report the beneficial effects of the molecule Fraisinib in counteracting lung tumors in both the A549 human adenocarcinoma cells and an NSCLC mouse model xenografted with this cell line. In addition, the identification of GARS1 as the drug target and the analysis of pathways deregulated by Fraisinib open new perspectives in the search for additional therapeutic adjuvants for this severe cancer.

Data availability statement

The datasets presented in this study can be found in online repositories. The names of the repository/repositories and accession number(s) can be found at: https://www.ebi.ac.uk/pride/archive/, PXD037653.

Ethics statements

Ethical approval was not required for the studies on humans in accordance with the local legislation and institutional requirements because only commercially available established cell lines were used. The animal study was approved by the toxicity experiments on Balb/c mice (23–26 g) and was performed in accordance with the European Communities Council Directive (86/609/EEC; 24 November 1986) regulating the welfare of experimental animals, and the experiments were approved by the Life Sciences and Health Research Ethics Committee (cer-svs) of the Institute of Biotechnology (University of Monastir, Tunisia; ethical approval no. 2019/02/I/CER-SVS/ISBM; 9 January 2019). Tumor growth experiments: Authorization no. 465/2020-PR; pursuant to article 31 of the legislative decree 4 March 2014, n. 26, acquired with prot. 0D183.4 of 10/16/2019 and integration of 30/04/2020, forwarded by IOM Ricerca S.r.l., registered office in Viagrande (CT), Via Penninazzo, 11, for the purposes of carrying out a research project as described in the documentation attached to the application. This study was conducted in accordance with the local legislation and institutional requirements.

Author contributions

IB: validation, writing–original draft, data curation, formal analysis, investigation, and methodology. TB: data curation, formal analysis, investigation, methodology, validation, writing–original draft, supervision, and writing–review and editing. LC-G: Data curation, investigation, methodology, validation, writing–original draft, and visualization. AP: data curation, investigation, methodology, formal analysis, supervision, and writing–review and editing. MP: formal analysis, investigation, methodology, supervision, writing–review and editing, and validation. AD: formal analysis, investigation, methodology, validation, data curation, software, visualization, and writing–original draft. AI: data curation, formal analysis, validation, visualization, writing–original draft, conceptualization, and supervision. SS: data curation, validation, investigation,

methodology, and writing–review and editing. CP: investigation, methodology, validation, and writing–review and editing. SFo: investigation, methodology, formal analysis, and writing–original draft. RG: investigation, methodology, validation, and writing–review and editing. CC: investigation, methodology, writing–review and editing, and formal analysis. DM: formal analysis, investigation, methodology, supervision, validation, visualization, writing–original draft, and writing–review and editing. GG: formal analysis, investigation, methodology, writing–review and editing, validation, and visualization. VL: investigation, methodology, validation, and writing–review and editing. SFi: investigation, methodology, and writing–review and editing. GD: writing–review and editing, conceptualization, funding acquisition, project administration, resources, visualization, and supervision. KT: writing–review and editing, data curation, formal analysis, investigation, methodology, validation. BC: data curation, formal analysis, investigation, methodology, and writing–review and editing. PR: data curation, resources, software, and writing–review and editing. EI: formal analysis, investigation, methodology, validation, and writing–review and editing. GV: data curation, formal analysis, methodology, software, and writing–review and editing. PB: conceptualization, data curation, formal analysis, investigation, methodology, software, supervision, and writing–review and editing. FK: conceptualization, investigation, methodology, writing–original draft, and writing–review and editing. CR: conceptualization, formal analysis, funding acquisition, investigation, project administration, resources, supervision, validation, visualization, writing–original draft, and writing–review and editing.

Funding

The authors declare financial support was received for the research, authorship, and/or publication of this article. GV and EI were partially supported by the Italian Ministry of Health (Fondi 5x1000 2018-2019 to CR). IB was partially supported by an STSM grant from the COST Action CA16231 "European Network on Vaccine Adjuvants." EI was supported by Fondazione Umberto Veronesi.

Acknowledgments

The authors acknowledge the support of the Italian Ministry of Health (Ricerca Corrente). This work was performed within the framework of COST Action CA17104 STRATAGEM "New diagnostic and therapeutic tools against multidrug resistant tumors." In addition, they thank Dr. Nicoletta Pedemonte e Dr. Valeria Tomati (UOC Genetica Medica, IRCCS Istituto Giannina Gaslini) for providing CFBE41o-cells and Dr. Patrizio Castagnola and Dr. Alessandra Forlani (IRCCS Ospedale Policlinico San Martino) for their help in cell cycle evaluation.

Conflict of interest

CR and GD are members of the Advisory Board of GIAM Pharma International S.A.R.L., Monthey (CH).

The remaining authors declare that the research was conducted in the absence of any commercial or financial relationships that could be construed as a potential conflict of interest.

The authors declare that they were editorial board members of Frontiers, at the time of submission. This had no impact on the peer review process and the final decision.

Publisher's note

Supplementary material

The Supplementary Material for this article can be found online at: https://www.frontiersin.org/articles/10.3389/fphar.2023.1258108/full#supplementary-material

References

Allen, W. E., Gale, P. A., Brown, C. T., Lynch, V. M., and Sessler, J. L. (1996). Binding of neutral substrates by calix[4]pyrroles. *J. Am. Chem. Soc.* 118, 12471–12472. doi:10.1021/ja9632217

Alpert, T., Herzel, L., and Neugebauer, K. M. (2017). Perfect timing: splic-ing and transcription rates in living cells. *Wiley Interdiscip. Rev. RNA* 8. doi:10.1002/wrna.1401

Baeyer, A. (1886). Ueber ein Condensations product von Pyrrol mit Aceton. *Ber. Dtsch. Chem. Ges.* 19, 2184–2185. doi:10.1002/cber.188601902121

Ben Toumia, I., Ponassi, M., Barboro, P., Iervasi, E., Var-gas, G. C., Banelli, B., et al. (2022). Two calix[4]pyrroles as potential therapeutics for castration resistant prostate cancer. *Invest. New Drugs* 40, 1185–1193. doi:10.1007/s10637-022-01294-8

Berman, H. M., Westbrook, J., Feng, Z., Gilliland, G., Bhat, T. N., Weissig, H., et al. (2000). The Protein Data Bank. *Nu-cleic Acids Res.* 28, 235–242. doi:10.1093/nar/28.1.235

Blackhall, F. H., Peters, S., Bubendorf, L., Dafni, U., Kerr, K. M., Hager, H., et al. (2014). Prevalence and clinical outcomes for patients with ALK-positive resected stage I to III adenocarcinoma: results from the European Thoracic Oncology Platform Lungscape Project. *J. Clin. Oncol.* 32, 2780–2787. doi:10.1200/JCO.2013.54.5921

Cader, M. Z., Ren, J., James, P. A., Bird, L. E., Talbot, K., and Stam-mers, D. K. (2007). Crystal structure of human wildtype and S581L-mutant glycyl-tRNA synthetase, an enzyme underlying distal spinal muscular atro-phy. *FEBS Lett.* 581, 2959–2964. doi:10.1016/j.febslet.2007.05.046

Cafeo, G., Carbotti, G., Cuzzola, A., Fabbi, M., Ferrini, S., Kohnke, F. H., et al. (2013). Drug delivery with a calixpyrrole--trans-Pt(II) complex. *J. Am. Chem. Soc.* 135, 2544–2551. doi:10.1021/ja307791j

Cafeo, G., Gattuso, G., Kohnke, F. H., Papanikolaou, G., Pro-fumo, A., and Rosano, C. (2014). Host-guest chemistry of aromatic-amide-linked bis- and tris-calix[4]pyrroles with bis-carboxylates and citrate anion. *Chemistry* 20, 1658–1668. doi:10.1002/chem.201303265

Cafeo, G., Kohnke, F. H., Mezzatesta, G., Profumo, A., Rosano, C., Villari, A., et al. (2015). Host-guest chemistry of a bis-calix[4]pyrrole derivative containing a trans/cis-switchable azobenzene unit with several aliphatic bis-carboxylates. *Chem. Eur. J.* 21, 5323–5327. doi:10.1002/chem.201406183

Chen, C. J., Chou, C. Y., Shu, K. H., Chen, H. C., Wang, M. C., Chang, C. C., et al. (2021). Discovery of novel protein biomarkers in urine for diagnosis of urothelial cancer using iTRAQ proteomics. *J. Proteome Res.* 20, 2953–2963. doi:10.1021/acs.jproteome.1c00164

Custelcean, R., Delmau, L. H., Moyer, B. A., Sessler, J. L., Cho, W. S., Gross, D., et al. (2005). Calix[4]pyrrole: an old yet new ion-pair receptor. *Angew. Chem. Int. Ed. Engl.* 44, 2537–2542. doi:10.1002/anie.200462945

Derks, J. L., van Suylen, R. J., Thunnissen, E., den Bakker, M. A., Groen, H. J., Smit, E. F., et al., and PALGA group (2017). Chemotherapy for pulmonary large cell neuroendocrine carcinomas: does the regimen matter? *Eur. Respir. J.* 49 (6), 1601838. Print 2017 Jun. PMID: 28572122. doi:10.1183/13993003.01838-2016

Deutsch, E. W., Bandeira, N., Sharma, V., Perez-Riverol, Y., Carver, J. J., Kundu, D. J., et al. (2020). The ProteomeXchange consortium in 2020: ena-bling 'big data' approaches in proteomics. *Nucleic Acids Res.* 48, D1145-D1152–D1152. doi:10.1093/nar/gkz984

Di Domizio, A., Vitriolo, A., Vistoli, G., and Pedretti, A. (2014). SPILLO-PBSS: detecting hidden binding sites within protein 3D-structures through a flexible structure-based approach. *J. Comput. Chem.* 35, 2005––2017. doi:10.1002/jcc.23714

Dorfer, V., Pichler, P., Stranzl, T., Stadlmann, J., Taus, T., Win-kler, S., et al. (2014). MS Amanda, a universal identification algorithm optimized for high accuracy tandem mass spectra. *J. proteome Res.* 13, 3679–3684. doi:10.1021/pr500202e

Ferguson, F., McLennan, A. G., Urbaniak, M. D., and Jones, N. J. (2020). Copeland Re-evaluation of diadenosine tetraphosphate (Ap4A) from a stress metabolite to *bona fide* secondary messenger. *Front. Mol. Biosci.* 17, 606807. doi:10.3389/fmolb.2020.606807

Ferrari, N., Granata, I., Capaia, M., Piccirillo, M., Guarra-cino, M. R., Venè, R., et al. (2017). Adaptive phenotype drives resistance to androgen deprivation therapy in prostate cancer. *Cell Commun. Signal* 5, 51. doi:10.1186/s12964-017-0206-x

Gale, P. A. (2011). From anion receptors to transporters. *Acc. Chem. Res.* 44, 216–226. doi:10.1021/ar100134p

Gale, P. A., Anzenbacher, P., and Sessler, J. L. (2001). Calixpyrroles II. *Coord. Chem. Rev.* 222, 57–102. doi:10.1016/s0010-8545(01)00346-0

Gale, P. A., Sessler, J. L., Kral, V., and Lynch, V. (1996). Calix[4]pyrroles: old yet new anion-binding agents. *J. Am. Chem. Soc.* 118, 5140–5141. doi:10.1021/ja960307r

Geretto, M., Ponassi, M., Casale, M., Pulliero, A., Cafeo, G., Malagreca, F., et al. (2018). A novel calix[4]pyrrole derivative as a potential anti-cancer agent that forms genotoxic adducts with DNA. *Sci. Rep.* 8, 11075. doi:10.1038/s41598-018-29314-9

Giatti, S., Di Domizio, A., Diviccaro, S., Falvo, E., Caruso, D., Contini, A., et al. (2021). Three-dimensional proteome-wide scale screening for the 5-alpha reductase inhibitor Finasteride: identification of a novel off-target. *J. Med. Chem.* 64, 4553–4566. doi:10.1021/acs.jmedchem.0c02039

Götz, K. H., Mex, M., Stuber, K., Offensperger, F., Scheffner, M., and Marx, A. (2019). Formation of the alarmones diadenosine triphosphate and tetraphosphate by ubiquitin- and ubiquitin-like-activating enzymes. *Cell Chem. Biol.* 26, 1535–1543. doi:10.1016/j.chembiol.2019.08.004

Grasso, G., Lanza, V., Malgieri, G., Fattorusso, R., Pietropao-lo, A., Rizzarelli, E., et al. (2015). The insulin degrading enzyme activates ubiquitin and promotes the formation of K48 and K63 diubiquitin. *Chem. Commun. (Camb).* 51, 15724–15727. doi:10.1039/c5cc06786c

Guan, Y., Gorenshteyn, D., Burmeister, M., Wong, A. K., Schimenti, J. C., Handel, M. A., et al. (2012). Tis-sue-Specific functional networks for prioritizing phenotype and disease genes. *PLOS Comput. Biol.* 8, e1002694. doi:10.1371/journal.pcbi.1002694

Guo, R. T., Chong, Y. E., Guo, M., and Yang, X. L. (2009). Crystal structures and biochemical analyses suggest a unique mechanism and role for human glycyl-tRNA synthetase in Ap4A homeostasis. *J. Biol. Chem.* 284, 28968–28976. doi:10.1074/jbc.M109.030692

Hashimoto, T., Kikkawa, U., and Kamada, S. (2011). Contribution of caspase(s) to the cell cycle regulation at mitotic phase. *PLoS One* 6, e18449. doi:10.1371/journal.pone.0018449

Jazaeri, A. A., Shibata, E., Park, J., Bryant, J. L., Conaway, M. R., Modesitt, S. C., et al. (2013). Overcoming platinum resistance in preclinical models of ovarian cancer using the neddylation inhibitor MLN4924. *Mol. Cancer Ther.* 12, 1958–1967. doi:10.1158/1535-7163.MCT-12-1028

Khosh Kish, E., Gamallat, Y., Choudhry, M., Ghosh, S., Seyedi, S., and Bismar, T. A. (2023). Glycyl-tRNA synthetase (GARS) expression is associat-ed with prostate cancer progression and its inhibition decreases migration, and invasion *in vitro*. *Int. J. Mol. Sci.* 24 (5), 4260. doi:10.3390/ijms24054260

Kwon, N. H., Fox, P. L., and Kim, S. (2019). Aminoacyl-tRNA synthetases as therapeutic targets. *Nat. Rev. Drug Discov.* 18, 629–650. doi:10.1038/s41573-019-0026-3

Lappano, R., Rosano, C., Pisano, A., Santolla, M. F., De Francesco, E. M., De Marco, P., et al. (2015). A calixpyrrole derivative acts as an antagonist to GPER, a G-protein coupled receptor: mechanisms and models. *Dis. Model Mech.* 8, 1237–1246. doi:10.1242/dmm.021071

Lee, K. A., Means, G. D., and Patterson, S. D. (2006). Phosphoproteomics: challenges and opportunities. *Curr. Proteomics* 3, 249–257. doi:10.2174/157016406780655559

Li, L., Wang, M., Yu, G., Chen, P., Li, H., Wei, D., et al. (2014). Overactivated neddylation pathway as a therapeutic target in lung cancer. *J. Natl. Cancer Inst.* 106 (6), dju083. doi:10.1093/jnci/dju083

Malacrida, A., Di Domizio, A., Bentivegna, A., Cislaghi, G., Messuti, E., Tabano, S. M., et al. (2022). MV1035 overcomes temozolomide resistance in patient-derived glioblastoma stem cell lines. *Biology* 11, 70. doi:10.3390/biology11010070

Małgorzata Juszczak, A, Katarzyna Walczak, B, Joanna Matysiak, C, MartaLemieszek, KA, Ewa Langner, A. B, MonikaKarpińska, MD, et al. (2016). New derivative of 2-(2,4-dihydroxyphenyl)thieno-1,3-thiazin-4-one (BChTT) elicits antiproliferative effect via p38-mediated cell cycle arrest in cancer cells. *Bioorg Med. Chem.* 24 (6), 1356–1361. doi:10.1016/j.bmc.2016.02.009

Mo, Z., Zhang, Q., Liu, Z., Lauer, J., Shi, Y., Sun, L., et al. (2016). Neddylation requires glycyl-tRNA synthetase to protect acti-vated E2. *Nat. Struct. Mol. Biol.* 23, 730–737. doi:10.1038/nsmb.3250

Park, M. C., Kang, T., Jin, D., Han, J. M., Kim, S. B., Park, Y. J., et al. (2012). Secreted human glycyl-tRNA synthetase implicated in defense against ERK-activated tumorigenesis. *Proc. Natl. Acad. Sci. U. S. A.* 109, E640–E647. doi:10.1073/pnas.1200194109

Parodi, F., Carosio, R., Ragusa, M., Di Pietro, C., Maugeri, M., Barbagallo, D., et al. (2016). Epigenetic dysregulation in neuroblastoma: a tale of miRNAs and DNA methylation. *Biochim. Biophys. Acta* 1859, 1502–1514. doi:10.1016/j.bbagrm.2016.10.006

Perez-Riverol, Y., Bai, J., Bandla, C., Hewapathirana, S., Gar-cía-Seisdedos, D., Kamatchinathan, S., et al. (2022). The PRIDE database resources in 2022: a Hub for mass spectrome-try-based proteomics evidences. *Nucleic Acids Res.* 50, D543–D552. doi:10.1093/nar/gkab1038

Qin, X., Hao, Z., Tian, Q., Zhang, Z., Zhou, C., and Xie, W. (2014). Cocrystal structures of glycyl-tRNA synthetase in complex with tRNA suggest multiple conformational states in glycylation. *J. Biol. Chem.* 289, 20359–20369. doi:10.1074/jbc.M114.557249

Reck, M., Popat, S., Reinmuth, N., De Ruysscher, D., Kerr, K. M., and Peters, S. (2014). Metastatic non-small-cell lung cancer (NSCLC): ESMO Clini-cal Practice Guidelines for diagnosis, treatment and follow-up. *Ann. Oncol.* 25 (Suppl. 3), 27–39. doi:10.1093/annonc/mdu199

Reck, M., and Rabe, K. F. (2017). Precision diagnosis and treatment for advanced non-small-cell lung cancer. *N. Engl. J. Med.* 377, 849–861. doi:10.1056/NEJMra1703413

Saar, M., Lavogina, D., Lust, H., Tamm, H., and Jaal, J. (2023). Immune checkpoint inhibitors modulate the cytotoxic effect of chemotherapy in lung adenocarcinoma cells. *Oncol. Lett.* 25 (4), 152. doi:10.3892/ol.2023.13738

Sangha, A. K., and Kantidakis, T. (2022). The aminoacyl-tRNA synthe-tase and tRNA expression levels are deregulated in cancer and correlate independently with patient survival. *Curr. Issues Mol. Biol.* 44, 3001–3019. doi:10.3390/cimb44070207

Sève, P., and Dumontet, C. (2005). Chemoresistance in non-small cell lung cancer. *Curr. Med. Chem. Anticancer Agents* 5 (1), 73–88. doi:10.2174/1568011053352604

Sonawane, A. R., Platig, J., Fagny, M., Chen, C. Y., Paulson, J. N., Lopes-Ramos, C. M., et al. (2017). Understanding tissue-specific gene regulation. *Cell Rep.* 21, 1077–1088. doi:10.1016/j.celrep.2017.10.001

Steuer, C. E., and Ramalingam, S. S. (2014). ALK-positive non-small cell lung cancer: mechanisms of resistance and emerging treatment options. *Cancer120* 120, 2392–2402. doi:10.1002/cncr.28597

Sung, H., Ferlay, J., Siegel, R. L., Laversanne, M., Soerjomata-ram, I., Jemal, A., et al. (2021). Global cancer statistics 2020: GLOBOCAN estimates of incidence and mortality worldwide for 36 cancers in 185 countries. *CA Cancer J. Clin.* 71, 209–249. doi:10.3322/caac.21660

Sung, Y., Yoon, I., Han, J. M., and Kim, S. (2022). Functional and pathologic association of aminoacyl-tRNA synthetases with cancer. *Exp. Mol. Med.* 54, 553–566. doi:10.1038/s12276-022-00765-5

Upson, R. H., Haugland, R. P., Malekzadeh, M. N., and Haugland, R. P. (1996). A spectrophotometric method to measure enzymatic activity in reactions that generate inorganic pyrophosphate. *Anal. Biochem.* 243, 41–45. doi:10.1006/abio.1996.0479

Wang, G., Reed, E., and Li, Q. Q. (2004). Molecular basis of cellular response to cisplatin chemotherapy in non-small cell lung cancer (Review). *On-col Rep.* 12, 955–965. doi:10.3892/or.12.5.955

Wang, J., Vallee, I., Dutta, A., Wang, Y., Mo, Z., Liu, Z., et al. (2020). Multi-omics database analysis of aminoacyl-tRNA synthetases in cancer. *Genes* 11, 1384. doi:10.3390/genes11111384

Wang, J., Yang, B., Wang, D., Han, R., Bi, Z., and Lin, L. (2022). GARS is implicated in poor survival and immune infiltration of hepatocellular car-cinoma. *Cell Signal* 94, 110302. doi:10.1016/j.cellsig.2022.110302

Wang, J., and Yang, X. L. (2020). Novel functions of cytoplasmic amino-acyl-tRNA synthetases shaping the hallmarks of cancer. *Enzymes* 48, 397–423. doi:10.1016/bs.enz.2020.06.005

Wang, M., Medeiros, B. C., Erba, H. P., DeAngelo, D. J., Giles, F. J., and Swords, R. T. (2011). Targeting protein neddylation: a novel therapeutic strategy for the treatment of cancer. *Expert Opin. Ther. Targets* 15, 253–264. doi:10.1517/14728222.2011.550877

Wood, S. L., Pernemalm, M., Crosbie, P. A., and Whetton, A. D. (2015). Mo-lecular histology of lung cancer: from targets to treatments. *Cancer Treat. Rev.* 41, 361–375. doi:10.1016/j.ctrv.2015.02.008

Wu, J., Savooji, J., and Liu, D. (2016). Second- and third-generation ALK inhibitors for non-small cell lung cancer. *J. Hematol. Oncol.* 9, 19. doi:10.1186/s13045-016-0251-8

Wu, J., Vallenius, T., Ovaska, K., Westermarck, J., Mäkelä, T. P., and Hautaniemi, S. (2009). Integrated network analysis platform for protein-protein interactions. *Nat. Methods* 6, 75–77. doi:10.1038/nmeth.1282

Yu, M., Luo, C., Huang, X., Chen, D., Li, S., Qi, H., et al. (2019). Amino acids stimulate glycyl-tRNA synthetase nuclear localization for mammalian target of rapamycin expression in bovine mammary epithelial cells. *J. Cell. Physiol.* 234, 7608–7621. doi:10.1002/jcp.27523

Zhang, X., Dong, W., Zhang, J., Liu, W., Yin, J., Shi, D., et al. (2021). A novel mitochondrial-related nuclear gene signature predicts over-all survival of lung adenocarcinoma patients. *Front. Cell Dev. Biol.* 9, 740487. doi:10.3389/fcell.2021.740487

frontiers | Frontiers in Pharmacology

TYPE Original Research
PUBLISHED 11 January 2024
DOI 10.3389/fphar.2023.1275558

OPEN ACCESS

EDITED BY
Vanessa Souza-Mello,
Rio de Janeiro State University, Brazil

REVIEWED BY
Vineet Mahajan,
University of Pittsburgh, United States
Yucong Xue,
Hebei University of Chinese Medicine, China
Wei Wang,
Jiangxi Provincial People's Hospital, China

*CORRESPONDENCE
Xi Chu,
chux2014@126.com
Zhenqing Sun,
szqszs356299@126.com
Li Chu,
chuli0614@126.com

†These authors have contributed equally to this work and share first authorship

RECEIVED 10 August 2023
ACCEPTED 15 December 2023
PUBLISHED 11 January 2024

CITATION
Qi J, Li H, Yang Y, Sun X, Wang J, Han X, Chu X, Sun Z and Chu L (2024), Mechanistic insights into the ameliorative effects of hypoxia-induced myocardial injury by *Corydalis yanhusuo* total alkaloids: based on network pharmacology and experiment verification.
Front. Pharmacol. 14:1275558.
doi: 10.3389/fphar.2023.1275558

Mechanistic insights into the ameliorative effects of hypoxia-induced myocardial injury by *Corydalis yanhusuo* total alkaloids: based on network pharmacology and experiment verification

Jiaying Qi[1†], Haoying Li[1†], Yakun Yang[1], Xiaoqi Sun[1], Jianxin Wang[1], Xue Han[1], Xi Chu[2*], Zhenqing Sun[3*] and Li Chu[1*]

[1]School of Pharmacy, Hebei University of Chinese Medicine, Shijiazhuang, Hebei, China, [2]The Fourth Hospital of Hebei Medical University, Shijiazhuang, Hebei, China, [3]Qingdao Hiser Hospital Affiliated of Qingdao University (Qingdao Traditional Chinese Medicine Hospital), Qingdao, Shandong, China

Introduction: *Corydalis yanhusuo* total alkaloids (CYTA) are the primary active ingredients in *yanhusuo*, known for their analgesic and cardioprotective effects. However, the mechanisms underlying the treatment of Myocardial ischemia (MI) with CYTA have not been reported. The purpose of this study was to explore the protective effect of CYTA on MI and its related mechanisms.

Methods: A network pharmacology was employed to shed light on the targets and mechanisms of CYTA's action on MI. The protective effect of CYTA against hypoxia damage was evaluated in H9c2 cells. Furthermore, the effects of CYTA on L-type Ca^{2+} current (I_{Ca-L}), contractile force, and Ca^{2+} transient in cardiomyocytes isolated from rats were investigated using the patch clamp technique and IonOptix system. The network pharmacology revealed that CYTA could regulate oxidative stress, apoptosis, and calcium signaling. Cellular experiments demonstrated that CYTA decreased levels of CK, LDH, and MDA, as well as ROS production and Ca^{2+} concentration. Additionally, CYTA improved apoptosis and increased the activities of SOD, CAT, and GSH-Px, along with the levels of ATP and Ca^{2+}-ATPase content and mitochondrial membrane potential. Moreover, CYTA inhibited I_{Ca-L}, cell contraction, and Ca^{2+} transient in cardiomyocytes.

Results: These findings suggest that CYTA has a protective effect on MI by inhibiting oxidative stress, mitochondrial damage, apoptosis and Ca^{2+} overload.

Discussion: The results prove that CYTA might be a potential natural compound in the field of MI treatment, and also provide a new scientific basis for the its utilization.

KEYWORDS

***Corydalis yanhusuo* total alkaloids, myocardial ischemia, network pharmacology, apoptosis, oxidative stress, L-type Ca^{2+} currents**

1 Introduction

Ischemic heart disease (IHD) is a serious cardiovascular disease that significantly threatens human health (Liu et al., 2021). In China, the incidence of IHD has been increasing yearly due to changes in lifestyle, dietary habits, an aging population, and other factors. It has now become the second leading cause of death in our population (Wong et al., 2013; Li and Zhang, 2022). Consequently, research on the prevention and treatment of IHD has garnered considerable attention. Currently, various clinical treatment methods are available for IHD, with drug treatment occupying an irreplaceable position. Western medicine has demonstrated remarkable efficacy in treating IHD and is widely used in clinical practice. However, some patients face limitations in its use due to contraindications, adverse drug reactions, and potential toxicity and side effects associated with long-term or combined medication. Therefore, the quest for safe and effective proprietary Chinese medicine for preventing and treating IHD has emerged as a crucial area of medical research (Yang et al., 2019).

The heart, the organ with the highest oxygen utilization and myocardial function demands in the body, is particularly susceptible to myocardial ischemia (MI). During MI, there is limited blood flow supply and an imbalance in oxygen delivery, resulting in severe myocardial hypoxia (Levraut et al., 2003). As such, MI is closely associated with hypoxia (Jin et al., 2023). The primary mechanisms underlying MI-induced damage to cell membranes and mitochondria involve the elevation of reactive oxygen species (ROS) due to hypoxia, intracellular Ca^{2+} overload, and impairment of mitochondrial energy synthesis. Mitochondrial damage serves as both a victim of hypoxia and an initiator of subsequent damage (Chang et al., 2023). The existence of Ca^{2+} is crucial, which is mainly reflected in not only maintaining the normal function of cells, but also participating in cell signal transduction, protein expression and degradation, myocardial contraction, relaxation and other processes (Xue et al., 2021). MI leads to increased permeability of myocardial cell membranes to ions, triggering an influx of Ca^{2+} and causing intracellular Ca^{2+} overload. Consequently, this inhibits mitochondrial respiratory function and induces lysosomal damage and hydrolase release, thereby exacerbating the cellular injury. During MI, mitochondrial oxidative phosphorylation is hindered, impairing ATP synthesis. In severe cases, mitochondrial swelling, crag disintegration, membrane fragmentation, and matrix spillover occur, resulting in irreversible damage (Nunnari and Suomalainen, 2012; Zorov et al., 2014). In addition, Ca^{2+} overload can also increase cell contractility, which in turn induces cardiac hypertrophy and apoptosis (Xue et al., 2021). Therefore, exploring the specific pathogenesis of MI will help to find a more appropriate strategy.

Yanhusuo is derived from the dried tubers of the Papaveraceae plant *Corydalis yanhusuo* and is recognized as a blood activator and pain reliever in traditional Chinese medicine. Its primary active components are alkaloids (Ling et al., 2006; Tian et al., 2020). *Yanhusuo* exhibits analgesic and sedative effects and significant therapeutic effects on coronary heart disease, angina pectoris, arrhythmia, and premature beats (Bi et al., 2021). Importantly, it has low toxic side effects and is suitable for long-term use (Tian et al., 2020). *Yanhusuo* extracts have been shown to contain various alkaloids that inhibit apoptosis, thus improving cardiac function (Ling et al., 2006). Among these alkaloids, tetrahydropalmatine (THP) is a notable active compound found in the total alkaloids of Corydalis yanhusuo. In a myocardial infarction model, THP has demonstrated antioxidant and anti-apoptotic properties, offering myocardial protection (Li and Zhang, 2022). So far, the specific mechanism by which CYTA acts on MI is not fully understood. Therefore, in order to find safer and more effective natural drugs to treat MI, it is essential to elucidate the molecular mechanism of action of CYTA.

The H9c2 cells were isolated from rat ventricular tissue, and despite their inability to contract, they still exhibit the functional characteristics of rat cardiomyocytes, rendering them ideal tools for *in vitro* simulation of cardiovascular disease models (Fang et al., 2018; Vanacore et al., 2018). Meanwhile, $CoCl_2$, a widely employed hypoxia inducer, has been extensively utilized for *in vitro* simulation of hypoxia/ischemia injury (Pecoraro et al., 2018; Han et al., 2022). Referred to the aforementioned theories, we hypothesized that CYTA might have a protective effect against MI. Therefore, in order to investigate the protective mechanism of CYTA against MI, a comprehensive network pharmacology approach was first performed to analyze the key proteins, pathways and mechanisms involved in the treatment of MI by CYTA. To experimentally validate these findings, H9c2 cells were employed as the experimental model, specifically utilizing the $CoCl_2$-induced hypoxia model. Furthermore, the effects of CYTA on L-type Ca^{2+} current ($I_{Ca\text{-}L}$), cell contractility, and Ca^{2+} transients were further investigated using acute isolated rat ventricular myocytes. By delving into the underlying mechanisms, this study aims to offer a more thorough understanding of how CYTA treats MI.

2 Materials and methods

2.1 Network pharmacology analysis

The alkaloid components of *Yanhusuo* were obtained from The Traditional Chinese Medicine Systems Pharmacology Database (TCMSP, https://old.tcmsp-e.com/index.php), along with literature databases. The collection of targets has been completed. The TCMSP database was searched with "*yanhusuo*" as the keyword, and all the alkaloid components were recorded in the results by selecting the classification of "ingredients." Subsequently, the detailed information of each alkaloid was checked, its related targets were recorded, and the duplicate values were removed, and the results were used as CYTA-related targets. The gene names corresponding to all target proteins were standardized using the UniProtKB database (https://www.uniprot.org/). The GeneCards database (https://www.genecards.org/) was searched for relevant targets with the keyword "myocardial ischemia," and all the target results were exported as MI-related genes.

The targets of CYTA and MI were inputted into the online Venn analysis tool (https://bioinfogp.cnb.csic.es/tools/venny/) to identify overlapping targets to be used as anti-MI targets for CYTA. The collected target information was then imported into the STRING database (https://string-db.org/), with the attribute set as *Homo sapiens* and the threshold set to 0.4, resulting in the retrieval of a protein interaction network (PPI) in TSV format. Subsequently, the files were imported into Cytoscape 3.6.1 to construct the PPI

network diagram. The Network Analyzer tool within the software was utilized to analyze the topological parameters of the network interaction graph, such as degree and betweenness centrality (BC), which indicate the degree of correlation between nodes in the network graph. By applying parameter values, key nodes in the network graph were identified, leading to the investigation of CYTA's mechanism on MI. Finally, the intersecting target genes underwent protein molecular function (MF), cell population (CC), biological process (BP), and KEGG analysis, which were performed using Metascape (https://metascape.org/gp/index.html). Throughout the analysis, a confidence level of $p < 0.01$ was employed.

2.2 Drugs and reagents

CYTA (purity ≥90%), purchased from Chengdu Dexter Biotechnology Co., LTD., was synthesized and dissolved in dimethyl sulfoxide (DMSO) as 100 mM stock solutions. It was diluted to a specific concentration when used. Cell Counting Kit-8 (CCK-8) was provided by Beijing Zhuo Man Biotechnology Co. in Beijing, China. Type II collagenase was obtained from Worthington Biochemical in Lakewood, United States. Isoprenaline (ISO) and verapamil (VER) were supplied by Hefeng Pharmaceutical Co. in Shanghai, China. Unlabeled reagents of analytical purity were obtained from Sigma Chemical Co. in Missouri, United States. All experiment kits, including CK (catalog: A0321-1), LDH (catalog: A020-1-2), SOD (catalog: A001-3-2), CAT (catalog: A007-1), MDA (catalog: A020-1-2), GSH-Px (catalog: A005-1-2), ATP (catalog: A095-11), Ca^{2+}-ATPase (catalog: A016-1-2), and BCA (catalog: A045-3), were purchased from Jiancheng BioEngineering Institute in Nanjing, China.

2.3 Cell culture and treatment

H9c2 cells (Bluefbio, Shanghai, China; catalog: BFN60804388) were cultured in High-sugar Dulbecco's Modified Eagle Medium (DMEM) (Gibco; Thermo Fisher Scientific, Waltham, United States) supplemented with 10% inactivated fetal bovine serum (FBS) (Gibco; Thermo Fisher Scientific, Waltham, United States) and 100 U/mL penicillin/streptomycin (Leagene Biotechnology; Beijing, China). The incubator maintained a stable temperature (37°C), CO_2 level (5%), pH (7.2–7.4), and high relative humidity (95%). Cells reached 80% confluency or higher after 2–3 days of growth in culture flasks. After washing with Phosphate-buffered saline (PBS) (Solarbio Life Sciences; Beijing, China), the cells were detached using 0.25 g/L trypsin (Leagene Biotechnology; Beijing, China). Cells with appropriate density were uniformly seeded in 96-well plates, 24-well plates, or 6-well plates for subsequent experiments.

2.4 Model establishment and experimental design

H9c2 cells were exposed to various concentrations of $CoCl_2$ (200, 400, 600, 800, and 1,000 μM) for 22 h and different concentrations of CYTA (1, 3, 10, 30, 100, and 300 μg/mL) to assess their impact on cell viability and determine the optimal concentrations of $CoCl_2$ and CYTA. At the end of the treatment, 10 μL of CCK-8 was added to each well to measure the absorbance value. Based on the aforementioned procedure, the optimal pretreatment concentration and time for CYTA were determined as 10 and 30 μg/mL for 4 h, respectively. The optimal concentration of $CoCl_2$ was found to be 800 μM. The experimental groups were categorized as follows: 1) Control (Con); 2) $CoCl_2$; 3) $CoCl_2$ + L-CYTA; 4) $CoCl_2$ + H-CYTA.

2.5 Assessment of biochemical analysis

After the treatment, the supernatant was collected to measure the release of CK and LDH, following the instructions provided with the kit. H9c2 cells were scraped and centrifuged to obtain the cell pellet. The pellet was resuspended in an appropriate amount of PBS and sonicated for fragmentation. The protein concentrations of each cell group were determined using the BCA kit and used for subsequent assays of SOD, MDA, CAT, GSH-Px, ATP, and Ca^{2+}-ATPase, following the instructions provided with the respective kits.

2.6 Assessment of ROS levels

Following the treatment, the medium was aspirated, and H9c2 cells cultured in 24-well plates were washed with PBS. Next, 500 μL of 2,7-dichlorodihydrofluorescein diacetate (DCFH-DA, Cayman Chemical Company, Michigan, United States) was added to each well and incubated for 20 min in a dark environment. Subsequently, the remaining dye was washed off with PBS, and fluorescence images were captured using a fluorescence microscope. The acquired images were analyzed quantitatively using Image-Pro Plus 6.0 software (Media Cybernetics, Inc.).

2.7 Assessment of Ca^{2+}

Following the treatment of H9c2 cells in 24-well plates, the plates were washed with PBS. Subsequently, 500 μL of 10 μmol/L Fluo-3 AM dye (Life Technologies, Carlsbad, United States) was added and incubated for 20 min in a light-free environment. After washing off the excess dye with PBS, fluorescent images were captured using a fluorescence microscope. The acquired images were subjected to quantitative analysis using Image-Pro Plus 6.0 software.

2.8 Assessment of mitochondrial membrane potential

After treating the cells in 24-well plates, 500 μL of Rhodamine 123 (Rh123, Yuanye Biotechnology, Shanghai, China) dye was added to each well. The cells were then incubated at 37°C in the dark for 20 min. Subsequently, the remaining dye in each well was washed off with PBS, and fluorescence images were captured using a fluorescence microscope. The acquired images were subjected to quantitative analysis using Image-Pro Plus 6.0 software.

2.9 Assessment of apoptosis

Following the treatment of cells cultured in 24-well plates, 500 μL of Hoechst-33258 staining solution (Beijing Solarbio Science & Technology, Beijing, China; Catalog: IH0060) at a concentration of 10 μg/mL was added to each well. The cells were then incubated in the dark at 37°C for 20 min. Subsequently, the residual dye in the cells was washed off with PBS. The cells were placed under a fluorescence microscope to capture fluorescence images. Finally, the acquired images were analyzed quantitatively using Image-Pro Plus 6.0 software.

2.10 Experimental animals

Forty male Sprague-Dawley (SD) rats aged 6–8 weeks and weighing 200 ± 20 g were obtained from the Experimental Animal Centre of Hebei Medical University. The rats were housed in a controlled environment with an ambient temperature of 21°C ± 1°C and a humidity level of 40%–60%. Rats were housed under 12/12 h light/dark cycle and up to five animals per cage. They had free access to food and water and were acclimated for 1 week before the experiments. All procedures followed the ethical guidelines for experimental animals set by the Hebei University of Traditional Chinese Medicine (approval number: 2103062). The rats were randomly divided into 2 groups: CON and ISO. To establish the myocardial infarction (MI) model, each rat received subcutaneous injections of ISO for two consecutive days (85 mg/kg/day) (Hosseini et al., 2022; Wahid et al., 2022). Subsequently, cardiomyocytes were acutely isolated from a single rat at a specific time point. This study was carried out following the recommendations of the Declaration of Helsinki. Animal experiments and methods were performed in accordance with the National Institutes of Health Guidelines for the Care and Use of Laboratory Animals.

2.11 Preparation of ventricular cardiomyocytes

The rats were anesthetized by intraperitoneal injection of sodium heparin (500 IU/KG) for 15 min, followed by an intraperitoneal injection of ethyl carbamate (1.0 g/KG). After the anesthesia was completed, the rat's thorax was opened to separate the aorta. The heart was quickly removed and placed in a Ca^{2+}-free Tyrode ice solution, and the cardiac aorta was inserted into the Langendorff device. The Ca^{2+}-free Tyrode solution was injected into the heart for 5 min in a thermostatic device at 37°C. The prepared enzyme solution was then perfused recurrently for 15–20 min to digest the myocardium, followed by rinsing with Ca^{2+}-free Tyrode solution to terminate digestion. Subsequently, the heart was placed in the Kreb's buffer, and the ventricular muscle was quickly torn to yield a final KB suspension of individual ventricular myocytes. This suspension was left to stand for 1 h at 4°C before the remaining procedures were conducted. The optimal time for the cells to be available is 8 h. All solutions used were continuously oxygenated at a perfusion rate of 4 mL/min to ensure a 100% oxygen content. The configuration details of the solutions used are presented in Table 1.

2.12 Electrophysiological recording

A suspension of ventricular myocytes was transferred to the cell recording chamber of the membrane clamp. Once the cells became stable and attached to the bottom of the recording chamber, an external solution of cells was added to suppress any interference from other currents. Cells with intact and clean edges, free from surface particles, clear striations, and at rest, were selected for the experiment. The whole-cell membrane clamp recording method was employed to hold the cells in place. After zeroing the internal and external potential difference, a borosilicate glass electrode (filled with internal solution, resistance 3–5 MΩ) was applied to the cell membrane and then sealed. The recorded streams with a 2 kHz filter were amplified using an Axopatch 200B amplifier (Axon Instruments, Union City, CA, United States) and analyzed using pCLAMP 10.2 software (protocol: pulse waveform of 10 mV, 1 ms; frequency duration of 10 Hz).

2.13 Contractility and Ca^{2+} transient measurement

To assess cardiomyocyte contractility, the cell suspension was gently introduced into the cell bath of the microscope. While the cells settled at the bottom of the bath, a calcium-free solution was perfused through the cells at a rate of 1 mL/min. Subsequently, the cardiomyocytes were stimulated to contract regularly at a frequency of 0.5 Hz (duration 2 ms) using a cell stimulator (MyoPacer, IonOptix), and the cell contractions were continuously recorded without any treatment using the IonOptix Myocardial Assay System (IonOptix, Milton, MA, United States). Following the recordings, the cells were returned to regular solution conditions.

Cardiomyocyte Ca^{2+} transients were recorded by observing changes in the fluorescent indicator. The cardiomyocytes were incubated with the fluorescent Ca^{2+} indicator, fluo2-AM (2 mM), for a duration of 10 min. The cell suspensions were then gently added to the bath, and cell excitation was induced by applying electric field stimulation through a sheet platinum electrode at a frequency of 0.5 Hz and a duration of 2 ms. The light from a 75 W UV xenon lamp was modulated by the electric field stimulation through a 340 or 380 nm filter to reach the ventricular myocytes, causing them to emit 510 nm light. The resulting fluorescence signal was examined using the IonOptix system.

2.14 Data analysis and statistics

The resulting experimental data were subjected to a one-way analysis of variance (ANOVA) followed by Tukey's *post hoc* test using Origin 9.1 software. The results were expressed as mean ± standard error (SEM). A p-value of less than 0.05 was considered statistically significant.

TABLE 1 Method of preparation of the solution.

Solution components (mM)	Enzyme solution	Tyrode's solution	External solution	Internal solution	Kreb's buffer
Hepes free acid (HEPES)	10	10	10	10	10
Glucose	10	10	10		10
$CaCl_2$	0.03	1.8	1.8		
$MgCl_2$	1	1	2		
Taurine	4.4	10			20
NaCl	135	135			
KCl	5.4	5.4			
NaH_2PO_4	0.33	0.33			
Bovine serum albumin	0.5[a]				
Collagenase type II	0.6[a]				
Tetraethylammonium chloride (TEA-Cl)			140	20	
CsCl				120	
Mg-ATP				5	
EGTA				10	1
$MgSO_4$					3
KCl					40
KH_2PO_4					25
KOH					80
Glutamic acid					50

Using NaOH, to adjust the pH of the enzyme solution and normal Tyrode's solution to 7.4. In contrast to normal Tyrode's solution, Ca^{2+}-free Tyrode's solution contains no $CaCl_2$ and taurine. Using CsOH, and KOH, the pH of the inteikrnal and external solutions and Kreb's buffer solutions were adjusted to 7.3 and 7.2, respectively.
[a]Unit in mg/mL.

TABLE 2 OB, DL values and molecule IDs for the 46 active ingredients of CYTA.

Mol ID	Molecule name	OB(%)	DL
MOL004071	Hyndarin	73.94	0.64
MOL004195	CORYDALINE	65.84	0.68
MOL000785	palmatine	64.6	0.65
MOL000787	Fumarine	59.26	0.83
MOL002903	(R)-Canadine	55.37	0.77
MOL004230	stylopine	48.25	0.85
MOL004203	Dehydrocorybulbine	46.97	0.63
MOL004205	Dehydrocorydalmine	43.9	0.59
MOL004204	dehydrocorydaline	41.98	0.68
MOL004216	13-methylpalmatrubine	40.97	0.63
MOL001454	berberine	36.86	0.78
MOL004209	13-methyldehydrocorydalmine	35.94	0.63
MOL000790	Isocorypalmine	35.77	0.59
MOL001458	coptisine	30.67	0.86

(Continued on following page)

TABLE 2 (*Continued*) OB, DL values and molecule IDs for the 46 active ingredients of CYTA.

Mol ID	Molecule name	OB(%)	DL
MOL004211	Glauvent	29.03	0.61
MOL004193	Clarkeanidine	86.65	0.54
MOL001460	Cryptopin	78.74	0.72
MOL004234	2,3,9,10-tetramethoxy-13-methyl-5,6-dihydroisoquinolino [2,1-b] isoquinolin-8-one	76.77	0.73
MOL000791	bicuculline	69.67	0.88
MOL004191	Capaurine	62.91	0.69
MOL004200	methyl-[2-(3,4,6,7-tetramethoxy-1-phenanthryl)ethyl]amine	61.15	0.44
MOL001463	Dihydrosanguinarine	59.31	0.86
MOL004232	tetrahydroprotopapaverine	57.28	0.33
MOL004226	Pseudoprotopine	53.75	0.83
MOL004196	Corydalmine	52.5	0.59
MOL000793	Bulbocapnine	47.54	0.69
MOL004198	Corynoline	46.06	0.85
MOL004210	(1S,8′R)-6,7-dimethoxy-2-methylspiro [3,4-dihydroisoquinoline-1,7′-6,8-dihydrocyclopenta[g][1,3]benzodioxole]-8′-ol	43.95	0.72
MOL004220	N-methyllaurotetanine	41.62	0.56
MOL004214	isocorybulbine	40.18	0.66
MOL004763	Izoteolin	39.53	0.51
MOL004202	dehydrocavidine	38.99	0.81
MOL004208	demethylcorydalmatine	38.99	0.54
MOL004225	pseudocoptisine	38.97	0.86
MOL004199	Corynoloxine	38.12	0.6
MOL001474	sanguinarine	37.81	0.86
MOL004197	Corydine	37.16	0.55
MOL002670	Cavidine	35.64	0.81
MOL004231	Tetrahydrocorysamine	34.17	0.86
MOL001461	Dihydrochelerythrine	32.73	0.81
MOL000217	(S)-Scoulerine	32.28	0.54
MOL004233	(+)-Thaliporphine	31.87	0.56
MOL004221	norglaucing	30.35	0.56
MOL004224	pontevedrine	30.28	0.71
MOL004290	(−)-alpha-N-methylcanadine	45.06	0.8
MOL004228	saulatine	42.74	0.79

3 Results

3.1 Network pharmacology analysis of potential targets and mechanisms of CYTA against MI

A comprehensive search was conducted on a total of 46 CYTA components using the TCMSP database and relevant literature (Table 2). Figure 1 illustrates the 549 targets associated with each component of CYTA retrieved from the TCMSP database. The MI-related genes were identified from the GeneCards database. Duplicate targets were removed, resulting in a total of 2649 MI-related targets. The Venn diagram (Figure 2A) demonstrates the intersection of potential targets between CYTA and MI, revealing 262 identical genes. To further examine the relationship among these 262 genes, the PPI network (Figure 2B) was generated using Cytoscape 3.6.1. The network represents proteins as nodes and their relationships as connecting lines, where nodes and connectors

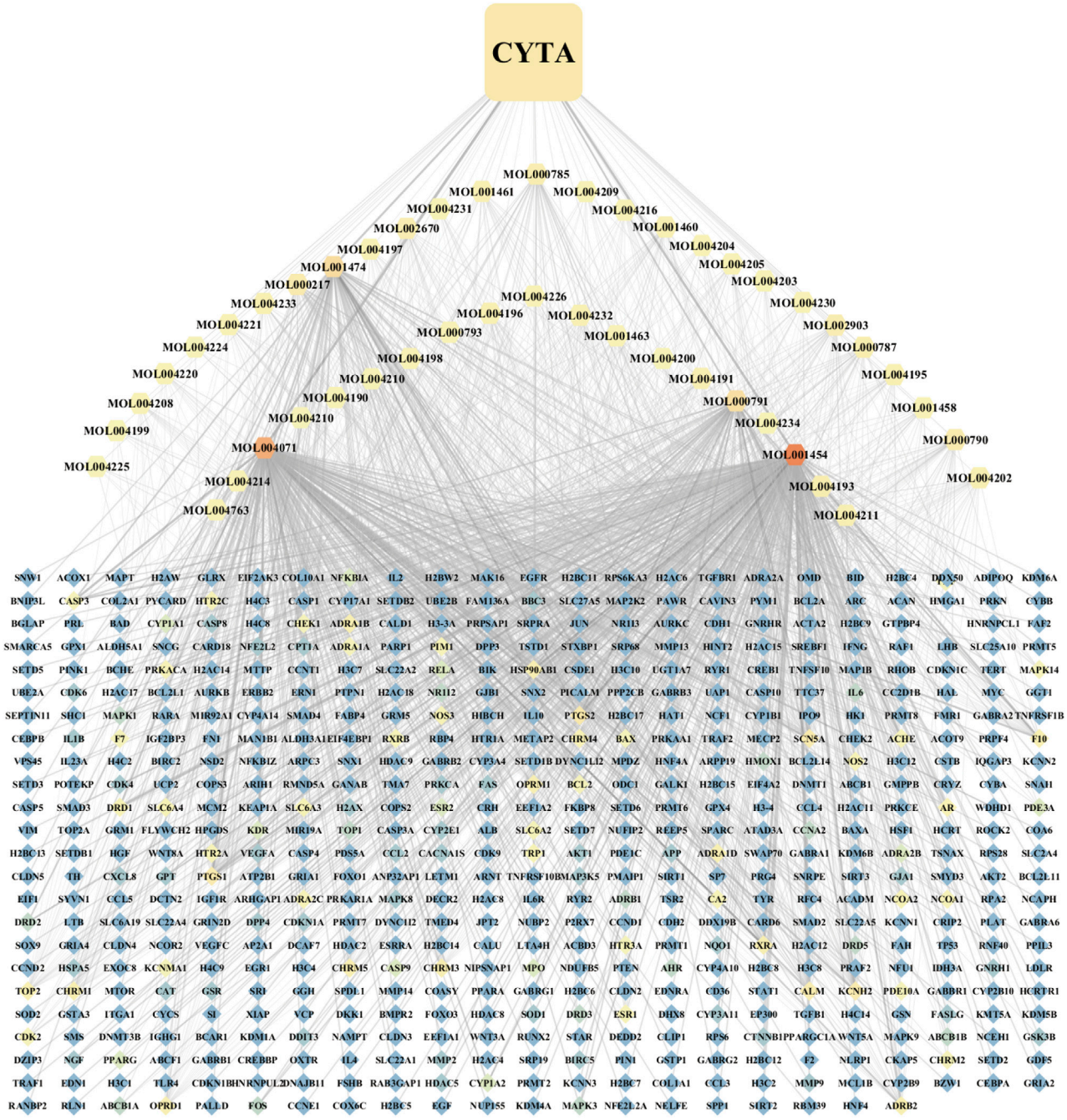

FIGURE 1
Component-target network diagram of CYTA.

withhigh degree and BC values tend to be brighter in color and *vice versa*.

The GO enrichment analysis yielded 185 BP items, 130 CC items, and 108 MF items. The BP analysis highlighted topics such as positive regulation of cell death, response to oxygen levels, regulation of neuron death, and apoptotic signaling pathways. Regarding CC, the targets were primarily associated with the cell membrane, nucleus, mitochondria, and endoplasmic reticulum. The MF analysis revealed that the intersecting targets were linked to kinase binding, protein domain-specific binding, and transcription factor binding, as depicted in Figure 3A.

In relation to the KEGG enrichment analysis of CYTA for MI, it identified 174 pathways. Further analysis of these pathways showed a strong association with apoptosis and the calcium signaling pathway. The top 20 results, based on the *p*-value, were selected and presented in a bubble diagram (Figure 3B). The results indicate the involvement of apoptosis, mitochondrial energy metabolism, and oxidative stress in the preventive effects of CYTA against MI. Additionally, based on the

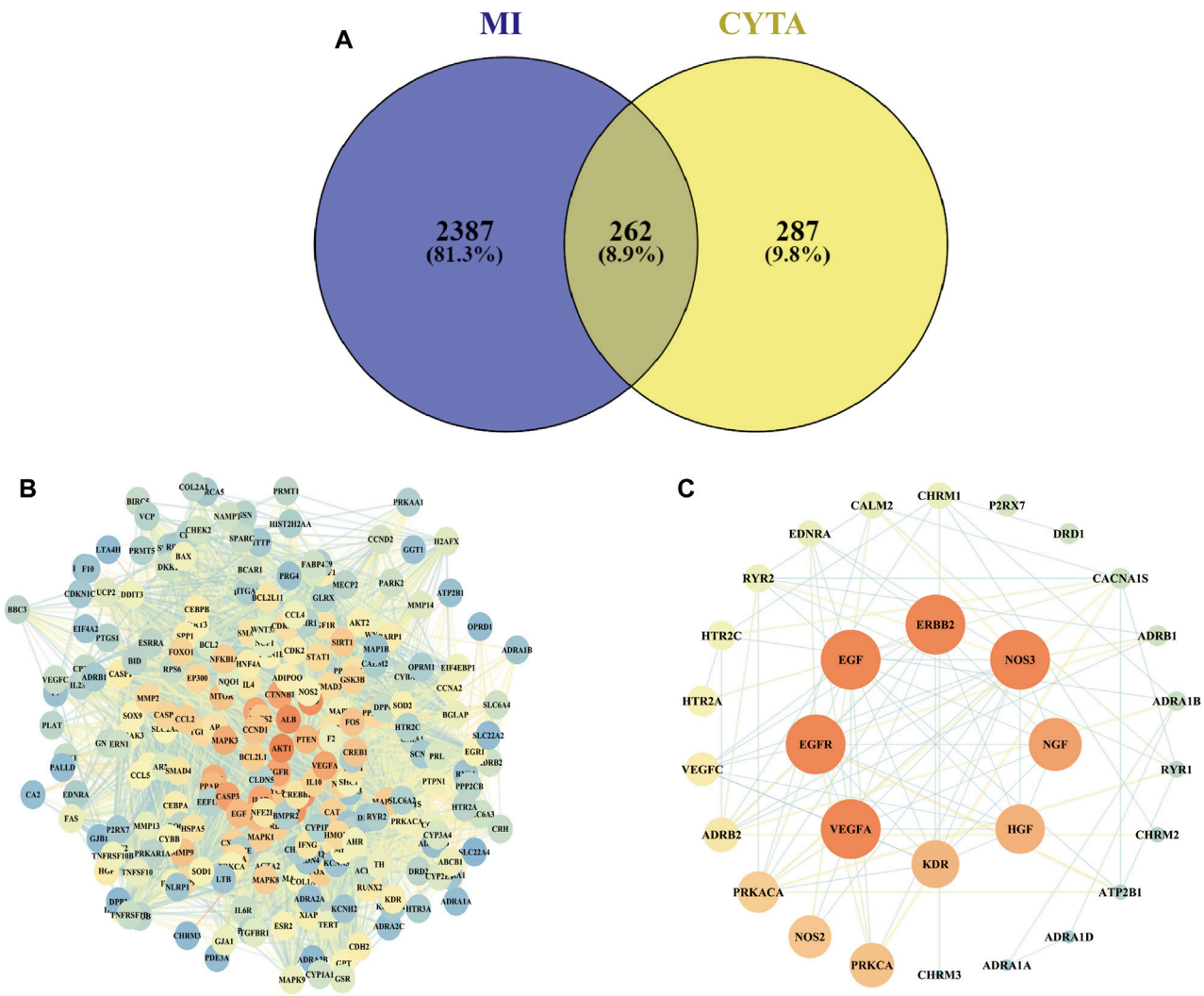

FIGURE 2
Target screening for CYTA against MI **(A)** The number of intersections between CYTA and MI targets. **(B)** PPI network diagram based on CYTA and MI intersection targets. **(C)** The targets are related to the calcium signaling pathway.

KEGG enrichment analysis, numerous targets were found to be closely associated with the calcium signaling pathway. Therefore, we extracted targets associated with the calcium signaling pathway (Figure 2C), where nodes and connecting lines with high degree values and BC tended to be larger and brighter in color, and *vice versa*.

3.2 Effects of different concentrations of CYTA in H9c2 cells viability

According to Figure 4B, concentrations of 1–100 μg/mL of CYTA did not exhibit significant inhibition of normal H9c2 cell proliferation ($p > 0.05$). However, at a 300 μg/mL concentration, an inhibition of normal H9c2 cell proliferation was observed ($p < 0.01$). Furthermore, at a concentration of 30 μg/mL, no inhibition of H9c2 cells was observed from 0 to 36 h ($p > 0.05$, Figure 4C). Based on these findings, dosing concentrations of 10 μg/mL and 30 μg/mL were selected.

3.3 Effect of CYTA in hypoxic H9c2 cells viability

The concentration of $CoCl_2$ that induced hypoxia was determined to be 800 μmol/L, as depicted in Figure 4A. Figure 4D shows that the survival of H9c2 cells was significantly reduced in the $CoCl_2$ group compared to the CON group ($p < 0.01$). However, pretreatment with either 10 or 30 μg/mL CYTA demonstrated a mitigating effect on hypoxic injury ($p < 0.05$ or 0.01).

3.4 Effects of CYTA on CK and LDH levels in hypoxic H9c2 cells

Figures 4E, F demonstrate that the release of CK and LDH into the extracellular medium was significantly elevated in the $CoCl_2$ group compared to the CON group ($p < 0.01$). In contrast, CYTA exhibited the ability to significantly decrease the levels of CK and LDH in the

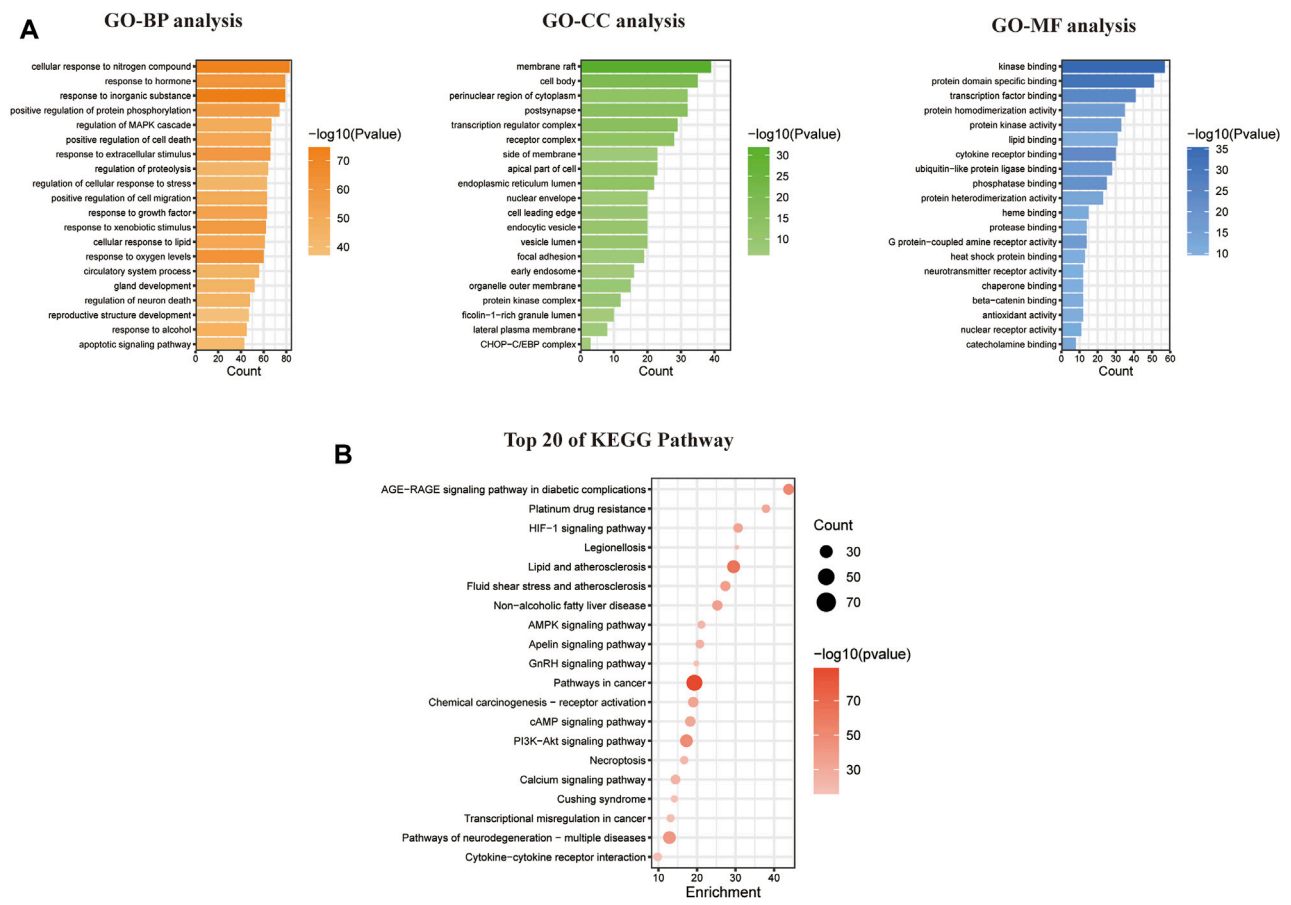

FIGURE 3
Enrichment analysis of GO and KEGG pathways based on CYTA and MI intersection targets. **(A)** GO analysis graphs of potential targets. **(B)** Enrichment analysis of the KEGG pathway for potential targets.

supernatant of hypoxic H9c2 cells ($p < 0.05$ or 0.01), indicating a mitigating effect of CYTA on cell injury.

3.5 Effects of CYTA on ROS levels in hypoxic H9c2 cells

The results obtained from the measurement of ROS can be interpreted such that a higher average fluorescence intensity value corresponds to increased ROS production in the cells. Compared to the normal group, the fluorescence intensity of ROS in H9c2 cells was significantly elevated in the $CoCl_2$ group ($p < 0.01$). However, in both the high and low-dose groups of CYTA, the fluorescence intensity of ROS in H9c2 cells was significantly reduced compared to the $CoCl_2$ group ($p < 0.05$ or 0.01). The results are depicted in Figures 5A, B.

3.6 Effects of CYTA on oxidative stress homeostasis in hypoxic H9c2 cells

As depicted in Figures 5C–F, the activities of SOD, GSH-Px, and CAT were decreased, while the activity of MDA was increased in the $CoCl_2$ group compared to the CON group ($p < 0.01$). Conversely, in the CYTA group, the activities of SOD, GSH-Px, and CAT were increased, and the level of MDA was decreased in the supernatant compared to the $CoCl_2$ group ($p < 0.05$ or 0.01).

3.7 Effects of CYTA on mitochondrial membrane potential in hypoxic H9c2 cells

As shown in Figures 6A, B, damage to the mitochondrial membrane resulted in a decrease in membrane potential. Rh123 fluorescence staining allowed the detection of changes in intracellular mitochondrial membrane potential. Compared to the CON group, the mitochondrial membrane potential of H9c2 cells was significantly reduced after hypoxic injury, and the difference was statistically significant ($p < 0.01$). However, after pretreatment with CYTA, the reduction in mitochondrial membrane potential was significantly improved in H9c2 cells compared to the hypoxic injury group ($p < 0.05$ or 0.01).

Both ATP content and Ca^{2+}-ATPase activity are direct and indirect indicators of mitochondrial function. Treatment with $CoCl_2$ significantly reduced the ATP content and Ca^{2+}-ATPase activity in H9c2 cells ($p < 0.01$). However, pretreatment with CYTA resulted in varying degrees of increased intracellular ATP content and Ca^{2+}-ATPase activity in H9c2 cells ($p < 0.05$ or 0.01) (Figures 6C, D).

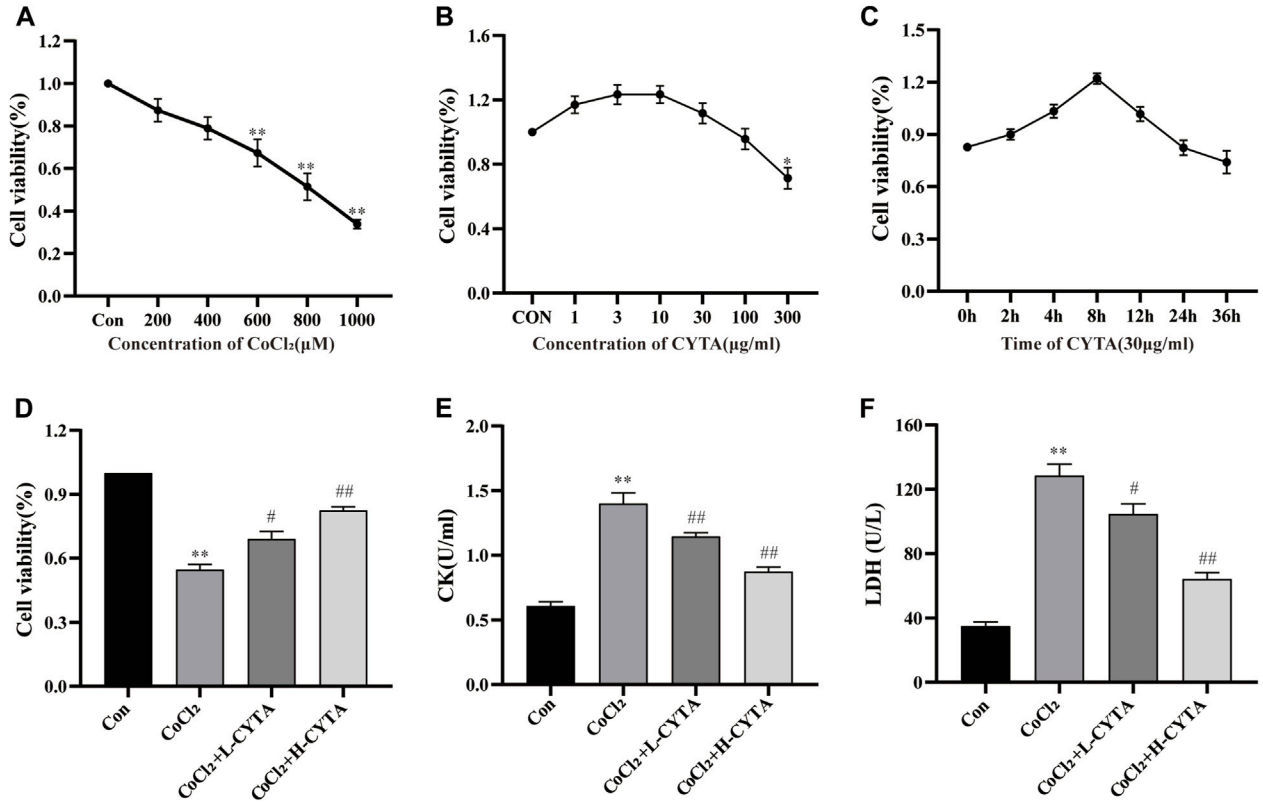

FIGURE 4
Determination of $CoCl_2$ and CYTA concentrations and the protective effects of CYTA on cardiac enzymes in hypoxic H9c2 cells. **(A)** H9c2 cells were incubated with $CoCl_2$ (200–1,000 μM) alone for 22 h **(B)** H9c2 cells were incubated with CYTA (1–300 μg/mL) alone for 24 h **(C)** Cells were incubated with CYTA (30 μg/mL) alone for 0–36 h **(D)** The protective effect of CYTA on H9C2 cells damaged by $CoCl_2$, CYTA was selected at 10 and 30 μg/mL for 4 h, $CoCl_2$ was selected at 800 μM. **(E,F)** The effects of CYTA treatment on LDH and CK levels in $CoCl_2$-induced H9c2 cell damage. Mean ± SEM, n = 3. *p < 0.05, **p < 0.01 versus CON group and #p < 0.05, ##p < 0.01 versus $CoCl_2$ group. Note: L-CYTA: 10 μg/mL and H-CYTA: 30 μg/mL.

3.8 Effects of CYTA on apoptosis in hypoxic H9c2 cells

Under fluorescence microscopy, the CON group showed no obvious apoptotic cells, with nuclei appearing light blue and having low fluorescence. In the $CoCl_2$ group, the nuclei exhibited uneven coloring, and apoptotic cells appeared bright blue with high fluorescence ($p < 0.01$). After CYTA treatment, the number of apoptotic cells gradually decreased (Figure 7A, $p < 0.05$ or 0.01). The apoptotic status of each cell group is depicted in Figure 7B.

3.9 Effects of CYTA on Ca^{2+} content in hypoxic H9c2 cells

The results are depicted in Figure 8. It is evident that $CoCl_2$ significantly increased the cytoplasmic Ca^{2+} content in H9c2 cells ($p < 0.01$), while pretreatment with CYTA significantly attenuated the increase in Ca^{2+} content ($p < 0.01$ or 0.05). These findings suggest that CYTA can regulate and maintain normal Ca^{2+} content in the cytoplasm of cardiomyocytes.

3.10 Verification of $I_{Ca\text{-}L}$

The high sensitivity of T-type Ca^{2+} channels to Ni^{2+} makes $NiCl_2$ a commonly employed specific blocker for T-type Ca^{2+} channels. Furthermore, it exhibits near-complete inhibition of the T-type calcium current while exerting minimal impact on the L-type calcium current (Lee et al., 1999). $NiCl_2$ was used to investigate its effect on the current at a concentration of 100 μM. Interestingly, the current was not inhibited by 100 μM $NiCl_2$, indicating that the recorded current was not a T-type Ca^{2+} current (Figures 9A, B) (Guan et al., 2015). In contrast, 1 μM VER almost completely blocked the current ($p < 0.01$), suggesting that the recorded current was $I_{Ca\text{-}L}$ (Figures 9C, D) (Zhu et al., 2016).

3.11 Inhibition of CYTA on $I_{Ca\text{-}L}$

The results demonstrate that CYTA at a concentration of 100 μg/mL inhibited $I_{Ca\text{-}L}$ in both normal and ischemic rat ventricular myocytes, resulting in inhibition rates of 61.60% ± 1.49% and 50.79% ± 2.26%, respectively ($p < 0.01$). Furthermore, following the administration of CYTA, extracellular fluid was used for washout, and the currents were partially restored to their pre-administration levels. This suggests that the inhibitory effect of CYTA on $I_{Ca\text{-}L}$ is reversible (Figures 10A–F).

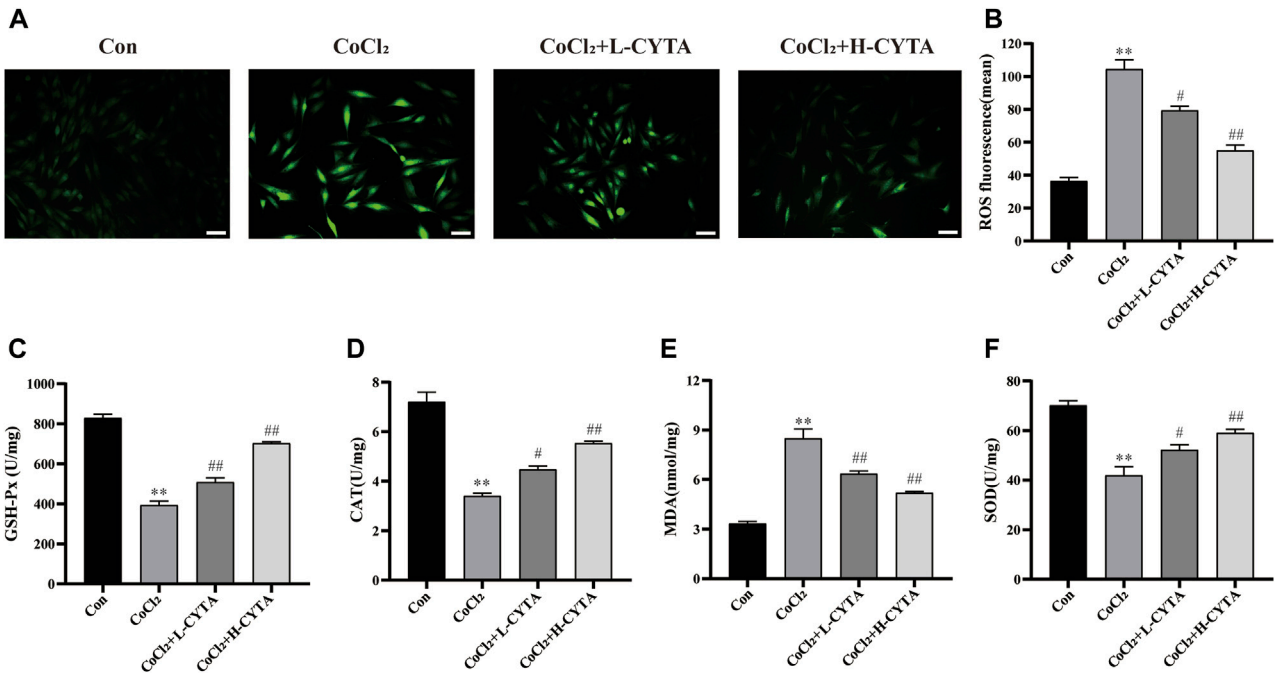

FIGURE 5
Effects of CYTA on intracellular ROS levels and oxidative stress indicators in hypoxic H9c2 cells. **(A)** Intracellular ROS levels observed under fluorescence microscopy (scale bar: 100 μm; magnification: ×200). Intense green fluorescence was displayed when intracellular ROS levels increased. **(B)** Results of the quantitative analysis of the mean fluorescence intensity of ROS. **(C–F)** Effect of CYTA on intracellular GSH-Px, CAT, MDA and SOD levels. Mean ± SEM, $n = 3$ or 6. $^{*}p < 0.05$, $^{**}p < 0.01$ versus CON group and $^{\#}p < 0.05$, $^{\#\#}p < 0.01$ versus $CoCl_2$ group. Note: L-CYTA: 10 μg/mL and H-CYTA: 30 μg/mL.

The results presented in these figures show a sequential increase in the inhibitory effect of CYTA on $I_{Ca\text{-}L}$ at concentrations of 1, 3, 10, 30, 100, and 300 μg/mL, resulting in inhibition rates of 2.12% ± 0.30%, 6.50% ± 0.56%, 14.45% ± 0.89%, 33.01% ± 1.95%, 62.17% ± 1.23%, and 75.65% ± 1.13%, respectively. This indicates a concentration-dependent effect of CYTA on $I_{Ca\text{-}L}$, with a half inhibition rate (IC50) of 43.60 ± 8.61 μg/mL (Figures 10G–I).

3.12 Effects of CYTA on $I_{Ca\text{-}L}$ current-voltage (I-V) curves in ventricular myocytes

Figure 11A shows the effect of CYTA (10, 30 and 100 μg/ml) and VER on the relationship between the I-V curves. As shown in Figure 11B, CYTA shifts the I-V curve in a concentration-dependent manner. At −20 mV, the amplitude of $I_{Ca\text{-}L}$ began to increase. In addition, the reversal potential of $I_{Ca\text{-}L}$ and the I-V curve did not change significantly.

3.13 Effects of CYTA on steady-state activation and inactivation of $I_{Ca\text{-}L}$

The results presented in Figures 11C, D indicate that CYTA at concentrations of 30 and 100 μg/mL did not significantly affect the steady-state activation-deactivation curve of $I_{Ca\text{-}L}$. The calculated values for $V_{1/2}$/slope (k) of the activation curves were −7.29 ± 1.14 mV/5.87 ± 0.99 mV, −9.64 ± 1.22 mV/5.70 ± 1.11 mV, and −10.84 ± 1.14 mV/5.56 ± 1.04 mV for 0, 30, and 100 μg/mL CYTA, respectively. Similarly, the $V_{1/2}$/slope (k) of the inactivation curves were −23.61 ± 0.73 mV/5.40 ± 0.23 mV, −29.25 ± 0.72 mV/3.97 ± 0.24, and −29.89 ± 0.11 mV/5.81 ± 0.69 mV, respectively.

3.14 Effects of CYTA on contractility and temporal parameters

Cell contractility was assessed at CYTA concentrations of 30 and 100 μg/mL, as depicted in Figures 12A, B. Figure 12C demonstrates that these concentrations of CYTA resulted in the inhibition of cell contraction by 25.27% ± 1.55% and 39.83% ± 1.68%, respectively ($p < 0.01$). Notably, the administration of extracellular fluid for washout partially restored cell contraction, indicating a reversible inhibitory effect of CYTA on ventricular myocyte contractility.

The time to 50% peak (Tp) is an important measure of cell contraction or Ca^{2+} elevation, while the time to 50% of baseline (Tr) is crucial for assessing cellular relaxation or Ca^{2+} reabsorption. Figures 12D, E show that both Tp and Tr were significantly lower in the CYTA group compared to the CON group ($p < 0.05$).

3.15 Effects of CYTA on Ca^{2+} transients

Figure 13A illustrates the impact of CYTA (100 μg/mL) on the peak change in Ca^{2+} transients. In Figure 13B, it is evident that a concentration of 100 μg/mL CYTA significantly inhibits the peak Ca^{2+} transient. Furthermore, Figure 13C demonstrates that CYTA at a concentration of 100 μg/mL resulted in a notable inhibition of the peak amplitude of cellular Ca^{2+} transient, with an inhibition rate of 38.48% ± 4.19% ($p < 0.01$).

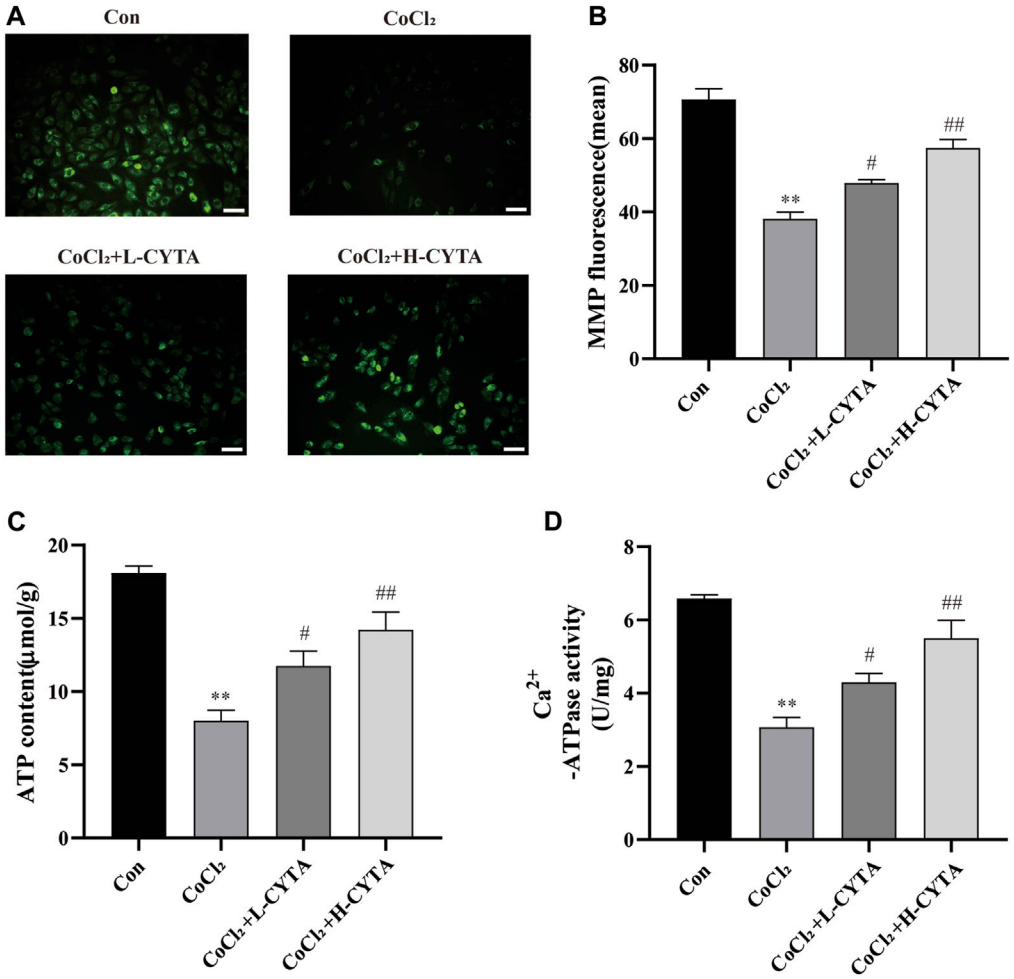

FIGURE 6
Effects of CYTA on MMP in hypoxic H9c2 cells. **(A)** Changes in the MMP of cells observed under fluorescence microscopy (scale bar: 100 μm; magnification: ×200). When the mitochondrial membrane potential was lost, the yellow-green fluorescence intensity within the mitochondria was significantly reduced. **(B)** Results of quantitative analysis of the mean fluorescence intensity of MMP **(C)** ATP content and **(D)** Ca^{2+}-ATPase activity were detected. Mean ± SEM, $n = 6$. $^{*}p < 0.05$, $^{**}p < 0.01$ versus CON group and $^{\#}p < 0.05$, $^{\#\#}p < 0.01$ versus $CoCl_2$ group. Note: L-CYTA: 10 μg/mL and H-CYTA: 30 μg/mL.

4 Discussion

Repeated or prolonged MI leads to non-adaptive remodeling of cardiomyocytes and expansion of extracellular matrix, which ultimately leads to dilation of cardiac chambers and systolic dysfunction, inducing diseases such as coronary heart disease and heart failure. Despite the increasing research on the prevention and treatment of IHD in recent years, IHD maintains a high mortality and morbidity rate. This condition remains a significant burden on individuals and healthcare resources worldwide (Severino et al., 2020). This study first utilized network pharmacology to explore the potential targets of action of CYTA in the treatment of MI, followed by experimental validation with H9c2 cells and acutely isolated ventricular myocytes in rats (Figure 14). Initially, it was demonstrated that CYTA could protect H9c2 cells from hypoxic injury, and the protective mechanism might be related to the inhibition of oxidative stress, apoptosis, and mitochondrial dysfunction. Most importantly, our findings suggest that CYTA safeguards the heart by inhibiting L-type Ca^{2+} channels (LTCCs), which consequently reduces cellular contraction and prevents Ca^{2+} overload.

Yanhusuo is a perennial herb from the poppy family and is commonly used in clinical practice as a traditional Chinese medicine (Li et al., 2022). It has been the subject of various pharmacological studies, which have reported its therapeutic effects on numerous cardiovascular diseases. Bi et al. (2021) used data mining to confirm that the frequency of *yanhusuo* in clinical prescriptions for the treatment of coronary artery disease in Chinese medicine is higher than 60%. In addition, previous studies have shown that *yanhusuo* extract and its constituents such as tetrahydropalmatie have the ability to reduce left ventricular end-diastolic pressure, enhance cardiac ejection function in rats, improve cardiac function, and significantly reduce the size of myocardial infarction, as well as having the ability to mitigate myocardial infarction with antiarrhythmic effects (Ling et al., 2006; Wu et al., 2007; Tian et al., 2020; Han et al., 2022). However, there are no studies exploring the effects of CYTA on LTCCs and contractility of

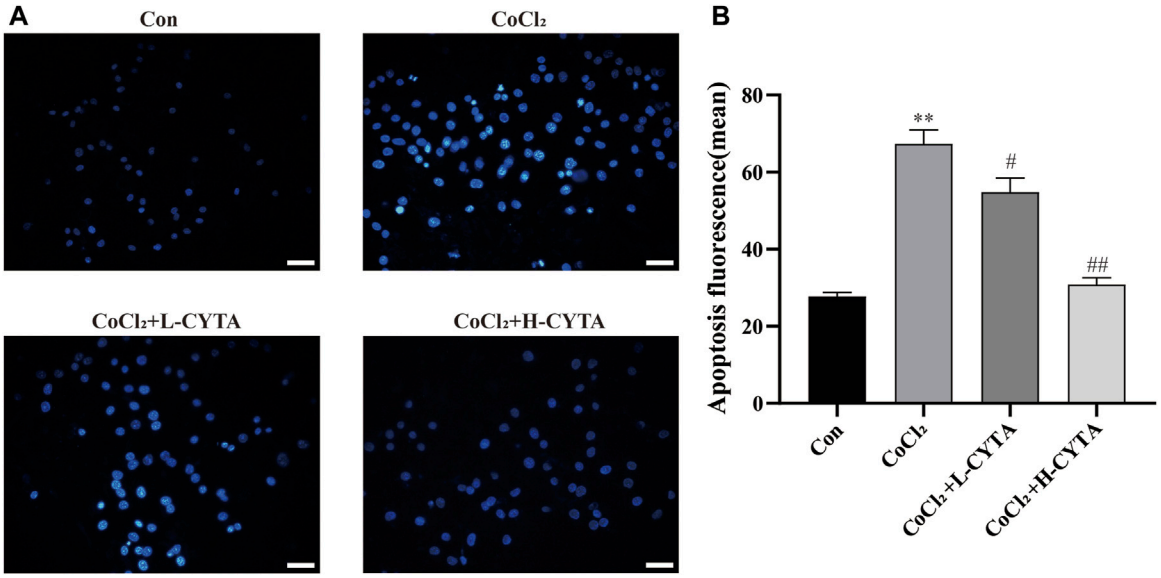

FIGURE 7
Effects of CYTA on apoptosis in hypoxic H9c2 cells. **(A)** Levels of apoptosis in H9c2 cells observed under fluorescence microscopy (scale bar: 100 μm; magnification: ×200). When cells apoptosis, the nuclei are bright blue fluorescence. **(B)** Results of quantitative analysis on the mean fluorescence intensity of apoptotic cells. Mean ± SEM, $n = 3$. $^{*}p < 0.05$, $^{**}p < 0.01$ versus CON group and $^{\#}p < 0.05$, $^{\#\#}p < 0.01$ versus $CoCl_2$ group. Note: L-CYTA: 10 μg/mL and H-CYTA: 30 μg/mL.

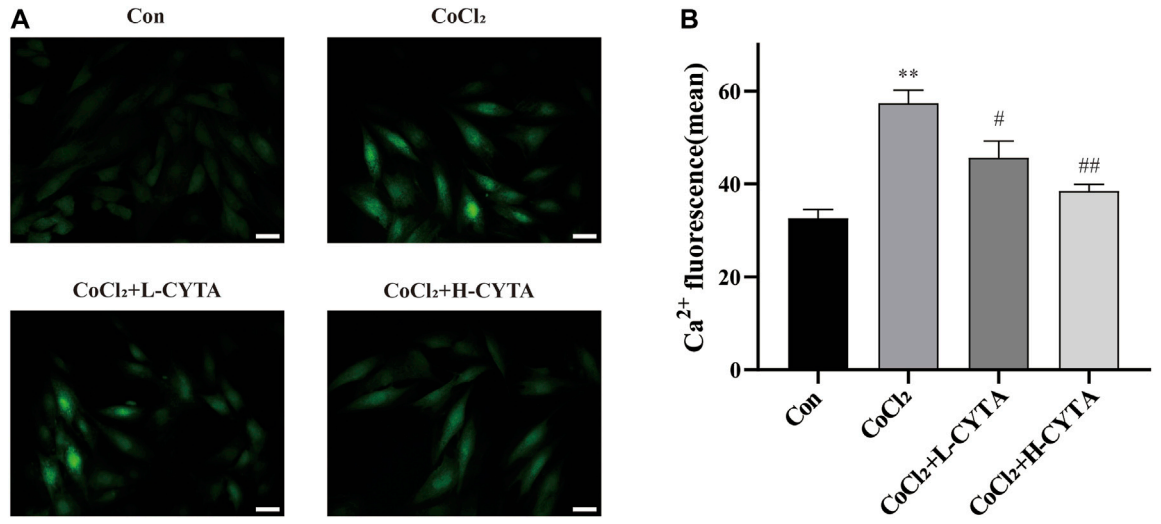

FIGURE 8
Effects of CYTA on intracellular Ca^{2+} concentration in hypoxic H9c2 cells. **(A)** Changes in intracellular Ca^{2+} concentration observed under fluorescence microscopy (scale bar:100 μm; magnification: ×200). The fluorescence changes became stronger when Fluo-3 combined with Ca^{2+}. **(B)** Results of the quantitative analysis on the mean fluorescence intensity of Ca^{2+}. Mean ± SEM, $n = 3$. $^{*}p < 0.05$, $^{**}p < 0.01$ versus CON group and $^{\#}p < 0.05$, $^{\#\#}p < 0.01$ versus $CoCl_2$ group. Note: L-CYTA: 10 μg/mL and H-CYTA: 30 μg/mL.

cardiomyocytes at the electrophysiologic level. It is well known that the membrane clamp is the gold standard for examining cellular electrophysiology. Currently, based on the electrophysiological method, numerous studies have been conducted on natural agents that can treat MI. For example, scholars such as Han et al. (2022); Guan et al. (2015) demonstrated that total flavones from *Acanthopanax senticosus* and *ginseng* total saponin have therapeutic effects on MI by inhibiting Ca^{2+} influx, respectively. Therefore, the present study is based on this to develop the experimental design.

Using the principles and techniques of modern network pharmacology, our study revealed that the therapeutic effects of CYTA on MI are attributed to its multi-component, multi-target, and multi-signaling pathway properties. Initially, we identified

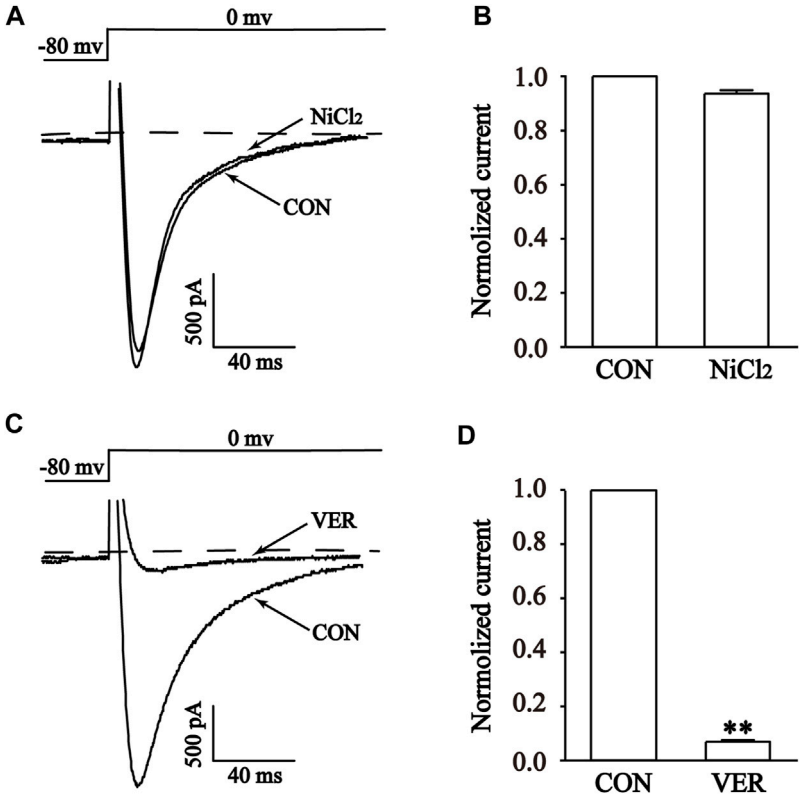

FIGURE 9
Validation of $I_{Ca\text{-}L}$ in isolated cardiomyocytes. Representative curves **(A,C)** and combined data **(B,D)** for steady-state activation of $I_{Ca\text{-}L}$ before and after using 1 μM Ver and 100 μM $NiCl_2$. Mean ± SEM, n = 10. Each group has 10 cells from 10 rat hearts. $^{**}p < 0.01$ versus CON group.

46 alkaloid components of CYTA (Table 2) through TCMSP and reference literature. Subsequently, we obtained 549 potential targets of CYTA (Figure 1) and 2649 MI-related targets. The intersection of these targets resulted in 262 cross-targets for further analysis (Figure 2A). Among the KEGG results, we specifically focused on the calcium signaling pathway as it appeared to be important in CYTA's efficacy against MI (Figure 3B). Consequently, we extracted and demonstrated 30 targets involved in the calcium signaling pathway (Figure 2C). Notably, CALM2, a calcium ion signal transducer protein, plays a role in activating CALM2 through calcium, subsequently regulating multiple signaling pathways (Boczek et al., 2016). Additionally, CACNA1S is recognized as one of the components of LTCCs (Kessi et al., 2021). Moreover, GO enrichment analysis revealed that the potential targets of CYTA could influence BPs related to MI, such as anti-oxidative stress and anti-apoptosis (Figure 3A).

Therefore, to investigate the effects of CYTA on cardiac oxidative stress injury, cell apoptosis, and calcium signaling regulation, we conducted experiments using both an H9c2 cell hypoxia model and a rat MI model. The $CoCl_2$ is a widely used and recognized chemical hypoxia simulation reagent. Co^{2+} can replace dried ammonia acyl of $CoCl_2$ hydroxylase (PHD) of Fe^{2+}, thereby enabling PHD inactivation. PHD plays a key role in the relationship between oxygen concentration and hypoxia-inducible factor (HIF) degradation. In addition, the presence of $CoCl_2$ can stabilize HIF under normoxic conditions and this stability can be maintained for several hours, which is not achieved under hypoxia-induced hypoxia. Thus, the model allows us a time window to manipulate and analyze samples under normoxic conditions (Munoz-Sanchez and Chanez-Cardenas, 2019). The optimal concentration of $CoCl_2$ for inducing hypoxia was determined using the CCK-8 method (Figure 4A). The measurement of CK and LDH release has been widely utilized as an adjunct method to verify myocardial damage (Long et al., 2012). Our results demonstrated that CYTA effectively protected H9c2 cells from $CoCl_2$-induced damage, as evidenced by the decreased release of CK and LDH (Figures 4E, F).

When cardiomyocytes experience hypoxic damage, the primary mechanisms involved are the increased production of ROS, intracellular Ca^{2+} overload, and impaired mitochondrial energy synthesis (Paradies et al., 2018). In recent years, with the in-depth research on the mechanism of myocardial ischemic injury, it has been found that large amount of ROS generation and its triggered lipid peroxidation reaction is one of the main mechanisms of myocardial ischemic injury (Neri et al., 2015; Han et al., 2022). Hypoxia leads to decreased ATP production and the entry of Ca^{2+} into cells, activating Ca^{2+}-dependent protein hydrolases, which convert xanthine dehydrogenase into xanthine oxidase. Consequently, a substantial amount of ROS is generated (Tsutsui et al., 2011). ROS reacts with unsaturated fatty acids, resulting in the production of lipid peroxides that further decompose into malondialdehyde (MDA). MDA combines with proteins containing free amino groups, phospholipid phosphoethanolamine, and nucleic acids (Zorov et al., 2014). This

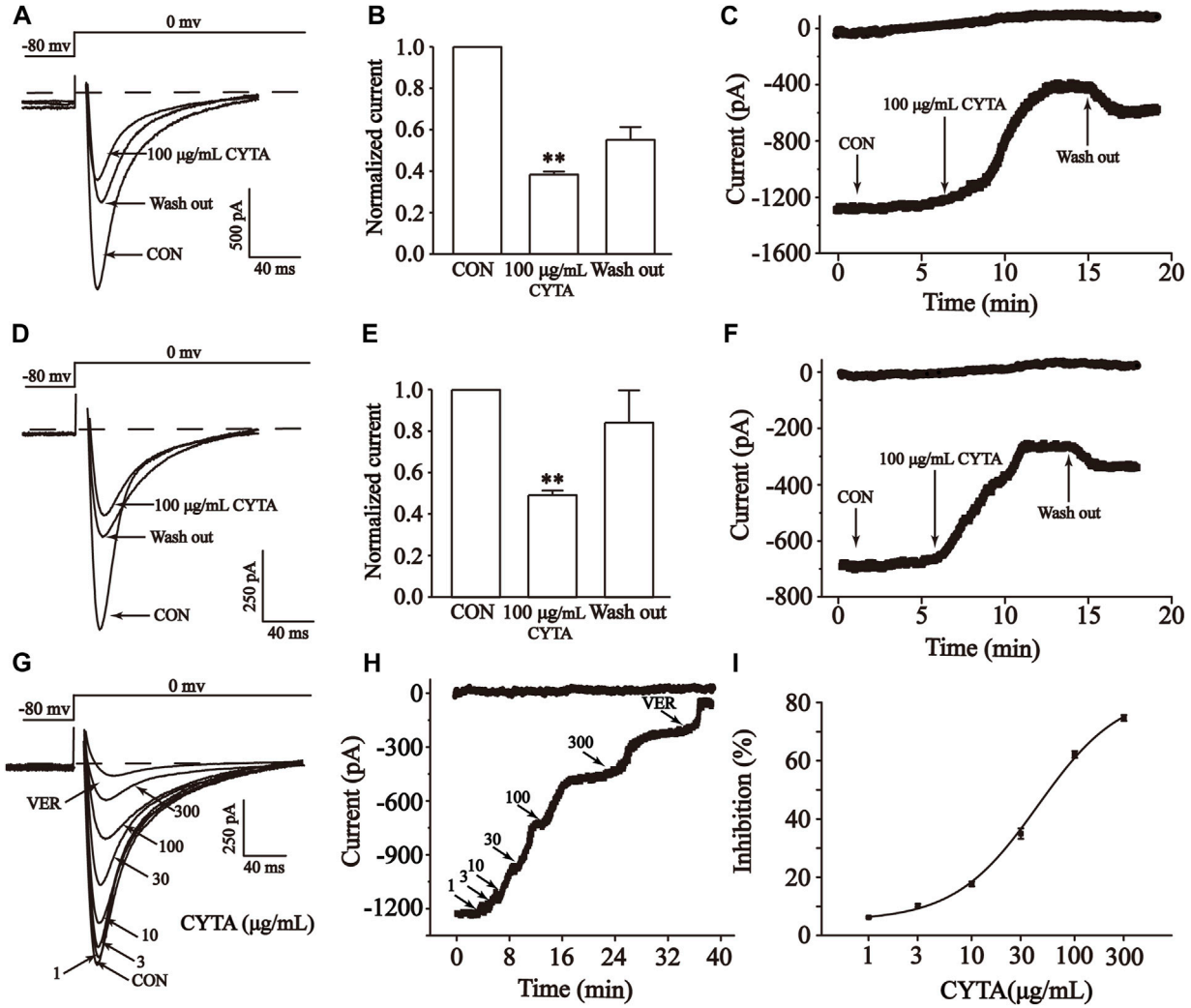

FIGURE 10
Effects of CYTA on $I_{Ca\text{-}L}$ in isolated cardiomyocytes. Effects on normal **(A–C)** and ischemic cardiomyocytes **(D–F)** $I_{Ca\text{-}L}$ were documented under CON, CYTA (100 μg/mL) and elution conditions **(A,D)** Representative examples of $I_{Ca\text{-}L}$, **(B,E)** summarized data and **(C,F)** time constant. Typical trajectory **(G)**, time constants **(H)** and dose versus percentage inhibition curves **(I)** for $I_{Ca\text{-}L}$ recorded at CON and 1, 3, 10, 30, 100 and 300 μM CYTA and 1 μM VER conditions. Mean ± SEM, n = 10. Each group has 10 cells from 10 rat hearts. $^{**}p < 0.01$ for CON group.

process leads to the formation of Schiff bases between MDA and free amino acids, such as proteins, phospholipid phosphoethanolamine, and nucleic acids, causing cross-linking between biomolecules.

These reactions ultimately result in protein denaturation, damage to the integrity of the myocardial cell membrane, increased membrane permeability, and the influx of extracellular Ca^{2+} into the intracellular space, leading to Ca^{2+} overload (Toescu, 2004; Wang et al., 2023). The accumulated intracellular Ca^{2+} can be absorbed by the sarcoplasmic reticulum and mitochondria, resulting in significant energy consumption. Additionally, the entry of Ca^{2+} into mitochondria can disrupt oxidative phosphorylation, thereby interfering with energy metabolism and directly reducing ATP production (Stanley, 2004). Therefore, the generation of ROS can induce cellular damage, while the damage to the cell membrane, alterations in the tissue microenvironment, and intracellular Ca^{2+} overload further accelerate cellular damage through a series of mechanisms (Barry, 1987).

It cannot be ignored that antioxidant enzymes such as CAT, SOD, GSH-Px play an important role in the process of cellular oxidative stress caused by ROS. CAT, also known as catalase, is an enzymatic scavenger that catalyzes the decomposition of H_2O_2 (Goyal and Basak, 2010). Another essential enzyme involved in scavenging free radicals is SOD, while MDA serves as an indicator of lipid peroxidation intensity (Tsutsui et al., 2011). GSH-Px catalyzes the decomposition of hydrogen peroxide within cells, reducing the peroxidation of polyunsaturated fatty acids in cell membranes by scavenging peroxides and hydroxyl radicals generated during cellular respiratory metabolism (Ferrari et al., 2004; Hall et al., 2009). The findings of our study revealed that CYTA reduced intracellular ROS levels and MDA content while increasing the activities of SOD, GSH-Px, and CAT (Figure 5). These results indicate that CYTA can counteract the oxidative stress damage in H9c2 cells through multiple pathways and improve the cellular antioxidant capacity.

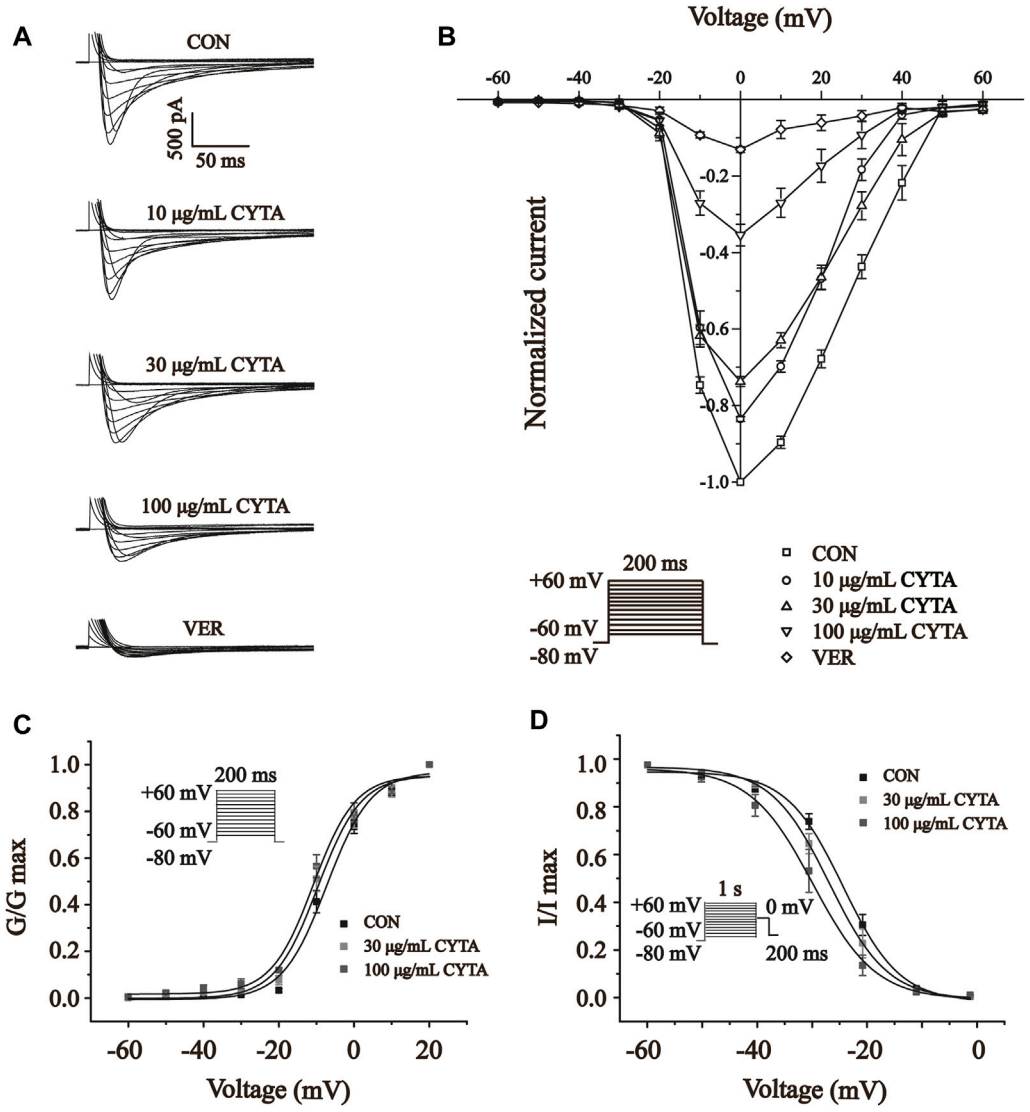

FIGURE 11
Effects of CYTA on $I_{Ca\text{-}L}$ current-voltage relationships (I-V curves) and $I_{Ca\text{-}L}$ steady-state activation and inactivation curves in isolated cardiomyocytes **(A)** Representative recording plots of $I_{Ca\text{-}L}$ recorded in isolated cardiomyocytes under CON, CYTA (10, 30 and 100 μg/mL) and VER (1 μM) conditions. **(B)** I-V relationship curves plotted at three consecutive concentrations of CYTA (10–100 μg/mL) and VER (1 μM) were given. Voltage Steady-state activation **(C)** and inactivation curves **(D)** of $I_{Ca\text{-}L}$ in ventricular myocytes before and after administration of different concentrations of CYTA (30 and 100 μg/mL). Mean ± SEM, n = 10. Each group has 10 cells from 10 rat hearts.

During myocardial hypoxia, mitochondrial oxidative phosphorylation was impeded, leading to impaired ATP synthesis. In severe cases, mitochondrial swelling, crag disintegration, membrane fragmentation, and matrix spillage occurred, causing irreversible damage and triggering apoptosis (Bernardi and Di Lisa, 2015; Bernardi et al., 2015). Therefore, this study examined intracellular ATP content, Ca^{2+}-ATPase activity, mitochondrial damage, and apoptosis. The results demonstrated that CYTA not only significantly improved intracellular ATP content and Ca^{2+}-ATPase activity (Figures 6C, D) but also reversed mitochondrial damage (Figures 6A, B) and apoptosis (Figure 7) induced by hypoxia. These findings suggest that CYTA possesses antioxidant and anti-apoptotic effects on cardiomyocytes.

Ca^{2+} is a crucial messenger that regulates various BPs *in vivo*, including myocardial excitation-contraction coupling (Hofmann et al., 2014). Therefore, maintaining Ca^{2+} homeostasis is essential for normal cardiac physiological function (Barry and Bridge, 1993). On the one hand, elevated intracellular calcium ions directly induce myocardial contraction (Bai et al., 2005); On the other hand, they also participate in regulating several calcium-dependent protease activities, serving as second messengers (Hofmann et al., 2014).

There are two types of calcium channels present in cardiomyocytes: voltage-gated calcium channels and calcium-releasing calcium channels. Voltage-gated calcium channels are categorized into T, L, N, P/Q, and R types based on their pharmacological and biophysical properties (Catterall, 2011). The low voltage-dependent calcium channels exclusively consist of the

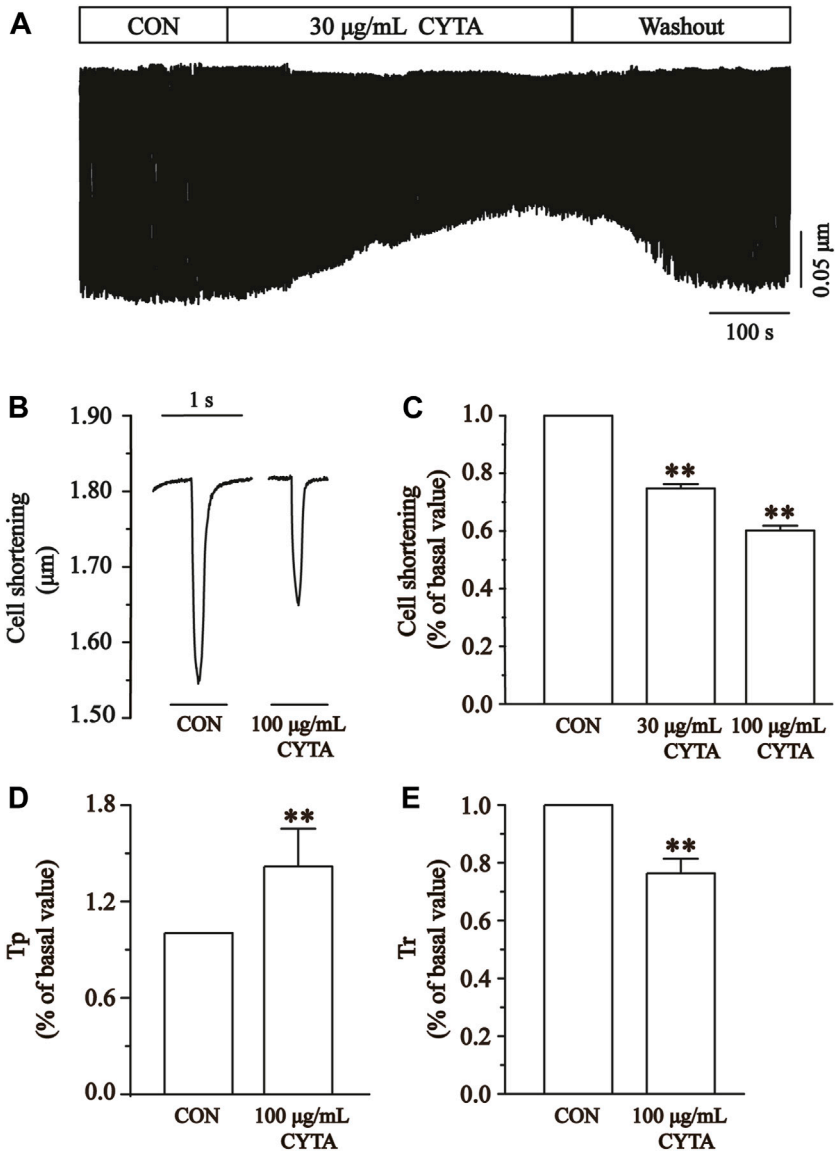

FIGURE 12
Effects of CYTA on cell contraction and time parameters of cell contraction in isolated cardiomyocytes. **(A)** The time progress of cell shortening was recorded in the existence or inexistence of 30 and 100 μg/mL CYTA. **(B)** Representative traces of cell shortening. **(C)** Statistical analysis of 30 and 100 μg/mL CYTA on cell shortening. **(D,E)** Statistical analysis results of Tp and Tr in the CON and 100 μg/mL CYTA. Mean ± SEM, $n = 8$. Each group has 8 cells from 8 rat hearts. $^{**}p < 0.01$ versus CON group.

T-type, which becomes activated and inactivated at relatively low membrane potentials (−70 to −60 mv) with a short duration. The high voltage-activated calcium channels encompass the L, N, P/Q, and R types, which activate at (−30 to −20 mv) and have a longer opening time (Catterall, 2011). Studies have reported that the VER exhibited significant anti-MI action in animal experiments and clinical studies. In addition, there are also studies using VER as a positive control group in animal experiment. Therefore, we chose VER as the positive control drug in the present (Han et al., 2022). Experimental results showed that the use of the specific $I_{Ca\text{-}L}$ blocker VER was able to almost completely eliminate the current, indicating the function of LTCCs in ventricular myocytes (Figure 9).

LTCCs are proteins found in the cardiomyocyte membrane. Ca^{2+} enters the cell through LTCCs, triggering the release of stored Ca^{2+} in the sarcoplasmic reticulum via sarcoplasmic reticulum calcium release channels. This process plays a crucial role in the excitation-contraction coupling of the heart, facilitating the propagation of action potentials predominantly during rapid depolarization. Moreover, it contributes to the formation and maintenance of the plateau phase of the myocardial action potential (Yamaoka and Kameyama, 2003).

Therefore, the effects of CYTA on LTCCs and cardiomyocyte contractility were explored in this research. The results showed that CYTA had a reversible inhibitory effect on LTCCs in both normal and ischemic rats (Figures 10A–F), and this inhibitory effect was concentration-dependent (Figures 10G–I). This demonstrated that CYTA had a calcium channel antagonist-like effect and was able to reduce Ca^{2+} entry into the cells. Furthermore, the relationship between CYTA and $I_{Ca\text{-}L}$ I-V curves reveals that CYTA can

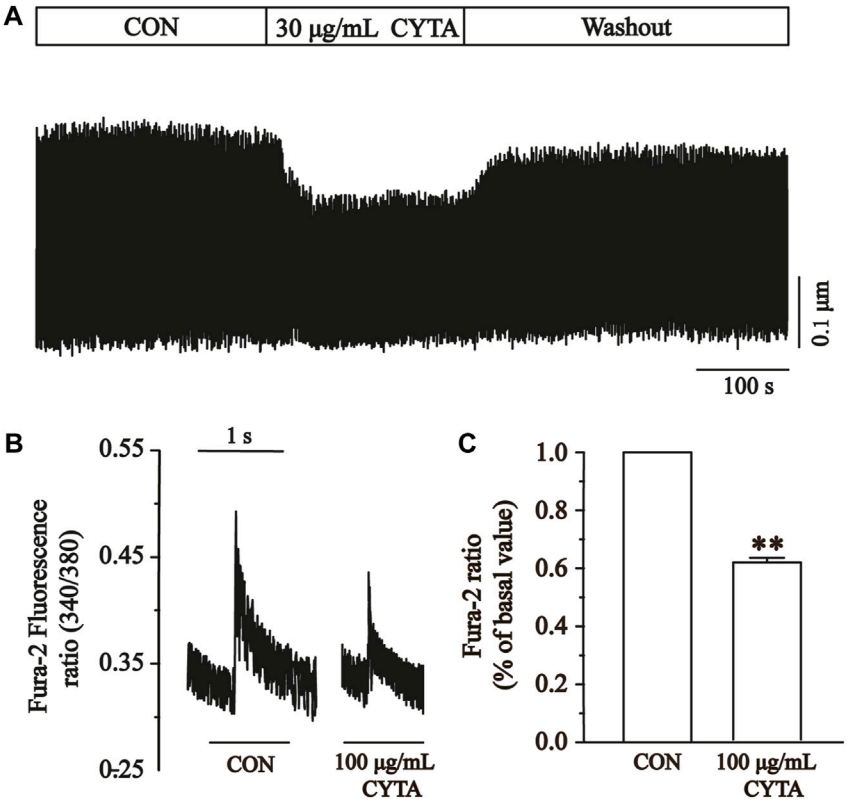

FIGURE 13
Effects of CYTA on Ca^{2+} transients in ventricular myocytes in isolated cardiomyocytes. Ca^{2+} transients recorded **(A)** in isolated cardiomyocytes in the presence or absence of CYTA (100 μg/mL) and representative trajectories **(B)** and summary data **(C)**. Mean ± SEM, $n = 6$. Each group has 9 cells from 9 rat hearts. $^{**}p < 0.01$ versus CON group.

concentration-dependently suppress $I_{Ca\text{-}L}$ peak current density while the activation and peak potentials remain unchanged. Consequently, this prolongs the action potential time course in cardiac myocytes, attenuates the rate of Ca^{2+} inward flow, and reduces myocardial contractility (Figure 11). Figure 11 indicates that CYTA does not significantly affect $I_{Ca\text{-}L}$ activation and inactivation kinetics, suggesting that CYTA does not alter the rate of $I_{Ca\text{-}L}$ activation and inactivation in rat ventricular myocytes.

When LTCCs are activated, it stimulates calcium influx, resulting in increased myocardial mechanical contraction and Ca^{2+} overload. The excessive contraction of cardiomyocytes leads to elevated oxygen consumption, potentially causing myocardial dysfunction and even cardiomyocyte death (Allen and Orchard, 1987; Crystal et al., 2013). Thus, inhibiting LTCCs can alleviate Ca^{2+} overload and hypercontractility of the myocardium.

The results indicate that CYTA effectively inhibits cardiomyocyte contractility (Figures 12A–C) and Ca^{2+} transients (Figure 13). Tp and Tr are critical temporal parameters that represent the rate of cell contraction and relaxation, respectively (Zhu et al., 2016). In conclusion, this study demonstrates that CYTA at a 100 μg/mL concentration significantly inhibits Tp and Tr (Figures 12D, E). These findings provide evidence that CYTA can hinder Ca^{2+} influx into cardiomyocytes by targeting LTCCs, reflecting the fact that CYTA has characteristics similar to those of antagonists of LTCCs. These findings all suggest that CYTA has potential for the treatment of MI.

Some limitations of this study should be considered. Our network pharmacology analysis revealed that SCN5A, KCNMA1, and KCNH2 are equally potential targets for MI treatment with CYTA. These targets are significant members of cell surface sodium and potassium channels (Bowlby et al., 2008; Li et al., 2018; Bailey et al., 2019). Apart from Ca^{2+} channels, the myocardial cell membrane also contains K^+ channels, Cl^- channels, and Na^+ channels, all of which play crucial roles in maintaining the normal physiological functions of the heart. The experimental subjects in this study consisted of cells isolated from the internal environment and H9c2 cells, thereby limiting the ability to fully replicate the complex physiological milieu *in vivo*. The H9c2 cells, despite sharing similar physiological and biochemical characteristics with primary cardiomyocytes, still exhibit distinctions in terms of cellular morphology, contractility, and gene expression (Zheng et al., 2021). Different species of animal experiments are needed to verify the protective effect of CYTA on MI. Electrophysiological studies from multiple directions, such as action potential duration, ion channel kinetics and the influence of membrane potential, should be carried out, which will deepen the understanding of CYTA. Therefore, the study of other electrophysiological aspects of CYTA will be an important area for future research and cannot be ignored. In the future, on the basis of the results of this study, the CYTA findings can be continuously verified in different experimental models to make the results reproducible and robust. And promote the transformation of scientific research to the clinical push CYTA speed up into clinical studies, clinical strategy for treatment of IHD to provide more.

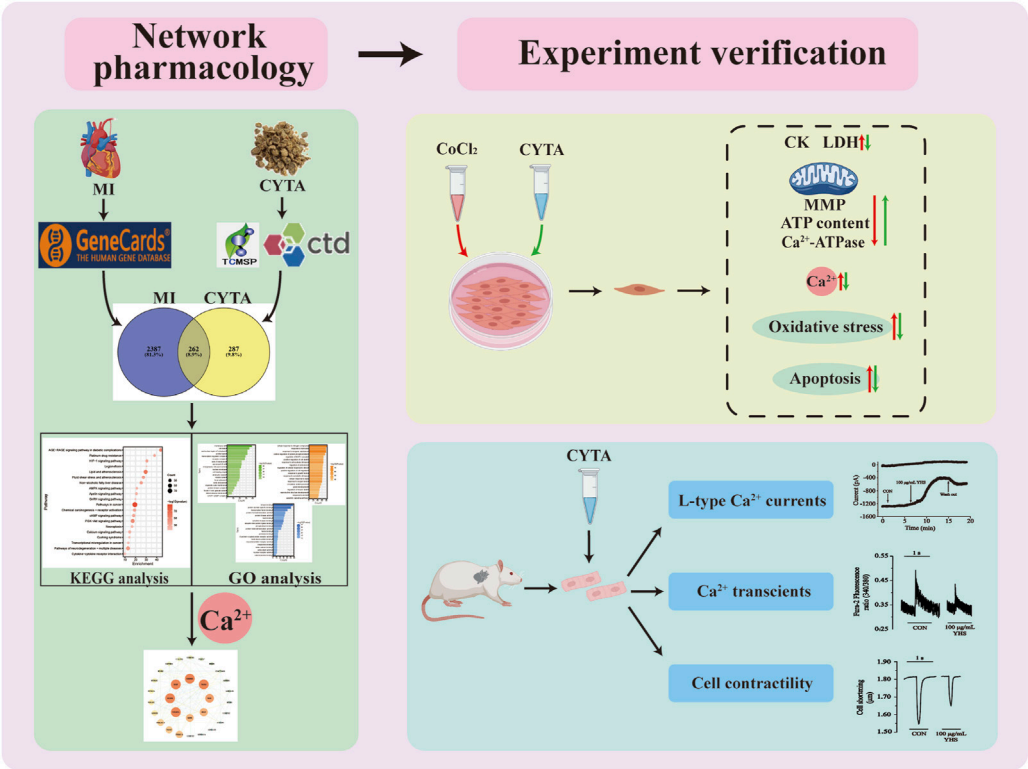

FIGURE 14
Workflow diagram for the discovery of potential mechanisms for CYTA against MI.

5 Conclusion

In summary, the present study demonstrates that CYTA has a significant protective effect against MI, and its protective mechanism may be related to attenuation of oxidative stress, improvement of mitochondrial function, reduction of cardiomyocyte apoptosis, and maintenance of Ca^{2+} homeostasis through LTCCs. The results obtained from this series of experiments using CYTA in the treatment of myocardial infarction provide new insights for future research and development of drugs for the treatment of IHD.

Data availability statement

The original contributions presented in the study are included in the article/Supplementary Material, further inquiries can be directed to the corresponding authors.

Ethics statement

The animal study was approved by the Hebei University of Chinese Medicine. The study was conducted in accordance with the local legislation and institutional requirements.

Author contributions

JQ: Methodology, Writing–original draft. HL: Writing–original draft. YY: Formal Analysis, Writing–review and editing. XS: Writing–review and editing, Software. JW: Writing–review and editing, Investigation. XH: Writing–review and editing, Data curation. XC: Writing–review and editing, Methodology. ZS: Methodology, Writing–review and editing. LC: Methodology, Writing–review and editing, Project administration.

Funding

The author(s) declare financial support was received for the research, authorship, and/or publication of this article. This work was supported by the Research Foundation of Natural Science of Hebei Province (Nos H2022206190 and H2022423306).

Conflict of interest

The authors declare that the research was conducted in the absence of any commercial or financial relationships that could be construed as a potential conflict of interest.

The reviewer YX declared a shared affiliation with the authors JQ, HL, YY, XS, JW, XH to the handling editor at the time of review.

Publisher's note

References

Allen, D. G., and Orchard, C. H. (1987). Myocardial contractile function during ischemia and hypoxia. *Circ. Res.* 60 (2), 153–168. doi:10.1161/01.res.60.2.153

Bai, C. X., Namekata, I., Kurokawa, J., Tanaka, H., Shigenobu, K., and Furukawa, T. (2005). Role of nitric oxide in Ca^{2+} sensitivity of the slowly activating delayed rectifier K^+ current in cardiac myocytes. *Circ. Res.* 96 (1), 64–72. doi:10.1161/01.RES.0000151846.19788.E0

Bailey, C. S., Moldenhauer, H. J., Park, S. M., Keros, S., and Meredith, A. L. (2019). KCNMA1-linked channelopathy. *J. Gen. Physiol.* 151 (10), 1173–1189. doi:10.1085/jgp.201912457

Barry, W. H. (1987). Mechanisms of myocardial cell injury during ischemia and reperfusion. *J. Card. Surg.* 2 (3), 375–383. doi:10.1111/j.1540-8191.1987.tb00196.x

Barry, W. H., and Bridge, J. H. (1993). Intracellular calcium homeostasis in cardiac myocytes. *Circulation* 87 (6), 1806–1815. doi:10.1161/01.cir.87.6.1806

Bernardi, P., and Di Lisa, F. (2015). The mitochondrial permeability transition pore: molecular nature and role as a target in cardioprotection. *J. Mol. Cell Cardiol.* 78, 100–106. doi:10.1016/j.yjmcc.2014.09.023

Bernardi, P., Rasola, A., Forte, M., and Lippe, G. (2015). The mitochondrial permeability transition pore: channel formation by F-ATP synthase, integration in signal transduction, and role in pathophysiology. *Physiol. Rev.* 95 (4), 1111–1155. doi:10.1152/physrev.00001.2015

Bi, S., Xu, L., Chen, S., Bu, S., and Xu, Y. (2021). Detection of herbal combinations and pharmacological mechanisms of clinical prescriptions for coronary heart disease using data mining and network pharmacology. *Evid. Based Complement. Altern. Med.* 2021, 9234984. doi:10.1155/2021/9234984

Boczek, N. J., Gomez-Hurtado, N., Ye, D., Calvert, M. L., Tester, D. J., Kryshtal, D., et al. (2016). Spectrum and prevalence of CALM1-, CALM2-, and CALM3-encoded calmodulin variants in long QT syndrome and functional characterization of a novel long QT syndrome-associated calmodulin missense variant, E141G. *Circ. Cardiovasc. Genet.* 9 (2), 136–146. doi:10.1161/CIRCGENETICS.115.001323

Bowlby, M. R., Peri, R., Zhang, H., and Dunlop, J. (2008). hERG (KCNH2 or Kv11.1) K^+ channels: screening for cardiac arrhythmia risk. *Curr. Drug Metab.* 9 (9), 965–970. doi:10.2174/138920008786485083

Catterall, W. A. (2011). Voltage-gated calcium channels. *Cold Spring Harb. Perspect. Biol.* 3 (8), a003947. doi:10.1101/cshperspect.a003947

Chang, X., Liu, J., Wang, Y., Guan, X., and Liu, R. (2023). Mitochondrial disorder and treatment of ischemic cardiomyopathy: potential and advantages of Chinese herbal medicine. *Biomed. Pharmacother.* 159, 114171. doi:10.1016/j.biopha.2022.114171

Crystal, G. J., Silver, J. M., and Salem, M. R. (2013). Mechanisms of increased right and left ventricular oxygen uptake during inotropic stimulation. *Life Sci.* 93 (2-3), 59–63. doi:10.1016/j.lfs.2013.05.011

Fang, Z., Luo, W., and Luo, Y. (2018). Protective effect of alpha-mangostin against $CoCl_2$-induced apoptosis by suppressing oxidative stress in H9c2 rat cardiomyoblasts. *Mol. Med. Rep.* 17 (5), 6697–6704. doi:10.3892/mmr.2018.8680

Ferrari, R., Guardigli, G., Mele, D., Percoco, G. F., Ceconi, C., and Curello, S. (2004). Oxidative stress during myocardial ischaemia and heart failure. *Curr. Pharm. Des.* 10 (14), 1699–1711. doi:10.2174/1381612043384718

Goyal, M. M., and Basak, A. (2010). Human catalase: looking for complete identity. *Protein Cell* 1 (10), 888–897. doi:10.1007/s13238-010-0113-z

Guan, S., Ma, J., Chu, X., Gao, Y., Zhang, Y., Zhang, X., et al. (2015). Effects of total flavones from Acanthopanax senticosus on L-type calcium channels, calcium transient and contractility in rat ventricular myocytes. *Phytother. Res.* 29 (4), 533–539. doi:10.1002/ptr.5278

Hall, A., Karplus, P. A., and Poole, L. B. (2009). Typical 2-cys peroxiredoxins--structures, mechanisms and functions. *FEBS J.* 276 (9), 2469–2477. doi:10.1111/j.1742-4658.2009.06985.x

Han, B. J., Cao, G. Y., Jia, L. Y., Zheng, G., Zhang, L., Sheng, P., et al. (2022a). Cardioprotective effects of tetrahydropalmatine on acute myocardial infarction in rats. *Am. J. Chin. Med.* 50 (7), 1887–1904. doi:10.1142/s0192415x2250080x

Han, X., Qi, J., Yang, Y., Zheng, B., Liu, M., Liu, Y., et al. (2022b). Protective mechanisms of 10-gingerol against myocardial ischemia may involve activation of JAK2/STAT3 pathway and regulation of $Ca^{(2+)}$ homeostasis. *Biomed. Pharmacother.* 151, 113082. doi:10.1016/j.biopha.2022.113082

Hofmann, F., Flockerzi, V., Kahl, S., and Wegener, J. W. (2014). L-Type CaV1.2 calcium channels: from *in vitro* findings to *in vivo* function. *Physiol. Rev.* 94 (1), 303–326. doi:10.1152/physrev.00016.2013

Hosseini, A., Rajabian, A., Sobhanifar, M. A., Alavi, M. S., Taghipour, Z., Hasanpour, M., et al. (2022). Attenuation of isoprenaline-induced myocardial infarction by rheum turkestanicum. *Biomed. Pharmacother.* 148, 112775. doi:10.1016/j.biopha.2022.112775

Jin, Y., Ren, W., Liu, J., Tang, X., Shi, X., Pan, D., et al. (2023). Identification and validation of potential hypoxia-related genes associated with coronary artery disease. *Front. Physiol.* 14, 1181510. doi:10.3389/fphys.2023.1181510

Kessi, M., Chen, B., Peng, J., Yan, F., Yang, L., and Yin, F. (2021). Calcium channelopathies and intellectual disability: a systematic review. *Orphanet J. Rare Dis.* 16 (1), 219. doi:10.1186/s13023-021-01850-0

Lee, J. H., Gomora, J. C., Cribbs, L. L., and Perez-Reyes, E. (1999). Nickel block of three cloned T-type calcium channels: low concentrations selectively block Alpha1H. *Biophys. J.* 77 (6), 3034–3042. doi:10.1016/s0006-3495(99)77134-1

Levraut, J., Iwase, H., Shao, Z. H., Vanden Hoek, T. L., and Schumacker, P. T. (2003). Cell death during ischemia: relationship to mitochondrial depolarization and ROS generation. *Am. J. Physiol. Heart Circ. Physiol.* 284 (2), H549–H558. doi:10.1152/ajpheart.00708.2002

Li, J., Wu, J., Huang, J., Cheng, Y., Wang, D., and Liu, Z. (2022). Uncovering the effect and mechanism of rhizoma Corydalis on myocardial infarction through an integrated network pharmacology approach and experimental verification. *Front. Pharmacol.* 13, 927488. doi:10.3389/fphar.2022.927488

Li, W., Yin, L., Shen, C., Hu, K., Ge, J., and Sun, A. (2018). SCN5A variants: association with cardiac disorders. *Front. Physiol.* 9, 1372. doi:10.3389/fphys.2018.01372

Li, Y., and Zhang, J. (2022). Disease burden and risk factors of ischemic heart disease in China during 1990-2019 based on the global burden of disease 2019 report: a systematic analysis. *Front. Public Health* 10, 973317. doi:10.3389/fpubh.2022.973317

Ling, H., Wu, L., and Li, L. (2006). Corydalis yanhusuo rhizoma extract reduces infarct size and improves heart function during myocardial ischemia/reperfusion by inhibiting apoptosis in rats. *Phytother. Res.* 20 (6), 448–453. doi:10.1002/ptr.1875

Liu, J., Bu, X., Wei, L., Wang, X., Lai, L., Dong, C., et al. (2021). Global burden of cardiovascular diseases attributable to hypertension in young adults from 1990 to 2019. *J. Hypertens.* 39 (12), 2488–2496. doi:10.1097/hjh.0000000000002958

Long, J., Gao, M., Kong, Y., Shen, X., Du, X., Son, Y. O., et al. (2012). Cardioprotective effect of total paeony glycosides against isoprenaline-induced myocardial ischemia in rats. *Phytomedicine* 19 (8-9), 672–676. doi:10.1016/j.phymed.2012.03.004

Munoz-Sanchez, J., and Chanez-Cardenas, M. E. (2019). The use of cobalt chloride as a chemical hypoxia model. *J. Appl. Toxicol.* 39 (4), 556–570. doi:10.1002/jat.3749

Neri, M., Fineschi, V., Di Paolo, M., Pomara, C., Riezzo, I., Turillazzi, E., et al. (2015). Cardiac oxidative stress and inflammatory cytokines response after myocardial infarction. *Curr. Vasc. Pharmacol.* 13 (1), 26–36. doi:10.2174/15701611113119990003

Nunnari, J., and Suomalainen, A. (2012). Mitochondria: in sickness and in health. *Cell* 148 (6), 1145–1159. doi:10.1016/j.cell.2012.02.035

Paradies, G., Paradies, V., Ruggiero, F. M., and Petrosillo, G. (2018). Mitochondrial bioenergetics and cardiolipin alterations in myocardial ischemia-reperfusion injury: implications for pharmacological cardioprotection. *Am. J. Physiol. Heart Circ. Physiol.* 315 (5), H1341–H1352. doi:10.1152/ajpheart.00028.2018

Pecoraro, M., Pinto, A., and Popolo, A. (2018). Inhibition of connexin 43 translocation on mitochondria accelerates $CoCl_2$-induced apoptotic response in a chemical model of hypoxia. *Toxicol. Vitro* 47, 120–128. doi:10.1016/j.tiv.2017.11.004

Severino, P., D'Amato, A., Pucci, M., Infusino, F., Adamo, F., Birtolo, L. I., et al. (2020). Ischemic heart disease pathophysiology paradigms overview: from plaque activation to microvascular dysfunction. *Int. J. Mol. Sci.* 21 (21), 8118. doi:10.3390/ijms21218118

Stanley, W. C. (2004). Myocardial energy metabolism during ischemia and the mechanisms of metabolic therapies. *J. Cardiovasc Pharmacol. Ther.* 9 (Suppl. 1), S31–S45. doi:10.1177/107424840400900104

Tian, B., Tian, M., and Huang, S. M. (2020). Advances in phytochemical and modern pharmacological research of rhizoma Corydalis. *Pharm. Biol.* 58 (1), 265–275. doi:10.1080/13880209.2020.1741651

Toescu, E. C. (2004). Hypoxia sensing and pathways of cytosolic Ca^{2+} increases. *Cell Calcium* 36 (3-4), 187–199. doi:10.1016/j.ceca.2004.02.019

Tsutsui, H., Kinugawa, S., and Matsushima, S. (2011). Oxidative stress and heart failure. *Am. J. Physiol. Heart Circ. Physiol.* 301 (6), H2181–H2190. doi:10.1152/ajpheart.00554.2011

Vanacore, D., Messina, G., Lama, S., Bitti, G., Ambrosio, P., Tenore, G., et al. (2018). Effect of restriction vegan diet's on muscle mass, oxidative status, and myocytes differentiation: a pilot study. *J. Cell. Physiology* 233 (12), 9345–9353. doi:10.1002/jcp.26427

Wahid, M., Saqib, F., Chicea, L., Ahmedah, H. T., Sajer, B. H., Marc Vlaic, R. A., et al. (2022). Metabolomics analysis delineates the therapeutic effects of hydroethanolic extract of cucumis sativus L. Seeds on hypertension and isoproterenol-induced myocardial infarction. *Biomed. Pharmacother.* 148, 112704. doi:10.1016/j.biopha.2022.112704

Wang, Y., Zhang, T., Nie, L., Zhang, Y., Wang, J., Liu, Q., et al. (2023). Digestibility of malondialdehyde-induced dietary advanced lipoxidation end products and their effects on hepatic lipid accumulation in Mice. *J. Agric. Food Chem.* 71 (27), 10403–10416. doi:10.1021/acs.jafc.3c01956

Wong, I. O., Cowling, B. J., Leung, G. M., and Schooling, C. M. (2013). Age-period-Cohort projections of ischaemic heart disease mortality by socio-economic position in a rapidly transitioning Chinese population. *PLoS One* 8 (4), e61495. doi:10.1371/journal.pone.0061495

Wu, L., Ling, H., Li, L., Jiang, L., and He, M. (2007). Beneficial effects of the extract from Corydalis yanhusuo in rats with heart failure following myocardial infarction. *J. Pharm. Pharmacol.* 59 (5), 695–701. doi:10.1211/jpp.59.5.0010

Xue, Y., Zhang, M., Zheng, B., Zhang, Y., Chu, X., Liu, Y., et al. (2021). [8]-Gingerol exerts anti-myocardial ischemic effects in rats via modulation of the MAPK signaling pathway and L-type Ca^{2+} channels. *Pharmacol. Res. Perspect.* 9 (5), e00852. doi:10.1002/prp2.852

Yamaoka, K., and Kameyama, M. (2003). Regulation of L-type Ca^{2+} channels in the heart: overview of recent advances. *Mol. Cell Biochem.* 253 (1-2), 3–13. doi:10.1023/a:1026036931170

Yang, X., He, T., Han, S., Zhang, X., Sun, Y., Xing, Y., et al. (2019). The role of traditional Chinese medicine in the regulation of oxidative stress in treating coronary heart disease. *Oxid. Med. Cell Longev.* 2019, 3231424. doi:10.1155/2019/3231424

Zheng, B., Qi, J., Liu, P., Zhang, M., Zhang, Y., Xue, Y., et al. (2021). 10-Gingerol alleviates hypoxia/reoxygenation-induced cardiomyocyte injury through inhibition of the wnt5a/frizzled-2 pathway. *Food Sci. Nutr.* 9 (7), 3917–3931. doi:10.1002/fsn3.2381

Zhu, F., Chu, X., Wang, H., Zhang, X., Zhang, Y., Liu, Z., et al. (2016). New findings on the effects of tannic acid: inhibition of L-type calcium channels, calcium transient and contractility in rat ventricular myocytes. *Phytother. Res.* 30 (3), 510–516. doi:10.1002/ptr.5558

Zorov, D. B., Juhaszova, M., and Sollott, S. J. (2014). Mitochondrial reactive oxygen species (ROS) and ROS-induced ROS release. *Physiol. Rev.* 94 (3), 909–950. doi:10.1152/physrev.00026.2013

frontiers | Frontiers in Pharmacology

TYPE Original Research
PUBLISHED 23 January 2024
DOI 10.3389/fphar.2024.1260603

OPEN ACCESS

EDITED BY
Jorge G. Farias,
Universidad de La Frontera, Chile

REVIEWED BY
Hee Eun Kang,
Catholic University of Korea, Republic of Korea
Muhammad Fawad Rasool,
Bahauddin Zakariya University, Pakistan

*CORRESPONDENCE
Muhammad Shahbaz,
iosurg@gmail.com
Haiyan Shi,
shihaiyan123@163.com

RECEIVED 18 July 2023
ACCEPTED 08 January 2024
PUBLISHED 23 January 2024

CITATION
Xu N, Ijaz M, Shu Y, Wang P, Ma L, Wang P, Ding H, Shahbaz M and Shi H (2024), The *in vivo* study on antioxidant activity of wendan decoction in treating hyperlipidemia: a pharmacokinetic-pharmacodynamic (PK-PD) model.
Front. Pharmacol. 15:1260603.
doi: 10.3389/fphar.2024.1260603

The *in vivo* study on antioxidant activity of wendan decoction in treating hyperlipidemia: a pharmacokinetic-pharmacodynamic (PK-PD) model

Nan Xu[1,2], Muhammad Ijaz[2,3], Yishuo Shu[4], Peng Wang[4], Lei Ma[1], Ping Wang[1], Hailing Ding[2], Muhammad Shahbaz[1,5]* and Haiyan Shi[2,4]*

[1]Laboratory of Chinese Medicine Preparation, Shandong Research Academy of Traditional Chinese Medicine, Jinan, China, [2]The Faculty of Medicine, Qilu Institute of Technology, Jinan, China, [3]Department of Pharmacology, School of Pharmaceutical Science, Shandong University, Jinan, China, [4]Shandong Medicine and Health Key Laboratory of Clinical Pharmacy, Department of Clinical Pharmacy, The First Affiliated Hospital of Shandong First Medical University, Shandong Provincial Qianfoshan Hospital, Shandong Engineering and Technology Research Center for Pediatric Drug Development, Jinan, China, [5]Research Center for Sectional and Imaging Anatomy, School of Basic Medical Science, Digital Human Institute, Shandong University, Jinan, Shandong, China

Background: Wendan Decoction (WDD) is a six-herb Chinese medicine recipe that was first mentioned in about 652 AD. It is frequently used to treat hyperlipidemic patients' clinical complaints. According to reports, oxidative stress has a significant role in hyperlipidemia.

Purpose: There has not yet been a thorough pharmacokinetic-pharmacodynamic (PK-PD) examination of the clinical efficacy of WDD in the context of hyperlipemia-related oxidative stress. Therefore, the goal of this research is to explore the antioxidant essence of WDD by developing a PK-PD model, ordering to assure its implication in treating hyperlipidemia in medical practice.

Methods: The model rats of foodborne hyperlipidemia were established by feeding with high-fat feed, and the lipid-lowering effect of WDD was explored. The plasma drug concentration of rats at different doses were measured by UPL-MS/MS technology, and PK parameters were calculated using Phoenix WinNonlin 8.1 software. The level of lipid peroxide (LPO) in plasma at different time points was measured by enzyme labeling instrument. Finally, the PK-PD model was established by using Phoenix WinNonlin 8.1 software, to explore the lipid-lowering effect of WDD and the relation between the dynamic changes of chemical components and antioxidant effect.

Results: The findings suggested that, WDD can reduce the levels of triglyceride (TG), total cholesterol (TC), and low-density lipoprotein cholesterol (LDL-C) in plasma, and high-density lipoprotein cholesterol (HDL-C) was related to the dosage. Between the peak drug levels and the WDD's maximal therapeutic response, there existed a hysteresis. WDD's effect-concentration curves

displayed a counterclockwise delaying loop. Alternatively, among the ten components of WDD, hesperetin, quercetin, naringenin and tangeretin might exert more significant effects in regulating the LPO levels in hyperlipidemic rats.

Conclusion: This study can be helpful for other investigators to study the lipid-lowering effect of WDD.

KEYWORDS

wendan decoction, hyperlipidemia, pharmacokinetic-pharmacodynamic model, antioxidant, lipid peroxide

1 Introduction

Hyperlipidemia, sometimes also termed as dyslipidemia, refers to the higher levels of lipids and cholesterol in the blood plasma (Kramer, 2020). Low-density lipoprotein (LDL) cholesterol (bad cholesterol) and high-density lipoprotein (HDL) cholesterol (good cholesterol) regulate the balance in the blood. An imbalance in the levels of LDL-cholesterol and HDL-cholesterol may leads to the cardiovascular complexities including myocardial infarction or even heart attack (Karr, 2017). A well-documented data has described that, the appropriate levels of HDL-C have the ability to exert the shielding effects on the endothelial functions in the patients with hyperlipidemia and hypercholesterolemia (Memon et al., 1995). Hyperlipidemia can be caused as a result of several factors, most common of which include, unhealthy lifestyle, an imbalanced diet, stress, being overweight, being alcoholic, smoking, physical inactivity, etc. Genetic factor, like familial hypercholesterolemia (FH) can also contribute to the hyperlipidemia. FH is reported to affect about 1 in every 250 people, and individuals with FH have very high levels of LDL-cholesterol at a very young age. Such people have a very high risk of getting the stroke or myocardial infarction (Warnholtz et al., 2001; Ansar et al., 2011). Oxidative stress and inflammation are thought to cause the excessive lipid aggregation in the non-adipose tissues (Okon et al., 2007). Oxidative stress can be caused as a result of the excessive production of the different kinds of free radicals, notably reactive oxygen species (ROS), reactive nitrogen species (RNS), and so on (Elesber et al., 2007; Abu-Saleh et al., 2021). Oxidative stress has been documented to induce an abnormal lipid metabolism (Jeong et al., 2012). Thus, depending on its pathogenesis, oxidative stress has become a key therapeutic target to treat the hyperlipidemia.

Traditional Chinese medicine (TCM), with thousands of years of history, has a significant impact on the management of illnesses, and then it bases its therapeutic approach on a number of different components. Daidzein plays an important role to treat the type 2 diabetes (Das et al., 2018), scopoletin and naringin have a significant role in the regulation of insulin (Jia et al., 2019; Jang et al., 2020), and glycyrrhetinic acid and formononetin play roles in the treatment of hypertension (Zhang et al., 2019; Li et al., 2020). Because of the complexity of TCM and its preparations, its challenging to select molecules as detection indexes. Thus, for studying the pharmacokinetics of TCM medicines, a useful foundation was laid by LC-MS/MS technology (Ji et al., 2018; Lu et al., 2019; Wan et al., 2020). The pharmacokinetics of Ban-Xia (BX), Zhu-Ru (ZR), Chen-Pi (CP), Zhi-Shi (ZS), Gan-Cao (GC), Sheng-Jiang (SJ), and other single herbs have been reported previously (Lin et al., 2009; Xu and Cheng, 2011; Tang et al., 2018; Li et al., 2019), but these compounds could not represent the pharmacokinetics of complex compounds in TCM.

WDD is one of the top ten classic prescriptions of traditional Chinese medicine. WDD was originated from "Bei ji qian jin yao fang (Essential Recipes for Emergent Use Worth a Thousand Gold)" by Tang Sun Simiao (Zhang et al., 2022). It was one of the first 100 classic prescriptions released and composed of Pinellia ternata (BX), Bambusae Caulis in Taenias (ZR), Citri Reticulatae Pericarpium (CP), Aurantii Fructus (ZS), Glycyrrhizae Radix et Rhizome (GC), Zingiberis Rhizoma Recens (SJ). Clinical studies have proved that WDD has significant therapeutic effects on depression, dyslipidemia, schizophrenia, insomnia, Alzheimer's disease and other nervous system disorders (Deng and Xu, 2017; Yan et al., 2017; Feng et al., 2019). This prescription is basically prescribed as an "expectorant" in clinical practice. Further, it is commonly used in clinical practice to treat the patients with gallbladder problems and phlegm disturbance such as neurosis, climacteric syndrome and epilepsy (Che et al., 2016; Jin et al., 2022). Previous studies have demonstrated the qualitative and quantitative determination of WDD based on LC-MS/MS technology. The main chemical components analyzed in WDD include flavonoids, alkaloids, coumarins and triterpenoids (Yang et al., 2017; Wang et al., 2021). Several reports have been made on the pharmacokinetics associated with certain key bioactive substances, such as liquiritigenin, isoliquiritigenin (Han et al., 2019), naringenin (Wang et al., 2020a), etc. Nevertheless, pharmacokinetic studies on the primary bioactive components of WDD are still lacking. Pharmacokinetic analyses of WDD's primary bioactive ingredients will help to understand the dynamic process and action mechanism of the main bioactive components of WDD *in vivo*. To date there has not been a pharmacokinetic (PK) and pharmacodynamic (PD) study documented on the *in vivo* antioxidant activity of WDD.

In order to relate WDD-PK profiles to important therapeutic aspects and to provide guidance on the therapeutic usage of this herb in clinical settings, this work aims to build an *in vivo* PK-PD model. Which in turn will lay a foundation for other researchers to further investigate the PK-PD attributes of this potent traditional herb.

2 Materials and methods

2.1 Materials and instruments

Hesperidin (wkq20030407), tangeretin (wkq20041611), naringin (wkq21020606), isoliquiritigenin (wkq18033006),

10.3389/fphar.2024.1260603

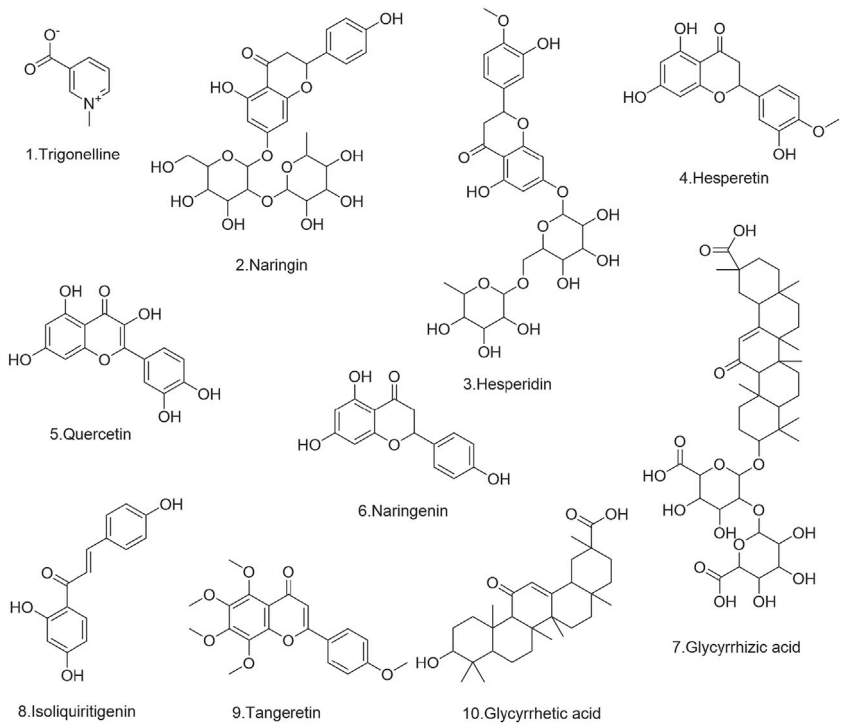

FIGURE 1
The structures of ten components of WDD.

TABLE 1 Mass spectrometric parameters for the 10 compounds and the internal standard.

Compounds	Chemical formula	Molecular weight	tR (min)	Scan mode	Q1 (m/z)	Q3 (m/z)	Collision energy (V)	Tube lens (V)
Trigonelline	$C_7H_7NO_2$	137.14	0.84	+	138.01	92.13	19.91	97
Naringin	$C_{27}H_{32}O_{14}$	580.53	3.71	-	579.2	459.16	22.99	234
Hesperidin	$C_{28}H_{34}O_{15}$	610.56	3.74	-	609.21	286.08	41.73	170
Hesperetin	$C_{16}H_{14}O_6$	302.28	3.75	+	303.11	177.13	16.84	133
Quercetin	$C_{15}H_{10}O_7$	302.24	4.03	-	301.06	151.04	21.09	149
Naringenin	$C_{15}H_{12}O_5$	272.25	4.51	-	271.03	119.05	26.52	124
Glycyrrhizic acid	$C_{42}H_{62}O_{16}$	822.93	4.55	+	823.52	453.39	19.87	171
Isoliquiritigenin	$C_{15}H_{12}O_4$	256.25	4.79	-	254.97	134.97	15.7	104
Tangeretin	$C_{20}H_{20}O_7$	372.37	6.03	+	373.17	358.13	19.07	167
Glycyrrhetinic acid	$C_{30}H_{46}O_4$	470.68	8.29	-	469.36	355.33	46.45	261
Furosemide	$C_{12}H_{11}ClN_2O_5S$	330.74	4.49	-	328.95	204.99	21.51	113

TABLE 2 Changes of blood lipid levels in rats after 12 weeks (mmol/L).

Group	TG	TC	LDL-C	HDL-C
NCG	0.44 ± 0.03	1.73 ± 0.30	0.30 ± 0.05	1.66 ± 0.23
MCG	1.41 ± 0.16**	2.65 ± 0.78**	0.58 ± 0.07*	0.92 ± 0.07*

*$p < 0.05$, **: $p < 0.01$.

glycyrrhetinic acid (wkq16070701), glycyrrhizic acid (wkq16032502), were obtained from the Sichuan Weikeqi Biological Technology Co., Ltd. (Sichuan, China). Hesperetin (PS000219), Trigonelline (PS000427), were provided by Sichuan Pu Si Biological Technology Co., Ltd. (Sichuan, China). Quercetin (100081–200406), and furosemide (as an internal standard), (100544–201503) were taken from the China Institute for

TABLE 3 Effect of WDD on the indexes of hyperlipidemia rats.

Group	Weight (g)	Liver wet weight (g)	TG (mmol/L)	TC (mmol/L)	LDL-C (mmol/L)	HDL-C (mmol/L)
NCG	469 ± 11	10.02 ± 1.68	0.42 ± 0.11	1.70 ± 0.17	0.30 ± 0.02	1.71 ± 0.25
MCG	611.33 ± 12.33	14.42 ± 1.48	1.44 ± 0.19	2.83 ± 0.45	0.61 ± 0.04	0.89 ± 0.04
LTG	525.00 ± 9.00*	10.87 ± 0.57	1.11 ± 0.16*	2.06 ± 0.15*	0.49 ± 0.04*	0.90 ± 0.05
HTG	503.33 ± 20.33*	11.82 ± 1.72	0.89 ± 0.08*	2.13 ± 0.10*	0.50 ± 0.04*	0.95 ± 0.05*

*$p < 0.05$.

TABLE 4 Standard curves and linear ranges of 10 compounds.

Compounds	Standard curves	r^2	Linear ranges (ng/mL)
Trigonelline	Y = 0.0030X+0.0532	0.9905	60–6,000
Naringin	Y = 0.0026X+0.0034	0.9926	6–600
Hesperidin	Y = 0.0018X+0.0037	0.9908	12–1,200
Hesperetin	Y = 0.0070X+0.0350	0.9903	30–3,000
Quercetin	Y = 0.0014X+0.1164	0.9912	13–1,300
Naringenin	Y = 0.0128X+0.0933	0.9907	7–700
Glycyrrhizic acid	Y = 0.0448X-0.1093	0.9931	5–500
Isoliquiritigenin	Y = 0.0360X-0.0907	0.9904	3–300
Tangeretin	Y = 0.1822X+1.0565	0.991	0.2–20
Glycyrrhetinic acid	Y = 0.0007X+0.0004	0.9908	30–3,000

Identification of Pharmaceutical and Biological Products (Beijing, China). The purity of all reference substances was above 98%. The structures of ten components of WDD are displayed in Figure 1.

Lipid peroxide (LPO) kit (EDL202107257) was supplied by Shanghai Yubo Biotechnology Co., LTD. (Shanghai, China). TG kit (20,210,723), LDL-C kit (20,210,723), HDL-C kit (20,210,723), and TC kit (20,210,723) were taken from Nanjing Jiancheng Bioengineering Institute (Nanjing, China). Acetonitrile and formic acid (chromatographic grade), were given by Fisher Scientific and Thermo Fisher Scientific Co., Ltd., respectively, whereas water was deionized water. High-fat blood feed (76.8% basic feed, 10% lard, 0.5% sodium cholate, 2.5% cholesterol, 10% egg yolk powder, 0.2% propylthiouracil) was purchased from Jinan Pengyue Experimental Animal Breeding Co., Ltd. (Jinan, China). Every single herb was purchased from Bozhou market (Anhui, China), and identified by Jin Guangqian, researcher of Shandong Academy of Traditional Chinese Medicine.

Mass spectrometry measurement was employed to Vanquish purification LC system, and triple quadrupole mass spectrometer (Thermo Scientific, United States), furnished with heated-electrospray ionization apparatus. Method setting, data acquisition and processing, and reporting were conducted using a Thermo Scientific Xcalibur software. Alpha1-4LSCplus freeze dryer (Germany CHRIST Freeze Dryer Co., LTD.). N-2110 rotary evaporator (Tokyo Physical and Chemical Instrument Co., LTD.). Xmark microplate reader (Bio-Rad Company), high-speed centrifuge HC-2518 (Anhui Zhongke Zhongjia Scientific Instrument Co., LTD.).

This research scheme has been approved by the Ethics Committee of Shandong Academy of Traditional Chinese Medicine (NO. SDZYY202201015). Animal-related experiments in this study were carried out according to the guideline "Guidance for Nonclinical Pharmacokinetics of Medicinal Products".

2.2 Preparation of WDD extract

10 g of pinellia ternata, 10 g of bran fried Fructus aurantii, 20 g of ginger, 10 g of raw bamboo, 5 g of fried licorice, 15 g of raw orange peel and 840 mL water, were accurately measured. Then, these ingredients were soaked for 30 min, decocted twice (2 h each time), filtered, combined, evaporated and concentrated. The above operation was repeated to obtain the extract of WDD. The resultant WDD extract was stored in a refrigerator at −20°C, which was filtered with 0.22 μm microporous membrane before analysis.

2.3 Development of hyperlipidemia rat model

50 SPF grade male SD rats (4 weeks, 180–200 g) were supplied by Jinan Pengyue Experimental Animal Breeding Co., LTD. (certification no. SCXK (LU) 20,190,003). The Study was approved by the Ethics Committee of The First Affiliated Hospital of Shandong First Medical University and Shandong Provincial Qianfoshan Hospital Prior to being utilized in

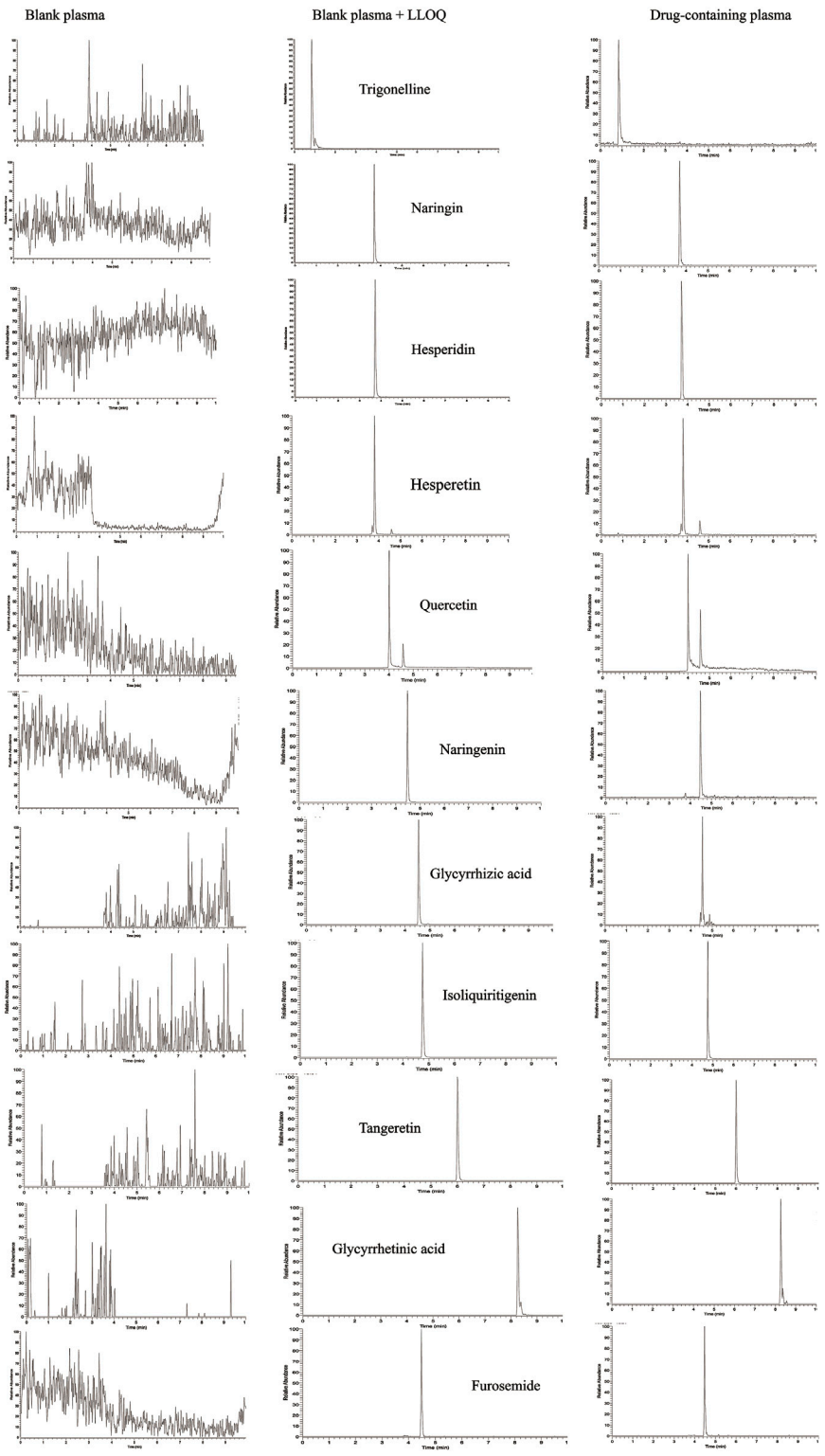

FIGURE 2
UPLC-MS chromatograms of ten components in WDD and Furosemide.

experiments, rats were kept for 7 days in an environmentally stable house (25°C ± 2°C, relative humidity 50% ± 5%, and 12 h light/dark cycle) having complete water accessibility, pathogen-free environment, and adaptive food. Rats with healthy blood lipid profiles were chosen after 1 week during adaptable feeding. Six of them were chosen to serve as NCG rats, and they were given a basic feed meal. The rest of the rats (to develop a hyperlipidemia model) were given a high-fat diet (HFD) over a 12-week period.

TABLE 5 Precision, accuracy, extraction recovery and matrix effects (n = 6).

Compounds	Concentrations (ng/mL)	Intra-day		Inter-day		Extraction recovery rate		Matrix effects	
		RSD (%)	RE (%)	RSD (%)	RE (%)	Recovery rate (%)	RSD (%)	Matrix effects (%)	RSD (%)
Trigonelline	60	12.26	13.86	9.08	5.52	103.84	8.03	98.90	6.24
	180	8.32	6.82	13.34	14.59	102.81	8.06	102.74	5.57
	3,000	12.48	1.39	2.11	6.07	103.15	4.84	102.39	5.11
	4,500	10.10	9.08	9.39	14.72	100.05	5.94	103.92	4.95
Naringin	6	3.38	19.80	10.34	5.70	100.13	2.80	100.77	3.51
	18	8.80	14.60	2.18	12.01	96.85	6.62	96.97	6.16
	300	13.53	12.55	1.64	10.10	97.95	3.53	98.07	5.64
	450	7.79	5.43	2.96	6.54	99.84	4.02	95.41	3.74
Hesperidin	12	5.52	14.36	13.01	4.35	97.56	2.77	100.03	2.28
	36	5.74	−6.94	5.17	−3.93	102.93	6.87	100.65	6.91
	600	4.84	2.47	3.79	−10.10	99.44	3.10	95.91	5.21
	900	8.35	1.11	3.16	−4.92	103.07	3.90	100.47	2.56
Hesperetin	30	11.83	8.41	12.54	−1.23	96.77	10.01	98.67	8.62
	90	12.69	5.54	7.82	10.70	98.55	6.19	103.98	8.31
	1,500	1.35	13.74	3.18	11.04	102.37	2.87	104.66	1.75
	2,250	8.15	14.11	10.02	10.73	96.52	2.73	106.30	6.52
Quercetin	13	5.52	8.79	7.43	8.57	98.06	3.84	101.71	3.52
	39	13.13	−6.73	3.78	−6.18	98.13	9.17	96.51	12.05
	650	5.57	2.44	6.60	1.55	94.32	9.59	100.78	5.57
	975	10.05	13.19	13.96	7.66	99.15	3.79	99.75	1.80
Naringenin	7	3.04	15.02	9.06	−0.17	99.42	1.60	99.38	2.64
	21	6.67	4.14	9.45	4.26	105.39	7.04	96.75	6.68
	350	5.69	−1.83	2.13	5.82	102.18	1.70	96.26	7.06
	525	6.07	−11.79	8.70	2.50	102.55	7.30	96.12	8.88
Glycyrrhizic acid	5	1.75	12.53	14.14	−5.11	99.56	2.26	99.91	2.00
	15	6.10	3.55	6.47	−3.53	105.20	5.70	99.49	7.88
	250	6.65	−12.25	5.35	−12.03	98.80	6.20	103.42	3.61
	375	11.37	−8.04	6.00	−7.37	106.05	5.99	98.76	3.22
Isoliquiritigenin	3	3.45	18.13	2.74	18.22	99.33	0.74	100.66	0.56
	9	5.62	12.90	4.43	3.44	102.61	2.68	97.59	2.97
	150	8.04	4.74	3.20	10.44	101.49	9.76	97.34	9.16
	225	9.08	3.66	11.65	9.18	97.16	7.96	102.26	6.94
Tangeretin	0.2	14.90	10.60	13.90	−1.97	101.41	7.86	99.91	8.16
	0.6	6.65	−12.50	9.90	6.29	98.67	5.84	94.80	5.44
	10	3.17	2.88	3.21	8.74	89.23	4.49	94.79	6.21
	15	5.56	3.07	9.18	−2.28	102.23	4.80	98.19	6.00

(Continued on following page)

TABLE 5 (*Continued*) Precision, accuracy, extraction recovery and matrix effects (n = 6).

Compounds	Concentrations (ng/mL)	Intra-day		Inter-day		Extraction recovery rate		Matrix effects	
		RSD (%)	RE (%)	RSD (%)	RE (%)	Recovery rate (%)	RSD (%)	Matrix effects (%)	RSD (%)
Glycyrrhetinic acid	30	19.33	−4.68	4.94	−2.03	98.67	7.44	101.16	7.22
	90	12.38	−6.57	11.96	7.73	102.17	8.98	97.88	11.91
	1,500	9.99	3.29	9.26	12.41	106.38	4.76	94.49	6.59
	2,250	7.61	8.99	12.67	12.67	106.48	5.44	103.14	3.53
IS	500					103.54	6.24	100.32	8.94

Afterwards, following a 12-h fasting, blood was drawn from each animal's mandibular vein and lipid panels (LDL-C, HDL-C, TC, and TG levels) were assessed to determine whether hyperlipidemia had been successfully induced. The rats with significant differences in body weights and blood lipid indexes were separated into a model group, a low-dose WDD group (LTG) and a high-dose WDD group (LTG) (n = 6 each). Fasting blood samples were taken to determine blood lipid indexes 12 h after administration.

2.4 Animal testing and samples gathering

Four groups (NCG, MCG, LTG, and HTG) of successfully modeled rats were established, with six rats in each group. LPO values of all the rats were assessed prior to therapy, and utilized as the baseline. Both the NCG and MCG groups received an equivalent amount of normal saline, whereas rats in the LTG and HTG groups received 2.2 g/100 g and 6.6 g/100 g of WDD by gavage, respectively. Before and after the administration, about 0.5 mL of blood was taken from orbital venous plexus at around 0.25, 0.5, 0.75, 1, 1.5, 2, 2.5, 3, 4, 6, 8, 10, 12, 24 h, and placed in a 1.5 mL heparinized centrifuge tube. Afterwards, centrifugation was carried out for 10 min at 6,000 rpm and the supernatant (200 μL) was divided into two separate storage tubes for PK and PD studies, and stored at −80°C.

2.5 Sample preparation and analysis

2.5.1 LC-MS/MS analytical conditions

2.5.1.1 Chromatographic conditions

Thermo Scientific Hypersil C18 analytical column (particle size: 1.9 μm, length: 100 mm, and diameter: 2.1 mm) was employed. Column operational conditions were like so, column temperature: 30°C, autosampler temperature: 4°C, whereas the flow rate: 0.3 mL/min. Injection volume: 3 μL, and mobile phase: aqueous solution containing 0.1% formic acid aqueous solution (A) and acetonitrile (B). Elution gradient: 0–0.5 min, 5% B; 0.5–2 min, 5%–8% B; 2–2.1 min, 40% B; 2.1–4 min, 40%–50% B; 4–6 min, 50%–60% B; 6–6.1 min, 60%–70% B; 6.1–8 min, 70%–80% B; 8–8.1 min, 80%–5% B; 8.1–10 min, 5% B.

2.5.1.2 Mass spectrometry conditions

Electrospray ion source (ESI) was used for mass spectrometry detection and analysis, both in positive and negative ion patterns. Nitrogen was kept as both of the auxiliary and sheath gas. The capillary temperature was 345°C, the atomizer temperature was 350°C, and the electrospray voltage was 3800 V. The mass spectrometry data for the 10 compounds and the internal standard (IS) are shown in Table 1.

2.5.2 Bioanalytical method validation

An appropriate amount of furosemide (IS) was taken, and furosemide solution with a concentration of 500 ng/mL was made in 50% acetonitrile. We prepared 2 mg/mL stock solutions of trigonelline, naringin, hesperidin, hesperetin, quercetin, naringenin, glycyrrhizic acid, isoliquiritigenin, tangeretin, and glycyrrhetinic acid in 50% acetonitrile. The above stock solutions were precisely pipetted and diluted with 50% acetonitrile solution, to make a mixture of working solutions, with concentrations: 60–6,000 ng/mL of trigonelline, 6–600 ng/mL of naringin, 12–1200 ng/mL of hesperidin, 30–3,000 ng/mL of hesperetin, 13–1,300 ng/mL of quercetin, 7–700 ng/mL of naringenin, 5–500 ng/mL of glycyrrhizic acid, 3–300 ng/mL of isoliquiritigenin, 0.2–20 ng/mL of tangeretin, and 30–3,000 ng/mL of glycyrrhetinic acid, respectively. The above mixed working solution was precisely measured and diluted with 50% acetonitrile into 4 different concentrations of Quality Control sample (QC) solutions (lower limit of quantification: low concentration: medium concentration: high concentration = 1:3:50:75). The precision, accuracy, linearity, recovery, and stability of the aforementioned solutions were then verified, in accordance with the standards for the verification of biological sample quantitative analytical methods.

2.5.3 Sample preparation

After accurately measuring 100 μL of plasma, 10 μL of the QC solution or the IS solution was supplemented, and the blend was vortexed for 30 s. Afterward, 300 μL of acetonitrile (as protein precipitant) was added, vortexed for 1 min, and then centrifuged (10 min at 12000 r/min). Finally, the supernatant was taken and stored for testing.

10.3389/fphar.2024.1260603

TABLE 6 Stability results of Wendan decoction compounds (n = 6).

Compounds	Concentrations (ng/mL)	Short-term stability		Sampler stability		Long-term stability		Freeze-thaw stability	
		RSD (%)	RE (%)	RSD (%)	RE (%)	RSD (%)	RE (%)	RSD (%)	RE (%)
Trigonelline	60	14.54	12.68	13.87	7.08	7.71	3.62	12.48	−5.67
	180	14.38	10.77	9.60	7.96	9.26	14.90	6.58	12.19
	3,000	6.88	13.86	14.55	−12.25	13.26	−9.25	13.68	9.63
	4,500	10.36	6.21	8.49	13.36	5.09	11.41	10.67	4.95
Naringin	6	2.93	18.35	3.64	17.64	2.29	15.77	5.00	19.78
	18	8.13	−3.41	9.49	−9.61	10.99	−14.52	11.80	−6.24
	300	10.71	3.38	6.55	7.71	11.13	12.08	11.05	8.72
	450	10.84	0.91	13.23	3.14	9.74	1.58	7.60	0.58
Hesperidin	12	2.98	11.61	2.46	9.97	2.33	11.00	4.50	7.52
	36	12.85	−2.17	12.43	−5.51	5.19	3.28	8.33	1.01
	600	6.74	−0.12	11.56	−5.29	10.60	1.54	8.51	−12.19
	900	6.56	4.63	10.11	7.61	7.85	9.13	11.46	4.61
Hesperetin	30	5.52	−2.74	7.53	4.94	8.71	3.99	13.44	−5.81
	90	3.61	14.70	4.57	13.49	9.93	9.48	10.12	11.59
	1,500	5.46	−1.22	10.24	0.14	8.69	−7.56	9.20	1.47
	2,250	6.08	5.43	7.17	3.47	6.17	9.31	7.38	−0.19
Quercetin	13	5.24	15.78	1.66	11.72	10.26	19.14	12.82	13.78
	39	8.29	−7.80	6.73	−6.42	8.74	6.92	13.28	3.42
	650	6.12	2.69	6.97	2.39	7.18	14.81	8.31	−2.45
	975	7.94	−2.18	7.41	4.02	4.60	3.33	9.04	−1.13
Naringenin	7	4.55	9.72	3.76	8.99	9.23	12.35	7.92	5.52
	21	8.16	−2.36	7.84	6.66	14.25	9.23	5.98	0.20
	350	9.33	1.75	13.17	9.39	9.60	12.97	12.63	2.80
	525	11.20	−12.08	14.79	−3.55	7.86	3.39	13.75	−9.80
Glycyrrhizic acid	5	5.01	15.73	2.89	10.97	4.83	12.94	2.95	7.12
	15	10.03	6.57	8.36	12.40	2.64	14.63	5.68	11.07
	250	8.58	−13.17	11.72	−0.40	14.07	7.02	6.72	−12.75
	375	8.90	−5.53	14.44	−2.04	5.32	0.59	9.82	−5.71
Isoliquiritigenin	3	5.43	15.82	1.88	13.76	1.28	13.34	2.71	12.48
	9	9.18	4.77	12.72	−7.52	7.16	−6.61	4.51	−11.70
	150	8.74	7.78	9.38	14.47	14.65	−3.26	12.08	−13.64
	225	12.39	−0.76	8.29	7.05	10.93	−7.04	14.53	−6.05
Tangeretin	0.2	13.26	18.32	15.09	12.80	15.54	−4.59	17.99	6.79
	0.6	10.65	0.90	8.53	4.40	11.56	10.86	10.67	5.38
	10	3.90	3.89	3.13	13.31	10.61	11.27	8.92	−2.42
	15	8.52	−5.20	10.46	−2.26	3.72	−1.29	9.67	−7.09

(Continued on following page)

TABLE 6 (*Continued*) Stability results of Wendan decoction compounds (n = 6).

Compounds	Concentrations (ng/mL)	Short-term stability		Sampler stability		Long-term stability		Freeze-thaw stability	
		RSD (%)	RE (%)	RSD (%)	RE (%)	RSD (%)	RE (%)	RSD (%)	RE (%)
Glycyrrhetinic acid	30	5.54	−7.16	18.51	−15.48	11.24	−3.30	13.23	−9.94
	90	5.69	5.72	12.35	3.07	13.01	11.11	8.99	5.66
	1,500	7.42	14.58	6.97	12.55	11.39	13.59	8.35	−2.83
	2,250	5.89	12.58	11.14	13.87	6.69	14.34	11.11	11.96

2.6 PK research

The standard curves produced for every specimen batch were used to calculate the trigonelline, naringin, hesperidin, hesperetin, quercetin, naringenin, glycyrrhizic acid, isoliquiritigenin, tangeretin and glycyrrhetinic acid plasma concentrations. The dose, plasma concentration and time after administration were imported into the NCA (Noncompartmental Analysis) module of Phoenix 8.1 to obtain the pharmacokinetic parameters. The Phoenix Model module of Phoenix software was used to establish the atrioventricular model of the drug. Akaike Information Criterion (AIC) rules were used to calculate the optimal PK model.

2.7 PK–PD research

Employing specialized ELISA kits and following the specified instructions, the values of plasma LPO were monitored over time. In order to assist the PK-PD modeling, LPO values were utilized to determine changes associated with treatment in the LTG via the given Eq. 1 (Huang et al., 2020):

$$\Delta LPO_{LTG} = LPO_{LTG} - LPO_{MCG} \quad (1)$$

('ΔLPO' refers to the variation in LPO from the initial levels)

Above PK model and a Sigmoid E_{max} model (Eq. 2) were used, to establish a PK-PD model on the basis of concentrations of plasma and LPO levels. A preliminary model of the PK-PD interaction was developed using the plasma concentrations of LPO as well as the 10 WDD ingredients in LTG rats.

$$E = E_{max} \times C^{\gamma} / ED_{50}^{\gamma} + C^{\gamma} \quad (2)$$

Where 'E' denotes the change in plasma LPO levels, 'C' indicates the concentration to drug effect, 'E_{max}' corresponds to the highest possible drug effect, 'ED50γ' indicates the dose that generates 50% of the E_{max}, and 'γ' signifies the halfway slope of the curve (an indicator of the concentration-effect correlation).

3 Results

3.1 Hyperlipidemia rat model study

Following 12 weeks of HFD feeding, the rats plasma lipid levels were determined. The findings demonstrated that, the model rats had much higher levels of lipids, as compared with the controls (Table 2). In particular, MCG rats were found with considerably higher levels of TC and TG than NCG rats ($p < 0.01$), whereas MCG rats were also observed with higher levels of LDL-C than NCG ($p < 0.05$), and lower levels of HDL-C than NCG ($p < 0.05$). Hence, these results verified the successful establishment of our hyperlipidemia rat model.

After administration of the low dose of WDD, the rats showed significant differences in weight, TG, TC and LDL-C levels in contrast to the model group rats, but the changes in HDL-C were not significant and did not differ significantly. After the administration of high-dose of WDD, the four lipid parameters examined varied considerably from the model group rats. These findings indicated that, WDD may achieve lipid-lowering effects by lowering plasma TC, TG and LDL-C levels, however no notable variations between HTG and LTG were seen (Table 3). Therefore, LTG group was selected to construct a PK-PD model.

3.2 Methodology study

3.2.1 Specificity

The lower limit of quantitation (LLOQ) refers to the signal-to-noise ratio of exactly 10, where an analyte can be reliably quantified (Trivedi et al., 2004; Duggan, 2019). The LLOQ and the blank plasma of IS rats were measured through the specificity analysis of rat blank plasma (Figure 2). The retention times of trigonelline, naringin, hesperidin, hesperetin, quercetin, naringenin, glycyrrhizic acid, isoliquiritigenin, tangeretin, glycyrrhetinic acid and furosemide were 0.84, 3.71, 3.74, 3.75, 4.03, 4.51, 4.55, 4.79, 6.03, 8.29, and 4.49 min respectively. The chromatographic peak patterns of each compound were good, and there was no interference from other impurity peaks in the plasma samples.

3.2.2 Standard curve and linear range

The linear regression equation and range of each substance to be measured were obtained by preparing 8 plasma solutions of mixed control at different concentration levels. The results indicated that, the correlation coefficient (r^2) of every single compound was >0.99, indicating that the linear relationship was good within this concentration range. Standard curves and linear ranges of 10 compounds were shown in Table 4. UPLC-MS chromatograms of 10 components in WDD and Furosemide were shown in Figure 2.

3.2.3 Precision and accuracy

The precision and accuracy (both intra- and inter-day) of QC samples of the substance to be measured were investigated. The

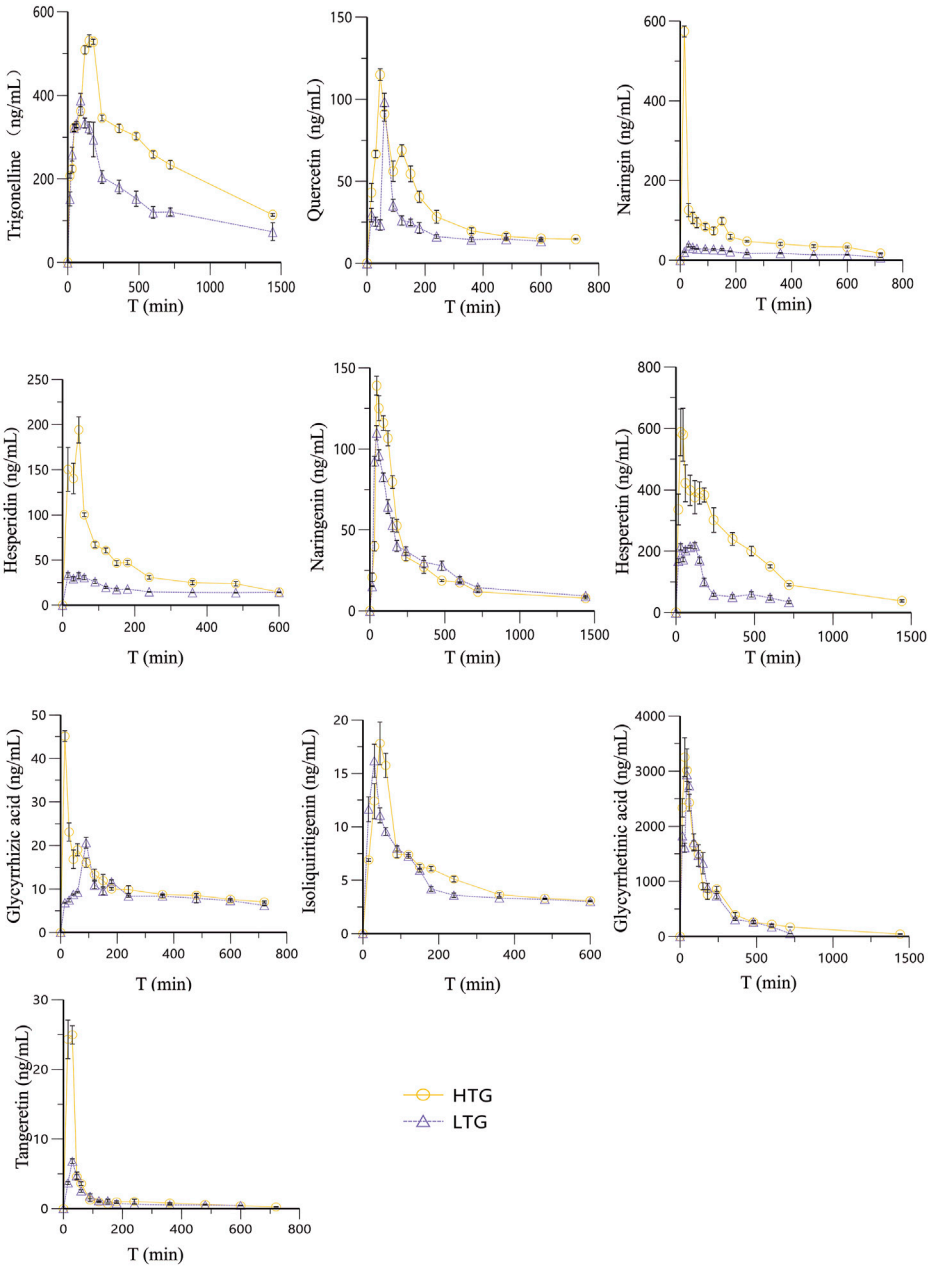

FIGURE 3
The Concentration-Time curves of ten components of WDD.

results showed that, the intra-day precision (RSD) was 1.35%–19.33%, and the inter-day precision (RSD) was 1.64%–14.14%. The intra-day accuracy (RE) was −12.50%-19.80%, and the inter-day accuracy (RE) was −12.03%-18.22% (Table 5), indicating that both of the precision and accuracy of the following procedure were good.

3.2.4 Extraction recovery and matrix effect

The results showed that, the extraction recoveries were greater than 89.23%, indicating that acetonitrile could be used as the extraction solvent for the above compounds, and the interference of other endogenous components could be excluded. The matrix effects of the 10 compounds ranged from 94.49% to 106.30%, and the RSD values ranged from 0.56% to 12.05%, indicating that, no interference of other endogenous components was there in the matrix of blood.

3.2.5 Stability

The stability results of QC specimens (at 4 different concentrations) showed that, the short-term stability and injector stability (RSD) of the 10 compounds to be tested ranged from 1.66% to 18.51%. Indicating that, the samples to

TABLE 7 Main pharmacokinetic parameters of the 10 chemical components of WDD (n = 6).

Ingredinent	Group	$t_{1/2}$(h)	T_{max} (h)	C_{max} (ng/mL)	AUC_{0-t} (ug*h/L)
Trigonelline	LTG	12.24 ± 1.65	1.50 ± 0.00	388.39 ± 25.84	3555.22 ± 299.53
	HTG	11.75 ± 1.81	2.67 ± 0.33	536.85 ± 7.69	6013.37 ± 96.43
Naringin	LTG	6.13 ± 0.94	0.54 ± 0.21	36.80 ± 4.99	209.74 ± 12.50
	HTG	5.00 ± 1.27	0.25 ± 0.00	574.53 ± 17.55	713.43 ± 46.42
Hesperidin	LTG	12.11 ± 5.52	0.67 ± 0.42	34.56 ± 3.22	171.66 ± 3.26
	HTG	4.19 ± 0.17	0.75 ± 0.00	194.13 ± 24.31	438.96 ± 13.31
Hesperetin	LTG	5.88 ± 3.39	1.42 ± 0.92	222.86 ± 8.19	1028.18 ± 23.75
	HTG	6.24 ± 0.36	0.67 ± 0.17	607.28 ± 129.68	3892.74 ± 147.13
Quercetin	LTG	31.10 ± 41.37	1.00 ± 0.00	98.36 ± 8.03	212.03 ± 9.39
	HTG	7.75 ± 12.99	0.75 ± 0.00	114.93 ± 4.83	370.18 ± 14.70
Naringenin	LTG	12.47 ± 4.08	0.75 ± 0.00	109.95 ± 6.80	587.10 ± 14.35
	HTG	11.69 ± 1.94	0.75 ± 0.00	139.03 ± 10.63	594.54 ± 15.42
Glycyrrhizic acid	LTG	10.80 ± 3.88	1.50 ± 0.00	20.64 ± 2.16	104.44 ± 5.97
	HTG	15.52 ± 7.44	0.25 ± 0.00	45.13 ± 2.30	128.19 ± 5.67
Isoliquiritigenin	LTG	27.45 ± 4.66	0.50 ± 0.00	16.19 ± 2.35	48.49 ± 0.82
	HTG	14.61 ± 9.00	0.79 ± 0.21	17.84 ± 3.31	54.94 ± 2.07
Tangeretin	LTG	8.83 ± 4.57	0.50 ± 0.00	6.80 ± 0.46	10.81 ± 0.32
	HTG	3.21 ± 0.89	0.38 ± 0.13	25.86 ± 2.98	22.39 ± 0.89
Glycyrrhetinic acid	LTG	2.30 ± 0.16	0.75 ± 0.00	2935.45 ± 220.30	8182.79 ± 499.70
	HTG	6.02 ± 0.92	0.54 ± 0.21	3282.24 ± 475.37	10176.26 ± 298.42

TABLE 8 PK-PD model equation for the chemical components of WDD.

Ingredient	Model	AIC	PK-PD equation
Trigonelline	Two-Compartment Model	−31.68	$E = 0.2378*C^{2.62}/(242.52^{2.62} + C^{2.62})$
Naringin	Two-Compartment Model	−5.88	$E = 0.1387*C^{7.41}/(13.40^{7.41} + C^{7.41})$
Hesperidin	One-Compartment Model	−0.31	$E = 0.1387*C^{8.69}/(13.63^{8.69} + C^{8.69})$
Hesperetin	One-Compartment Model	10.89	$E = 0.1387*C^{4.87}/(58.47^{4.87} + C^{4.87})$
Quercetin	Two-Compartment Model	18.54	$E = 0.1241*C^{5.72}/(10.98^{5.72} + C^{5.72})$
Naringenin	One-Compartment Model	22.89	$E = 0.1387*C^{7.84}/(32.66^{7.84} + C^{7.84})$
Glycyrrhizic acid	One-Compartment Model	62.87	$E = 0.1387*C^{13.46}/(7.46^{13.46} + C^{13.46})$
Isoliquiritigenin	Two-Compartment Model	−8.47	$E = 0.1399*C^{7.10}/(3.03^{7.10} + C^{7.10})$
Tangeretin	Two-Compartment Model	29.75	$E = 0.1390*C^{13.18}/(242.52^{13.18} + C^{13.18})$
Glycyrrhetinic acid	One-Compartment Model	3.90	$E = 0.1398*C^{2.35}/(244.50^{2.35} + C^{2.35})$

be tested were stable within 2 h at room temperature and within 24 h in the injector (4°C). The RSD values of long-term stability and freeze-thaw cycle stability were between 1.28% and 19.99%, and samples were stable after three repeated freeze-thaw cycles, suggesting that the samples to be tested could be stored at −80°C for 14 days, as detailed in Table 6.

3.3 PK profiles in hyperlipidemia rats

After the rats were given different doses of WDD by gavage, the established LC-MS/MS method was applied to quantitatively analyze the 10 substances to be measured in the rat's plasma. The blood drug concentrations were obtained at different time points

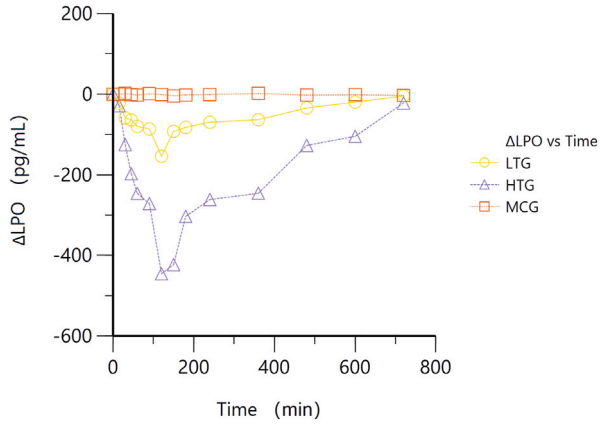

FIGURE 4
ΔLPO_{LTG}-Time curves of MCG, LTG and HTG groups.

and the drug-time curves of each compound were shown in Figure 3. Phoenix 8.1 software was used to calculate the non-compartment model to obtain its pharmacokinetic parameters (Table 7).

The results showed that, 10 components of WDD could be detected in plasma at 0.25 h. Equivalent dose: from the aspect of time of reaching the peak, hesperetin and isoliquiritigenin have the shortest time of reaching the peak, only 0.5 h, and the components with the longest time of reaching the peak are glycyrrhizic acid and trigonelline, 1.5 h. From the perspective of half-life, the half-life of glycyrrhetinic acid was the shortest, only 2.3 h, and that of quercetin was the longest, up to 31.1 h. High dose: the peak time of hesperetin and isoliquiritigenin was the shortest, only 0.25 h, and the component with the longest peak time was trigonelline, up to 2.67 h. In terms of half-life, hesperetin has the shortest half-life, only 3.21 h, and glycyrrhizic acid has the longest time, up to 15.52 h. In terms of the level of exposure *in vivo*, the area under the curve (AUC) of glycyrrhetinic acid in rat's plasma was the largest at both doses, indicating that it has good bioavailability. The ideal biochemical processing of these 10 substances in rats was better defined by the two-compartment PK model, according to AIC values (Table 8).

3.4 PD research

The average change in LPO levels in WDD treatment groups was evaluated by means of the effect-time curve for MCG, LTG and HTG groups (Figure 4). After treatment with WDD, the LPO levels in the two treatment groups showed a trend of decreasing first and then increasing, indicating that WDD can inhibit the level of LPO. The lowest level of LPO in the treatment group was observed in 2 h, whereas the LPO level in the high-dose group was severely inhibited. Thus, it is suggested that the inhibition of LPO level by WDD may be related to the dose. It can be seen that the LPO level in the WDD treatment group is significantly decreased than that at the beginning, which also proves the inhibitory effect of WDD on the level of LPO. Indicating that, this reduction could be one of the mechanisms of WDD to help in treating the hyperlipidemia.

3.5 PK-PD research

The PK-PD simulation was then carried out by employing the final collected data. The drug effect-concentration curves of ten components are shown in Figure 5. A sigmoid E_{max} model provided the most accurate descriptions of ten substances and LPO concentrations, with calculated parameters for trigonelline, naringin, hesperidin, hesperetin, quercetin, naringenin, glycyrrhizic acid, isoliquiritigenin, tangeretin and glycyrrhetinic acid, were determined using this model. Table 8 displays the final quantified PK-PD formulas for each group that incorporate drug levels and LPO effects.

4 Discussion

Hyperlipidemia is a kind of metabolic disorder caused by defective lipid metabolism in the body, which can cause systemic and cardiovascular disorders, i.e., atherosclerosis (Tannock, 2008; Nofer, 2010; Tietge, 2014; Navar-Boggan et al., 2015; Zhao et al., 2018; Suh et al., 2022). High fat diet intake and improper lipid metabolism could both contribute to the development of hyperlipidemic disorders (Joy et al., 2007; Bai et al., 2015; Matey-Hernandez et al., 2018; Rodríguez-Borjabad et al., 2021). In this study, a hyperlipidemia rat model was established, so as to study the PK-PD characteristics of the ten components of WDD. The *in vivo* PK-PD studies are considered to be extremely crucial in constructing the new drug molecules, in order to direct their clinical application (Wang et al., 2020b). PK analysis gives an insight into the several attributes of a drug, including drug-plasma concentration, half-life, the onset of action, etc. (Chaudhary and Dion, 2013). On the other hand, PD analysis analyzes the drug effect and the mechanism of action of a new drug (Cui et al., 2022). In order to understand the connection of particular components in a complex preparation with efficacy or toxicity, the precise study of the PK-PD relationship is valuable, Flavonoids have been proven to exert the protective effects, including antioxidant and anti-inflammatory effects, by eliminating the free radicals (Rajendran et al., 2004; Nauser and Gebicki, 2019; Kejík et al., 2021). Hence, it is been proposed that flavonoids and associated metabolites contain antioxidant effects and can prevent oxidative injury brought on by hyperlipidemia (Pietta, 2000; Sun et al., 2021). WDD components, including naringin, hesperidin, hesperetin, quercetin, naringenin, isoliquiritigenin, and tangeretin contain flavonoids as principal bioactive compounds. In addition, WDD also contains active alkaloids, such as trigonelline, glycyrrhizic acid and glycyrrhetinic acid.

Several studies have confirmed that these components have different degrees of lipid-lowering effects. Naringin has a strong effect on reducing lipids and protecting liver in hyperlipidemia mice (Yu et al., 2022). Hesperidin can reduce altered redox homeostasis in experimental hyperlipidemia rat models (Kumar et al., 2020). Compared with the control group, the body weight,

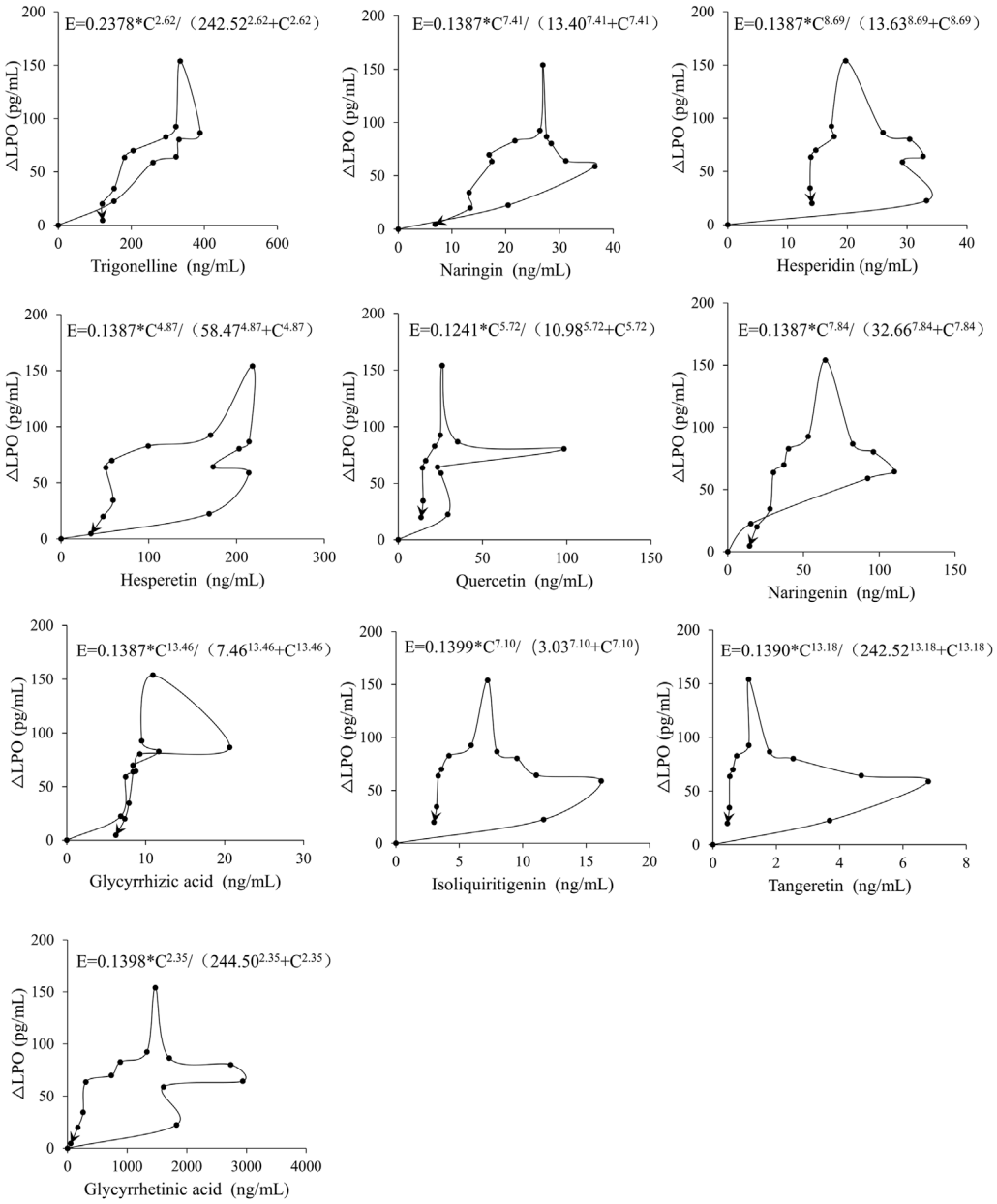

FIGURE 5
The Effect-Concentration curves of ten components.

obesity index, serum TC, TG, liver TC, TG and free fatty acid levels of hyperlipidemia hamsters treated with hesperetin were significantly decreased (Shi et al., 2023). Available evidence from randomized controlled trials suggests that quercetin supplementation does not have any clinically relevant effect on plasma lipids, except for a significant reduction in triglycerides at doses above 50 mg/day (Sahebkar, 2017). Supplementation with the natural compound naringenin can directly act on high cholesterol induced liver damage (Chtourou et al., 2015). Citrus flavonoids such as tangeretin have been shown to play a significant role in the treatment of dyslipidemia, insulin resistance, hepatic steatosis, obesity and atherosclerosis (Mulvihill et al., 2016). Trigonelline is reported to have a variety of biological activities, such as protecting the heart and liver, treating high blood sugar, hypercholesterolemia, nerve and hormone disorders, and cancer (Mohamadi et al., 2018). Glycyrrhizic acid can increase HDL and has anti-atherosclerotic properties (Eu et al., 2010).

The *in vivo* PK and PD parameters of such components in Hyperlipidemic environment have not yet been examined. Therefore, we constructed the current investigation as an *in vivo* PK-PD evaluation of trigonelline, hesperidin, hesperetin, naringenin, naringin, glycyrrhizic acid, isoliquiritigenin, tangeretin, quercetin, and glycyrrhetinic acid in hyperlipidemia. Studies have approved that, malondialdehyde (MDA), and such other polyunsaturated fatty acids can be used to

determine the oxidative stress and LPO in disease process related to hyperlipidemia (Ayala et al., 2014; Li et al., 2018). The rise of LPO level is the result of the automatic oxidation of polyunsaturated fatty acids, which can promote the production of MDA and other toxic compounds. In this study, we choose LPO level as the main PD index, measured by model animals with significant elevations in plasma (Figure 4), which is in line with previous studies (Chang et al., 2011; Guo et al., 2022).

Earlier in this study, we tested methanol and acetonitrile as organic solvents for the removal of protein macromolecules, and finally found that acetonitrile was superior to methanol. The plasma matrix effect and elution durations of trigonelline, naringin, hesperidin, hesperetin, quercetin, naringenin, glycyrrhizic acid, isoliquiritigenin, tangeretin, and glycyrrhetinic acid were assessed, and the results showed that these plasma components are optimally segregated using 0.1% formic acid in water and acetonitrile. Then, using a rat model of hyperlipidemia, we carried out PK and PD study on the WDD components.

All the rats in LTG and HTG WDD-treated groups were analyzed in parallel with each other, correlating the plasma concentrations of trigonelline, naringin, hesperidin, hesperetin, quercetin, naringenin, glycyrrhizic acid, isoliquiritigenin, tangeretin and glycyrrhetinic acid. Major PK variables were analyzed using UPLC-MS such as $t_{1/2}$, T_{max}, C_{max} and AUC_{0-t}. The LPO results determined by PD analysis were combined with treatment-related changes in the LTG and HTG to establish a PK-PD model. Rats in the HTG group showed substantially higher C_{max} and AUC_{0-t} for each of the 10 tested WDD ingredients than those in the LTG group. As compared with LTG group, $t_{1/2}$ of glycyrrhizic acid and glycyrrhetinic acid in HTG group were significantly prolonged, and T_{max} was significantly decreased, suggesting that the intestinal absorption rate of these two substances might be accelerated with the increase of dosage, and prolonged metabolic time in the body. The $t_{1/2}$ of hesperidin, quercetin, isoliquiritigenin, and tangeretin were significantly shortened and T_{max} was significantly decreased, indicating that the intestinal absorption and metabolism were expediated with increasing dose. The alterations in the gut flora brought on by oxidative stress and hyperlipidemia might help the body to absorb glycyrrhizic acid, glycyrrhetinic acid, hesperidin, quercetin, isoliquiritigenin and tangeretin. For trigonelline, hesperetin and naringenin, different doses did not cause significant changes in $t_{1/2}$ and T_{max}. The pharmacokinetic and pharmacodynamic relevance of the 10 major WDD compounds was investigated, based on trends in concentration as well as in LPO values. Subsequent results indicated that, ED_{50} values of isoliquiritigenin, glycyrrhizic acid, quercetin, naringin, hesperidin, naringenin, hesperetin were smaller. It indicated that, each component has a greater influence on the levels of LPO. These results suggest that, flavonoids are the main active components of WDD in lowering blood lipids. Our previous study has proved the shielding effects of WDD on HUVEC cells damage by palmitic-acid (Xu et al., 2023). Whereas, our present study has validated the lipid-lowering nature of the potent WDD in rats' plasma. Suggesting that, both studies may provide a foundation for other researchers to further investigate the antihyperlipidemic effects of WDD.

5 Conclusion

In the interest of better comprehending the antioxidant activity of this TCM formulation, we examined the PK and PD attributes of 10 major components of WDD (trigonelline, naringin, hesperidin, hesperetin, quercetin, naringenin, glycyrrhizic acid, isoliquiritigenin, tangeretin and glycyrrhetinic acid) *in vivo*. So as to assess the efficacy of the exclusive dosage of WDD in decreasing the LPO blood levels in the hyperlipidemia *in vivo*, we effectively built the sigmoid E_{max} PK-PD model. The consequent results of this study may provide data for ensuing investigations of PK/PD properties of WDD, in order to direct its therapeutic use in medical settings.

Data availability statement

The original contributions presented in the study are included in the article/supplementary material, further inquiries can be directed to the corresponding authors.

Author contributions

NX: Conceptualization, Data curation, Formal Analysis, Funding acquisition, Investigation, Methodology, Project administration, Resources, Software, Supervision, Validation, Visualization, Writing–original draft, Writing–review and editing. MI: Conceptualization, Data curation, Formal Analysis, Funding acquisition, Investigation, Methodology, Project administration, Resources, Software, Visualization, Writing–original draft, Writing–review and editing. YS: Conceptualization, Data curation, Formal Analysis, Funding acquisition, Investigation, Methodology, Project administration, Resources, Visualization, Writing–original draft, Writing–review and editing. PeW: Conceptualization, Data curation, Formal Analysis, Investigation, Methodology, Project administration, Software, Visualization, Writing–original draft, Writing–review and editing. LM: Conceptualization, Data curation, Formal Analysis, Investigation, Methodology, Software, Visualization, Writing–original draft, Writing–review and editing. PiW: Conceptualization, Data curation, Formal Analysis, Funding acquisition, Investigation, Methodology, Project administration, Resources, Software, Supervision, Validation, Writing–original draft, Writing–review and editing. HD: Conceptualization, Data curation, Formal Analysis, Investigation, Methodology, Software, Validation, Visualization, Writing–original draft, Writing–review and editing. MSh: Conceptualization, Data curation, Formal Analysis, Funding acquisition, Investigation, Methodology, Project administration, Resources, Software, Supervision, Validation, Visualization, Writing–original draft, Writing–review and editing. H-yS: Conceptualization, Data curation, Formal Analysis, Funding acquisition, Investigation, Methodology, Project administration, Resources, Software, Supervision, Writing–original draft.

Funding

The author(s) declare financial support was received for the research, authorship, and/or publication of this article. Funding Information: Key Project of Shandong Natural Science Foundation (ZR2020KH017); National Natural Science Foundation Project (82,074,052); New 20 clauses universities in Jinan City Introduce Innovation Team Projects (202,333,021); Key Projects of Traditional Chinese Medicine Technology Projects in Shandong Province (2021Z048); Shandong Province Science and Technology Small and Medium Enterprises Innovation Ability Enhancement Project (2022TSGC1057); Jinan Science and Technology Small and Medium Enterprises Innovation Ability Enhancement Project (2022TSGC1057); Shandong Province Traditional Chinese Medicine Technology Project (Z-2023012).

Conflict of interest

The authors declare that the research was conducted in the absence of any commercial or financial relationships that could be construed as a potential conflict of interest.

Publisher's note

References

Abu-Saleh, N., Yaseen, H., Kinaneh, S., Khamaisi, M., and Abassi, Z. (2021). Combination of hyperglycaemia and hyperlipidaemia induces endothelial dysfunction: role of the endothelin and nitric oxide systems. *J. Cell. Mol. Med.* 25 (4), 1884–1895. doi:10.1111/jcmm.15787

Ansar, S., Koska, J., and Reaven, P. D. (2011). Postprandial hyperlipidemia, endothelial dysfunction and cardiovascular risk: focus on incretins. *Cardiovasc. Diabetol.* 10, 61. doi:10.1186/1475-2840-10-61

Ayala, A., Muñoz, M. F., and Argüelles, S. (2014). Lipid peroxidation: production, metabolism, and signaling mechanisms of malondialdehyde and 4-hydroxy-2-nonenal. *Oxidative Med. Cell. Longev.* 2014, 360438. doi:10.1155/2014/360438

Bai, J., Zheng, S., Jiang, D., Han, T., Li, Y., Zhang, Y., et al. (2015). Oxidative stress contributes to abnormal glucose metabolism and insulin sensitivity in two hyperlipidemia models. *Int. J. Clin. Exp. Pathology* 8, 13193–13200.

Chang, C.Ju, Tzeng, T. F., Liou, S. S., Chang, Y. S., and Liu, I. M. (2011). Kaempferol regulates the lipid-profile in high-fat diet-fed rats through an increase in hepatic PPARα levels. *Planta Medica.* 77, 1876–1882. doi:10.1055/s-0031-1279992

Chaudhary, H. R., and Dion, R. B. (2013). The single dose poloxamer 407 model of hyperlipidemia; systemic effects on lipids assessed using pharmacokinetic methods, and its effects on adipokines. *J. Pharm. Pharm. Sci.* 16 (1), 65–73. doi:10.18433/j37g7m

Che, Y., Yao, K., Xi, Y., Chen, Z., Li, Y., Yu, N., et al. (2016). Wendan decoction for treatment of schizophrenia: a systematic review of randomized controlled trials. *Chin. J. Integr. Med.* 22, 302–310. doi:10.1007/s11655-015-2047-z

Chtourou, Y., Slima, A. B., Makni, M., Gdoura, R., and Fetoui, H. (2015). Naringenin protects cardiac hypercholesterolemia-induced oxidative stress and subsequent necroptosis in rats. *Pharmacol. Rep.* 67 (6), 1090–1097. doi:10.1016/j.pharep.2015.04.002

Cui, M., Zhu, F., Yin, Y., Sui, Y., Yan, X., and Chen, T. (2022). Influence of gegenqinlian decoction on pharmacokinetics and pharmacodynamics of atorvastatin calcium in hyperlipidemic rats. *Eur. J. drug metabolism Pharmacokinet.* 47 (1), 117–126. doi:10.1007/s13318-021-00738-5

Das, D., Sarkar, S., Bordoloi, J., Wann, S. B., Kalita, J., and Manna, P. (2018). Daidzein, its effects on impaired glucose and lipid metabolism and vascular inflammation associated with type 2 diabetes. *BioFactors Oxf. Engl.* 44, 407–417. doi:10.1002/biof.1439

Deng, H., and Xu, J. (2017). Wendan decoction (Traditional Chinese medicine) for schizophrenia. *Cochrane database Syst. Rev.* 6, CD012217. doi:10.1002/14651858.CD012217.pub2

Duggan, J. X. (2019). Quantification below the LLOQ in regulated LC-MS/MS assays: a review of bioanalytical considerations and cautions. *Bioanalysis* 11 (8), 797–814. doi:10.4155/bio-2018-0261

Elesber, A. A., Redfield, M. M., Rihal, C. S., Prasad, A., Lavi, S., Lennon, R., et al. (2007). Coronary endothelial dysfunction and hyperlipidemia are independently associated with diastolic dysfunction in humans. *Am. heart J.* 153 (6), 1081–1087. doi:10.1016/j.ahj.2007.03.007

Eu, C. H., Lim, W. Y., Ton, S. H., and bin Abdul Kadir, K. (2010). Glycyrrhizic acid improved lipoprotein lipase expression, insulin sensitivity, serum lipid and lipid deposition in high-fat diet-induced obese rats. *Lipids Health Dis.* 9, 81. doi:10.1186/1476-511X-9-81

Feng, W., Ye, X., Lv, H., Hou, C., and Chen, Y. (2019). Wendan decoction for dyslipidemia: protocol for a systematic review and meta-analysis. *Medicine* 98, e14159. doi:10.1097/MD.0000000000014159

Guo, Z., Ali, Q., Abaidullah, M., Gao, Z., Diao, X., Liu, B., et al. (2022). High fat diet-induced hyperlipidemia and tissue steatosis in rabbits through modulating ileal microbiota. *Appl. Microbiol. Biotechnol.* 106, 7187–7207. doi:10.1007/s00253-022-12203-7

Han, Y. J., Kang, B., Yang, E. J., Choi, M. K., and Song, I. S. (2019). Simultaneous determination and pharmacokinetic characterization of glycyrrhizin, isoliquiritigenin, liquiritigenin, and liquiritin in rat plasma following oral administration of Glycyrrhizae Radix extract. *Mol. (Basel, Switz.* 24, 1816. doi:10.3390/molecules24091816

Huang, P., Tang, Y., Li, C., et al. (2020). Correlation study between the pharmacokinetics of seven main active ingredients of Mahuang decoction and its pharmacodynamics in asthmatic rats. *J. Pharm. Biomed. Anal.* 183, 113144. doi:10.1016/j.jpba.2020.113144

Jang, J. H., Park, J. E., and Han, J. S. (2020). Scopoletin increases glucose uptake through activation of PI3K and AMPK signaling pathway and improves insulin sensitivity in 3T3-L1 cells. *Nutr. Res. (New York, N.Y.)* 74, 52–61. doi:10.1016/j.nutres.2019.12.003

Jeong, K., Monica, M., Sruti, C., and Michael, J. (2012). Role of lipotoxicity in endothelial dysfunction. *Heart Fail.* 8 (4), 589–607. doi:10.1016/j.hfc.2012.06.012

Ji, B., Zhao, Y., Yu, P., Yang, B., Zhou, C., and Yu, Z. (2018). LC-ESI-MS/MS method for simultaneous determination of eleven bioactive compounds in rat plasma after oral administration of Ling-Gui-Zhu-Gan Decoction and its application to a pharmacokinetics study. *Talanta* 190, 450–459. doi:10.1016/j.talanta.2018.08.020

Jia, B., Wang, Y., Yu, G., Cheng, Y., Yang, C., Cao, F., et al. (2019). Naringenin ameliorates insulin resistance by modulating endoplasmic reticulum stress in hepatitis C virus-infected liver. *Biomedecine Pharmacother.* 115, 108848. doi:10.1016/j.biopha.2019.108848

Jin, Q., Li, J., Chen, G. Y., Wu, Z. Y., Liu, X. Y., Liu, Y., et al. (2022). Network and experimental Pharmacology to decode the action of wendan decoction against generalized anxiety disorder. *Drug Des. Dev. Ther.* 16, 3297–3314. doi:10.2147/DDDT.S367871

Joy, T., Keogh, H. M., Hadigan, C., Lee, H., Dolan, S. E., Fitch, K., et al. (2007). Dietary fat intake and relationship to serum lipid levels in HIV-infected patients with metabolic abnormalities in the HAART era. *AIDS Lond. Engl.* 21, 1591–1600. doi:10.1097/QAD.0b013e32823644ff

Karr, S. (2017). Epidemiology and management of hyperlipidemia. *Am. J. Manag. care* 23 (9), S139–S148.

Kejík, Z., Kaplánek, R., Masařík, M., Babula, P., Matkowski, A., Filipenský, P., et al. (2021). Iron complexes of flavonoids-antioxidant capacity and beyond. *Int. J. Mol. Sci.* 22, 646. doi:10.3390/ijms22020646

Kramer, A. (2020). An overview of the beneficial effects of exercise on health and performance. *Adv. Exp. Med. Biol.* 1228, 3–22. doi:10.1007/978-981-15-1792-1_1

Kumar, R., Akhtar, F., and Rizvi, S. I. (2020). Hesperidin attenuates altered redox homeostasis in an experimental hyperlipidaemic model of rat. *Clin. Exp. Pharmacol. Physiol.* 47 (4), 571–582. doi:10.1111/1440-1681.13221

Li, L.-L., Cui, Y., Guo, X. H., Ma, K., Tian, P., Feng, J., et al. (2019). Pharmacokinetics and tissue distribution of gingerols and shogaols from ginger (*Zingiber officinale* rosc.) in rats by UPLC-Q-Exactive-HRMS. *Mol. (Basel, Switz.* 24, 3–512. doi:10.3390/molecules24030512

Li, W., Jiang, N., Li, B., Wan, M., Chang, X., Liu, H., et al. (2018). Antioxidant activity of purified ulvan in hyperlipidemic mice. *Int. J. Biol. Macromol.* 113, 971–975. doi:10.1016/j.ijbiomac.2018.02.104

Li, W., Jiang, Y. H., Wang, Y., Zhao, M., Hou, G. J., Hu, H. Z., et al. (2020). Protective effects of combination of Radix astragali and Radix salviae miltiorrhizae on kidney of spontaneously hypertensive rats and renal intrinsic cells. *Chin. J. Integr. Med.* 26 (1), 46–53. doi:10.1007/s11655-019-3071-1

Lin, W., Yao, J., and Zhou, J. P. (2009). Preparation of self-assemble nobiletin proliposomes and its pharmacokinetics in rats. *Yao Xue Xue Bao* 44 (2), 192–196.

Lu, Y.-Y., Chen, J. F., Song, J. Y., Du, Z. Y., Wang, J. L., Qian, Y., et al. (2019). Pharmacokinetics study of 16 representative components from Baoyuan Decoction in rat plasma by LC-MS/MS with a large-volume direct injection method. *Phytomedicine* 57, 148–157. doi:10.1016/j.phymed.2018.09.002

Matey-Hernandez, M. L., Williams, F. M. K., Potter, T., Valdes, A. M., Spector, T. D., and Menni, C. (2018). Genetic and microbiome influence on lipid metabolism and dyslipidemia. *Physiol. genomics* 50 (2), 117–126. doi:10.1152/physiolgenomics.00053.2017

Memon, R. A., and Gilani, A. H. (1995). An update on hyperlipidemia and its management. *JPMA. J. Pak. Med. Assoc.* 45 (10), 275–282.

Mohamadi, N., Sharififar, F., Pournamdari, M., and Ansari, M. (2018). A review on biosynthesis, analytical techniques, and pharmacological activities of trigonelline as a plant alkaloid. *J. Diet. Suppl.* 15 (2), 207–222. doi:10.1080/19390211.2017.1329244

Mulvihill, E. E., Burke, A. C., and Huff, M. W. (2016). Citrus flavonoids as regulators of lipoprotein metabolism and atherosclerosis. *Annu. Rev. Nutr.* 36, 275–299. doi:10.1146/annurev-nutr-071715-050718

Nauser, T., and Gebicki, J. M. (2019). Fast reaction of carbon free radicals with flavonoids and other aromatic compounds. *Archives Biochem. biophysics* 674, 108107. doi:10.1016/j.abb.2019.108107

Navar-Boggan, A. M., Peterson, E. D., D'Agostino, R. B., Neely, B., Sniderman, A. D., and Pencina, M. J. (2015). Hyperlipidemia in early adulthood increases long-term risk of coronary heart disease. *Circulation* 131 (5), 451–458. doi:10.1161/CIRCULATIONAHA.114.012477

Nofer, J.-R. (2010). Hyperlipidemia and cardiovascular disease: should we abandon HDL cholesterol as a therapeutic target in coronary heart disease. *Curr. Opin. Lipidol.* 21 (4), 392–393. doi:10.1097/MOL.0b013e32833c224d

Okon, E. B., Chung, A. W. Y., Zhang, H., Laher, I., and van Breemen, C. (2007). Hyperglycemia and hyperlipidemia are associated with endothelial dysfunction during the development of type 2 diabetes. *Can. J. physiology Pharmacol.* 85 (5), 562–567. doi:10.1139/y07-026

Pietta, P. G. (2000). Flavonoids as antioxidants. *J. Nat. Prod.* 63, 1035–1042. doi:10.1021/np9904509

Rajendran, M., Manisankar, P., Gandhidasan, R., and Murugesan, R. (2004). Free radicals scavenging efficiency of a few naturally occurring flavonoids: a comparative study. *J. Agric. food Chem.* 52 (24), 7389–7394. doi:10.1021/jf0400718

Rodríguez-Borjabad, C., Narveud, I., Christensen, J. J., Ulven, S. M., Malo, A. I., Ibarretxe, D., et al. (2021). Dietary intake and lipid levels in Norwegian and Spanish children with familial hypercholesterolemia. *Nutr. metabolism, Cardiovasc. Dis.* 31 (4), 1299–1307. doi:10.1016/j.numecd.2020.12.002

Sahebkar, A. (2017). Effects of quercetin supplementation on lipid profile: a systematic review and meta-analysis of randomized controlled trials. *Crit. Rev. Food Sci. Nutr.* 57 (4), 666–676. doi:10.1080/10408398.2014.948609

Shi, L., Zou, M., Zhou, X., Wang, S., Meng, W., and Lan, Z. (2023). Comparison of protective effects of hesperetin and pectolinarigenin on high-fat diet-induced hyperlipidemia and hepatic steatosis in Golden Syrian hamsters. *Exp. Anim.* 72 (1), 123–131. doi:10.1538/expanim.22-0115

Suh, J. S., Kim, S. Y. J., Lee, S. H., Kim, R. H., and Park, N. H. (2022). Hyperlipidemia is necessary for the initiation and progression of atherosclerosis by severe periodontitis in mice. *Mol. Med. Rep.* 26 (2), 273. doi:10.3892/mmr.2022.12789

Sun, J., Wang, Z., Chen, L., and Sun, G. (2021). Hypolipidemic effects and preliminary mechanism of Chrysanthemum flavonoids, its main components luteolin and luteoloside in hyperlipidemia rats. *Antioxidants (Basel, Switz.* 10, 1309. doi:10.3390/antiox10081309

Tang, X., Zhao, H., Jiang, W., Zhang, S., Guo, S., Gao, X., et al. (2018). Pharmacokinetics and pharmacodynamics of citrus peel extract in lipopolysaccharide-induced acute lung injury combined with Pinelliae Rhizoma Praeparatum. *Food and Funct.* 9, 5880–5890. doi:10.1039/c8fo01337c

Tannock, L. R. (2008). Advances in the management of hyperlipidemia-induced atherosclerosis. *Expert Rev. Cardiovasc. Ther.* 6 (3), 369–383. doi:10.1586/14779072.6.3.369

Tietge, U. J. F. (2014). Hyperlipidemia and cardiovascular disease: inflammation, dyslipidemia, and atherosclerosis. *Curr. Opin. Lipidol.* 25 (1), 94–95. doi:10.1097/MOL.0000000000000051

Trivedi, R. K., Kallem, R. R., Mamidi, R. N. V. S., Mullangi, R., and Srinivas, N. R. (2004). Determination of lipoic acid in rat plasma by LC-MS/MS with electrospray ionization: assay development, validation and application to a pharamcokinetic study. *Biomed. Chromatogr. BMC* 18 (9), 681–686. doi:10.1002/bmc.375

Wan, H., Pan, L., Wang, Y., Li, C., Yu, L., Zhou, H., et al. (2020). Pharmacokinetics of seven major active components of Mahuang decoction in rat blood and brain by LC-MS/MS coupled to microdialysis sampling. *Naunyn-Schmiedeberg's archives Pharmacol.* 393, 1559–1571. doi:10.1007/s00210-019-01786-0

Wang, B., Shen, J., Zhou, Q., Meng, D., He, Y., Chen, F., et al. (2020a). Effects of naringenin on the pharmacokinetics of tofacitinib in rats. *Pharm. Biol.* 58 (1), 225–230. doi:10.1080/13880209.2020.1738504

Wang, L., Li, W., Cheng, D., Guo, Y., Wu, R., Yin, R., et al. (2020b). Pharmacokinetics and pharmacodynamics of three oral formulations of curcumin in rats. *J. Pharmacokinet. pharmacodynamics* 47 (2), 131–144. doi:10.1007/s10928-020-09675-3

Wang, Q., Zou, Z., Zhang, Y., Lin, P., Lan, T., Qin, Z., et al. (2021). Characterization of chemical profile and quantification of major representative components of Wendan decoction, a classical traditional Chinese medicine formula. *J. Sep. Sci.* 44 (5), 1036–1061. doi:10.1002/jssc.202000952

Warnholtz, A., Mollnau, H., Oelze, M., Wendt, M., and Münzel, T. (2001). Antioxidants and endothelial dysfunction in hyperlipidemia. *Curr. Hypertens. Rep.* 3, 53–60. doi:10.1007/s11906-001-0081-z

Xu, D., and Cheng, K. (2011). Determination of liquiritin, naringin, hesperidin and glycyrrhizic acid in extractive of Wendan formula by RP-HPLC. *China J. Chin. materia medica* 36 (1), 45–47. doi:10.4268/cjcmm20110110

Xu, N., Ijaz, M., Shi, H., Shahbaz, M., Cai, M., Wang, P., et al. (2023). Screening of active ingredients from wendan decoction in alleviating palmitic acid-induced endothelial cell injury. *Mol. (Basel, Switz.* 28, 1328. doi:10.3390/molecules28031328

Yan, X., Wang, Y., Li, X., Li, Z., Zhang, Y., Cai, X., et al. (2017). Wendan decoction for primary insomnia: protocol for a systematic review and meta-analysis. *Medicine* 96, e8906, e8906. doi:10.1097/MD.0000000000008906

Yang, Y., Wang, X., Zhao, C., Tian, G., Zhang, H., Xiao, H., et al. (2017). Chemical mapping of essential oils, flavonoids and carotenoids in citrus peels by Raman microscopy. *J. food Sci.* 82 (12), 2840–2846. doi:10.1111/1750-3841.13952

Yu, X., Meng, X., Yan, Y., Wang, H., and Zhang, L. (2022). Extraction of naringin from pomelo and its therapeutic potentials against hyperlipidemia. *Molecules* 27 (24), 9033. doi:10.3390/molecules27249033

Zhang, M., Chang, Z., Zhao, F., Zhang, P., Hao, Y. J., Yan, L., et al. (2019). Protective effects of 18β-glycyrrhetinic acid on monocrotaline-induced pulmonary arterial hypertension in rats. *Front. Pharmacol.* 10, 13. doi:10.3389/fphar.2019.00013

Zhang, Y., Liu, T., Zhang, L., Pu, Z., Yan, Z., and Hua, H. (2022). Wendan decoction in the treatment of nonalcoholic fatty liver disease: a systematic review and meta-analysis. *Front. Pharmacol.* 13, 1039611. doi:10.3389/fphar.2022.1039611

Zhao, Y., Yang, Y., Xing, R., Cui, X., Xiao, Y., Xie, L., et al. (2018). Hyperlipidemia induces typical atherosclerosis development in Ldlr and Apoe deficient rats. *Atherosclerosis* 271, 26–35. doi:10.1016/j.atherosclerosis.2018.02.015

frontiers | Frontiers in Pharmacology

TYPE Original Research
PUBLISHED 26 February 2024
DOI 10.3389/fphar.2024.1235639

OPEN ACCESS

EDITED BY
Jorge G. Farias,
Universidad de La Frontera, Chile

REVIEWED BY
Kaijian Hou,
Shantou University, China
Benli Su,
Second Hospital of Dalian Medical University, China

*CORRESPONDENCE
Shaohong Yu,
sutcm2006@163.com
Zhongwen Zhang,
zhangzhongwen@sdu.edu.cn

†These authors have contributed equally to this work and share first authorship

RECEIVED 06 June 2023
ACCEPTED 29 January 2024
PUBLISHED 26 February 2024

CITATION
Liu Y, Ma W, Fu H, Zhang Z, Yin Y, Wang Y, Liu W, Yu S and Zhang Z (2024), Efficacy of polyethylene glycol loxenatide for type 2 diabetes mellitus patients: a systematic review and meta-analysis.
Front. Pharmacol. 15:1235639.
doi: 10.3389/fphar.2024.1235639

Efficacy of polyethylene glycol loxenatide for type 2 diabetes mellitus patients: a systematic review and meta-analysis

Yibo Liu[1,2†], Wenjing Ma[2†], Hui Fu[3], Zhe Zhang[4], Yanyan Yin[5], Yongchun Wang[2], Wei Liu[4], Shaohong Yu[2,6*] and Zhongwen Zhang[7*]

[1]Department of Endocrinology and Metabology, Rehabilitation Hospital, The Second Affiliated Hospital of Shandong University of Traditional Chinese Medicine, The Third Affiliated Hospital of Shandong First Medical University, Jinan, China, [2]Rehabilitation Hospital, The Second Affiliated Hospital of Shandong University of Traditional Chinese Medicine, Jinan, China, [3]Medical Integration and Practice Center, Shandong University, Jinan, China, [4]Shandong University of Traditional Chinese Medicine, Jinan, China, [5]Shandong Provincial Medical Association, Jinan, China, [6]Teaching and Research Section of Internal Medicine, College of Medicine, Shandong University of Traditional Chinese Medicine, Jinan, China, [7]Shandong Provincial Key Laboratory for Rheumatic Disease and Translational Medicine, Department of Endocrinology and Metabology, The First Affiliated Hospital of Shandong First Medical University and Shandong Provincial Qianfoshan Hospital, The Third Affiliated Hospital of Shandong First Medical University, Jinan, China

Objective: Some studies have proved that polyethylene glycol loxenatide (PEG-Loxe) has significant effects on controlling blood glucose and body weight in patients with type 2 diabetes mellitus (T2DM), but there is still some controversy over the improvement of blood lipid profiles (BLP) and blood pressure (BP), and more evidences are needed to verify such effects. Therefore, this study was conducted to provide a comprehensive evaluation of the efficacy of PEG-Loxe in improving blood glucose (BG), BLP, BP, body mass index (BMI), and body weight (BW) in patients with T2DM for clinical reference.

Methods: Randomized controlled trials (RCT) in which PEG-Loxe was applied to treat T2DM were retrieved by searching PubMed, Cochrane Library, Embase, Medline, Scopus, Web of Science, China National Knowledge Infrastructure, China Scientific Journal, Wanfang Data, and SinoMed databases. Outcome measures included BG, BLP, BP, BMI, and BW. RevMan 5.3 software was used to perform data analysis.

Results: Eighteen trials were identified involving 2,166 patients. In experimental group 1,260 patients received PEG-Loxe alone or with other hypoglycemic agents, while in control group 906 patients received placebo or other hypoglycemic agents. In the overall analysis, PEG-Loxe significantly reduced the levels of glycosylated hemoglobin (HbA1c), fasting plasma glucose (FPG), 2-h postprandial blood glucose (2-h PBG), BMI, and BW compared with control group. However, it had no obvious effect on total cholesterol (TC), triglycerides (TG), low-density lipoprotein cholesterol (LDL-C), high-density lipoprotein cholesterol (HDL-C), systolic blood pressure (SBP), and diastolic blood pressure (DBP).

Conclusion: PEG-Loxe has better hypoglycemic effects compared with placebo in patients with T2DM, but could not significantly improved TG, LDL-C, HDL-C,

SBP, and DBP. And the combination of conventional hypoglycemic drugs (CHD) and PEG-Loxe could more effectively improve the levels of HbA1c, FPG, 2-h PBG, TC, TG, BMI, and BW compared with CHD in T2DM patients.

Systematic Review Registration: www.inplasy.com, identifier INPLASY202350106

KEYWORDS

polyethylene glycol loxenatide, type 2 diabetes mellitus, blood glucose, blood lipid profiles, blood pressure, body mass index, body weight, meta-analysis

1 Introduction

Diabetes is one of the most serious and long-term chronic diseases and is also one of the top 10 causes of death in adults. Therefore, it poses a major threat to individual, family and global health (Saeedi et al., 2019). According to the International Diabetes Federation, more than 500 million individuals suffered from diabetes in 2021 worldwide, and it is expected that the number of patients will increase by 200 million in 2045. In 2021, the global health costs associated with diabetes were evaluated at 966 billion U.S. dollars, and this number is expected to reach 1,054 billion U.S. dollars by 2045 (Williams et al., 2020; Sun et al., 2022). With the aging of the global population and changes in lifestyle, there would be more people suffering from diabetes and more cost spending diabetes. Type 2 diabetes mellitus (T2DM), the most prevalent diabetes, accounts for more than 90% diabetic patients (Zheng et al., 2018; Khan et al., 2019). T2DM is a metabolic disease induced by a variety of causes. It would lead to insulin deficiency, insulin resistance, and persistently elevated blood glucose levels. In a long-term hyperglycemic internal environment, blood vessels and nerves would undergo pathological changes, which could damage the organs such as heart, kidneys, and eyes (Chatterjee et al., 2017; Ahmad et al., 2022). Since there is no radical cure for T2DM at present, blood glucose and weight control are particularly critical in its treatment process (Davies et al., 2022).

In recent years, since glucagon-like peptide-1 receptor agonists (GLP-1RAs) have significant hypoglycemic effects and multiple benefits for diabetic patients, they have been recommended in major guidelines. GLP-1RAs are potent hypoglycemic agents with the function to promote glucose-dependent insulin secretion from pancreatic beta-cells by binding to glucagon-like peptide-1 receptor (GLP-1R) and inhibiting glucagon secretion (Drucker, 2018). The degradation and destroy of GLP-1RAs are slow, so the effect of

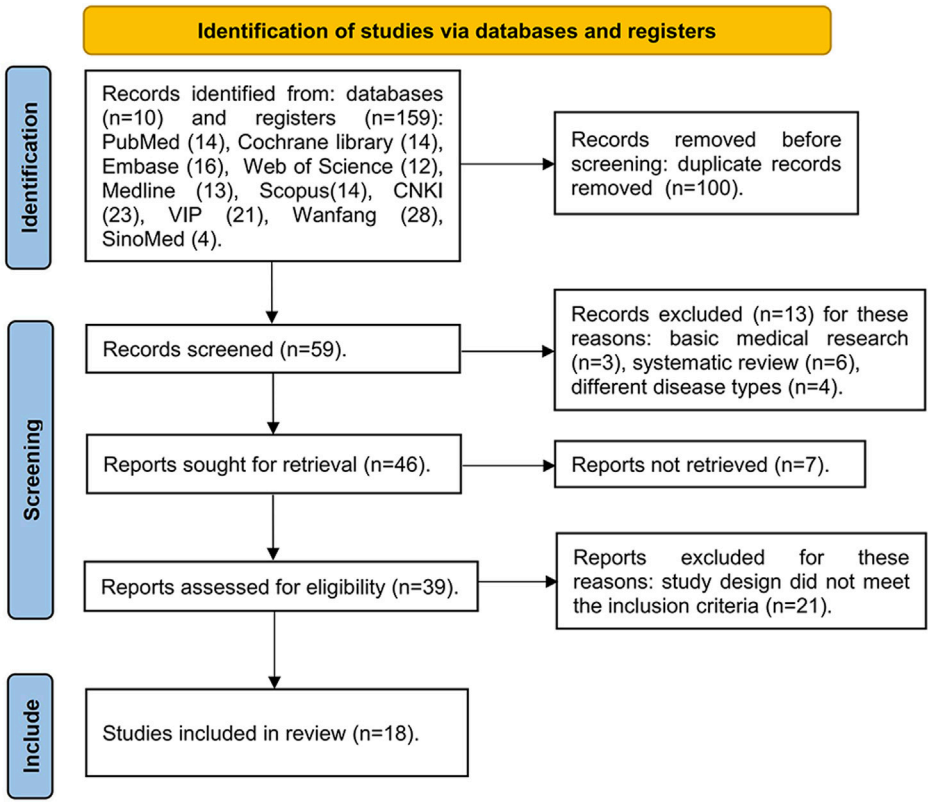

FIGURE 1
The flowchart of literature search.

TABLE 1 The characteristics of the included studies.

ID	Group	Sample size	Mean age, years	Intervention measures	Treatment time, weeks	Outcome indicator
Yang (2022)	Experimental group	40	55.89 ± 2.52	PEG-Loxe 0.1 mg	12	HbAlc, FPG, and 2-h PBG
	Control group	40	55.82 ± 2.56	Insulin glargine		
Wan et al. (2023)	Experimental group	35	63.31 ± 6.43	PEG-Loxe 0.2 mg + Insulin glargine + Metformin	12	HbAlc, FPG, TC, TG, LDL-C, and BMI
	Control group	35	63.25 ± 6.36	Insulin glargine + Metformin		
Zhang Y. et al. (2023)	Experimental group	41	53.50 ± 5.43	PEG-Loxe 0.2 mg + Metformin	12	HbA1c, FBG, 2-h PBG, TC, TG, LDL-C, HDL-C
	Control group	41	53.00 ± 5.45	Metformin		
Zhong (2023)	Experimental group	30	53.30 ± 10.86	PEG-Loxe 0.2 mg + Insulin glargine	12	HbA1c, FBG, 2-h PBG, TC, TG
	Control group	30	52.50 ± 10.88	Insulin glargine		
Zhou et al. (2023)	Experimental group	40	46.8 ± 11.3	PEG-Loxe 0.2 mg + Metformin	12	HbA1c, FBG, 2-h PBG, TC, TG, LDL-C, HDL-C, SBP, DBP, and BMI
	Control group	40	47.2 ± 12.1	Metformin		
Li et al. (2021)	Experimental group	30	47.7 ± 6.8	PEG-Loxe 0.1 mg + Metformin/ Acarbose	12	HbAlc, FPG, 2-h PBG, and BMI
	Control group	30	47.2 ± 7.3	Metformin/Acarbose		
Tian et al. (2022)	Experimental group	35	50 ± 13.00	PEG-Loxe 0.2 mg + Metformin	12	HbA1c, FBG, 2-h PBG, BMI, and BW
	Control group	34	50 ± 13.00	Sodium chloride injection + Metformin		
Zhao et al. (2022)	Experimental group	56	46.72 ± 9.34	PEG-Loxe 0.2 mg + Metformin	12	HbA1c, FBG, 2-h PBG, TC, TG, LDL-C, HDL-C, and BMI
	Control group	54	47.89 ± 8.95	Metformin		
Li K. et al. (2022)	Experimental group	50	52.34 ± 4.15	PEG-Loxe 0.2 mg + Metformin	12	FPG, 2-h PBG, TG, TC, LDL-C, and HDL-C
	Control group	50	52.56 ± 4.08	Metformin		
Liang et al. (2021)	Experimental group	62	53.8 ± 8.5	PEG-Loxe 0.2 mg	24	HbAlc, FPG, 2-h PBG, TG, TC, HDL-C, LDL-C, and BMI
	Control group	62	54.1 ± 7.9	Multiple oral hypoglycemic drugs or oral drugs combined with insulin		
Wang and Zhao (2021)	Experimental group	37	59.78 ± 14.76	PEG-Loxe 0.2 mg	12	HbAlc, FPG, 2-h PBG, and BMI
	Control group	37	58.36 ± 14.63	Insulin glargine		
Yao et al. (2017)	Experimental group	13	53.6 ± 9.90	PEG-Loxe 0.1 mg	12	HbAlc, FPG, and 2-h PBG
		12	53.6 ± 9.90	PEG-Loxe 0.2 mg		
	Control group	11	53.6 ± 9.90	Placebo		
Gao et al. (2020)	Experimental group	179	53.60 ± 10.50	PEG-Loxe 0.1 mg + Metformin	24	HbA1c, FPG, 2-h PBG, TC, TG, HDL-C, LDL-C, SBP, DBP, and BW
		175	52.80 ± 10.60	PEG-Loxe 0.2 mg + Metformin		
	Control group	179	52.30 ± 10.70	Placebo + Metformin		
Shuai et al. (2020)	Experimental group	124	50.50 ± 10.40	PEG-Loxe 0.1 mg	24	HbA1c, FPG, 2-h PBG, TC, TG, HDL-C, LDL-C, SBP, DBP, and BW
		116	52.40 ± 11.50	PEG-Loxe 0.2 mg		
	Control group	121	51.50 ± 10.90	Placebo		

(Continued on following page)

TABLE 1 (*Continued*) The characteristics of the included studies.

ID	Group	Sample size	Mean age, years	Intervention measures	Treatment time, weeks	Outcome indicator
Chen et al. (2017)	Experimental group	41	52.60 ± 8.40	PEG-Loxe 0.1 mg + Metformin	12	HbA1c, FPG, 2-h PBG, TC, TG, HDL-C, LDL-C, SBP, DBP, and BW
		39	49.80 ± 10.90	PEG-Loxe 0.2 mg + Metformin		
	Control group	38	53.50 ± 10.20	Placebo + Metformin		
Zhang S. et al. (2023)	Experimental group	35	68.30 ± 10.40	PEG-Loxe 0.2 mg + Metformin	24	HbA1c
	Control group	34	67.40 ± 10.20	Insulin glargine + Metformin		
Song et al. (2023)	Experimental group	50	51.38 ± 6.39	PEG-Loxe 0.2 mg + Metformin + Insulin	24	HbA1c, FPG, 2-h PBG, TC,TG, HDL-C, LDL-C, BW, and BMI
	Control group	50	51.49 ± 6.67	Metformin + Insulin		
Li X. Y. et al. (2022)	Experimental group	20	63.29 ± 1.27	PEG-Loxe 0.2 mg + Metformin	12	FPG, 2-h PBG, TG, HDL-C, and LDL-C
	Control group	20	64.23 ± 1.31	Metformin		

PEG-Loxe, polyethylene glycol loxenatide; HbA1c: glycosylated hemoglobin; FPG, fasting plasma glucose; 2-h PBG, 2-h postprandial blood glucose; TC, total cholesterol; TG, triglycerides; LDL-C, low-density lipoprotein cholesterol; HDL-C, high-density lipoprotein cholesterol; SBP, systolic blood pressure; DBP, diastolic blood pressure; BMI, body mass index; BW, body weight.

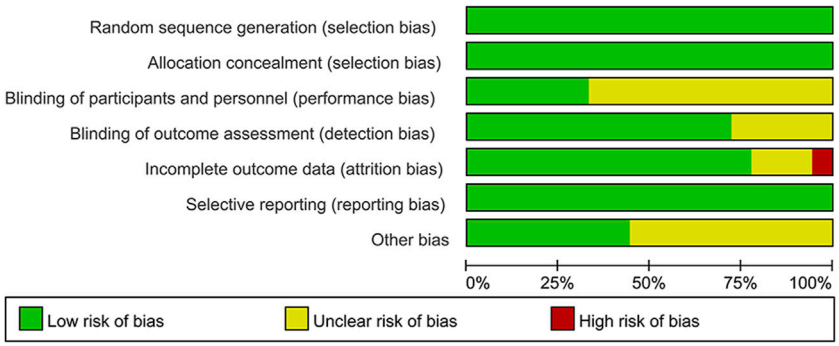

FIGURE 2
Risk of bias graph.

reducing blood glucose (BG) could be maintained for a long time (Chen et al., 2017). In addition, GLP-1RAs have the advantages of reducing BG without increasing the incidence of hypoglycemia (Drucker and Nauck, 2006). Therefore, the 2020 American Association of Clinical Endocrinologists guidelines recommend GLP-1RAs as the drug of choice after metformin (Garber et al., 2020). Polyethylene glycol loxenatide (PEG-Loxe), a new agent of the GLP-1RAs, was approved for clinical application in China In 2019. It was synthesized by replacing the chemical structure of exenatide at the N-terminal positions 2, 14, 28, and 39, and modified by polyethylene glycol (PEG). PEG-Loxe could further resist the rapid degradation of dipeptidyl peptidase-IV (DPP-4), reduce the toxicity and its antigenic immunity, prolong the mean half-life (131.8–139.8 h) and duration of action, and improve its bioavailability, compliance, and the therapeutic effect in the body, with better effects compared with exenatide (Yang et al., 2015; Chen et al., 2017). In terms of the hypoglycemic effect, studies have reported that PEG-Loxe is likely to inhibit β-cell apoptosis to promote the expression of GLP-1R, thereby activating the insulin PI3K/AKT pathway, promoting insulin synthesis and secretion, and thus exerting a hypoglycemic effect (Zhang et al., 2021). PEG-Loxe has shown a good effect on controlling BG in patients with T2DM, but there are still some controversy over the improvement of BLP and few clinical evidence for reducing BW. Therefore, we aimed to comprehensively evaluate the efficacy of PEG-Loxe for BG, BLP, BP, body mass index (BMI), and BW.

2 Materials and methods

The protocol and report of this study followed the "Preferred Reporting Items for Systematic Reviews and Meta-Analyses (PRISMA)" statement (Page et al., 2021) and were registered in the INPLASYInternational Platform of Registered Systematic Review and Meta-analysis Protocols (identifier: INPLASY202350106. DOI number: 10.37766/inplasy 2023.5.0106).

TABLE 2 The results of overall analysis.

Index	Dosage (mg)	n	Sample size	Effect model	Overall effect: Heterogeneity (P_h, I^2%); MD (95% CI); Z-test (Z-values, P_Z)
HbA1c	0.1	6	846	Random	$P_h < 0.00001$, 98%; −0.91 (−1.05, −0.76); 12.16, $P_Z < 0.00001$
	0.2	14	1,169		
FPG	0.1	7	886	Random	$P_h < 0.00001$, 97%; −1.22 (−1.42, −1.02); 12.06, $P_Z < 0.00001$
	0.2	14	1,545		
2-h PBG	0.1	7	886	Random	$P_h < 0.00001$, 97%; −1.84 (−2.16, −1.53); 11.37, $P_Z < 0.00001$
	0.2	13	1,475		
TC	0.1	3	682	Random	$P_h < 0.00001$, 93%; −0.44 (−0.68, 0.19); 3.48, $P_Z = 0.0005$
	0.2	11	1,384		
TG	0.1	3	682	Random	$P_h < 0.00001$, 97%; −0.59 (−0.98, 0.19); 2.92, $P_Z = 0.004$
	0.2	11	1,384		
LDL-C	0.1	4	722	Random	$P_h < 0.00001$, 93%; −0.16 (−0.34, 0.02); 1.79, $P_Z = 0.07$
	0.2	10	1,324		
HDL-C	0.1	3	682	Random	$P_h < 0.00001$, 88%; 0.07 (−0.01, 0.14); 1.77, $P_Z = 0.08$
	0.2	9	1,254		
SBP	0.1	3	344	Random	$P_h < 0.00001$, 93%; 0.17 (−0.90, 1.24); 0.31, $P_Z = 0.75$
	0.2	4	370		
DBP	0.1	3	344	Random	$P_h < 0.00001$, 95%; −0.39 (−1.20, 0.42); 0.95, Pz = 0.34
	0.2	4	370		
BMI	0.1	2	418	Random	$P_h < 0.00001$, 82%; −1.68 (−2.20, −1.17); 6.44, $P_Z < 0.00001$
	0.2	9	1,048		
BW	0.1	2	603	Random	$P_h < 0.00001$, 96%; −2.71 (−4.97, −0.45); 2.35, $P_Z = 0.02$
	0.2	5	870		

P_h, *p*-values for heterogeneity of Q-test; MD, mean difference; CI, confidence interval; Pz, *p*-values for Z-test; $P_Z < 0.05$, shows a significant difference; HbA1c, glycosylated hemoglobin; FPG, fasting plasma glucose; 2-h PBG, 2-h postprandial blood glucose; TC, total cholesterol; TG, triglycerides; LDL-C, low-density lipoprotein cholesterol; HDL-C, high-density lipoprotein cholesterol; SBP, systolic blood pressure; DBP, diastolic blood pressure; BMI, body mass index; and BW, body weight.

2.1 Literature search strategies

Literature was retrieved in the PubMed, Cochrane Library, Embase, Medline, Scopus, Web of Science, China National Knowledge Infrastructure (CNKI), China Scientific Journal, Wanfang Data, and SinoMed databases. The search terms were "polyethylene glycol loxenatide" or "PEG-Loxe" or "PEX168" in combination with "randomized controlled trial," "randomized controlled trials" "RCT," "RCTs," "type 2 diabetes mellitus" or "diabetes mellitus" or "diabetes mellitus, type 2," or "T2DM." The complete search strategies of databases were shown in Supplementary Table S1.

2.2 The inclusion and exclusion criteria

The inclusion criteria followed the PICOS principle. T2DM patients with FPG≥11.1 mmol/L, HbA1c ≥ 9.0%; BMI≥27 kg/m^2, age≥18 years old; Patients in experimental group received PEG-Loxe alone or along with other hypoglycemic agents, and patients in control group received placebo or other hypoglycemic agents; The dose of PEG-Loxe was 0.1 mg or 0.2 mg. Outcome indicators involved HbA1c, FPG, 2-h PBG, TC, TG, LDL-C, HDL-C, SBP, DBP, BMI and BW; RCT published in English or Chinese.

The exclusion criteria were shown as follows: the study design was scientific research achievements, systematic reviews, and animal experiments; trials that did not report related information; the full text could not be obtained; other intervention measures existed; patients that combined with other severe diseases or limb dysfunction, and serious complications of T2DM.

2.3 Quality assessment and data extraction

The quality assessment and data extraction were conducted by 2 researchers independently, with disagreements resolved by consensus. The quality of the included studies was assessed according to six aspects: random sequence generation (selection bias), allocation concealment (selection bias), blinding of participants and personnel (performance bias), blinding of

TABLE 3 The results of subgroup analysis.

Index	Heterogeneity (P_h, I^2%); MD (95% CI); Z-test (Z-values, P_Z)							
	Intervention measure subgroup				Dosage subgroup		Treatment time subgroup	
	PEG-Loxe + CHD		PEG-Loxe					
	CHD	CHD + Placebo	CHD	Placebo	0.1 mg	0.2 mg	12 weeks	24 weeks
HbA1c	P_h < 0.00001, 96%	P_h = 0.008, 75%	P_h = 0.06, 71%	P_h < 0.00001, 99%	P_h = 0.03, 60%	P_h < 0.00001, 99%	P_h < 0.00001, 90%	P_h < 0.00001, 100%
	−1.04 (−1.38, −0.69)	−0.81 (−0.84, −0.77)	−0.72 (−2.30, 0.86)	−1.05 (−1.34, −0.76)	−0.83 (−0.88, −0.79)	−1.01 (−1.35, −0.66)	−1.16 (−1.57, −0.75)	−0.59 (−0.89, −0.28)
	5.86, P_z < 0.00001	43.24, P_z < 0.00001	0.90, P_z = 0.37	7.07, P_z < 0.00001	39.02, P_z < 0.00001	12.16, P_z < 0.00001	5.55, P_z < 0.00001	3.57, P_z = 0.0002
FPG	P_h = 0.10, 37%	P_h < 0.00001, 100%	P_h = 0.0002, 93%	P_h < 0.00001, 97%	P_h < 0.00001, 96%	P_h < 0.00001, 87%	P_h = 0.03, 46%	P_h < 0.00001, 99%
	−1.04 (−1.25, −0.84)	−1.23 (−2.32, −0.15)	−1.21 (−3.03, 0.60)	−1.43 (−1.80, −1.06)	−1.28 (−1.58, −0.98)	−1.19 (−1.37, −1.00)	−1.10 (−1.37, −0.83)	−1.16 (−1.45, −0.87)
	10.10, P_z < 0.00001	2.23, P_z = 0.03	1.31, P_z = 0.19	7.52, P_z < 0.00001	8.38, P_z < 0.00001	12.62, P_z < 0.00001	7.94, P_z < 0.00001	7.74, P_z < 0.00001
2-h PBG	P_h = 0.05, 50%	P_h < 0.00001, 86%	P_h = 0.004, 88%	P_h < 0.00001, 99%	P_h < 0.0001, 80%	P_h < 0.00001, 97%	P_h < 0.0001, 69%	P_h < 0.00001, 99%
	−2.15 (−2.70, −1.59)	−1.59 (−1.85, −1.32)	−1.27 (−3.53, 0.99)	−2.12 (−3.35, −0.90)	−1.33 (−1.56, −1.10)	−1.91 (−2.42, −1.41)	−2.20 (−2.74, −1.66)	−1.57 (−2.04, −1.10)
	7.58, P_z < 0.00001	11.41, P_h < 0.00001	1.10, P_z = 0.27	3.40, P_z = 0.0007	11.37, P_z < 0.00001	7.42, P_z < 0.00001	7.97, P_z < 0.00001	6.51, P_z < 0.00001
TC	P_h < 0.00001, 87%	P_h < 0.0001, 87%	NA	P_h = 0.52, 0%	P_h = 0.0008, 86%	P_h < 0.00001, 92%	P_h < 0.0001, 81%	P_h < 0.00001, 94%
	−0.77 (−1.06, −0.48)	−0.10 (−0.44, 0.24)		0.23 (0.07, 0.40)	−0.03 (−0.41, 0.36)	−0.55 (−0.83, −0.27)	−0.71 (−1.00, −0.42)	0.09 (−0.24, 0.42)
	5.24, P_z < 0.00001	0.58, P_z = 0.56		2.78, P_z = 0.005	0.14, P_z = 0.89	3.82, P_z = 0.0001	4.78, P_z < 0.00001	0.54, P_z = 0.59
TG	P_h < 0.00001, 98%	P_h = 0.90, 0%	NA	P_h = 0.56, 0%	P_h = 0.18, 39%	P_h < 0.00001, 98%	P_h < 0.0001, 98%	P_h = 0.007, 79%
	−1.05 (−1.57, −0.52)	0.11 (−0.07, 0.30)		0.14 (−0.28, 0.56)	−0.03 (−0.31, 0.24)	−0.80 (−1.28, −0.32)	−0.89 (−1.54, −0.23)	−0.02 (−0.31, 0.28)
	3.98, P_z = 0.0001	1.21, P_z = 0.22		0.65, P_z = 0.52	0.24, P_z = 0.81	3.25, P_z = 0.001	2.64, P_z = 0.008	0.01, P_z = 0.92
LDL-C	P_h < 0.00001), 95%	P_h < 0.00001, 90%	NA	P_h = 0.51, 0%	P_h = 0.04, 64%	P_h < 0.00001, 95%	P_h < 0.00001, 93%	P_h = 0.04, 59%
	−0.27 (−0.56, 0.01)	−0.02 (−0.33, 0.29)		−0.00 (−0.14, 0.13)	0.00 (−0.21, 0.21)	−0.21 (−0.44, 0.02)	−0.34 (−0.65, 0.02)	0.13 (0.04, 0.22)
	1.87, P_z = 0.06	0.13, P_z = 0.90		0.05, P_z = 0.96	0.01, P_z = 0.99	1.79, P_z = 0.07	2.12, P_z = 0.03	2.71, P_z = 0.007
HDL-C	P_h < 0.00001, 91%	P_h = 0.01, 72%	NA	P_h = 0.63, 0%	P_h = 0.01, 74%	P_h < 0.00001, 91%	P_h < 0.00001, 92%	P_h = 0.03, 63%
	0.10 (−0.09, 0.28)	0.01 (−0.06, 0.08)		0.01 (−0.03, 0.05)	0.06 (−0.02, 0.14)	0.06 (−0.05, 0.17)	0.06 (−0.10, 0.22)	0.04 (0.00, 0.09)
	1.02, P_z = 0.31	0.31, P_z = 0.76		0.51, P_z = 0.61	1.48, P_z = 0.14	1.03, P_z = 0.30	0.72, P_z = 0.47	1.83, P_z = 0.07
SBP	NA	P_h < 0.00001, 96%	NA	P_h = 0.80, 0%	P_h = 0.41, 0%	P_h = 0.0002, 85%	P_h = 0.0006, 87%	P_h < 0.00001, 96%
		−0.11 (−0.27, 0.04)		3.04 (−0.19, 6.26)	0.52 (−0.30, 0.74)	−0.46 (−3.38, −2.46)	−0.14 (−6.61, 6.33)	0.39 (−0.70, 1.49)
		1.42, P_z = 0.16		1.85, P_z = 0.06	4.57, P_z < 0.00001	0.31, P_z = 0.76	0.04, P_z = 0.97	0.70, P_z = 0.48

(Continued on following page)

TABLE 3 (*Continued*) The results of subgroup analysis.

Index	Heterogeneity (P_h, I^2%); MD (95% CI); Z-test (Z-values, P_Z)							
	Intervention measure subgroup				Dosage subgroup		Treatment time subgroup	
	PEG-Loxe + CHD		PEG-Loxe					
	CHD	CHD + Placebo	CHD	Placebo	0.1 mg	0.2 mg	12 weeks	24 weeks
DBP	NA	P_h < 0.00001, 96%	NA	P_h = 0.82, 0%	P_h = 0.10, 57%	P_h = 0.001, 81%	P_h = 0.0009, 86%	P_h < 0.00001, 97%
		−0.79 (−0.90, −0.68)		2.72 (0.37, 5.07)	0.30 (−0.99, 1.59)	−0.68 (−2.32, 0.96)	0.54 (−3.68, 4.77)	−0.40 (−1.28, 0.48)
		14.13, P_z < 0.00001		2.27, P_z = 0.02	0.45, P_z = 0.65	0.81, P_z = 0.42	0.25, P_z = 0.80	0.90, P_z = 0.37
BMI	P_h = 0.002, 69%	P_h = 1.00, 0%	NA	NA	P_h = 0.06, 72%	P_h < 0.00001, 80%	P_h = 0.002, 69%	P_h < 0.00001, 91%
	−2.04 (−2.49, −1.58)	−0.10 (−0.66, 0.46)			−0.96 (−3.06, 1.15)	−1.82 (−2.32, −1.33)	−2.06 (−2.57, −1.56)	−0.68 (−1.93, 0.56)
	8.74, P_z < 0.00001	Z = 0.35, P_z = 0.72			0.89, P_z = 0.37	7.24, P_z < 0.00001	8.00, P_z < 0.00001	1.07, P_z = 0.28
BW	P_h = 0.03, 72%	P_h = 0.96, 0%	NA	P_h = 0.54, 0%	P_h = 0.93, 0%	P_h < 0.00001, 96%	P_h = 0.44, 0%	P_h < 0.00001, 96%
	−7.01 (−9.97, −4.04)	0.35 (−1.71, 2.40)		0.30 (−0.14, 0.73)	0.42 (−0.17, 1.02)	−2.71 (−4.97, −0.45)	−8.76 (−11.18, −6.34)	−0.86 (−3.12, 1.40)
	4.53, P_z < 0.00001	0.33, P_z = 0.74		1.35, P_z = 0.18	1.40, P_z = 0.16	2.35, P_z = 0.02	7.09, P_z < 0.00001	0.75, P_z = 0.45

P_h, *p*-values for heterogeneity of Q-test; MD, mean difference; CI, confidence interval; P_z, *p*-values for Z-test; $P_Z < 0.05$, shows a significant difference; PEG-Loxe, polyethylene glycol loxenatide; CHD, conventional hypoglycemic drugs; PEG-Loxe + CHD, polyethylene glycol loxenatide combined with conventional hypoglycemic drugs; CHD + Placebo, conventional hypoglycemic drugs combined with Placebo; HbA1c, glycosylated hemoglobin; FPG, fasting plasma glucose; 2-h PBG, 2-h postprandial blood glucose; TC, total cholesterol; TG, triglycerides; LDL-C, low-density lipoprotein cholesterol; HDL-C, high-density lipoprotein cholesterol; SBP, systolic blood pressure; DBP, diastolic blood pressure; BMI, body mass index; BW, body weight; NA, not available.

outcome assessment (detection bias), incomplete outcome data (attrition bias), and selective reporting (reporting bias), which are detailed described in the Cochrane Collaboration Risk-of-Bias Tool (Higgins et al., 2011). Information extracted from each study included the first author, year of publication, sample size, age range, intervention measures, duration, and outcomes.

2.4 Statistical analysis

RevMan 5.3 software was used for data analysis. Mean difference (MD) and 95% confidence intervals (CI) were used to represent continuous variables. $p < 0.05$ was considered statistically significant. The statistical heterogeneity was evaluated by Chi-square and I^2 tests. According to section-10–10-four to one of Cochrane Handbook for Systematic Reviews of Intervention, the confidence interval of estimate around the random effects was wider than the fixed effects when heterogeneity was present. Therefore, results of non-heterogeneous (I^2<50%) and heterogeneous (I^2>50%) were analyzed by fixed or random effects models for calculating the pooled effect, respectively (Cumpston et al., 2019). Subgroup analysis was performed based on different intervention measures, dosages and treatment time. The experimental group was divided into PEG-Loxe combined with conventional hypoglycemic drugs (PEG-Loxe + CHD) group and PEG-Loxe group, while the control group was divided into CHD group, CHD combined with placebo (CHD + Placebo) group and Placebo group. PEG-Loxe group was further divided into 0.1 mg and 0.2 mg subgroup. And treatment courses were divided into 12 and 24 weeks. In addition, sensitivity analysis was executed when statistically significant heterogeneity was observed (Patsopoulos et al., 2008; Ruppar, 2020).

3 Results

3.1 Study selection and characteristics

One hundred and fifty-nine relevant articles were retrieved, 59 articles were obtained after eliminating duplicate articles, 46 articles were screened after reading the titles and abstracts, and finally 18 articles (Chen et al., 2017; Yao et al., 2017; Gao et al., 2020; Li et al., 2021; Liang et al., 2021; Shuai et al., 2021; Wang and Zhao, 2021; Li K. et al., 2022; Li X. Y. et al., 2022; Tian et al., 2022; Yang, 2022; Zhao et al., 2022; Song et al., 2023; Wan et al., 2023; Zhang S. et al., 2023; Zhang Y. et al., 2023; Zhong, 2023; Zhou et al., 2023) were included after full-text reading, involving 2,166 patients in total (experimental group: 1,260 patients; control group: 906 patients). The literature search process is shown in Figure 1. Table 1 presents the basic information of these articles. The risk of bias assessments of the studies are showed in Figure 2.

10.3389/fphar.2024.1235639

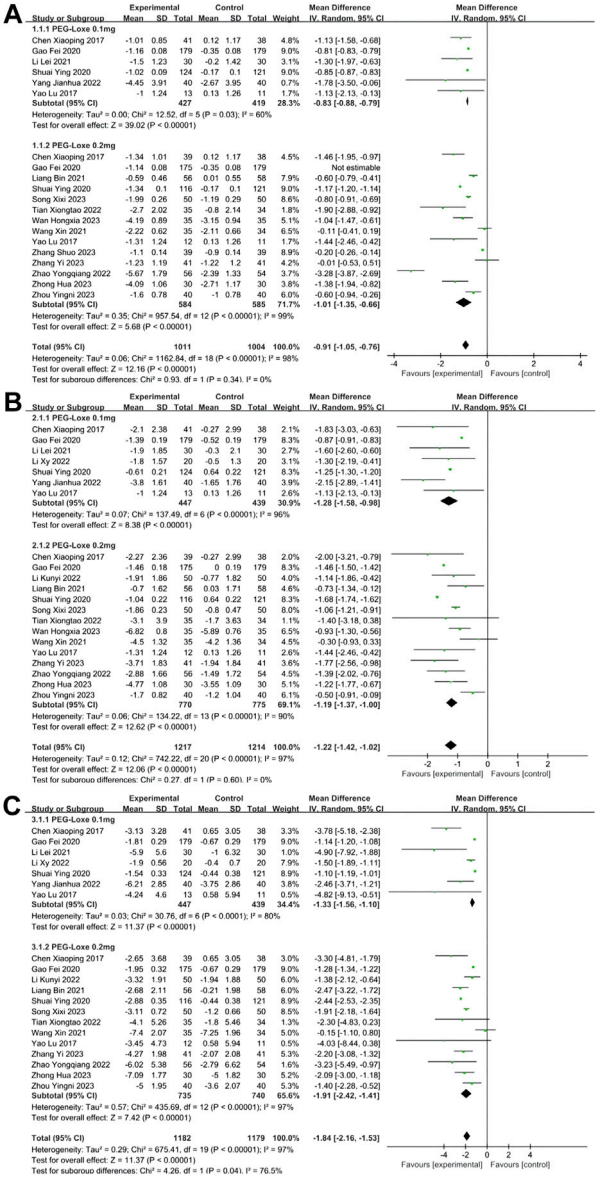

FIGURE 3
The forest plot of meta-analysis of blood glucose. **(A)** The forest plot of meta-analysis of HbA1c. **(B)** The forest plot of meta-analysis of FPG. **(C)** The forest plot of meta-analysis of 2-h PBG.

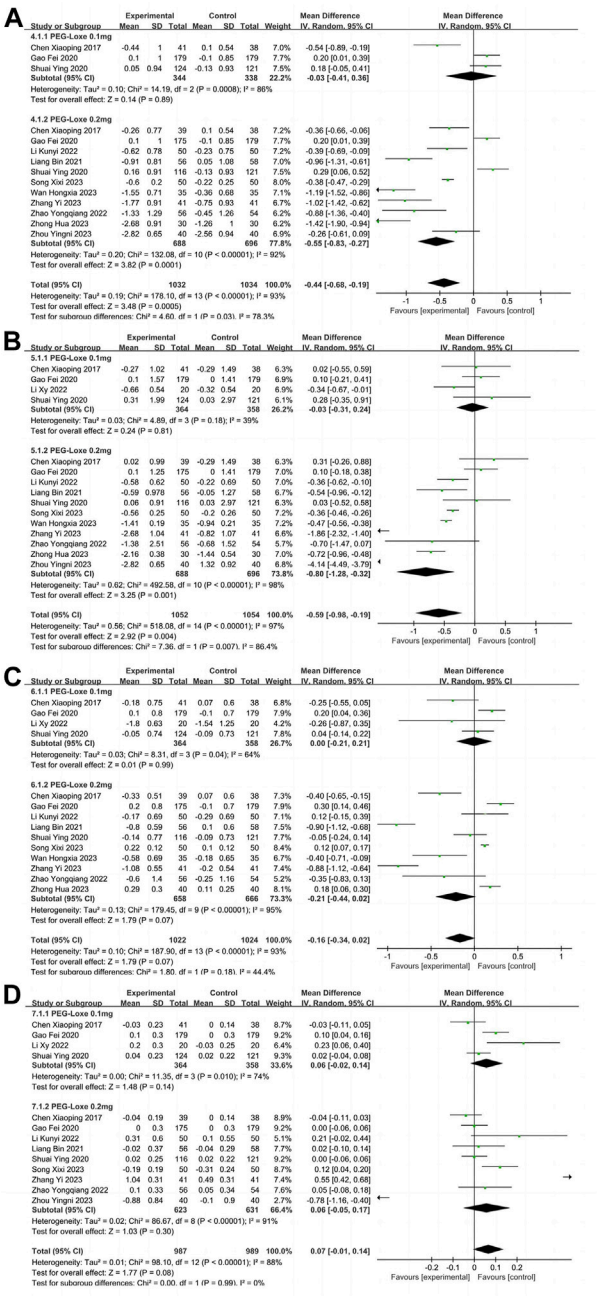

FIGURE 4
The forest plot of meta-analysis of blood lipid profiles. **(A)** The forest plot of meta-analysis of TC. **(B)** The forest plot of meta-analysis of TG. **(C)** The forest plot of meta-analysis of LDL-C. **(D)** The forest plot of meta-analysis of HDL-C.

3.2 The results of meta-analyses

The results of overall and subgroup analysis are present in Tables 2, 3, respectively.

3.2.1 Meta-analysis of BG: HbA1c; FPG; 2-h PBG

HbA1c was reported in 16 studies (Chen et al., 2017; Yao et al., 2017; Gao et al., 2020; Li et al., 2021; Liang et al., 2021; Shuai et al., 2021; Wang and Zhao, 2021; Tian et al., 2022; Yang, 2022; Zhao et al., 2022; Song et al., 2023; Wan et al., 2023; Zhang S. et al., 2023; Zhang Y. et al., 2023; Zhong, 2023; Zhou et al., 2023), whereas FPG and 2-h PBG were reported in 17 (Chen et al., 2017; Yao et al., 2017; Gao et al., 2020; Li et al., 2021; Liang et al., 2021; Shuai et al., 2021; Wang and Zhao, 2021; Li K. et al., 2022; Li X. Y. et al., 2022; Tian et al., 2022; Yang, 2022; Zhao et al., 2022; Song et al., 2023; Wan et al., 2023; Zhang S. et al., 2023; Zhong, 2023; Zhou et al., 2023) and 16 studies (Chen et al., 2017; Yao et al., 2017; Gao et al., 2020; Li et al., 2021; Liang et al., 2021; Shuai et al., 2021; Wang and Zhao, 2021; Li K. et al., 2022; Li X. Y. et al., 2022; Tian et al., 2022; Yang, 2022; Zhao et al., 2022; Song et al., 2023; Zhang Y. et al., 2023; Zhong, 2023; Zhou et al., 2023), respectively. Meta-analysis showed that PEG-Loxe significantly reduced the levels of HbA1c (MD = −0.91; 95% CI, −1.05 to −0.76; P_Z<0.00001; I^2 = 98%),

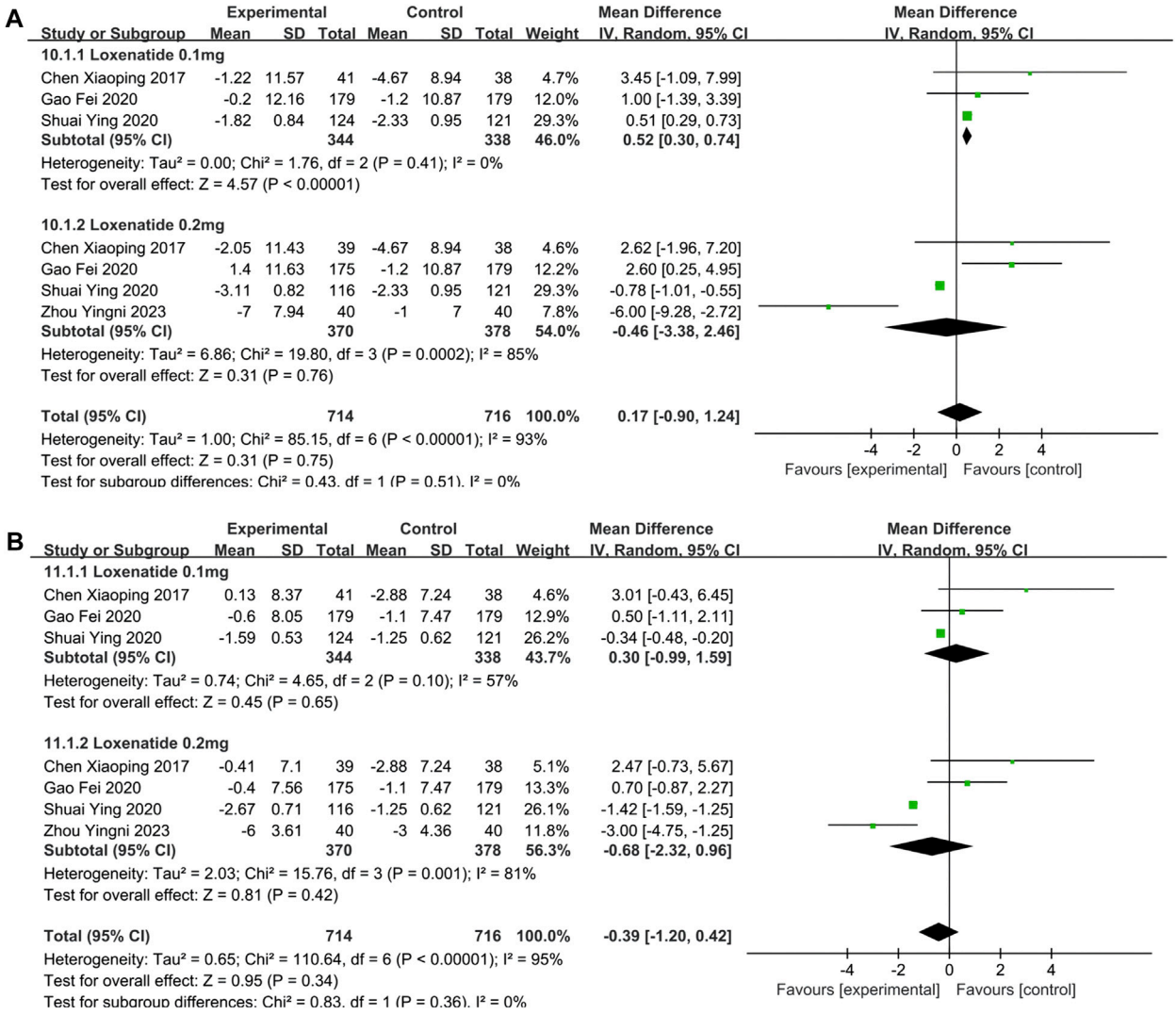

FIGURE 5
The forest plot of meta-analysis of SBP and DBP. **(A)** The forest plot of meta-analysis of SBP. **(B)** The forest plot of meta-analysis of DBP.

FPG (MD = −1.22; 95% CI, −1.42 to −1.02; P_Z<0.0001; I^2 = 97%) and 2-h PBG (MD = −1.84, 95% CI, −2.16 to −1.53; P_Z<0.00001; I^2 = 97%) in experimental group compared those in control group (Table 2). The forest plots of meta-analysis of HbA1c, FPG and 2-h PBG are showed in Figures 3A–C, respectively. Results obtained from subgroup analyses are shown in Table 3. In 0.2 mg subgroup, the decreased levels of HbA1c (MD = −1.01; 95% CI, −1.35 to −0.66; P_Z<0.00001; I^2 = 99%), FPG (MD = −1.19; 95% CI, −1.37 to −1.00; P_Z<0.00001; I^2 = 87%) and 2-h PBG (MD = −1.91; 95% CI, −2.42 to −1.41; P_Z<0.00001; I^2 = 97%) were more significant than the levels of HbA1c (MD = −0.83; 95% CI, −0.88 to −0.79; P_Z = 0.0001; I^2 = 60%), FPG (MD = −1.28; 95% CI, −1.58 to −0.98; P_Z<0.00001; I^2 = 96%) and 2-h PBG (MD = −1.33; 95% CI, −1.56 to −1.10; P_Z<0.0001; I^2 = 80%) in 0.1 mg subgroup. Subgroup analysis indicated that the HbA1c and 2-h PBG lowering effects in PEG-Loxe + CHD group were better than that in CHD group and CHD + Placebo group (P_Z≤0.05). The glucose-lowering effect in PEG-Loxe group was better than that in Placebo group (P_Z≤0.00001). Other results were not of statistical difference. In addition, subgroup analysis also showed that the high heterogeneity of HbA1c was caused by intervention measures and dosages, and heterogeneity of FPG was caused by intervention measures and treatment time, and heterogeneity of 2-h PBG was caused by intervention measures and treatment time.

3.2.2 Meta-analysis of BLP: TC; TG; LDL-C; HDL-C

TC, TG, LDL-C and HDL-C were reported in 11 (Chen et al., 2017; Gao et al., 2020; Liang et al., 2021; Shuai et al., 2021; Li K. et al., 2022; Zhao et al., 2022; Song et al., 2023; Wan et al., 2023; Zhang S. et al., 2023; Zhong, 2023; Zhou et al., 2023), 12, (Chen et al., 2017; Gao et al., 2020; Liang et al., 2021; Shuai et al., 2021; Li K. et al., 2022; Li X. Y. et al., 2022; Zhao et al., 2022; Song et al., 2023; Wan et al., 2023; Zhang Y. et al., 2023; Zhong, 2023; Zhou et al., 2023), 11 (Chen et al., 2017; Gao et al., 2020; Liang et al., 2021; Shuai et al., 2021; Li K. et al., 2022; Li X. Y. et al., 2022; Zhao et al., 2022; Song et al., 2023; Wan et al., 2023; Zhang S. et al., 2023; Zhou et al., 2023), and 10 (Chen et al., 2017; Gao et al., 2020; Liang et al., 2021; Shuai et al., 2021; Li K. et al., 2022; Li X. Y. et al., 2022; Zhao et al., 2022; Song

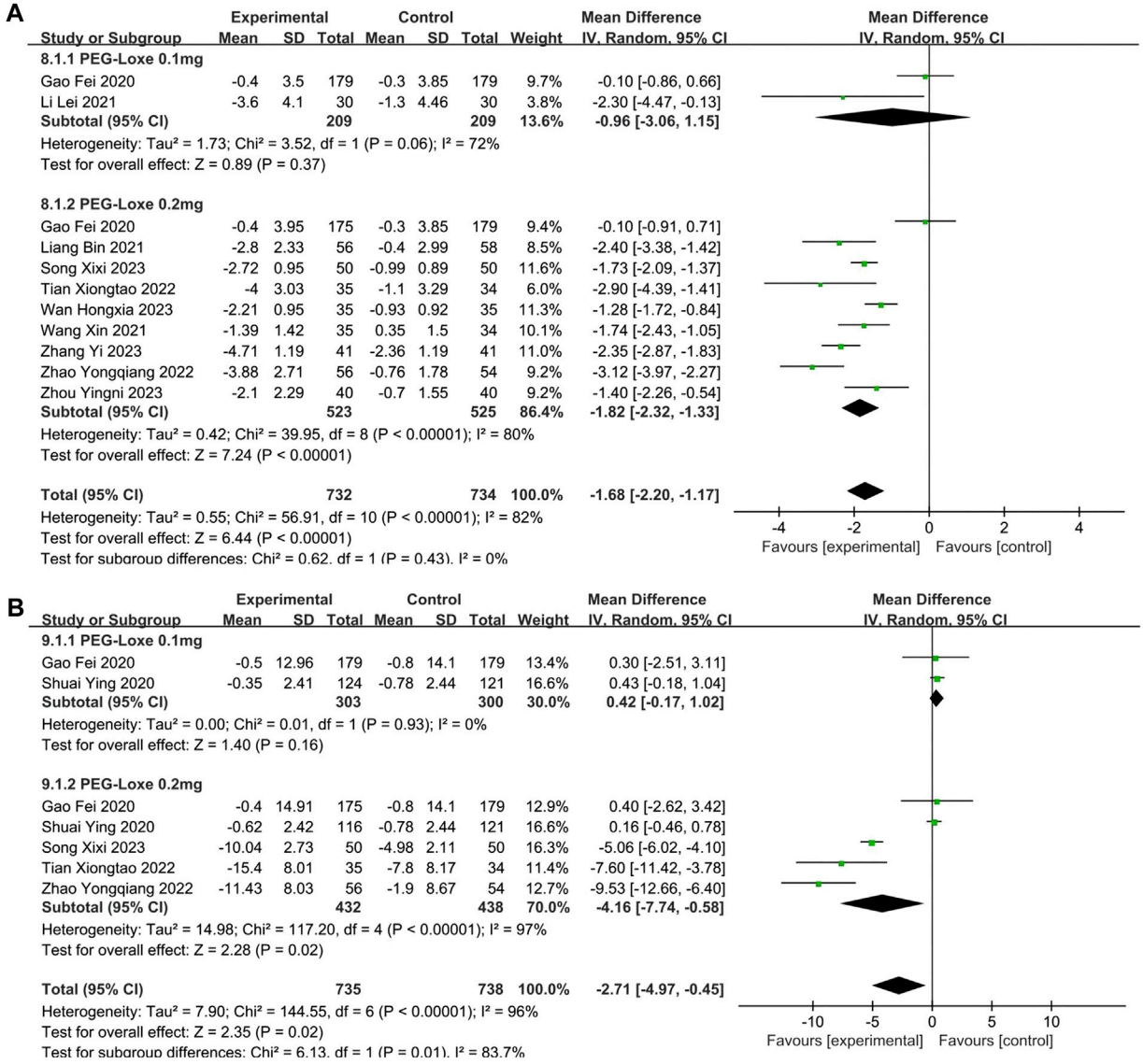

FIGURE 6
The forest plot of meta-analysis of BMI and BW. **(A)** The forest plot of meta-analysis of BMI. **(B)** The forest plot of meta-analysis of BW.

et al., 2023; Zhang Y. et al., 2023; Zhou et al., 2023) studies, respectively. In Table 2, the overall analysis of BLP showed that changes of TC (MD = −0.44; 95% CI, −0.68 to 0.19; $P_Z = 0.0005$; $I^2 = 93\%$), TG (MD = −0.59; 95% CI, −0.98 to 0.19; $P_Z = 0.004$; $I^2 = 97\%$), LDL-C (MD = −0.16; 95% CI, −0.34 to 0.02; $P_Z = 0.07$; $I^2 = 93\%$), and HDL-C (MD = 0.07; 95% CI, −0.01 to 0.14; $P_Z = 0.08$; $I^2 = 88\%$) in experimental group were not statistically significant compared with control group. The forest plot of meta-analysis of TC, TG, LDL-C, and HDL-C are shown in Figures 4A–D, respectively. Since the control group was treated with placebo or other CHD, the difference in BLP between the experimental and control groups might have been less significant than what would have been observed in control group with only placebo applied. In Table 3, Intervention measure subgroup analysis showed that the effect of reducing TC and TG of PEG-Loxe + CHD group were better than those in CHD group ($P_Z \leq 0.00001$), and the improvement effect of PEG Loxe on TC did not show any advantage compared with Placebo group ($P_Z = 0.005$). In 0.2 mg subgroup, the decreased levels of TC and TG were significant. Treatment time subgroup showed that the changes in TC at 12 weeks, LDL-C at 12 and 24 weeks were statistically significant. And other results were not of statistical difference. In addition, subgroup analysis also showed that the high heterogeneities of TC, LDL-C, and HDL-C were caused by the intervention measures, and the high heterogeneity of TG was caused by intervention measures and dosages.

3.2.3 Meta-analysis of BP: SBP and DBP

SBP and DBP were reported in 4 studies (Chen et al., 2017; Gao et al., 2020; Shuai et al., 2021; Zhou et al., 2023). In Table 2, the overall analysis of BP showed that changes of SBP (MD = 0.17; 95% CI, −0.90 to 1.24; $P_Z = 0.75$; $I^2 = 93\%$) and DBP (MD = −0.39; 95% CI, −1.20 to 0.42; $P_Z = 0.34$; $I^2 = 95\%$) in experimental group were not statistically significant compared with control group. The forest plot of meta-analysis of SBPand DBP are shown in Figures 5A, B,

respectively. In Table 3, intervention measure subgroup analysis showed that the effect of reducing DBP of PEG-Loxe + CHD group were better than those in CHD + Placebo group ($P_z < 0.00001$), and the improvement effect of PEG Loxe on DBP did not show any advantage compared with Placebo group ($P_Z = 0.02$). And other groups were not statistically different. In addition, subgroup analysis also showed that the high heterogeneities of SBP and DBP were caused by the intervention measures.

3.2.4 Meta-analysis of BMI and BW

The changes in BMI and BW were reported by 10 (Gao et al., 2020; Li et al., 2021; Liang et al., 2021; Wang and Zhao, 2021; Tian et al., 2022; Zhao et al., 2022; Song et al., 2023; Wan et al., 2023; Zhang S. et al., 2023; Zhou et al., 2023) and 5 (Gao et al., 2020; Shuai et al., 2021; Tian et al., 2022; Zhao et al., 2022; Song et al., 2023) studies, respectively. Significant reductions in BMI (MD = −1.68; 95% CI, −2.20 to −1.17; $P_Z < 0.00001$; $I^2 = 82\%$) and BW (MD = −2.71; 95% CI, −4.97 to −0.45; $P_Z = 0.02$; $I^2 = 96\%$) are shown in Table 2. The forest plot of meta-analysis of BMI and BW are shown in Figures 6A, B, respectively. In Table 3, subgroup analyses on intervention measures showed that the effect of reducing BMI and BW in PEG-Loxe + CHD group were better than that in CHD group ($P_Z < 0.0001$), 0.2 mg PEG-Loxe caused a statistically significant change in BMI ($P_Z < 0.00001$) and BW ($P_Z = 0.004$) in dosages subgroup. In treatment time subgroup, PEG-Loxe caused statistically significant changes in BMI and BW ($P_Z < 0.00001$) at 12 weeks, while other results were not of statistical difference. In addition, subgroup analysis also showed that the high heterogeneity of BMI was caused by intervention measures, and the high heterogeneity of BW was intervention measures, dosage and treatment time.

4 Sensitivity analysis

Sensitivity analysis was performed on the combined results of the indicators. The results of the meta-analysis were considered robust as there was no significant change in the combined effect size after removing a trial at a time.

5 Discussion

This is the first study to systematically assess the effects of PEG-Loxe on BG, BLP, BP, BMI, and BW. The overall results showed that PEG-Loxe was significantly effective in reducing HbA1c, FPG, 2-h PBG, BMI, and BW in patients with T2DM, but was not effective for improving TC, TG, HDL-C, LDL-C, SBP, and DBP. This suggested that PEG-Loxe might have a significant effect on lowering BG and reducing BW. We divided participants into subgroups based on different intervention measures, dosages, and treatment time. Then a comprehensive subgroup analysis was performed according to different variables to explain or explore the sources of heterogeneity. The above variables were identified as the source of high heterogeneity in the research results through subgroup analysis. In addition, the results of subgroup analysis showed that PEG-Loxe combined with CHD showed better effects in reducing HbA1c, FPG, 2-h PBG, TC, TG, BMI, and BW compared with CHD. And PEG-Loxe showed better hypoglycemic effects than placebo. In each subgroup, the heterogeneity of the results was greatly reduced.

Chronic hyperglycemia was the most typical pathologic manifestation of T2DM. Hyperglycemia increased the urine output of patients, which could lead to electrolyte disorders, hypertonic diuresis, and dehydration of the body (Fayfman et al., 2017; Sun et al., 2020). Also, hyperglycemia could cause diabetic nephropathy in patients with T2DM. The early symptoms of diabetic nephropathy are proteinuria and edema, while the late stage is renal failure that was the main cause of death in T2DM (Samsu, 2021). Hyperglycemia state could lead to excessive breakdown of fat and protein, and further secondary infections, such as boils of skin, wound infection, lung infection, and urinary tract infection (Nagendra et al., 2000). Long term of hyperglycemia has a toxic effect on the pancreatic islet beta-cells, and would accelerate the pancreatic islet beta-cells apoptosis and pancreatic islet failure, leading to gradual deterioration of the condition (Eizirik et al., 2020). In addition, long term hyperglycemia in diabetic patients would damage large vessels and micro-vessels, and sensory nerves and autonomic nerves, which would cause the occurrence and development of chronic complications such as cardiovascular and cerebrovascular diseases, diabetes nephropathy, retinopathy, peripheral neuropathy, diabetes foot gangrene (Jia et al., 2018; Eckel et al., 2021). Overweight and obesity are risk factors for cardiovascular disease, and it can affect cardiovascular health by influencing metabolic syndromes such as insulin resistance and dyslipidemia (Kachur et al., 2017; Che et al., 2018). Therefore, it could be concluded that control of BG and BW is important in the treatment of T2DM (Davies et al., 2022). The weight loss effect of PEG-Loxe may inhibit the development of T2DM patients to T2DM complicated with cardiovascular disease.

PEG-Loxe reduces HbA1c in a similar manner to other GLP-1RAs. More importantly, it is the only GLP-1RA that increases the therapeutic dosage without increasing the risk of hypoglycemia (Jiang et al., 2021). Therefore, PEG-Loxe has multiple therapeutic advantages. In terms of mechanism of action, PEG-Loxe improves beta-cells function and plays a hypoglycemic role by stimulating insulin secretion, inhibiting glucagon secretion, improving insulin resistance, and inhibiting hepatic glucose output by activating insulin phosphatidyl inositol 3-kinase/protein kinase B (PI3K/AKT) pathway (Rameshrad et al., 2020; Ard et al., 2021; Zeng et al., 2021; Zhang et al., 2021). Other studies have found that PEG-Loxe could regulate the expression of chemerin and omentin through its hypoglycemic effect (Li X. Y. et al., 2022). In addition, PEG-Loxe can delay gastric emptying and suppress patients' appetite, thereby reducing their food intake and ultimately reducing their weight (Drucker et al., 2017). And studies have reported that PEG-Loxe could regulating gut microbiota to protect vascular endothelial cell function in T2DM patients (Chen et al., 2022). Since there are few studies on the mechanism of PEG-Loxe, further studies are needed to prove its specific pharmacological mechanism.

There exist a couple of limitations in the research. Firstly, meta-analysis results showed some heterogeneity. We found that intervention measures, dosages and course of treatment were the causes of high heterogeneity by subgroup analysis. Secondly,

since the control group was treated with a placebo or other hypoglycemic agents, the difference of meta-analysis in BLP between the experimental and control groups might have been less significant than what would have been observed in the control group with only placebo applied. And in some studies, BLP were not the primary endpoint, so enrolled patients may not have dyslipidemia, which may be why no difference in BLP was observed. Thirdly, since PEG-Loxe is a novel drug, meta-analysis was limited by sample sizes and a short study period, and its long-term efficacy cannot be evaluated temporarily, longer duration of observation is need in further. Besides, PEG-Loxe is independently developed in China, and correspondingly 11 of the 18 studies included were published in Chinese journals, and the conclusions of the meta-analysis may be more applicable for East Asian. And SBP and DBP indicators were reported in 4 studies only, the results of its meta-analysis need to be viewed with caution. In the future, more high-quality, large-sample, multicenter RCTs of PEG-Loxe for T2DM should be performed.

In summary, PEG-Loxe is a promising drug in controlling BG and BW for patients with T2DM, and is worthy of promoting in clinical practice. In the future, more high-quality, large-sample, multicenter RCTs should be conducted to explore its impact on blood lipids further and provide a more rational basis and reference for treating T2DM clinically.

6 Conclusion

PEG-Loxe has better hypoglycemic effects compared with placebo in patients with T2DM, but could not significantly improved TC, TG, LDL-C, HDL-C, SBP, DBP and BW. And the combination of CHD and PEG-Loxe could more effectively improve the levels of HbA1c, FPG, 2-h PBG, TC, TG, BMI, and BW compared with CHD in T2DM patients.

Data availability statement

The original contributions presented in the study are included in the article/Supplementary Material, further inquiries can be directed to the corresponding authors.

Author contributions

SY and ZZ contributed to study conception and design. YL and WM contributed to analysis of data, literature review and preparation of the manuscript. SY, ZZ, YL, HF, ZZ, YY, YW, and WL contributed to revise the manuscript critically. All authors contributed to the article and approved the submitted version.

Funding

This work was supported by the National Natural Science Foundation of China (no. 82000788), Key Technology Research and Development Program of Shandong (no. 2018GSF118176), Basic and Applied Basic Research Foundation of Guangdong Province (no. 2019A1515110023), Postdoctoral Research Foundation of China (no. 2021M702040), and Natural Science Foundation of Shandong Province (no. ZR2016HQ26).

Conflict of interest

The authors declare that the research was conducted in the absence of any commercial or financial relationships that could be construed as a potential conflict of interest.

Publisher's note

Supplementary material

The Supplementary Material for this article can be found online at: https://www.frontiersin.org/articles/10.3389/fphar.2024.1235639/full#supplementary-material

References

Ahmad, E., Lim, S., Lamptey, R., Webb, D. R., and Davies, M. J. (2022). Type 2 diabetes. *Lancet* 400 (10365), 1803–1820. doi:10.1016/s0140-6736(22)01655-5

Ard, J., Fitch, A., Fruh, S., and Herman, L. (2021). Weight loss and maintenance related to the mechanism of action of glucagon-like peptide 1 receptor agonists. *Adv. Ther.* 38 (6), 2821–2839. doi:10.1007/s12325-021-01710-0

Chatterjee, S., Khunti, K., and Davies, M. J. (2017). Type 2 diabetes. *Lancet* 389 (10085), 2239–2251. doi:10.1016/s0140-6736(17)30058-2

Che, L., Xu, L., Huang, Y., and Yu, C. (2018). Clinical utility of the revised cardiac risk index in older Chinese patients with known coronary artery disease. *Clin. Interv. Aging* 13, 35–41. doi:10.2147/cia.s144832

Chen, F., He, L., Li, J., Yang, S., Zhang, B., Zhu, D., et al. (2022). Polyethylene glycol loxenatide injection (GLP-1) protects vascular endothelial cell function in middle-aged and elderly patients with type 2 diabetes by regulating gut microbiota. *Front. Mol. Biosci.* 9, 879294. doi:10.3389/fmolb.2022.879294

Chen, X., Lv, X., Yang, G., Lu, D., Piao, C., Zhang, X., et al. (2017). Polyethylene glycol loxenatide injections added to metformin effectively improve glycemic control and exhibit favorable safety in type 2 diabetic patients. *J. Diabetes* 9 (2), 158–167. doi:10.1111/1753-0407.12397

Cumpston, M., Li, T., Page, M. J., Chandler, J., Welch, V. A., Higgins, J. P., et al. (2019). Updated guidance for trusted systematic reviews: a new edition of the Cochrane Handbook for Systematic Reviews of Interventions. *Cochrane Database Syst. Rev.* 10, Ed000142. doi:10.1002/14651858.ed000142

Davies, M. J., Aroda, V. R., Collins, B. S., Gabbay, R. A., Green, J., Maruthur, N. M., et al. (2022). Management of hyperglycemia in type 2 diabetes, 2022. A consensus report by the American diabetes association (ada) and the European association for the study of diabetes (easd). *Diabetes Care* 45 (11), 2753–2786. doi:10.2337/dci22-0034

Drucker, D. J. (2018). Mechanisms of action and therapeutic application of glucagon-like peptide-1. *Cell Metab.* 27 (4), 740–756. doi:10.1016/j.cmet.2018.03.001

Drucker, D. J., Habener, J. F., and Holst, J. J. (2017). Discovery, characterization, and clinical development of the glucagon-like peptides. *J. Clin. Invest* 127 (12), 4217–4227. doi:10.1172/jci97233

Drucker, D. J., and Nauck, M. A. (2006). The incretin system: glucagon-like peptide-1 receptor agonists and dipeptidyl peptidase-4 inhibitors in type 2 diabetes. *Lancet* 368 (9548), 1696–1705. doi:10.1016/s0140-6736(06)69705-5

Eckel, R. H., Bornfeldt, K. E., and Goldberg, I. J. (2021). Cardiovascular disease in diabetes, beyond glucose. *Cell Metab.* 33 (8), 1519–1545. doi:10.1016/j.cmet.2021.07.001

Eizirik, D. L., Pasquali, L., and Cnop, M. (2020). Pancreatic β-cells in type 1 and type 2 diabetes mellitus: different pathways to failure. *Nat. Rev. Endocrinol.* 16 (7), 349–362. doi:10.1038/s41574-020-0355-7

Fayfman, M., Pasquel, F. J., and Umpierrez, G. E. (2017). Management of hyperglycemic crises: diabetic ketoacidosis and hyperglycemic hyperosmolar state. *Med. Clin. North Am.* 101 (3), 587–606. doi:10.1016/j.mcna.2016.12.011

Gao, F., Lv, X., Mo, Z., Ma, J., Zhang, Q., Yang, G., et al. (2020). Efficacy and safety of polyethylene glycol loxenatide as add-on to metformin in patients with type 2 diabetes: a multicentre, randomized, double-blind, placebo-controlled, phase 3b trial. *Diabetes Obes. Metab.* 22 (12), 2375–2383. doi:10.1111/dom.14163

Garber, A. J., Handelsman, Y., Grunberger, G., Einhorn, D., Abrahamson, M. J., Barzilay, J. I., et al. (2020). Consensus statement by the american association of clinical endocrinologists and american college of endocrinology on the comprehensive type 2 diabetes management algorithm - 2020 executive summary. *Endocr. Pract.* 26 (1), 107–139. doi:10.4158/cs-2019-0472

Higgins, J. P., Altman, D. G., Gøtzsche, P. C., Jüni, P., Moher, D., Oxman, A. D., et al. (2011). The Cochrane Collaboration's tool for assessing risk of bias in randomised trials. *Bmj* 343, d5928. doi:10.1136/bmj.d5928

Jia, G., Whaley-Connell, A., and Sowers, J. R. (2018). Diabetic cardiomyopathy: a hyperglycaemia- and insulin-resistance-induced heart disease. *Diabetologia* 61 (1), 21–28. doi:10.1007/s00125-017-4390-4

Jiang, Y., Liu, J., Chen, X., Yang, W., Jia, W., and Wu, J. (2021). Efficacy and safety of glucagon-like peptide 1 receptor agonists for the treatment of type 2 diabetes mellitus: a network meta-analysis. *Adv. Ther.* 38 (3), 1470–1482. doi:10.1007/s12325-021-01637-6

Kachur, S., Lavie, C. J., de Schutter, A., Milani, R. V., and Ventura, H. O. (2017). Obesity and cardiovascular diseases. *Minerva Med.* 108 (3), 212–228. doi:10.23736/s0026-4806.17.05022-4

Khan, R. M. M., Chua, Z. J. Y., Tan, J. C., Yang, Y., Liao, Z., and Zhao, Y. (2019). From pre-diabetes to diabetes: diagnosis, treatments and translational research. *Med. Kaunas.* 55 (9), 546. doi:10.3390/medicina55090546

Li, K., Li, Z., and Li, G. (2022). Effects of loxenatide combined with metformin on metabolic markers in obese patients with type 2 diabetes [in Chinese]. *J. Med. Theory Pract.* 35 (05), 772–774. doi:10.19381/j.issn.1001-7585.2022.05.017

Li, L., Wang, F., Li, M., and Jiang, S. (2021). A randomized controlled trial Polyethylene Glycol Loxenatide Injection for patients with type 2 diabetes mellitus [in Chinese]. *China Med. Her.* 18 (18), 68–71.

Li, X. Y., Li, C. P., Zhang, C. Y., Zhang, S., Chen, J. X., Zhu, D., et al. (2022). Effect of polyethylene Glycol Loxenatide (long-acting GLP-1RA) on lipid, glucose levels and weight in type 2 diabetes mellitus patients with obesity. *Eur. Rev. Med. Pharmacol. Sci.* 26 (21), 7996–8003. doi:10.26355/eurrev_202211_30153

Liang, B., Li, L., and Wei, D. (2021). Clinical efficacy of polyethylene glycol losenatide combined with metformin in patients with type 2 diabetes mellitus [in Chinese]. *J. North Sichuan Med. Coll.* 36 (02), 246–249.

Nagendra, L., Boro, H., and Mannar, V. (2000). in *Bacterial infections in diabetes-Endotext*. Editors K. R. Feingold, B. Anawalt, M. R. Blackman, A. Boyce, G. Chrousos, E. Corpas, et al. (South Dartmouth (MA): MDText.com, Inc).

Page, M. J., McKenzie, J. E., Bossuyt, P. M., Boutron, I., Hoffmann, T. C., Mulrow, C. D., et al. (2021). The PRISMA 2020 statement: an updated guideline for reporting systematic reviews. *Bmj* 372, n71. doi:10.1136/bmj.n71

Patsopoulos, N. A., Evangelou, E., and Ioannidis, J. P. (2008). Sensitivity of between-study heterogeneity in meta-analysis: proposed metrics and empirical evaluation. *Int. J. Epidemiol.* 37 (5), 1148–1157. doi:10.1093/ije/dyn065

Rameshrad, M., Razavi, B. M., Lalau, J. D., De Broe, M. E., and Hosseinzadeh, H. (2020). An overview of glucagon-like peptide-1 receptor agonists for the treatment of metabolic syndrome: a drug repositioning. *Iran. J. Basic Med. Sci.* 23 (5), 556–568. doi:10.22038/ijbms.2020.41638.9832

Ruppar, T. (2020). Meta-analysis: how to quantify and explain heterogeneity? *Eur. J. Cardiovasc Nurs.* 19 (7), 646–652. doi:10.1177/1474515120944014

Saeedi, P., Petersohn, I., Salpea, P., Malanda, B., Karuranga, S., Unwin, N., et al. (2019). Global and regional diabetes prevalence estimates for 2019 and projections for 2030 and 2045: results from the international diabetes federation diabetes atlas, 9th edition. *Diabetes Res. Clin. Pract.* 157, 107843. doi:10.1016/j.diabres.2019.107843

Samsu, N. (2021). Diabetic nephropathy: challenges in pathogenesis, diagnosis, and treatment. *Biomed. Res. Int.* 2021, 1497449. doi:10.1155/2021/1497449

Shuai, Y., Yang, G., Zhang, Q., Li, W., Luo, Y., Ma, J., et al. (2021). Efficacy and safety of polyethylene glycol loxenatide monotherapy in type 2 diabetes patients: a multicentre, randomized, double-blind, placebo-controlled phase 3a clinical trial. *Diabetes Obes. Metab.* 23 (1), 116–124. doi:10.1111/dom.14198

Song, X., Yao, M., Li, Z., Guo, S., Yin, F., and Li, R. (2023). Clinical efficacy of polyethylene glycol loxenatide in the treatment of obese or overweight patients with type 2 diabetes mellitus. *J. Coll. Physicians Surgeons–Pakistan JCPSP* 33 (12), 1390–1394. doi:10.29271/jcpsp.2023.12.1390

Sun, H., Saeedi, P., Karuranga, S., Pinkepank, M., Ogurtsova, K., Duncan, B. B., et al. (2022). IDF Diabetes Atlas: global, regional and country-level diabetes prevalence estimates for 2021 and projections for 2045. *Diabetes Res. Clin. Pract.* 183, 109119. doi:10.1016/j.diabres.2021.109119

Sun, Y., Roumelioti, M. E., Ganta, K., Glew, R. H., Gibb, J., Vigil, D., et al. (2020). Dialysis-associated hyperglycemia: manifestations and treatment. *Int. Urol. Nephrol.* 52 (3), 505–517. doi:10.1007/s11255-019-02373-1

Tian, X., Liu, L., and Liu, X. (2022). Efficacy and safety of polyethylene glycol loxenatide injection combined with metformin in obese patients with newly diagnosed type 2 diabetes [in Chinese]. *Chin. Remedies Clin.* 22 (03), 197–200.

Wan, H. X., Cao, H., Chen, W., Shen, D. Q., Wang, L. L., Su, X. H., et al. (2023). Effects of early combination of glucagon-like peptide-1 receptor agonist on blood glucose and pancreatic β -cell function in obese patients with newly diagnosed type 2 diabetes mellitus [in Chinese]. *Diabetes New World* 26 (11), 24–27+41. doi:10.16658/j.cnki.1672-4062.2023.11.024

Wang, X., and Zhao, Y. (2021). Observation on the clinical efficacy of polyethylene glycol loxenatide injection and insulin glargine in the treatment of type 2 diabetes mellitus [in Chinese]. *Chin. J. Mod. Drug Appl.* 15 (19), 156–159. doi:10.14164/j.cnki.cn11-5581/r.2021.19.059

Williams, R., Karuranga, S., Malanda, B., Saeedi, P., Basit, A., Besançon, S., et al. (2020). Global and regional estimates and projections of diabetes-related health expenditure: results from the International Diabetes Federation Diabetes Atlas, 9th edition. *Diabetes Res. Clin. Pract.* 162, 108072. doi:10.1016/j.diabres.2020.108072

Yang, G. R., Zhao, X. L., Jin, F., Shi, L. H., and Yang, J. K. (2015). Pharmacokinetics and pharmacodynamics of a polyethylene glycol (PEG)-conjugated GLP-receptor agonist once weekly in Chinese patients with type 2 diabetes. *J. Clin. Pharmacol.* 55 (2), 152–158. doi:10.1002/jcph.386

Yang, J. H. (2022). Analysis of the effect of polyethylene glycol loxenatide combined with long-acting insulin on blood glucose control in patients with type 2 diabetes mellitus [in Chinese]. *Diabetes New World* 25 (7), 71–74. doi:10.16658/j.cnki.1672-4062.2022.07.071

Yao, L., Wu, Y., Tian, G., Wang, X., and Zhang, F. (2017). Curative effect of polyethylene glycol loxenatide injection combined with metformin in patients with type 2 diabetes mellitus [in Chinese]. *Chin. J. Evidence-Bases Cardiovasc. Med.* 9 (05), 577–579.

Zeng, Q., Li, N., Pan, X. F., Chen, L., and Pan, A. (2021). Clinical management and treatment of obesity in China. *Lancet Diabetes Endocrinol.* 9 (6), 393–405. doi:10.1016/s2213-8587(21)00047-4

Zhang, S., Zhang, C., Chen, J., Deng, F., Wu, Z., Zhu, D., et al. (2023). Efficacy of polyethylene glycol loxenatide versus insulin glargine on glycemic control in patients with type 2 diabetes: a randomized, open-label, parallel-group trial. *Front. Pharmacol.* 14, 1171399. doi:10.3389/fphar.2023.1171399

Zhang, Y., Li, Y., Zhao, J., Wang, C., Deng, B., Zhang, Q., et al. (2021). Protective effects and mechanisms of polyethylene glycol loxenatide against hyperglycemia and liver injury in db/db diabetic mice. *Front. Pharmacol.* 12, 781856. doi:10.3389/fphar.2021.781856

Zhang, Y., Liu, Y. N., and Cheng, Y. J. (2023). Effect of polyethylene glycol losenatide injection combined with metformin on primary diagnosis of obese type 2 diabetes mellitus [in Chinese]. *Diabetes New World* 26 (09), 95–98. doi:10.16658/j.cnki.1672-4062.2023.09.095

Zhao, Y., Qin, X., and Tian, D. (2022). Effect of polyethylene glycol losenatide injection combined with metformin in the treatment of obese type 2 diabetes mellitus and its effect on serum antioxidant factors and inflammatory factors [in Chinese]. *Chin. J. Drug Abuse Prev. Treat.* 28 (01), 77–81. doi:10.15900/j.cnki.zylf1995.2022.01.017

Zheng, Y., Ley, S. H., and Hu, F. B. (2018). Global aetiology and epidemiology of type 2 diabetes mellitus and its complications. *Nat. Rev. Endocrinol.* 14 (2), 88–98. doi:10.1038/nrendo.2017.151

Zhong, H. (2023). Effects of Polyethylene glycol loxenatide combined with insulin glargine in treatment of patients with type 2 diabetes [in Chinese]. *Med. J. Chin. People's Health* 35 (23), 64–66+70.

Zhou, Y. N., Shi, M., Lai, J. B., Li, X. M., and Liu, X. Y. (2023). Efficacy of PEX168 combined with metformin in newly diagnosed obese patients with type 2 diabetes mellitus [in Chinese]. *J. Pract. Med.* 39 (2), 170–174. doi:10.3969/j.issn.1006-5725.2023.02.008

Frontiers in Pharmacology

Explores the interactions between chemicals and living beings

The most cited journal in its field, which advances access to pharmacological discoveries to prevent and treat human disease.

Discover the latest Research Topics

See more →

Frontiers

Avenue du Tribunal-Fédéral 34
1005 Lausanne, Switzerland
frontiersin.org

Contact us

+41 (0)21 510 17 00
frontiersin.org/about/contact